Carbon NanoTubes (CNTs) for the development of high-performance and smart composites

Abstract

Carbon NanoTubes (CNTs) have drawn enormous attention in recent years due to their outstanding multifunctional properties. In particular, the addition of CNTs as nanofillers for the development of new composite materials not only enhances the mechanical properties of the pristine material, but also confers new piezoresistive properties. In this way, the appearance of external loadings can be correlated to measurable variations of the electrical properties of the composite or, in other words, the material turns into a self-sensing composite. This multifunctional feature is in line with the new paradigm of Structural Health Monitoring (SHM) that advocates the use of smart materials/structures to solve the scalability issue on full-scale civil engineering structures. Despite a considerable number of works can be found in the literature on the experimental characterization or development of pilot applications of these composites, there exists a gap on the theoretical modeling of their behavior that needs to be addressed.

All the efforts of this thesis have focused on the modeling of the mechanical, piezoresistive and electromechanical properties of CNT-reinforced composites for the development of high-strength and smart structures. In particular, the developed approaches have been formulated on the basis of the mean-field homogenization theory. The major physically meaningful mechanisms that underlie the electrical transport of these composites, namely electron hopping and conductive networking, have been distinguished within a percolative-type framework. The theoretical formulation also copes with the effect of arbitrary three-dimensional strain states on the overall electrical conductivity. The developed formulation has been shown suitable to be included in a multiphysics 3D finite element code. Finally, a novel piezoresistive/piezoelectric equivalent circuit has been proposed for the analysis of the electromechanical response of CNT-reinforced cement-based materials in the time domain. The effectiveness and accuracy of the proposed approaches have been verified by different experiments under laboratory conditions.

Ph.D. Thesis **Enrique García Macías**

Carbon NanoTubes (CNTs) for the development of high-performance and smart composites

Ph.D. Enrique García Macías 2017/2018

Tesis Doctoral
Ph.D. Thesis

Carbon NanoTubes (CNTs) for the development of high-performance and smart composites

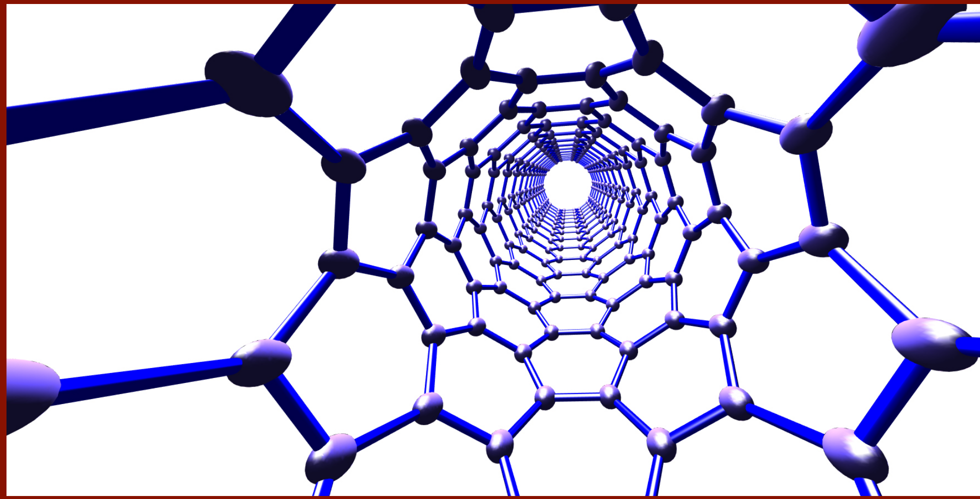

Autor: Enrique García Macías
Director: Andrés Sáez Pérez
Co-director: Rafael Castro Triguero

Department of Continuum Mechanics
and Structural Analysis
School of Engineering
Universidad de Sevilla

Sevilla, 2017-2018

Tesis Doctoral
Ph.D. Thesis

Carbon NanoTubes (CNTs) for the development of high-performance and smart composites

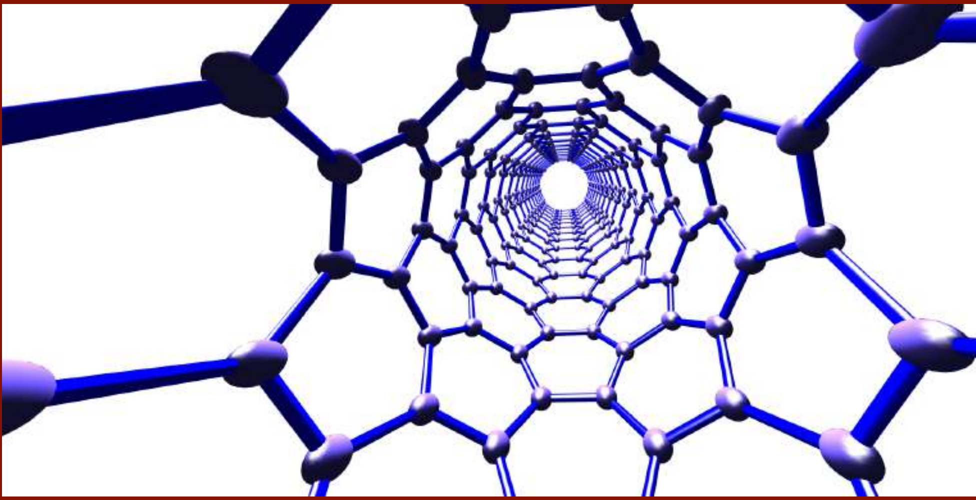

Autor: Enrique García Macías
Director: Andrés Sáez Pérez
Co-director: Rafael Castro Triguero

Department of Continuum Mechanics
and Structural Analysis
School of Engineering
Universidad de Sevilla

Sevilla, 2017-2018

Tesis Doctoral
Ph.D. Thesis

Carbon NanoTubes (CNTs) for the development of high-performance and smart composites

Autor:
Enrique García Macías

Director:
Andrés Sáez Pérez
Catedrático de Universidad
Universidad de Sevilla

Co-director:
Rafael Castro Triguero
Profesor Contratado Doctor
Universidad de Córdoba

Department of Continuum Mechanics
and Structural Analysis
School of Engineering
Universidad de Sevilla

2017-2018

Tesis Doctoral: Carbon NanoTubes (CNTs) for the development of high-performance and smart composites

Autor: Enrique García Macías

Director: Andrés Sáez Pérez. Co-director: Rafael Castro Triguero

El tribunal nombrado para juzgar la Tesis arriba indicada, compuesto por los siguientes doctores:

Presidente:

Vocales:

Secretario:

acuerdan otorgarle la calificación de:

El Secretario del Tribunal

Fecha:

Resumen

Los nanotubos de carbono han atraído una enorme atención en los últimos años debido a sus propiedades multifuncionales sobresalientes. Un número cada vez mayor de trabajos de investigación de primera línea centran su interés en la búsqueda de aplicaciones prácticas que den uso de las notables propiedades de los nanotubos de carbono, incluyendo una elevada resistencia mecánica, propiedades piezorestivas, alta conductividad eléctrica, ligereza, excelente estabilidad química y térmica. En concreto, los estudios más recientes plantean dos grandes ramas de aplicación: fabricación de estructuras aligeradas de alta resistencia, y desarrollo de estructuras inteligentes. Con respecto a la primera línea de aplicación, el desarrollo de materiales compuestos ligeros de alta resistencia conecta con la creciente tendencia de la ingeniería estructural a incorporar materiales compuestos innovadores. Ejemplos recientes como el avión comercial Boeing 787, en el que la mitad del peso fue diseñado con materiales compuestos, predicen un futuro auspicioso para los nanotubos de carbono en la ingeniería aeronáutica. Sin embargo, aún resulta más interesante el comportamiento piezorresistivo de los compuestos reforzados con nanotubos de carbono, ya que posibilita la creación de estructuras que no sólo presentan altas capacidades portantes y reducido peso específico, sino que también ofrecen capacidades de auto-detección de deformaciones. Cuando el material se ve sometido a una deformación externa, en virtud de dicha propiedad piezoresistiva, la conductividad eléctrica varía de modo que es posible correlacionar su respuesta eléctrica con el campo deformacional aplicado. Estas propiedades multifuncionales entroncan con el nuevo paradigma de la Vigilancia de la Salud Estructural el cual aboga por el uso de materiales/estructuras inteligentes para resolver el problema de escalabilidad. En este contexto, la estructura o parte de ella presenta capacidades de auto-detección de tal manera que el mantenimiento basado en la condición puede llevarse a cabo sin necesidad de incluir sensores externos. En ambas líneas, la mayoría de las investigaciones han centrado el estudio en la experimentación, siendo mucho menor el número de trabajos que plantean modelos teóricos capaces de simular las propiedades mecánicas, eléctricas y electromecánicas de estos compuestos.

Desde un punto de vista mecánico, existen estudios experimentales que informan acerca de los efectos perjudiciales sobre la respuesta macroscópica de aspectos micromecánicos tales como la tendencia a formar aglomerados, así como la curvatura de los nanotubos de carbono. Es por ello esencial desarrollar modelos teóricos que incorporen estos efectos y asistan al diseño de elementos estructurales reforzados con nanotubos de carbono. Respecto al estudio de las propiedades de conductividad y piezoresistividad, es esencial desarrollar formulaciones teóricas capaces de abordar la optimización de las propiedades de autodetección de deformaciones. Asimismo, es crucial comprender los diferentes mecanismos físicos que rigen la conductividad eléctrica de estos compuestos, de modo que sea posible incorporar su efecto diferencial dentro de un marco teórico. Por último, también es fundamental avanzar hacia el dominio del tiempo con el fin de desarrollar aplicaciones de vigilancia de la salud estructural basada en vibraciones.

Con todo ello, los esfuerzos de esta tesis se han centrado en el modelado de las propiedades mecánicas, conductivas y electromecánicas de los compuestos reforzados con nanotubos de carbono para el desarrollo de estructuras inteligentes y de alta resistencia. Estas dos aplicaciones, a saber, compuestos de alta resistencia e inteligentes, han sido enmarcadas en el ámbito de los materiales poliméricos y de cemento, respectivamente. La razón de esta distinción se debe a la presunción de que los compuestos poliméricos pueden encontrar aplicaciones directas como paneles de fuselaje para estructuras de aeronaves, así como refuerzos mecánicos sobre estructuras pre-existentes. En cuanto al uso de nanotubos de carbono como inclusiones multifuncionales para compuestos inteligentes, tanto los materiales poliméricos como los de base cemento ofrecen una amplia gama de aplicaciones potenciales. Sin embargo, la similitud entre los compuestos de base cemento y el hormigón estructural convencional sugiere la idea de desarrollar sensores embebidos que ofrezcan una monitorización continua integrada sin comprometer a priori la durabilidad de la estructura huésped. Tanto las propiedades mecánicas como las conductivas han sido estudiadas mediante métodos de homogeneización de campo medio. Aspectos micromecánicos tales como la relación de aspecto, el contenido, la distribución de la orientación, la ondulación o la aglomeración de los nanotubos se han estudiado en detalle e incorporado al análisis de diferentes elementos estructurales. De manera similar, se han estudiado las propiedades de conductividad eléctrica y auto-detección de deformaciones bajo cargas cuasi-estáticas mediante modelos mixtos de homogenización micromecánica de Mori-Tanaka. Los principales mecanismos que gobiernan las propiedades de transporte eléctrico de estos compuestos, a saber, los efectos de túnel cuántico y la formación de canales conductores, se han incorporado por separado en las simulaciones a través de la teoría de percolación de fibras conductoras. Los resultados teóricos han sido validados con éxito mediante experimentos en condiciones de laboratorio. Finalmente, se ha desarrollado un nuevo circuito equivalente piezorresistivo/piezoeléctrico para el modelado electromecánico de materiales de base cemento reforzado con nanotubos de carbono en el dominio del tiempo. Con los experimentos como base de validación, se ha demostrado que el enfoque propuesto proporciona resultados precisos y ofrece un marco teórico apto para aplicaciones de procesamiento de señales y monitorización de la salud estructural.

Se espera que el trabajo desarrollado en esta tesis pueda proporcionar herramientas valiosas que permitan profundizar en la comprensión de los principales aspectos físicos que controlan las propiedades mecánicas, eléctricas y electromecánicas de los compuestos reforzados con nanotubos de carbono. Además, se espera que los resultados presentados en esta tesis impulsen el desarrollo de materiales compuestos auto-sensibles embebidos para aplicaciones de vigilancia de la salud estructural.

Keywords: *Aglomeración, Nanotubo de carbono, Compuestos de base cemento, Material funcionalmente gradado, Micromecánica, Piezoresistividad, Compuesto polimérico, Material auto-sensible, Hormigón inteligente, Monitorización de la saludo estructural, Curvatura*

Abstract

Carbon nanotubes have drawn enormous attention in recent years due to their outstanding multifunctional properties. A constantly growing number of works at the front line of research pursue potential applications of their remarkable physical properties, including elevated load-bearing capacity, piezoresistive properties, high electrical conductivity, lightness, and excellent chemical and thermal stability. In particular, most recent works contemplate two different application branches: manufacture of light-weight high-strength structures, and development of smart structures. With regard to the first line of application, the development of high-strength lightweight composites connects with the growing tendency of structural engineering to incorporate advanced composite materials. Recent noticeable examples such as the commercial aircraft Boeing 787, in which half of the total weight was designed with composite materials, predict an auspicious future for carbon nanotubes in aircraft structures. Nonetheless, what is even more interesting is the piezoresistive behavior of carbon nanotube-reinforced composites, which allows us to create structures that are not only high-strength and lightweight but also strain-sensitive. When the composites are subjected to external strain fields, in virtue of such piezoresistive properties, the overall electrical conductivity varies in such a way that it is possible to correlate the electrical response with the deformational state of the material. These multifunctional properties are in line with the new paradigm of Structural Health Monitoring which advocates the use of smart materials/structures to solve the scalability issue. In this context, the structure or part of it presents self-sensing capabilities in such a way that the condition-based maintenance can be conducted without necessitating external off-the-shelf sensors. In both lines, most investigations have focused on experimentation. Conversely, the number of theoretical models capable of simulating the mechanical, electrical, and electromechanical properties of these composites is still scarce.

From a mechanical point of view, experiments have reported about the detrimental effects of micromechanical aspects such as agglomeration of fillers and curviness on the macroscopic properties. Hence, it is essential to develop theoretical models that allow us to include these effects and assist the design of composite structural elements. With regard to the study of the conductivity and piezoresistivity of carbon nanotube-reinforced composites, it is essential to develop theoretical formulations capable of tackling the optimization of their strain sensitivity. In addition, it is crucial to understand the different physical mechanisms that govern the electrical conductivity of these composites and include them separately in the theoretical framework. Finally, it is also fundamental to move towards the time domain in order to develop applications for vibration-based structural health monitoring.

Overall, all the efforts of this thesis have been put into the modeling of the mechanical, conductive and electromechanical properties of carbon nanotube-reinforced composites for the development of high-strength and smart structures. These two applications, namely high-strength and smart composites, have been framed in the realm of polymeric and cement-based materials, respectively. The reason for this distinction is the idea that polymer composites with high load-bearing capacity can find direct applications as fuselage panels for aircraft structures, as well as mechanical reinforcements attached to pre-existing structures. With regard to the use of carbon nanotubes as fillers for smart composites, both polymer and cement-based materials offer an enormous range of potential applications. Nonetheless, the similarity between cement-based composites and regular structural concrete suggests the idea of developing continuous embedded monitoring systems without compromising the durability of the hosting structure a priori. Both mechanical and conductive properties have been studied by means of mean-field homogenization methods. Micromechanical aspects such as filler aspect ratio, content, orientation distribution, waviness or agglomeration have been studied in detail and incorporated to the analysis of different structural elements. Similarly, the electrical conductivity and strain-sensing properties of these composites under quasi-static loadings have been studied by means of mixed Mori-Tanaka micromechanics models. The main mechanisms that underlie the electrical conduction of these composites, namely quantum tunneling effects and conductive networks, have been distinguished by a percolative-type behavior. The theoretical results have been successfully validated by means of experiments under laboratory conditions. Finally, a novel piezoresistive/piezoelectric equivalent lumped circuit has been developed for the electromechanical modeling of carbon nanotube-reinforced cement-based materials in the time domain. With experiments as validating basis, the proposed approach has been shown to provide accurate results and offers a theoretical framework readily applicable to signal processing applications and structural health monitoring.

The work developed in this thesis is envisaged to provide valuable tools to further the understanding of the main physical aspects that control the mechanical, electrical and electromechanical properties of composites doped with carbon nanotubes. Furthermore, it is expected to boost the development of embedded self-sensing carbon nanotube-reinforced composites for structural health monitoring applications.

Keywords: *Agglomeration, Carbon nanotube, Cement-matrix composites, Functionally graded material, Micromechanics, Piezoresistivity, Polymer composite, Self-sensing material, Smart concrete, Structural Health Monitoring, Waviness*

Co-Authorship Statement

■ Refereed Journal Papers:

(A) **Title:** Static and free vibration analysis of functionally graded carbon nanotube reinforced skew plates.

Authors: **García-Macías, Enrique**, Castro-Triguero, Rafael, Flores, Erick I. Saavedra, Friswell, Michael I. and Gallego, Rafael.

Reference: Composite Structures 140 (2016) 473-490.

(B) **Title:** Metamodel-based approach for stochastic free vibration analysis of functionally graded carbon nanotube reinforced plates.

Authors: **García-Macías, Enrique**, Castro-Triguero, Rafael, Friswell, Michael I., Adhikari, Sondipon and Sáez, Andrés.

Reference: Composite Structures 152 (2016) 183-198.

(C) **Title:** Buckling analysis of functionally graded carbon nanotube-reinforced curved panels under axial compression and shear.

Authors: **García-Macías, Enrique**, Rodríguez-Tembleque, Luis, Castro-Triguero, Rafael and Sáez, Andrés.

Reference: Composites Part B: Engineering 108 (2017) 243-256.

(D) **Title:** Micromechanics modeling of the electrical conductivity of carbon nanotube cement-matrix composites.

Authors: **García-Macías, Enrique**, D’Alessandro, Antonella, Castro-Triguero, Rafael, Pérez-Mira, Domingo and Ubertini, Filippo.

Reference: Composites Part B: Engineering 108 (2017) 451-469.

(E) **Title:** Micromechanics modeling of the uniaxial strain-sensing property of carbon nanotube cement-matrix composites for SHM applications.

Authors: **García-Macías, Enrique**, D'Alessandro, Antonella, Castro-Triguero, Rafael, Pérez-Mira, Domingo and Ubertini, Filippo.

Reference: Composite Structures 163 (2017) 195-215.

(F) **Title:** Enhanced lumped circuit model for smart nanocomposite cement-based sensors under dynamic compressive loading conditions.

Authors: **García-Macías, Enrique**, Downey, Austin, D'Alessandro, Antonella, Castro-Triguero, Rafael, Laflamme, Simon and Ubertini, Filippo.

Reference: Sensors and Actuators A: Physical 260 (2017) 45-57.

(G) **Title:** Multi-scale model updating of a timber footbridge using experimental vibration data.

Authors: Castro-Triguero, Rafael, **García-Macías, Enrique**, Saavedra Flores, Erick, Friswell, Michael I. and Gallego, Rafael.

Reference: Engineering Computations 34.3 (2017) 754-780.

(H) **Title:** Eshelby-Mori-Tanaka approach for post-buckling analysis of axially compressed functionally graded CNT/polymer composite cylindrical panels.

Authors: **García-Macías, Enrique**, Rodríguez-Tembleque, Luis, Castro-Triguero, Rafael and Sáez, Andrés.

Reference: Composites Part B: Engineering 128 (2017) 208-224.

(I) **Title:** Bending and free vibration analysis of functionally graded graphene vs. carbon nanotube reinforced composite panels.

Authors: **García-Macías, Enrique**, Rodríguez-Tembleque, Luis and Sáez, Andrés.

Reference: Composite Structures 186 (2018) 123-138.

Refereed Journal Papers under review:

(J) **Title:** Coupled effect of CNT waviness and agglomeration: A case study of vibrational analysis of CNT/polymer skew plates.

Authors: **García-Macías, Enrique** and Castro-Triguero, Rafael.

Reference: Composite Structures. Submission date: 08-01-2018.

(K) **Title:** 3D modeling of piezoresistive carbon nanotube smart concrete.

Authors: **García-Macías, Enrique**, Castro-Triguero, Rafael, Sáez, Andrés and Ubertini, Filippo.

Reference: Computer Methods in Applied Mechanics and Engineering. Submission date: 03-11-2017.

International conference papers:

(A) **Title:** Uncertainty Analysis of Mechanical Behavior of Functionally Graded Carbon Nanotube Composite Materials.

Authors: **García-Macías, Enrique**, Castro-Triguero, Rafael, Friswell, Michael, Sáez, Andrés and Gallego, Rafael.

Reference: Model Validation and Uncertainty Quantification, 2016 Volume 3 (pp. 59-72) Springer International Publishing.

(B) **Title:** Two Metamodeling Techniques for Optimization of Carbon Nanotube Reinforced Composite Shells.

Authors: **García-Macías, Enrique**, Castro-Triguero, Rafael, Adhikari, Sondipon, Friswell, Michael and Sáez, Andrés.

Reference: 2nd International Conference on Mechanics of Composites (MECHCOMP 2016), Porto, Portugal, 11-14 July 2016.

(C) **Title:** Continuous and embedded solutions for SHM of concrete structures using changing electrical potential in self-sensing cement-based composites.

Authors: Austin Downey, **García-Macías, Enrique**, D'Alessandro, Antonella, Laflamme, Simon, Castro-Triguero, Rafael and Ubertini, Filippo.

Reference: SPIE, Nondestructive Characterization and Monitoring of Advanced Materials, Aerospace, and Civil Infrastructure 2017.

(D) **Title:** Free vibration analysis of graphene sheet- and carbon nanotube-reinforced polymer plates.

Authors: **García-Macías, Enrique**, Rodríguez-Tembleque, Luis and Sáez, Andrés.

Reference: 4th International Conference on Mechanical Models in Structural Engineering (CMMOST 2017), Madrid, Spain, 29 Nov-01 Dec 2017.

A mi familia
A mis profesores

Acknowledgments

First and foremost, I would like to express my sincere gratitude to my advisors Andrés Sáez and Rafael Castro. Being your Ph.D. student has been truly an honor and a rewarding experience. I am deeply indebted to Rafael Castro, who offered me the first research opportunity back in 2013 and guided my first steps in Science. I appreciate all your contributions of time, ideas, and, above all, your joy and enthusiasm that have been contagious all along. It has been also a great privilege to work under the supervision of Andrés Sáez, whose wealth of experience and insightful comments and suggestions have played an essential role in my research. During the toughest times of this thesis, you gave me the support and the freedom I needed to continue. I am also thankful for the excellent examples you both have provided me as successful scientists and committed professors.

I must also show my gratitude to the rest of the members of the group that have immensely contributed to my personal and professional growth at the University of Seville. Especially, I would like to thank Luis Rodríguez-Tembleque for his helpful advice and collaboration. It is also acknowledged the collaboration of Victor Compán and Federico Buroni. Thank you to my colleague Pablo Pachón for his collaboration and for demonstrating that there exist scientists with a huge sense of humor. Thanks to the strong willingness of my advisors to collaborate, I have enjoyed the unique opportunity to work with many excellent researchers from other universities. In particular, I praise the enormous amount of help and teaching by Felipe García and Germán Castillo from the University of Málaga, and Rafael Gallego from the University of Granada. Thank you to Javier Jiménez and David Bullejos from the University of Córdoba for your incredibly helpful discussions on electronics. My special gratitude goes to Alejandro E. Martínez, with whom I discovered my true passion for Science and Research. Other past group members that I have had the pleasure to work with or alongside are the graduate students Alberto Merino, Millán, Juan Navas and Andres Pérez, and my office mate Miguel Ángel Gómez. I cannot forget mentioning Germán Ayuso, who I met when he was just an undergraduate student and, to this day, he is doing an amazing Ph. D. at the University of Swansea. It is so relieving that there exist some other fools in the world fond of talking about finite element modeling and computing well into the night hours.

My sincere thanks also go to professor Michael Ian Friswell for his hospitality during my first research stay at the University of Swansea. I feel deeply honored to have had the chance to work with such a renowned group and to witness their cutting-edge research. I really appreciate his wise advice and unmatched eloquence, which were extraordinarily motivating during the first stages of my thesis. I also wish to thank some other members of the College of Engineering, including Sondipon Adhikari for his aid and collaboration on the uncertainty analysis of composite materials, and Rubén Sevilla for his discussions on surrogate modeling. Especially, I thank Antonio Gil for his invaluable discussions on finite element implementation, as well as his enthusiasm and dedication that were definitely a great source of inspiration.

A key milestone in my Ph. D. experience was undoubtedly my research stay at the University of Perugia. I express my deep gratitude and admiration to professor Filippo Ubertini, who kindly hosted me and offered his support and collaboration since the very beginning. All this experience was nothing short of amazing and I could not enumerate all the invaluable lessons I learned. Nevertheless, if I had to choose one motto for this period, I would say "fundamental research is important but keeping an eye on experimentation and hands-on application". I also express special appreciation to Antonella D'Alessandro who made the experimental specimens and conducted most of the experiments used in my thesis. Thank you to other co-workers, lab and office mates such as Andrea Meoni, Gabriele Comanducci, Nicola Cavalagli, Anna Laura Pisello, and Alban Kita. I would also like to acknowledge the group of Materials Science and Technology, especially to Marco Rallini, for the fabrication and inspection of the specimens used for the experimental validation of some of the developed homogenization models.

I also want to show my gratitude to other remarkable colleagues I have had the enormous luck to work with, such as Simon Laflamme and Austin Downey from the University of Iowa State, and Erick Saavedra and Carlos Guzmán from the University of Santiago.

I gratefully acknowledge the funding sources that made this Ph. D. thesis possible. I was funded by the Ministerio de Economía y Competitividad of Spain under the project DPI2014-53947-R, and I was honored with a FPU contract-fellowship from the Spanish Ministry of Education of Spain Ref: FPU13/04892. My work was also supported by the Corporación Tecnológica de Andalucía (CTA) and AZVI S.A.

Last but not the least, I would like to thank my beloved family: my parents and my brothers for their endless support throughout writing this thesis and my life. My time at Seville was made delightful in large part due to the many friends and fellows that I came across with along the way. I am thankful for all those memorable times spent with friends, especially for my "S.P. crew" and that million excuses to escape from the daily routine and just fool around, and for Bruno, whom I consider my best friend ever since I can remember and understands my sense of humor better than anyone. And most of all for my loving, kindhearted, encouraging, and patient Sabrina whose faithful support during all the toughest stages of this Ph.D. is so appreciated. Specially acknowledged is his thorough supervision of the artwork of my research articles or, as she rather saying, "those little colorful nanotubes". Thank you.

Enrique García Macías
Universidad de Sevilla
February 2018

Table of Contents

Notation

θ, γ, ψ	Euler angles
β	Polar angle
$\mathbf{g}$	Transformation matrix
$\mathbf{\Omega}$	Orientation Distribution Function (ODF)
$\mathbf{A}$	Concentration tensor
$\mathbf{A}^{dil}$	Dilute concentration tensor
$\mathbf{I}$	Identity tensor
$\mathbf{S}$	Eshelby’s tensor
f_r	Volume fraction of inclusions
f_m	Volume fraction of matrix
f_{CNT}	Volume fractions of CNTs
w_{CNT}	Mass content of CNTs with respect to mass of cement
$\mathbf{C}_f$	Constitutive tensor of inclusions
$\mathbf{C}_m$	Constitutive tensor of matrix
$\mathbf{C}^{MT}$	Overall Mori-Tanaka stiffness tensor
$\mathbf{C}^{SC}$	Overall Self-consistent stiffness tensor
$\mathbf{C}_V$	Voigt stiffness tensor
$\mathbf{C}_R$	Reuss stiffness tensor
$E_{\|\|}$	Longitudinal elastic modulus
$E_{\perp}$	Transverse elastic modulus
λ	Wave length
θ^w	Helical spiral angle
L^{wavy}	Length of helical curve
D_h	Diameter of helical curve
δ	Polar angle of helical curve
V_r	Total volume of CNTs
V	Total volume of RVE
$V_r^{bundles}$	Volume of CNTs agglomerated in bundles
V_r^m	Volume of CNTs dispersed in matrix

ξ, ζ	Agglomeration parameters
ρ^m	Density of matrix
ρ^{CNT}	Density of CNTs
ks	Transverse shear correction factor
r_c	Radius of CNTs
L_{C-C}	Length of carbon-carbon bonds
φ	Fiber orientation angle
$\bar{\lambda}$	Non-dimensional frequency parameter
$\bar{w}$	Non-dimensional central deflection
k_σ	Non-dimensional buckling load intensity factor
MSE	Mean square error
k	Power-law index
d_a	Average separation distance among CNTs
d_c	Critical separation distance among CNTs
f_c	Percolation threshold
R_{int}	Resistance to electron tunneling
σ_{int}	Electrical conductivity of interphase
V_o	Height of the tunneling potential barrier
m	Mass of an electron
e	Electric charge of an electron
$\hbar$	Reduced Planck's constant
A_c	Contact area of CNTs
L_{CNT}	Length of CNTs
D_{CNT}	Diameter of CNTs
σ_c	Electrical conductivity of CNTs
σ_m	Electrical conductivity of matrix
f_{eff}	Volume fraction of effective solid fillers
$\tilde{\sigma}^L$	Longitudinal electrical conductivity of effective solid filler
$\tilde{\sigma}^T$	Transverse electrical conductivity of effective solid filler
$\boldsymbol{\sigma}_{cnt}$	Electrical conductivity tensor of effective filler
$\boldsymbol{\sigma}_m$	Electrical conductivity tensor of matrix
χ	Percentage of CNTs connected forming conductive networks
L^{str}	Length of equivalent straight filler
J	Electrical flux
A_r	Aspect ratio of CNTs
A_e	Aspect ratio of prolate bundles
$\boldsymbol{\sigma}_{N,EH}$	Electrical conductivity given by electron hopping mechanism
$\boldsymbol{\sigma}_{N,CN}$	Electrical conductivity given by conductive network mechanism
σ_{spc}	Equivalent conductivity accounting for electrodes
w_{cem}	Weight of cement
S_σ	Sensitivity coefficient
λ^-	Gauge factor under compressive stresses
λ^+	Gauge factor under tensile stresses

C_1	Constant of proportionality between strain and inter-particle distance
C_2	Constant of proportionality between strain and potential height
$\Delta R/R_o$	Relative change in electrical resistance
λ_C	Gauge factor based on the relative capacitance change
R_{ip}	Internal resistance
C_{ip}	Internal capacitance
R_{pm}	Interface resistance
C_{pm}	Interface capacitance
R_{ct}	Contact resistance
S_q	Piezoelectric parameter of CNT cement-based sensor
FRF	Frequency response function

1 Introduction

> *Saying that we should stop nanoscience is tantamount to saying we should stop science.*
>
> Harry Kroto

1.1 Motivation

Since their detailed structural characterization by Ijima [143] in 1991, Carbon NanoTubes (CNTs) have generated an enormous activity in many areas of science and engineering. Their unprecedented mechanical, thermal and electronic properties suggest that CNTs are ideal reinforcing fillers for the development of high-performance composite materials. Specifically, most attention has focused on two main potential applications, namely CNTs as mechanical reinforcements for lightweight and high-strength composites, and as smart fillers for self-sensing composites. Among all possible candidate matrix materials, polymer materials are particularly apt for the development of mechanical reinforcements for pre-existing structures, whilst cement-based materials are especially well-suited for developing embeddable sensors. On one hand, thanks to their excellent corrosion resistance, relatively low unit cost, and facile processing, polymers are extensively used in a diverse range of engineering applications. The development of CNT-reinforced polymer nanocomposites blends the excellent properties of polymers with the multi-functional properties of CNTs, what makes it possible to develop manifold applications such as high strength reinforcing coatings, conductive glue, gas storage devices, sensors, energy storage devices, light-weight aircraft applications, etc. On the other hand, a large portion of the worldwide civil infrastructures is constituted by concrete. The growing concern with the aging and structural degradation of civil infrastructures makes condition-based maintenance of the utmost importance for structural engineering. However, traditional monitoring systems require substantial costs and complex signal processing software, what discourages infrastructure owners due to low return on investments. The development of CNT-reinforced cement-based composites allows for conceiving continuous embedded strain-sensing systems, which would entail substantial improvements in the cost-effectiveness of SHM solutions for geometrically large systems. These composites exhibit strain-sensing capabilities (i.e. composites themselves also behave as sensors) by means of measurable variations of their electrical properties under applied mechanical deformations. Once embedded, CNT-reinforced cement-based materials form a mechanically strong bond with the monitored structure without substantially compromising its durability a priori. Thus, it is possible to create a continuously distributed set of strain sensors within the structure with limited maintenance.

1.2 State of the art review

Carbon Nanotubes (CNTs) are an allotrope of carbon consisting of rolled-up graphene sheets that form concentric cylinders. Depending on the number of layers, two different types of CNTs can be found, namely Single-Walled Carbon Nanotubes (SWCNTs), and Multiple-Walled Carbon Nanotubes (WMCNTs) [27, 359]. SWCNTs consist of a single graphene layer rolled seamlessly to form a cylinder with diameters ranging from 0.5 to 5 nm, and lengths of up to centimeters (see figure 1.1(a)). MWCNTs are defined as arrays of concentrically arranged graphene layers with sensibly larger diameters from several nanometers up to 200 nm, and lengths of ten of microns (see figure 1.1(b)). The question of who actually discovered CNTs is shrouded in great uncertainty, a fact that may explain why no Nobel Prizes have been yet awarded in this area [128]. A significant milestone was made by Oberlin and co-workers [234] in 1976 with one of the first images of a nanotube resembling a SWCNT, although this was not explicitly claimed by the authors. It was only after Ijima's report [143] in 1991 where the structure of CNTs was described in detail, when the global scientific attention was turned to these novel nanoparticles.

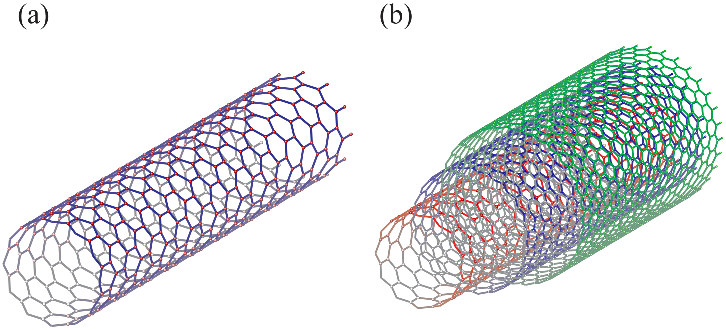

Figure 1.1 (a) Single-Walled Carbon NanoTube (CNT) and (b) Multi-Walled Carbon NanoTube (MWCNT).

The properties of CNTs depend upon the structure, morphology, diameter, and length of the tubes. The structure of CNTs is defined by their chirality, which is defined by a chiral vector, $\vec{C}_h$, and the chiral angle, θ, as represented in Fig.1.2. The chiral vector indicates the way in which a layer graphene is rolled-up to form a nanotube, and is defined as [98]:

$$\vec{C}_h = n\vec{a}_1 + m\vec{a}_2 \tag{1.1}$$

where the chiral integers (n,m) indicate the number of steps along the carbon bonds of the hexagonal lattice, $\vec{a}_1$ and $\vec{a}_2$ are the unit cell vectors of the two-dimensional lattice formed by the graphene sheet. Particular cases are found for $(n,0)$ and (n,n), or the so-called "zig-zag" and "armchair" structures (Figs. 1.2 (b) and (c)). The chirality of CNTs has a huge impact on their physical properties and, in particular, on their mechanical and electrical properties.

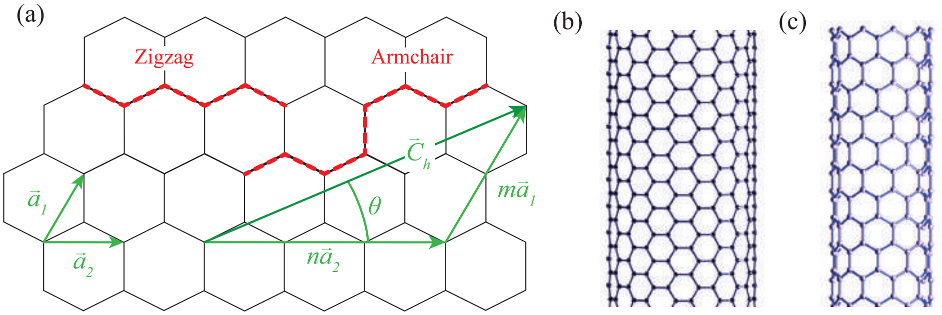

Figure 1.2 (a) Conventional rolled up model for CNTs (n,m) is formed by rolling a graphene sheet along the chiral vector $\vec{C}_h$. (b) Special cases of armchair tubes (n,n), and (b) zig-zag tubes $(n,0)$.

One of the most remarkable properties of CNTs is their exceptional mechanical properties due to their chemical bonding composed entirely of C-C covalent sp^2 bonds. Both experimental and theoretical investigations show extraordinary stiffness properties of individual CNTs with Young's moduli around 1 TPa [361], and ultimate tensile strengths of 100-200 GPa [355, 247, 178, 371, 71, 65]. These properties largely exceed those of any previously existing material and, thus, CNTs are considered the strongest material yet discovered by humankind. Particularly enlightening is the comparison with high-strength steel, whose Young's modulus is around 200 GPa, that is to say, one-fifth of the Young's modulus of CNTs. In addition, densities of CNTs can be as low as 1.3 g/cm^3, one-sixth of that of stainless steel. The elastic response of CNTs to deformation is also remarkable. CNTs can sustain up to 15% tensile strain before fracture [371, 197], and reversible bending up to angles of 100° [144]. All these features open up broad possibilities for the use of CNTs as lightweight, highly elastic, and very strong doping fillers for high-performance composite materials.

Despite the outstanding mechanical properties of CNTs, their unique electrical properties have received the greatest attention. Depending on the chirality, it has been theoretically proved that CNTs electrically behave as either a metal or a semiconductor material, similar to copper and silicon, respectively [213, 117, 308, 153]. SWCNTs are metallic if the chiral integers (n,m) are: $n=m$ (armchair CNTs) or $n-m=3i$, with i being an integer, whilst other structures lead to a semiconducting behavior [235]. The geometry of CNTs determines their electronic band structures and, therefore, the energy band gap. The energy band gap, E_g, of semiconducting CNTs is given by [190]:

$$E_g = \frac{\gamma_o L_{C-C}}{r_c} \tag{1.2}$$

where γ_o is the carbon-carbon (C-C) tight binding overlap energy (2.45 eV), L_{C-C} is the length of C-C bonds ($\approx$ 1.42 Å), and r_c is the radius of the nanotube. The electrical conductance of CNTs is given by [211]:

$$G = G_o M = \frac{2e^2}{\hbar} M \tag{1.3}$$

where $G_o = (2e^2)/\hbar = 1/12.9\ \mathrm{k}\Omega^{-1}$ is the quantum unit of the conductance, and e and $\hbar$ are the charge on one electron and Planck's constant, respectively [97, 153]. M is the apparent number of conducting channels including electron-electron and intertube coupling effects, as well as intrinsic channels. Ebbesen *et al.* [78] utilized a four-probe configuration by lithographic deposition of tungsten leads across individual MWCNTs, and reported values of electrical conductivities in the range of 10^7-10^8 S/m. The electronic properties of MWCNTs are defined by their multiple-shell structure, including the electrical properties of the tubes along with additional electronic couplings between the different shells. In addition, metallic CNTs are reported to exhibit ballistic electron transport at room temperature, that is to say, every electron injected into the nanotube at one end should come out the other end without heat dissipation [211]. In this case, the electrical resistance is not dependent upon the CNT length and Ohm's law does not apply [25, 248]. Furthermore, Wei *et al.* [342] reported that CNTs can carry current densities up to 109 A/cm^2, well above any other known material. In summary, all these exceptional electronic properties suggest the use of CNTs as electrically conductive fillers for smart composite materials.

1.2.1 Mechanical behavior of CNT-reinforced composites

The aforementioned unique mechanical properties of CNTs have spurred a considerable amount of research on the development of high-strength nanocomposites. The exceptional properties of CNTs, in combination with the relatively low cost and facile processing of polymers, open a large number of applications such as aircraft structures, tribological components, reinforcing coatings, wind turbine blades, sports equipment, etc. [57, 297, 217]. In virtue of the large disparity between the properties of CNTs and most matrix materials, an increasing number of publications report about the outstanding enhancements of the mechanical properties of composites doped with small concentrations of CNTs. For instance, Qian *et al.* [250] dispersed MWCNTs throughout polystyrene with a concentration of 1wt.%, reaching increases with respect to the pristine polymer in elastic modulus and break stress of 36-42% and ~25%, respectively. Andrews *et al.* [15] developed SWCNT-loaded isotropic petroleum pitch matrices. Those authors found that the tensile strength and elastic modulus with 5wt.% content of purified SWCNTs increased by about 90 and 150%, respectively. Biercuk *et al.* [28] reported monotonic increase in Vickers harness up to a factor of 3.5 by doping epoxy with 2wt.% of SWCNTs. A number of studies show that, after a critical CNT content in the matrix, the mechanical properties of CNT-polymer composites decrease with increasing CNT content and, even, these properties decrease below the neat matrix material [58, 168]. Chen *et al.* [48] produced polycarbonate/MWCNT nanocomposites and reported that a content of 1wt.% of CNTs yielded 4.5% increase in tensile strength with respect to the neat polymer. Higher filler contents resulted in a loss of fluidity and worse dispersion and, consequently, weakened mechanical properties. All these results evidence that filler dispersion holds a very crucial role in the preparation of CNT-reinforced composites.

Many efforts have been also devoted to the development of CNT-cement based composites. In this regard, an extensive review work was recently conducted by Siddique and Mehta [286]. It is worth noting the work by Chaipanich *et al.* [44] who investigated the compressive strength of fly ash cement mortars doped with 0.5 and 1wt.% of CNTs. Their results showed that the highest compressive strength at 28 days was found for samples with 1wt.% concentration of CNTs, reaching a mean value of 51.8 MPa that largely exceeded the reference strength of 47.2 MPa of neat mortars. SEM inspections by those authors revealed a good interaction between CNTs and the fly ash cement matrix, resulting in a denser microstructure. A similar work was done Morsy *et al.* [221] who analyzed the behavior of cementitious matrices doped with MWCNTs contents from 0 to 0.1wt.%. Their results displayed increasing compressive strengths with the CNTs content until an optimal amount of 0.02wt.%, followed by considerable reductions. The increases in cement mortar strength with CNTs loaded up to 0.02wt.% were ascribed to the cross-link of CNTs with the hydration products and, as a result, less formation of micro-cracks. At higher contents, on the contrary, CNTs tend to form agglomerates around the cement grains, leading to partial hydration and weak bonds between the hydrated products. Also, CNTs may not be properly wetted by cement, causing filler pullout and the appearance and propagation of micro-cracks. Konsta-Gdoutos and co-authors [166, 165] investigated the effect of the MWCNT aspect ratio on the mechanical properties of CNT-reinforced cement pastes. In agreement with other studies in the literature [294], it was concluded that the CNT aspect ratio critically determines the optimum filler concentration or, alternatively, the difficulty in obtaining good filler dispersions. Another noteworthy contribution was done by Abu Al-Rub *et al.* [1] who reported increases in the flexural strength of MWCNT/cement composites with respect to plain cement paste up to 269% with 0.2wt.% MWCNTs.

1.2.1.1 Functionally graded CNT-reinforced composites

Functionally graded materials (FGMs) belong to a branch of advanced materials characterized by spatially varying properties, such as gradation of the filler concentration or orientation as schematically illustrated in Fig. 1.3. This concept has promoted the development of a wide range of applications since its origin in 1984 (see e.g. [326]). Unlike laminated materials, FGMs exhibit smooth and continuous variations of their material properties and, therefore, prevent delamination and debonding failures caused by stress concentrations at the interfaces [105, 32, 156]. In the realm of CNT-reinforced composites, the idea of developing cost-efficient FG-CNT Reinforced Composites (FG-CNTRCs) has drawn an increasing attention in recent years. The high manufacturing cost of CNTs remains an important obstacle to the extensive manufacturing of these composites. Hence, the design of FG-CNTRCs would allow us to devise doping gradations of CNTs so that the overall stiffness is maximized with a minimum filler content. Inspired by this idea, Shen [279] proposed the use of non-uniform distributions of CNTs within an isotropic matrix. In that work, nonlinear vibration of FG-CNTRC plates in thermal environments was presented. Following this trace, researchers have employed many different methodologies to model FG-CNTRCs, most of which are collected in a recent review by Liew *et al.* [191]. A noteworthy contribution was done by Zhu *et al.* [390] who investigated the vibrational properties of FG-CNTRC plates by using a finite element model based, including homogenized mechanical properties by the Extended Rule of Mixtures (EROM). Ke *et al.* [155] conducted nonlinear free vibration analysis of FG-CNTRC Timoshenko beams and a Ritz method solved by a direct iterative technique. Their numerical results showed that symmetrical distributions of CNTs across the thickness with maximum concentrations at the bottom and the top of the beams lead to stiffer structures. Shen and Zhang [280] analyzed the thermal buckling and postbuckling behavior of uniform and symmetric FG-CNTRC plates under in-plane temperature variation. Their results showed that the buckling temperature as well as thermal postbuckling strength of the plate can be increased by functionally graded reinforcements. Aragh *et al.* [18] proposed an Eshelby-Mori-Tanaka approach and a 2-D generalized differential quadrature method to investigate the vibrational behavior of rectangular plates resting on elastic foundations. Yas and Heshmati used the Timoshenko beam theory to analyze the vibration of straight uniform [367] and non-uniform [133] FG-CNTRC beams subjected to moving loads. A state-space Levy method was proposed by Zhang *et al.* [383] to analyze the vibrational properties of FG-CNTRC plates subjected to in-plane loads. Wu and Li [357] used a unified formulation of Reissner's mixed variational theorem based finite prism methods to study the free vibration behavior of FG-CNTRC plates. Free vibration analyses of quadrilateral laminated plates were carried out by Malekzadeh and Zarei [202] using first shear deformation theory and discretization of the spatial derivatives by the differential quadrature method. Lei *et al.* [175] presented parametric studies of the dynamic stability of CNTRC-FG cylindrical panels under static and periodic axial force using the mesh-free-kp-Ritz method and the Eshelby-Mori-Tanaka homogenization framework. Zhang and Liew [375] presented detailed parametric studies of the large deflection behaviors of quadrilateral FG-CNTRCs for different types of CNT

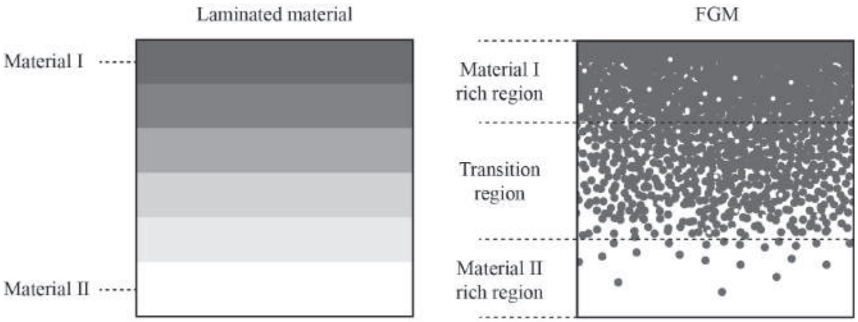

Figure 1.3 Schematic illustration of laminated composite and Functionally Graded Material (FGM).

distributions. Geometrically nonlinear large deformation analysis of FG-CNT skew plates resting on Pasternak foundations was carried out by Zhang and Liew [380]. Some other results can be found in the literature dealing with the buckling analysis of FG-CNTRC thick plates resting on Winkler [377] and Pasternak foundations [382], free vibration analysis of triangular plates [378], cylindrical panels [379, 173], three-dimensional free vibration analysis of FG-CNTRC plates [278], vibration of thick FG-CNTRC plates resting on elastic Winkler foundations [376], vibration analysis of FG-CNTRC thick plates with elastically restrained edges [375], etc.

1.2.1.2 Waviness and agglomeration effects on CNT-reinforced composites

It has been extensively reported in the literature that due to a high aspect ratio, up to 10^6 [57], as well as a very low bending stiffness, CNTs usually exhibit a certain degree of waviness [276, 330, 246], as can be observed in Fig. 1.4. All results in the literature agree to report curviness as a detrimental factor to mechanical performance. Finite element simulations have been proposed by Fisher *et al.* [93] and Bradshaw *et al.* [34] to analyze planar sinusoidal CNTs. The results demonstrated that filler waviness induces substantial decreases in the effective elastic moduli in the fiber direction. Another noteworthy contribution was done by Shi *et al.* [282] who extended the Mori-Tanaka method for three-dimensional helical CNTs. In this case, the results showed that composites doped with aligned wavy CNTs experience critical reductions in the longitudinal modulus, whilst the lateral modulus slightly increases. Yanase *et al.* [364] proposed an ad hoc Eshelby tensor to account for planar sinusoidal CNTs. Matveeva *et al.* [209] studied both sinusoidal and helical models by finite element-based homogenization methods, analytical models and molecular dynamics simulations. It was shown that both geometries significantly reduce the longitudinal elastic stiffness of the composite in the fiber direction.

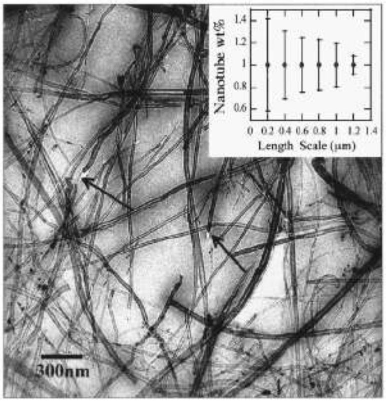

Figure 1.4 TEM micrograph illustrating the dispersion of 1wt.% MWNT incorporated in polystyrene. Source: [250].

Finally, a second important phenomenon to be taken into account in the simulation of CNT-based nanocomposites is the appearance of non-uniform spatial distributions of CNTs. Due to the electronic configuration of the tube walls and their high specific surface area, and therefore, large van de Waals' (vdW) attraction forces [9, 186, 352], CNTs tend to agglomerate in bundles as illustrated in the Transmission Electron Micrograph (TEM) in Fig. 1.5. Although there exists a variety of techniques to improve the dispersion of the fillers, such as the use of dispersants or sonication, the achievement of uniform CNT dispersions is still an intricate task. A noticeable contribution in this respect is the work by Shi *et al.* [282] who introduced a two-parameter agglomeration model. Their results demonstrated substantial decreases of the elastic modulus of the composites, what highlights the widespread thought of agglomeration as defects in the microstructure. Although only a few works report about this issue, the two-parameter agglomeration method has been widely accepted. For example, some efforts have been made in the study of the influence of agglomeration on the mechanical response of full-scale CNT-reinforced structural elements (see e.g. [316, 17, 18, 150]).

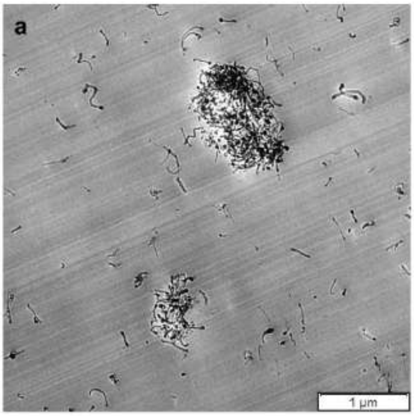

Figure 1.5 TEM micrograph illustrating the dispersion of 1wt.% MWNT incorporated in polycarbonate. Source: [242].

1.2.2 Electrical behavior of CNT-reinforced composites

In light of the reported outstanding electrical conductivity of CNTs, several orders of magnitude higher than most matrix materials, as well as their piezoresitive properties, the number of research works devoted to the development of conductive and strain-sensing CNT-reinforced composites has incredibly increased in recent years.

1.2.2.1 Mechanisms of electrical conductivity

Both theoretical and experimental results have evidenced a percolation-like behavior [47, 52, 348], that is to say, the conductivity varies only slightly for ranges of CNT concentrations below and above a certain critical concentration, so-called percolation threshold, at which abrupt increases of the overall electrical conductivity are observed. These behavior has been found for both polymer and cement-based composites as shown in Figs. 1.6 and 1.7. The first figure, Fig. 1.6, corresponds to Fig. 1 in the study of Sobha and

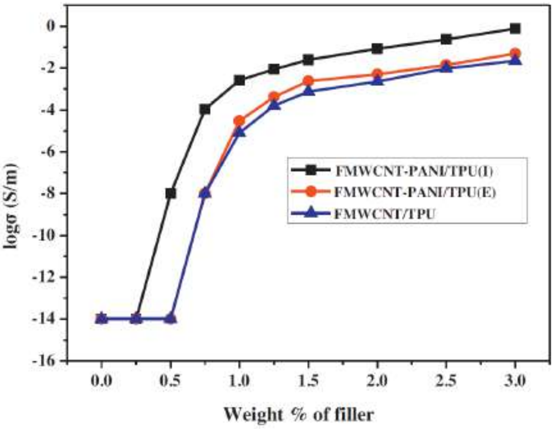

Figure 1.6 Electrical conductivity of various composites as a function of the weight of the filler. Source: [290].

Narayanankutty [290]. That research work reports about the experimental characterization of Polyanilini (PANI) Functionalised MWCNT (FMWCNT) based Thermoplastic Polyurethane (TPU) films. In addition, those authors also prepared the composites with solution casting methods using FMWCNT coated with polyaniline by in-situ and ex-situ polymerization of anililine, corresponding to FMWCNT-PANI/TPU (I) and FMWCNT-PANI/TPU (E), respectively. In that study, the initially insulating TPU, with an electrical conductivity of 10^{-14} S/cm, raised up to 1.1E-4 S/m in the case of FMWCNT-PANI/TPU (I) as shown in Fig. 1.6. The sharp increase in conductivity, ascribed to a percolation-like phenomenon, occurs at 1wt.% filler concentration. A similar behavior has been reported for cement-based materials. Fig. 1.7 shows some of the results obtained by D'Alessandro *et al.* [61] for MWCNT-reinforced cement-based materials. In particular, Fig. 1.7 shows the electrical conductivity of MWCNT reinforced cement paste versus mass content expressed as a percentage with respect to the mass of cement. In that work, different manufacturing techniques were compared for the optimization of electrically conductive cement-based nanocomposites, including sonication (SO) with low dispersant/mass of MWCNTs ratio 1:1 (Fig. 1.7(a)), sonication (SO) with high dispersant/mass of MWCNTs ratio 10:1 (Fig. 1.7(b)), an mechanical mixing (ME) with high dispersant/mass of MWCNTs ratio 10:1 (Fig. 1.7(c)). The results concluded that the overall electrical conductivity of MWCNT-reinforced concretes, mortars and cement-pastes is governed by a percolation-like behavior.

Most researchers agree explaining this percolation behavior by means of two different conductive mechanisms as shown in Fig. 1.8: electron hopping at the nanoscale and conductive networks at the microscale [345, 47, 185, 46]. From quantum mechanics, electron hopping or quantum tunneling is characterized by the transfer of electrons intra-tube or from one CNT to an adjacent tube. The probability of occurrence of this mechanism is highly dependent on the distance between tubes [119, 123]. At low CNT concentrations, electron hopping governs the electrical conductivity of the composite. With increasing

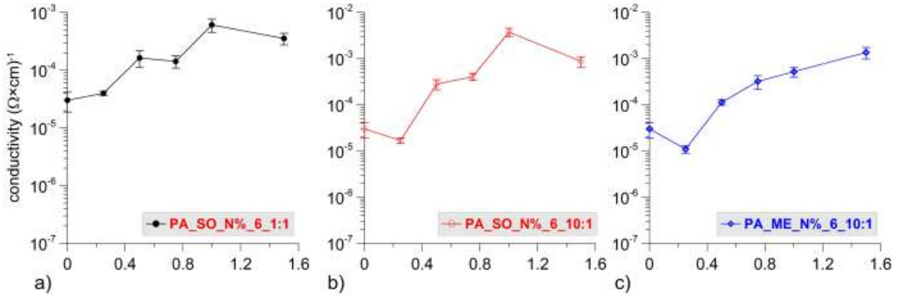

Figure 1.7 Electrical conductivity of MWCNT reinforced paste versus MWCNTs mass content expressed as a percentage with respect to the mass of cement, in AC electrical characterization tests. Source: [61].

CNT concentration, the separation distance among CNTs decreases until adjacent fibers touch one another resulting in a continuous electrically microscale conductive path. The conductivity of composites with CNT concentrations above the percolation threshold is believed to be dominated by this second mechanism.

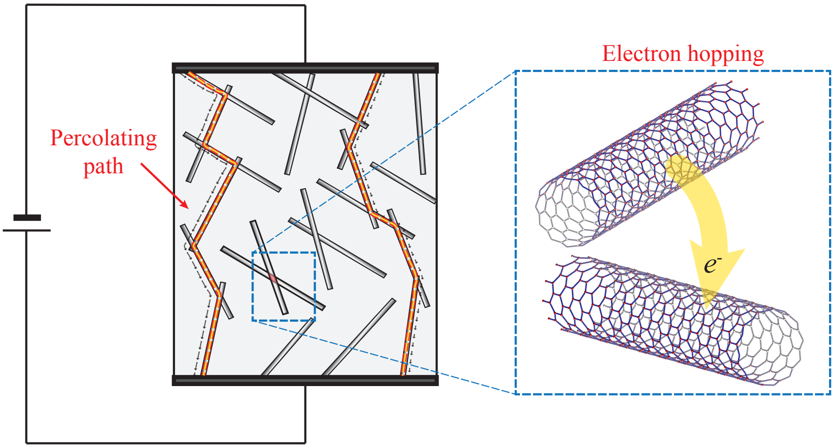

Figure 1.8 Schematics of the contribution of electron hopping and conductive network mechanisms to the overall electrical conductivity of CNT nanocomposites.

Together with the interesting aforementioned conductive properties of CNT-reinforced composites, results in the literature evidence the existence of variations in the electrical conductivity of these nanocomposites under the presence of external strains [179, 239, 51, 140, 212, 126], a feature that enables a huge range of applications as strain transducers and monitoring applications. For instance, Fig. 1.9 shows the resistance change ratio ($\Delta R/R_0\%$) versus strain of CNT-reinforced polymer composites studied by Hu *et al.* [140]. In that work, both numerical and experimental studies were conducted to characterize the piezoresistivity of CNT/epoxy films. From this figure, it can be seen that the traction and

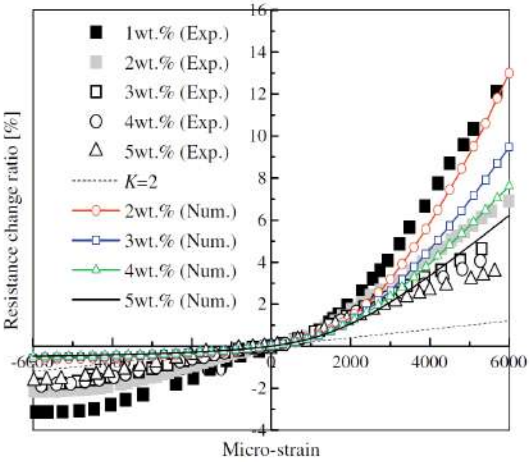

Figure 1.9 Comparison of numerical and experimental results of resistance change ratio ($\Delta R/R_0$%) versus strain of CNT/epoxy films. Source: [140].

compression strains increases and decreases the resistance of the composites. Another noticeable aspect is composites exhibit higher sensitivity values for low filler contents, reaching the maximum values in this case for filler contents of 1wt.%. A similar behavior has been also reported for CNT-reinforced cement-based composites. An example is the one shown in Fig. 1.10 from the research work of Materazzi *et al.* [205]. In a similar way, Materazzi and co-authors analyzed the strain-sensing behavior of cement pastes doped with MWCNTs. The results highlighted a good correlation between measured applied strain and internal electrical resistance, a fact that demonstrates the applicability of these nanocomposites as self-sensing strain transducers.

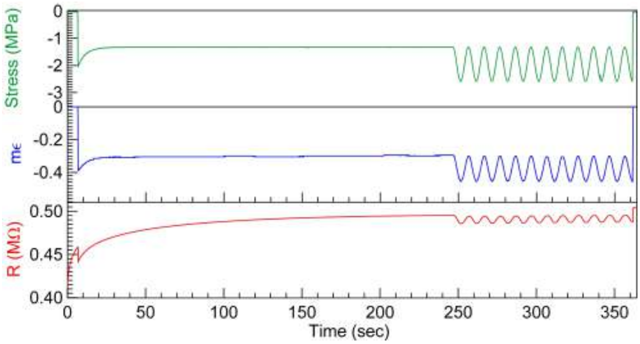

Figure 1.10 Time series of axial stress, measured strain and measured electrical resistance of MWNCT cement paste composite under a sinusoidal compressive load of frequency 0.1 Hz. Source: [205].

In view of the physical mechanisms governing the electrical conductivity of CNT-reinforced composites, the origin of the self-sensing property is due to the tampering of these mechanisms induced by external mechanical strains. In particular, three major expected changes during stretching/compressing have been suggested in the literature [85, 139]: (i) composite volume expansion, (ii) reorientation of fillers and (iii) changes in the percolation threshold. The first mechanism refers to the change of volume experienced by compressible materials when subjected to strain. Given that CNTs are much stiffer than the matrix, the volume change is mainly sustained by the matrix phase, while the volume change of fillers can be neglected. Hence, a change in the overall volume with an unaltered volume of fillers induces changes in the CNT volume fraction [243, 85, 113]. This change eventually causes the breakdown of existing conductive paths or the formation of new ones due to the change of the distance between CNTs. With regard to the second mechanism, experiments have shown that CNTs tend to re-orient in the direction of the stretching [51, 338, 12]. Under the assumption of initial random distributions of CNTs, strain induced orientation changes result in a growing anisotropy and, consequently, in changes in the effective electrical properties of the composite. Finally, many researchers agree that strain induced orientation also influences the percolation threshold. This is due to the fact that aligned fillers presumably have less likelihood to get in contact and form connecting networks [192, 115, 373].

1.2.2.2 Modeling of the electrical conductivity of CNT-reinforced composites

Most of the literature on CNT cement-based composites has focused on their fabrication process and experimental characterization. Theoretical studies coping with the explanation of the physical principles underlying the conductive mechanisms of these composites are rather scant. Among these contributions, it is noteworthy the application of lumped-circuit models of carbon fiber cement paste sensors based on series-parallel arrays of electrical resistors and capacitors [184, 121, 124, 126, 63]. A larger number of publications can be found concerning the modeling of polymeric materials doped with CNTs. Monte Carlo (MC) simulations haven been widely employed to predict the electrical conductivity of the nanocomposites [231, 200, 384, 198]. Nevertheless, MC simulations are computationally expensive and do not offer an explicit formulation useful for design purposes. Thus, the development of analytical models has attained more attention. Traditionally, a three-parameter power law fit taken from classic percolation theory has been widely used for determining the percolation threshold [159, 116]. However, since this model requires experimental data to be fitted, it cannot be used for design purposes nor let distinguish the two conductive mechanisms. Alternatively, other authors have attempted to predict the overall electrical conductivity of CNT nanocomposites by means of different micromechanics theories. Among them, it is worthy mentioning the work of Deng and Zheng [66] who developed a simplified micromechanics model to evaluate the effective electrical conductivity for CNT composites. This approach allowed to reproduce percolation, conductive networks, conductivity anisotropy and waviness of CNTs with good agreements with some experimental data from the literature. A similar approach was employed by Takeda *et al.* [303] for the analytical characterization of the electrical conductivity of CNT-based polymer composites. The predictions from the analytical model showed a good correlation with experimental results measured by alternating current impedance spectroscopy. Another relevant contribution was made by Seidel and Lagoudas [275] who proposed a Mori-Tanaka micromechanics model [220, 131] for the study of the individual influence of electron hopping and the formation of conductive networks on the electrical conductivity of CNT-polymer composites. In that work, the electron hopping mechanism was simulated by means of a conductive interphase surrounding the tubes, whilst conductive networks were represented by changes in the CNT aspect ratios. Despite the promising capabilities of this new approach, great discrepancies were observed compared to experimental data. The origin of these discrepancies was attributed by Feng and Jiang [87] to the assumption of the electrical conductivity and thickness of the interphase as constant, as well as the isolated effect of electron hopping and conductive networks before and after the percolation, respectively. These authors proposed an extension of the latter approach by considering the coupled effect of electron hopping and conductive networks on the overall conductivity with better agreement with experimental data. The simulation results also indicated that the sizes of CNTs have significant influence on the percolation threshold and, consequently, on the overall conductivity of the nanocomposites.

1.2.2.3 Modeling of the piezoresistivity of CNT-reinforced composites

Only a very scant number of studies has faced the prediction of the piezoresistivity properties of CNT-based composites. The work of Lin *et al.* [192] is worth noting, as it presented an application of the Monte Carlo method to investigate the stretching/compression effects on the electrical properties of fiber-filled composites. Their results showed that the deformation could shift the percolation threshold of the composites. Theodosiou and Saravanos [311] analyzed the piezoresistive response of CNTs with an atomistic model and the overall behavior of CNT-polymer composites at macroscale by a numerical CNT percolation model. That work concluded that the nanotube resistance and the tunneling effect were the dominant mechanisms of the strain-sensitivity of CNT-reinforced composites. Yasuoka *et al.* [368] simulated the strain-sensitivity of CNT-based composites by using a circuit simulator analogue to percolation network. It was shown that the piezoresistivity exhibits high levels of non-linearity, conclusion that well agrees with the experimental evidence. In that work, the stretching effects on percolation threshold was simulated by an excluded volume approach [43]. The results reaffirmed the non-linear behavior of the strain-sensing capability, more critical for CNT concentrations near the percolation threshold. A similar work has been recently carried out by Feng and Jiang [85]. The authors extended their previous works [87] in order to take into account the stretching effects. Despite finding gross differences in comparison to some experimental data of CNT/polymer composites with low CNT concentration, the proposed framework proved capable of qualitatively implementing the three major effects induced by stretching.

It is also noted that most theoretical works in the literature are limited to uni-axial loadings, while approaches concerning three-dimensional strain states are very scarce. A noteworthy contribution was done by Alamusi and Hu [5] who utilized a three-dimensional resistor network with Simmon's contact resistance among CNTs [287], in combination with a fiber re-orientation model [309]. Tallman and Wang [305] extended the theoretical approach proposed by Takeda *et al.* [303] for the piezoresistivity modeling of CNT composites subjected to arbitrary dilations. Bi-axial stretching effects were also investigated by Feng and Jiang [88], who presented closed-form expressions of the filler orientation distributions for such loading configurations. Recently, Wang *et al.* [336] developed a 2D RVE to simulate the electromechanical response of silicone elastomer loaded with carbon black. In that work, comparison analyses against experimental data demonstrated the importance of large deformation effects on the non-linear electrical response of the composites. Notwithstanding all these efforts, a generalized micromechanical scheme allowing for the modeling of the electro-mechanical response of CNT-reinforced cement-matrix composites under arbitrary 3D strain states is still lacking in the literature.

1.2.2.4 Modeling of waviness and agglomeration effects on piezoresistive CNT-reinforced composites

It should be mentioned that most of the existing theoretical studies on the electrical properties of CNT-reinforced composites assume straight conductive fillers. Conversely, only a few researchers have reported on the effects of waviness on the overall electrical properties of CNT nanocomposites. By assuming a simple sinusoidal shape, Yi at al. [370], Berhan and Sastry [26] and Fisher *et al.* [93] showed that CNT waviness induces considerable increases of the percolation threshold and decreases of the overall conductivity. Similar conclusions were reached by approximating wavy CNTs as elongated polygons by Li *et al.* [177], or by introducing equivalent straight fibers into a simplified micromechanics models, as reported by Deng and Zheng [66] and Takeda *et al.* [303]. A second important phenomenon that occurs in CNT composites is the agglomeration of fibers. The difficulty in obtaining good dispersion of the nanotubes is related to the circumstance that CNTs tend to form agglomerates and bundles. This phenomenon is attributed to the electronic configuration of tube walls and their high specific surface area which favors the appearance of large vdW attraction forces among nanotubes [9, 186, 352]. Although it is reported in the literature that bundles can substantially decrease the overall conductivity of the composites since they inhibit the formation of conductive networks [147], only a few contributions have attempted the theoretical simulation of heterogeneous filler dispersions. Along these lines, it is worth noting the works of Weng [350] and Yang and co-authors [365]. The results showed that the inhibition of conductive networks induced by filler clustering leads to important increases in the percolation threshold. With regard to the strain-sensing capabilities, waviness and agglomeration apparently have important influence on the piezoresistivity of CNT-based composites, although this has not been thoroughly investigated. Thereof, implementation of non-straightness and agglomeration of CNTs are essential phenomena to be included in a rigorous theoretical modeling.

1.2.3 Smart CNT-reinforced composites for SHM applications

1.2.3.1 Literature review on SHM applications of CNT-reinforced composites

The growing concern on the critical socio-economical impact of civil infrastructures, as well as the aging process and the appearance of extreme natural events, have impelled great advances in the realm of Structural Health Monitoring (SHM) in the last decades. Nevertheless, conventional sensors such as off-the-shelf accelerometers or strain gauges only provide quasi-point measurements and, thus, may not detect the appearance of damages if their location is not properly defined [122]. Recently, fiber-optic sensors have been successfully used for distributed sensing applications [81, 110]. Fiber-optic sensors offer some advantages as they can be embedded in the structure and monitor the strain along their length. However, these conventional solutions are hardly scalable to large-scale infrastructures without incurring high costs and complex signal processing algorithms. In addition, the application of most conventional monitoring systems to long-term systems, capable of detecting the appearance of damages so that reparation measures can be conducted, require a substantial investment. The rapid growth of nanotechnologies has opened a wide range of possibilities in sensor developments, including multifunctional materials that enable substantial improvements in the cost-effectiveness of SHM solutions for geometrically large systems. A specially interesting potential application of these new technologies is in concrete infrastructures through embedded continuous monitoring systems. In particular, there is a growing concern with the lifetime of these structures because of concrete's wide material discreteness and complex service environments [2, 206]. The new development of multifunctional and smart materials, and particularly electrically conductive CNT cement-based composites, opens up a wide range of possibilities in the realm of SHM [118, 325, 92]. On the basis of the piezoresistive properties of CNT-reinforced composites, i.e. composites themselves behave as sensors by means of measurable variations of their electrical properties under applied mechanical deformations [99, 171, 324], many researchers have striven to prove the feasibility of these composites as strain sensors for condition-based maintenance applications. This exceptional property, together with the similarity and compatibility between these composites and structural concrete, can be used to develop durable distributed embedded strain-sensing systems with low maintenance cost in applications to large-scale concrete structures [184, 120, 136, 277, 121, 125, 123].

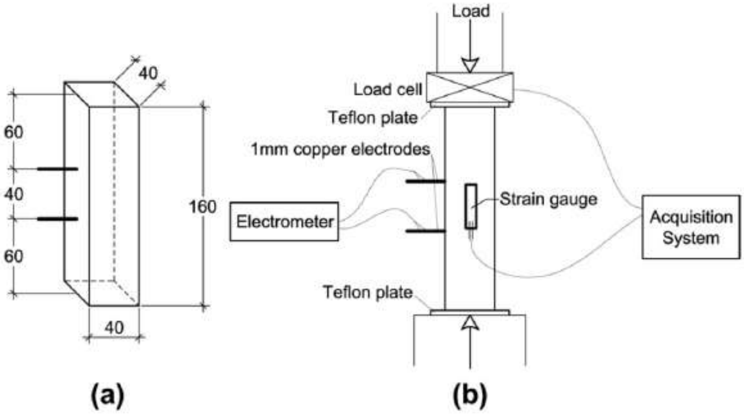

Figure 1.11 Sketch of the sensor (a) and of the measurement system (b) with dimensions in mm. Source: [205].

It is worth noting the work of Han *et al.* [124] who investigated the potential application of MWCNT/cement composites as embedded strain sensors for traffic monitoring. With vehicular loading experiments, the authors reported good corresponding relationships between compressive stress and the electrical resistance of the sensors. Saafi [262] developed cement-CNT sensors for crack detection in concrete structures. Interfaced to a low cost wireless communication system, the cement-CNT sensors were embedded into 100x100x100 mm^3 concrete beams. The results proved the potential of CNT-reinforced cement pastes as sensors for crack detection in a three-point bending test, where crack initiation resulted in a sudden increase in the effective resistance. Howser *et al.* [137] reported the fabrication of self-consolidating concrete doped with carbon nanofibers for the development of strain-sensing shear columns. The results demonstrated the appearance of peaks and valleys in the electrical resistance traces of the concrete matching the strain in the columns. It is also worth noting the work of Materazzi *et al.* [205] who reported on the applicability of carbon nanotube-cement based sensors for measuring dynamically varying strain in concrete structures. Under laboratory conditions, the electrical response of prismatic specimens (see Fig. 1.11) made of carbon nanotube-cement composite was analyzed under sinusoidal stress-stains in the typical frequency range of large civil structures. The results of the experimental tests demonstrated that a sinusoidal compression load as input produces a sinusoidal variation of the electrical resistance as output. Test with sweep variation in the axial load frequency allowed a more in-depth study of the specimens' dynamic response. A very close correlation was observed between the measured electrical resistance and the axial strain. Subsequently, the works of Ubertini *et al.* [323, 325] further

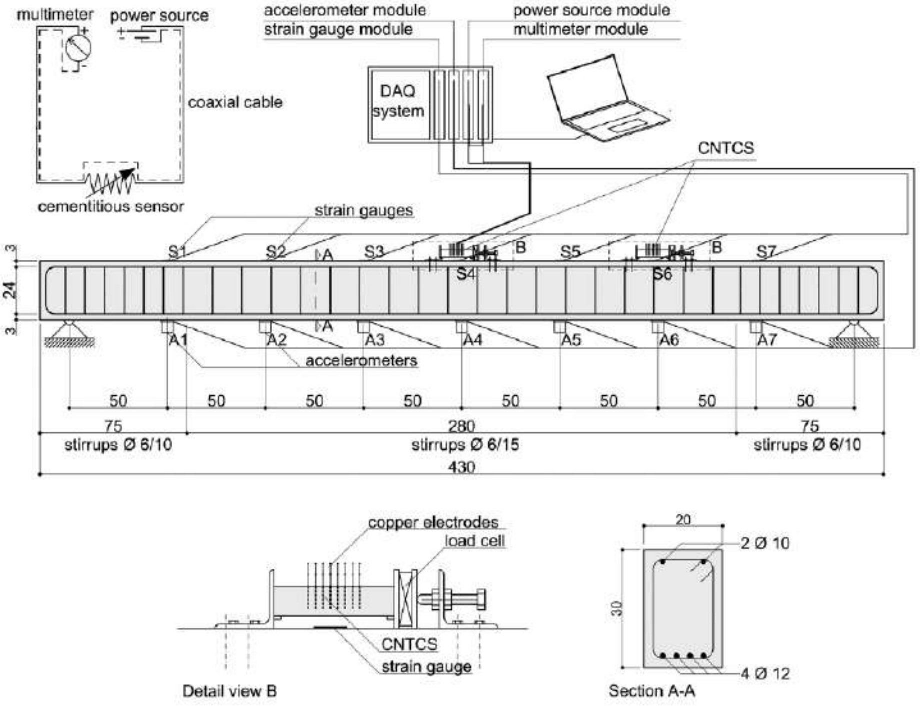

Figure 1.12 Layout of the experimental setup and plans of the investigated reinforced concrete beam with dimensions in cm. Source: [325].

the study of the potential application of CNT-reinforced cement-based sensors in the out-only modal identification for SHM of large concrete structures (see Fig. 1.12). The studies were conducted though laboratory tests on a steel-reinforced concrete beam. The experimental results, benchmarked against traditional accelerometers, demonstrated that the CNT-reinforced Cement composites (CNTCs) allowed for modal identification over a frequency range up to 500 Hz.

Naeem *et al.* [226] analyzed the stress and crack sensing capabilities of MWCNT/cement composites subjected to flexural loadings. Those authors furthered the study of these nanocomposites for the flexural stress/crack sensing by embedding long prismatic MWCNT/cement in different locations of reinforced mortar beams. Steep changes in the resistance were reported at failure of the mortar in flexural crack sensing tests, demonstrating the applicability of MWCNT cement-based nanocomposites as embedded continuous transducers for crack detection applications. Most of the research studies focuses on Direct Current (DC) resistivity measurements. Some of the previous refereed research studies [205, 323, 325] reported on the limitations of DC resistance measurement of self-sensing multi-functional structural materials due to the time-based drift in the material's measured electrical output. This phenomenon is often attributed to the material polarization, changes in the material's dielectric constant, the piezoelectric effect or the combination of other electrical effects. The electrical polarization of CNTCS results in signal distortions at low frequencies that can be eliminated using high-pass filtering as shown in [325]. Nevertheless, this effect may prevent the application of CNT-reinforced cement-based composites to structures with relatively low resonant frequencies. In order to avoid this issue, Alternating Current (AC) measurements have been shown to offer alternative suitable solutions. In this line, a noteworthy contribution is the work by Downey *et al.* [74] who proposed a novel biphasic DC measurement approach for use in the resistance measurement of self-sensing multi-functional structural materials. According to that approach, the elimination of the drift is achieved through applying a periodic charge/discharge signal in the form of an alternating square wave. In addition, that approach was shown to allow for simultaneous, multi-channel acquisition of adjacent electrodes in the CNTCS, what opens a vast range of applications in the realm of continuous distributed sensing solutions. The authors demonstrated the applicability of the proposed approach for damage detection and lo-

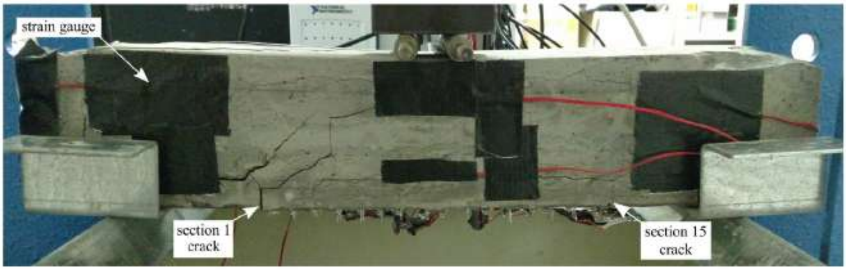

Figure 1.13 Test specimen showing the damage of a 100x100x500 mm^3 steel reinforced CNT/cement composite beam loaded in a four-point bending configuration. Source: [74].

calization using two CNT-reinforced cement-based composite beams. First, controlled damage was introduced into a 40x40x160 mm^3 beam to detect and localize damage within the multi-sectioned MWCNT beam. Thereafter, a 100x100x500 mm^3 steel reinforced cement composite beam was loaded past failure in a four-point bending configuration as shown in Fig. 1.13. Changes in the beams internal resistance were successfully tracked to provide damage detection and localization. CNT-reinforced polymers have been also investigated as dynamic strain sensors. For instance, Kang *et al.* [154] developed 10wt.% CNT-reinforced Poly(methyl methacrylate) (PMMA) strain sensors. Under laboratory conditions, the authors bonded CNT/PMMA sensors with dimensions 50x4x0.08 mm to an aluminum cantilever using a spray-on techniques. Their results demonstrated close correlations between the electrical resistance and the monitored vibration of the beam. Additionally, the authors simulated the appearance and propagation of damage cutting part of the section of the sensor, and found significant changes in the electrical resistance and capacitance of the sensors. In this line, application of CNT/polymer dynamic strain sensors are particularly well-suited for pre-existing structures, as well as for stretchable electronics in bioengineering, wearable fabric strain sensors [337].

1.2.3.2 Electromechanical modeling of CNT-reinforced dynamic strain transducers

Although a vast effort has been put into understanding the physical mechanisms governing the strain sensitivity of CNT reinforced nanocomposites, none of the above mentioned methodologies offers suitable approaches for analyzing their dynamic response, essential for applications in the form of dynamic strain sensors. Cement-based materials primarily behave as dielectrics. When a dielectric material is exposed to an electric field, the molecular dipoles tend to get oriented in the direction of the field and create an induced electric field opposite to the applied one. As a consequence of this phenomenon, termed polarization, the electric current decreases over time under the application of a constant potential difference [346, 40]. Polarization, together with the strain-varying electrical properties, must be taken into account when simulating DC resistivity measurements. To do so, equivalent lumped-circuit models are being imposed as they provide a feasible and tractable framework to simulate electric time-varying systems. It is noticeable the work of Kang *et al.* [154] who performed Electrochemical Impedance Spectroscopy (EIS) testing to characterize the electrical properties of SWNT/PMMA sensors. On this basis, the authors proposed a modified Randles circuit to represent the dynamic behavior of the sensors. In a similar way to other works, strain sensing was enabled by a linear relationship between the variation of the relative change of the internal electrical resistance and the axial strain. This type of approaches neglects any kind of nonlinearity in the response, what limits their application to small deformation ranges and filler contents away from the percolation threshold. A similar study is the one of Loh *et al.* [195] on SWCNT-poly(sodium 4-styrene-sulfonate)/vinyl alcohol (SWNT-PSS/PVA) thin films. An RC-circuit model was formulated from frequency-domain EIS to fit the numerical results to the experimental data. The contact resistance, the double layer capacitance and the bulk resistance were defined exponentially decaying with time and a good agreement with the experiments was obtained. Also, Materazzi *et al.* [205] conducted an experimental campaign to assess the change in the electrical resistance of CNTCSs under the action of sinusoidal compression loads. The analyses showed that the variation of the amplitude of the electrical resistance increases with the frequency of excitation. Following the trace of that work, D'Alessandro *et al*. [63] proposed a Randles equivalent circuit based electromechanical modeling of CNTRCs as shown in Fig. 1.14, similar to the one proposed by Han *et al*. [126]. The lumped-circuit consisted of two resistors and a capacitor, accounting for the contact resistance (cables and electrodes), internal dissipation and electric polarization. An important conclusion was that the dynamic response of CNTRCs is not monochromatic, but rather contains superharmonics. However, while the presence of superharmonics was anticipated by the model, the increasing amplitude of the response with increasing frequency was not reproduced. Sanli *et al*. [270] proposed an RC equivalent circuit based on the impedance response of sensitive CNT/epoxy films. An interesting aspect of that work is the consideration of not only internal resistance dependence on external strain, but also strain-dependent capacitance.

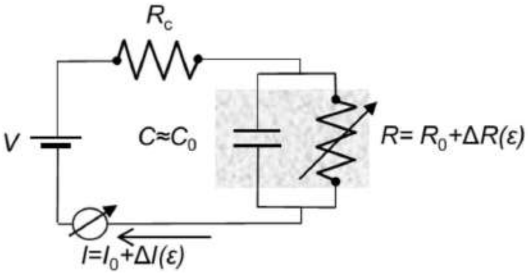

Figure 1.14 Piezoresistive electromechanical model of a CNTCS. Source: [63].

1.3 Objectives and scope

In general terms, the scope of this thesis comprises the analysis of the potential applications of carbon nanotubes as mechanical reinforcements and smart inclusions. In virtue of the multifunctional properties of CNTs, these two applications are not independent. Along these lines, the use of CNTs as additives not only enhances the load-bearing capacity of structures but also confers strain sensing capabilities.

The interest of the first branch of applications primarily focuses on the development of structural reinforcements for rehabilitation/strengthening of pre-existing structures. In this line, the works conducted in this thesis aim at implementing mechanical micromechanics approaches capable of estimating the load-transfer mechanisms in CNT-reinforced composites, as well as predicting the macroscopic response of full-scale structural elements. It is also intended to investigate the weakening effects in the microstructure, including the filler waviness or agglomeration.

On the other hand, the second line of applications focuses on the piezoresistivity properties of CNT-reinforced composites for the development of embeddable sensors. The second goal of this thesis, therefore, concerns the development of micromechanics approaches for the evaluation of the electrical properties of CNT-reinforced composites. Specifically, the analysis comprises the evaluation of the physical mechanisms underlying the electrical transport, electrical conductivity, and piezoresistivity properties under the action of uniaxial and general three-dimensional strain states.

On the basis of these two pursued applications, two different matrix materials are considered, namely polymer and cement-based composites. Polymers offer a great range of possibilities for developing reinforcing coatings, including a large variety of geometries that can be easily incorporated into pre-existing infrastructures. On the other hand, CNT-reinforced cement-based composites exhibit similar characteristics to structural concrete. This fact suggests the possibility of developing embedded sensing systems with substantial improvements in the cost-effectiveness of the monitoring of large-scale concrete structures and without compromising the durability. Although the theoretical framework of the works conducted for both applications is similar, the presented results focus on these two matrix materials according to the aforementioned criterion.

Finally, the ultimate goal of this thesis is to use the previously developed approaches for the evaluation of the potential application of CNT-reinforced composites in the realm of SHM. Especially interesting is the application of CNT-reinforced sensors to output-only Operational Modal Analysis (OMA). A premise in this goal is that the incorporation of certain CNT-reinforced structural members represents a mechanical reinforcement and, at the same time, the same members also behave as sensors. This would enable us to infer the dynamic properties of the whole structure in operational conditions without necessitating external off-the-shelf sensors. In this line, this thesis comprises a preliminary experience in the application of ambient-vibration OMA techniques with conventional accelerometers. Afterward, it is intended to extend the previously developed approaches in the time-domain and ascertain the dynamic properties of CNT-reinforced composites.

Overall, the main goals of this thesis can be listed as follows:

1. Analysis of the potential of CNTs as mechanical reinforcements for high-strength composites.
    - Development of advanced micromechanics models of the mechanical response of CNT-reinforced composites, including critical microstructural features such as complex filler arrangement, waviness, and agglomeration.
    - Investigation of the design optimization possibilities of FG-CNTRCs structures.
    - Analysis of the uncertainty propagation of the main design variables on the macroscopic response of FG-CNTRCs.
2. Analysis of the potential of CNTs as reinforcements for smart composites.
    - Development of advanced micromechanics models of the electrical conductivity of CNTCs, incorporating separately the contributions of the different physical mechanisms that govern the electric transport properties.
    - Study of the piezoresistivity properties of CNTCs under uniaxial strain loadings. Specifically, it is intended to incorporate within the previously developed approaches the strain-induced disturbances on the physical mechanisms underlying the overall conductivity.

  - Extension of the previously developed micromechanics approaches to account for general three-dimensional strain states. This aims at evaluating the potentials of CNTCs as static strain transducers within a theoretical multi-physics framework.

3. Analysis of potential applications of CNT-reinforced materials in the realm of SHM.

   - Development of equivalent lumped circuits apt for estimating the response of CNTCs in the time domain. In light of the literature review, the modeling must reproduce the major features reported by experimentation: (i) the electrical response of sensors contains superharmonics when subjected to sinusoidal loadings; and (ii) the frequency response function increases with the frequency of excitation.

   - Comprehensive evaluation of potential applications of CNT-based sensors for static and dynamic monitoring of full-scale civil infrastructures.

1.4 Thesis structure

In view of the aforementioned objectives, the remainder of this thesis has been structured in three chapters as follows:

Chapter 2 presents the main contributions of this thesis in the realm of carbon nanotubes as mechanical reinforcements. Section 2.1 provides a literature review on the micromechanics modeling of CNTRCs, FG-CNTRCs, and the uncertainty propagation analysis of CNTRCs. Section 2.2 overviews the main mechanical homogenization approaches for CNTRCs, including complex filler arrangements, waviness and agglomeration effects. Section 2.3 presents the theoretical fundamentals for FG-CNTRCs. Section 2.4 introduces the theoretical background of the uncertainty propagation analysis of FG-CNTRCs, and surrogate modeling. Section 2.5 presents the numerical results and discussion. Here, Subsection 2.5.1 presents the numerical results of the mean-field homogenization of FG-CNTRCs, Subsections 2.5.2 and 2.5.3 show the analysis results of the macroscopic response of FG-CNTRC full-scale structural elements, 2.5.4 presents a case study of uncertainty propagation analysis of the vibrational properties of FG-CNTRC plates, and 2.5.5 shows a comparison analysis of the stiffening effects of composite plates doped with CNTs and graphene. Finally, Section 2.6 concludes this chapter. The results and conclusions of this chapter cover the first objective of this thesis.

Chapter 3 shows the works conducted in this thesis on the modeling of the electrical conductivity and piezoresistivity properties of CNTCSs. First, a literature review is presented in Section 3.1. Afterward, Section 3.3 overviews the mixed micromechanics approach developed for the prediction of the electrical conductivity of CNTCSs. Sections 3.3 and 3.4 present the theoretical formulation of the micromechanics modeling of the piezoresistivity properties of CNTCSs under uniaxial and three-dimensional strain loadings, respectively. Section 3.5 presents the numerical results and comparison analyses with experimental data and, finally, Section 3.6 concludes this chapter. The achievements reported in this chapter complete the second objective of this thesis.

Chapter 4 furnishes the studies conducted in this thesis on the potential use of CNT-reinforced composites for SHM applications in civil engineering structures. Section 4.1 presents a literature review on the application of smart materials in the realm of SHM of civil infrastructures, as well as the electromechanical modeling of the dynamic response of CNTCSs. Section 4.2 introduces the principles of ambient-vibration SHM, including an application case of the OMA campaign conducted in the Montoro footbridge in Córdoba, Spain. Section 4.3 presents a novel equivalent-lumped circuit for the electromechanical modeling of CNTCSs. The validation and numerical results are presented in Section 4.4 and, finally, Section 4.5 concludes this chapter. The third and last goal of this thesis is fulfilled by the studies conducted in this chapter.

Finally, **Chapter 5** summarizes the main contributions and conclusions of this thesis, as well as possible future developments.

For the sake of clarity, the structure of this thesis is illustrated in Fig. 1.15. As previously indicated, the study of high-strength and smart materials has been framed in the realm of polymeric and cementitious composites. Nevertheless, the developed micromechanics approaches are general enough to be extended to other types of composites.

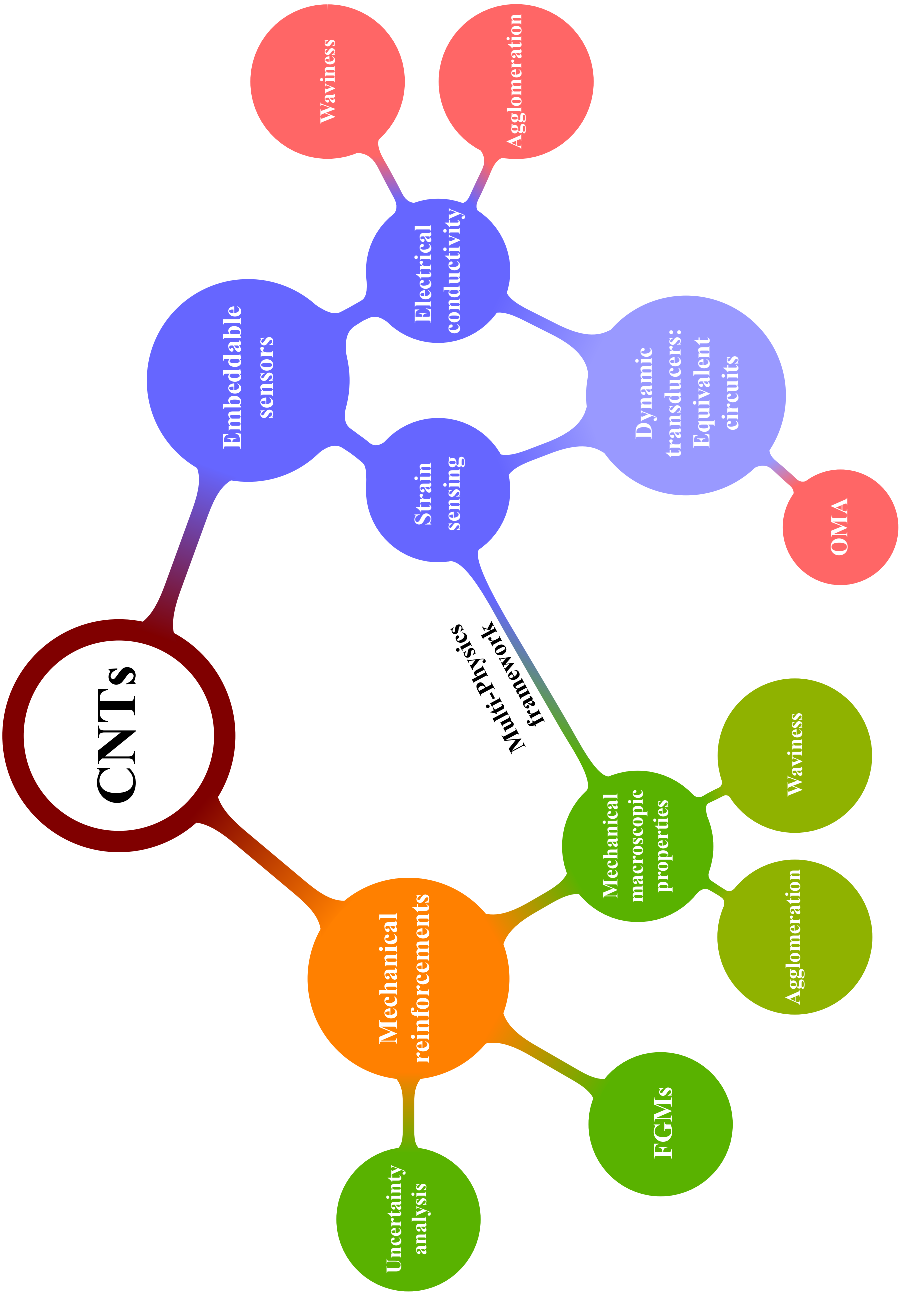

Figure 1.15 Mind map of the thesis structure.

2 CNTs as additives for high-strength composites

This second chapter of the thesis focuses on the works conducted in the realm of carbon nanotubes as additives for the development of high-performance composites, including the results published in the articles A, B, C, H, I and J.

2.1 Introduction

The exceptional mechanical, thermal and electrical properties of carbon nanotubes have spurred a considerable amount of research in recent years. In particular, the elastic moduli of CNTs have been shown to be greater than 1 TPa [361] and their ultimate tensile strengths around 150 GPa [65], largely exceeding those of any previously existing material. In addition, an increasing number of publications report about the outstanding enhancements of the mechanical properties of polymeric matrices doped with small concentrations of CNTs [57, 297], making them one of the most promising additives for the development of high-performance and lightweight composites. For instance, Qian *et al.* [250] dispersed MWCNTs throughout polystyrene with a concentration of 1wt.%, reaching increases with respect to the neat polymer in elastic modulus and break stress of 36-42% and ~25%, respectively. Andrews *et al.* [15] developed SWCNTs loaded isotropic petroleum pitch matrices and found that the tensile strength and elastic modulus with 5wt.% content of purified SWCNTs increased by about 90 and 150%, respectively. In this context, theoretical models capable of predicting the overall mechanical properties of CNT-reinforced composites are of pivotal importance for assisting their design. Since nanotechnology and, in particular, the synthesis of carbon nanotubes, is still in a process of development, the manufacturing cost of CNT-reinforced structural elements is very limiting. Hence, theoretical models must account for realistic filler configurations so that CNT-reinforced composites can be optimized.

In light of the potential applications of CNTs as mechanical reinforcements, the first goal of this thesis focuses on the development of advanced micromechanics models of the mechanical response of CNT-reinforced composites. Hence, the fist efforts have been put into considering manufacturing-induced complex orientation distribution of fillers, as well as filler waviness and agglomeration effects. Moreover, another interesting application to maximize the cost-efficiency of CNT-reinforced composites is the development of Functionally Graded Materials (FGMs). FGMs shows promise for developing tailor-made structural elements that meet superior load-bearing requirements. These advanced materials are defined by spatially continuous varying properties, such as gradation of doping concentration or orientation across the thickness [326]. Unlike laminated materials, FGMs exhibit smooth and continuous variations of their material properties and, therefore, prevent delamination and debonding failures caused by stress concentrations at interfaces [105, 32, 156]. Finally, efforts have been also put into the stochastic design of FG-CNTRCs and the uncertainty propagation analysis of the main design variables.

In this context, the conducted studies have been categorized into three different sections: analytical mechanical homogenization approaches (Section 2.2), FG-CNTRCs (Section 2.3), and uncertainty analysis of FG-CNTRCs (Section 2.4). The review of the state of art follows hereafter according to the previously mentioned categories, Section 2.5 summarizes some of the most relevant results achieved in the course of this part of the thesis and, finally, Section 2.6 concludes this chapter.

Throughout this chapter, a boldface letter stands for a fourth-order tensor, $\mathbf{A} \equiv A_{ijkl}$, and a colon between two tensors denotes inner product, $\mathbf{A} : \mathbf{B} \equiv A_{ijkl}B_{klmn}$.

2.1.1 Analytical mechanical homogenization of CNT-reinforced composites

Along with the encouraging results from experimentation, much effort has been devoted to the development of theoretical models capable of providing reliable estimates of the overall elastic moduli of CNT-reinforced composites, essential for design and optimization purposes. Since Molecular Dynamics (MD) and multi-scale finite element simulations [114, 392, 127, 285, 6] are limited to systems with a small number of atoms due to their high costs of computation, homogenization approaches based on the mean-field homogenization theory have drawn an increasing attention. In particular, a large number of recent publications in the realm of CNT nanocomposites have been conducted by the Extended Rule of Mixtures (EROM) [174, 381, 101, 157] and the Mori-Tanaka (MT) [18, 380, 150, 104] method. The EROM is based upon a modification of the classical Voigt and Reuss bounds by the so-called efficiency parameters in order to fit the results from an MD or multi-scale simulation [279]. Although many authors have been attracted by the simplicity of this approach, it is highly dependent on a more complex simulation and only singular filler arrangements can be modeled. The MT model, on the contrary, enables the simulation of more complex configurations such as misoriented distribution of fillers, curviness and agglomeration effects [282]. However, numerous research works report about some inconsistencies and limitations of this methodology, such as diagonal asymmetry of the estimated constitutive tensors and violation of the Hashin-Shtrikman-Walpole bounds for some filler configurations.

A large majority of the research studies using the MT approach assumes that CNTs are fully aligned or randomly oriented in the matrix. However, in real CNT/polymer nanocomposites, fillers orientations are governed by complicated flow fields induced in the manufacturing process. Unless special measures are undertaken, the CNTs are randomly distributed in the matrix. There exists a number of works in the literature on techniques of aligning CNTs, including slicing [3], chemical vapor decomposition [50], melt processing [214], mechanical stretching [33], electrophoresis [362], application of magnetic fields [4, 106, 158] and electrospinning [75, 160, 267]. However, a drawback of most of these alignment processes stems from the loss of alignment when combining the nanotubes with the polymer matrix [160, 39]. Hence, CNTs are generally oriented somewhere between the two extremes, random and fully aligned. Therefore, orientation distributions of CNTs throughout polymer matrices must be studied in statistical terms.

Although the MT method provides an apparently favorable theoretical framework for the consideration of general CNT orientation distributions, a few research works in the literature report that the MT method may provide diagonally asymmetric stiffness tensors, as well as may violate the Hashin-Shtrikman-Walpole bounds [232, 252, 89, 24]. Qiu and Weng [252] showed that, only in the case of fully aligned inclusions, the effective stiffness tensor provided by the MT approach preserves the symmetry and stays within the Hashin-Shtrikman-Walpole (HSW) bounds. Hashin and Shtrikman introduced variational principles for heterogeneous materials with statistically isotropic microstructures [129, 130]. The Hashin-Shtrikman (HS) variational principles consist of an alternative representation of the minimum potential/complementary energy principles in terms of piecewise constant polarization fields relative to a reference material. This framework allows rigorous bounds to be obtained by choosing suitable reference materials. The HS bounds, although originally restricted to isotropic phases, were generalized by Walpole [333, 334, 335] to anisotropic phases. The HSW bounds are the tightest bounds that can be stated irrespective of the geometry of the microstructure and, therefore, are always valid if the composite phases are firmly bonded together and homogeneously distributed. Nevertheless, Qiu and Weng [252] showed that the MT method provides elastic moduli outside the HSW bounds for randomly oriented rod-like transversely isotropic inclusions, as typically assumed for CNTs. Therefore, the MT approach cannot be considered acceptable in these cases. Gommers *et al.* [112] even revealed that for two-phase composite materials some of the MT moduli can exceed the Voigt bound, less restrictive than the upper HSW bound. Another source of criticism of the MT method concerns its estimates at high filler concentrations. As discussed by Ferrari and Johnson [91], the MT estimates depend upon the matrix moduli at limit filler contents close to one, that is to say only inclusions, what discourages the use of the MT method for high volume fractions. Finally, it has been demonstrated that the MT model does not guarantee the diagonal symmetry of the estimated stiffness tensors for non-aligned phases [24, 232, 252, 89]. From an energy argument, a constitutive tensor must possess diagonal symmetry. Otherwise, the effective media would not possess strain energy function and, thus, would not correspond to a conservative material. Therefore, the use of the MT is only justified in the cases in which symmetry is ensured such as [89]: (i) random orientation distribution of inclusions, (ii) perfect alignment of inclusions, (iii) isotropic inclusions, and (iv) spherical inclusions. Amongst these cases, only (ii) and (iii) are sufficient for the MT stiffness not to exhibit dependence on the matrix material properties at the unitary filler concentration limit. Thence, the use of the MT method is counter-productive for two-phase composites doped with high concentrations of anisotropic fibers, even if these are spherical or randomly oriented.

In light of the aforementioned deficiencies, some authors have sought alternative approaches. One of the first solutions was presented by Walpole [335] who suggested a normalization of the strain concentration tensors to overcome the asymmetry inconsistency of the MT method. That approach was successfully adopted by Imakuma and Nemat-Nasser [146] and Nemat-Nasser and Obata [227] in their self-consistent modeling of finite deformations of polycristalline solids. In the literature, some other research works can be found on the homogenization of composites with anisotropic inclusions exhibiting non-trivial orientation distributions [245, 302, 204, 272, 273], as well as non-dilute volume fractions of the reinforcement phase [318, 319, 320, 219, 41]. It is worth noting the contribution by Ferrari [90], and posteriorly adopted by Dunn *et al.* [76], who proposed using the strain-concentration tensor to be given by the MT concentration tensor for perfectly aligned short fibers. In those works, Ferrari's approach was proved to provide diagonally symmetric stiffness tensors for general filler orientation distributions, and identically results to the MT method for fully aligned configurations. Ferrari's approach was also utilized by Gommers *et al.* [112] for textile composite materials with similar conclusions. Another relevant work was the one by Schjødt-Thomsen and Pyrz (STP) [274] who proposed a novel micromechanics approach based upon the direct integration of the MT stiffness tensor for perfectly aligned inclusions. Hence, the orientation distribution is accounted for by averaging the constitutive tensor weighted by an orientation distribution function. Since it is well known that the MT stiffness tensor of composites doped with anisotropic fully aligned inclusions is symmetric [252], the STP approach always provides diagonally symmetric estimates. Odegard *et al.* [236] presented an interesting multiscale technique to compute the effective elastic properties of CNT-reinforced polymer composites. In that work, different orientation distributions of fibers were analyzed by the MT approach based on Marzari and Ferrari's results [204]. Zhupanska [393] studied the applicability of the MT method to estimate the elastic moduli of buckypaper doped with non-trivial orientation distributions of SWCNTs. In a similar way to the analysis in Qiu and Weng [252], the degree of asymmetry of the MT stiffness estimates with different misoriented SWCNTs distributions was analyzed. In the case of randomly dispersed SWCNTs, their results also showed that the MT method only provides estimates comprised between the HSW bounds for moderate filler contents, yielding inadmissible results for high filler concentrations.

It has been extensively reported in the literature that due to a high aspect ratio, up to 10^6 [57], as well as a very low bending stiffness, CNTs usually exhibit a certain degree of waviness [276, 330, 246]. Also, all results in the literature agree to report curviness as a detrimental factor to the macroscopic mechanical performance of CNT-based composites. Finite element simulations have been proposed by Fisher *et al.* [93] and Bradshaw *et al.* [34] to analyze planar sinusoidal CNTs as proposed by Hsiao and Daniel [138]. In those works, two different methodologies, so-called Effective Reinforcing Modulus (ERM) and Numerical Strain Concentration Tensor (NSCT), were presented. The ERM approach consists of replacing the wavy CNTs by equivalent straight fibers with a reduced Young's modulus extracted from the finite element simulations. On the contrary, in the NSCT method, the dilute strain concentration tensor is evaluated numerically. Bradshaw and co-authors compared both methodologies and also proposed an Analytical Long Wavelength (ALW) model based on the Eshelby's equivalent inclusion method. Their results demonstrated that planar sinusoidal CNTs lead to orthotropic composites with substantial decreases in the effective elastic moduli in the fiber direction. The authors also showed that the numerical solutions tend to the analytical ALW results for increasing fiber wavelength-to-diameter ratios. In the case of random distributions of wavy fibers, the effective Young's modulus was shown to be decreasing with respect to wavelength-to-diameter ratio. Conversely, since the ALW model is based on the assumption of wavy fibers as a continuous sequence of misoriented straight fibers, the analytical results were shown insensitive to curviness for filler random distributions. Another noteworthy contribution was done by Shi *et al.* [282] who extended the MT method for three-dimensional helical CNTs. In this case, the results showed that composites doped with aligned wavy CNTs experience critical reductions in the longitudinal modulus, whilst the lateral modulus slightly increases. Yanase *et al.* [364] proposed an ad hoc Eshelby tensor to account for planar sinusoidal CNTs. In their model, the integration of localized changes in orientation was combined with the MT model to derive closed-form solutions of the effective stiffness. Matveeva *et al.* [209] studied both sinusoidal and helical models by finite element-based homogenization methods, analytical models and MD simulations. It was shown that both geometries significantly reduce the longitudinal elastic stiffness of the composite in the fiber direction.

Finally, a second important phenomenon to be taken into account in the simulation of CNT-based nanocomposites is the appearance of non-uniform spatial distributions of CNTs. Due to the electronic configuration of the tube walls and their high specific surface area, and therefore, large vdW attraction forces [9, 186, 352], CNTs tend to agglomerate in bundles. Although there exists a variety of techniques to improve the dispersion of the fillers, such as the use of dispersants or sonication, the achievement of uniform CNT dispersions is still an intricate task. A noticeable contribution in this respect is the work by Shi *et al.* [282] who introduced a two-parameter agglomeration model. That approach consists of considering the agglomerates as ellipsoidal inclusions so that one can conduct the homogenization process in two separate steps. First, the effective properties of the surrounding matrix and the bundles, i.e. matrix doped with low and high CNT volume fractions, respectively, are computed. Secondly, the bundles are now considered as ellipsoidal inclusions embedded in the surrounding composite matrix. To this aim, two agglomeration parameters are defined, one controlling the ratio of CNT volume within the bundles with respect to the total CNT volume, and another setting the volume ratio of bundles with respect to the total volume of the composite. Their results demonstrated substantial weakening effects of agglomeration in the macroscopic elastic moduli of CNT-reinforced composites.

2.1.2 Functionally graded CNT-reinforced structures

Drawn by the exceptional properties of CNTs as mechanical reinforcements, the number of publications dealing with the static and dynamic analysis of CNTRC structural elements have increased considerably in recent years. Wuite and Adali [358] studied the bending behavior of classical symmetric cross-ply and angle-ply laminated beams reinforced by aligned CNTs and isotropic beams reinforced by randomly oriented CNTs. By using a micromechanical constitutive model based on the Mori-Tanaka method, they highlighted that small concentrations of CNTs lead to significant improvements in the stiffness of the composite beams. Vodenitcharova and Zhang [331] developed a continuum model for the uniform bending and bending-induced buckling of a straight nanocomposite beam with circular cross section reinforced by a SWNT. Their results showed that although the addition of SWNTs to a matrix material increases the macroscopic load carrying capacity, SWCNTs locally buckle at smaller bending angles and greater flattening ratios for thicker matrix layers. Formica *et al.* [95] studied the vibrational properties of cantilevered CNTRC plates with the Mori-Tanaka approach and finite element modeling. Their results demonstrated the ability of CNTs to tune the vibrational properties of composites and increase the fundamental frequencies up to 500%. These exceptional properties have motivated many researchers to attempt to optimize the contribution of CNTs. Arani *et al.* [19] investigated analytically and numerically the buckling behavior of CNTRC rectangular plates. Based on the classical laminate plate theory and the third-order shear deformation theory for moderately thick plates, those authors optimized the orientation of CNTs to achieve the highest critical loads. Another example is the research work conducted by Rokni *et al.* [260]. By dividing a beam along its longitudinal and thickness direction with the inclusion proportion as the design variable, and given a total weight CNTs, those authors proposed a new two-dimensional optimum distribution of reinforcements in polymer composite micro-beams to maximize the fundamental natural frequency.

A promising direction is the application of CNTs as reinforcements in functionally graded materials (FGMs). These materials are inhomogeneous composites characterized by smooth and continuous variations in both compositional profile and material properties, feature that eludes characteristic issues of laminates such as delamination and debonding [105, 32, 156]. In addition, FGMs allow designers to optimize the contribution of each phase of the composite, which has led to an extensive number of applications in many engineering fields. It is worth noting the research work by Zhu *et al.* [390] who conducted bending and free vibration analysis of FG-CNTRC plates by using a finite element model based on the first-order shear deformation plate theory. Ke *et al.* [155] presented nonlinear free vibration analysis of FG-CNTRC beams within the framework of Timoshenko beam theory and Ritz method solved by a direct iterative technique. A remarkable conclusion of that work is that symmetrical distributions of CNTs provide the highest linear and nonlinear natural frequencies. Zhang *et al.* [391] proposed a meshless local Petrov-Galerkin approach based on the moving Kriging interpolation technique to analyze the geometrically nonlinear thermoelastic behavior of functionally graded plates in thermal environments. Aragh *et al.* [18] utilized the Eshelby-Mori-Tanaka approach along with a 2-D generalized differential quadrature method to investigate the vibrational behavior of rectangular plates resting on elastic foundations. Alibeigloo and Liew [7] studied the bending behavior of FG-CNTRC plates with simply supported edges subjected to thermo-mechanical loading conditions by the 3D elasticity theory and using the Fourier series expansion and state-space method. That work was extended by Alibeigloo and Emtehani [8] for various boundary conditions by using the differential quadrature method. Zhang *et al.* [383] proposed a state-space Levy method for the vibration analysis of FG-CNTRC plates subjected to in-plane loads based on higher-order shear deformation theory. In accordance with previous studies, those authors concluded that symmetrical distributions of CNTs, with maximum filler concentrations at the top and bottom faces of the plates, yield the largest resonant frequencies and buckling loads.

2.1.3 Uncertainty analysis of CNT-reinforced composites

There is still a lack of deeper knowledge of the uncertainty associated with the incorporation of CNTs into functionally graded composite materials. Moreover, the uncertainty propagation in nanocomposite structures remains an unsolved issue. Rouhi and Rohani [261] analyzed the probabilistic response characteristics of a thin-walled nanocomposite cylinder subjected to buckling instability. They employed micromechanical approaches based on the Eshelby-Mori-Tanaka method for the mathematical modeling of randomly distributed carbon nanofibers (CNFs) in a thermoset polymer material. By using a dual metamodeling procedure, uncertainty in CNF material properties, CNF waviness and CNF-matrix interphase were taken into consideration to carry out a reliability-based design optimization in terms of a prescribed maximum probability of failure. Ghasemi *et al.* [108] proposed a Kriging metamodel-based probabilistic optimization procedure. By linking the different scales (nano-, micro-, meso- and macro- scales) by multi-scale analysis, the Eshelby-Mori-Tanaka model and finite element method, they considered three different uncertainty sources: material uncertainties (length, waviness, agglomeration, orientation and dispersion of CNTs), structural uncertainties (geometry, boundary and loading conditions) and modeling uncertainties (discretization and approximation errors). Their results showed that the failure probability strongly depends on the CNT parameters, especially the CNT volume fraction and the waviness. In addition, they also concluded that the influence of the CNT agglomeration is nearly negligible.

Most researchers restrict the aim of their studies to the analysis of composite materials with uniform or linear grading profiles. However, because of its manufacturing complexity, FG-CNTRC structures may be expected to present process-induced uncertainties that make these linear distributions rather improbable. Thus, two main sources of uncertainty must be considered: uncertainty in the material properties (matrix/CNT) and uncertainty in the reinforcement grading profile which, in turn, propagates the prior uncertainties within the thickness of the specimen. In order to increase the computational efficiency, the expensive-to-evaluate finite element models can be surrogated by more computationally efficient metamodels. In particular, a special attention has been devoted to the Kriging and the Random Sampling High-Dimensional Model Representation (RS-HDMR) surrogate models. The RS-HDMR approach has been employed in many different fields [183, 55, 224]. For instance, the uncertainty of the dynamic characteristics of angle-ply composite plates was studied by Dey *et al.* [70], as well as the effects of noise on stochastic frequency response functions [68], and thermal uncertainty propagation in laminated composite plates [67]. Dey *et al.* [69] also employed the Kriging metamodel to analyze the uncertainty propagation in the free vibration characteristics of laminated shallow doubly curved shells.

2.2 Analytical mechanical homogenization techniques [1]

In the realm of CNT nanocomposites, the Extended Rule of Mixtures (EROM) and the Mori-Tanaka (MT) method are widely used for the determination of the macroscopic mechanical properties. The theoretical framework of both approaches are outlined below.

---

[1] An extended version of this section is found in paper J.

2.2.1 Extended Rule of Mixtures (EROM)

The EROM is based upon a modification of the classical Voigt and Reuss bounds. Under the assumption of fully aligned CNTs, the effective material properties of CNTRCs can be expressed as [279]:

$$E_{11} = \eta_1 f_r E_{11}^{CNT} + f_m E^m \tag{2.1a}$$

$$\frac{\eta_2}{E_{22}} = \frac{f_r}{E_{22}^{CNT}} + \frac{f_m}{E^m} \tag{2.1b}$$

$$\frac{\eta_3}{G_{12}} = \frac{f_r}{G_{12}^{CNT}} + \frac{f_m}{G^m} \tag{2.1c}$$

where E_{11}^{CNT}, E_{22}^{CNT} and G_{12}^{CNT} indicate the Young's moduli and shear modulus of CNTs, respectively, and E^m and G^m represent the corresponding properties of the isotropic matrix. In order to account for the scale-dependent material properties, the CNT efficiency parameters, η_j (j=1,2,3), are introduced and can be calculated by matching the effective properties of the CNTRC obtained from a MD or multi-scale simulation with those from the rule of mixtures. f_r and f_m are respectively the volume fractions of the carbon nanotubes and matrix, whose sum equals one. Similarly, the thermal expansion coefficients in the longitudinal and transverse directions, α_{11} and α_{22}, Poisson's ratio ν_{12} and the density ρ of the nanocomposites can be determined in a similar same way as:

$$\nu_{12} = f_r \nu_{12}^{CNT} + f_m \nu^m \tag{2.2a}$$

$$\rho = f_r \rho^{CNT} + f_m \rho^m \tag{2.2b}$$

$$\alpha_{11} = f_r \alpha_{11}^{CNT} + f_m \alpha^m \tag{2.2c}$$

$$\alpha_{22} = (1+\nu_{12}^{CNT}) f_r \alpha_{22}^{CNT} + (1+\nu^m) f_m \alpha^m - \nu_{12}\alpha_{11} \tag{2.2d}$$

where ν_{12}^{CNT} and ν^m are Poisson's ratios, and α_{11}^{CNT}, α_{22}^{CNT} and α^m are the thermal expansion coefficients of the CNT and matrix, respectively. In addition, we assume that $G_{23} = G_{13} = G_{12}$. The rest of the other effective mechanical properties are defined as follows:

$$\begin{aligned} &E_{33} = E_{22}, \quad && G_{13} = G_{12}, \quad && \nu_{23} = \tfrac{E_{22}}{2G_{23}} - 1, \\ &\nu_{13} = \nu_{12}, && \nu_{31} = \nu_{21}, && \nu_{32} = \nu_{23}, \\ &\nu_{21} = \nu_{12}\tfrac{E_{22}}{E_{11}} \end{aligned} \tag{2.3}$$

2.2.2 Fundamentals of effective medium theory

Let V denote the Representative Volume Element (RVE) in Fig. 2.1 of a linear elastic polymer matrix doped with dispersed CNTs. It is assumed that the RVE contains a sufficient number of fillers in such a way that the overall properties of the composite are statistically represented [228]. It is assumed that the CNTs are transversely isotropic ellipsoidal inclusions dispersed according to an arbitrary orientation distribution. The matrix is defined isotropic and perfect bonding between phases is assumed. In accordance with the notation of Hill [134] and Walpole [335], the tensor of elastic moduli of the CNTs, $\mathbf{C}_f$, can be denoted as $\mathbf{C}_f = (2k_r,l_r,n_r,2m_r,2p_r)$, where k_r, l_r, m_r, n_r and p_r are fiber Hill's elastic moduli [134]; k_r is the plane-strain bulk modulus normal to the fiber direction, n_r is the uniaxial tension modulus in the fiber direction, l_r is the associated cross modulus, m_r and p_r are the shear moduli in planes normal and parallel to the fiber direction, respectively. Similarly, the tensor of elastic moduli of the matrix phase can be noted as $\mathbf{C}_m = (3\kappa_m,2\mu_m)$, with κ_m and μ_m being the matrix's bulk and shear moduli, respectively. In conjunction with the used notations, the constitutive matrix for inclusions with transversely isotropic properties (local x_2'' is the axis of material symmetry) takes the form:

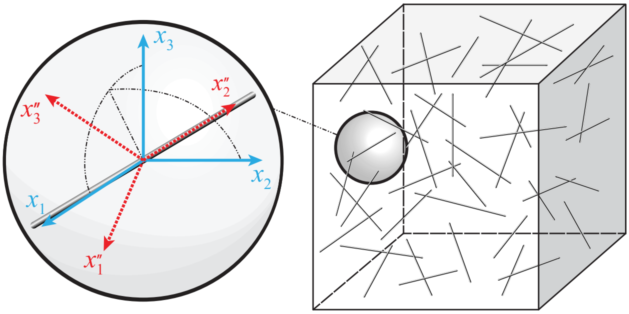

Figure 2.1 Representative Volume Element (RVE) including well dispersed straight CNTs.

$$\mathbf{C}_f = \begin{bmatrix} k_r+m_r & l_r & k_r-m_r & 0 & 0 & 0 \\ l_r & n_r & l_r & 0 & 0 & 0 \\ k_r-m_r & l_r & k_r+m_r & 0 & 0 & 0 \\ 0 & 0 & 0 & p_r & 0 & 0 \\ 0 & 0 & 0 & 0 & m_r & 0 \\ 0 & 0 & 0 & 0 & 0 & p_r \end{bmatrix} \tag{2.4}$$

The material properties of the composite can be also expressed in terms of engineering constants as [317]:

$$E_{11} = n_r - \frac{l^2}{k_r}, \quad E_{22} = \frac{4m_r(k_r - l_r^2)}{k - l^2 + m_r n_r}, \tag{2.5}$$

$$\nu_{12} = \nu_{13} = \frac{l_r}{2k_r}, \quad \nu_{23} = \frac{n_r(k_r - m_r) - l_r^2}{n_r(k_r + m_r) - l_r^2}, \tag{2.6}$$

$$G_{12} = G_{13} = p_r \tag{2.7}$$

In order to describe the filler orientation, a reference local coordinate system $\mathrm{K}'' \equiv \left\{0; x_1'' x_2'' x_3''\right\}$ is associated with each fiber. In this thesis, it is assumed that all the inclusions in the two-phase composite are equal and defined as ellipsoids with an aspect ratio $a_1 = a_3 < a_2$, being the major axis aligned in the local x_2'' direction as indicated in Fig. 2.2. In general, three Euler angles, θ, γ and ψ, are required to describe the relative orientation of any orthogonal coordinate system with respect to the global one, K$\equiv\{0;x_1x_2x_3\}$. Hence, the transformation consists of three successive rotations. According to the aforementioned filler configuration, θ stands for a rotation angle around the x_2 axis and transforms the global coordinate system K into an auxiliary coordinate system K$'$, γ denotes the rotation angle around the resultant x_1' and, finally, ψ is the rotation angle around x_2''. Since x_2'' axis is parallel to the axis of rotational symmetry of the ellipsoids, rotation around this axis produces no change. Therefore, ψ can be chosen arbitrarily, e.g. ψ=0. The resultant configuration is shown in Fig. 2.2, where the polar and azimuthal angles, θ and γ, are defined by:

$$\theta \equiv \widehat{x_1x_1'}, \quad \gamma \equiv \widehat{x_3'x_3''} \tag{2.8}$$

The base vectors $\mathbf{e}_i$ and $\mathbf{e}_i''$ of the global and local coordinate systems are thus related via the transformation matrix $\mathbf{g}$:

$$\mathbf{e}_i'' = g_{ij}\mathbf{e}_j \tag{2.9}$$

where $\mathbf{g}$ is defined by the successive rotation around x_2 and x_1 axes, R_1 and R_2, leading to:

$$\mathbf{g} = [R_1(\gamma)]\,[R_2(\theta)] = \begin{bmatrix} \cos(\gamma) & 0 & \sin(\gamma) \\ -\sin(\theta)\sin(\gamma) & \cos(\theta) & \cos(\gamma)\sin(\theta) \\ -\cos(\theta)\sin(\gamma) & -\sin(\theta) & \cos(\theta)\cos(\gamma) \end{bmatrix} \tag{2.10}$$

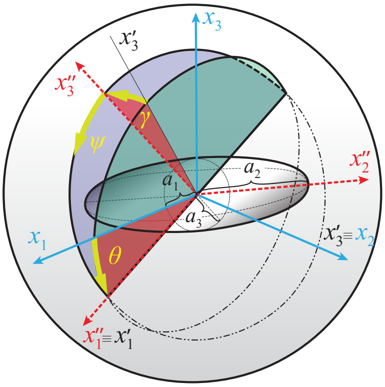

Figure 2.2 Euler angles defining the relation between the orientation of an ellipsoidal inclusion with an aspect ratio $a_1 = a_3 < a_2$ in the local coordinate system, $\left\{0;x_1''x_2''x_3''\right\}$ and the global coordinate system, $\left\{0;x_1x_2x_3\right\}$.

Hence, the coordinate transformation of a fourth-rank tensor $\mathbf{P}$ into the local coordinate system K$''$ is explicitly represented in terms of the transformation matrix as:

$$P_{ijlk}'' = g_{ip}g_{jq}g_{kr}g_{ls}P_{pqrs} \tag{2.11}$$

Due to the high number of fillers contained in the RVE, the description of their orientation field is of statistical nature. The probability of a fiber lying in an infinitesimal range of angles θ and $\theta + \mathrm{d}\theta$, and γ and $\gamma + \mathrm{d}\gamma$ is given by $\Omega(\theta,\gamma)\sin(\theta)\mathrm{d}\theta\mathrm{d}\gamma$, with $\Omega(\theta,\gamma)$ being the so-called Orientation Distribution Function (ODF). Any ODF must satisfy the following normalization condition:

$$\int_0^{2\pi}\int_0^{\pi/2}\Omega(\theta,\gamma)\sin(\theta)\mathrm{d}\theta\mathrm{d}\gamma = 1 \tag{2.12}$$

The integration of any ODF weighted function $F(\theta,\gamma)$ over all possible orientations in the Euler space, also referred to as the orientational average of F, $\langle F\rangle$, is defined through:

$$\langle F\rangle = \int_0^{2\pi}\int_0^{\pi/2} F(\theta,\gamma)\Omega(\theta,\gamma)\sin(\theta)\mathrm{d}\theta\mathrm{d}\gamma \tag{2.13}$$

Throughout this work, the superscripts "f" and "m" refer the corresponding quantity to the inclusion and matrix occupied portions of V. With this convention, the relationships between the total average strain and stress tensors in the RVE, $\overline{\varepsilon}$ and $\overline{\sigma}$, respectively, are defined by the rule of mixtures as follows:

$$\overline{\varepsilon} = f_r\left\langle\overline{\varepsilon}^f\right\rangle + (1 - f_r)\overline{\varepsilon}^m \tag{2.14}$$

$$\overline{\sigma} = f_r\left\langle\overline{\sigma}^f\right\rangle + (1 - f_r)\overline{\sigma}^m \tag{2.15}$$

Here, $\overline{\varepsilon}^m$ and $\overline{\sigma}^m$ are the average strain and stress in the matrix, and $\overline{\varepsilon}^f$ and $\overline{\sigma}^f$ are the corresponding orientation-dependent average fields in a typical inclusion. f_r denotes the volume fraction occupied by the inclusions and, therefore, the volume fraction of the matrix is $f_m = 1 - f_r$. In addition, the interaction between the average inclusion strain with the corresponding average matrix strain is governed by the strain concentration tensor $\mathbf{A}$ as:

$$\overline{\varepsilon}^f = \mathbf{A} : \overline{\varepsilon}^m \tag{2.16}$$

Let us note that tensor $\mathbf{A}$ is not necessarily diagonally symmetric, $A_{ijkl} \neq A_{klij}$, although minor symmetry is always guaranteed, that is $A_{ijkl} = A_{jikl} = A_{ijlk}$. Equations (2.14), (2.15), and (2.16), as well as the linear elastic constitutive laws for both phases, namely CNTs and matrix as $\overline{\sigma}^f = \mathbf{C}_f : \overline{\varepsilon}^f$ and $\overline{\sigma}^m = \mathbf{C}_m : \overline{\varepsilon}^m$, respectively, suffice to identify the equivalent material effective stiffness $\mathbf{C}$ defined through $\overline{\sigma} = \mathbf{C} : \overline{\varepsilon}$, and whose resulting expression reads:

$$\mathbf{C} = \mathbf{C}_m + f_r\left\langle\left(\mathbf{C}_f - \mathbf{C}_m\right) : \mathbf{A}\right\rangle \tag{2.17}$$

Different assumptions on the tensor $\mathbf{A}$ correspond to different effective medium theories.

2.2.3 Mean-field micromechanics modeling

On the basis of the previously outlined framework, it is clear that the estimate of the effective stiffness tensor depends upon the definition of the concentration tensor $\mathbf{A}$. Various micromechanics models have been proposed in the literature, amongst which the Mori-Tanaka and the self-consistent effective-medium approaches are the most commonly used. In addition, in the light of the previously mentioned limitations of the Mori-Tanaka method, some alternative approaches have been proposed in the literature. In particular, it is worth noting the approaches proposed by Ferrari [90] and Schjødt-Thomsen and Pyrz [274]. The basic assumptions and fundamentals of these approaches are reviewed below.

2.2.3.1 Mori-Tanaka approach

The Mori-Tanaka (MT) method [220] is one of the most commonly used homogenization approaches due to its simplicity. The MT method allows extending the theory of Eshelby [82, 83], restricted to one single inclusion embedded in a semi-infinite elastic, homogeneous and isotropic medium, to the case of a finite domain doped with multiple inhomogeneities. The Eshelby-Mori-Tanaka method, also known as the equivalent inclusion-average stress method, is based on the equivalent elastic inclusion idea of Eshelby and the concept of average stress in the matrix stated by Mori-Tanaka. The Eshelby's equivalent inclusion method [82] showed that the strain concentration tensor for the limit case of a single anisotropic ellipsoidal inhomogeneity in an infinite matrix, $\mathbf{A}^{dil}$, is defined as:

$$\mathbf{A}^{dil} = \left[\mathbf{I} + \mathbf{S} : \mathbf{C}_m^{-1} : \left(\mathbf{C}_f - \mathbf{C}_m\right)\right]^{-1} \tag{2.18}$$

where $\mathbf{I}$ (I_{ijkl}) is the fourth rank identity tensor, and $\mathbf{S}$ is the Eshelby's tensor, well documented in Mura [225]. Also, further details can be found in Appendix C. Let us remark that, in the case of ellipsoidal inclusions embedded in an isotropic medium, the Eshelby's tensor depends upon the aspect ratio of the inclusions and the Poisson's ratio of the matrix. Then, at non-dilute volumetric fiber concentrations, the effective elastic tensor given by the Eshelby-Mori-Tanaka method writes according to Benveniste's revision [23]:

$$\mathbf{C}^{MT} = \mathbf{C}_m + f_r \left\langle \left(\mathbf{C}_f - \mathbf{C}_m\right) : \mathbf{A}^{MT} \right\rangle \tag{2.19}$$

with the strain concentration tensor $\mathbf{A}^{MT}$:

$$\mathbf{A}^{MT} = \mathbf{A}^{dil} : \left[(1 - f_r)\mathbf{I} + f_r \left\langle \mathbf{A}^{dil} \right\rangle\right]^{-1} \tag{2.20}$$

Hence, Eq. (2.19) can be rearranged in a more compact form as:

$$\mathbf{C}^{MT} = \left(f_m \mathbf{C}_m + f_r \left\langle \mathbf{C}_r : \mathbf{A}^{dil} \right\rangle\right) : \left(f_r \mathbf{I} + f_r \left\langle \mathbf{A}^{dil} \right\rangle\right)^{-1} \tag{2.21}$$

In the case of perfectly aligned fillers, the orientational averages are omitted and the stiffness tensor can be cast into:

$$\mathbf{C}^{MT} = \left(f_m \mathbf{C}_m + f_r \mathbf{C}_r : \mathbf{A}^{dil}\right) : \left(f_r \mathbf{I} + f_r \mathbf{A}^{dil}\right)^{-1} \tag{2.22}$$

The MT approach has been successfully applied to two-phase composite materials. However, the application of the MT method to multi-phase composites containing reinforcements with either different geometries or alignments has been showed questionable.

2.2.3.2 Self-consistent effective-medium approach

In the case of high volume fractions of inhomogeneities, the non-interaction hypothesis of the Mori-Tanaka method becomes uncertain. Typically, an alternative strategy for obtaining mean field estimates for the elastic behavior of non-dilute inhomogeneous materials is the Self-Consistent (SC) method. The SC method approximates the interaction between the phases by assuming that inclusions are embedded in an infinite volume of an effective medium with yet unknown elastic tensor C^*. Hence, the effective stiffness tensor provided by the so-called classical self-consistent scheme writes [134]:

$$\mathbf{C}^{SC} = \mathbf{C}^* + f_r \left\langle \left(\mathbf{C}_f - \mathbf{C}^* \right) : \mathbf{A}^{SC} \right\rangle \tag{2.23}$$

where $\mathbf{A}^{SC}$ reads:

$$\mathbf{A}^{SC} = \left[\mathbf{I} + \mathbf{S}^* : (\mathbf{C}^*)^{-1} : (\mathbf{C}_r - \mathbf{C}^*) \right]^{-1} \tag{2.24}$$

Now Eshelby's tensor S^* is a function of the effective stiffness tensor C^* instead of C_m. Since the effective stiffness tensor C^* is not known a priori, the self-consistent method is an implicit method and must be solved by an iterative algorithm. An additional change is that Eshelby's tensor S^* depends on C^*, which is now transversely isotropic. Expressions for Eshelby's tensor for an ellipsoid of revolution in a transversely isotropic matrix were given by Chou *et al.* [54] and by Lin and Mura [193], and are included in the Appendix D.

2.2.3.3 Extended Mori-Tanaka approaches

As previously discussed, a few research works in the literature report that the MT method may provide diagonally asymmetric stiffness tensors, as well as may violate the Hashin-Shtrikman-Walpole bounds [24, 232, 252, 89]. From Eqs. (2.17) and (2.20), note that the effective stiffness tensor $\mathbf{C}^{MT}$ is diagonally symmetric, i.e. $C^{MT}_{ijkl} = C^{MT}_{klij}$, if and only if the term $\left\langle \left(\mathbf{C}_f - \mathbf{C}_m \right) : \mathbf{A}^{MT} \right\rangle$ is symmetric for non-vanishing values of f_r. Nonetheless, several works in the literature conclude that this condition is not met for general two-phase composites [89, 187, 274], what results in unacceptable stiffness tensors from an energy argument. The main reason for this asymmetry is attributed to the strain concentration tensors which are generally diagonally non-symmetric [77]. Therefore, the use of the MT is only justified in cases in which symmetry is guaranteed such as [89]:

1. Random orientation distribution of inclusions.
2. Perfect alignment of the inclusions.
3. Isotropic inclusions.
4. Spherical inclusions.

It may be noted that neither disk-like ($a_3 = 0$) nor cylindrical ($a_3 = \infty$) inclusions, being the latter typically used for describing CNTs, suffice to ensure symmetry in general. A second weakness of the MT method concerns questionable predictions at high filler concentrations. In particular, as discussed by Ferrari and Johnson [91], the resulting $\mathbf{C}^{MT}$ in Eq. (2.19) depends on the matrix moduli for f_r approaching one. Of the symmetry-ensuring conditions listed above, only (2) and (3) are sufficient for the Mori-Tanaka stiffness not to exhibit dependence on the matrix material properties at the limit filler concentration $f_r = 1$. This fact discourages the use of the MT method for two-phase composites with high concentration of anisotropic fillers, even if these are spherical or randomly oriented. Qui and Weng [252] proved that, only in the case of perfect alignment, the effective stiffness tensor obtained using the MT approach preserves the symmetry and stays within the Hashin-Shtrikman-Walpole (HSW) bounds.

In view of the aforementioned issues, some authors have sought alternative approaches. These include the approaches proposed by Ferrari [90], and later developed by Dunn *et al.* [76] for two-phase composites, as well as the STP approach [274].

- Dunn (DUN) approach

  Following the studies of Ferrari [90], Dunn *et al.* [76] proposed using the strain-concentration tensor to be given by the MT concentration tensor for perfectly aligned fibers as follows:

$$\mathbf{A}^{DUN} = \mathbf{A}^{dil} : \left[(1-f_r)\mathbf{I} + f_r\mathbf{A}^{dil}\right]^{-1} \tag{2.25}$$

  thus, the stiffness tensor for two-phase composites with inclusions of identical shape reads:

$$\mathbf{C}^{DUN} = \mathbf{C}_m + f_r\left[\left\langle \mathbf{C}_f : \mathbf{A}^{DUN}\right\rangle - (1-f_r)\left\langle \mathbf{A}^{DUN}\right\rangle\right] \tag{2.26}$$

- Schjødt-Thomsen and Pyrz (STP) approach

  Another prominent alternative is the one proposed by Schjødt-Thomsen and Pyrz (STP) [274]. That approach utilizes a direct integration of the MT stiffness tensor for the case of perfectly aligned fibers in Eq. (2.22) with respect to the ODF as:

$$\mathbf{C}^{STP} = \int_0^{2\pi}\int_0^{\pi/2} \mathbf{C}(\theta,\gamma)\Omega(\theta,\gamma)\sin(\theta)\mathrm{d}\theta\mathrm{d}\gamma \tag{2.27}$$

  with $C(\theta,\gamma)_{ijkl} = g_{ip}g_{jq}g_{kr}g_{ls}C(0,0)^{MT}_{pqrs}$.

2.2.4 Modeling of CNT waviness

A large number of experimental investigations have reported about the wavy state of CNTs dispersed in composites [276, 330, 246]. Due to their large aspect ratio, with typical lengths between 0.1 and 10 µm and diameters ranging from 10 to 15 nm, as well as very low bending stiffness, CNTs usually present a certain degree of waviness. In order to characterize the waviness of CNTs, different curved geometries have been proposed in the literature such as planar sinusoidal curves [138, 93, 322, 369, 364], helixes [282, 103, 102] or polylines with straight segments [21, 73]. In the present work, both planar sinusoidal and helical approaches, as sketched in Figs. 2.3 (a) and (b), respectively, are compared. Both microstructures are assumed to be periodic and, therefore, it is sufficient to consider one single period to compute their macroscopic stiffness. Three different approaches are considered, namely the MT method by Shi *et al.* [282], the extension of the STP approach for wavy CNTs, and the ad hoc Eshelby's tensor approach by Yanase *et al.* [364]. The theoretical background of these approaches is outlined below.

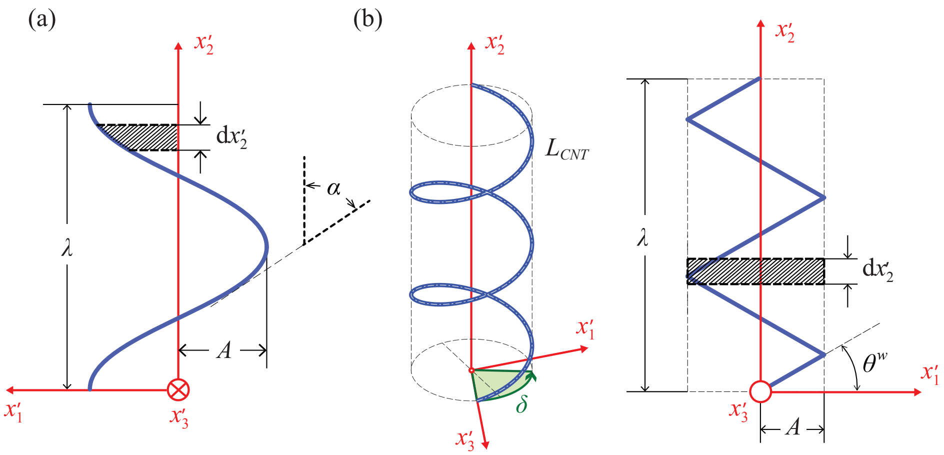

Figure 2.3 Planar sinusoidal (a) and helical model (b) of a curved CNT.

2.2.4.1 Planar sinusoidal geometry

The planar sinusoidal approach in Fig. 2.3 (a) is defined in the $x'_1 - x'_2$ plane by its amplitude, A, and wave length, λ, as:

$$x'_3 = 0, \quad x'_2 = x'_2, \quad x'_1 = A\cos\frac{2\pi x'_2}{\lambda} \quad x'_2 \in [0,\lambda] \tag{2.28}$$

Eshelby-Mori-Tanaka approach The application of the MT framework to the study of wavy CNT-reinforced composites was first conducted by Shi *et al.* [282] for the analysis of helical nanotubes. The main hypothesis of this approach is that, when the filler wavelength becomes far larger than its amplitude, the average strain in the filler section approaches that of an infinitely long straight fiber. Hence, the average strain at every differential slice, dx'_2, can be estimated as that of an infinitely long straight fiber oriented at an angle $\alpha(x'_2)$. On this basis, the approach proposed by Shi *et al.* [282] can be extended to planar sinusoidal CNTs as follows:

$$\begin{aligned}\mathbf{C}^{MT} = {} & \left[\frac{f_r}{V_c}\int_0^{\lambda}\left(\mathbf{C}_r(y):\mathbf{A}(\alpha(y),0):\mathbf{C}_m^{-1}\right)\mathrm{d}V_c + f_m\mathbf{I}\right]: \\ & :\left[\frac{f_r}{V_c}\int_0^{\lambda}\left(\mathbf{A}(\alpha(y),0):\mathbf{C}_m^{-1}\right)\mathrm{d}V_c + f_m\mathbf{C}_m^{-1}\right]^{-1}\end{aligned} \tag{2.29}$$

with V_c being the volume of a CNT. The angle $\alpha(x_2')$ can be obtained by differentiating Eq. (2.28), what yields:

$$\alpha(x_2') = \tan^{-1}\left[\frac{\mathrm{d}x_1'}{\mathrm{d}x_2'}\right] = \tan^{-1}\left[-\frac{2\pi A}{\lambda}\sin\left(\frac{2\pi x_2'}{\lambda}\right)\right] \tag{2.30}$$

The volume occupied by the infinitesimal slice, $\mathrm{d}V_c$, of a CNT with diameter d_c is given by:

$$\mathrm{d}V_c = \frac{\pi d_c^2}{4}\frac{\mathrm{d}x_2'}{\cos\alpha(x_2')} \tag{2.31}$$

and therefore

$$V_c = \frac{\pi d_c^2}{4}\int_0^\lambda \frac{\mathrm{d}x_2'}{\cos\alpha(x_2')} = \frac{\pi d_c^2}{4} I_v \tag{2.32}$$

Then, Eq. (2.29) can be rearranged as follows:

$$\begin{aligned}\mathbf{C}^{MT} =& \left[\frac{f_r}{I_v}\int_0^\lambda \left(\mathbf{C}_r(x_2') : \mathbf{A}(\alpha(x_2'),0) : \mathbf{C}_m^{-1}\right)\frac{\mathrm{d}x_2'}{\cos\alpha(x_2')} + f_m\mathbf{I}\right] : \\ &: \left[\frac{f_r}{I_v}\int_0^\lambda \left(\mathbf{A}(\alpha(x_2'),0) : \mathbf{C}_m^{-1}\right)\frac{\mathrm{d}x_2'}{\cos\alpha(x_2')} + f_m\mathbf{C}_m^{-1}\right]^{-1}\end{aligned} \tag{2.33}$$

Schjødt-Thomsen and Pyrz (STP) approach The direct integration of the STP approach can be also applied in this context integrating the stiffness tensor along the curved trace as:

$$\mathbf{C}^{STP} = \frac{1}{I_v}\int_0^\lambda \frac{\mathbf{C}(\alpha(x_2'),0)}{\cos\alpha(x_2')}\mathrm{d}x_2' \tag{2.34}$$

being $\mathbf{C}(\alpha(x_2'),0)$ the MT estimate for straight fibers with polar angle $\alpha(x_2')$.

Ad hoc Eshelby's tensor approach An ad hoc Eshelby's tensor to account for waviness effects was proposed by Yanase (YNS) *et al.* [364]. According to this model, the effective stiffness of wavy CNT-reinforced composites is evaluated by the following integral:

$$\overline{\mathbf{C}} = \frac{1}{I_v}\int_0^\lambda \frac{\mathbf{C}^*(\alpha(x_2'),0)}{\cos\alpha(x_2')}\mathrm{d}x_2' \tag{2.35}$$

with $\mathbf{C}^*$ being the solution of the Eshelby's equivalent problem as:

$$\mathbf{C}^* = \mathbf{C}_m + f_r\left(\mathbf{C}_f - \mathbf{C}_m\right) : \mathbf{A}^{dil} \tag{2.36}$$

In order to reproduce Eq. (2.35) with the Eshelby's equivalent inclusion method, an ad hoc Eshelby's tensor, $\overline{\mathbf{S}}$, can be evaluated as follows:

$$\overline{\mathbf{S}} = \lim_{f_r \to 0} \left[f_r \left((\mathbf{C}_m)^{-1} : \overline{\mathbf{C}} - \mathbf{I} \right)^{-1} - \left(\mathbf{C}_f - \mathbf{C}_m \right)^{-1} : \mathbf{C}_m \right] \tag{2.37}$$

where the limit is taken to exclude the far-field interaction. Moreover, if the wavy fibers are randomly oriented, the ad hoc Eshelby's tensor of Eq. (2.37) can be integrated around the alignment axis, x_2':

$$\mathbf{S}^* = \frac{1}{2\pi} \int_0^{2\pi} \overline{\mathbf{S}}(0,\gamma)\mathrm{d}\gamma \tag{2.38}$$

Now, the effective stiffness of wavy CNT-reinforced composites at non-dilute regimes can be computed by the MT method as:

$$\mathbf{C}^{YNS} = (f_m \mathbf{C}_m + f_r \langle \mathbf{C}_r : \mathbf{A}^* \rangle) : (f_r \mathbf{I} + f_r \langle \mathbf{A}^* \rangle)^{-1} \tag{2.39}$$

where

$$\mathbf{A}^* = \left[\mathbf{I} + \mathbf{S}^* : \mathbf{C}_m^{-1} : \left(\mathbf{C}_f - \mathbf{C}_m \right) \right]^{-1} \tag{2.40}$$

2.2.4.2 Helical geometry

The helical curve is parametrized by its radius, A, spiral angle, θ^w, and polar angle, δ, as:

$$x_1' = A\sin\delta, \quad x_2' = x_2', \quad x_3' = A\cos\delta \quad x_2' \in [0,\lambda] \tag{2.41}$$

where the wave length can be expressed as $\lambda = L\sin\theta^w$, being $L = \delta A/\cos\theta^w$ the length of the curve. The spiral angle θ^w ranges from 0 to $\pi/2$ and governs the curvature of the filler. For instance, $\theta^w = \pi/2$ corresponds to a straight CNT, while $\theta^w = 0$ corresponds to a circular CNT.

Eshelby-Mori-Tanaka approach In this case, the helical approach was developed by Shi *et al.* [282] as:

$$\begin{aligned} \mathbf{C}^{MT} = & \left[\frac{f_r}{\delta} \int_0^\delta \left(\mathbf{C}_r(\theta^w,s) : \mathbf{A}(\theta^w,s) : \mathbf{C}_m^{-1} \right) \mathrm{d}s + f_m \mathbf{I} \right] : \\ & : \left[\frac{f_r}{\delta} \int_0^\delta \left(\mathbf{A}(\theta^w,s) : \mathbf{C}_m^{-1} \right) \mathrm{d}s + f_m \mathbf{C}_m^{-1} \right]^{-1} \end{aligned} \tag{2.42}$$

Schjødt-Thomsen and Pyrz (STP) approach In a similar way to planar sinusoidal configurations, the STP approach can be also applied to helical nanotubes as follows:

$$\mathbf{C}^{STP} = \frac{1}{\delta} \int_0^\delta \mathbf{C}(\theta^w,\gamma)\mathrm{d}\gamma \tag{2.43}$$

being in this case $\mathbf{C}(\theta^w, s)$ the MT estimate for straight fillers with constant polar angle θ^w and azimuthal angle γ varying from 0 to δ.

Ah hoc Eshelby's tensor approach Finally, the YNS approach can be extended to helical geometries as:

$$\overline{\mathbf{C}}^{YNS} = \frac{1}{\delta}\int_0^{\delta} \mathbf{C}^*(\theta^w, \gamma)\mathrm{d}\gamma \tag{2.44}$$

with $\mathbf{C}^*$ being the Eshelby's equivalent inclusion solution given in Eq. (2.36). In this case, helical wavy nanotubes affect both transverse directions and, thus, the integral in Eq. (2.38) is not required to model random orientations of CNTs. Hence, Eq. (2.39) can be directly used with the strain concentration tensor $\mathbf{A}^*$:

$$\mathbf{A}^* = \left[\mathbf{I} + \overline{\mathbf{S}} : \mathbf{C}_m^{-1} : \left(\mathbf{C}_f - \mathbf{C}_m\right)\right]^{-1} \tag{2.45}$$

2.2.5 Modeling of CNT agglomeration

A second important phenomenon to be taken into consideration for the simulation of CNT nano-reinforced composites is the appearance of non-uniform spatial distributions of nanoinclusions. The difficulty in obtaining good fiber dispersions is related to the circumstance that CNTs tend to agglomerate in bundles. This effect is attributed to the electronic configuration of tube walls and their high specific surface area which increases the vdW attraction forces among nanotubes [9, 186, 352]. In order to model the effective mechanical properties of non-uniform distributions of CNTs, the two-parameter agglomeration model introduced by Shi *et al.* [282] is here adopted. This approach differentiates two regions, one with high CNT concentration, corresponding to clusters, and another with low CNT concentration, i.e. the surrounding composite. Therefore, the total volume of CNTs, V_r, dispersed in the RVE, V, can be divided into the following two parts:

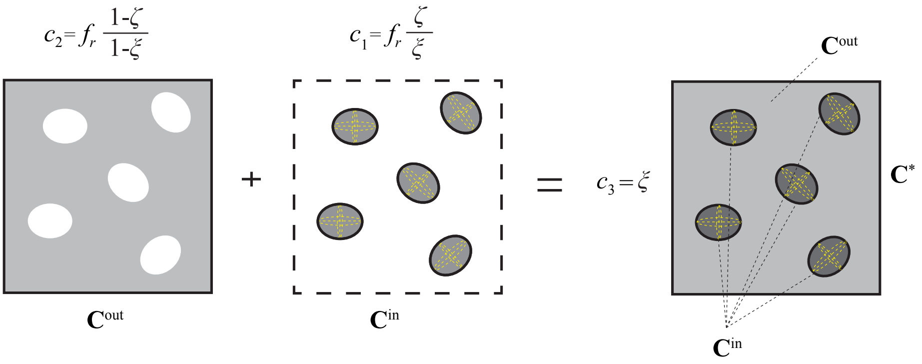

Figure 2.4 Schematic representation of the two parameter agglomeration model.

$$V_r = V_r^{bundles} + V_r^m \tag{2.46}$$

where $V_r^{bundles}$ and V_r^m denote the volumes of CNTs dispersed in the bundles and in the matrix, respectively. In order to characterize the agglomeration of CNTs in bundles, Shi *et al.* [282] introduced two parameters, ξ and ζ, as follows:

$$\xi = \frac{V_{bundles}}{V}, \quad \zeta = \frac{V_r^{bundles}}{V_r} \tag{2.47}$$

where $V_{bundles}$ is the volume occupied by the bundles in the RVE. The agglomeration parameter ξ represents the volume ratio of bundles with respect to the total volume of the RVE. On the other hand, ζ stands for the volume ratio of CNTs within the bundles with respect to the total volume of fillers. This pair of parameters unequivocally determine the agglomeration scheme as outlined in Fig. 2.4. After some straightforward manipulations, the CNT volume fractions in the bundles and the surrounding composite, c_1 and c_2, respectively, can be expressed as:

$$c_1 = f_r \frac{\zeta}{\xi}, \quad c_2 = f_r \frac{1-\zeta}{1-\xi} \tag{2.48}$$

being f_r the total volume fraction in the composite. It can be extracted from Eq. (2.48) that $\zeta \geq \xi$ must be met in order to impose a higher filler concentration in the clusters. The limit case $\zeta = \xi$ represents an uniform distribution of the fillers, whilst the heterogeneity degree grows for larger values of ζ with limit case of $\zeta = \min(1, \xi/f_r)$. Hence, the homogenization process can be carried out in two steps. Firstly, the overall constitutive tensor of the inclusions, $\mathbf{C}^{\text{in}}$, and the surrounding composite, $\mathbf{C}^{\text{out}}$, are obtained considering the polymer as the matrix phase and the nanotubes as inclusion phase with concentrations c_1 and c_2, respectively. Secondly, the effective constitutive tensor of the composite, $\mathbf{C}^*$, is computed considering the surrounding composite as matrix material and bundles as inclusions. On this basis, whichever of the previously presented micromechanical models can be extended to account for agglomeration.

In this thesis, two different configurations have been studied, namely randomly oriented CNTs, and a novel configuration of fully aligned CNTs as schematically represented in Fig. 2.5 (a) and (b), respectively. The case of an isotropic matrix doped with randomly distributed rod-like inclusions with spherical bundles was studied by Shi *et al.* [282]. In that work, closed-form expressions of the elastic moduli of the effective composite were presented, as collected in Appendix E. In the case of fully aligned fillers with agglomeration effect, both the bundles and the surrounding matrix are transversely isotropic and, therefore, the Eshelby's tensor of the clusters must be accordingly defined. In a similar way to the self-consistent approach, the Eshelby's tensor for the case of transversely isotropic inclusions embedded in a transversely isotropic matrix is defined in Appendix D.

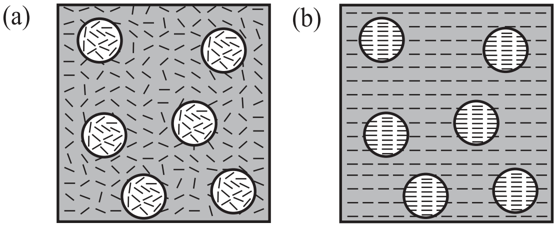

Figure 2.5 Schematic representation of agglomeration configurations: (a) randomly oriented and (b) uniaxially aligned CNTs.

2.3 Functionally graded CNT-reinforced composites

Typically, FGMs are defined for shell-like structures, and four different distributions of the filler content are commonly used, namely UD, FG-V, FG-O and FG-X. UD-CNTRC represents the uniform distribution whilst FG-V, FG-O and FG-X CNTRC are linear distributions of carbon nanotubes along the thickness direction. According to these distributions (Fig. 2.6), the CNT volume fractions, $f_{CNT}(z)$, is defined as a function of z, which runs along the thickness of the structure $[-t/2, t/2]$, are given by:

$$\begin{aligned} f_{CNT} &= f^*_{CNT} && \text{(UD CNTRC)} \\ f_{CNT} &= \tfrac{4|z|}{t} f^*_{CNT} && \text{(FG-X CNTRC)} \\ f_{CNT} &= (1+\tfrac{2z}{t}) f^*_{CNT} && \text{(FG-V CNTRC)} \\ f_{CNT} &= 2(1-\tfrac{2|z|}{t}) f^*_{CNT} && \text{(FG-O CNTRC)} \end{aligned} \tag{2.49}$$

with f^*_{CNT} the volume fraction of CNTs that can be calculated from the mass fraction of nanotubes, w_{CNT}, as:

$$f^*_{CNT} = \frac{w_{CNT}}{w_{CNT} + (\rho^{CNT}/\rho^m) - (\rho^{CNT}/\rho^m) w_{CNT}} \tag{2.50}$$

where ρ^m and ρ^{CNT} are the densities of the matrix and CNTs, respectively. Hence, the cases of uniformly distributed (UD), i.e. $f_{CNT} = f^*_{CNT}$, and functionally graded (FG) CNTRCs have the same value of mass fraction of CNTs.

2.4 Uncertainty analysis [2]

FG-CNTRC structures are difficult to manufacture according to its exact design specifications due to their inherent complexity and undesirable process-induced uncertainties. Since the mechanical properties of the constituent materials may vary statistically, along with process-induced uncertainties, the mass and stiffness properties of FG-CNTRCs

---

[2] An extended version of this section is found in paper B.

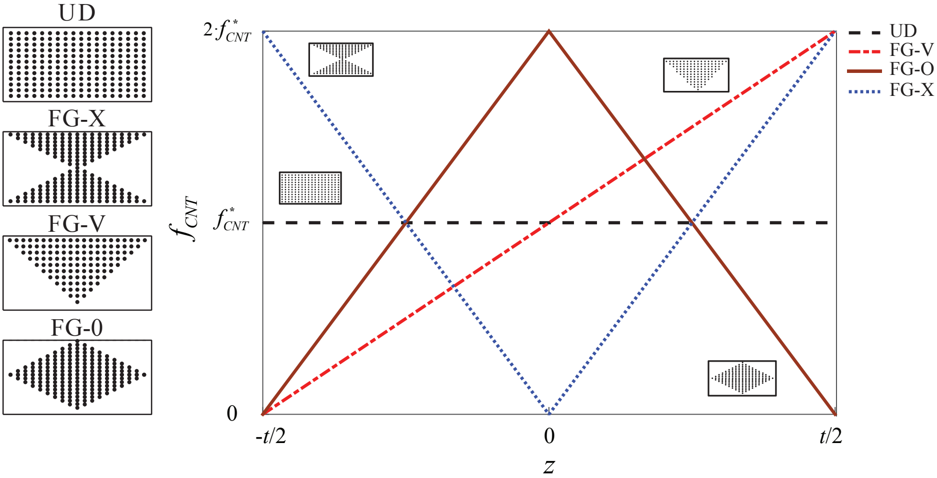

Figure 2.6 Variation of nanotube volume fraction (f_{CNT}) along the radial direction for types of FG-V, FG-O, FG-X and UD.

are stochastic in nature. Thus, two main sources of uncertainty must be considered: (i) uncertainty in the material properties, (ii) uncertainty associated with the leap from nano to macroscale through an homogenization framework, and (iii) uncertainty in the reinforcement grading profile which, in turn, propagates the prior uncertainties within the thickness of the specimen.

To this aim, the reinforcement grading profile can be considered as a general distribution shape function $f(z)$. For a given volume fraction of inclusions f^*_{CNT}, the distribution of CNTs as a function of the z coordinate across the thickness of the specimen can be derived as:

$$f_{CNT}(z) = f^*_{CNT} \cdot \frac{f(z) \cdot t}{\int_{-t/2}^{t/2} f(z)\mathrm{d}z} \tag{2.51}$$

Different expressions for this distribution shape function can be assumed. Some of the most employed distributions in the literature are power-law functions (P-FGM), exponential functions (E-FGM) and sigmoid functions (S-FGM) [132]. In the following analyses, P-FGM functions are selected. For instance, in the case of FG-V and FG-X distributions, the CNT volume fraction defined by P-FGM, P-FGV and P-FGX respectively, adopts the following expressions:

$$\begin{array}{ll} f(z) = \left(\frac{t-2z}{2t}\right)^k & \text{(P-FGV)} \\ f(z) = \begin{cases} \left(\frac{2}{t}z\right)^k & 0 \leq z \leq \frac{t}{2} \\ \left(-\frac{2}{t}z\right)^k & -\frac{t}{2} \leq z \leq 0 \end{cases} & \text{(P-FGX)} \end{array} \tag{2.52}$$

where the variation around the linear case ($k = 1$) is controlled by the power-law index k. Fig. 2.7 shows the different profiles obtained by P-FGV and P-FGX for different values of the power law index.

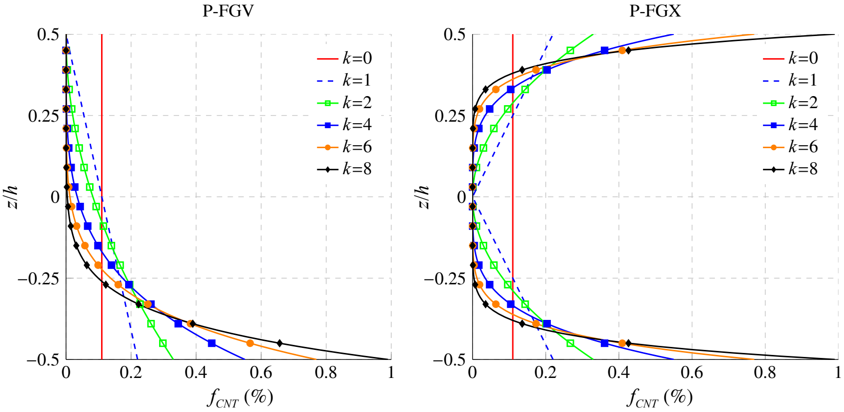

Figure 2.7 Variation of the CNT volume fraction through the thickness defined by the power-law distribution function for different power law indices k, based on FG-V and FG-X linear distributions, namely P-FGV and P-FGX ($f^*_{CNT} = 0.11$).

In addition, in order to increase the computational efficiency, the expensive-to-evaluate finite element models can be surrogated by more computationally efficient metamodels. In this thesis, two different surrogate modelings have been utilized, namely Kriging and RS-HDMR. In these two cases, the actual finite element model is replaced by a response surface model, making the process computationally efficient and cost efficient. Random samples are drawn uniformly over the entire domain ensuring good prediction capability of the constructed metamodels in the whole design space including the tail regions. The theoretical basis of these two metamodels is reviewed below.

2.4.1 Surrogate modeling

In this section, two metamodels are introduced, including the Kriging and Random Sampling High Dimensional Model Representation (RS-HDMR) models. In general, a surrogate model is an approximation of the Input/Output of a main model. The main purpose of a surrogate model is to fit the outcome obtained by a large model, costly in terms of computation, in a more compact and cost-effective way. Let us define a set of m observations, so called design sites $X = [x_1, \dots, x_m]^T$ with $x_i \in \mathbb{R}^n$, and a set of corresponding outputs $Y = [y_1, \dots, y_m]^T$ with $y_i \in \mathbb{R}^q$.

2.4.1.1 Kriging metamodel

The Kriging model, originated in geostatistics [207], is a commonly used method of interpolation (prediction) for spatial data. This model expresses the unknown function of interest $y(x)$ for a n dimensional input $x \subseteq D \subseteq \mathbb{R}^n$, as the sum of a regression model $y_r(x)$ and a stochastic function $\mathcal{F}(x)$ as follows [266]:

$$y(x) = y_r(x) + \mathcal{F}(x) \tag{2.53}$$

the function $\mathcal{F}(x)$ is the realization of a stochastic process with mean zero, variance σ^2 and non-zero covariance, $y_r(x)$ is a known regression function dependent on p regression parameters $\beta = \left[\beta_1, \ldots, \beta_p\right]$ and defined functions $f_j : \mathbb{R}^n \rightarrow \mathbb{R}$ [196]:

$$y_r(\beta, x) = f(x)^T \beta \tag{2.54}$$

It can be understood that $y_r(x)$ globally approximates the design space, meanwhile $\mathcal{F}(x)$ creates the localized deviations so that the Kriging model interpolates the m-sampled data points. The covariance matrix of $\mathcal{F}(x)$ is:

$$Cov\left[\mathcal{F}(x^i)\mathcal{F}(x^j)\right] = \sigma^2 R\left[R(\theta, x^i, x^j)\right] \tag{2.55}$$

between any two of the m-sampled data points x^i and x^j. R is a $m \times m$ symmetric matrix with ones along the diagonal. $R_{ij} = R(\theta, x^i, x^j)$ is the correlation model with parameters $\theta = \left[\theta_1, \ldots, \theta_{\acute{l}}\right]$. The user can specify a wide variety of correlation functions [162, 216, 265] dependent on θ parameters. For example, in the case of a Gaussian correlation function:

$$R(x^i, x^j) = \exp\left[-\sum_{k=1}^{\acute{l}} \theta_k \left|x_k^i - x_k^j\right|^2\right] \tag{2.56}$$

The relation between the predicted estimates, $\hat{y}(x)$ of the response $y(x)$ at an untried point x is defined by the Kriging predictor as follows:

$$\hat{y}(x) = f(x)^T \cdot \beta^* + r(x)^T (Y - F \cdot \beta^*) \tag{2.57}$$

where Y is a column vector of length m that contains the sample values of the frequency responses and F is the $m \times p$ observability matrix $F_{ij} = f_j(x_i)$. $r(x)$ is a vector with the correlations between the design sites and x:

$$r^T(x) = [R(\theta, x_1, x), \ldots, R(\theta, x_m, x)]^T \tag{2.58}$$

The regression problem $F \cdot \beta \approx Y$ has the generalized least squares solution:

$$\beta^* = (F^T \cdot R^{-1} F)^{-1} \cdot F^T \cdot R^{-1} \cdot Y \tag{2.59}$$

and the variance estimate:

$$\sigma^2 = \frac{1}{m}(Y - F \cdot \beta^*)^T \cdot R^{-1} \cdot (Y - F \cdot \beta^*) \tag{2.60}$$

The matrix R and therefore β^* and σ^2, depend on θ. The optimal choice of θ^* is defined as the maximum likelihood estimator (e.g. best guesses), i.e. the maximizer of:

$$\underset{\theta>0}{max.}\Gamma(\theta_k) = \frac{1}{2}(m \cdot \ln \sigma^2 + \ln |R|) \tag{2.61}$$

where $|R|$ is the determinant of R. This optimization process results in a k-dimensional unconstrained non-linear optimization problem. Note that for a given set of design data the matrices β^* and the parameters θ_k are fixed. For every new x we just have to compute the vectors $f(x) \in \mathbb{R}^p$ and $x \in \mathbb{R}^m$ and add two simple products. After obtaining the Kriging surrogate model, it is possible to compute an approximation error to evaluate the accuracy of the predicted results. The mean squared error (MSE) of the predictor is defined by:

$$MSE = E\left[(\hat{y}(x) - y(x))^2\right] \tag{2.62}$$

2.4.1.2 Random Sampling High Dimensional Model Representation HDMR

The RS-HDMR method is a set of tools explored by Rabitz *et al.* [253] in order to express the input-output mapping of a high dimensional model with a large number of input variables and a reduced number of samples [181, 395]. The relationship between the input $X = [x_1, \ldots, x_m]^T$ and output variables $X = [f(x_1), \ldots, f(x_m)]^T$ is expressed as [293, 292]:

$$f(X) = f_0 + \sum_{i=1}^{n} f_i(x_i) + \sum_{1 \le i < j \le n} f_{ij}(x_i, x_j) + \ldots + f_{12\ldots n}(x_1, x_2, \ldots, x_m) \tag{2.63}$$

here the term f_0 is a constant (zeroth order) that stands for the mean contribution of all the inputs to the outputs. The function $f_i(x_i)$ is a first order term giving the effect of variable x_i acting independently upon the output $f(X)$. The function $f_{ij}(x_i, x_j)$ is a second order term describing the cooperative effects of the x_i and x_j upon the output $f(X)$. The higher order terms reflect the cooperative effects of increasing numbers of input variables acting together to influence the output $f(X)$. The last term, $f_{(12\ldots m)}(x_1, x_2, \ldots, x_m)$, reflects any residual mth order correlated contribution of all input variables. In most cases, terms up to second order are enough to provide accurate results [182]. The component functions are determined through and averaging process. Firstly, all the input variables are rescaled in the range [0,1]. Hence, the output response function is defined in the domain of a unit hypercube $K^m = \{(x_1, x_2, \ldots, x_m), i = 1, \ldots, m\}$. The component functions of the RS-HDMR have the following form:

$$f_0 = \int_{K^m} f(x)\mathrm{d}x \tag{2.64a}$$

$$f_i(x_i) = \int_{K^{m-1}} f(x)\mathrm{d}x^i - f_0 \tag{2.64b}$$

$$f_{ij}(x_i, x_j) = \int_{K^{m-2}} f(x)\mathrm{d}x^{ij} - f_i(x_i) - f_0 \tag{2.64c}$$

where $\mathrm{d}x^i$ stands for the product $\mathrm{d}x_1\mathrm{d}x_2\ldots\mathrm{d}x_n$ without $\mathrm{d}x_i$, whereas $\mathrm{d}x^{ij}$ denotes the same product without $\mathrm{d}x_i$ and $\mathrm{d}x_j$. The last term $f_{12\ldots n}(x_1, x_2, \ldots, x_n)$ is evaluated from the difference between $f(x)$ and all the other component functions. The zeroth order term f_0 is calculated by the average value of all $f(X)$. The determination of the higher component functions requires the evaluation of high-dimensional integrals that can be approximately calculated by direct Monte-Carlo integration. However this integration demands high computational cost. Approximations by analytical basis functions, such as orthonormal polynomials, provide accurate results with considerably less sampling effort. Thus the first and second order component functions are expressed as:

$$f_i(x_i) \approx \sum_{r=1}^{k} \alpha_r^i \varphi_r(x_i) \tag{2.65a}$$

$$f_{ij}(x_i,x_j) \approx \sum_{p=1}^{l} \sum_{q=1}^{\acute{l}} \beta_{pq}^{ij} \varphi_p(x_i) \varphi_q(x_j) \tag{2.65b}$$

where k, l and $\acute{l}$ represent the order of the polynomial expansion, α_r^i and β_{pq}^{ij} are constant coefficients to be determined, and $\varphi_r(x_i)$, $\varphi_p(x_i)$ and $\varphi_q\left(x_j\right)$ are the orthonormal basis functions. An orthonormal basis function $\varphi_k(x)$ has the following properties in a domain $[a,b]$:

$$\text{Zero mean:} \quad \int_a^b \varphi_k(x)\mathrm{d}x = 0, \quad k = 1,2,\ldots \tag{2.66a}$$

$$\text{Unit norm:} \quad \int_a^b \varphi_k^2(x)\mathrm{d}x = 1, \quad k = 1,2,\ldots \tag{2.66b}$$

$$\text{Mutually orthogonal:} \quad \int_a^b \varphi_k(x)\varphi_l(x)\mathrm{d}x = 0, \quad k \neq l\ldots \tag{2.66c}$$

From the above condition, the orthonormal polynomials are constructed in the domain [0,1] as:

$$\begin{aligned}
\varphi_1(x) &= \sqrt{3}(2x-1) \\
\varphi_2(x) &= 6\sqrt{5}\left(x^2 - x + \tfrac{1}{6}\right) \\
\varphi_3(x) &= 20\sqrt{7}\left(x^3 - \tfrac{3}{2}x^2 + \tfrac{3}{5}x - \tfrac{1}{20}\right) \\
&\vdots
\end{aligned} \tag{2.67}$$

The expansion coefficients α_r^i and β_{pq}^{ij} can be determined by a minimization process and Monte Carlo integration which leads to:

$$\alpha_r^i \approx \frac{1}{N} \sum_{s=1}^{N} f\left(x^{(s)}\right) \varphi_r\left(x_i^{(s)}\right) \tag{2.68a}$$

$$\beta_{pq}^{ij} \approx \frac{1}{N} \sum_{s=1}^{N} f\left(x^{(s)}\right) \varphi_p\left(x_i^{(s)}\right) \varphi_q\left(x_j^{(s)}\right) \tag{2.68b}$$

Note that only a set of random samples N is necessary to determine all the RS-HDMR component functions. The MC integration for calculating the expansion coefficients α and β controls the accuracy of RS-HDMR. Variance reduction methods can be employed to improve the accuracy of the Monte Carlo integration without increasing the sample size N. Two methods, the correlation method [181] and ratio control variate method [180] have been successfully applied in connection with the RS-HDMR. In both cases the determination of the expansion coefficients is an iterative process and requires an analytical reference function which has to be similar to $f(x)$. A truncated RS-HDMR expansion can be used as a reference function by calculating its expansion coefficients with a direct Monte Carlo integration. Since the HDMR component functions are independent, the order of the polynomial approximation can be chosen separately for each component function in order to improve the accuracy of the final surrogate model. Thereupon, Ziehn and Tomlin [394] developed an optimization method based on the least square method, which determines the best polynomial order for each of the component functions. Furthermore, a threshold criterion proposed by Ziehn and Tomlin [396] allows to exclude unimportant component functions from the RS-HDMR expansion. The final equation of RS-HDMR up to second order component functions are expressed as:

$$f(X) = f_0 + \sum_{i=1}^{n}\sum_{r=1}^{k}\alpha_r^i\varphi_r(x_i) + \sum_{1\leq i<j\leq n}\sum_{p=1}^{l}\sum_{q=1}^{\acute{l}}\beta_{pq}^{ij}\varphi_p(x_i)\varphi_q(x_j) \tag{2.69}$$

In order to quantify the contribution of each uncertainty source in the response, a global sensitivity analysis based on RS-HDMR is employed in this study. The orthogonal relationship between the component functions of the RS-HDMR expression implies that the component functions are independent and their action contributes independently to the overall output response. This fact suggests that each individual component function has a direct statistical correlation with the output. Hence, the sensitivity of each component function can be determined by calculating the total and partial variances. The total variance (D) is computed using MC integration for a set of N samples ($X^{(s)} = \left(x_1^{(s)}, x_2^{(s)}, \ldots, x_n^{(s)}\right)$, $s = 1,2,\ldots,N$ and is defined by:

$$D = \int_{K^n} f^2(X)\mathrm{d}X - f_o^2 \approx \frac{1}{N}\sum_{s=1}^{N} f^2\left(X^{(s)}\right) - f_o^2 \tag{2.70}$$

The partial variances (D_i and D_{ij}) obtained by using the properties of orthonormal polynomials are expressed as follows:

$$D_i = \int_0^1 f_i^2(x_i)\mathrm{d}x_i \approx \int_0^1 \left[\sum_{r=1}^{k}\alpha_r^i\varphi_r(x_i)\right]^2 \mathrm{d}x_i = \sum_{r=1}^{k}\left(\alpha_r^i\right)^2 \tag{2.71a}$$

$$D_{ij} = \int_0^1\int_0^1 f_{ij}^2(x_i,x_j)\mathrm{d}x_i\mathrm{d}x_j \approx \int_0^1\int_0^1 \left[\sum_{p=1}^{l}\sum_{q=1}^{\acute{l}}\beta_{pq}^{ij}\varphi_p(x_i)\varphi_q(x_j)\right] = \sum_{p=1}^{l}\sum_{q=1}^{\acute{l}}\left(\beta_{pq}\right)^2 \tag{2.71b}$$

Finally, the sensitivity indices ($S_{i_1,\ldots,i_s}$) are given by:

$$S_{i_1,\ldots,i_s} = \frac{D_{i_1,\ldots,i_s}}{D}, 1 \leq i_1 \leq i_2 \ldots \leq i_n \leq n \tag{2.72}$$

so that, $\sum_{i=1}^{n} S_i + \sum_{1\leq i<j\leq n}^{n} S_{ij} + \ldots + S_{1,2,\ldots n} = 1$.

The quality of the proposed approximations is appraised by checking the coefficient of determination (R^2). To ensure accuracy, the value of R^2 must be close to one and is expressed as:

$$R^2 = \frac{SS_R}{SS_T} = 1 - \frac{SS_E}{SS_T} \quad (0 \leq R^2 \leq 1) \tag{2.73}$$

where $SS_T = SS_E + SS_R$ is the total sum of squares, and SS_R and SS_E are the regression sum of squares and the residual sum of squares, respectively. The quality of the surrogate models can also be determined by the Relative Error (RE), computed as:

$$RE(\%) = \frac{\left|F - F'\right|}{F} \times 100 \tag{2.74}$$

where F is the actual response and F' is the approximated response using the surrogate models.

2.5 Results and discussion

In this section, a comprehensive comparison of the previously indicated homogenization approaches of the macroscopic properties of CNT-reinforced composites is presented. Afterward, the mechanical behavior of different CNT-reinforced structures is investigated, including FG-CNT reinforced rectangular flat panels, skew shells and cylindrical curved panels.

2.5.1 Overall mechanical properties of CNT-reinforced composites

2.5.1.1 Introduction

In this set of analyses, numerical results are conducted in order to highlight the correctness of the previously introduced approaches for different CNT arrangements. In particular, the discussion focuses on the diagonal symmetry consistency and comparison with reference boundaries, such as the Voigt/Reuss (VR) and Hashin-Shtriman-Walpole (HSW) bounds. Case studies of uniform filler dispersions, effects of non-straightness, as well as effects of agglomeration are presented. For illustrative purposes, the polymer matrix is selected as a thermosetting polymer Epon 862/EPI cure W with elastic properties E_m=2.55 GPa and ν_m=0.2. As reinforcing phase, different SWCNTs are studied with Hill's elastic moduli included in the research work of Tornabene *et al.* [316] and collected in Table 2.1.

2.5.1.2 Numerical results

Polymer doped with well dispersed straight CNTs First, uniform dispersions of uniaxially aligned straight CNTs are studied. Traditionally, bounds on the elastic properties of composites are useful for assessing the validity of homogenization approaches as well as for assisting the design of engineered composite materials. In this set of tests, the VR bounds, as well as the HSW bounds have been considered. Voigt [332] and Reuss [258] adopted iso-strain and iso-stress hypotheses to estimate the effective composite stiffness

Table 2.1 Hill's elastic moduli for several Single-Walled Carbon Nanotubes (SWCNTs) [281, 316].

CNT	k_r [GPa]	l_r [GPa]	m_r [GPa]	n_r [GPa]	p_r [GPa]
SWCNT (5,5)	536	184	132	2143	791
SWCNT (10,10)	271	88	17	1089	442
SWCNT (15,15)	181	58	5	726	301
SWCNT (20,20)	136	43	2	545	227
SWCNT (50,50)	55	17	0.1	218	92

tensor, respectively. In other words, the stiffness of Voigt composites, $\mathbf{C}_V$, is defined by the weighted volume average of the stiffness matrices of the constituent phases, whilst the compliance of Reuss composites, $\mathbf{M}_R = \mathbf{C}_R^{-1}$, is obtained by the weighted volume average of the compliance matrices of the constituent phases, that is, in the case of a two-phase composite:

$$\mathbf{C}_V = f_m \mathbf{C}_m + f_r \mathbf{C}_r \tag{2.75}$$

$$\mathbf{M}_R = f_m \mathbf{M}_m + f_r \mathbf{M}_r \tag{2.76}$$

Tighter bounds were developed by Hashin and Shtrikman (HS) by introducing variational principles for heterogeneous materials with statistically isotropic microstructures [129, 130]. The HS variational principles consist of an alternative representation of the minimum potential/complementary energy principles in terms of piecewise constant polarization fields relative to a reference material. This framework allows rigorous bounds to be obtained by choosing suitable reference materials. Considering reference materials with infinite or zero stiffness, Voigt and Reuss bounds are obtained, respectively, as particular cases of the HS bounds. Although originally restricted to isotropic phases, the HS bounds were generalized by Walpole [333, 334, 335] to anisotropic phases. In the case of uniaxially aligned circular fibers, Weng [349] showed that the MT model coincides with the lower HSW bound if the matrix is the softest phase and vice versa.

Figure 2.8 shows the effective elastic moduli of polymer composites reinforced by aligned straight (10,10) SWCNTs. The longitudinal, $E_{||}$, and transverse elastic moduli, $E_{\perp}$, are shown versus the volume fraction f_r of CNTs, and whose expressions can be related to Hill's elastic moduli as:

$$E_{||} = n - \frac{l^2}{k}, \quad E_{\perp} = \frac{4m\left(kn - l^2\right)}{kn - l^2 + mn} \tag{2.77}$$

The previously outlined homogenization approaches are compared, namely the MT method, dilute Eshelby's solution, self-consistent approach, as well as the Voigt/Reuss and HSM bounds. Let us remark that, in the case of fully aligned inclusions, all the analyzed approaches are well known to provide diagonally symmetric predictions. For this reason, the analysis of the diagonal symmetry is obviated in this test. It is noted that CNTs are highly anisotropic, with longitudinal Young's modulus two orders of magnitude higher than the transverse one. It is observed in Fig. 2.8 that, because of the anisotropy of CNTs, $E_{||}$ increases much more rapidly with the volume fraction f_r than $E_{\perp}$. Very little

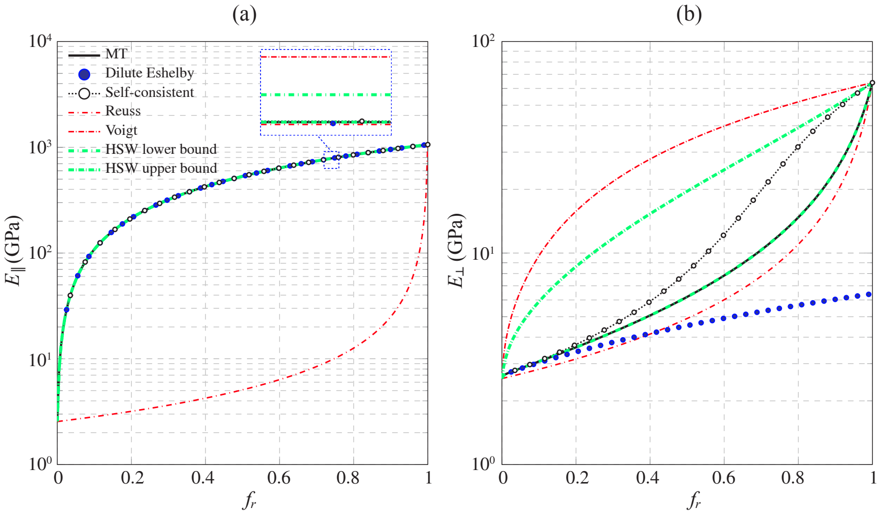

Figure 2.8 Effective Young's modulus in the longitudinal direction $E_{||}$ (a) and in the transverse direction $E_{\perp}$ (b) versus filler volume fraction f_r of Epon 862/EPI cure W reinforced by aligned, infinitely long straight (10,10) SWCNTs.

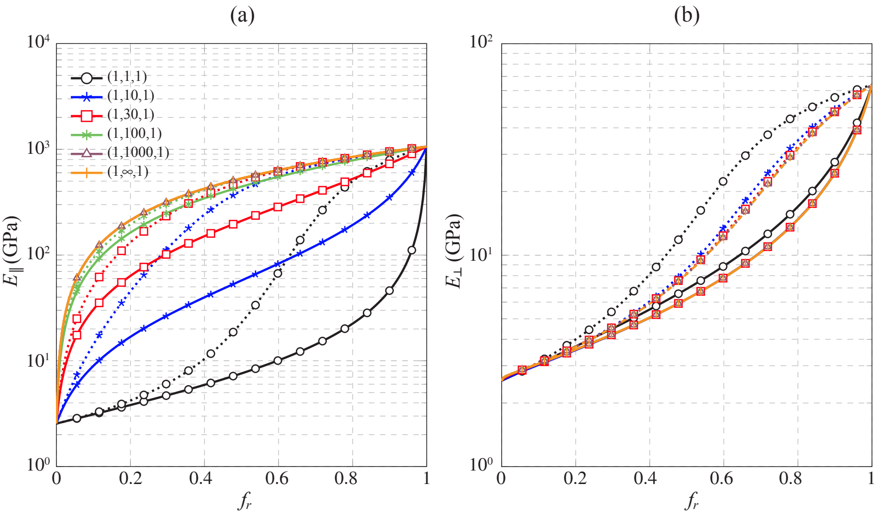

Figure 2.9 Effective Young's modulus in the longitudinal direction $E_{||}$ (a) and in the transverse direction $E_{\perp}$ (b) versus filler volume fraction f_r of Epon 862/EPI cure W reinforced by aligned, straight (10,10) SWCNTs with different aspect ratios, estimated by the Mori-Tanaka and self-consistent approaches, corresponding to solid and dotted lines, respectively.

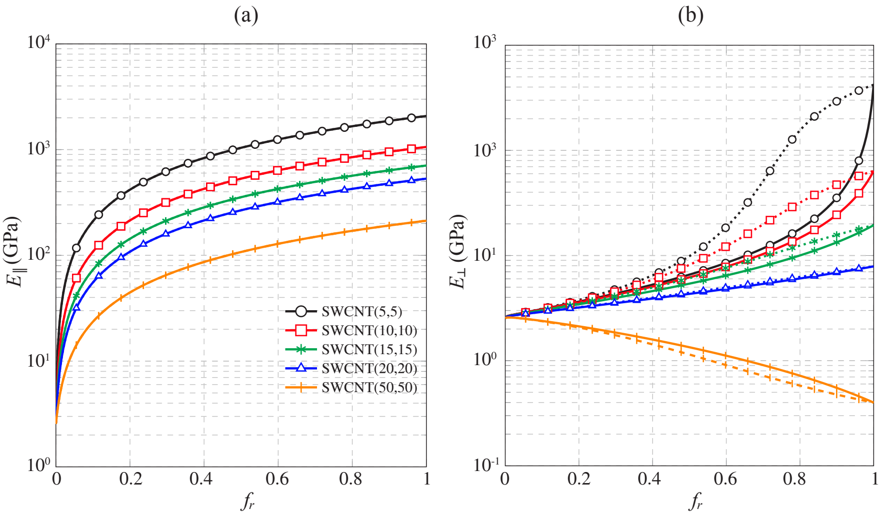

Figure 2.10 Effective Young's modulus in the longitudinal direction $E_{\parallel}$ (a) and in the transverse direction $E_{\perp}$ (b) versus filler volume fraction f_r of Epon 862/EPI reinforced by different aligned, straight (10,10) SWCNTs, estimated by the Mori-Tanaka and self-consistent approaches, corresponding to solid and dotted lines, respectively.

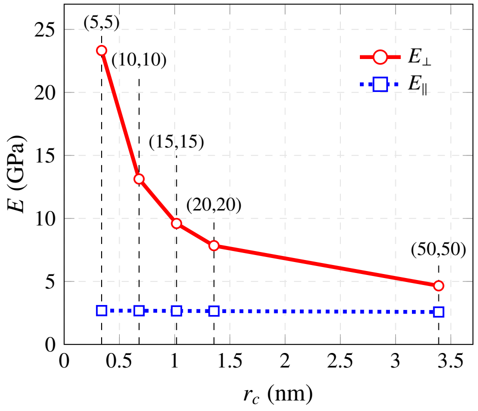

Figure 2.11 Longitudinal $E_{\parallel}$ and transverse $E_{\perp}$ Young's moduli as a function of CNT radius.

differences are found for $E_{\parallel}$ among the different methods (see Fig. 2.8 (a)). On the contrary, larger differences arise for $E_{\perp}$ in Fig. 2.8 (b). The dilute Eshelby's approach ignores any interaction between the particles so it is only valid for low filler volume fractions f_r (asymptotically correct to $\mathcal{O}(f_r)$). The MT estimates coincide with the lower HSW bound as expected. In the case of the self-consistent scheme, it shows a typical behavior which approximates the lower/upper HSW bounds at low and high volume fractions, respectively, and displays a transition sigmoid curve in-between.

The longitudinal and transverse Young's moduli of polymers reinforced by CNTs with different aspect ratios (a_1,a_2,a_3) are shown in Figs. 2.9 (a) and (b), respectively. In particular, nanotubes range from spherical particles, i.e. (1,1,1), to infinitely long fibers, (1,∞,1). Effective properties have been estimated by the MT method and the self-consistent approach, corresponding to solid and dotted lines in Fig. 2.9, respectively. It can be seen in Fig. 2.9 (a) that $E_{||}$ increases with increasing CNTs lengths. Let us remark that the estimates by both the MT and self-consistent approaches get closer as the CNT aspect ratio increases. Conversely, in the case of $E_{\perp}$ in Fig. 2.9 (b), it can be seen that increases of the aspect ratio of the fibers lead to decreases of $E_{\perp}$. This dependence is expected because of the well-known effect of the increase in load transfer with increases in reinforcement length and volume fraction.

Finally, Fig. 2.10 shows the Young's moduli $E_{||}$ and $E_{\perp}$ for the different armchair chiralities presented in Table 2.1. It can be seen that SWCNTs (5,5) and (50,50) yield the maximum and minimum moduli, respectively. These results are in accordance with the theoretical results of Popov *et al.* [249] who showed that both longitudinal and transverse Young's moduli decrease with CNT radius. Fig. 2.11 shows $E_{||}$ and $E_{\perp}$ for different CNT radii. For armchair SWCNTs with chiral vector integers (n,n), the radius of the CNTs, r_c, can be computed as $r_c = 3\frac{nL_{C-C}}{2\pi}$, being L_{C-C}=0.142 nm the length of the C-C bonds. It can be seen in Fig. 2.11 that both moduli substantially decrease with the CNT radii. It is also interesting to remark that the degree of anisotropy is also decreasing with CNT radii. This fact explains the decreasing Young's moduli in Fig. 2.10 for increasing chiral vector integers (n,n). In particular, SWCNTs (50,50) even reduce the transverse Young's modulus $E_{\perp}$. This chiral configuration corresponds to tube radius of 0.339 Å and has a transverse modulus of 0.4 GPa, less than the Young's modulus of the polymer matrix.

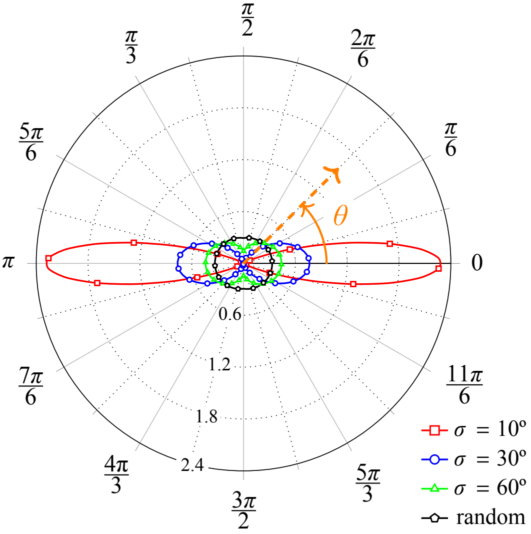

Figure 2.12 Polar plot of the symmetric truncated normal orientation distribution function $\Omega(\theta)$ for various standard deviations σ.

Let us move to the analysis of the cases with orientational dependence in the CNT distributions. We already noted that the averaging procedure does not ensure the diagonal symmetry of the orientation-dependent constitutive tensors and, thus, the symmetry condition has to be checked. In this research work, ODFs have been defined as truncated Gaussian distribution functions with azimuthal symmetry so that Ω is independent of γ. Characterized by a mean value $\mu = 0^\circ$ and a standard deviation σ, the ODF can be expressed as a function of the polar angle θ as:

$$\Omega(\theta) = \frac{e^{-\frac{\theta^2}{2\sigma^2}}}{\sqrt{2\pi}\sigma \operatorname{erf}\left(\frac{\pi}{2\sqrt{2}\sigma}\right)} \tag{2.78}$$

with erf(x) being the error function formally defined as:

$$\operatorname{erf}(x) = \frac{2}{\sqrt{\pi}} \int_0^x e^{-u^2} du \tag{2.79}$$

In order to meet the normalization condition of Eq. (2.12), the orientational average of any function $F(\theta,\gamma)$ defined in Eq. (2.13) is substituted by:

$$\langle F(\theta,\gamma) \rangle = \frac{\int_0^{2\pi}\int_0^{\pi/2} F(\theta,\gamma)\Omega(\theta)\sin\theta d\theta d\gamma}{\int_0^{2\pi}\int_0^{\pi/2} \Omega(\theta)\sin\theta d\theta d\gamma} \tag{2.80}$$

Simpson's rule for the numerical integration of these definite integrals has been implemented. Fig. 2.12 furnishes the ODFs for different standard deviations, $\sigma = 10^\circ$, 30°, 60° and $\Omega(\theta) = 1$, corresponding to a completely random distribution.

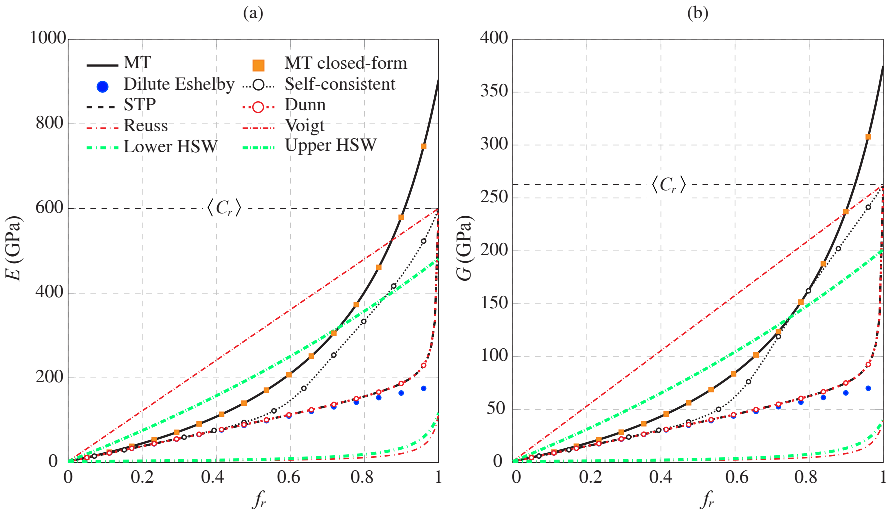

Figure 2.13 Young's modulus (a) and shear modulus (b) of Epon 862/EPI cure W reinforced by randomly oriented straight (10,10) SWCNTs.

First, the stiffness tensors computed by the MT, SC, STP and DUN approaches are compared against theoretical bounds on elastic moduli for random filler arrangements ($\Omega(\theta)$). The RS/VT bounds can be extended for the case of randomly dispersed CNTs by averaging Eqs. (2.75) and (2.76). On the other hand, explicit expressions of the HSW bounds for randomly oriented long fibers are given in [335] and collected in Appendix F. Figs. 2.13 (a) and (b) show the Young's and shear moduli as functions of the filler volume fraction f_r, respectively. A first important conclusion is that the MT solution violates the HSW bound at a filler concentration around 67%. In addition, the MT solution even violates the VT bound, fact that agrees with the previous results by Qiu and Weng [252]. The violation of the HSW bounds limits the applicability of the MT solution for high volume fractions of CNTs. Nevertheless, the MT approach remains important in practical applications, where CNT volume fractions are usually below 10%. With regard to the extended MT approaches, note that all the solutions converge to the VT bound at f_r=1. For validation purposes, the orientational average $\langle C_r \rangle$, corresponding to the VT bound at f_r=1, has been computed by the closed-form solutions given by Zheng *et al.* [387], detailed in Appendix G. The convergence of the numerical solution demonstrates the validity of the implemented approach. The SC scheme also violates the upper HSW bound although does lay within the VT/RS bounds. It is also observed that the DUN and STP approaches yield very close results and are comprised between the HSW bounds. With regard to the diagonal symmetry of the tensors, the estimates of the different used approaches have been reported to be symmetric for random filler arrangements and, therefore, discussion on this regard is omitted.

Finally, let us focus on misoriented CNT distributions. In this case, the diagonal symmetry of the estimates has to be checked. An asymmetry factor AF_{12} can be defined to this end as follows [252]:

$$AF_{ij} = 2\frac{C(i,j) - C(j,i)}{C(i,j) + C(j,i)}, \quad i \neq j \tag{2.81}$$

being $C(i,j)$ the components of the stiffness tensor in Voigt notation. Fig. 2.14 shows the asymmetry factor of the MT stiffness tensor versus the orientation standard deviation σ for various filler contents. It can be observed that all the curves start at zero, as expected for fully aligned CNTs ($\sigma = 0°$). In addition, all the asymmetry factors tend to zero for high standard deviation values, σ, until the limit case of randomly oriented CNTs where $\Omega(\theta) = 1$. It can be seen that the asymmetry factor increases with higher filler contents, reaching maximum values around $\sigma = 10°$. It is important to note that, in the case of infinitely long fibers, the asymmetry factors are not excessively large. Nevertheless, these estimates cannot be used in structural applications since the resulting constitutive tensors are not positive definite. The predictions of the DUN and STP approaches always yield diagonally symmetric stiffness tensors, that is zero asymmetry factors for every σ, so they have been omitted in Fig. 2.14.

Finally, the stiffness tensors of CNT-reinforced composites with a certain degree of misalignment are studied. As previously discussed, Dunn and STP approaches yield similar results and, therefore, only the estimates by the STP approach are shown for clarity in the results. Assuming orientation distribution functions with azimuthal symmetry, the composite material is transversely isotropic, with $x_1 - x_3$ as the symmetry plane. Fig. 2.15

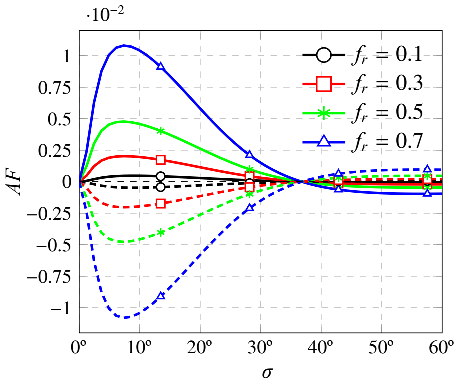

Figure 2.14 Asymmetry factor AF as a function of the orientation standard deviation σ for a symmetric truncated normal distribution obtained using the MT approach with different SWCNT (5,5) concentrations. Solid and dashed lines stand for AF_{12} and AF_{23}, respectively.

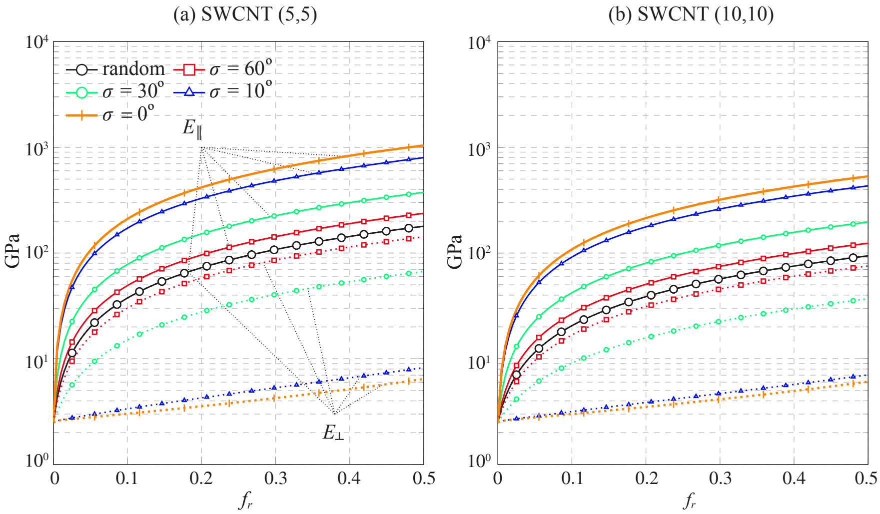

Figure 2.15 Longitudinal $E_{||}$ and transverse $E_\perp$ Young's moduli as a function of volume fraction with different degrees of nanotube misalignment, for Epon 862/EPI reinforced by armchair SWCNTs with chiralities (5,5) (a) and (10,10) (b).

shows the longitudinal $E_{||}$ and transverse $E_\perp$ Young's moduli as a function of the CNT volume fraction with different degrees of nanotube alignment. Two different chiralities have been analyzed, namely (5,5) and (10,10). The elastic moduli of the nanocomposites doped with general ODFs of nanotubes are bounded by those obtained for the cases of fully aligned ($\sigma = 0^\circ$) and randomly oriented nanotubes ($\Omega(\theta) = 1$). In this case, no explicit bounds for arbitrary ODFs are known (the procedure developed by Walpole only provides explicit bounds for random orientation distributions). It is clearly shown in Fig. 2.15 that a variation of the alignment degree has a significant effect on the macroscopic Young's moduli. As σ increases and decreases, $E_{||}$ approaches that of the random and fully aligned configurations, respectively. The opposite conclusions can be extracted for $E_{\perp}$. This behavior can be better understood if one represents the variation of $E_{||}$ and $E_{\perp}$ for varying orientation standard deviations, σ, as shown in Fig. 2.16. It can be extracted from this analysis that the anisotropy of the composite decreases with the degree of misalignment, reaching a limit point, $\Omega(\theta) = 1$, which corresponds to the random filler arrangement and exhibits isotropic properties.

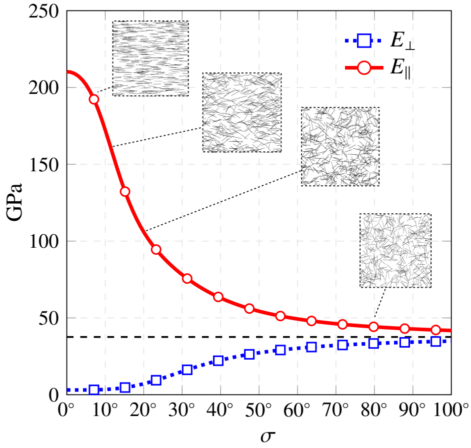

Figure 2.16 Longitudinal $E_{||}$ and transverse $E_{\perp}$ Young's moduli as a function of orientation standard deviation σ of SWCNTs (5,5) with azimuthal symmetry (f_r=0.1).

In summary, the conclusions drawn from the consistency conditions, i.e. diagonal symmetry and HSW-VR bounds, are outlined in Fig. 2.17.

Effect of non-straightness of fibers In this subsection, the effect of CNT waviness is investigated by the MT, YNS, and STP approaches. First, the diagonal symmetry condition must be verified. The direct integrations of the stiffness tensors appearing in both the YNS and STP approaches ensure this condition is fulfilled. Nonetheless, this is not the case for the MT estimates. Figs. 2.18 (a) and (b) depict the asymmetry factors (AF_{12} and AF_{23}) as functions of the spiral angle θ^w and various filler volume fractions with fully aligned (6,6) and (50,50) helical SWCNTs as reinforcing fillers, respectively. In both cases, the MT estimates are highly asymmetric, particularly for spiral angles $\theta^w = 0°$, corresponding to circular fillers. As expected, the asymmetry condition is fulfilled ($AF_{ij} = 0$) for straight fillers, i.e. $\theta^w = 90°$. Interestingly, it is noted that (50,50) SWCNTs lead to larger asymmetry factors, whereby it is extracted that lesser anisotropic fillers yield more asymmetric estimates in Eq. (2.42). These results demonstrate that the MT approach cannot be directly applied to model CNT-reinforced composites with waviness effects and it is thereupon disregarded.

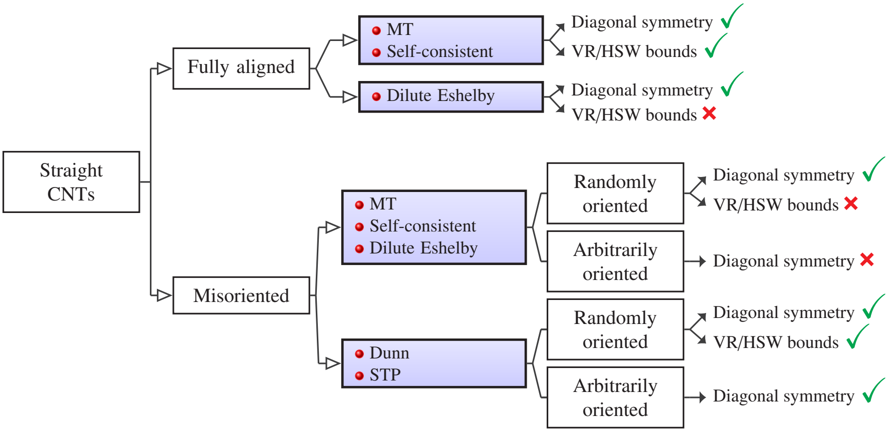

Figure 2.17 Flowchart presenting a condensed summary of the results on the evaluation of the consistency conditions of micromechanics approaches for composites reinforced by straight CNTs.

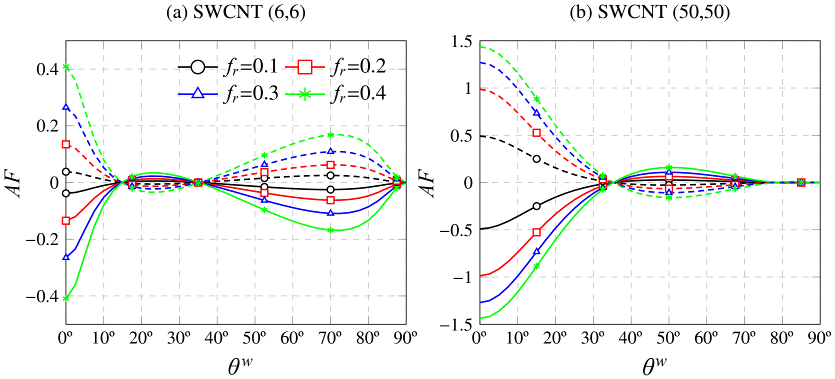

Figure 2.18 Asymmetry factors AF_{ij} as functions of the spiral angle θ^w for helical CNT-reinforced Epon 862/EPI obtained using the MT approach with different SWCNT (6,6) (a) and SWCNT (50,50) (b) concentrations. Solid and dashed lines stand for AF_{12} and AF_{23}, respectively.

Fig. 2.19 shows the elastic moduli of composites doped with fully aligned wavy SWCNTs (5,5) computed by the YNS and STP approaches. A volume fraction $f_r = 0.01$ is selected, and helical and planar sinusoidal configurations are depicted by solid and dashed lines, respectively. In order to compare both geometries, a waviness parameter is designated as A/λ. E_{22} stands for the macroscopic longitudinal Young's modulus, E_{11} and E_{33} are the transverse Young's moduli, and G_{12} denotes the longitudinal shear modulus of the composite. It is first observed that composites are orthotropic for planar sinusoidal geometries and transversely isotropic for the helical ones. Also, it is noted that the longitudinal Young's modulus E_{22} rapidly decreases as the waviness increases. With helical

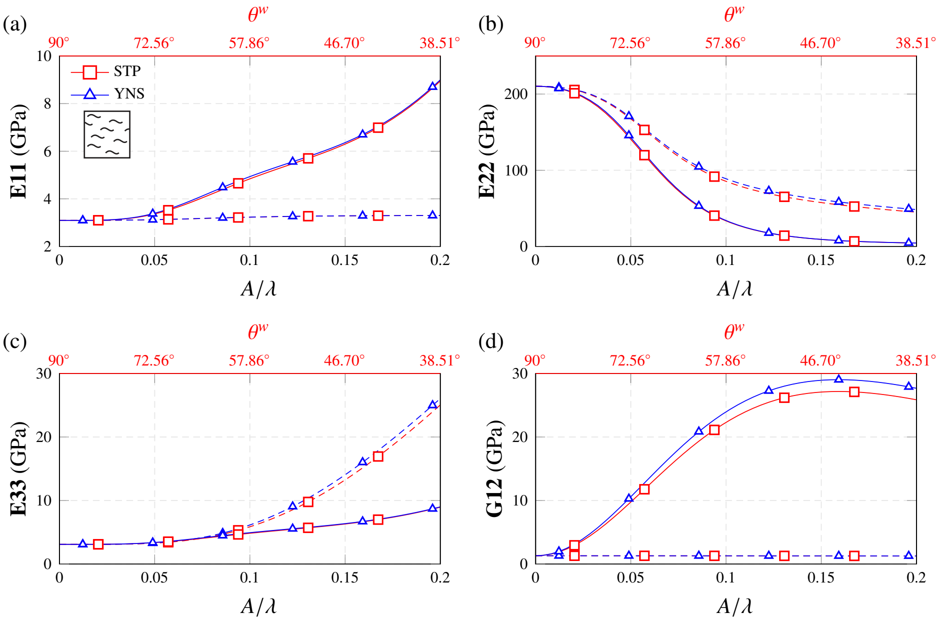

Figure 2.19 Elastic moduli predicted for Epon 862/EPI reinforced by fully aligned wavy SWCNTs (5,5) (f_r=0.1). Solid and dashed lines denote helical and planar sinusoidal configurations, respectively.

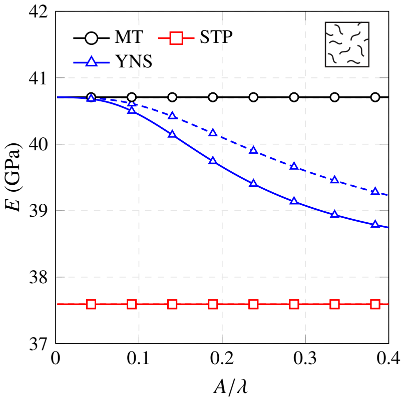

Figure 2.20 Elastic moduli predicted for Epon 862/EPI reinforced by randomly oriented wavy SWCNTs (5,5) (f_r=0.1). Solid and dashed lines denote helical and planar sinusoidal configurations, respectively.

configurations, more pronounced reductions are found in E_{22}, while the transverse moduli $E_{11} = E_{33}$ slightly increase with the CNT waviness. For planar sinusoidal configurations, on the other hand, E_{33} substantially increases since the fillers are defined on the x_2-x_3 plane, whilst E_{11} remains approximately constant. With regard to the different homogenization approaches, it can be seen that the STP and YNS approaches provide similar estimates, with slight differences in the macroscopic shear moduli.

Finally, the estimates for the case of randomly distributed wavy CNTs are furnished in Fig. 2.20. Interestingly, both the MT and STP approaches yield estimates that are insensitive to waviness, unlike the YNS approach. The explanation of this behavior lies in the assumption of wavy fibers as consecutive infinitely long fibers. On the contrary, the YNS approach considers an ad hoc Eshelby's tensor, resulting in a modified definition of the microstructure of the composite. Hence, decreasing Young's and shear moduli are found for larger waviness parameters with both helical and planar sinusoidal configurations, with more acute reductions in the latter case.

Effect of agglomeration Finally, in this set of analyses, the agglomeration schemes presented in Section 2.2.5 are studied. For illustrative purposes, a global filler volume fraction is selected as $f_r = 0.1$. In the case of randomly oriented CNTs, i.e. case (a) in Fig. 2.5, the variations of the effective Young's and shear moduli with respect to the agglomeration parameter ζ are shown in Figs. 2.21 (a) and (b), respectively. The agglomeration parameter ξ is kept constant at a value of 0.2. The effective properties

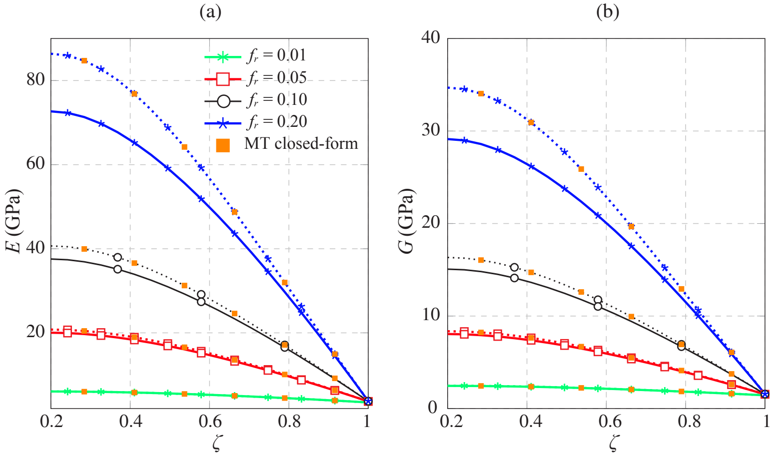

Figure 2.21 Macroscopic Young's modulus (a) and shear modulus (b) of Epon 862/EPI reinforced by randomly oriented SWCNTs (5,5) with agglomeration parameter ξ=0.2 and varying agglomeration parameter ζ (f_r=0.1). Dashed and solid lines denote estimates by the MT and SPT approaches, respectively.

have been estimated by the MT and STP approaches, corresponding to dashed and solid lines, respectively. In addition, for validation purposes, the closed-form solution obtained by Shi *et al.* [282], and contained in Appendix E, has been also included. It can be seen that the closed-form solution and the MT numerical results perfectly match, what proves a further validation of the implemented numerical framework. For both approaches, with the increase in the relative amount of ζ, that is to say, a larger number of CNTs agglomerated in clusters, the macroscopic elastic moduli experience substantial decreases. Let us remark that this weakening effect is more severe for higher filler concentrations. The STP approach provides lower results what finds the same explanation as in the previous analyses.

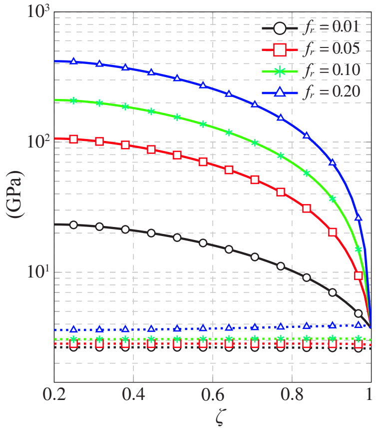

Figure 2.22 Macroscopic Young's and shear moduli of Epon 862/EPI reinforced by fully aligned SWCNTs (5,5) with agglomeration parameter ξ=0.2 and varying agglomeration parameter ζ (f_r=0.1). Dashed and solid lines denote estimates by the MT and SPT approaches, respectively.

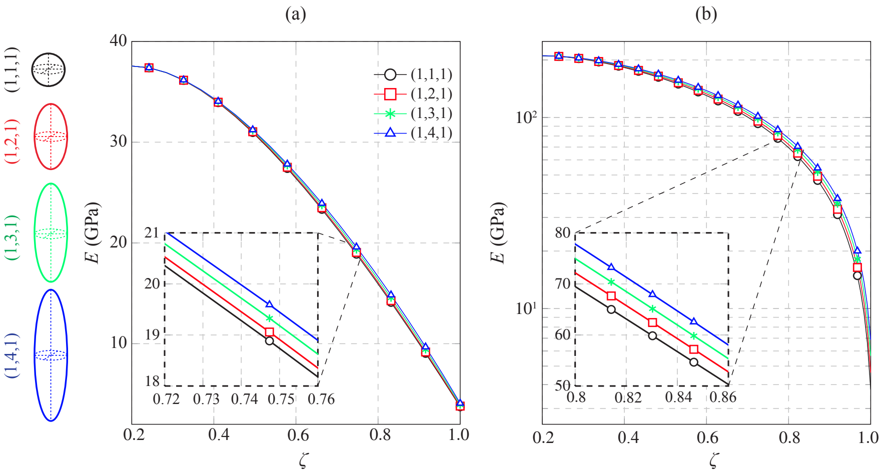

Figure 2.23 Effect of bundles aspect ratio (a_1,a_2,a_3) on the effective elastic properties of CNT reinforced Epon 862/EPI: (a) Young's modulus of composites doped with randomly oriented CNTs, (b) longitudinal Young's modulus of composites doped with uniaxially aligned CNTs (SWCNT (5,5), ξ=0.2, f_r=0.1).

In the case of composites doped with uniaxially aligned CNTs, i.e. case (a) in Fig. 2.5, the effective elastic properties are transversely isotropic. Fig. 2.22 shows the longitudinal, $E_{||}$, and transverse elastic moduli, $E_{\perp}$, as a function of the agglomeration parameter ζ. The agglomeration parameter ξ is also kept constant at a value of 0.2. In this case, the weakening effect induced by agglomeration is even more severe in the case of $E_{||}$. Conversely, CNT agglomeration has little effect on the lateral moduli $E_{\perp}$ which can even experience slight increases at high filler concentrations.

Finally, the effect of different aspect ratios (a_1,a_2,a_3) of the bundles has been also studied by the STP approach as shown in Fig. 2.23. Four different aspect ratios have been selected considering different lengths of the ellipsoids along the x_2 axis, namely (1,1,1), (1,2,1), (1,3,1) and (1,4,1). It can be extracted that for both configurations, (a) randomly oriented CNTs and (b) uniaxially aligned CNTs, the bundle aspect ratio has limited effect on the elastic properties. It is also interesting to note that the spherical bundles (1,1,1) yield the strongest weakening effect.

Coupled effect of waviness and agglomeration The coupled effect of waviness and agglomeration for randomly oriented CNT-reinforced polymers is investigated in Fig. 2.24. In this figure, the macroscopic Young's modulus is depicted against the helical spiral angle θ^w. The agglomeration parameter ξ is kept constant at a value of 0.2, and three different values of ζ are selected, namely ζ = 0.2, 0.3 and 0.4. Also, the global filler volume fraction is chosen as f_r = 0.1. Given that the MT approach for randomly oriented filler arrangements is insensitive to waviness as previously shown in Fig. 2.20, the YNS approach is combined with the two-parameter agglomeration model for this purpose. It is observed that the elastic modulus E decreases with higher agglomeration levels, that is to say, with larger ζ parameters. In addition, when waviness is also incorporated ($\theta^w < 90°$), further reductions are found. For instance, in the case of $\xi = 0.2$ and $\zeta = 0.4$ and straight fillers, a reduction of 10.5% in the overall Young's modulus is found. However, when

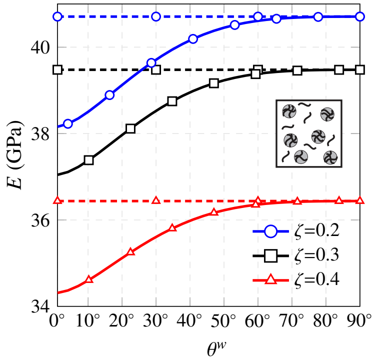

Figure 2.24 Macroscopic Young's modulus of Epon 862/EPI reinforced by randomly oriented wavy SWCNTs (5,5) with agglomeration parameter ξ=0.2 and varying agglomeration parameter ζ as a function of the spiral angle θ^w (a_1=a_2=a_3, f_r=0.1). Dashed lines denote the corresponding magnitudes for randomly oriented straight fillers.

$\theta^w = 30^\circ$, the Young's modulus is further reduced up to 12.7%. Therefore, it is concluded that when both phenomena act simultaneously, their weakening effects add up.

2.5.1.3 Conclusions

This subsection has presented a critical comparison of different mean-field homogenization approaches for CNT-reinforced polymer composites with waviness and agglomeration effects. Firstly, the MT, SC, DUN and STP approaches have been compared in terms of diagonal symmetry and against the HSW and RS/VT bounds for misoriented CNT arrangements. Afterward, the MT, STP and YNS approaches have been analyzed for both planar sinusoidal and three-dimensional helical CNTs, including fully aligned and randomly oriented wavy filler arrangements. Through a two-parameter agglomeration framework, the influence of filler agglomeration on the macroscopic stiffness of CNT-reinforced composites has been also investigated. The results have evidenced that the MT method fails to simulate the coupled effect of waviness and agglomeration, providing estimates that are insensitive to waviness for random filler arrangements. Furthermore, it has been shown that the MT predictions for composites doped with fully aligned wavy CNTs are highly asymmetric and, thus, physically inadmissible. By considering the combination of the YNS approach and the two-parameter agglomeration model, it has been shown that the weakening effects of waviness and agglomeration add up when acting simultaneously.

The key findings of this work can be summarized as follows:

- It has been shown that the MT solution violates the HSW bounds at filler volume fractions above 67% for randomly oriented CNTs, unlike the DUN and STP approaches which always provide diagonally symmetric estimates.
- In the case of fully aligned wavy CNTs, the MT approach has been reported to provide highly asymmetric stiffness tensors and, thus, physically inadmissible estimates.
- Filler agglomeration has been proven to induce detrimental effects on the mechanical properties for both randomly oriented and fully aligned CNTs, with more severe effects in the latter.
- The results have evidenced that filler waviness and agglomeration have coupled weakening effects when acting together. It has been shown that only the YNS approach in combination with the two-parameter agglomeration model can properly account for both phenomena simultaneously.

2.5.2 Static and free vibration analysis of FG-CNTRC skew plates [3]

2.5.2.1 Introduction

As an example of the mechanical enhancements of CNTs in the mechanical response of full-scale structural elements, FG-CNTRC skew plates have been studied. Figure 2.25 shows the configuration of considered skew plates, with length a, width b, thickness t, skew angle α, and fiber orientation angle φ. UD-CNTRC, FG-V, FG-O and FG-X distributions are assumed across the thickness direction of the composite skew plates. In this study, the EROM approach is employed to compute the macroscopic elastic moduli of the composites. An efficient finite element formulation based on the Hu-Washizu principle has been developed to obtain approximate solutions for static and free vibration of various types of FG-CNTRC skew plates with moderate thickness. The shell theory is formulated in oblique coordinates and includes the effects of transverse shear strains by the first-order shear deformation theory (FSDT). An invariant definition of the elastic transversely isotropic tensor based on the representation theorem is also defined in oblique coordinates. Independent approximations of displacements (bilinear), strains and stresses (piecewise constant within subregions) provide a consistent mechanism to formulate four-noded skew elements with a total of twenty degrees of freedom. A set of eigenvalue equations for the FG-CNTRC skew plate vibration is derived, from which the natural frequencies and mode shapes can be obtained. Further information on the formulation of this element can be found in Appendix A.

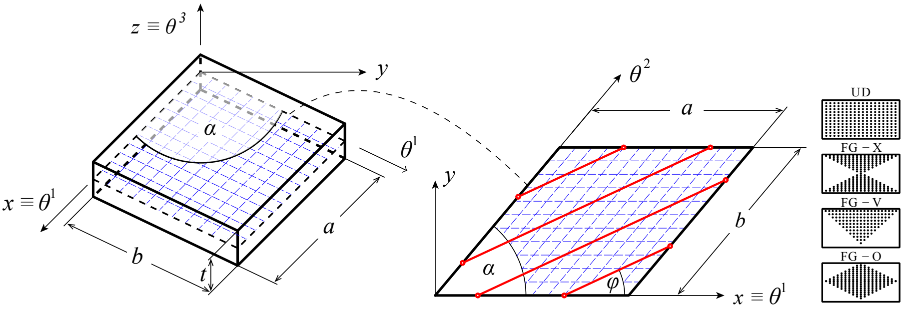

Figure 2.25 Geometry and configurations of the functionally graded carbon nanotube-reinforced (FG-CNTRC) skew plates.

Poly (methyl methacrylate), referred to as PMMA, is selected as matrix phase. The armchair (10,10) SWCNTs are selected as reinforcements with properties taken from the MD simulation carried out by Shen and Zhang [280]. The material properties of these two constituent phases are summarized in Table 2.2. In this study, it is assumed that the effective material properties are independent of the geometry of the CNTRC plates. The material properties of PMMA/CNT composites are taken from the MD results reported

---

[3] An extended version of this subsection is found in paper A.

by Han and Elliot [127], whereby the CNT efficiency parameters can be computed as presented in Table 2.3 [280].

Table 2.2 Material properties of Poly (methyl methacrylate)(PMMA) and Poly{(*m*-phenylenevinylene)-*co*-[(2,5-dioctoxy-*p*-phenylene)vinylene]} (PmPV) at room temperature of 300 K and (10,10) single walled carbon nanotubes (SWCNT).

(10,10) SWCNT [280]	PMMA (T = 300 K) [127]	PmPV (T=300 K) [390]
$E_{11}^{CNT} = 5.6466$ TPa	$E^m = 2.5$ GPa	$E^m = 2.1$ GPa
$E_{22}^{CNT} = 7.0800$ TPa	$\nu^m = 0.34$	$\nu^m = 0.34$
$G_{12}^{CNT} = 1.9445$ TPa	$\alpha^m = 51.75 \times 10^{-6}/K$	$\alpha^m = 51.75 \times 10^{-6}/K$
$\nu_{12}^{CNT} = 0.175$	$\rho^m = 1.15$ g/m^3	$\rho^m = 1.15$ g/m^3
$\rho^{CNT} = 1.40$ g/m^3		

Table 2.3 Comparison of Young's moduli for PMMA/CNT composites reinforced by (10,10) SWCNT at T=300 K with MD simulation [280].

f_{CNT}^*	MD [280]		Rule of mixtures			
	E_{11}[GPa]	E_{22} [GPa]	E_{11} [GPa]	η_1	E_{22} [GPa]	η_2
0.12	94.6	2.9	94.8	0.137	2.9	1.022
0.17	138.2	4.9	138.7	0.142	4.9	1.626
0.28	224.2	5.5	224.0	0.141	5.5	1.585

Studies are conducted on the static response of functionally graded PMMA/CNT skew plates under uniform transverse loads (q_o), the free vibration of FG skew plates with symmetrical and unsymmetrical reinforcement distributions and, finally, the influence of fiber direction on the natural frequencies is also investigated. The various non-dimensional parameters used throughout this subsection are defined as:

$$\text{Non-dimensional frequency parameter}: \bar{\lambda} = \omega \frac{b^2}{t} \sqrt{\frac{\rho^m}{E^m}}, \tag{2.82a}$$

$$\text{Non-dimensional central deflection}: \bar{w} = \frac{w_o}{t} \tag{2.82b}$$

where w_o is the vertical deflection at the central point, and ω stands for the natural frequencies in rad/s.

2.5.2.2 Numerical results

Several numerical examples are provided to investigate the bending behavior of FG-CNTRC skew plates under uniform transverse loading $q_o = -0.1$ MPa. In order to demonstrate the accuracy of the FE model used in the present study, results computed by the commercial FE software ANSYS (SHELL181, four-noded element with six degrees of freedom at each node) are also provided for the same mesh density. Table 2.4 shows the non-dimensional central deflection $\bar{w}$ for the four types of FG CNTRC skew plates subjected to a uniform transverse load q_o, considering different values of width-to-thickness ratio (b/t=10, 50) and varying skew angles for simply supported (SSSS) boundary conditions. It is noticeable that the volume fraction of the CNTs has a deep influence on the central deflection of the plates. For instance, for uniform distributions only 6% increase in the volume fraction of CNT may lead to more than 60% decrease in the central deflection. Likewise, the values of non-dimensional deflections decrease as the skew angle increases. It is also noted that the central deflections of FG-V and FG-O CNTRC plates are larger than the deflections of UD-CNTRC plates, while those of the FG-X CNTRC plates are substantially smaller. This is because the profile of the reinforcement distribution direcly affects the stiffness of the plates. Such results highlight the advantage of FG materials, in which a desired stiffness can be achieved by tailoring the distribution of CNTs along the thickness direction of the plates. Overall, it is concluded that fillers distributed close to the top and bottom induce higher stiffness values of plates.

Table 2.4 Effects of CNT volume fraction f_{CNT} and width-to-thickness ratio (b/t) on the non-dimensional central deflection $\bar{w}$ for CNTRC skew plates under a uniformly distributed load $q_0 = -0.1$ MPa with SSSS boundary conditions (a/b=1, $\varphi = 0^\circ$).

f_{CNT}	b/t	α	UD		FG-X		FG-V		FG-O	
			Present	ANSYS	Present	ANSYS	Present	ANSYS	Present	ANSYS
0.12	10	90	2.831E-03	2.828E-03	2.274E-03	2.271E-03	2.983E-03	2.980E-03	4.341E-03	4.337E-03
		60	2.698E-03	2.558E-03	2.245E-03	2.094E-03	2.812E-03	2.678E-03	3.824E-03	3.719E-03
		30	1.181E-03	1.115E-03	1.073E-03	9.917E-04	1.200E-03	1.141E-03	1.364E-03	1.335E-03
	50	90	1.134E+00	1.133E+00	7.736E-01	7.733E-01	1.232E+00	1.232E+00	2.105E+00	2.105E+00
		60	1.045E+00	1.040E+00	7.376E-01	7.329E-01	1.125E+00	1.120E+00	1.797E+00	1.794E+00
		30	4.300E-01	4.267E-01	3.489E-01	3.443E-01	4.586E-01	4.528E-01	5.721E-01	5.719E-01
0.17	10	90	1.836E-03	1.834E-03	1.450E-03	1.448E-03	1.935E-03	1.933E-03	2.866E-03	2.863E-03
		60	1.720E-03	1.641E-03	1.404E-03	1.320E-03	1.789E-03	1.715E-03	2.480E-03	2.423E-03
		30	7.186E-04	6.847E-04	6.361E-04	5.956E-04	7.248E-04	6.960E-04	8.440E-04	8.308E-04
	50	90	7.732E-01	7.731E-01	5.277E-01	5.275E-01	8.404E-01	8.403E-01	1.436E+00	1.436E+00
		60	7.008E-01	6.984E-01	4.940E-01	4.914E-01	7.533E-01	7.509E-01	1.204E+00	1.202E+00
		30	2.710E-01	2.694E-01	2.162E-01	2.139E-01	2.873E-01	2.838E-01	3.639E-01	3.642E-01
0.28	10	90	1.320E-03	1.318E-03	1.047E-03	1.045E-03	1.359E-03	1.357E-03	1.988E-03	1.986E-03
		60	1.291E-03	1.210E-03	1.041E-03	9.641E-04	1.305E-03	1.233E-03	1.820E-03	1.756E-03
		30	6.040E-04	5.611E-04	4.992E-04	4.600E-04	5.824E-04	5.487E-04	7.218E-04	6.945E-04
	50	90	4.841E-01	4.839E-01	3.281E-01	3.280E-01	5.278E-01	5.276E-01	9.280E-01	9.279E-01
		60	4.570E-01	4.546E-01	3.150E-01	3.126E-01	4.905E-01	4.883E-01	8.245E-01	8.226E-01
		30	2.069E-01	2.046E-01	1.530E-01	1.506E-01	2.134E-01	2.106E-01	2.965E-01	2.957E-01

The results of the free vibration analyses for simply supported FG-CNTRC skew plates are given in Table 2.5. The presented four filler FG distributions are considered with CNT volume fractions of 12%, 17% and 28%. The plate geometry is defined by the following parameters, a/b=1 and b/t=10, 50. Here, the results are also compared to those from the commercial code ANSYS. Firstly, it is observed that higher skew angles give stiffer behaviors and, therefore, higher frequency parameters. This can be explained in terms of the plate area and the perpendicular distance between the non-skew edges. With higher skew angles, the distance between the non-skew edges decreases which raises the frequency values. Furthermore, larger CNT volume fractions lead to higher values of frequency due to an increase in the macroscopic stiffness of the plates. Moreover, as could be previously seen in the bending simulations, we observe that the FG-X plates lead to the stiffest solutions and possess the highest frequency parameters. The explanation of this phenomenon is the same as mentioned before; reinforcements distributed closer to the extremes result in stiffer plates than those distributed nearer to the mid-plane. Fig. 2.26 shows the vibration mode shapes of fully clamped (CCCC) UD-CNTRC plates (f^*_{CNT} = 12%, $a/b = 1$ and $t/b = 0.02$) for skew angles $\alpha = 90°$, $60°$, and $30°$. It is observed from these figures that mode crossing occurs as the skew angle increases.

Table 2.5 Comparison study of frequency parameter $\bar{\lambda}_1$ of skew plates with SSSS boundary conditions ($a/b = 1$, $\varphi = 0°$).

Skew angle	f_{CNT}	b/t	Mode	Types							
				UD		FG-V		FG-O		FG-X	
				Present	ANSYS	Present	ANSYS	Present	ANSYS	Present	ANSYS
90°	0.12	10	1	14.181	14.254	13.859	13.934	11.576	11.644	15.734	15.810
			2	18.364	18.611	18.185	18.433	16.410	16.642	19.717	19.976
			3	28.090	28.710	28.086	28.707	26.660	27.272	29.345	29.972
		50	1	17.808	17.807	17.167	17.164	13.264	13.263	21.343	21.341
			2	22.378	22.372	21.931	21.913	18.738	18.738	25.525	25.515
			3	34.465	34.485	34.320	34.293	31.696	31.727	37.247	37.259
	0.28	10	1	20.343	20.443	20.135	20.239	16.737	16.831	22.798	22.904
			2	25.656	25.998	25.748	26.090	22.491	22.810	28.579	28.944
			3	38.461	39.303	39.124	39.976	35.516	36.364	42.446	43.304
		50	1	26.620	26.617	25.670	25.673	19.515	19.513	32.167	32.164
			2	32.274	32.262	31.779	31.775	25.893	25.889	38.150	38.134
			3	47.900	47.916	48.312	48.345	41.894	41.924	55.183	55.200
60°	0.12	10	1	14.592	15.087	14.327	14.784	12.350	12.617	15.933	16.596
			2	21.101	21.661	20.926	21.465	19.411	19.824	22.313	22.987
			3	32.873	34.092	32.583	33.819	31.282	32.395	34.098	35.414
		50	1	18.756	18.792	18.137	18.164	14.430	14.442	22.176	22.242
			2	26.386	26.413	25.886	25.888	22.941	22.956	29.410	29.457
			3	43.260	43.332	42.738	42.734	39.956	40.020	46.293	46.380
	0.28	10	1	20.691	21.498	20.640	21.373	17.549	17.995	23.004	24.033
			2	29.170	30.019	29.401	30.207	26.304	26.923	32.254	33.247
			3	44.903	46.607	45.412	47.128	42.055	43.558	48.975	50.908
		50	1	27.766	27.837	26.930	26.993	20.869	20.892	33.329	33.451
			2	37.466	37.515	37.094	37.142	31.174	31.194	43.775	43.859
			3	59.776	59.882	60.014	60.128	52.887	52.967	68.437	68.579
30°	0.12	10	1	22.026	23.037	21.874	22.764	20.556	21.132	23.076	24.369
			2	35.790	38.414	35.393	37.696	34.218	36.220	36.920	39.851
			3	48.488	53.298	48.046	52.222	46.768	50.579	49.692	54.883
		50	1	29.557	29.680	28.675	28.721	25.707	25.717	32.750	32.979
			2	55.280	55.701	52.700	52.908	48.992	49.207	59.842	60.416
			3	87.659	88.906	82.247	82.849	75.991	76.537	95.834	97.611
	0.28	10	1	30.267	31.889	30.870	32.269	27.752	28.780	33.281	35.161
			2	48.805	52.635	49.540	52.880	46.258	49.343	52.755	56.928
			3	65.977	72.898	67.116	73.145	63.538	69.423	70.563	77.795
		50	1	41.856	42.098	41.319	41.478	35.068	35.121	48.609	49.020
			2	77.179	77.849	74.931	75.438	66.601	66.936	88.338	89.322
			3	123.376	125.438	117.376	118.770	104.682	105.621	141.233	144.254

Taking advantage of the invariant definition of the constitutive tensor for transversely isotropic materials (as given in Appendix A), which is characterized by a unit vector parallel to the axis of transverse isotropy, $\vec{n} = (\cos\varphi, \sin\varphi, 0)$, we analyze the influence of the angle φ on the frequency parameters $\bar{\lambda}$. Fig. 2.27 shows the variation of the first frequency

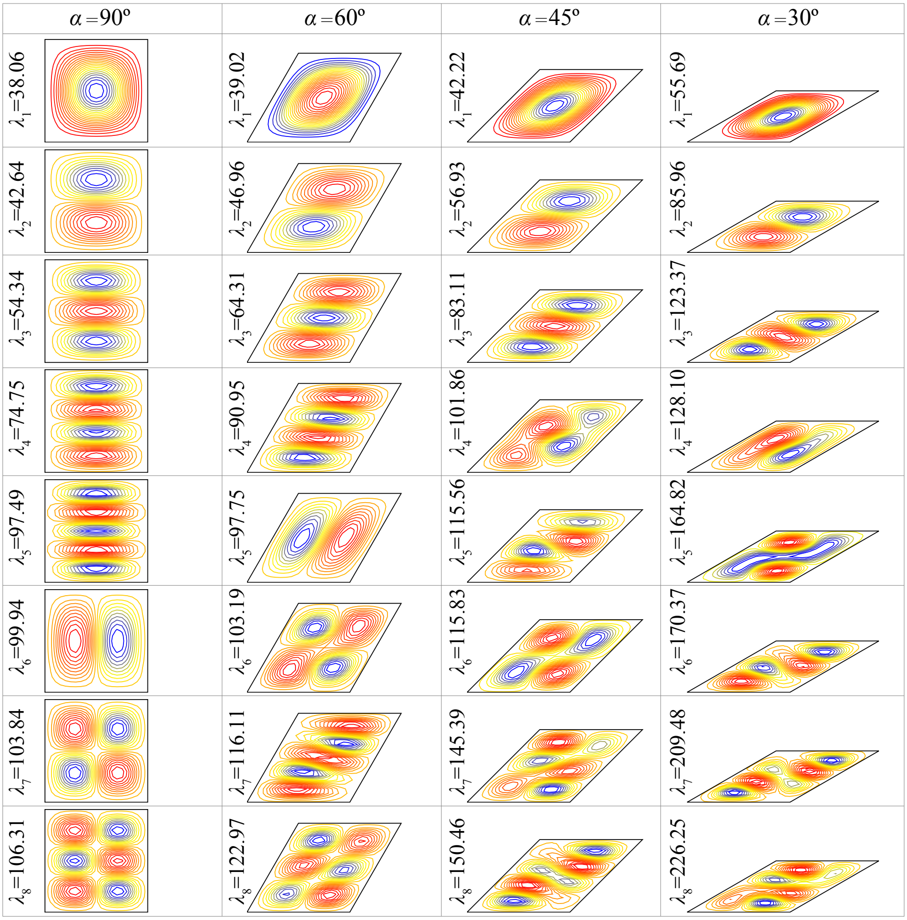

Figure 2.26 First eight mode shapes of a fully clamped (CCCC) UD-CNTRC skew plate for skew angles $\alpha = 90^\circ$, 60°, 45° and 30°, $f^*_{CNT} = 12\%$, $a/b = 1$, $t/b = 0.02$ and $\varphi = 0^\circ$.

parameter for several values of skew angle α and two boundary conditions, namely CCCC and SSSS. As in all the previous analyses, the frequency parameters increase for higher values of the skew angle. Moreover, the results for skew angles of $\alpha = 90^\circ$ are symmetric about $\varphi = 90^\circ$. In contrast, the curves for higher skew angles present increasing levels of asymmetry. This is due to the increment of stiffness provided by the fibers coupled with the stiffening effect of the skew angle. The curves can be separated into two sets divided around $\varphi = 90^\circ$. With SSSS boundary conditions, it is clear that the increase in stiffness is associated with fibers aligning the direction of the longest diagonal. Otherwise, the frequency values for the second set decreases in all cases for fiber angles above $\varphi = 90^\circ$. In the case of CCCC boundary conditions, this behavior is repeated although the maximum values are approximately obtained with fibers aligned in the horizontal Cartesian direction.

These results show the importance of taking into consideration the aligning direction of CNTs in order to optimize the mechanical response of the FG-CNTRC skew plates. For example, with a skew angle of $\alpha = 30°$ and SSSS boundary conditions, the variation of φ may increase the first frequency parameter by up to 11.7% and decrease it by up to 18.6%.

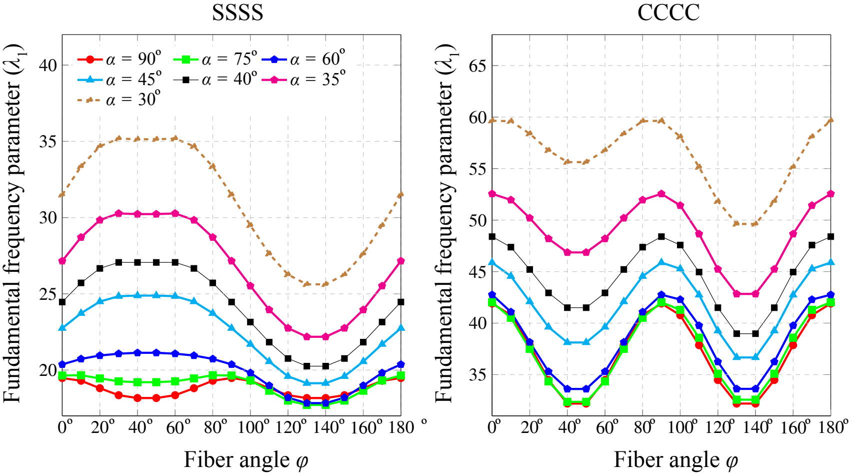

Figure 2.27 Effect of fiber angle φ on the first frequency parameter $\bar{\lambda}_1$ of a CNTRC skew plate (UD-CNTRC, $f_{CNT} = 12\%$, $a/b = 1$, $b/t = 50$).

2.5.2.3 Conclusions

In this subsection, static and free vibration analyses of moderately thick FG-CNTRC skew plates have been presented. An efficient finite element formulation based on the Hu-Washizu principle has been developed. The shell theory is formulated in oblique coordinates and includes the effects of transverse shear strains by first-order shear deformation theory (FSDT). An invariant definition of the elastic transversely isotropic tensor based on the representation theorem is defined in oblique coordinates. Independent approximations of displacements (bilinear), strains and stresses (piecewise constant within subregions) provide a consistent mechanism to formulate four-noded skew elements with a total number of twenty degrees of freedom. A set of eigenvalue equations for the FG-CNTRC skew plate vibration is derived, from which the natural frequencies and mode shapes can be obtained. Detailed parametric studies have been carried out to investigate the influences of skew angle, carbon nanotube volume fraction, plate thickness-to-width ratio, plate aspect ratio, boundary condition and distribution profile of reinforcements (uniform and three non-uniform distributions) on the static and free vibration characteristics of the FG-CNTRC skew plates. The results have been compared to commercial code ANSYS and limited existing bibliography with very good agreement.

2.5.3 Buckling and post-buckling analysis of FG-CNTRC curved panels [4]

2.5.3.1 Introduction

The FG-CNTRC curved cylindrical panels analyzed in this research work are sketched in Fig. 2.28. The panel is defined by an x-y-z curvilinear coordinate system with the origin at the center of the panel. The x-axis is parallel to the straight edges, the z-axis is directed outward the surface of the panel, and the y-axis is the circumferential coordinate. Displacements u, v and w refer to the mid-surface axial, circumferential and out-of-plane displacements, respectively. Rotational degrees of freedom noted as ϕ_x and ϕ_y stand for rotations around x- and y-axis, respectively. The axial compression loading condition is defined by an uniformly distributed load N_x along the curved edges. The panel is assumed to be thin and of width b, straight length a, radius R, span angle 2β, and uniform constant thickness t. The rise of the curved edges, h, can be computed by simple trigonometric relations as $h = R(1-\cos\beta)$. The CNTs are assumed to be uniaxially aligned at φ degrees with respect to the axial direction (x-axis). A local material coordinate system, $\{0 - x_1 x_2 x_3\}$, is defined at every point on the mid-plane with x_1 aligned in the fiber direction, x_2 on the panel mid-plane, and x_3 normal to the panel. In addition, CNTs are functionally graded across the thickness of the panel by four different distributions, namely UD, FG-V, FG-O and FG-X.

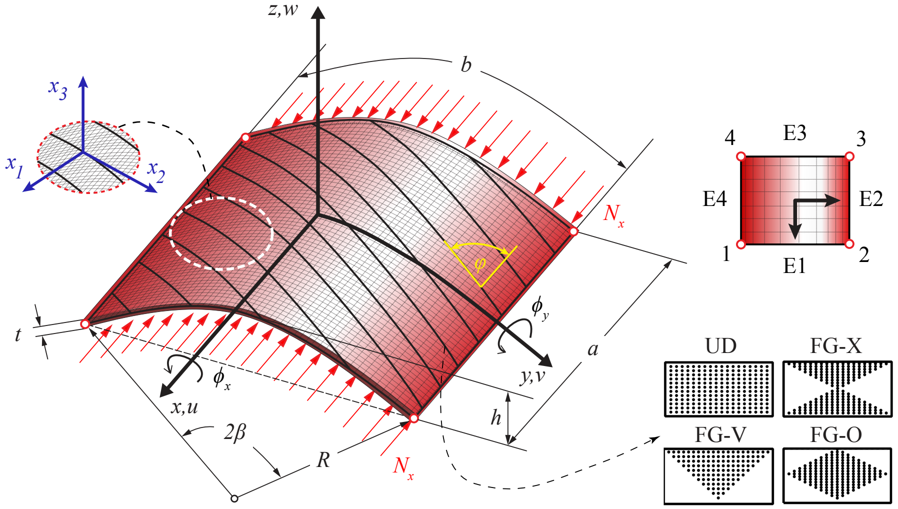

Figure 2.28 Geometry and coordinate system of FG-CNTRC cylindrical panel.

The aim of this set of analyses concerns, firstly, the study of the linear buckling behavior of FG-CNTRC curved panels under uniform axial compression and shear and, finally, the post-buckling behavior of FG-CNTRC curved panels under axial compression. PmPV and PMMA are considered as the matrix materials in the linear buckling and post-buckling analysis, respectively. The material properties of these polymers are summarized in

---

[4] An extended version of this subsection is found in papers C and H.

Table. 2.2. The armchair (10,10) SWCNTs are selected in both cases as reinforcing phase. The effective mechanical properties of the composite are computed by the Eshelby-Mori-Tanaka model unless otherwise indicated. The following representative values of the Hill's elastic moduli of CNTs: n_r=450 GPa, k_r=30 GPa, m_r=p_r=1 GPa and l_r=10 GPa, have been taken from the analytical results of Popov *et al.* [249]. In the case of different thermal environments, the temperature-dependent mechanical properties of (10,10) SWCNTs are indicated in Table. 2.6.

Table 2.6 Temperature-dependent material properties for (10,10) SWCNT (L=9.26 nm, R=0.68 nm, h=0.067 nm, $\nu_{12}^{CNT} = 0.175$) [280].

Temperature (K)	E_{11}^{CNT} [TPa]	E_{22}^{CNT} [TPa]	G_{12}^{CNT} [TPa]	α_{11}^{CNT} ($\times10^{-6}$/K)	α_{22}^{CNT} ($\times10^{-6}$/K)
300	5.6466	7.0800	1.9445	3.4584	5.1682
400	5.5679	6.9814	1.9703	4.1496	5.0905
500	5.5308	6.9348	1.9643	4.5361	5.0189
700	5.4744	6.8641	1.9644	4.6677	4.8943
1000	5.2814	6.6220	1.9451	4.2800	4.7532

2.5.3.2 Numerical results

Linear buckling The numerical studies are conducted with the commercial software ANSYS v15.0. The panels are modeled with the standard structural shell element, Shell 181 [299]. This element type is a quadrilateral 4-nodes element involving both bending and membrane properties with three rotational and three translational degrees of freedom per node. This element is suitable for thin to moderately-thick shell structures. In order to implement functionally graded sections, the preintegrated sections module of ANSYS is employed. This module permits the specification of the membrane, bending and coupling stiffness matrices of the shells (for further information in this regard see Appendix A). All the foregoing results are defined by the non-dimensional buckling load intensity factor as follows:

$$k_\sigma = \frac{\sigma_{cr}}{\sigma_E}; \quad \sigma_E = \frac{\pi^2 E_m}{12(1-\nu_m^2)}\left(\frac{t}{b}\right)^2 \tag{2.83}$$

The cylindrical shells are considered simply supported on all edges (w=0); along the curved edge 1 (loaded one) the longitudinal displacements are allowed but restricted while in the curved edge 3 are restrained. The straight edges 2 and 4 are free to wave in the circumferential direction. The external load is introduced by means of a uniform compression on the edge 1 in the longitudinal direction. For illustrative purposes, a constant length of b=100 cm and thickness $t = b/50$ are selected in the subsequent analyses.

The effect of the fiber orientation angle φ on the critical buckling load is analyzed for different reinforcement distributions and curvature in Fig. 2.29. The results show that in the case of flat shells (h/R=0) the buckling load intensity factor presents positive curvature with respect to the fiber angle φ. This fact favors the origin of peak values for fibers aligned approximately with the diagonal direction of the shell. Moreover, among the different distributions of CNTs, FG-X distribution leads to the largest buckling loads whilst the

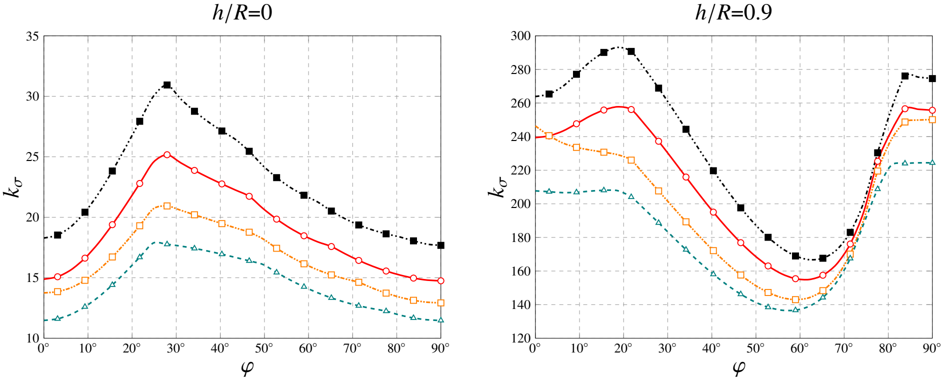

Figure 2.29 Effect of fiber angle φ on the buckling load intensity factor k_σ of a FG-CNTRC panel subjected to compressive forces N_b (SSSS, b=100cm, a=2· b, t=b/50, R=b/2, f^*_{CNT}=0.11) for different profiles: UD (—○—), FG-V (—□—), FG-O (—△—) and FG-X (- - -).

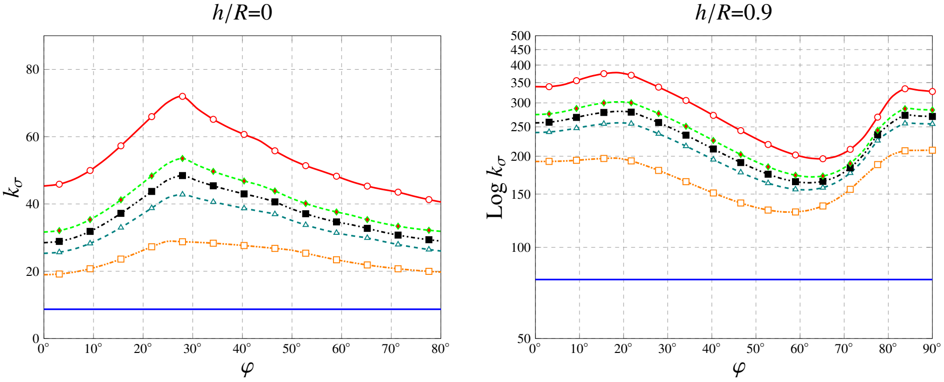

Figure 2.30 Effect of fiber angle φ on the buckling load intensity factor k_σ of a UD-CNTRC panel subjected to compressive forces N_b (SSSS, b=100 cm, a=2· b, t=b/50, R=b/2) for different SWCNT volume fractions: f^*_{CNT}=0.00 (———), f^*_{CNT}=0.05 (···□···), f^*_{CNT}=0.11 (- - △ - -), f^*_{CNT}=0.14 (···■···), f^*_{CNT}=0.17 (- - -◆- - -), and f^*_{CNT}=0.30 (——○——).

FG-O distribution conducts to the minimum values. This is because the profile of the reinforcement distribution affects the stiffness of the shells. Also, this circumstance points out the advantage of FG materials, in which a desired stiffness can be achieved by adjusting the distribution of CNTs along the thickness direction of the shells. It is concluded that reinforcements distributed close to the top and bottom induce higher stiffness values of shells. Another essential aspect is the influence of the fiber direction. In the case of flat shells, for every reinforcement distribution the critical buckling load increases up to 40% with respect to the shells with fibers aligned in the axial direction. In the case of curved shells (h/R=0.9), the curvature significantly increases the buckling load values

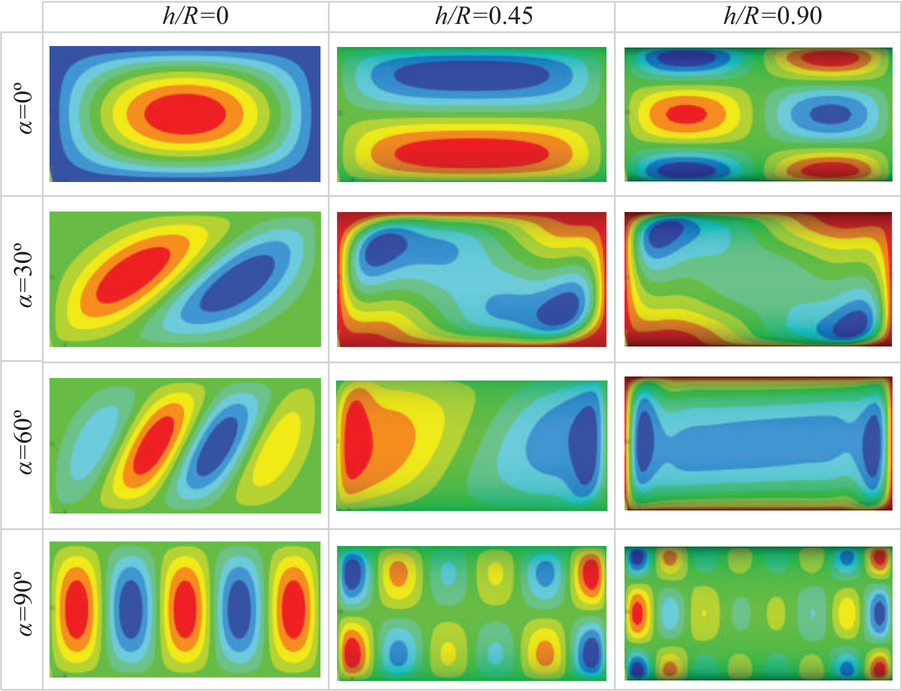

Figure 2.31 Plan view of the first elastic buckling modes for UD-CNTRC flat panel ($h/R = 0$) and curved panels ($h/R = 0.45, 0.9$) subjected to compressive loading for different fiber orientation angles φ (SSSS, b=100 cm, a=2· b, t=b/50, f^*_{CNT}=0.11).

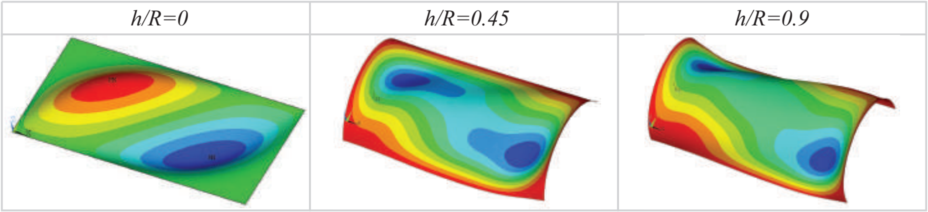

Figure 2.32 Perspective view of the first elastic buckling modes for UD-CNTRC flat panel ($h/R = 0$) and curved panels (h/R=0.45, 0.9) subjected to compressive loading with fiber orientation angle φ of 30° (SSSS, b=100 cm, a=2· b, t=b/50, f^*_{CNT}=0.11).

with respect to the flat configuration. However, this more complex geometry distorts the relationship between the buckling load factor and the fiber orientation angle. It is noticeable that despite the fiber distributions conserve their relative order, there is a range of angles, approximately between 70° and 85°, in which they do not show a significant difference. Similar conclusions can be extracted by varying the CNT volume fraction f^*_{CNT} as in Fig. 2.30. In this figure, it is represented the buckling load intensity factor for different fiber orientation angles φ and UD-CNTRC panels with increasing CNT volume fractions. The results show that the buckling load intensity factors have higher values when the CNT volume fraction is larger as it raises the stiffness of the panels. The curvature parameter h/R and the fiber angle φ also have a substantial influence on the shape of the first buckling mode as can be clearly seen in Figs. 2.31 and 2.32.

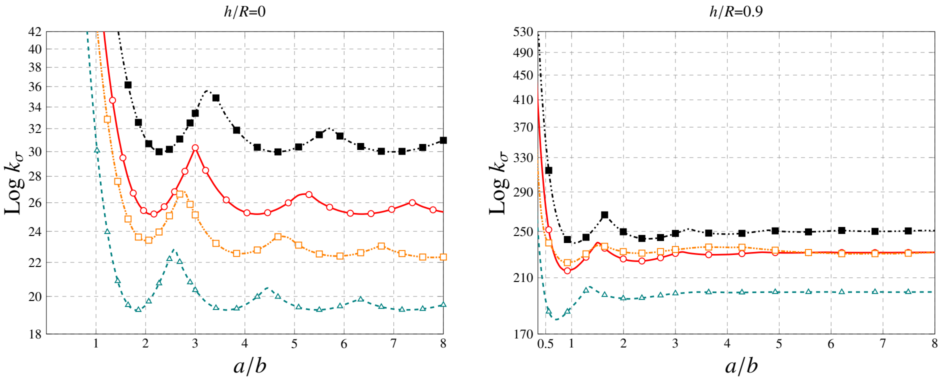

Figure 2.33 Variation of the buckling load intensity factor k_σ of FG-CNTRC panels versus plate aspect ratio under axial compression (SSSS, b=100cm, t=b/50, f^*_{CNT}=0.11, φ=0°) for different profiles: UD (—○—), FG-V (—□—), FG-O (—△—) and FG-X (- - -).

Fig. 2.33 shows the buckling load parameters for simply supported FG-CNTRC curved panels with aspect ratio a/b changing from 0.5 to 8. It can be seen that the buckling load parameters decrease as the plate aspect ratio increases due to the activation of buckling modes with higher number of waves. I is also noticeable that the FG-V and UD distributions show similar results in the curved configuration. This fact, which can also be observed in Fig. 2.29, results in the inversion of the order of these two curves for certain values of fiber orientation angles and aspect ratios.

The effect of different uniform temperature environments (T=300K, 400K and 500K) on the buckling load parameters of FG-CNTRC curved panels with different reinforcement distributions are shown in Table 2.7. For this study, the EROM is used to predict the effective material properties of CNTRCs. Both CNTs and the matrix phase are assumed temperature-dependent. To this end, CNT elastic moduli are taken from Table 2.6, and the Young's modulus of PmPV is defined as $E^m = (3.52 \times 0.0047T)$ GPa, with $T = T_0 + \Delta T$ and the room temperature T_0 = 300 K. It can be seen that the buckling load intensity factors decrease as temperature increases. This is because an increment of the temperature reduces the elastic moduli of CNTRCs shells since material properties of the matrix and SWCNTs are assumed to be temperature-dependent. As in previous analyses, we also found here that FG-X and FG-O CNTRC shells have the highest and lowest values of buckling load intensity factors, respectively, in different temperature environments.

The buckling behavior of simply supported FG-CNTRC curved shells subjected to shear loading N_{xy} is also analyzed. The shear forces have been applied in the form of uniform shell edge loads along the middle surface of the plates. Fig. 2.34 shows the loading

Table 2.7 Effect of environment temperature on the buckling load intensity factor (k_σ=σ_{cr}/σ_E; σ_E=$\left(\pi^2 E_{(m,T=300K)}/12\left(1-\nu^2_{(m,T=300K)}\right)\right)(t/b)^2$) of FG-CNTRC curved panels under axial compression (SSSS, b=100 cm, a=2· b, t=b/50, f^*_{CNT}=0.11, φ=0°).

T (K)	h/R	Type of CNTRC			
		UD	FG-V	FG-O	FG-X
300	0	15.57	13.76	10.52	20.68
	0.45	121.13	120.76	99.79	131.73
	0.9	268.10	268.04	223.02	310.36
400	0	12.66	10.80	7.86	17.45
	0.45	74.04	77.06	65.65	81.95
	0.9	176.42	176.33	145.27	192.27
500	0	9.41	7.56	5.15	13.41
	0.45	23.27	23.93	17.76	28.56
	0.9	49.41	50.51	39.85	58.67

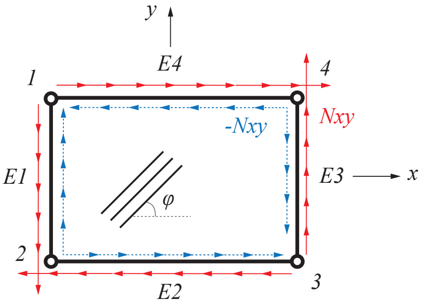

Figure 2.34 Positive (+N_{xy}) and negative (-N_{xy}) shear loading of a FG-CNTRC curved shell.

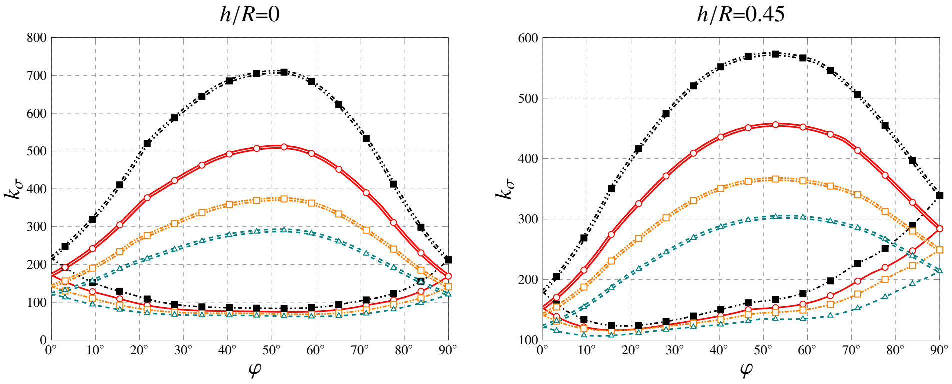

Figure 2.35 Effect of fiber angle φ on the buckling load intensity factor k_σ of a FG-CNTRC flat panel subjected to tangential forces (+N_{xy} "-", -N_{xy} "=") for different profiles: UD (—○—), FG-V (—□—), FG-O (—△—) and FG-X (- - -); (SSSS, b=100 cm, $a=b$, $t=b/50$, f^*_{CNT}=0.11).

conditions considered in these analyses. Fig. 2.35 shows the effect of the fiber angle φ on the buckling load factor k_σ for square flat and curved shells. The critical loads of the FG-CNTRC panels under negative shear are higher than those of under positive shear for every fiber angle. This is because in the former case the compressive component of the shear is more closely aligned with the fibers. Furthermore, like in the case of compressive loadings, fiber orientation angles aligned with the diagonal of the panels (45°) conduct to higher buckling loads. For further illustration of these results, the first buckling modes of UD-CNTRC panels for different fiber orientation angles and h/R ratios are also depicted in Fig. 2.36.

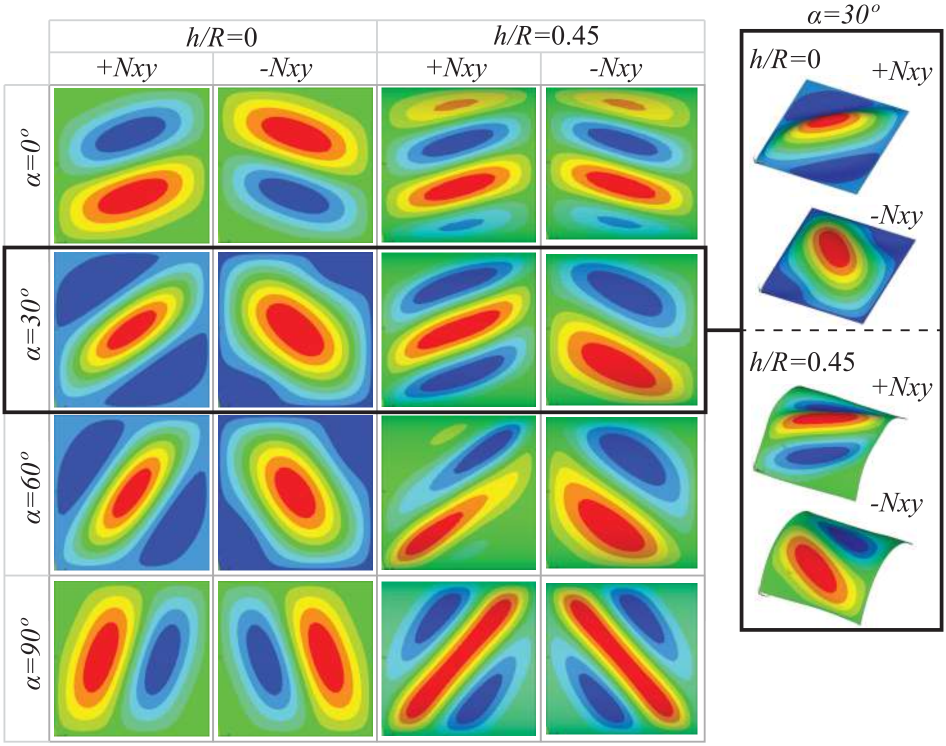

Figure 2.36 First elastic buckling modes of simply supported UD-CNTRC flat panel (h/R=0) and curved panel (h/R=0.9) under shear forces with different fiber orientation angles α (b=100 cm, $a = b$, $t = b/50$, f^*_{CNT}=0.11).

Post-buckling analysis For the subsequent analyses, the geometrical properties $a = b = 0.2$ m, t =a/50, and h =0.025b are set up, unless otherwise indicated. In order to evaluate the imperfection sensitivity of the panels, a small initial imperfection, $w_0 = 0.1t$, is also considered in the transverse direction following the first buckling mode. Axial loads are presented in non-dimensional form as $N_b = N_x a^2/E_m t^3$. Two types of boundary conditions are considered in the numerical analyses: clamped curved edges and simply supported straight edges (CSCS), and four edges simply supported (SSSS). In this study, the arc-length method has been selected as the numerical approach for predicting the non-linear buckling behavior.

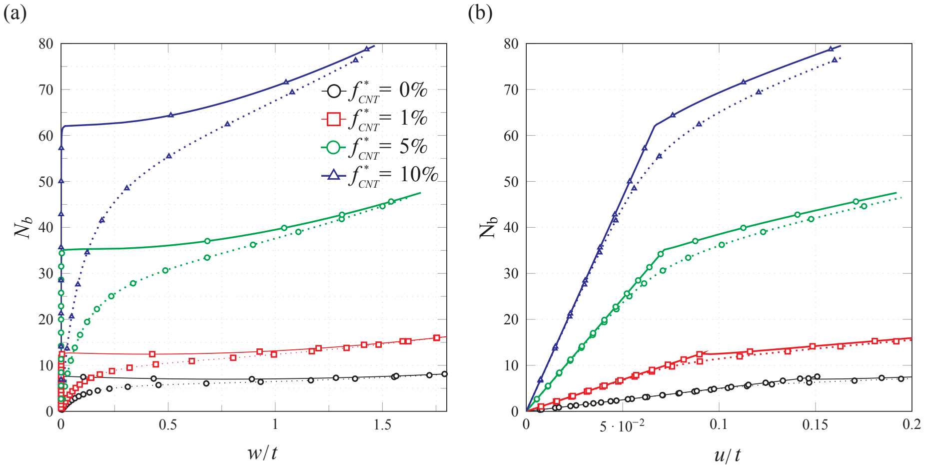

Figure 2.37 Non-dimensional central deflection (a) and end-shortening (b) of uniaxially compressed FG-CNTRC curved panels with CSCS boundary conditions and different SWCNT contents (UD, a=b=1 m, $t = a/50$, h =0.025b, $\varphi = 0^\circ$). Solid and dotted lines denote the results for perfect and imperfect ($w_0 = 0.1t$) panels, respectively.

Firstly, the post-buckling paths of FG-CNTRC curved panels are analyzed for different filler contents. In particular, CNT volume fractions of 0, 1, 5 and 10% are selected as shown in Fig. 2.37. Uniform (UD) distributions of nanotubes are considered as well as CSCS boundary conditions. Figs. 2.37 (a) and (b) show the non-dimensional central deflection (w/t) and end-shortening (u/t), respectively. We first note that the limit points and the subsequent snap-through buckling paths, as in the case of neat polymer f^*_{CNT}=0%, tend to disappear as the filler content grows. In these cases, as for instance a filler content of f^*_{CNT}=10%, the central deflection increases slowly in the pre-buckling stage and increases very fast in the post-buckling stage. In addition, the relationship between the end-shortening and the load parameter is almost bi-linear. As expected, higher SWCNT contents lead to stiffer panels and, therefore, higher critical buckling loads. For example, a filler content of 5% yields an increase of the critical buckling load of five times that of the neat polymer, f^*_{CNT}=0%. The increases in the bending stiffness of the panels can be clearly seen in Fig. 2.37 (a) where, in the post-buckling stage, the slope of the equilibrium path increases admitting higher load levels. In terms of axial stiffness, similar conclusions can be extracted from Fig. 2.37 (b).

The post-buckling behavior of FG-CNTRC curved panels with different CNTs distributions, namely UD, FG-V, FG-O, and FG-X, is studied for CSCS and SSSS boundary conditions in Figs. 2.38 (a) and (b), and (c) and (d), respectively. First of all, let us focus on the V type distribution. It can be seen in Fig. 2.38 (c) that the FG-V distribution does not exhibit a critical buckling load and presents an unstable response (the analysis with initial imperfection has been omitted for clarity). As already discussed by other authors

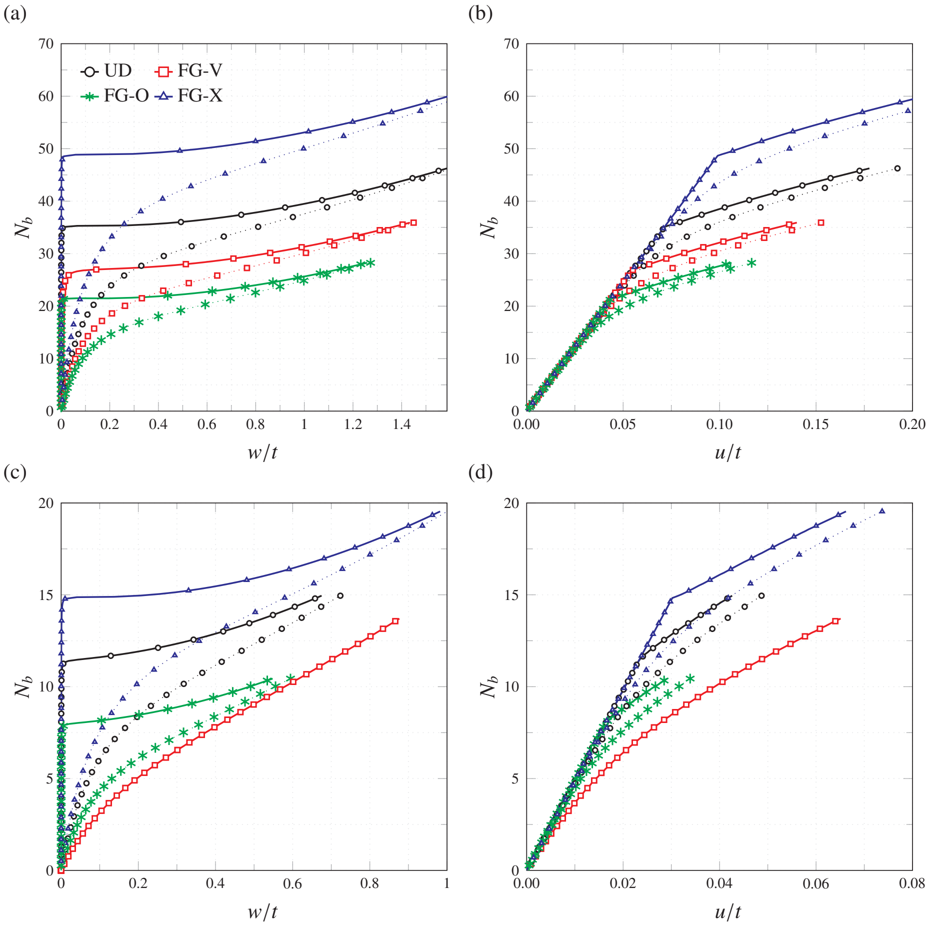

Figure 2.38 Post-buckling path of FG-CNTRC curved panels with CSCS, (a) and (b), and SSSS, (c) and (d), boundary conditions and different SWCNTs distributions (a=b=1 m, t =a/50 , h =0.025b, $f^*_{CNT} = 0.12$, $\varphi = 0°$). Solid and dotted lines denote the results for perfect and imperfect ($w_0 = 0.1t$) panels, respectively.

[385, 386], this behavior is explained by the coupling between membrane and bending stiffnesses induced by the asymmetry of the distribution. Conversely, this coupling is lost in the case of CSCS boundary condition as shown in Fig. 2.38 (a). In this case, the rotational restraint deletes the bending-extension coupling and the panels thus exhibit typical pre- and post-buckling behaviors. With respect to the rest of distributions, it can be seen that FG-O leads to the lowest post-buckling strength, while FG-X yields the highest post-buckling strength among the four types of distributions for both boundary conditions. In the case of CSCS boundary condition, where FG-V does originate initially stable panels, CNTs distributed according to FG-V profile yields post-buckling paths between those by UD and FG-O. It can be therefore concluded that CNTs distributed close to the top and bottom surfaces increase more efficiently the stiffness and post-buckling strength of the FG-CNTRC cylindrical panels than CNTs distributed near the mid-plane.

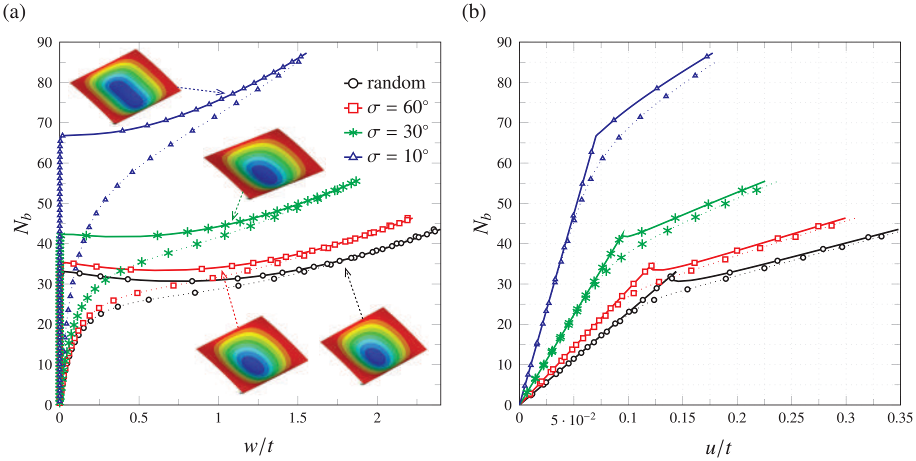

Figure 2.39 Non-dimensional central deflection (a) and end-shortening (b) of uniaxially compressed FG-CNTRC curved panels with CSCS boundary conditions and different SWCNT misalignment degrees (UD, a=b=1 m, t =a/50 , h =0.025b, f^*_{CNT} = 0.12, φ = 0°). Solid and dotted lines denote the results for perfect and imperfect (w_0 = 0.1t) panels, respectively.

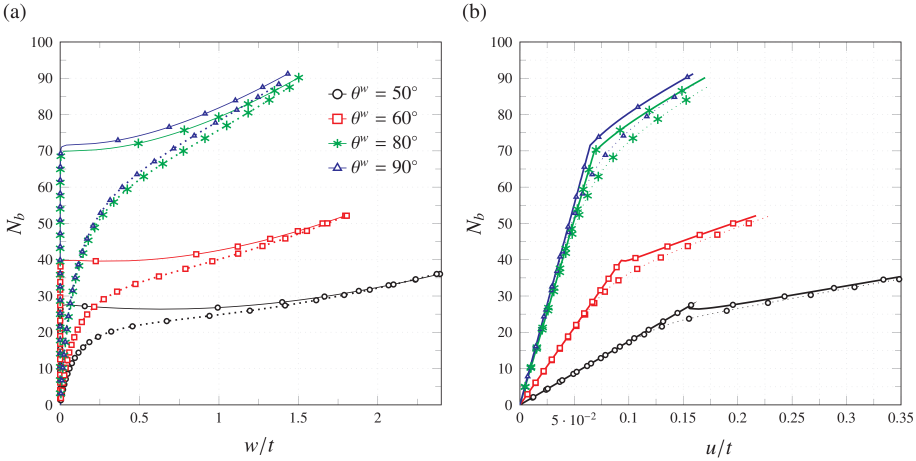

Figure 2.40 Non-dimensional central deflection (a) and end-shortening (b) of uniaxially compressed FG-CNTRC curved panels with CSCS boundary conditions and different degrees of CNT waviness (UD, a=b=1 m, t =a/50 , h =0.025b, f^*_{CNT} = 0.12, φ = 0°). Solid and dotted lines denote the results for perfect and imperfect (w_0 = 0.1t) panels, respectively.

The influence of CNTs misalignment on the post-buckling behavior of UD-CNTRC curved panels is also investigated. To this aim, the orientation distribution function in Eq. (2.78) is adopted here. This type of distribution is said to have azimuthal symmetric and, thus, only one Euler angle is needed for its definition. Hence, the orientation distribution function, $\Omega(\theta)$, is defined as a truncated Gaussian distribution with mean value $\theta = 0^\circ$, and θ ranging from $-\pi/2$ to $\pi/2$, with standard deviation σ. Any general orientation distribution is comprised between the limit cases of fully aligned, $\sigma = 0^\circ$, and randomly oriented fillers, $\Omega(\theta) = 1$. In the case of fully aligned, the overall composites are transversely isotropic, whilst randomly oriented CNTs yield isotropic composites. Thence, the degree of anisotropy depends upon the alignment of the fillers.

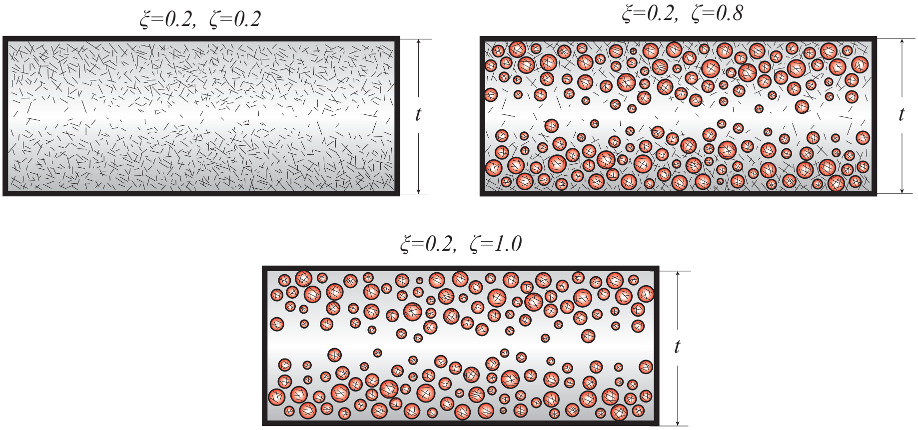

Figure 2.41 Schematic illustration of the variation of the parameters ξ and ζ of the two-parameter agglomeration model for a FG-X filler distribution.

On this basis, Fig. 2.39 shows the post-buckling behavior of UD-CNTRC curved panels with different degrees of CNTs misalignment. It is observed that misalignment of fillers has a substantial effect on the critical buckling loads. The highest critical buckling loads are obtained for fully aligned SWCNTs configurations, i.e. $\sigma = 0^\circ$, and decrease with the misalignment degree, i.e. with decreasing standard deviation values. In addition, not only the critical buckling loads are affected, but also the slope of both central deflection and end-shortening curves. Misalignment of fillers also has a deep influence on the buckling modes as shown in Fig. 2.39. This fact is of crucial relevance in the design of FG-CNTRC fuselage panels. The orientation distribution of CNTs embedded in polymer matrices depends upon the manufacturing process. Unless special measures are taken, nanotubes are randomly oriented within the matrix. There exist several techniques in the literature for the aligning of the nanotubes, such as the application of high magnetic fields. However, these techniques are usually expensive and hardly scalable, so the mechanical enhancements must be properly justified. This sort of results supports the importance of developing cost-efficient aligning techniques for the development of high-performance composites.

The effect of CNTs waviness is also studied for different spiral angles θ^w as shown in Fig. 2.40. It can be observed in Fig. 2.40 (a) that spiral angles below 80° induce substantial decreases in the critical buckling load. Similarly, it is clearly displayed in Fig. 2.40 (b) that waviness has an important effect on the axial stiffness of the panels, and severe reductions of the slope of the equilibrium paths can be observed. It can be seen that a sharp reduction is found for spiral angles between 60° and 80°. It is also worth noting the influence of CNTs waviness on the shape of the post-buckling equilibrium paths. It can be seen that for decreasing spiral angles θ^w, and thus decreasing CNTs anisotropy, the post-buckling paths exhibit a limit point and a snap-through transition regime, as it is the case for $\theta^w = 50°$. Nonetheless, as θ^w increases, the snap-though transition tends to disappear and the post-buckling paths exhibit almost bi-linear behaviors.

Finally, the effect of agglomeration of SWCNTs is studied. Following the theoretical framework outlined in Section 2.2.5, the two-parameter agglomeration model can be readily applied to functionally graded materials as illustrated in Fig. 2.41. Hence, the analyses are conducted with the first agglomeration parameter fixed at ζ=0.2, and the post-buckling paths are obtained for ξ parameters varying between the limit values of 0.2 and 1. Let us recall that limit cases ζ=ξ=0.2 and ζ=0.2, ξ=1 correspond to uniform dispersions and fillers located at bundles, respectively. Fig. 2.42 shows the post-buckling equilibrium paths for FG-CNTRC curved panels with different agglomeration degrees and CSCS boundary condition. A first important conclusion is that agglomeration has a detrimental effect on the mechanical behavior of FG-CNTRCs. For example, in the case of the deflection of UD distribution, Fig. 2.42 (a), CNTs located only within the bundles (ξ=1) originates a reduction of the critical buckling load of more than three times. The same effect can be observed for all the filler distributions and, therefore, it can be concluded that agglomeration always reduces both the critical buckling load and the post-buckling stiffness. This conclusion has a pivotal importance for the design of high-performance FG-CNTRCs. Although there exist a few techniques to improve the dispersion of CNTs, achieving uniform distribution of fillers remains a challenging task. Nevertheless, as observed in these analyses, mitigating the agglomeration effects is of critical importance for the development of high strength CNT reinforced composites. Finally, it is worth noting that, as in previous analyses, the stiffest post-buckling paths are obtained for FG-X filler distributions. UD, FG-V and FG-0 distributions provide, in decreasing order, lesser critical buckling loads and non-dimensional force parameters. Therefore, the discussion on the greater efficiency of filler distributions with CNTs close to the top and bottom panel surfaces can be also made here.

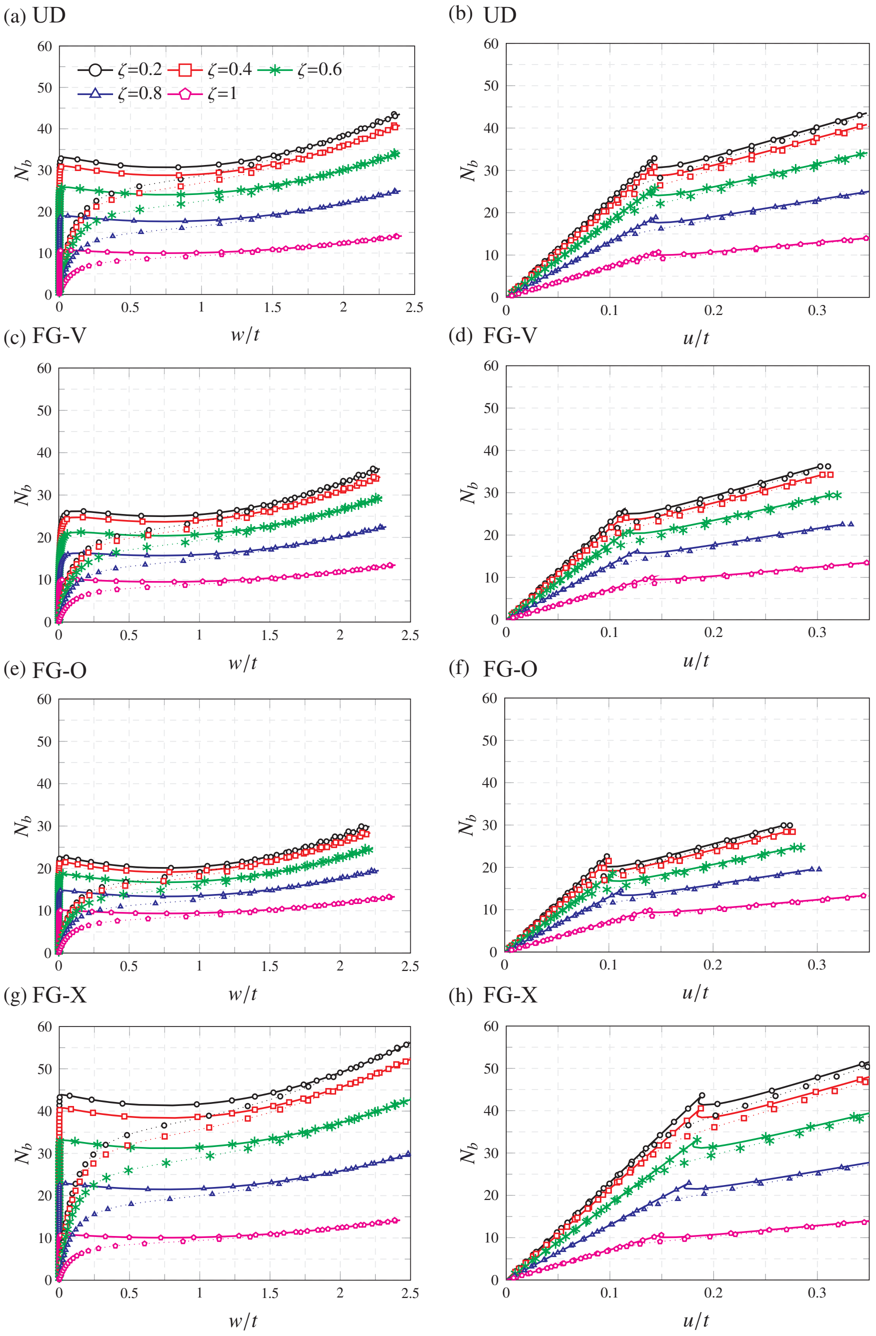
(a) UD (b) UD

(c) FG-V (d) FG-V

(e) FG-O (f) FG-O

(g) FG-X (h) FG-X

Figure 2.42 Non-dimensional central deflection and end-shortening of uniaxially compressed FG-CNTRC curved panels with UD, (a) and (b), FG-V (c) and (d), FG-O, (e) and (f), and FG-X, (g) and (h), SWCNT distributions (CSCS, ξ=0.2, a=b=1 m, t =a/50 , $h = 0.025b$, $f_{CNT}^{*} = 0.12$, $\varphi = 0^{\circ}$). Solid and dotted lines denote the results for perfect and imperfect ($w_0 = 0.1t$) panels, respectively.

2.5.3.3 Conclusions

In this subsection, the critical buckling of FG-CNTRC cylindrical curved panels under compression and shear forces have been first investigated by finite elements analyses. The plates are reinforced by SWCNTs and effective material properties of CNTRC plates are estimated either by the Eshelby-Mori-Tanaka approach or the EROM. Detailed case studies illustrate the influence of fiber angle, aspect ratio, temperature, SWCNTs grading profile and curvature. The key contributions of this study can be summarized as follows:

- The buckling load intensity factor of flat panels subjected to compressive loading presents positive curvature with respect to the fiber orientation angle. One clear maximum peak is found for fiber orientations aligned with the diagonal of the panel. On the contrary, the effects of the fiber orientation angle on the buckling load factor become more complex as the curvature increases. It is shown a change from curves with one single maximum peak to curves with one minimum and two maximum peaks.
- FG-X distribution leads to the largest buckling loads in all the studied cases whilst the FG-O distribution conducts to the minimum values. It is concluded that reinforcements distributed close to the top and bottom induce higher stiffness values.
- In the case of curved panels, it is found some fiber orientation angle ranges in which there is not a big difference among the different CNT distributions. In particular, for curved panels with ratio h/R=0.9, in the range of fiber angles between 70° and 85°, all the fiber distributions present very similar results.
- In all cases, the buckling load intensity factors have higher values when the volume fraction of CNT is larger as it raises the stiffness of the panels.
- In the case of curved configurations under compressive loading, slight differences on the buckling loads are found for FG-V and UD distributions with certain values of fiber orientation angle and aspect ratio. This fact even results in the inversion of the relative order of these two distributions.
- The buckling load intensity factors decrease as temperature increases in FG-CNTRC curved panels subjected to compressive and tangential forces as a result of the temperature-dependent material properties.
- The critical loads of the FG-CNTRC panels under the negative shear are higher than those of positive shear for all fiber angles, exhibiting a maximum value for fibers approximately aligned with the diagonal direction ($\varphi = 45^\circ$).

Secondly, the influence of micromechanical aspects such as the filler orientation, orientation distribution of fillers, waviness and agglomeration on the post-buckling behavior of uniaxially compressed FG-CNTRC curved panels has been investigated. The main findings of this research work can be summarized as follows:

- It has been shown that CNTs orientation has a critical effect on the linear buckling and post-buckling behavior of FG-CNTRC panels. Fibers orientation has a deep impact on the buckling modes and, therefore, the post-buckling equilibrium paths are also heavily influenced.

- FG-V distribution has been shown initially unstable for SSSS conditions. This behavior is ascribed to the coupling between membrane and bending stiffnesses due to the asymmetry of the distribution. Conversely, it has been shown that this coupling is lost in the case of CSCS by means of rotational restraints at curved edges. In this case, the panels have been shown to exhibit typical pre- and post-buckling behavior.
- It has been also illustrated that the orientation distribution of CNTs has a substantial effect of on the post-buckling behavior of FG-CNTRCs. The maximum buckling loads have been found for fully aligned SWCNTs configurations, and decreasing with the CNTs misalignment degree. Since the anisotropy of the resulting composite depends upon the CNTs orientation distribution, it has been shown that the overall stiffness of FG-CNTRC curved panels is highly affected by the orientation distribution of CNTs and, likewise, so are the slopes of both central deflection and end-shortening curves.
- The results have shown that the CNT waviness induces substantial reductions in the critical buckling loads as well as severe reductions of the slopes of the equilibrium paths. This behavior has been explained by the reduction of the longitudinal effective Young’s modulus induced by curviness.
- It has been shown that agglomeration degrades the post-buckling strength for all the fiber distributions. Hence, agglomeration of CNTs in bundles can be understood as defects in the microstructure of the composite. These results strengthen the importance of dispersion techniques for the development of high-performance composites.

2.5.4 Uncertainty propagation in the dynamic behavior of FG-CNTRC plates

2.5.4.1 Introduction

This subsection investigates the effects of the randomness in CNT distribution coupled with the material uncertainties on the vibrational properties of FG-CNTRC plates. FG-CNTRC plates with uniform thickness h, length a and width b are analyzed as shown in Fig. 2.43. Two main sources of stochasticity are considered for FG-CNT plates: the material properties of the composite phases such as the elastic modulus and the Poisson's ratio of the isotropic matrix, mass densities of the matrix and the CNTs, longitudinal and transverse elastic modulus of the CNTs, CNT volume fraction, as well as variations with respect to the linear distribution of CNTs by a power-law model defined by the power-law index k. A variation of ±10% of the uniformly distributed input parameters is assumed for the material variables. In the case of randomness in the CNTs distribution, a truncated Gaussian distribution is set up with a mean value of $\bar{k} = 1$ and a standard deviation of $\sigma_k = 0.2$ in the range $0 \leq k \leq 2$. Fig. 2.44 shows the envelope of all the possible P-FGV reinforcement grading profiles with $f^*_{CNT} = 0.11$ provided by the truncated Gaussian distribution. The random variables mentioned above are examined in three sequential stages:

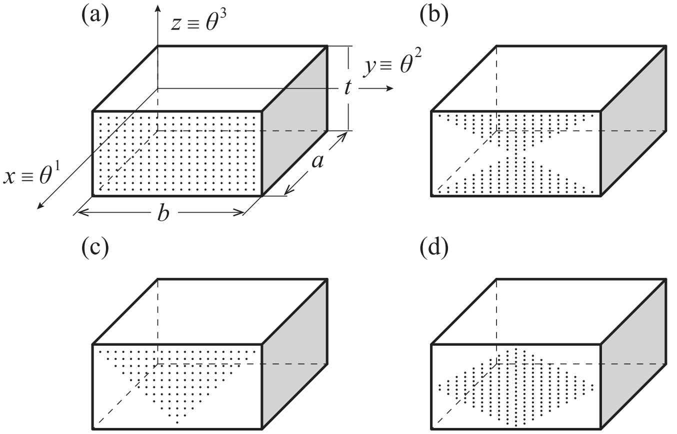

Figure 2.43 Geometry and linear configurations of the functionally graded carbon nanotube-reinforced (FG-CNTRC) plates. (a) UD CNTRC plate; (b) FG-V CNTRC plate; (c) FG-O CNTRC plate; (d) FG-X CNTRC plate.

1. Variation of the material parameters ($k = 1$): $\left\{E_m; \rho_m; f_m; E_{11}^{CNT}; E_{22}^{CNT}; \rho_{CNT}; f_{CNT}\right\}$
2. Variation of the reinforcement grading profile: $\{k\}$
3. Combined variation of (**1**) and (**2**).

The first three natural frequencies are considered as the outputs. The random input variables are scaled randomly in the range 0 to 1, hence, the output response functions are thus defined in the domain of an unit hypercube $K^n = \{(x_1, \dots, x_n), i = 1, \dots, n\}$. Fig. 2.45 shows a general flowchart describing the uncertainty representation and propagation steps. Firstly, an initial sample of the design space is generated by Monte Carlo Simulations (MCSs) and the finite element code based on the Hu-Washizu principle and detailed in Appendix A. Afterward, the initial samples are used in the construction of the surrogate models. The quality of these initial sample points governs the accuracy of the metamodels. Therefore, the quasi-random sequence of Sobol [291] is utilized to ensure a good uniform distribution of the sample points. The response surface thus represents the result of the structural analysis encompassing every reasonable combination of all the input variables. From this, thousands of combinations of all design variables can be created (via simulation) and a pseudo-analysis performed for each variable set, by simply adopting the corresponding surface values. Once the metamodels are built, they can be used to obtain a representative population of the first three stochastic natural frequencies and, finally, statistical analysis of the generated data is carried out.

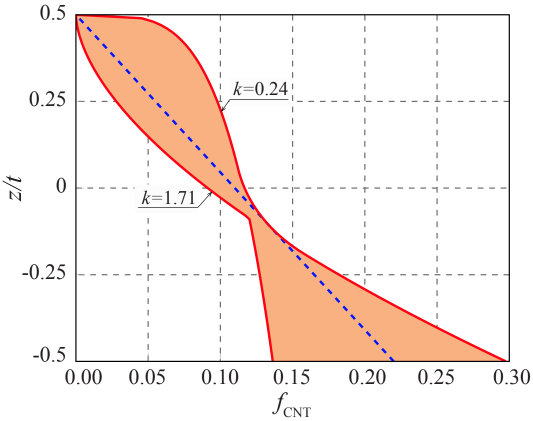

Figure 2.44 Envelope of all possible grading profiles provided by a FG-V power-law distribution (P-FGV) with $f^*_{CNT} = 0.11$ with different power-law indices (k) according to a truncated Gaussian distribution $\left(\bar{k} = 1, \sigma_k = 0.5\right)$.

In the present study, PmPV and (10,10) SWCNTs are selected as the matrix and the reinforcing phases, respectively. The material properties of these two phases are summarized in Table 2.2. The detailed mean material properties of PmPV/CNT for the FG-CNTRC plates are selected from the MD results reported by Han and Elliot [127]. The CNT efficiency parameters η_j can be determined by matching the Young's moduli E_{11} and E_{22} with the counterparts computed by the rule of mixtures. For example, $\eta_1 = 0.149$ and $\eta_2 = 0.934$ for the case of $f^*_{CNT} = 0.11$, and $\eta_1 = 0.150$ and $\eta_2 = 0.941$ for the case of $f^*_{CNT} = 0.14$, and $\eta_1 = 0.149$ and $\eta_2 = 1.381$ for the case of $f^*_{CNT} = 0.17$. In addition, we assume that $\eta_3 = \eta_2$ and $G_{23} = G_{13} = G_{12}$. A fully clamped FG-CNTRC plate is considered having square plan form $a/b = 1$ and length to thickness ratio $a/t = 10$. The resonant frequencies

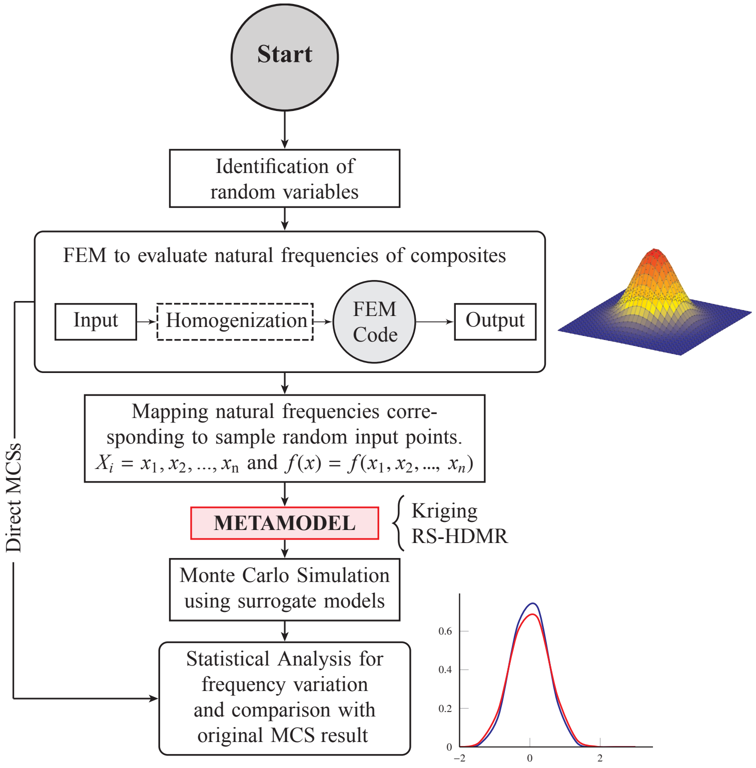

Figure 2.45 Flowchart of stochastic free vibration analysis of FG-CNTRC plates using Kriging and RS-HDMR metamodels.

are presented in non-dimensional form as follows:

$$\bar{\lambda} = \omega \frac{b^2}{\pi^2}\sqrt{\frac{\rho^m t}{D}}; \quad D = E^m t^3/12\left[1-(\nu^m)^2\right] \tag{2.84}$$

2.5.4.2 Results

The random input variables are scaled randomly in the range 0 to 1. For the material variables, a lower and upper limits of ±10% variation are assumed with respect to the mean values for the uniformly distributed input parameters. In the case of the reinforcement grading profile, a truncated Gaussian distribution ($\bar{k} = 1$, $\sigma_k = 0.5$)(1,0.5) is set up for values of k varying from 0 to 2. Metamodels are formed to generate the first three natural frequencies of CCCC FG-CNTRC plates. In the case of the Kriging metamodels, a second order polynomial regression function and a Gaussian correlation are employed. For the RS-HDMR metamodels, first and second order component functions with orthonormal polynomials up to third order are utilized.

Fig. 2.46 shows the Probability Density Functions (PDFs) obtained by the original MCS with respect to the first natural frequency ($\bar{\lambda}_1$) for simultaneous variation of the

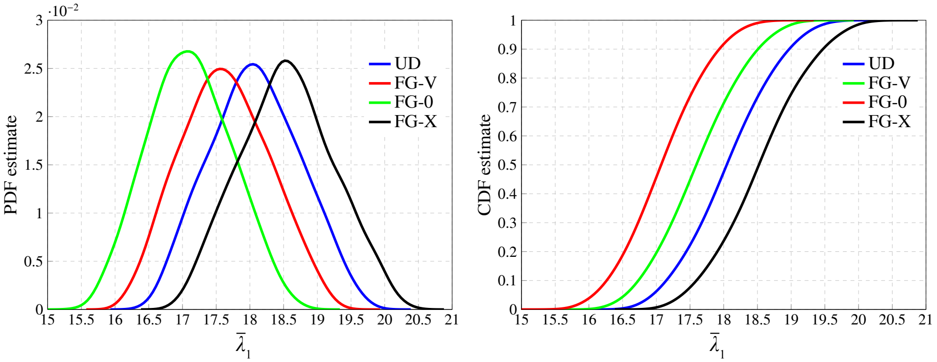

Figure 2.46 Probability density functions (PDF) and cumulative density functions (CDF) of CCCC FG-CNTRC plates with linear grading profiles and simultaneous variation of the material parameters. ($a/b = 1$, $t/b = 0.1$ and $\overline{f}^{*}_{CNT} = 0.11$, 10.000 samples).

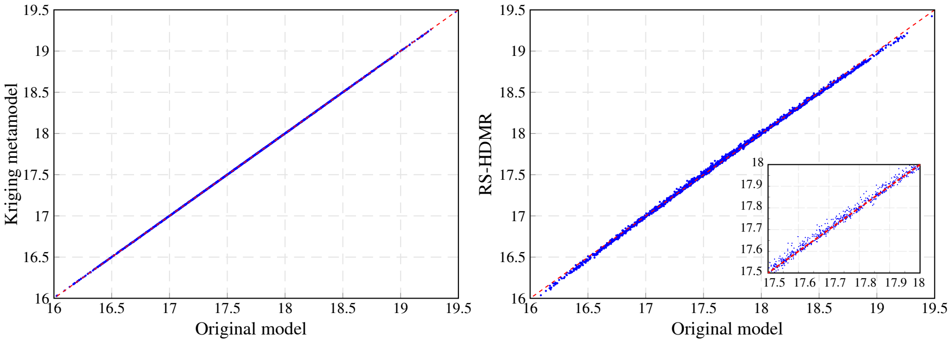

Figure 2.47 Scatter plot of Kriging and RS-HDMR metamodels with respect to the original model for the first natural frequency ($\bar{\lambda}_1$) for simultaneous variation of the material parameters (CCCC UD-CNTRC plate, $a/b = 1$, $t/b = 0.1$, $\overline{f}^{*}_{CNT} = 0.11$).

material parameters for fully clamped FG-CNTRC plates with four different linear grading profiles (UD, FG-V, FG-O and FG-X). It can be seen that the FG-X plates lead to the stiffest solutions and possess the highest frequency parameters. The explanation of this phenomenon is that reinforcements distributed closer to the extremes result in stiffener plates than those distributed nearer to the mid-plane. Fig. 2.47 shows a sample scatter plot describing the relationship between the original FE model and the constructed metamodels for natural frequencies. The low scatter of the points around the diagonal line corroborates that the metamodels are both formed with accuracy. Due to space limitations, in all the subsequent analyses, only results of the uncertainty of the FG-V distribution (P-FGV) are presented.

Fig. 2.48 shows the comparison of the PDFs obtained by direct MCSs and the two surrogate models presented in section 2.4.1 for the three cases of uncertainty. All the plots obtained by both metamodels are checked and found to be in good agreement ensuring

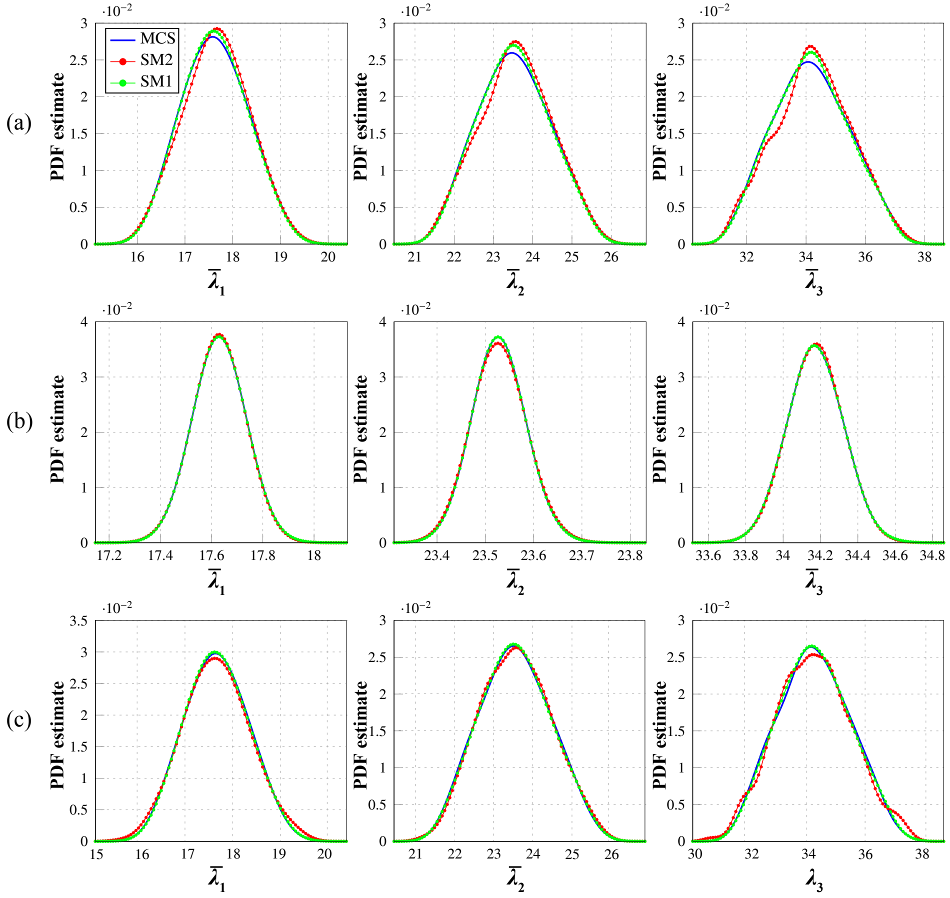

Figure 2.48 Comparison of the probability density functions (PDF) of the first three natural frequencies of P-FGV CCCC plates obtained by direct MCS (10.000 samples), Kriging (SM1) and RS-HDMR (SM2) metamodels (256 samples). (a) variation of the material parameters with linear reinforcement profile, (b) variation of the reinforcement grading profile and (c) combined variation. ($a/b = 1$, $t/b = 0.1$, $\overline{f}^*_{CNT} = 0.11$).

efficiency and accuracy. Global sensitivity analyses using RS-HDMR are performed for significant input parameter screening. The sensitivity indices for each input parameter (including the interaction effects) corresponding to different output responses are shown in Fig. 2.49. It is observed that the matrix parameters have a predominant effect on sensitivity. A significant effect of the power-law index k is found on the first and third natural frequencies with considerable contribution from the volume fraction of inclusions f^*_{CNT}. It is also noticeable the null sensitivity due to random variation of the transverse elastic modulus of CNTs, E_{22}^{CNT}. Table 2.8 represents the minimum values, maximum values, mean values and Standard Deviation (SD) using the two proposed metamodels for the first three natural frequencies obtained due to individual variability of all the variables.

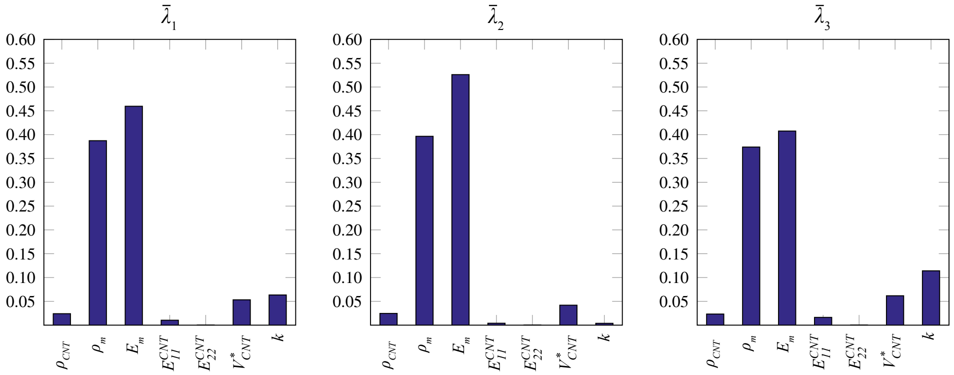

Figure 2.49 Sensitivity indices with respect to the first three natural frequencies for combined variation of all the variables of CCCC P-FGV plates ($a/b = 1$, $t/b = 0.1$, $\overline{f}_{CNT}^* = 0.11$, 256 samples).

Table 2.8 Uncertainty analysis due to individual variability of all the input variables by a Kriging and RS-HDMR meatamodels (256 samples) for the first two natural frequencies for CCCC P-FGV plates. ($a/b = 1$, $t/b = 0.1$ and $\overline{f}_{CNT}^* = 0.11$, SD: standard deviation).

Metamodel	ρ_{CNT}		ρ_m		E_m		E_{11}^{CNT}		E_{22}^{CNT}		f_{CNT}^*		k	
	$\bar{\lambda}_1$	$\bar{\lambda}_2$	$\bar{\lambda}_1$	$\bar{\lambda}_2$	$\bar{\lambda}_1$	$\bar{\lambda}_2$	$\bar{\lambda}_1$	$\bar{\lambda}_2$	$\bar{\lambda}_1$	$\bar{\lambda}_2$	$\bar{\lambda}_1$	$\bar{\lambda}_2$	$\bar{\lambda}_1$	$\bar{\lambda}_2$
KRIGING														
Min.	17.51	23.37	16.91	22.56	16.86	22.40	17.48	23.43	17.63	23.52	17.41	23.32	17.26	23.46
Max.	17.75	23.68	18.45	24.62	18.35	24.58	17.76	23.61	17.63	23.53	17.84	23.73	17.97	23.68
Mean	17.63	23.53	17.65	23.55	17.62	23.51	17.63	23.52	17.63	23.52	17.63	23.52	17.63	23.53
SD	0.07	0.09	0.44	0.59	0.43	0.63	0.08	0.05	0.00	0.00	0.12	0.12	0.09	0.03
RS-HDMR														
Min.	17.50	23.38	16.91	22.51	16.85	22.44	17.48	23.54	17.62	23.53	17.41	23.33	17.27	23.47
Max.	17.75	23.70	18.44	24.56	18.35	24.63	17.74	23.54	17.62	23.54	17.82	23.73	18.07	23.75
Mean	17.63	23.54	17.64	23.53	17.62	23.54	17.62	23.54	17.62	23.53	17.62	23.53	17.63	23.54
SD	0.07	0.09	0.44	0.59	0.43	0.63	0.08	0.00	0.00	0.00	0.12	0.12	0.09	0.03

Finally, some new physical insights are drawn on the dynamic behavior of P-FGV plates by studying the transient response in the frequency domain and a comparison of the stochastic and deterministic mode shapes. The transient response of a CCCC P-FGV plate under impulse loading is considered to ascertain the corresponding amplitude (in dB) of the frequency response function (FRF) as represented in Fig. 2.50. The Effective Independence method (EFI) [152] was employed to select the optimal positions of three points, two response points (P-1 and P-2) and one driving point (DP). This methodology is based on the maximization of the determinant of the Fisher information matrix (FIM), defined as the product of the mode shape matrix and its transpose. The principal idea of this method is based on the linear independence of the mode shapes. Proportional Rayleigh damping is assumed by imposing damping ratios of 1% for the first two natural modes. Higher frequency shows wider volatility in the simulation bounds of FRF compared to the lower frequency ranges. It is noticeable that the isolated randomness in the power-law index (k) does not lead to great differences in the FRFs. Nevertheless, its simultaneous variation along with the material parameters enlarges the shifts around the resonance peaks

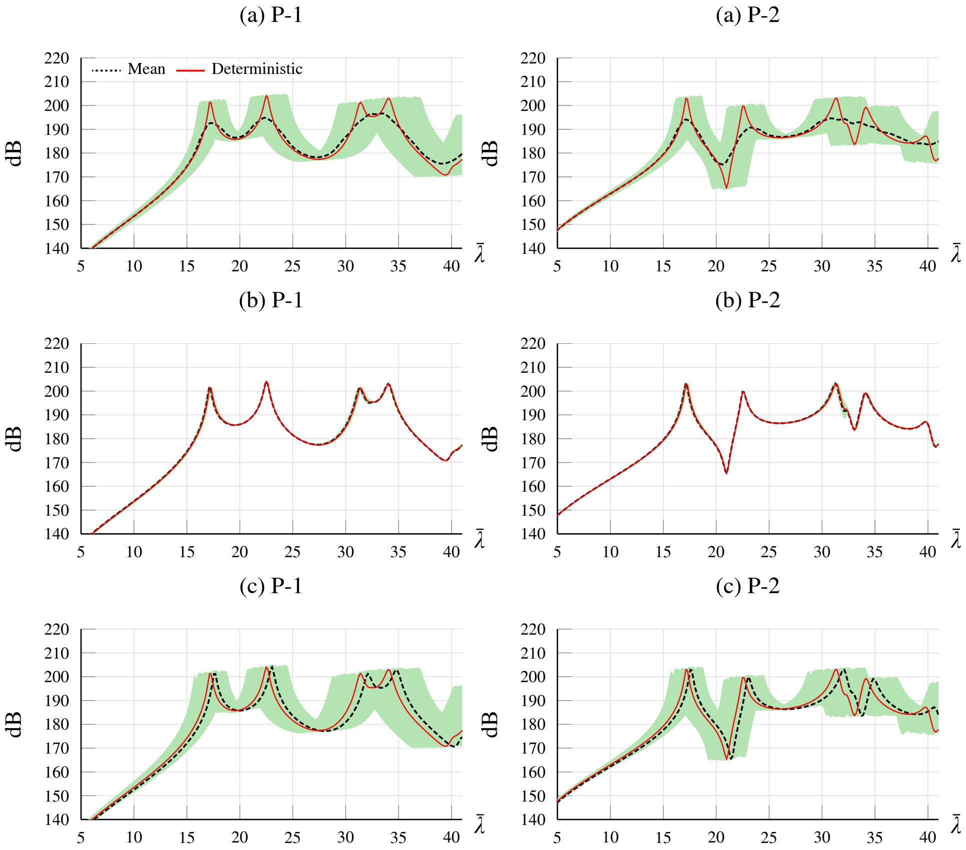
(a) P-1

(a) P-2

(b) P-1

(b) P-2

(c) P-1

(c) P-2

Figure 2.50 Frequency response function (FRF) plot of simulation bounds, simulation mean and deterministic mean of P-FGV CCCC plates obtained by direct MCS (10.000 samples), Kriging and RS-HDMR metamodels (256 samples). (a) variation of the material parameters with linear reinforcement profile, (b) variation of the reinforcement grading profile and (c) combined variation. ($a/b = 1$, $t/b = 0.1$, $f^*_{CNT} = 0.11$, P-1:{0.67a,0.33b}, P-2:{0.33a,0.58b}, DP:{0.67a,0.67b}).

and widens the FRF bounds. This can be attributed to the propagating effect of k, which not only incorporates variation by itself, but also scatters the randomness of the rest of the variables (set up at mid-plane level) along the thickness of the plates. Fig. 2.51 shows the comparison between the deterministic modes and the mean of the stochastic modes through the assessment of the MAC (Modal Assurance Criterion) matrix. In the case of the uncertainty in the material parameters (a), the mode shapes do not change substantially with zero values along the diagonal of the matrix. On the contrary, the incorporation of the uncertainty in the power-law index (k) does change the characteristics of some mode shapes. This effect, which remains in stage (c) with simultaneous variation of all the input parameters, highlights the propagating effect of k along the thickness of the plates.

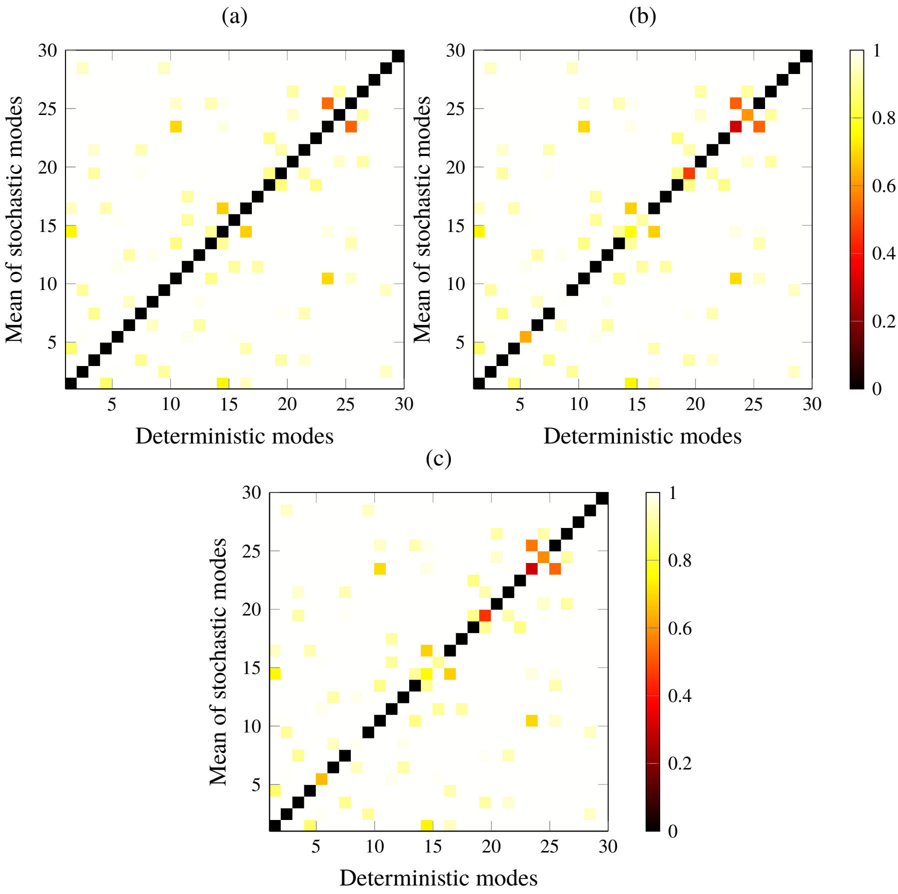

Figure 2.51 1-MAC matrix comparing the deterministic modes and the mean of the stochastic modes of P-FGV CCCC plates obtained by direct MCS (10.000 samples), Kriging and RS-HDMR metamodels (256 samples). (a) variation of the material parameters with linear reinforcement profile, (b) variation of the reinforcement grading profile and (c) combined variation. ($a/b = 1$, $t/b = 0.1$, $f^*_{CNT} = 0.11$).

2.5.4.3 Conclusions

This subsection has illustrated the influence of randomness in the CNT distribution when acting simultaneously with uncertainty in the CNT/matrix material properties on the vibrational properties of FG-CNTRC plates. The feasibility of applying metamodel-based approaches using Kriging and RS-HDMR has been shown in the realm of stochastic analysis. Although the same sampling size as in direct Monte Carlo Simulation (sample size of 10.000) has been considered, the number of FE analysis is much less compared to direct MCS and is equal to the number of representative samples (sample size of 256) required to construct the metamodels. It has been observed that both metamodels can handle a large number of input parameters. The metamodels formed from a small set of samples have been found to establish accuracy and computational efficiency. The obtained results, including probability density functions and cumulative distribution functions employing Kriging and RS-HDMR metamodels, have been compared with the results from direct MCSs. It has been observed that the matrix parameters have a predominant effect on sensitivity. A significant effect of the power-law index (k) has been found on the first and third natural frequencies with considerable contribution from the volume fraction of inclusions (f^*_{CNT}). Interestingly, null sensitivity has been identified for the transverse elastic modulus of CNTs (E^*_{CNT}). The volume fraction of CNTs (f^*_{CNT}) has been found to hold the maximum sensitivity for the second natural frequency. New dynamic analyses, transient response under impulse loading and the MAC matrix between the mean stochastic and deterministic mode shapes, have highlighted the propagating effect of the power-law index (k). Process-induced uncertainties in the reinforcement grading profile of FG-CNTRC plates will thus propagate all the sources of uncertainty defined at mid-plane level along the thickness. The key contributions of this study can be summarized as follows:

- The CNT distribution is considered as a source of uncertainty. Power-law distribution functions provide a parametrization of the CNT distribution along the thickness, suitable to characterize uncertainty.
- Metamodel-based approaches using Kriging and RS-HDMR metamodels have been shown efficient techniques to evaluate the uncertainty propagation on the vibrational properties of FG-CNTRC plates.
- The power-law index (k) has an important effect on bending stiffness of FG-CNTRC plates. Any uncertainty in the material parameters set up at mid-plane level is propagated along the thickness of the plates by means of the index k.

2.5.5 Free vibration of carbon nanotube/graphene reinforced composite plates[5]

2.5.5.1 Introduction

Despite the large number of publications in the literature concerning the study of CNTs, a change in tendency is being observed in recent years. To illustrate this, Fig. 2.52 depicts the number of publications in the open literature containing the keywords carbon nanotube and graphene. Shortly after the work by Ijima [143] in 1991, a steady increase in the number of works is found regarding the study of CNTs. However, this number has tended to stabilize for the last five years. Conversely, the interest for graphene began later, although the growth rate of publications containing the keyword graphene has enormously increased, exceeding in number those studies on CNTs. An important milestone in this curve is found in 2004, when professors Andre Geim and Konstantin Novoselov isolated graphene for the first time at the University of Manchester [233]. In recognition of their breakthrough, the pair were awarded the Nobel Prize in Physics in 2010. Aspects such as the high manufacturing cost of CNTs, difficulty in obtaining adequate uniform dispersions, as well as the highly anisotropic properties of CNTs, explain this change in tendency. In contrast, recent investigations agree to indicate the superior properties of graphene and its derivatives [203, 217, 372, 188]. It is noteworthy the experimental study of Rafiee *et al.* [254] who compared the effective mechanical properties of epoxy loaded with graphene, SWCNTs, and MWCNTs at nanofiller concentrations of 0.1wt.%. Their results showed that graphene led to Young's moduli 31% higher than those of pristine epoxy, whilst only 3% increments were reached by SWCNTs. Their results also reported that Graphene sheet-Reinforced Composites (GRCs) outperformed those doped with CNTs in terms of toughness and fatigue behavior. The superiority of graphene is ascribed to its high specific surface area and nanofiller/matrix interlocking, as well as its two-dimensional geometry, which enables more uniform filler distributions in comparison to CNTs. These excellent

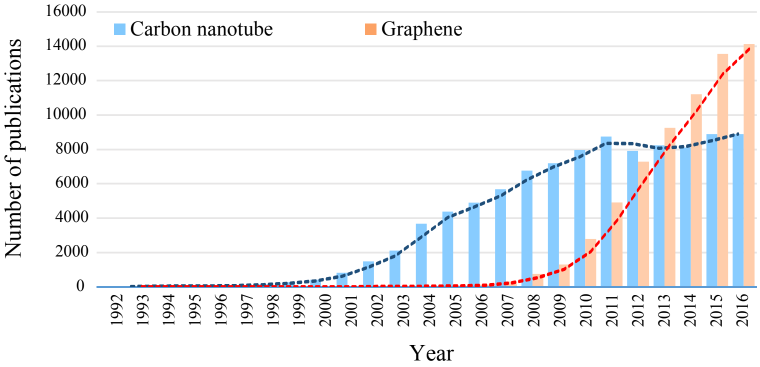

Figure 2.52 Number of indexed publications containing the keywords carbon nanotubes and Graphene. Data source: Scopus.

---

[5] An extended version of this subsection is found in paper I.

properties showcased by graphene, together with its low manufacturing cost [366], make GRCs a promising multifunctional composite in the shorter run.

In light of this change of paradigm, this subsection evaluates the stiffening effects of carbon nanotubes and graphene on the vibrational properties of composite plates. In particular, this subsection collects the results of some of the works done during the last stages of this thesis. The objective here is twofold: to extend the previously developed micromechanics models to account for different filler reinforcements such as, in this case, graphene, and to compare the macroscopic vibrational behavior of CNT- and GNP-reinforced plates.

Figure 2.53 shows the polymer nanocomposite plates studied in this subsection, with length a, width b, and thickness t. In order to define the graphene microstructure, a local coordinate system x'_1-x'_2-x'_3 is set up. Thence, Graphite NanoPlatelets (GNPs) lay on the x'_1-x'_2 planes with x'_3-axis normal to their surface. In the case of fully aligned GRC plates, GNPs are assumed to be arranged in the global x_1-x_2 plane that is parallel to the mid-plane of the plate as sketched in Fig. 2.53. The overall properties of both composites are estimated by the Mori-Tanaka micromechanics model, and the numerical simulations are conducted with a self-developed Reissner's four-noded shell finite element code.

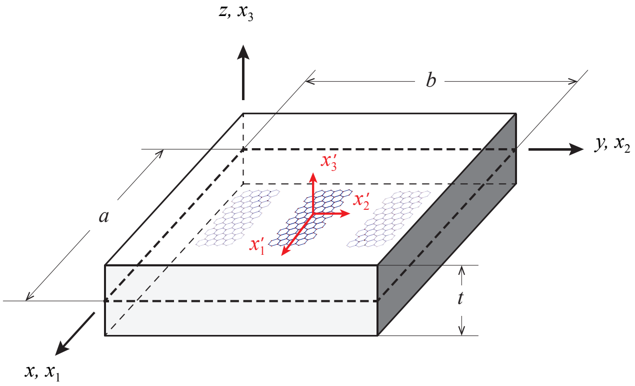

Figure 2.53 Geometry and coordinate system of GRC polymer plates.

In practical nanocomposites, 2D graphene sheets have a tendency to stack up and form multi-layered graphite due to the steric effect and the vdW interaction between different sheets. The shape of graphite influences the stiffening effect due to its dominance in the Eshelby's tensor. We inspect the situation where GNPs stack up in the shape of ellipsoids with two semi-major axes equal in length, i.e. $a_1 = a_2$, and a semi-minor axis a_3 defined by the aspect ratio a_3/a_1 representing the thickness of the resulting restacked graphene sheets, as shown in Fig. 2.54. On this basis, the Eshelby's tensor can be reckoned by Eq. (6.54) in Appendix C. When tensile loads are transferred to the stacked graphene sheets, vdW bonding between layers is likely to fail before graphitic carbon-carbon bonding, leading to further exfoliation of the particle. For this reason, the in-plane elastic moduli remain similar to those of graphene sheets although the out-of plane modulus approximates that of graphite, as shown in the molecular mechanics calculations of Chou *et al.* [53].

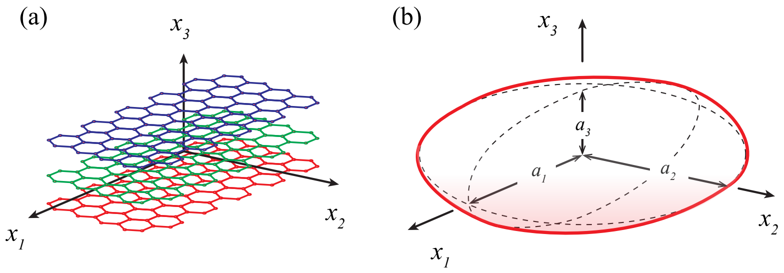

Figure 2.54 Schematic representation of restacking of graphene sheets forming multi-layered graphite (a) and equivalent ellipsoid (b).

With regard to the different constituents analyzed in this work, the elastic moduli and mass density of the different phases are summarized in Table 2.9. The in-plane Young's modulus and Poisson's ratio of graphene sheets have been assumed $E_{11} = 1020$ GPa and $\nu_{12} = 0.4$, respectively, in accordance with Lee *et al.* [172] and Reddy *et al.* [257]. The out-of-plane modulus E_{33} and the shear modulus G_{13} are assumed to be 100 times the in-plane modulus, while the Poisson's ratio ν_{31} is taken as 1% of ν_{12}, i.e. $E_{33} = G_{13} = 102000$ GPa and $\nu_{31}=0.004$ [148]. Hence, the stiffness tensor for graphene sheet inclusions can be denoted as $\mathbf{C}_r^{graphene}=(2k_r,l_r,n_r,2m_r,2p_r) = (1700,6.8,102000,738,204000)$ GPa. With regard to restacked graphene sheets, according to the molecular mechanics simulations of Chou *et al.* [53] and the work of Ji *et al.* [148], the stiffness tensor for restacked graphene sheets is chosen as $\mathbf{C}_r^{graphite} = (1240,15,36.5,880,8)$ GPa. On the other hand, SWCNTs have been also considered for comparison purposes. According to the results by Popov *et al.* [249], the stiffness tensor for (5,5) SWCNTs is denoted as $\mathbf{C}_r^{CNT} = (60,10,450,2,2)$ GPa. Finally, the matrix material studied in this work is polystyrene with Young's modulus $E_m = 1.9$ GPa and Poisson's ratio $\nu_m=0.3$ so that its isotropic stiffness tensor can be denoted as $\mathbf{C}_m = (3\kappa_m,2\mu_m) = (4.75,1.46)$, with κ_m and μ_m being the matrix's bulk and shear moduli, respectively. The resonant frequencies are presented in non-dimensional form as follows:

$$\bar{\lambda} = \omega\frac{b^2}{\pi^2}\sqrt{\frac{\rho^m t}{D}}; \quad D = E^m t^3/12\left[1-(\nu^m)^2\right] \tag{2.85}$$

Table 2.9 Hill's elastic moduli (k,l,n,m,p) and mass density (ρ) of constituent phases, Ref. [254, 148, 29, 249, 312].

	Graphene	Graphite	CNT		Polystyrene
k_r (GPa)	850.0	620.0	30.0	E_m (GPa)	1.9
l_r (GPa)	6.8	15.0	10.0	ν_m	0.3
n_r (GPa)	102000.0	36.5	450.0	ρ_m (kg/m^3)	1040
m_r (GPa)	369.0	440.0	1.0		
p_r (GPa)	102000.0	4.0	1.0		
ρ_r (kg/m^3)	2250	1060	1400		

2.5.5.2 Numerical results

Free vibration of GRC polymer plates The effect of the filler content on the free vibration behavior of fully aligned GRC plates is analyzed in Fig. 2.55 for both simply supported (SSSS) (a) and simply supported with one free edge (SSSF) (b) boundary conditions. For comparison purposes, both GNP and SWCNT nanofillers are studied with properties defined in Table 2.9, corresponding to solid and dashed lines, respectively. The first three mode shapes for both nanocomposites and boundary conditions are depicted in Fig. 2.56. It is evidenced that the stiffening effect of GNPs overtakes that of CNTs for all the natural frequencies. For instance, the addition of graphene at a volume fraction of 0.05 rises the fundamental frequency $\overline{\lambda}_1$ of the SSSS composite plates up to five times that of the neat polymer, whilst CNTs only doubles this value. Let us remark that, in the case of GRCs, the second and third natural frequencies overlap due to symmetry about $x-z$ and $y-z$ planes, in accordance with the mode shapes shown in Fig. 2.56. It is observed that the characteristic mode shapes are disordered due to the in-plane anisotropy of CNT-reinforced composites. For example, it is observed that the third bending mode for CNT-reinforced composites corresponds to the third mode shape, while for GNP-reinforced composites it does not appear until the sixth mode shape.

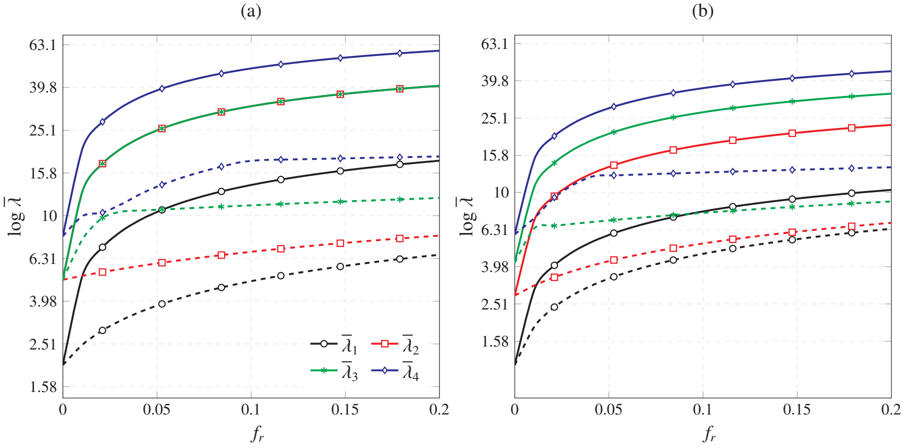

Figure 2.55 Non-dimensional natural frequencies versus filler volume fraction for fully aligned GNP- and CNT-reinforced composite plates, corresponding to solid and dashed lines, respectively ($a/b = 1$, $t = a/50$, SSSS (a) and SSSF (b) boundary conditions).

The comparison between the stiffening effect of GNPs and CNTs is also conducted for randomly oriented configurations as shown in Fig. 2.57 (a) and (b), respectively. Thence, frequency values obtained for fully aligned nanofillers are denoted with solid lines, while those obtained for randomly oriented configurations are denoted with dashed lines. When fillers are randomly oriented, both composites exhibit isotropic properties and, thus, the second and third natural frequencies coincide. In both cases, the fundamental frequencies of plates doped with fully aligned fillers surpass those with randomly oriented fillers. However, in some other cases, e.g. fourth mode shape in Fig. 2.57 (b), it can be observed

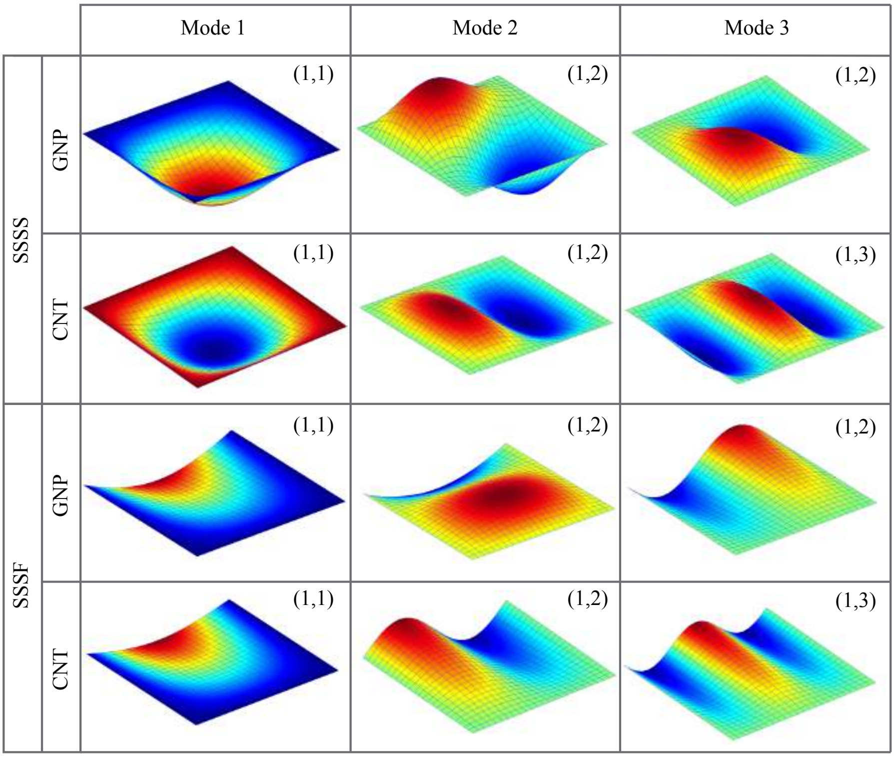

Figure 2.56 First three mode shapes of fully aligned GNP- and CNT-reinforced composite plates with SSSS and SSSF boundary conditions ($a/b = 1$, $t = a/50$, $f_r = 0.2$).

that the resonant frequencies are higher for random configurations. This fact is ascribed to the loss of anisotropy when fillers are randomly oriented. In order to further explain these results, the elastic moduli obtained for both nanofillers and configurations are shown in Fig. 2.58. Both nanofillers exhibit highly anisotropic properties when fully aligned, being the longitudinal elastic modulus, $E_{||}$, several orders of magnitude higher than the transverse modulus, $E_{\perp}$. However, when nanofillers are randomly oriented, composites exhibit isotropic properties with lesser $E_{||}$ but higher $E_{\perp}$ in comparison to fully aligned configurations. This fact, along with mode shapes shown in Fig. 2.56, gives response to the higher frequencies of some mode shapes for randomly oriented filler configurations. When the number of sine waves increases, the contribution of the transverse bending stiffness so does and, therefore, randomly oriented configurations may result in higher natural frequencies. With regard to the comparison between nanofillers, GNPs lead to much stiffer composites so that similar conclusions to the previous analysis can be extracted here. It is interesting to note that for CNT-reinforced composites, the structural behavior is considerably different for fully aligned and random orientation configurations. When CNTs are aligned in the x_2 direction, the composite exhibits transversely isotropic properties with

x_2 as transverse isotropy axis. As the content of CNTs increases, the anisotropy degree of the composite plates so does and, therefore, the first mode shapes begin to be defined by a higher number of sine waves perpendicular to the filler direction. On the other hand, fully aligned GNPs are defined parallel to the mid-plane of the plate. In this case, assuming plane stress conditions, the behavior of the GRC plates is isotropic and, thus, the mode shapes do not change substantially for randomly oriented configurations.

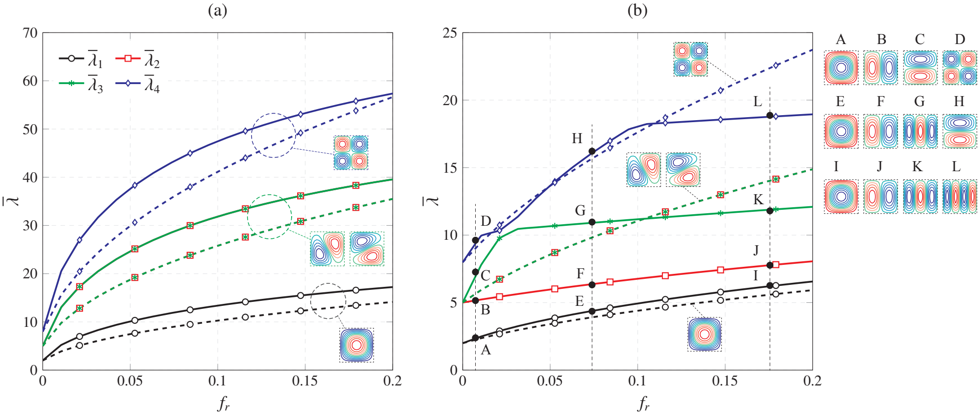

Figure 2.57 Non-dimensional natural frequencies for GNP- (a) and CNT-reinforced composite plates (b) versus filler volume fraction with fully aligned and randomly oriented filler configurations, corresponding to solid and dashed lines, respectively ($a/b = 1$, $t = a/50$, SSSS boundary condition).

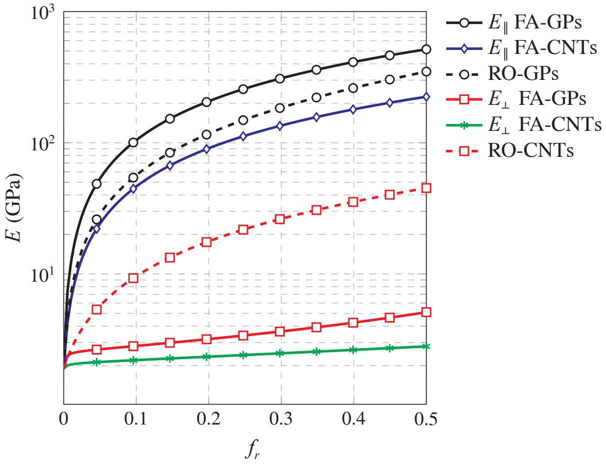

Figure 2.58 Elastic moduli versus filler content for GNP- and CNT-reinforced polymer composites with Fully Aligned (FA) and Randomly Oriented (RO) filler configurations.

Effect of restacking of graphene sheets on the bending and vibrational behavior of GRC polymer plates The restacking effects on the fundamental frequency of SSSS GRC plates are inspected in Fig. 2.59. Fully aligned and randomly oriented configurations are studied and denoted with solid and dashed lines, respectively. In accordance with Fig. 2.54, the restacking of graphene sheets forming multi-layered graphite platelets can be modeled by ellipsoidal inclusions with aspect ratios a_3/a_1. As previously discussed, graphene sheets can stack up forming multiple sheets. When tensile loads are transferred to the stacked graphene sheets, the vdW bonding between layers is likely to fail before graphitic carbon-carbon bonding, leading to further exfoliation of the particle. Hence, the material properties of the graphene sheets with restacking effects are taken as those defined for graphite in Table 2.9. It is extracted that for increasing number of stacked graphite layers, i.e. higher aspect ratio a_3/a_1, the overall stiffness decreases for both cases. It is especially critical for aspect ratios a_3/a_1 above E-3 where the most drastic reductions are found. These results evidence that the stiffening effect of graphene sheets may be dramatically reduced when a considerable fraction of fillers stacks up forming platelets of graphite.

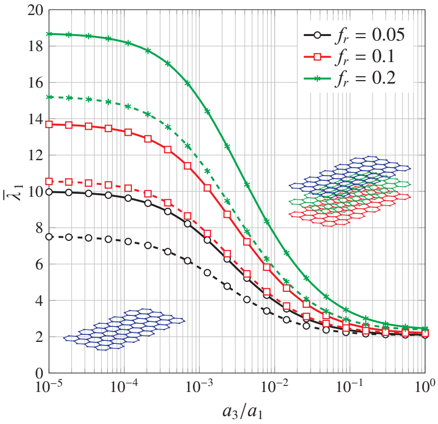

Figure 2.59 Non-dimensional fundamental frequency of a composite plate reinforced by graphene sheets with restacking effects ($a/b = 1$, $t = a/50$, SSSS boundary condition, solid and dashed lines denote fully aligned and randomly oriented configurations, respectively).

2.5.5.3 Conclusions

This subsection has presented a study of the bending and vibrational behavior of GRC plates by means of a Mori-Tanaka micromechanics model, including harmful effects related to restacking of graphene sheets. In order to highlight the superior load bearing capacity of GNPs compared to CNTs, detailed parametric analyses have been presented. Micromechanical aspects such as filler content and distribution have been investigated. Overall, the key findings of this work can be summarized as follows:

- The stiffening effect of GNPs as mechanical additives have been shown superior in comparison to CNTs. In both fully aligned and randomly oriented configurations, graphene has been shown to provide stiffer macroscopic properties for the same filler content.

- Agglomeration of fillers into clusters may be understood as a mechanical defect in the microstructure of the composite. The results demonstrated critical reductions of the resonant frequency as the heterogeneity degree of the filler dispersion increases.
- The restacking of graphene sheets into graphite platelets is a limiting factor of the macroscopic behavior of these composites. The numerical results have showed dramatic reductions of the effective resonant frequencies for higher fractions of graphene sheets lumped into graphite platelets.

2.6 Conclusions

This chapter has presented the main contributions of this thesis in the study of the potential applications of CNTs for the development of high-strength composites. First, advanced micromechanics models have been implemented to estimate the overall stiffness tensor of CNT/reinforced composites. In light of the micrograph inspections reported in the literature, common microstructural features such as filler waviness and agglomeration have been considered. The developed homogenization approaches have been employed to analyze the potential enhancements of CNTs in the macroscopic response of certain structural elements, namely flat shells, skew shells, and cylindrical panels. Furthermore, numerical studies have been conducted to assess the design optimization possibilities of FG-CNTRCs. Finally, in order to perform optimization or uncertainty propagation analyses, as well as the considerable number of variables involved in the microstructure, Kriging and RS-HDMR surrogate models have been implemented. In this way, it has been possible to substitute the finite element simulations, which are very costly in terms of computation, and generate large populations of simulations apt for conducting statistical analyses of the macroscopic response of FG-CNTRCs. Overall, the main conclusions reached along this chapter can be summarized in the following key points:

- The theoretical simulations of the overall properties of CNTRCs demonstrate large enhancements of the mechanical properties with small filler concentrations. These results support the idea of developing light-weight high-strength composite structural elements such as fuselage panels, high-performance tribological engineering components, reinforcing coatings for damaged infrastructures, etc.
- The mean-field homogenization theory of Eshelby-Mori-Tanaka exhibits some shortcomings for the analysis of general distributions of CNTs. In particular, it has been shown that its estimates violate the Hashin-Shtrikman-Walpole and Voigt/Reuss bounds for random filler arrangements. Also, in the case of misoriented filler arrangements or fully aligned wavy configurations, the stiffness tensors computed by the MT model are diagonally asymmetric and, thus, physically inadmissible.
- The numerical results have evidenced that filler waviness and agglomeration have coupled weakening effects when acting together. It has been shown that only the

consideration of ad hoc Eshelby's tensors for wavy filler configurations, along with the two-parameter agglomeration model, can properly account for both phenomena simultaneously.

- The results have highlighted that the use of functionally graded doping of CNTs opens many design optimization possibilities. In particular, all the conducted analyses have revealed that fillers concentrated at sections far from the mid-surface of the element yield the stiffest responses.
- Uncertainty propagation analyses have shown a high sensitivity of the vibrational properties of FG-CNTRC plates to variations of the matrix material properties, filler volume fraction and distribution across the thickness, and elastic moduli of CNTs. Also, power-law distribution functions have been shown to provide a parametrization of the CNT distribution suitable for characterizing uncertainties stemming from the manufacturing process. The Kriging and RS-HDMR surrogate models have been shown robust and computationally efficient for such uncertainty analyses.

On the whole, it is concluded that the first goal pursued in this thesis on the analysis of CNTs as mechanical reinforcements for high-strength composites has been fulfilled.

3 CNTs as additives for smart composites

This third chapter of the thesis presents the works conducted on the realm of carbon nanotubes as additives for the development of smart composites, including the results published in the articles D, E and K.

3.1 Introduction

Recent advances in the field of Nanotechnology have led to the development of new multi-functional and smart materials. In particular, electrically conductive Carbon NanoTube (CNT) cement-based composites open a vast field of applications in SHM [118, 325, 92]. CNTs exhibit electrical conductivities between 1000 and 200000 S/cm [78], that is several orders of magnitude larger than most polymeric and cementitious materials. As a result of these properties, along with high aspect ratio, small diameter, lightness and excellent chemical and thermal stability, CNTs can be used as additives to produce multifunctional composites [313]. However, what is even more interesting is the piezoresistive behavior of these composites. In virtue of this property, these composites exhibit strain-sensing capabilities by means of measurable variations of their electrical properties under applied mechanical deformations [99, 171, 324]. This unique property, coupled with the similarity between these composites and structural concrete, suggests the possibility of developing distributed strain-sensing systems that would entail substantial improvements in the cost-effectiveness of large-scale concrete structures [184, 120, 136, 277, 121, 125, 123]. Cementitious composites also have a similar durability to the monitored structure, which allows long-term applications. However, works reporting the development of theoretical models capable of simulating the relationship between external mechanical strains and the effective electrical conductivity is still scant.

In this context, the second objective of this thesis is twofold:

- Modeling of the electrical conductivity of CNT-reinforced composites. Along these lines, the research works are intended to determine the macroscopic conductivity in the absence of external loading, σ^o, or alternatively the macroscopic resistivity, $\rho^o = (\sigma^o)^{-1}$.
- Modeling of the strain-sensitivity of CNT-reinforced composites. To this end, the previously developed theoretical formulation should be extended to determine the variation of the conductivity tensor $\Delta\boldsymbol{\rho}$ under the action of an external strain field $\boldsymbol{\varepsilon}$. In this way, it would be possible to relate the electrical and mechanical fields through a multiphysics simulation as $\Delta\rho_{ij}/\rho^o = \Pi_{ijkl}\varepsilon_{kl}$, with Π_{ijkl} being the components of the piezoresistivity tensor.

Following the trace of the micromechanics modeling of the mechanical properties of composites previously overviewed, this chapter collects the works conducted on their extension to the homogenization of the electrical conductivity and piezoresistivy of CNTRCs. In a similar way to the previous chapter, a special interest has been put into the analysis of the influence of waviness and agglomeration effects. Novel mixed-micromechanics approaches have been proposed for the modeling of the effective electrical conductivity and piezoresistivity of CNT-reinforced composites. In addition, an experimental campaign was conducted to characterize the electrical properties of CNT-reinforced cement-based materials, namely cement, mortar and concrete, to serve as validation benchmark. Excellent agreements were found with the developed theoretical models what proves the accuracy of the proposed approaches.

The present chapter is organized as follows. A detailed review of the state-of-the-art of the modeling of the conductivity and strain-sensing properties of CNT-reinforced composites is presented in Sections 3.1.1 and 3.1.2, respectively. Section 3.2 outlines the theoretical framework of the models developed for the electrical conductivity of CNT-reinforced cement-based materials. Sections 3.3 and 3.4 review the extensions of the latter approaches to incorporate uniaxial and three-dimensional strain states, respectively. Section 3.5 includes the numerical results and comparison with experimental data and, finally, Section 3.6 concludes this chapter.

In this chapter, a boldface letter stands for a second-order tensor, $\mathbf{A} \equiv A_{ij}$, unless otherwise indicated.

3.1.1 Conductivity of CNT-reinforced composites

Over the last decade, many experimental results have put in evidence the percolation-like nature of the electrical conductivity of cement-based composites [47, 52, 348]. In this way, the conductivity of composites varies only slightly for ranges of CNT concentrations below and above a certain critical concentration, so-called percolation threshold, at which abrupt increases are observed. Most researchers agree explaining this percolation behavior by means of two different conductive mechanisms: electron hopping (or quantum tunneling) and conductive networking [345, 47, 185, 46]. From quantum mechanics, electron hopping is characterized by a transfer of electrons intra-tube or from one CNT to an adjacent tube. The probability of occurrence of this mechanism is highly dependent on the distance between tubes [119, 123]. At low CNT concentrations, electron hopping governs the electrical conductivity of the composite. With increasing CNT concentration, the separation distance among CNTs decreases until adjacent fibers touch one another resulting in a continuous electrically microscale conductive path. The conductivity of composites with CNT concentrations above the percolation threshold is believed to be dominated by this second mechanism.

Most of the literature on CNT cement-based composites has focused on their fabrication process and experimental characterization. Theoretical studies coping with the explanation of the physical principles underlying the conductive mechanisms of these composites are rather scant. Among these contributions, it is noteworthy the application of lumped-circuit models of carbon fiber cement paste sensors based on series-parallel arrays of electrical resistors and capacitors [184, 121, 124, 63, 126]. A larger number of publications is found concerning the modeling of polymeric materials doped with carbon nanotubes. Monte Carlo (MC) simulations haven been widely employed to predict the electrical conductivity of nanocomposites [231, 200, 384, 198]. Nevertheless, MC simulations are computationally expensive and do not offer an explicit formulation useful for design purposes. Thus, the development of analytical models has attained more attention. Traditionally, a three-parameter power law fit taken from classic percolation theory has been widely used for determining the percolation threshold [159, 116]. However, since this model requires experimental data to be fitted, it cannot be used for design purposes nor let distinguish the two conductive mechanisms. Alternatively, other authors have attempted to predict the overall electrical conductivity of CNT nanocomposites by means of micromechanics theories. Among them, it is worth mentioning the work of Deng and Zheng [66] who developed a simplified micromechanics model to evaluate the effective electrical conductivity of CNT-based composites. That approach made it possible to reproduce percolation, conductive networks, conductivity anisotropy and CNT waviness with reasonably good agreements with some experimental data from the literature. A similar approach was employed by Takeda *et al.* [303] for the analytical characterization of the electrical conductivity of CNT-reinforced polymer composites. The predictions provided by that analytical model showed a good correlation with experimental results measured by alternating current impedance spectroscopy. Another relevant contribution was made by Seidel and Lagoudas [275] who proposed a Mori-Tanaka micromechanics model [220, 131] for the study of the individual influence of electron hopping and conductive networking mechanisms on the electrical conductivity of CNT-polymer composites. In that work, the electron hopping mechanism was simulated by means of conductive interphases surrounding the tubes, whilst conductive networks were represented by changes of the CNT aspect ratios. Despite the promising capabilities of this new approach, great discrepancies were observed compared to experimental data. The origin of these discrepancies was attributed by Feng and Jiang [87] to the assumption of the electrical conductivity and thickness of the interphase as constant, as well as the isolated effect of electron hopping and conductive networks before and after the percolation, respectively. Those authors proposed an extension of the latter approach by considering the coupled effect of electron hopping and conductive networks on the overall conductivity, achieving better agreement with experimental data. Their simulation results also indicated that the CNT aspect ratio plays a key role in the definition of the percolation threshold and, consequently, in the overall conductivity of the nanocomposites.

It should be mentioned that most of the existing theoretical studies of the electrical properties have assumed straight conductive fillers. However, plenty of experiments have shown that CNTs in composites typically present a certain degree of waviness [276, 330, 246], which is due to their large aspect ratio and low bending stiffness. In this regard, some researchers have reported on the effects of waviness on the overall electrical properties of CNT nanocomposites. By assuming a simple sinusoidal shape, Yi *et al*. [370], Berhan and Sastry [26] and Fisher *et al*. [93] showed that CNT waviness induces considerable increases in the percolation threshold and decreases in the overall conductivity. Similar conclusions were reached by approximating wavy CNTs as elongated polygons by Li *et al*. [177], or by introducing equivalent straight fibers into simplified micromechanics models, as reported by Deng and Zheng [66] and Takeda *et al*. [303]. A second important phenomenon that is commonly present in CNT-based composites is the agglomeration of fillers. The difficulty in obtaining good dispersions of nanotubes is related to the circumstance that CNTs tend to form agglomerates and bundles. This phenomenon is attributed to the electronic configuration of tube walls and their high specific surface area which favors the appearance of large vdW attraction forces among CNTs [9, 186, 352]. Although it has been reported in the literature that bundles can substantially decrease the overall conductivity of composites since they inhibit the formation of conductive networks [147], only a few contributions have attempted to theoretically simulate of this effect. Along these lines, it is worth noting the works of Weng [350] and Yang and co-authors [365]. Their results showed that the inhibition of conductive networks induced by clustering leads to important increases in the percolation threshold. It is thereby essential to develop rigorous theoretical models capable of simulating CNT waviness and clustering for the correct comprehension of the physical principles that govern the conductivity of CNT cement-based composites, as well as for the development of effective tools for their design.

3.1.2 Strain-sensing capabilities of CNT-reinforced composites

The origin of the self-sensing property of CNT-reinforced composites is attributed to the tampering of the mechanisms underlying the overall conductivity when external strains are applied. In particular, three major expected changes during stretching/compressing have been suggested in the literature [85, 139]: (i) composite volume expansion, (ii) reorientation of fillers and (iii) changes in the percolation threshold. The first mechanism refers to the change of volume experienced by compressible materials when subjected to dilation strain. Given that CNTs are much stiffer than the matrix, the volumetric expansion of fillers can be neglected, being only sustained by the matrix. Hence, a change in the overall volume with an unaltered volume of fillers induces changes in the CNT volume fraction [243, 85, 113]. This change eventually causes the breakdown of some existing conductive paths or the formation of new ones due to the change of the distance between CNTs. With regard to the second mechanism, experiments have shown that CNTs tend to re-orient in the direction of the stretching [51, 338, 12]. Under the assumption of initial random distributions of CNTs, the strain-induced filler reorientation results in a growing anisotropy degree and, consequently, in changes in the effective electrical properties of the composite. Finally, many researchers agree that strain-induced reorientation also alters the percolation threshold. This is ascribed to the fact that aligned fillers presumably have less likelihood to get in contact and form connecting networks [115, 373].

In the literature, most studies to date have focused on the fabrication and experimental analysis of CNT-based composites. In the light of the promising potential of these composites as smart materials, much effort has been put into the experimental characterization and the development of new applications as sensors [374, 194, 118, 140, 137, 164, 323, 325, 62]. Nevertheless, the number of theoretical studies that allow for tailoring the properties of these composites and for properly interpreting their outputs is much smaller. The work of Lin *et al*. [192] is worth noting, as it presented an application of the Monte Carlo method to investigate the stretching/compression effects on the electrical properties of fiber-filled composites. Their results showed that deformation can shift the percolation threshold of the composites. Theodosiou and Saravanos [311] analyzed the piezoresistive response of CNTs by an atomistic model, as well as the macroscopic behavior of CNT-polymer composites by a numerical percolation model. That work concluded that the nanotube resistance and the tunneling effect are the dominant mechanisms in the strain-sensitivity of the composites. Yasuoka *et al*. [368] simulated the strain-sensitivity of CNT-based composites by using a circuit simulator analogue to a percolation network. It was shown that piezoresistivity exhibits a high level of non-linearity, a conclusion that agrees well with the experimental evidence. A similar work was carried out by Feng and Jiang [85, 88]. Those authors extended their previous works on the modeling of the overall electrical conductivity of CNT-reinforced composites [87] in order to take into account the stretching effects. Despite finding gross differences in comparison to some experimental data for CNT/polymer composites doped with low CNT concentrations, the proposed framework proved capable of qualitatively implementing the three major effects induced by stretching.

It should be also mentioned that most theoretical works in the literature restrict their analyses to uni-axial loadings, whilst those estimating the response of these composites under general three-dimensional strain states are sorely lacking. In this line, it is worth noting the contribution of Alamusi and Hu [5] who utilized the three-dimensional resistor network previously proposed by Hu *et al.* [141], and incorporated Simmon's contact resistance among CNTs [287] along with a fiber re-orientation model [309]. Tallman and Wang [305] extended the theoretical formulation developed by Takeda *et al.* [303] for the piezoresistivity modeling of CNT composites subjected to arbitrary dilations. The case of bi-axial stretching was also studied by Feng and Jiang [88] who presented closed-form expressions of the filler orientation distribution functions for such loading configurations. It should be also remarked the recent work by Wang *et al.* [336] who developed a two-dimensional representative volume element to simulate the electromechanical response of silicone elastomer doped with carbon black. In that work, comparison analyses against experimental data for laterally constrained uni-axial stretching demonstrated the importance of large deformation effects on the non-linear electrical response of the composites. Despite these developments, there is no a generalized micromechanical scheme allowing for the modeling of the electro-mechanical response of CNT-reinforced cement-matrix composites under arbitrary 3D strain states. The present chapter of this thesis is intended to address this gap.

3.2 Conductivity of CNT-reinforced composites[1]

3.2.1 Composites reinforced with randomly oriented straight CNTs

In this section, carbon nanotubes are assumed to be straight, uniformly and randomly dispersed throughout a cementitious matrix. Based on the Eshelby-Mori-Tanaka mean-field homogenization framework, the electron hopping mechanism is simulated by means of a conductive interphase surrounding the tubes, whilst conductive networks are represented by changes in the CNT aspect ratios.

3.2.1.1 Tunneling resistance: Thickness and conductivity of the interphase

The electron hopping is characterized by the transfer of electrons between proximate tubes. The physical origin of this transfer is a quantum tunneling effect which defines the penetration or tunneling of an electron through a potential barrier. The transmission probability decays exponentially with the increase in the width and height of the potential barrier [353, 259]. In the case of CNT-reinforced composites, the potential barrier is defined by the insulating gap of matrix d_a between proximate non-connected tubes [119, 123]. The upper limit distance for MWCNTs in conductive networks, in other words, the cut-off distance for tunneling effects, has been taken as d_c=0.5 nm [347, 360], which is the maximum possible thickness of a cementitious medium separating two adjacent MWCNTs that allows the tunneling penetration of electrons (See Fig. 3.1). Due to a lack of information in the literature on the estimation of the average separation distance between CNTs without electrical contact, an assumption of $d_a = d_c$ has been made on this quantity in the present work. When the separation distance of CNTs is larger than d_c with CNT volume fraction f_{CNT} less than the percolation threshold f_c, it is regarded that CNTs are more independent rather than electrically connected to each other. In this situation, electron hopping dominates the electrical conductivity of the composite. When conductive networks are formed after the percolation, several works in the literature have demonstrated that the average separation distance d_a between adjacent MWCNTs follows a power-law description [10, 303, 87]. Here, we use the expression proposed by Deng and Zheng [66]:

$$d_a = \begin{cases} d_c & 0 \le f_{CNT} < f_c \\ d_c \left(\dfrac{fc}{f_{CNT}} \right)^{1/3} & f_c \le f_{CNT} \le 1 \end{cases} \tag{3.1}$$

Simmons [288] derived a generalized formula for the electric tunneling effect between similar electrodes separated by a thin insulating film. If we assume the thickness of insulating film in the contact area of crossing CNTs to be uniform and neglect the variation of barrier height along the thickness, the formula of the resistance to electron tunneling R_{int} for a rectangular potential barrier can be employed [176]:

$$R_{int}(d_a) = \frac{d_a \hbar^2}{A_c e^2 \left(2mV_o^{1/2}\right)} \exp\left(\frac{4\pi d_a}{\hbar} \left(2mV_o\right)^{1/2} \right) \tag{3.2}$$

---

[1] An extended version of this section is found in paper D.

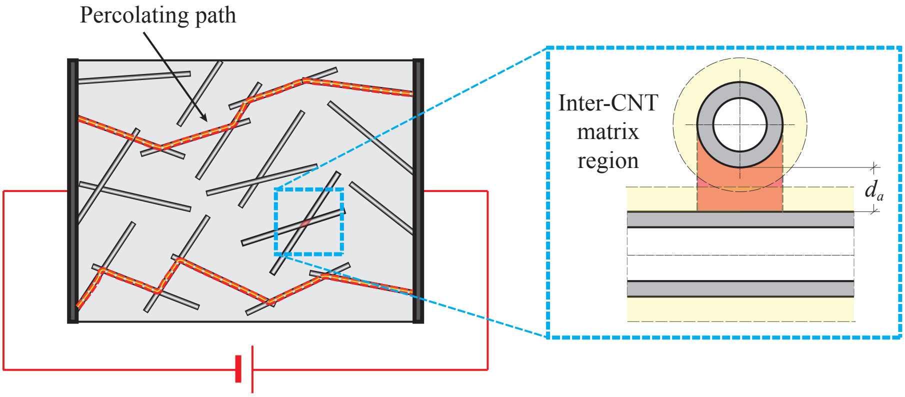

Figure 3.1 Schematic representation of the contribution of electron hopping and conductive network mechanisms to the overall electrical conductivity of CNT nanocomposites.

where V_o is the height of the tunneling potential barrier, m and e are the mass and the electric charge of an electron, respectively, A_c is the contact area of MWCNTs and $\hbar$ is the reduced Planck's constant. A reference value of 0.36 eV has been taken for the height of the tunneling potential barrier based on the experimental results of Wen and Chung [347]. This effect has been incorporated into the simulation through a conductive interphase layer surrounding the nanotubes, whose thickness, t, and electrical conductivity, σ_{int}, can be expressed correspondingly as:

$$t = \frac{1}{2}d_a, \quad \sigma_{int} = \frac{d_a}{A_c R_{int}(d_a)} \tag{3.3}$$

Assuming a constant average separation among MWCNTs without electrical contact may result in an overestimated electrical conductivity of the nanocomposites for CNT volume fractions below and around the percolation threshold. However, the contribution of conductive networks becomes more dominating with the increase of CNT volume fraction, allowing to neglect this overestimation above percolation [87].

3.2.1.2 Nanoscale composite cylinder model for CNTs

As discussed above, the electron hopping mechanism among MWCNTs distributed in the matrix is simulated by the formation of a continuum interphase layer surrounding the nanotubes. In order to capture this interphase layer and the hollow nature of MWCNTs, a widely-accepted effective composite cylinder model can be used to determine the effective electrical conductivity of MWCNTs together with the surrounding interphases. Fig. 3.2 shows the composite cylinder assemblage which consists of a MWCNT (length L_{CNT} and diameter $D_{CNT} = 2r_c$) and the surrounding interphase with a thickness of t. In this work, MWCNTs have been treated as solid cylinders instead of hollow tubes due to the difficulty in obtaining the actual electrical conductivity of MWCNTs considering the nanoscale structures. The effective longitudinal and transverse electrical conductivity of the equivalent cylinders, $\tilde{\sigma}^L$ and $\tilde{\sigma}^T$, respectively, can be obtained in a local coordinate system $\{x_1, x_2, x_3\}$ by applying the Maxwell's equations and the law-of-mixture rule as [363, 87]:

$$\tilde{\sigma}^L = \frac{(L_{CNT}+2t)\sigma_{int}\left[\sigma_c^L r_c^2 + \sigma_{int}\left(2r_c t + t^2\right)\right]}{2\sigma_c^L r_c^2 t + 2\sigma_{int}(2r_c t + t^2)t + \sigma_{int} L_{CNT}(r_c+t)^2} \tag{3.4}$$

$$\tilde{\sigma}^T = \frac{\sigma_{int}}{L_{CNT}+2t}\left[L_{CNT}\frac{2r_c^2\sigma_c^T + \left(\sigma_c^T+\sigma_{int}\right)\left(t^2+2r_c t\right)}{2r_c^2\sigma_{int} + \left(\sigma_c^T+\sigma_{int}\right)\left(t^2+2r_c t\right)} + 2t\right] \tag{3.5}$$

where σ_c denotes the electrical conductivity of the MWCNT and the superscripts "L" and "T" represent the longitudinal and the transverse directions, respectively. The volume fraction f_{eff} of the effective solid fillers can be obtained in terms of the CNT volume fraction f_{CNT} as follows:

$$f_{eff} = \frac{(r_c+t)^2(L_{CNT}+2t)}{r_c^2 L_{CNT}} f_{CNT} \tag{3.6}$$

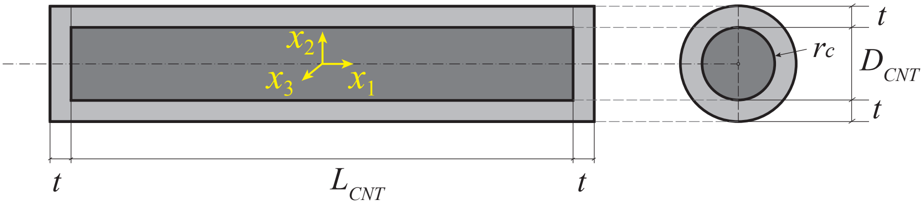

Figure 3.2 Equivalent composite cylinder.

In this way, the composite itself is composed of two phases: the matrix and the effective solid fibers. For this two-phase composite, a micromechanics model can be applied to determine its overall electrical conductivity.

3.2.1.3 Mixed micromechanics model

Let us consider a RVE of cementitious matrix doped with randomly dispersed straight MWCNTs as shown in Fig. 3.3. It is assumed that the RVE contains a sufficient number of fillers in such a way that the overall properties of the composite are statistically represented. The effective properties of the RVE can be estimated by means of the electrical counterpart of the mean-field homogenization model of Eshelby-Mori-Tanaka.

As discussed in the previous section, MWCNTs together with the surrounding interphases can be simulated as equivalent solid fillers. The orientation of a straight filler aligned in the local x_1' direction is characterized by two Euler angles θ and γ, as shown in Fig. 3.3. According to the far-field particle interactions assumption of the Mori-Tanaka method, the effective electric conductivity $\boldsymbol{\sigma}_{eff}$ of the nanocomposite can be determined by averaging over all possible orientations of the fillers in the RVE according to the following expression [237]:

$$\boldsymbol{\sigma}_{eff} = \boldsymbol{\sigma}_m + f_{eff} \frac{\int_0^{2\pi}\int_0^{\pi} \Omega(\theta,\gamma)\,(\boldsymbol{\sigma}_{cnt} - \boldsymbol{\sigma}_m)\,\mathbf{A}\sin(\theta)\,\mathrm{d}\theta\mathrm{d}\gamma}{\int_0^{2\pi}\int_0^{\pi} \Omega(\theta,\gamma)\sin(\theta)\,\mathrm{d}\theta\mathrm{d}\gamma} \tag{3.7}$$

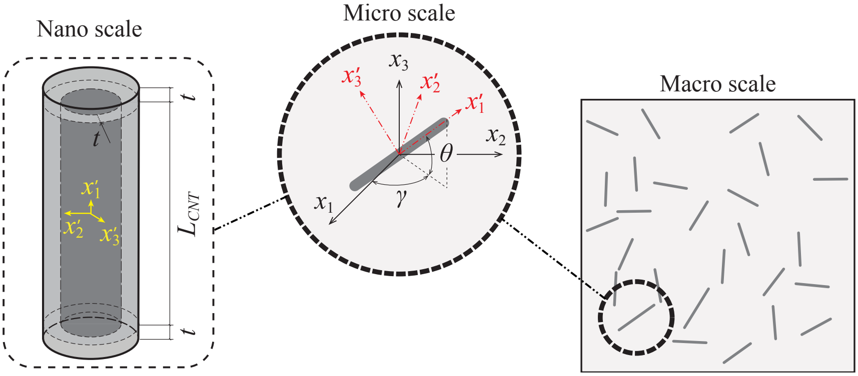

Figure 3.3 Representative Volume Element (RVE) including straight CNTs.

where $\Omega(\theta,\gamma)$ is the Orientation Distribution Function (ODF); f_{eff} is the effective volume fraction of the equivalent filler defined in Eq. (3.6); $\boldsymbol{\sigma}_{cnt}$ and $\boldsymbol{\sigma}_m$ are the electrical conductivity tensors of the effective filler and the matrix, respectively; and $\mathbf{A}$ is the electric field concentration tensor. In the case of completely random oriented fillers, the orientation distribution function is constantly equal to one, $\Omega(\theta,\gamma) = 1$. The base vectors e_i and e'_i of the global (x_1,x_2,x_3) and the local coordinate systems (x'_1,x'_2,x'_3) are related via the transformation matrix $\mathbf{Q}$:

$$e_i = Q_{ij}e'_j \tag{3.8}$$

where $\mathbf{Q}$ is given by:

$$\mathbf{Q} = \begin{bmatrix} \cos\gamma\sin\theta & \sin\gamma\sin\theta & \cos\theta \\ -\sin\gamma & \cos\gamma & 0 \\ -\cos\gamma\cos\theta & -\sin\gamma\cos\theta & \sin\theta \end{bmatrix} \tag{3.9}$$

Each straight MWCNT is modeled as an equivalent solid cylinder with transversely isotropic electrical conductivity tensor in the local coordinate system, $\boldsymbol{\sigma}'_{cnt}$, given as [275]:

$$\boldsymbol{\sigma}'_{cnt} = \begin{bmatrix} \tilde{\sigma}^L & 0 & 0 \\ 0 & \tilde{\sigma}^T & 0 \\ 0 & 0 & \tilde{\sigma}^T \end{bmatrix} \tag{3.10}$$

with $\tilde{\sigma}^L$ and $\tilde{\sigma}^T$ being the longitudinal and transverse electrical conductivity of the effective filler as obtained in Eqs. (3.4) and (3.5), respectively. Based on the assumption of uniform and random distribution of fillers, the electric field concentration tensor **A** in the global coordinate system can be expressed as [87]:

$$\mathbf{A} = \mathbf{Q}^T\tilde{\mathbf{T}}\mathbf{Q}\left\{\left(1-f_{eff}\right)\mathbf{I}+\frac{f_{eff}}{4\pi}\int_0^{2\pi}\int_0^{\pi}\left\{\mathbf{Q}^T\tilde{\mathbf{T}}\mathbf{Q}\right\}\sin(\theta)\,\mathrm{d}\theta\mathrm{d}\gamma\right\}^{-1} \tag{3.11}$$

where

$$\tilde{\mathbf{T}} = \left\{\mathbf{I}+\mathbf{S}(\sigma_m)^{-1}(\tilde{\sigma}-\sigma_m)\right\}^{-1} \tag{3.12}$$

with $\mathbf{I}$ (I_{ij}) and $\mathbf{S}$ (S_{ij}) being the second-order identity tensor and the Eshelby tensor of the effective filler, respectively. The Eshelby's tensor of a prolate spheroid ($a_2 = a_3 < a_1$) aligned in the x_1' direction is given by [310]:

$$\mathbf{S} = \begin{bmatrix} S_{11} & 0 & 0 \\ 0 & S_{22} & 0 \\ 0 & 0 & S_{33} \end{bmatrix} \tag{3.13}$$

where

$$S_{22} = S_{33} = \frac{A_{re}}{2\left(A_{re}^2-1\right)^{3/2}}\left[A_{re}\left(A_{re}^2-1\right)^{1/2}-\cosh^{-1}A_{re}\right] \tag{3.14a}$$

$$S_{11} = 1-2S_{22} \tag{3.14b}$$

with A_{re} being the aspect ratio of the effective filler, i.e. A_{re}=$(L_{CNT}+2t)/(D_{CNT}+2t)$.

As mentioned before, several experiments and simulations have demonstrated that CNT-cement nanocomposites have a percolation-like behavior displaying a sharp increase in the electrical conductivity after the CNT volume fraction reaches a certain threshold [47, 52, 348]. For a two-phase nanocomposite with a uniformly random distribution of CNTs, the percolation threshold, f_c, can be approximately determined by the following analytical expression [100, 66]:

$$f_c(H) = \frac{9H(1-H)}{2+15H-9H^2}, \quad H = \frac{1}{A_r^2-1}\left[\frac{A_r}{\sqrt{A_r^2-1}}\ln\left(A_r+\sqrt{A_r^2-1}\right)-1\right] \tag{3.15}$$

where A_r is the aspect ratio of the MWCNT, i.e. $A_r = L_{CNT}/D_{CNT}$. The percolation threshold f_c denotes the onset of the percolation process. Before this critical value ($f_{CNT} < f_c$), electron hopping is the only mechanism that contributes to the electrical conductivity. Nonetheless, once percolation starts ($f_{CNT} = f_c$), a certain number of MWCNTs begin to be electrically connected forming conductive networks. Hence, for volume fractions above the percolation threshold, a percentage $\mathcal{X}$ of MWCNTs are connected forming conductive networks whilst the rest, $1-\mathcal{X}$, are not yet connected and only electron hopping contributes to the overall conductivity of the composite. According to Deng and Zheng [66], the relative amount of percolated MWCNTs, $\mathcal{X}$, can be approximately estimated as:

$$\mathcal{X} = \begin{cases} 0 & 0 \leq f_{CNT} < f_c \\ \dfrac{f_{CNT}^{1/3} - f_c^{1/3}}{1 - f_c^{1/3}} & f_c \leq f_{CNT} \leq 1 \end{cases} \tag{3.16}$$

From the above analysis, it is concluded that both electron hopping (EH) and conductive networks (CN) contribute to the electrical conductivity of the composite after percolation, while only electron hopping takes place before this critical value. Therefore, the expression of the overall electrical conductivity of CNT-cement nanocomposites from Eq. (3.7) can be extended by the sum of both mechanisms as follows:

$$\boldsymbol{\sigma}_{eff} = \boldsymbol{\sigma}_m + \boldsymbol{\sigma}_{N,EH} + \boldsymbol{\sigma}_{N,CN} \tag{3.17}$$

where $\boldsymbol{\sigma}_{N,EH}$ and $\boldsymbol{\sigma}_{N,CN}$ denote the electrical conductivity provided by electron hopping and conductive network mechanisms, respectively, and are defined as:

$$\boldsymbol{\sigma}_{N,EH} = (1 - \mathcal{X}) \frac{1}{4\pi} \int_0^{2\pi} \int_0^{\pi} \left\{ f_{eff} \left(\boldsymbol{\sigma}_{EH} - \boldsymbol{\sigma}_m \right) \mathbf{A}_{EH} \right\} \sin(\theta) \, \mathrm{d}\theta \mathrm{d}\gamma \tag{3.18}$$

$$\boldsymbol{\sigma}_{N,CN} = \mathcal{X} \frac{1}{4\pi} \int_0^{2\pi} \int_0^{\pi} \left\{ f_{eff} \left(\boldsymbol{\sigma}_{CN} - \boldsymbol{\sigma}_m \right) \mathbf{A}_{CN} \right\} \sin(\theta) \, \mathrm{d}\theta \mathrm{d}\gamma \tag{3.19}$$

In the case of MWCNTs forming conductive networks, several adjacent fibers are electrically connected resulting in a continuous conductive path. This effect can be modeled by considering infinite aspect ratio of the MWCNTs as proposed by Seidel and Lagoudas [275]. Therefore, quantities associated with electron hopping correspond to the real MWCNTs aspect ratio ($a_2 = a_3 = r_c, \quad a_1 = L_{CNT}$), while quantities related to conductive networks correspond to an infinite aspect ratio ($a_2 = a_3 = r_c, \quad a_1 \to \infty$).

3.2.2 Composites reinforced with randomly oriented curved CNTs

In order to support the development of the analytical micromechanics model of electrical conduction in CNT cement-matrix composites, morphological analyses have been carried out on water suspensions and cementitious materials doped with MWCNTs, appropriately realized with different dispersing procedures. The results have shown that most MWCNTs in cement-based composites exist in a curved state, what is attributed to their low bending stiffness due to the small tube diameter (10-15 nm). Figure 3.4 shows two examples of Scanning Electron Microscope (SEM) images, at the same magnification, of MWCNTs in water suspensions obtained after sonication by use of lignosulfonic acid sodium salt (SLS) dispersant (Fig. 3.4 (a)), and using just mechanical mixing without dispersant (Fig. 3.4 (b)). The micrographs show a homogeneous dispersion of the carbon fillers in the sonicated mix and the presence of visible bundles in the mechanically mixed one. Experimental investigations have also concerned the influence of different amounts of dispersant on the morphology of MWCNTs in water suspensions after mixing. Figure 3.5 shows the SEM images of MWCNTs dispersed in water solution realized with surfactant added in the concentrations of 1:1 (Fig. 3.5 (a)) and 10:1 (Figs. 3.5 (b) and 3.5 (c)) with respect to the mass of the carbon nanotubes. The addition methods used for the dispersions were sonication (Figs. 3.5 (a) and 3.5 (b)) and mechanical mixing (Fig. 3.4 (c)). All the SEM images of the MWCNT-added water suspensions, realized for the dispersion analyses, have demonstrated that the carbon nanotubes exhibit similar characteristic curved geometries.

From this analysis, it can be extracted that the geometry of curved MWCNTs can be approximated by an helical curve. The geometry of this curve (Fig. 3.6) is defined by the diameter D_h, the spiral angle θ^w and the polar angle δ. The length L^{wavy} of the curved CNT is defined by these parameters as:

$$L^{wavy} = \frac{\delta D_h}{2\cos\theta^w} \tag{3.20}$$

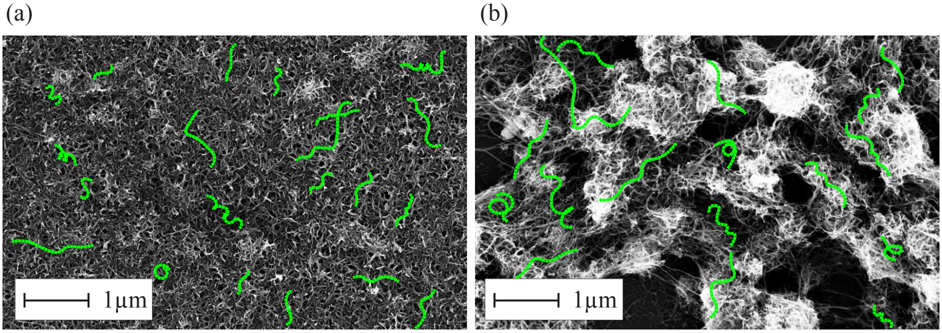

Figure 3.4 SEM pictures of MWCNTs in aqueous suspensions with physical dispersant after sonication (a) and without dispersant after mechanical mixing (b). (The green dashed lines represent some of the helical wavy geometries detected in the inspections).

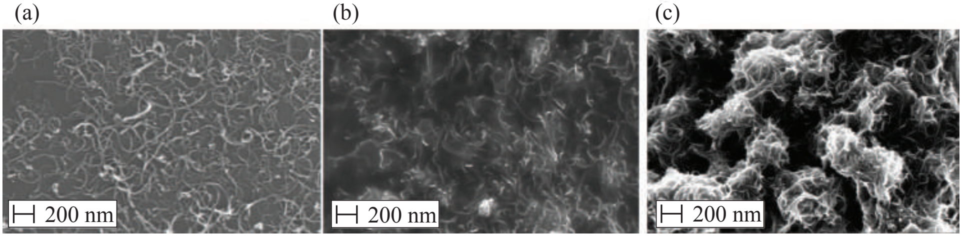

Figure 3.5 SEM pictures of MWCNTs in aqueous suspensions sonicated with the SLS dispersant in the 1:1 (a) and 10:1 (b) amounts, and mechanically mixed using the SLS dispersant in the 10:1 amount (c).

The waviness of a MWCNT is governed by its spiral angle, θ^w. For example, $\theta^w = \pi/2$ corresponds to a straight configuration, while $\theta^w = 0$ corresponds to a circular MWCNT. The consideration of the waviness effect into the micromechanics modeling requires the conversion of the wavy CNTs into equivalent straight fillers of length L^{str} [66, 303, 86]. A wavy MWCNT can be regarded as an equivalent straight fiber with the capability of

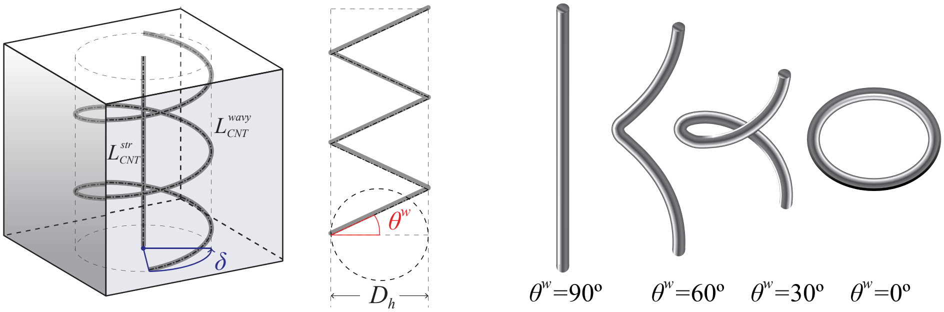

Figure 3.6 Helical model of a curved MWCNT and its equivalent straight counterpart.

(i) conducting the same electric flux J; and (ii) transporting the same amount of electric charges [87]. When the wavy MWCNT is subjected to a potential difference ΔV, the electrical flux J can be approximated by [66]:

$$J = \sigma_c^{wavy} \frac{\Delta V}{L^{wavy}} \tag{3.21}$$

Hence, the first condition (i) defines the effective electrical conductivity of the equivalent straight MWCNT as:

$$\sigma_c^{str} = \alpha \sigma_c^{wavy} \tag{3.22}$$

with $\alpha = L^{str}/L^{wavy} = \sin\theta^w$ the length ratio. The second condition (ii) imposes the same electrical charge through the wavy and the equivalent straight fillers and, thus, the same electrical resistance:

$$R_{cnt}^{str} = R_{cnt}^{wavy} \tag{3.23}$$

The combination of Eqs. (3.22) and (3.23) results in a condition of equal diameters for the wavy and the straight fillers, $D^{str} = D^{wavy}$. Finally, due to the reduction of the MWCNTs length from L^{wavy} to L^{str}, the volume fraction of the fillers must be updated to $f^{str} = \alpha f^{wavy}$, with f^{wavy} being the volume fraction of the wavy MWCNTs.

3.2.3 Modeling of CNT agglomeration effects

The large surface area of MWCNTs originates substantial vdW attraction forces what makes MWCNTs easy to form agglomerates in bundles [276, 284]. The resulting spatial distribution of nano-inclusions within the matrix is non-uniform, so some local regions present higher concentrations of MWCNTs than the average in the composite. Fig. 3.7 shows two SEM pictures of MWCNTs dispersed in water solution with low content of dispersant after sonication, taken with magnification factors of 5000 and 1000, respectively. They clearly illustrate some typical carbon nanotube agglomerations occurring in aqueous suspensions, whose geometries can be approximately defined as ellipsoidal. Hence, in order to include the agglomeration effect in the proposed micromechanics approach, the bundles are assumed as ellipsoidal inclusions ($a_2 = a_3 \neq a_1$) with distinct conductive properties from the surrounding material. To this end, the two parameter agglomeration model introduced by Shi *et al.* [282], and previously outlined in section 2.2.5, has been adapted in this work to model the conductivity of non-uniformly distributed MWCNT-reinforced cement composites.

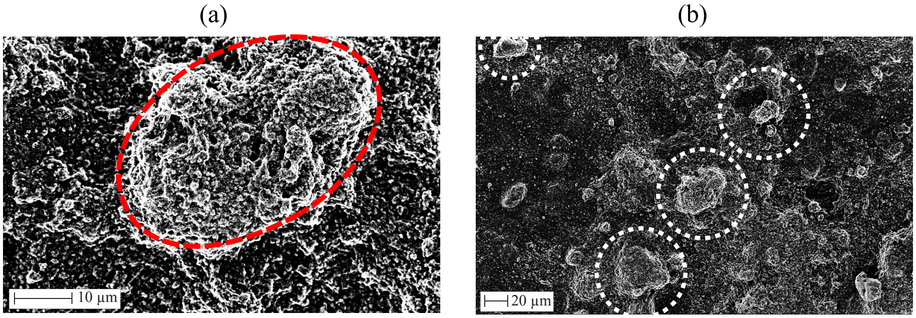

Figure 3.7 SEM pictures of MWCNTs in aqueous suspension with magnification factors of 5000× (a) and 1000× (b).

The homogenization procedure defined in Eq. (3.17) has been therefore applied in two separate steps: inside the bundles and in the surrounding matrix. The homogenization of these two new phases has been carried out taking into account the ellipsoidal geometry of the bundles. To this purpose, the Eshelby's tensor for an ellipsoid inclusion with symmetric axis x'_3 has been used, whose expression is given by:

$$S_{22} = S_{33} = \begin{cases} \dfrac{A_e}{2\left(A_e^2-1\right)^{3/2}}\left[A_e\left(A_e^2-1^{1/2}\right)-\cosh^{-1}A_e\right]; & A_e \geq 1 \\ \dfrac{A_e}{2\left(A_e^2-1\right)^{3/2}}\left[cos^{-1}A_e-A_e\left(1-A_e^2\right)^{1/2}\right]; & A_e \geq 1 \end{cases} \tag{3.24}$$

with A_e the aspect ratio of the ellipsoid ($A_e = a_1/a_2$) and $S_{11}=1-2S_{22}$.

3.3 Uniaxial strain-sensing capabilities of CNT-reinforced composites[2]

In this section, a micromechanics modeling of the uniaxial piezoresistivity of CNT-reinforced cement-matrix composites is developed as an extension of the previously described approach. The origin of the strain sensing capabilities of the cement-based nanocomposites is attributed to three main mechanisms: (i) volume expansion and reorientation of CNTs, (ii) changes in the conductive networks, and (iii) changes in the tunneling resistance. The following sections separately present the modeling approach for each of these contributions.

---

[2] An extended version of this section is found in paper E.

3.3.1 Volume expansion and reorientation of CNTs

Let us consider a three-dimensional affine deformation cell containing an embedded effective solid filler before and after the application of a uniaxial strain ε as shown in Fig. 3.13. Under the assumption of large deformations, the volume of the cell changes from $V_o^c = l_o^3$ to $V^c = l_o^3(1+\varepsilon)^{1-2\nu}$, with ν being the Poisson's ratio of the composite. Moreover, assuming that the deformation of the composite is mainly sustained by the matrix, the volume of the nano-inclusions remains constant and, therefore, the volume expansion induces changes in the CNT volume fraction as follows [85]:

$$f_{CNT}^{*} = \frac{V_o^c f_{CNT}}{V^c} = \frac{f_{CNT}}{(1+\varepsilon)^{1-2\nu}} \tag{3.25}$$

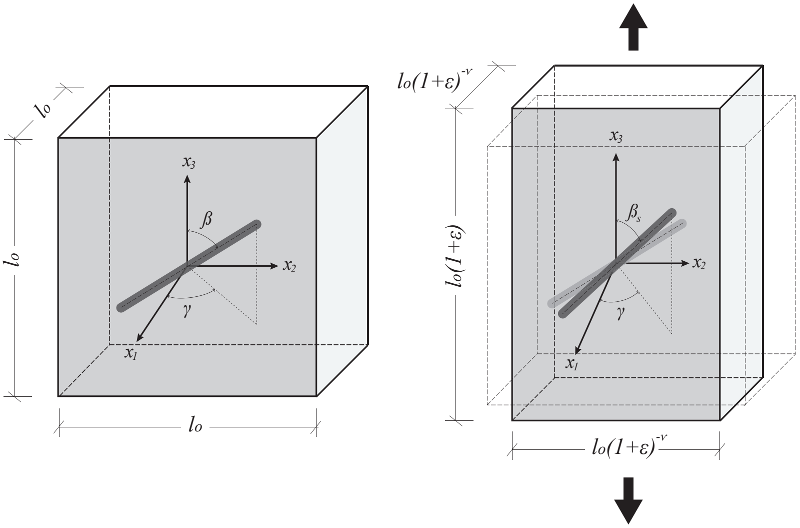

Figure 3.8 Schematic representation of the volume expansion and reorientation of a conductive filler within a deformable cell subjected to uni-axial strain ε.

Likewise, it can be noted from Fig. 3.13 that the strain ε also originates a re-alignment of the fiber along the strain direction x_3. This change of orientation is characterized by a decrease in the complementary polar angle from $\pi/2-\beta$ to $\pi/2-\beta_s$, with negligible variation of the azimuth angle γ [85]. The new complementary polar angle β_s can be expressed in terms of its initial value β as follows [309]:

$$\tan\beta_s = (1+\varepsilon)^{1+\nu}\tan\beta \tag{3.26}$$

This change of the polar angle of the fillers results in a change of the ODF from $\Omega(\pi/2-\beta,\gamma)$ to $\Omega(\pi/2-\beta_s,\gamma)$. After the application of the strain, the initially randomly distributed fillers ($\Omega(\pi/2-\beta,\gamma)=1$) tend to align in the strain direction and, therefore, the randomness of the nanofillers distribution is reduced. In order to obtain the resulting ODF, the condition of a constant number of fillers before and after the application of the strain has been applied. To this end, and assuming a total number of N fillers distributed in the RVE, the number of fillers lying in the orientation range $(\beta, \beta + \mathrm{d}\beta) \times (\gamma, \gamma + \mathrm{d}\gamma)$ can be computed as [85]:

$$\mathrm{d}N_{\substack{\beta,\beta+\mathrm{d}\beta \\ \gamma,\gamma+\mathrm{d}\gamma}} = \frac{1}{\pi} N \Omega(\pi/2 - \beta, \gamma) \sin\beta \mathrm{d}\beta \mathrm{d}\gamma \tag{3.27}$$

Accordingly, the total number of fillers must be the same after the application of the strain within the range $(\beta_s, \beta_s + \mathrm{d}\beta_s) \times (\gamma, \gamma + \mathrm{d}\gamma)$:

$$\mathrm{d}N_{\substack{\beta_s,\beta_s+\mathrm{d}\beta_s \\ \gamma,\gamma+\mathrm{d}\gamma}} = \mathrm{d}N_{\substack{\beta,\beta+\mathrm{d}\beta \\ \gamma,\gamma+\mathrm{d}\gamma}} \tag{3.28}$$

Substituting Eq. (3.26) into Eq. (3.28), and expressing θ as $\pi/2 - \beta$ (see Fig. 3.13), the resulting ODF, $\Omega(\theta, \gamma)$, is determined as:

$$\Omega(\pi/2 - \beta, \gamma) = \frac{(1+\varepsilon)^{\frac{1+\nu}{2}}}{\left[(1+\varepsilon)^{-(1+\nu)} \cos^2(\pi/2 - \beta) + (1+\varepsilon)^{(1+\nu)} \sin^2(\pi/2 - \beta)\right]^{\frac{3}{2}}} \tag{3.29}$$

Fig. 3.9 shows the variation of the ODF with the strain ε and the polar angle β. In the unloaded case, $\varepsilon = 0$, the ODF remains constant and equal to 1 for every polar angle, corresponding to the uniform random distribution. It is also observed that, for increasing traction ($\varepsilon > 0$), the ODF gives more weight to complementary polar angles close to 0 and π, that is to say, more fibers tend to re-align in the direction of the strain. On the contrary, it is worth noting that for increasing compression ($\varepsilon < 0$), the ODF has higher values for polar angles around $\pi/2$ and, therefore, the fibers tend to re-align in the transverse direction of the strain.

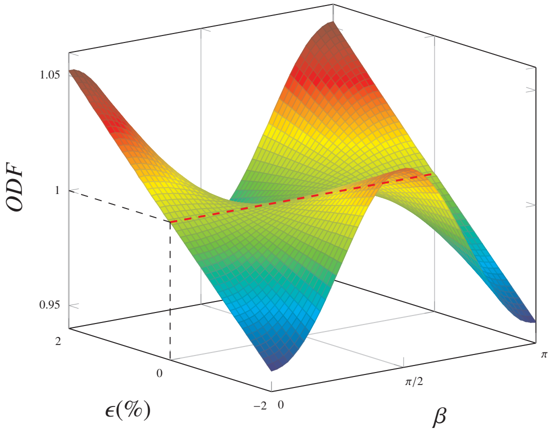

Figure 3.9 Variation of $\Omega(\theta, \gamma)$ (ODF) with strain ε and complementary polar angle β ($\nu = 0.3$).

3.3.2 Change in the conductive networks

Piezoresistivity of CNT nanocomposites is also due to the breakage of conductive networks induced by strain. As previously discussed, the reorientation of the fibers decreases the randomness of the CNT distribution as the strain increases. Hence, it can be intuitively understood that the probability of forming conductive paths must be altered, which corresponds to the change in the percolation threshold f_c.

Komoro and Makishima [163] proposed a stochastic approach for the calculation of the number of filler contacts in general disordered systems doped with rod-like inclusions with constant length and diameter. According to that work, a filler “A” with a given orientation (θ,γ) comes into contact with a second filler “B” with orientation (θ',γ') if the center of mass of the former is located within the neighborhood region of the latter. The neighborhood region is defined when the fiber B is slid over both sides of the fiber A from one end to the other, keeping the direction and the contact point on B unchanged (see Fig. 3.10). In these two sweepings, the axis of B makes two rhombuses near both sides of A, conforming a parallelepiped. The volume of this region is $V = 2D_{CNT}L_{CNT}^2 \sin\tau$, with τ being the angle between the two nanofillers. Based on the defined number of contacts in a volume V along with the probability of formation of a contact, the mean distance among contacts, $\overline{b}_{KM}$, is given by:

$$\overline{b}_{KM} = \frac{\pi D_{CNT}}{8 I f_{CNT}} \tag{3.30}$$

where

$$I = \int_0^{\pi} \mathrm{d}\theta \int_0^{\pi} J(\gamma,\theta)\Omega(\theta,\gamma)\sin\theta \mathrm{d}\gamma \tag{3.31}$$

$$J(\theta,\gamma) = \int_0^{\pi} \mathrm{d}\theta' \int_0^{\pi} \sin\tau\Omega(\theta',\gamma')\sin\theta' \mathrm{d}\gamma' \tag{3.32}$$

$$\sin\tau = \left[1 - \{\cos\theta\cos\theta' + \cos(\gamma-\gamma')\sin\theta\sin\theta'\}^2\right]^{1/2} \tag{3.33}$$

It should be mentioned that Komoro and Makishima did not consider the changes in the contact probability with successive contacts. Pan [238] reported about this issue and proposed an extended approach by considering that an existing contact reduces the effective contact length of a filler, which reduces the probability of forming a new contact. A new expression of the mean distance among inclusions $\overline{b}_{Pan}$ was given as:

$$\overline{b}_{Pan} = \frac{(\pi + 4 f_{CNT}\eta) D_{CNT}}{8 f_{CNT} I} \tag{3.34}$$

where

$$\eta = \int_0^{\pi} \mathrm{d}\gamma \int_0^{\pi} J(\theta,\gamma)K(\theta,\gamma)\sin\theta \mathrm{d}\theta \tag{3.35}$$

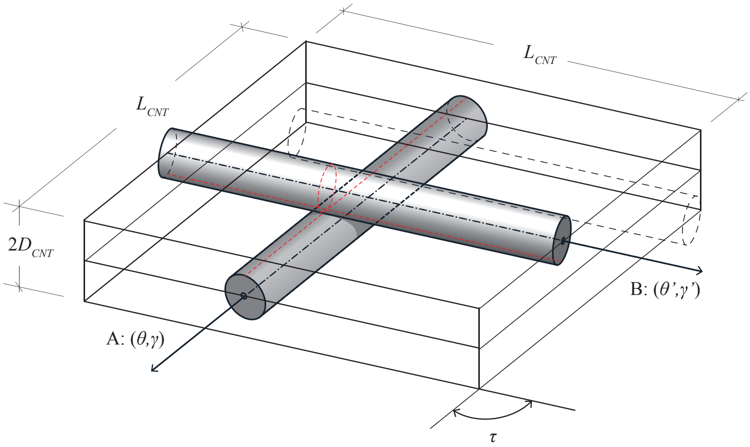

Figure 3.10 Neighborhood of the contact region of a fiber A of orientation (θ,γ) defined by the parallelepiped formed by a second fiber B of orientation (θ',γ') sliding over both sides of the former.

$$K(\theta,\gamma) = \int_0^{\pi} \mathrm{d}\gamma' \int_0^{\pi} \frac{\Omega(\theta',\gamma')\sin\theta'}{\sin\tau(\theta,\gamma,\theta',\gamma')}\mathrm{d}\theta' \tag{3.36}$$

Finally, it is worth noting that each nanofiller must have at least two contact points to be part of a conductive network in the nanocomposite [283]. Alternatively, the mean distance between contacts should be at least half of the filler length to attain the percolation threshold. Kumar and Rawal [169] defined a coverage parameter, $\Gamma = b/L_{CNT}$, which represents the number of contacts formed on a given filler length. In the case of percolated nanofillers, this quantity is such that $\Gamma \leq 0.5$. Those authors also proposed a mean coverage parameter, $\overline{\Gamma} = \overline{b}/L_{CNT}$, as the probability of percolation of the composite. Furthermore, it has been reported in the literature that the distance between the contacts exhibit an exponential distribution [59, 315] and, similarly, a mean coverage parameter $\overline{\Gamma}$ can be defined as [169]:

$$P(\Gamma) = (1/\overline{\Gamma})\exp\left(-\Gamma/\overline{\Gamma}\right) \tag{3.37}$$

Zheng *et al.* [388] reported that the statistical percolation threshold is reached when 50% of the sample percolates, this is:

$$\int_0^{0.5} P(\Gamma)\mathrm{d}\Gamma = -\exp(0.5/\overline{\Gamma}) + 1 = 0.5 \tag{3.38}$$

where a value $\overline{\Gamma}$ of 0.72 is extracted. Finally, combining this result with Eqs. (3.31) and (3.34), the percolation threshold can be computed using the Komori-Makishima and Pan's models as:

$$f_c^{KM} = \frac{\pi}{5.77 A_r I}, \quad f_c^{Pan} = \frac{\pi}{5.77 A_r I - 4\eta} \tag{3.39}$$

with A_r being the aspect ratio of the nanofillers, i.e. L_{CNT}/D_{CNT}. Kumar and Rawal [169] reported that there are only slight differences between the Komori and Makishima and Pan's models since the percolation threshold is often reached at significantly low nanofiller concentrations. Similar conclusions were also obtained in the present work and, therefore, all the results that are provided thereafter are obtained by using the Komoro and Makishima's model. This methodology has allowed us to relate the externally applied deformation with the variation of the percolation threshold through the ODF, as previously defined in Eq. (3.29). Fig. 3.11 shows the variation of the percolation threshold with respect to the nanofiller aspect ratio and for different strain levels. For mere illustrative purposes, unrealistically high strain levels are considered to highlight the strain-induced variations. It can be extracted from this figure that, due to the reorientation of the fillers caused by the strain, some conductive paths disappear and consequently the percolation threshold increases. In addition, Fig. 3.12 (a) shows different orientation distribution functions for polar angles varying from 0 to π under different levels of uni-axial strain. As already discussed in the previous section, in the case of stretching ($\varepsilon > 0$), the nanotubes tend to re-align in the direction of the strain, whilst in the case of compression ($\varepsilon < 0$), the tendency is the opposite and the fillers tend to re-align perpendicularly to the strain. In both cases, the loss of randomness of the nanofillers distribution leads to lesser probability of forming conductive paths as it can be seen in Fig. 3.12 (b). Hence, it can be concluded from this figure that both compression and traction lead to higher percolation thresholds.

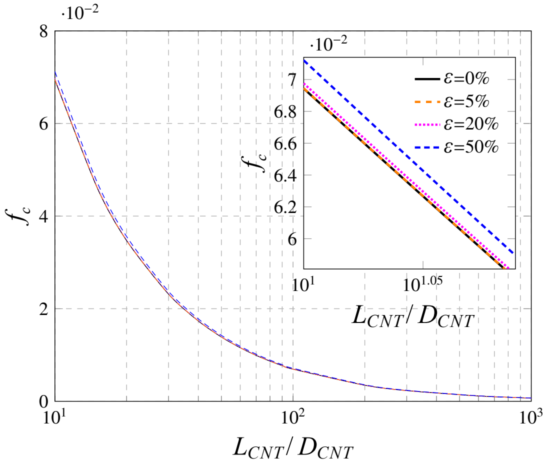

Figure 3.11 Percolation threshold versus CNTs volume fraction under different strain levels (ν=0.3).

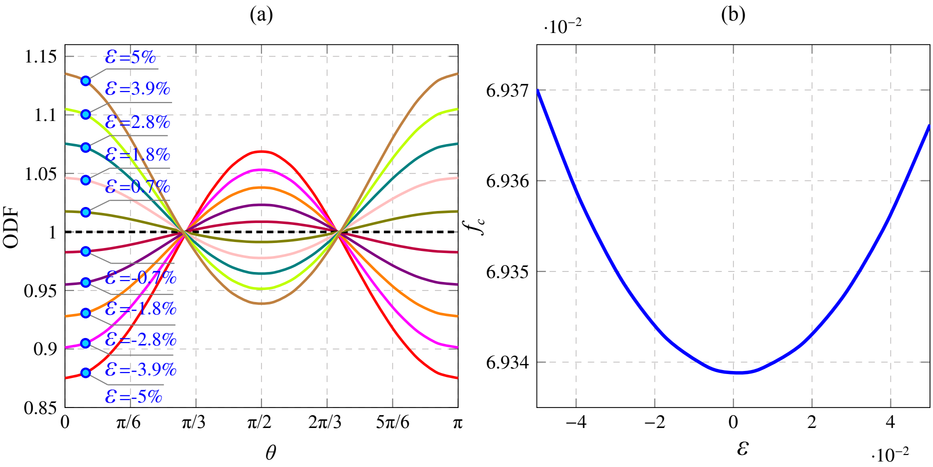

Figure 3.12 Orientation distribution functions under different strain levels (a), and variation of the percolation threshold with respect to the strain level (b) (ν=0.3).

3.3.3 Change in the tunneling resistance

The third mechanism originating the strain-sensing property of the composites is related to the circumstance that electron hopping is altered when a deformation is applied because of changes in the inter-particle distance. It has been reported in the literature that, when a nanocomposite is deformed under external strain, the change of the nanotube resistance is expected to be negligible because of the extremely small elastic deformation in nanotubes resulting from their high elastic modulus, while the large deformation in the inter-nanotube matrix due to its low modulus contributes to the electrical resistance change of the composite [170]. It has been also reported in the literature that, at relatively low strains ($< 10^{-4}$), the inter-particle distance and the height of the potential barrier change proportionally with the strain [290] as follows:

$$d_a = d_{a,0}(1 + C_1\varepsilon) \tag{3.40}$$

$$V_o = V_o^0(1 + C_2\varepsilon) \tag{3.41}$$

where $d_{a,0}$ and V_o^0 are the initial inter-particle distance and potential height at zero strain, respectively, and C_1 and C_2 are constants. The constants C_1 and C_2 can be obtained by fitting experimental data. There still exists a lack of information in the literature about this aspect and, therefore, further future research is needed in order to develop a fully experimental independent tool for design purposes.

3.4 Three-dimensional strain-sensing capabilities of CNT-reinforced composites[3]

In this section, the previously presented formulation is extended to account for general three-dimensional strain states. In particular, dilation and distortion strain states are analyzed in order to construct the three-dimensional piezoresistivity matrices, apt to be applied in steady-state piezoresistive analyses in a finite element code. In a similar way to the previous section, strain-induced alterations are divided into (i) volume expansion and reorientation of fillers, (ii) changes in the conductive networks, and (iii) changes in the tunneling resistance.

3.4.1 Volume expansion and reorientation of CNTs under 3D strain states

Two different strain states are considered, namely dilation and distortion. The main purpose of this section is to study the volume expansion and reorientation of fillers under both strain conditions. New closed-form expressions of the ODFs are presented for affine deformation of cubic cells of random arrangements of fillers under three-dimensional dilation and shear strains.

3.4.1.1 Dilation strain

Let us retake the deformable cubic cell of side l_o loaded with an embedded filler before and after the application of a 3D strain state (ε_1,ε_2,ε_3) as shown in Fig. 3.13. The volume of the cell changes from $V_o = l_o^3$ to $V = l_o^3(1+\varepsilon_1)(1+\varepsilon_2)(1+\varepsilon_3)$=$l_o^3\bar{\varepsilon}_1\bar{\varepsilon}_2\bar{\varepsilon}_3$. It is assumed that the filler remains inextensible because its stiffness is considerably higher than that of the matrix. In this way, the deformation of the composite is mainly sustained by the matrix and, therefore, the volume expansion induces changes in the CNT volume fraction as follows:

$$f^* = \frac{V_o f_{CNT}}{V} = \frac{f_{CNT}}{\bar{\varepsilon}_1\bar{\varepsilon}_2\bar{\varepsilon}_3} \tag{3.42}$$

Likewise, it can be noted from Fig. 3.13 that the strains also originate a re-alignment of the fiber. This change of orientation is characterized by a change of the Euler angles from (β,γ) to (β',γ'). Correspondingly, the relationships between the coordinates of the upper end of the filler in the cell before (x_1,x_2,x_3) and after (x_1',x_2',x_3') the tri-axial strain are determined in terms of the Euler angles as:

$$\frac{x_1'}{x_1} = \frac{u' \sin\beta' \cos\gamma'}{u \sin\beta \cos\gamma} = \bar{\varepsilon}_1 \tag{3.43a}$$

$$\frac{x_2'}{x_2} = \frac{u' \sin\beta' \sin\gamma'}{u \sin\beta \sin\gamma} = \bar{\varepsilon}_2 \tag{3.43b}$$

$$\frac{x_3'}{x_3} = \frac{u' \cos\beta'}{u \cos\beta} = \bar{\varepsilon}_3 \tag{3.43c}$$

---

[3] An extended version of this section is found in paper K.

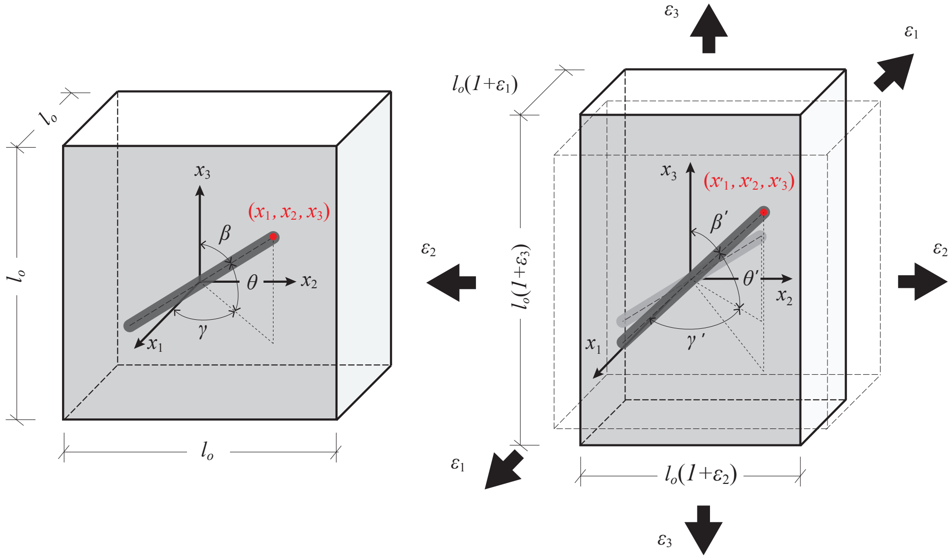

Figure 3.13 Schematic representation of the volume expansion and reorientation of a conductive filler within a deformable cell subjected to a triaxial strain state (ε_1,ε_2,ε_3).

where u and u' are the half lengths of the filler before and after the application of the distortion, respectively. Since the filler is considerably stiffer than the matrix, it is assumed as inextensible, that is $u' = u$. This change of the Euler angles of the filler results in a change of the ODF from $\Omega(\beta,\gamma)$ to $\Omega(\beta',\gamma')$. After the application of strain, the initially randomly oriented fillers ($\Omega(\beta,\gamma) = 1$) tend to re-align and, therefore, the randomness of the nanofillers arrangement is reduced. In order to obtain the resulting ODF, the condition of a constant number of fillers before and after the application of strain can be applied. In this regard, considering a total number of N fillers distributed in the RVE, the number of fillers dN lying in the orientation range $(\beta,\beta+\mathrm{d}\beta)\times(\gamma,\gamma+\mathrm{d}\gamma)$ can be computed as [85]:

$$\mathrm{d}N_{\substack{\beta,\beta+\mathrm{d}\beta\\ \gamma,\gamma+\mathrm{d}\gamma}} = \frac{1}{\pi}N\Omega(\beta,\gamma)\sin\beta\mathrm{d}\beta\mathrm{d}\gamma \tag{3.44}$$

The total number of fillers must remain constant after the application of the strain within the range $(\beta',\beta'+\mathrm{d}\beta')\times(\gamma',\gamma'+\mathrm{d}\gamma')$, what yields:

$$\mathrm{d}N_{\substack{\beta',\beta'+\mathrm{d}\beta'\\ \gamma',\gamma'+\mathrm{d}\gamma'}} = \mathrm{d}N_{\substack{\beta,\beta+\mathrm{d}\beta\\ \gamma,\gamma+\mathrm{d}\gamma}} \tag{3.45}$$

Substituting Eqs. (3.43) and (3.44) into Eq. (3.45), and considering that $\Omega(\beta,\gamma) = 1$ since CNTs are assumed randomly oriented in the undeformed configuration, the resulting

ODF, $\Omega(\beta',\gamma')$, is determined after some manipulations as:

$$\Omega(\beta',\gamma') = \frac{\bar{\varepsilon}_1^2\bar{\varepsilon}_2^2\bar{\varepsilon}_3^2}{\left[\bar{\varepsilon}_2^2\bar{\varepsilon}_1^2\cos^2\beta' + \bar{\varepsilon}_3^2\left(\bar{\varepsilon}_2^2\cos^2\gamma' + \bar{\varepsilon}_1^2\sin^2\gamma'\right)\sin^2\beta'\right]^{3/2}} \tag{3.46}$$

In the absence of strains, i.e. $\varepsilon_1 = \varepsilon_2 = \varepsilon_3 = 0$ or equivalently $\bar{\varepsilon}_1 = \bar{\varepsilon}_2 = \bar{\varepsilon}_3 = 1$, the ODF in Eq. (3.46) reduces to 1 as expected for a random orientation distribution. Figs. 3.14 (a) and (b) show the variation of the ODF with the uni-axial strain ε_3 and the polar angle β for laterally unconstrained ($1+\varepsilon_1 = 1+\varepsilon_2 = (1+\varepsilon_3)^{-\nu}$) and constrained conditions ($\varepsilon_1 = \varepsilon_2 = 0$), respectively. For illustrative purposes, a Poisson's ratio of $\nu = 0.45$ is assumed. In both cases, when strains are zero, the ODF remains constant and equal to 1 for every polar angle, corresponding to the random orientation distribution case as previously indicated. It is also observed that, for increasing stretching ($\varepsilon_3 > 0$), the ODF gives more weight to polar angles close to 0 and π, what indicates that more nanotubes tend to re-align in the direction of the strain. On the contrary, for increasing compression ($\varepsilon_3 < 0$), the ODF has higher values for polar angles around $\pi/2$ and, therefore, the nanotubes tend to re-align in the transverse direction of the strain. With regard to the lateral conditions, it is observed that the randomness of the orientation is less altered when the composite is laterally constrained.

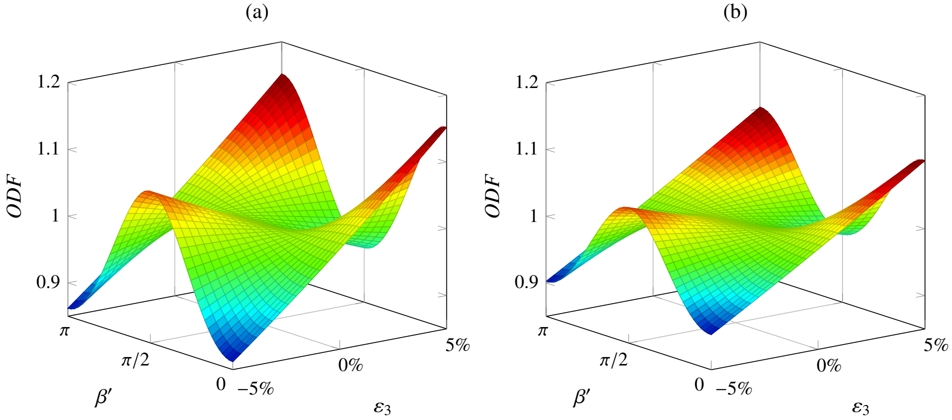

Figure 3.14 Variation of $\Omega(\beta',\gamma')$ (ODF) with strain ε_3 and polar angle β' for laterally unconstrained (a) and constrained (b) conditions ($\nu = 0.45$).

Fig. 3.15 (a) shows the ODF under bi-axial stretching with $\varepsilon_3 = 5\%$ and $\varepsilon_2 = 0.25 \cdot 5\%$ and laterally unconstrained condition, that is, $\bar{\varepsilon}_1 = [(1+\varepsilon_3)(1+\varepsilon_2)]^{-\frac{\nu}{1-\nu}}$. Similarly, Fig. 3.15 (b) shows the ODF under bi-axial stretching with $\varepsilon_3 = \varepsilon_2 = 5\%$ and laterally unconstrained condition. It is noted that such high strain values are not physically possible for concrete and cement-based materials, but are here considered for generality, as the derived ODFs can be used for different CNT-reinforced composites, as well as for illustrative purposes. From these figures, it can be seen that the strain tends to re-align the fillers along the stretching directions ($\gamma' = \pi/2$ and $\beta' = 0, \pi$). Comparing the ODFs in Figs. 3.15 (a) and (b), it is concluded that increasing the stretching in the x_2 direction increases the re-alignment of fillers along that direction.

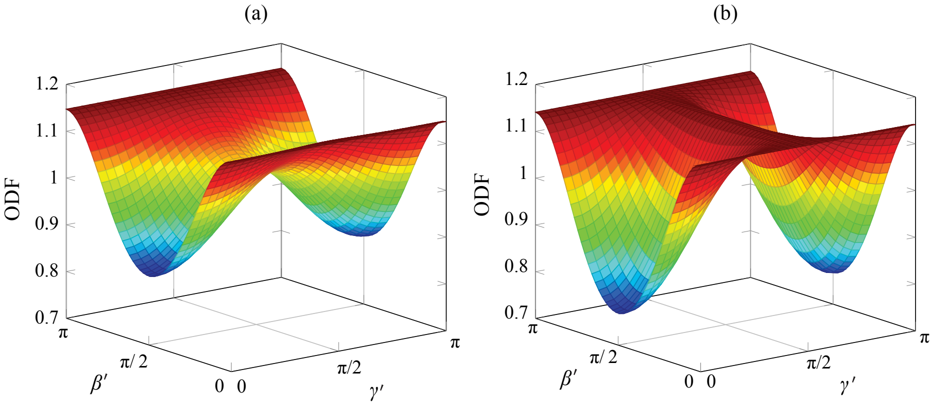

Figure 3.15 Variation of $\Omega(\beta',\gamma')$ (ODF) with polar β' and azimuthal angle γ' under bi-axial stretching (a) $\varepsilon_3 = 5\%, \varepsilon_2 = 0.25 \cdot 5\%$ and (b) $\varepsilon_3 = 5\%, \varepsilon_2 = 5\%$ in laterally unconstrained conditions ($\nu = 0.45$).

Finally, in order to further the comprehension of Eq. (3.46), the ODFs obtained for uni-axial stretching along the (a) x_1, (b) x_2 and (c) x_3 directions with laterally constrained conditions are depicted in Fig. 3.16. It is observed that, in all cases, stretching induces a re-alignment of the fillers in the strain direction.

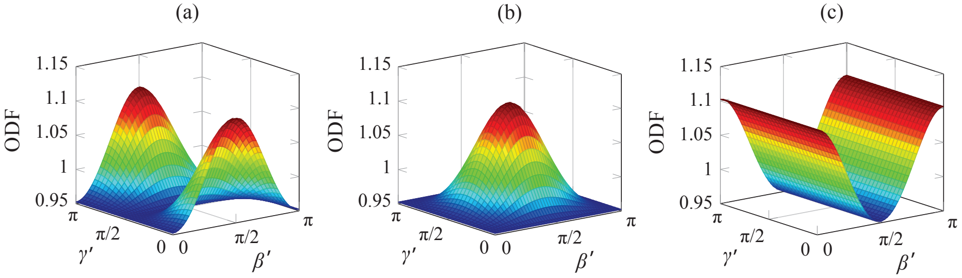

Figure 3.16 Variation of $\Omega(\beta',\gamma')$ (ODF) with polar β' and azimuthal angle γ' with uni-axial stretching along the (a) x_1, (b) x_2 and (c) x_3 directions under laterally constrained conditions ($\varepsilon_i = 5\%$, $\overline{\varepsilon}_j = 1$ $j \neq i$, $\nu = 0.45$).

3.4.1.2 Distortion strain

Let us now consider a deformable cubic cell containing an embedded filler before and after the application of a distortion ε_{32} as shown in Fig. 3.17. In this case, distortion does not originate any volume change although it does induce re-orientation of the filler. In order to study the deformed configuration, two auxiliary planes A and B are defined as indicated in the figure. Plane A is parallel to the $x_2 - x_3$ plane and contains the upper end of the filler. On the other hand, plane B is defined by the x_3-axis and the upper end of the filler. An auxiliary angle α is defined as the angle between the x_3-axis and the orthogonal projection of the filler onto plane A. It is observed that once the distortion is applied, both planes transform into rhombuses. It is hypothesized that the filler re-aligns in the diagonal direction of both rhombuses. Hence, this assumption completely determines the orientation of the filler after the application of strain, irrespective of the deformed filler length u'. In a similar way to the previous case, it is assumed that the strain is mainly held by the matrix and the filler is assumed inextensible, i.e. $u' = u$. In the particular case of ε_{32}, it is also observed that the polar angle changes from β to β', while the azimuthal angle remains unaltered. Using trigonometric relations in Fig. 3.17, the following relations can be extracted:

$$\tan\alpha' = \frac{\sin\beta\sin\gamma}{\cos\beta + 2\varepsilon_{32}\sin\beta\sin\gamma} \tag{3.47}$$

$$\tan\beta' = \frac{\tan\alpha'}{\sin\gamma} \tag{3.48}$$

and substitution of Eq. (3.47) into Eq. (3.48) leads to:

$$\tan\beta = \frac{\tan\beta'}{1 - 2\varepsilon_{32}\sin\gamma\tan\beta'} \tag{3.49}$$

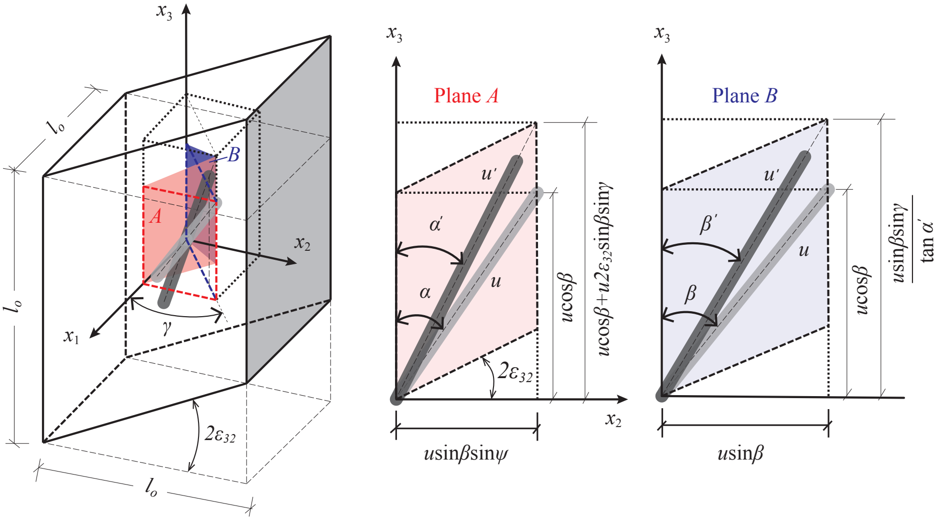

Figure 3.17 Schematic representation of reorientation of a conductive filler within a deformable cell subjected to a distortion ε_{32}.

In the same way as in the previous case, the total number of fillers must remain constant within the range $(\beta',\beta'+\mathrm{d}\beta')\times(\gamma,\gamma+\mathrm{d}\gamma)$, that is:

$$\mathrm{d}N_{\substack{\beta',\beta'+\mathrm{d}\beta' \\ \gamma,\gamma+\mathrm{d}\gamma}} = \mathrm{d}N_{\substack{\beta,\beta+\mathrm{d}\beta \\ \gamma,\gamma+\mathrm{d}\gamma}} \tag{3.50}$$

Substituting Eq. (3.49) into Eq. (3.50), the resulting ODF, $\Omega(\gamma,\beta')$, is determined after some manipulation as:

$$\Omega(\beta',\gamma) = \left(1 - 4\varepsilon_{32}\sin\gamma\sin\beta'\cos\beta' + 4\varepsilon_{32}^2\sin^2\gamma\sin^2\beta'^2\right)^{-3/2} \tag{3.51}$$

Fig. 3.18 shows the ODF under distortion strain $\varepsilon_{32} = 0.1$. It is observed that the ODF has a symmetry about γ. In addition, it is observed that the ODF gives more weight to fillers with polar angles β close to 0, whilst lesser values are found for those with polar angles close to π. According to Fig. 3.17, fillers tend to align in the $\beta = 0$, $\gamma = \pi/2$ direction. It is also noticeable that the limit cases of $\beta = 0,\pi$, and $\gamma = 0,\pi$ correspond to unitary ODF values. This fact is readily observed in Fig. 3.17 as these fillers do not experience any change in their orientation.

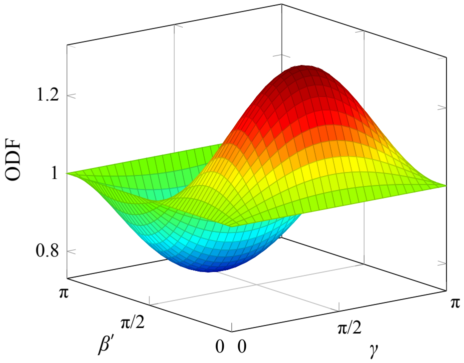

Figure 3.18 Variation of $\Omega(\beta',\gamma)$ (ODF) with polar β' and azimuthal angle γ with distortion strain $\varepsilon_{32} = 0.1$ ($\nu = 0.45$).

3.4.2 Change in the conductive networks and in the tunneling resistance

On the basis of the previously obtained ODFs, the Komori-Makishima model in Eq. (3.39) can be readily applied to determine the influence of arbitrary strain cases on the percolation threshold. Uni-axial dilation and distortion conditions are shown in Fig. 3.19. Fig. 3.19(a) shows the relative variation of the percolation threshold with respect to the unstrained value, f_c^o, for laterally constrained and unconstrained conditions. In both cases, compression/stretching leads to a loss of randomness of the nanofillers orientation distribution and, therefore, lesser probability of forming conductive paths. It is interesting to point out that, when the transverse displacements are constrained, the strain-induced variations of the percolation threshold are smaller that those computed with unconstrained conditions. Finally, it is worth noting that the variations are almost identical under compression ($\varepsilon < 0$)

and tension ($\varepsilon > 0$), the latter yielding slightly lower values. On the other hand, Fig. 3.19(b) shows the relative variation of the percolation threshold under distortion strain ε_{12}. In a similar way, the application of distortion yields losses in the randomness of the fillers orientation distribution and, consequently, increases in the percolation threshold. In this case, both positive and negative distortion strains lead to identical values.

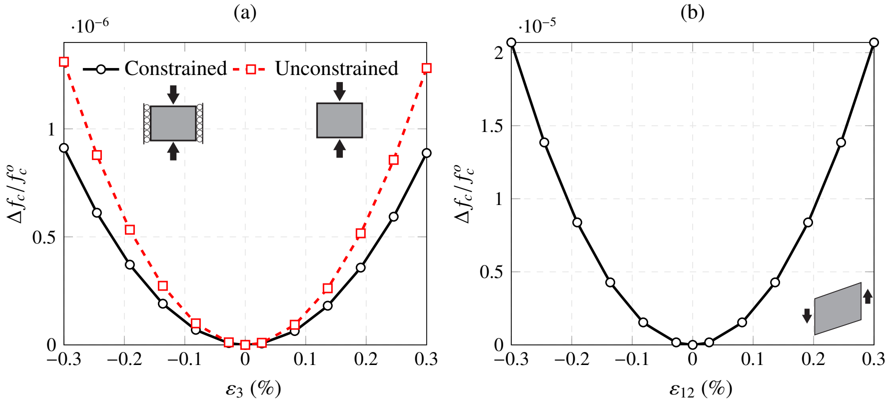

Figure 3.19 Variation of the percolation threshold with respect to the strain level ($\nu = 0.2$) under laterally constrained and unconstrained conditions (a) and distortion (b) assuming $L_{CNT} = 1$ μm, D_{CNT}=10 nm.

Fig. 3.20 depicts the variations of the ratio $\mathcal{X}/\mathcal{X}_o$ with strain, being $\mathcal{X}_o$ and $\mathcal{X}$ the fraction of percolated CNTs (see Eq. (3.16)) before and after the application of strain, respectively. Conditions of laterally constrained and unconstrained uni-axial dilation with different Poisson's ratio are compared along with distortion conditions. Under tensile strains, it is observed that the amount of percolated nanotubes decreases with increasing strain. In this case, the loss of randomness of the fillers and the subsequent higher percolation thresholds, as well as the volume expansion, yield the breakage of electrically conductive paths. However, under compressive strains, these two mechanisms generate opposite effects. Although the percolation threshold increases with higher compressive strains, the increase of the effective filler volume fraction dominates the small range of deformation and, therefore, increasing compressions imply larger numbers of conductive paths. In addition, laterally constrained and unconstrained conditions with different Poisson's ratios are compared. First, it is important to note that the constrained conditions exhibit greater variations in the number of percolated CNTs. As previously shown in Fig. 3.19, the percolation threshold increases more slowly, and also the strain-induced volume expansion has a greater effect in the case of laterally constrained systems. With regard to the effect of the Poisson's ratio for unconstrained systems, it is observed that decreasing the Poisson's ratio leads to higher variations of the number of percolated CNTs. In particular, the limit case of $\nu = 0$ corresponds to the case of a laterally constrained system. In the case of shear strain, both positive and negative distortions generate the breakage of conductive paths. From a mathematical point of view, the variation of the percolation threshold solely contributes to the strain-sensitivity. The re-orientation of the fillers induced by shear strains always generates a loss of randomness of the filler orientation distribution and, thus, strains also cause increasing percolation thresholds and a decreasing number of conductive paths. Finally, Fig. 3.21 plots $\mathcal{X}/\mathcal{X}_o$ versus uni-axial strain with laterally constrained and unconstrained composites with different filler contents. It is noted that the fraction of percolated CNTs is more sensitive to strain for composites with lower CNT volume fraction.

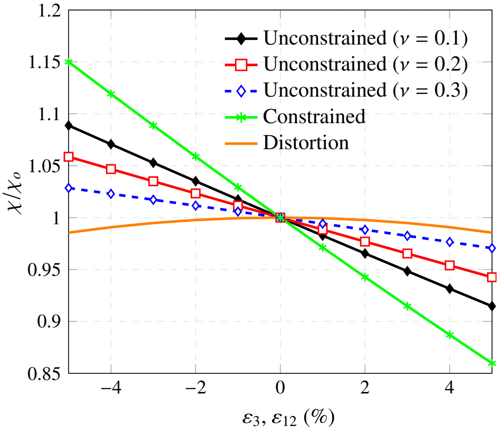

Figure 3.20 Variation of normalized percentage of percolated CNTs (ξ/ξ_o) versus strain for different strain conditions (f_{CNT} = 0.5%, L_{CNT} = 3 µm, D_{CNT}=15 nm).

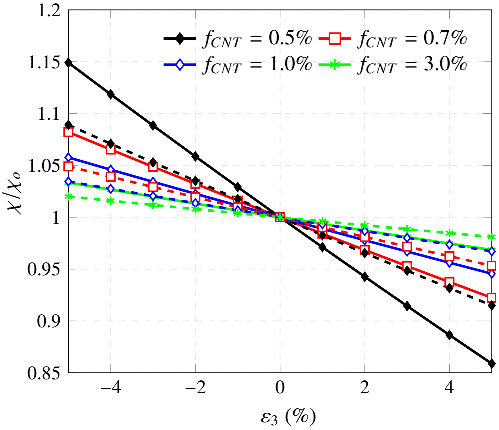

Figure 3.21 Variation of normalized percentage of percolated CNTs (ξ/ξ_o) versus strain for composites with different filler concentration and uni-axial dilation. (L_{CNT} = 3 µm, D_{CNT}=15 nm, ν = 0.2). Solid and dashed lines denote laterally constrained and unconstrained conditions.

With regard to the strain-induced changes in the tunneling resistance, there exists a gap in the literature on the determination of the inter-particle distance and the height of the potential barrier under general 3D strain states. In a simplified manner, the same hypothesis of linear dependence between the inter-particle distance and the height of the potential barrier with the strain in Eqs. (3.40) and (3.41) is assumed for dilation cases. With regard to the distortion cases, the variation of the inter-particle properties is presumably smaller than under dilation and, due to the difficulty in its theoretical determination, it is assumed to be strain-independent.

3.4.3 Steady-State Piezoresistivity analysis

Modeling the piezoresistive behavior of CNT-reinforced smart concretes under arbitrary 3D strain states requires linking the equations related to the electrical behavior of the material with those describing the mechanical strain state, or alternatively the stress state assuming the material to behave as linear elastic. On the basis of the presented micromechanics approach, the electrical resistivity tensor $\boldsymbol{\rho}_{eff}$, which can be directly computed as the inverse of the conductivity tensor $\boldsymbol{\sigma}_{eff}$ in Eq. (3.17), i.e. $\boldsymbol{\rho}_{eff} = \boldsymbol{\sigma}_{eff}^{-1}$, relates the current intensity vector, $\mathbf{J}$, to the electric field vector, $\mathbf{E}$, as $\mathbf{E} = \boldsymbol{\rho}_{eff}\mathbf{J}$. This relation can be written in matrix notation as:

$$\begin{Bmatrix} E_1 \\ E_2 \\ E_3 \end{Bmatrix} = \begin{bmatrix} \rho_1 & \rho_6 & \rho_5 \\ \rho_6 & \rho_2 & \rho_4 \\ \rho_5 & \rho_4 & \rho_3 \end{bmatrix} \begin{Bmatrix} J_1 \\ J_2 \\ J_3 \end{Bmatrix} \tag{3.52}$$

When the composite is not subjected to any strain, the assumption of randomly oriented fillers leads to diagonal resistivity matrices with equal components ρ_0, i.e. $\rho_1 = \rho_2 = \rho_3 = \rho_0$ and $\rho_4 = \rho_5 = \rho_6 = 0$. After the application of strain, each component of the resistivity matrix changes. In general, the new components of the resistivity tensor can be written as follows:

$$\begin{Bmatrix} \rho_1 \\ \rho_2 \\ \rho_3 \\ \rho_4 \\ \rho_5 \\ \rho_6 \end{Bmatrix} = \begin{Bmatrix} \rho_0 \\ \rho_0 \\ \rho_0 \\ 0 \\ 0 \\ 0 \end{Bmatrix} + \begin{Bmatrix} \Delta\rho_1 \\ \Delta\rho_2 \\ \Delta\rho_3 \\ \Delta\rho_4 \\ \Delta\rho_5 \\ \Delta\rho_6 \end{Bmatrix} \tag{3.53}$$

which can be related to the strain in the composite through:

$$\boldsymbol{\rho}_{eff} = \boldsymbol{\rho}_{eff}^{o}(\mathbf{I} + \mathbf{r}) \tag{3.54}$$

where $\boldsymbol{\rho}_{eff}^{o} = (\boldsymbol{\sigma}_{eff}^{o})^{-1}$ is the resistivity matrix of the unloaded composite and $\mathbf{r}$ is the relative change in resistivity defined as $\mathbf{r} = \boldsymbol{\Pi}\boldsymbol{\varepsilon}$. The connection between the relative change in resistivity and the strain tensor is the $\boldsymbol{\Pi}$ matrix whose components Π_{ijkl} are denoted in Voigt notation as λ_{ij}. It is hypothesized that CNT-reinforced composites possess cubic crystal symmetry, in a similar way to silicon [149], and only three $\lambda-$coefficients are needed. Hence, $\mathbf{r} = \boldsymbol{\Pi}\boldsymbol{\varepsilon}$ in matrix notation becomes:

$$\begin{Bmatrix} \Delta\rho_1/\rho_0 \\ \Delta\rho_2/\rho_0 \\ \Delta\rho_3/\rho_0 \\ \Delta\rho_4/\rho_0 \\ \Delta\rho_5/\rho_0 \\ \Delta\rho_6/\rho_0 \end{Bmatrix} = \begin{bmatrix} \lambda_{11} & \lambda_{12} & \lambda_{12} & 0 & 0 & 0 \\ \lambda_{12} & \lambda_{11} & \lambda_{12} & 0 & 0 & 0 \\ \lambda_{12} & \lambda_{12} & \lambda_{11} & 0 & 0 & 0 \\ 0 & 0 & 0 & \lambda_{44} & 0 & 0 \\ 0 & 0 & 0 & 0 & \lambda_{44} & 0 \\ 0 & 0 & 0 & 0 & 0 & \lambda_{44} \end{bmatrix} \begin{Bmatrix} \varepsilon_1 \\ \varepsilon_2 \\ \varepsilon_3 \\ 2\varepsilon_{23} \\ 2\varepsilon_{13} \\ 2\varepsilon_{12} \end{Bmatrix} \tag{3.55}$$

Discussion on the correctness of this assumption is provided in subsequent parametric analyses. Among the three independent λ–coefficients in Eq. (3.55), λ_{11} depicts the piezoresistive effect along one principal crystal axis for strains applied in this principal crystal axis (longitudinal piezoresistive effect), λ_{12} relates the piezoresistive effect along one principal crystal axis for strains applied in one perpendicular crystal axis (transverse piezoresistive effect), and λ_{44} describes the piezoresistive effect on an out-of-plane electric field by the change of the in-plane current induced by in-plane shear stress. In order to compute the independent coefficients in $\boldsymbol{\Pi}$, only two virtual experiments are needed, namely laterally constrained uni-axial dilation and distortion as follows:

$$\text{Dilation:} \quad \begin{Bmatrix} \Delta\rho_1/\rho_0 \\ \Delta\rho_2/\rho_0 \\ \Delta\rho_3/\rho_0 \end{Bmatrix} = \begin{bmatrix} \lambda_{11} & \lambda_{12} & \lambda_{12} \\ \lambda_{12} & \lambda_{11} & \lambda_{12} \\ \lambda_{12} & \lambda_{12} & \lambda_{11} \end{bmatrix} \begin{Bmatrix} 0 \\ 0 \\ \varepsilon_3 \end{Bmatrix} = \boldsymbol{\Pi}^{dil} \begin{Bmatrix} 0 \\ 0 \\ \varepsilon_3 \end{Bmatrix} \tag{3.56}$$

$$\text{Distortion:} \quad \begin{Bmatrix} \Delta\rho_4/\rho_0 \\ \Delta\rho_5/\rho_0 \\ \Delta\rho_6/\rho_0 \end{Bmatrix} = \begin{bmatrix} \lambda_{44} & 0 & 0 \\ 0 & \lambda_{44} & 0 \\ 0 & 0 & \lambda_{44} \end{bmatrix} \begin{Bmatrix} 0 \\ 0 \\ 2\varepsilon_{12} \end{Bmatrix} = \boldsymbol{\Pi}^{dis} \begin{Bmatrix} 0 \\ 0 \\ 2\varepsilon_{12} \end{Bmatrix} \tag{3.57}$$

3.5 Results and discussion

3.5.1 Experimental characterization campaign

In order to validate the analytical models developed in the current work, the modeling results have been compared to the experimental data carried out in the specimens made of composite cement paste (PA), mortar (MO) and concrete (CO) doped with MWCNTs. Multi-walled carbon nanotubes type Graphistrength C100 from Arkema have been used as conductive nanoinclusions in the cementitious matrices. Table 3.1 reports the main physical, chemical and mechanical properties of the MWCNTs utilized for the fabrication of the composites. Cement paste, mortar and concrete samples have been realized adding different quantities of MWCNTs, namely 0, 0.25, 0.5, 0.75, 1.0 and 1.5% with respect to the weight of cement. Table 3.2 summarizes the mix design of all the cementitious materials. Two different dispersant concentrations have been used, namely 1:1 and 10:1 with respect to the mass of the carbon nanotube fillers. The cement is pozzolanic, type 42.5. Sand and gravel had nominal dimensions between 0-4 mm and 4-8 mm, respectively. A plasticizer has been added to obtain similar workability for all the admixtures, with the same water/cement ratio of 0.45.

The cementitious samples are cube-shaped, with sides of 51 mm and five embedded stainless steel electrodes placed at a mutual distance of 10 mm. The electrodes are nets made of 0.5 mm diameter wires and mesh of 6 mm. In the case of concrete samples, the embedded part was modified, cutting alternatively the vertical wires, resulting in a final mutual distance of 12 mm. Figures 3.22 (a) and 3.22 (b) report the geometry of the specimens and of the electrodes, together with the picture of a cured sample. Figure 3.22 (c) shows the setup of the experimental electrical tests carried out between two next electrodes at a distance of 10 mm, by use of a high precision LCR meter, model HM8018 [62].

Table 3.1 Main characteristics of MWCNTs used in the experiments (from Ref. [210]).

Property	Value	Property	Value
Mean agglomerate size	200-500 μm	Apparent density	50-150 kg/m^3
Mean number of walls	5-15 μm	Weight loss at 105 °C	<1%
Outer mean diameter	10-15 nm	Thermal Conductivity	>3000 W/(mK)
Length	0.1-10 μm	Electric Conductivity	up to 10^7 (Ωm)$^{-1}$
Carbon content	>90% in weight	Young Modulus	>1 TPa
Surface area	100-250 m$^2/g$	Tensile strength	About 150 GPa

Table 3.2 Mix designs of cementitious samples with six different concentrations of MWCNTs (the ratio ν between the mass of MWCNTs and cement varies from 0 to 1.5%). C_{0i} and C_i are the masses of cement in normal materials and with MWCNTs, respectively. ΔV_p, ΔV_m and ΔV_c are the total volumes of MWCNTs plus dispersant for paste, mortar and concrete nanomaterials, respectively, while η is the ratio between dispersant and MWCNTs, equal to 1 or to 10 [62].

Components	Paste kg/m^3		Mortar kg/m^3		Concrete kg/m^3	
	Normal	With MWCNTs	Normal	With MWCNTs	Normal	With MWCNTs
Cement 42.5N	C_{0p}=1277	$C_p=C_{0p}\,\frac{1\text{m}^3}{1\text{m}^3+\Delta V_p}$	C_{0m}=654	$C_m=C_{0m}\,\frac{1\text{m}^3}{1\text{m}^3+\Delta V_m}$	C_{0c}=524	$C_c=C_{0c}\,\frac{1\text{m}^3}{1\text{m}^3+\Delta V_c}$
Water	W_{0p}=574	0.45C_p	W_{0m}=294	0.45C_m	W_{0c}=234	0.45C_c
MWCNTs	-	νC_p	-	νC_m	-	νC_c
Dispersant	-	$\eta\nu C_p$	-	$\eta\nu C_m$	-	$\eta\nu C_c$
Sand	-	-	1308	2C_m	951	1.81C_c
Gravel	-	-	-	-	638	1.22C_c
Plasticizer	-	Var	-	Var	2.62	Var
W/C ratio	0.45	0.45	0.45	0.45	0.45	0.45

Figure 3.23 sketches the preparation procedure for the paste, mortar and concrete samples with MWCNTs. In the first step the carbon nanotubes were added to the water solution with the surfactant through a preliminary mixing (Fig. 3.23 (a) and 3.23 (b)) and then were dispersed by use of a sonicator (Fig. 3.23 (c)) or a mechanical stirrer (Fig. 3.23 (c1)). After that, the obtained nano-modified suspension and the plasticizer were added to the cement and mixed (Fig. 3.23 (d)). The mixes were poured into oiled molds for curing, and the electrodes were embedded (Fig. 3.23 (e)). After a few days, the samples were unmolded to complete the curing in controlled laboratory conditions (Fig. 3.23 (f)). The dispersion and the morphology of MWCNTs in both water suspensions and cementitious materials were analyzed by use of SEM micrographs (Fig. 3.23 (c1) and 3.23 (f1)). SEM inspections have demonstrated that the MWCNTs dispersed in cementitious hardened matrices (paste,

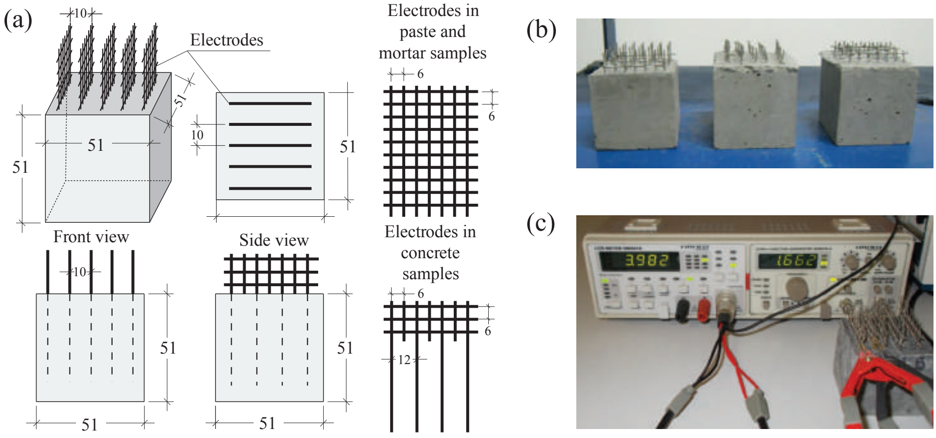

Figure 3.22 Geometry and dimensions of the cementitious samples and of the electrodes (a), picture of some samples with the embedded electrodes (b), and setup of the experimental electrical tests (c) (units in mm).

mortar and concrete) show wavy shapes similar to the ones observed after their dispersion in water solutions (Fig. 3.24). Fig. 3.25 shows the good dispersion obtained in the water suspensions after sonication (Fig. 3.25 (a)) and in a hardened mortar matrix after curing (Fig. 3.25 (b)).

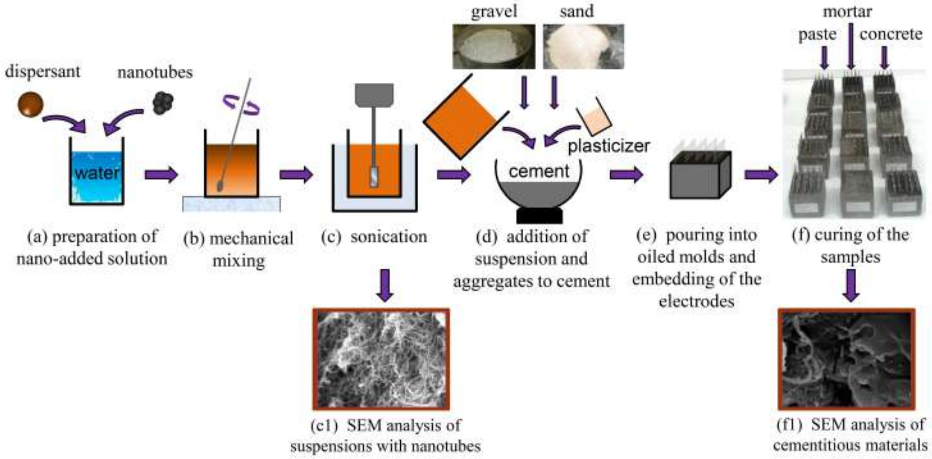

Figure 3.23 Preparation procedure of paste, mortar and concrete samples with MWCNTs.

The strain sensing capabilities of the cementitious composites were investigated subjected the samples to cyclic axial compression loads with increasing loads (Fig. 3.26 (a)), by use of a servo-controlled pneumatic universal testing machine of 14kN load capacity, model IPC Global UTM14P. Fig. 3.26 (b) is a detailed view of a samples during the setup

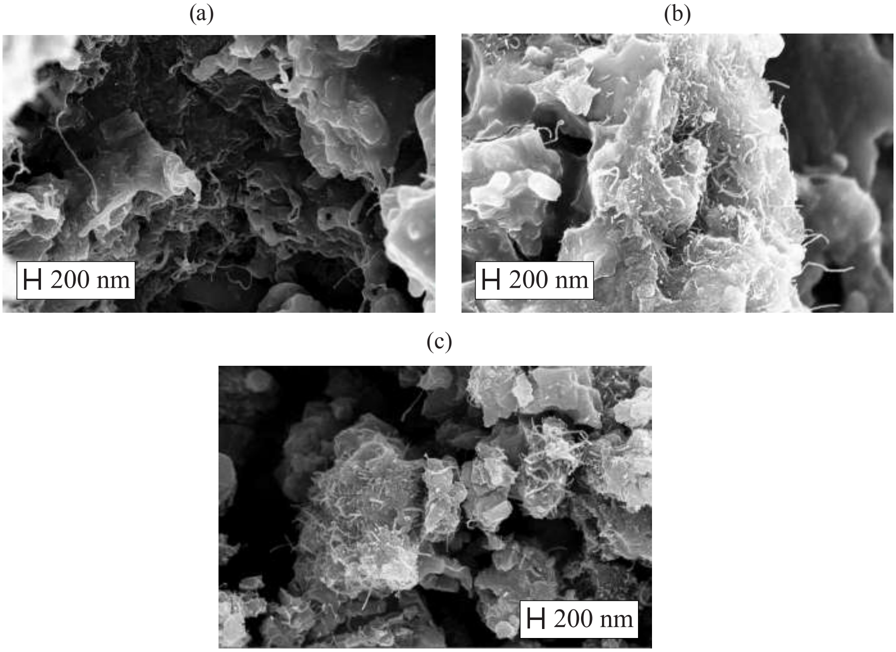

Figure 3.24 SEM pictures of MWCNTs dispersed using the SLS dispersant and sonicated with the SLS dispersant in the 1:1 (a) and 10:1 (b) amounts, and mechanically mixed using the SLS dispersant in the 10:1 amount (c).

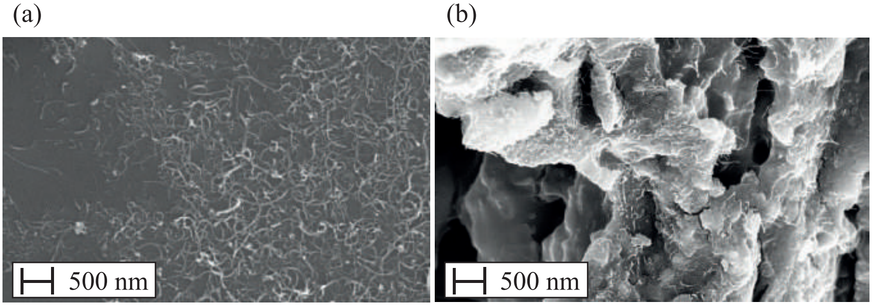

Figure 3.25 SEM pictures of MWCNTs dispersed in water solution (a) and in a mortar matrix (b).

of the mechanical tests. The strain sensing properties were investigated by measuring the current passing through two electrodes placed at a distance of 10 mm under the application of a stabilized voltage of 2.5 V. The source measure unit and the high speed digital multimeter were model NI PXI4130 and NI PXI4071 devices, respectively. Two electrical strain gauges 2 cm long, with a nominal resistance of 120 Ω and a gauge factor of about 2 were also attached at opposite faces of the specimens and acquired using a data acquisition card, model NI PXIe-4330. Strain-induced incremental variation in electrical resistance of the composites, $\Delta R(t)$, was obtained by dividing the applied voltage, V, by the incremental variation in measured current intensity, $\Delta I(t)$. Under the assumption of small strains, the correlation between the relative change in resistance, $\Delta R/R_o$, and the applied compressive strain, ε, can be modeled likewise conventional strain gauges as:

$$\frac{\Delta R}{R_o} = \lambda^{-}\varepsilon, \quad \varepsilon < 0 \tag{3.58}$$

where λ^{-} is the so-called gauge factor. Although only compression tests were carried out, the presented approach also allows to model tensile stresses. As further discussed in the next section, the piezoresistive behavior of CNT-reinforced composites is slightly different under compressive and tensile stresses. Hence, superscripts "–" and "+" are used for gauge factors in the case of compressive ($\varepsilon < 0$) and tensile ($\varepsilon > 0$) strains, respectively.

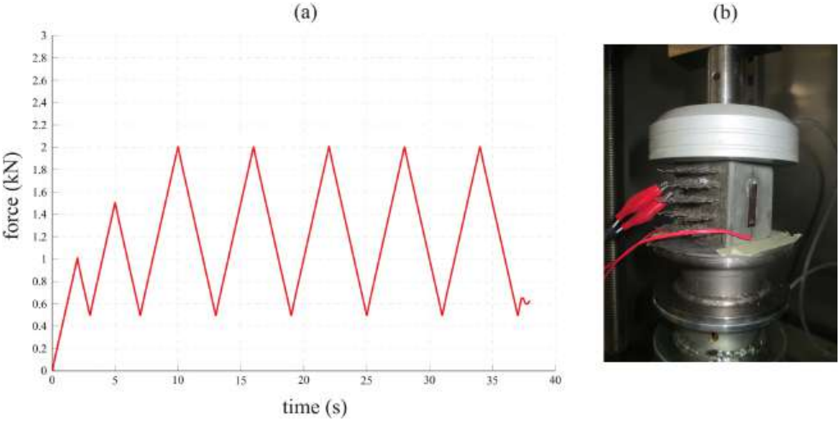

Figure 3.26 Applied compression load (a) and uniaxial testing setup (b).

3.5.2 Conductivity of CNT-reinforced cement-matrix composites

3.5.2.1 Introduction

In this section, the proposed analytical model is tested against experimental data from MWCNT-reinforced cement paste, mortar and concrete experimental specimens. Moreover, the influence of the different variables affecting the overall electrical conductivity is also examined. In our calculations, the electrical conductivities of the three different matrices have been selected as 2.8×10^{-3} S/m, 1.04×10^{-3} S/m and 2.92×10^{-4} S/m, for cement paste (PA), cement mortar (MO) and concrete (CO), respectively [230, 189]. In order to compare the theoretical and experimental results, it must be taken into account the resistivity of the electrodes and the contact resistance [121]. Hence, an equivalent in series circuit with conductivity σ_{spc} has been defined, in which the resistivity of the electrodes and the contact resistance have been computed so that the initial plain configuration conductivity (f_{CNT}=0) is fitted. Having regard to the commercial specifications of MWCNTs (Table. 3.1), the electrical conductivity of MWCNTs has been set in the range 10^{0}-10^{7} S/m. The values of the constants used in the Simmon's model for the evaluation of the interphase conductivity in Eq. (3.2) are given in Table 3.3. For practical convenience, the concentration f_{CNT}

of carbon nanotubes is usually expressed in the literature in terms of mass fraction with respect to the mass of cement, w_{cem}, as follows:

$$w_{CNT} = \frac{\rho^{CNT}}{w_{cem}} f_{CNT} \tag{3.59}$$

with ρ^{CNT} being the density of the carbon nanotubes, taken as 150 kg/m^3, and w_{cem} the weight of cement per unit (m^3) of composite as given in Table. 3.2.

Table 3.3 Physical constants used in Simmon's model.

Mass of electron m	9.10938291×10^{-31} kg
Electric charge of an electron e	$-1.602176565\times10^{-19}$ C
Reduced Planck's constant $\hbar$	6.626068×10^{-34} m^{2}kg/s

3.5.2.2 Numerical results

Effects of constituents properties Firstly, the effects of the CNT diameter and length on the overall electrical conductivity of MWCNT-cement paste nanocomposites are shown in Figs. 3.27 (a) and (b), respectively. It can be observed that both quantities have a significant effect on the percolating phase, while a moderate effect is found after percolation. The overall electrical conductivity increases with the increase in MWCNT length or the decrease in MWCNT diameter. This behavior is attributed to the greater likelihood of forming conductive networks of fibers with larger aspect ratio. Furthermore, it is observed that a reduction of the CNT length results in an increase in the percolation threshold, while a reduction of the CNT diameter produces the opposite effect. It can be concluded from these results that the electrical conductivity of MWCNT-cement based specimens can be enhanced with the addition of carbon nanotubes with higher aspect ratio.

In Fig. 3.28, it is shown the electrical conductivity of MWCNT-cement nanocomposites for different matrix materials, namely cement paste, mortar and concrete. It can be seen that, for every MWCNT concentration, the cement paste composites exhibit the highest values of conductivity whereas the concrete composites are the least conductive, circumstance that matches well the experimental experience. A key aspect of the electrical behavior of cement-based carbon nanotube composites is the uniformity of the dispersion of the nanoinclusions. As discussed above, different types of dispersants were employed for this purpose during the experimental campaign. It has been reported in the literature that dispersants create a partially isolating coating on the carbon nanotubes which can even inhibit the contact between the fibers [339]. This effect can be interpreted as an increment in the height of the tunneling potential barrier V_o and, therefore, a reduction of the electron hopping contribution. Fig. 3.29 shows the electrical conductivity of MWCNT-cement paste nanocomposites with different values of V_o. It is evidenced in this figure that the potential barrier height V_o has substantial effect on the overall electrical conductivity of the composite before percolation. Higher values of V_o lead to higher percolation thresholds, while limited differences are found after percolation. It can be extracted from this analysis that the employment of dispersant delays the percolation process, exhibiting more acute effects for MWCNTs concentration below percolation threshold.

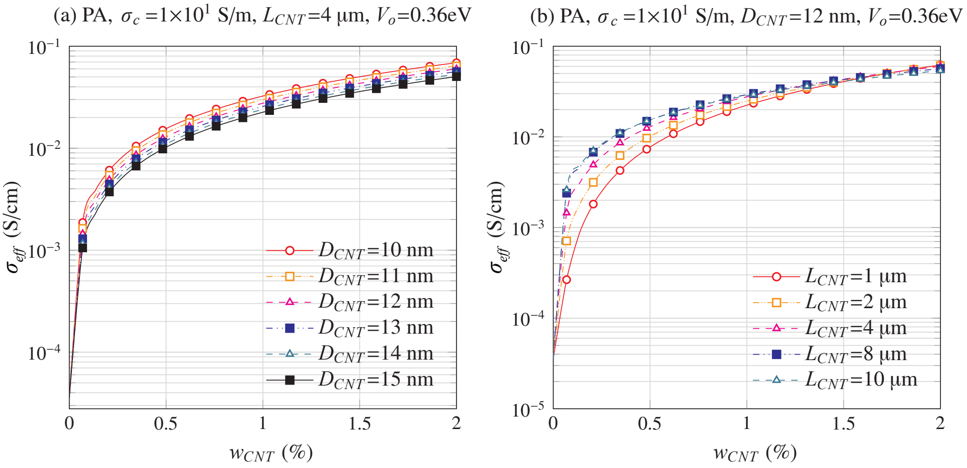

Figure 3.27 Effect of MWCNTs diameter (a) and length (b) on the electrical conductivity of MWCNT-cement paste nanocomposites.

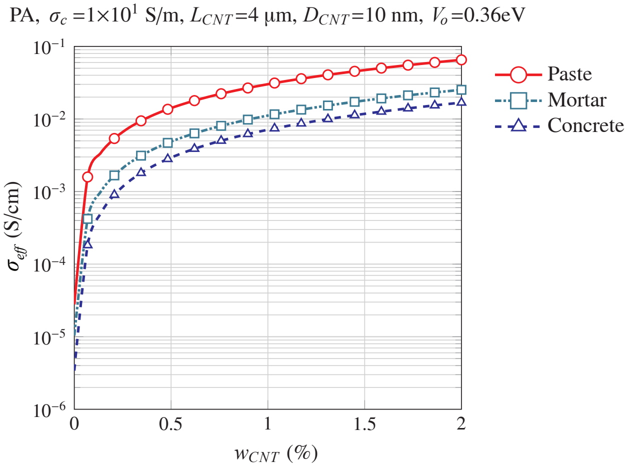

Figure 3.28 Electrical conductivity of MWCNT nanocomposites with different matrix materials: cement paste, mortar and concrete.

Fig. 3.30 (a) demonstrates the effects of MWCNTs electrical conductivity σ_c on the overall conductivity of MWCNT cement paste nanocomposites. The analytical results obtained without considering the contribution of the conductive networks mechanism (CN) is also represented for illustrative purposes. It can be seen that, for low MWCNT concentrations before percolation, little differences are found among the modeling results with and without conductive networking mechanism. Nevertheless, once the percolation threshold is reached, the conductive networking mechanism becomes dominant and, therefore, big differences appear between these two models. The predicted results are also

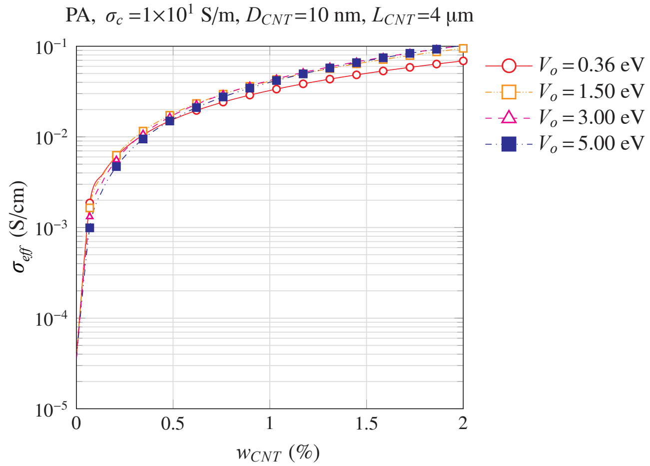

Figure 3.29 Effect of the electric potential barrier V_o on the electrical conductivity of MWCNT-cement paste nanocomposites.

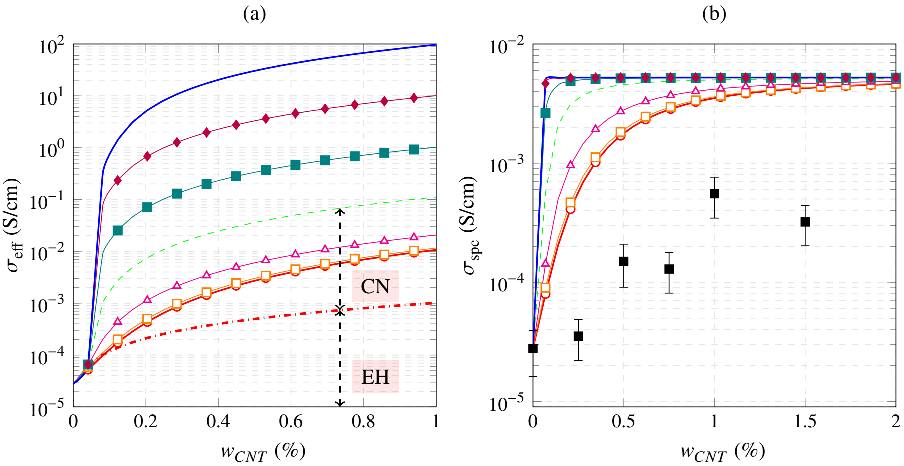

Figure 3.30 Effect of MWCNTs electrical conductivity σ_c on the effective conductivity of MWCNT-cement paste nanocomposites (a), and comparison with experimental data (b) (PA-SO-N‰-6-1:1; V_o=1.5eV; L_{CNT} = 1 µm; D_{CNT} = 15 nm; —○— σ_c=1e-2 S/cm; —□— σ_c=1e-1 S/cm; —△— σ_c=1e+0 S/cm; - - - σ_c=1e+1 S/cm; —■— σ_c=1e+2 S/cm; —◆— σ_c=1e+3 S/cm; —— σ_c=1e+4 S/cm; -·-· σ_c=1e+1 S/cm (No conductive networks); ■ experimental data; the error bars denote ± standard deviation intervals, with standard deviations computed by varying the electrodes).

compared to the experimental data in Fig. 3.30 (b). In this first comparison, large differences are found among the experimental and theoretical results. The analytical estimations of the overall electrical conductivity are noticeably larger than the measurements carried out in the specimens. Furthermore, it can also be noticed that the percolation process predicted by the micromechanics modeling takes place before what is registered in the experimental specimens. The origin of these discrepancies may be attributed to waviness and agglomeration effects as it is shown in the following analyses.

Effects of MWCNTs waviness In this section, the effect of MWCNTs waviness is investigated. The comparison analysis of Fig. 3.30 (b) is here updated for the case of σ_c=1e+0 S/cm with four wavy geometries, corresponding to helical angles of 90°, 80°, 60° and 30°. It can be seen in Fig. 3.31 that the main effect of non-straightness of the fibers is a delay of the percolation process. This effect is attributed to the reduction of the length from wavy to equivalent straight fiber, what leads to an increment of the percolation threshold. However, the electrical conductivity predicted by the micromechanics modeling is still larger than the experimental data. This difference may be due to imperfections associated with a non-uniform nanoinclusions distribution, that is to say, agglomeration.

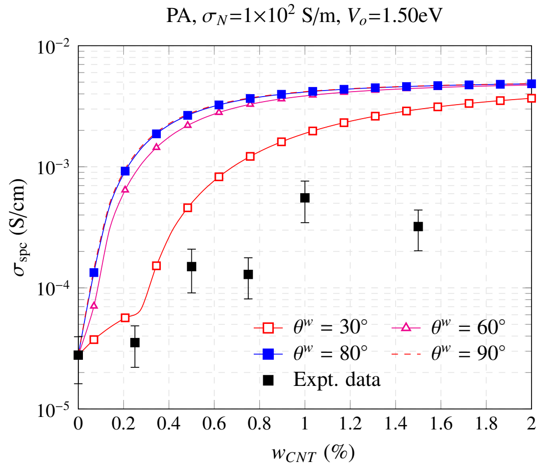

Figure 3.31 Effect of the MWCNT waviness on the electrical conductivity of the MWCNT cement paste nanocomposite (PA-SO-N%-6-1:1); the error bars denote ± standard deviation intervals, with standard deviations computed by varying the electrodes (L_{CNT} = 1 μm, D_{CNT} = 15 nm).

Effects of MWCNTs agglomeration The effect of MWCNTs agglomeration in spherical bundles on the conductivity of cement-based composites has been also analyzed. In Figs. 3.32 (a) and (b), it is shown the overall conductivity for different agglomeration parameters ξ and ζ, respectively. It is extracted from this analysis that the CNT distribution has a strong influence on the overall conductivity of the composite. In Fig. 3.32 (a), the volume fraction of MWCNTs within the bundles is set at 90% ($\zeta = 0.9$), whereas the ratio between the volume of the bundles and the total volume of the RVE varies from 10 to 90%. It can be noticed that the percolation process takes place sequentially within and outside the bundles. At the contrary, in Fig. 3.32 (b), the volume fraction of the bundles is set at

40% and the ratio of MWCNTs concentration within them ranges from 40 to 90%. The higher is the concentration of MWCNTs within the clusters, the lesser is the nanoinclusions uniformity and, thus, the lesser is the overall conductivity of the composite.

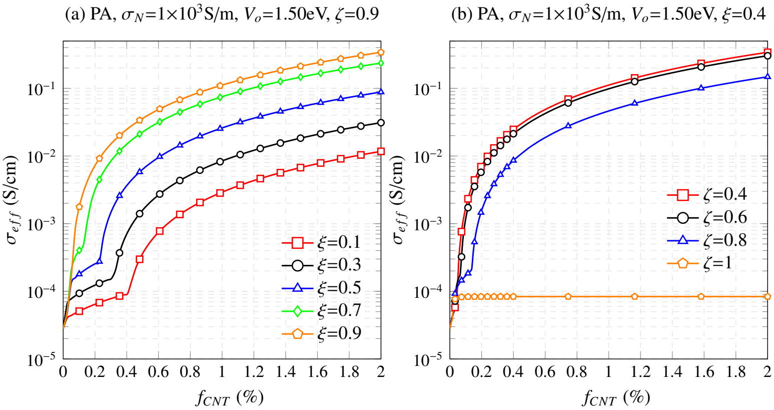

Figure 3.32 Effect of the MWCNTs agglomeration on the electrical conductivity of the MWCNT cement paste nanocomposite (a_1/a_3 = 1, L_{CNT} = 1 µm, D_{CNT}=15 nm).

Comparison analyses with cement-based specimens In light of the previous studies, the combination of waviness and agglomeration can give an explanation to the discrepancies with the experimental data observed in the first comparison analyses. Hereafter, the proposed micromechanics approach with consideration of waviness and clustering effects is compared to the experimental results, including cement paste, mortar and concrete composites. Fig. 3.33 shows the comparison between the modeling results and the experimental data for different matrix materials and manufacturing processes. The waviness of the MWCNTs has been defined with a spiral angle of 50° in all cases except for sonicated specimens with high dispersant concentrations (10:1). It is found that the analytical results agree well with the experimental data when the CNT electrical conductivity are set between 1E+2 S/m and 1E+3 S/m. It can be seen that generally the addition of larger dispersant concentrations can be simulated with larger agglomeration parameters. Furthermore, the incorporation of dispersant acts as a partially isolating coating on the surface of the nanotubes, what has been simulated by an increment of the potential barrier V_o. In particular values of 1.5 and 3 eV have been taken for the cases of low (1:1) and high dispersant (10:1) concentration, respectively. The influence of the manufacturing process, sonication (SO) or mechanical (ME), has been taken into account via different agglomeration parameters, generally stricter in the case of mechanical mixing. It is noticeable the cases of cement paste and mortar specimens in which the dispersant has a special effect on the uniformity of the composite. In these cases, the absence of gravel reduces the advantages of sonication with respect to mechanical mixing, leading to more uniform dispersions of nanotubes with mechanical mixing and high dispersant concentration than with sonication and low dispersant concentrations.

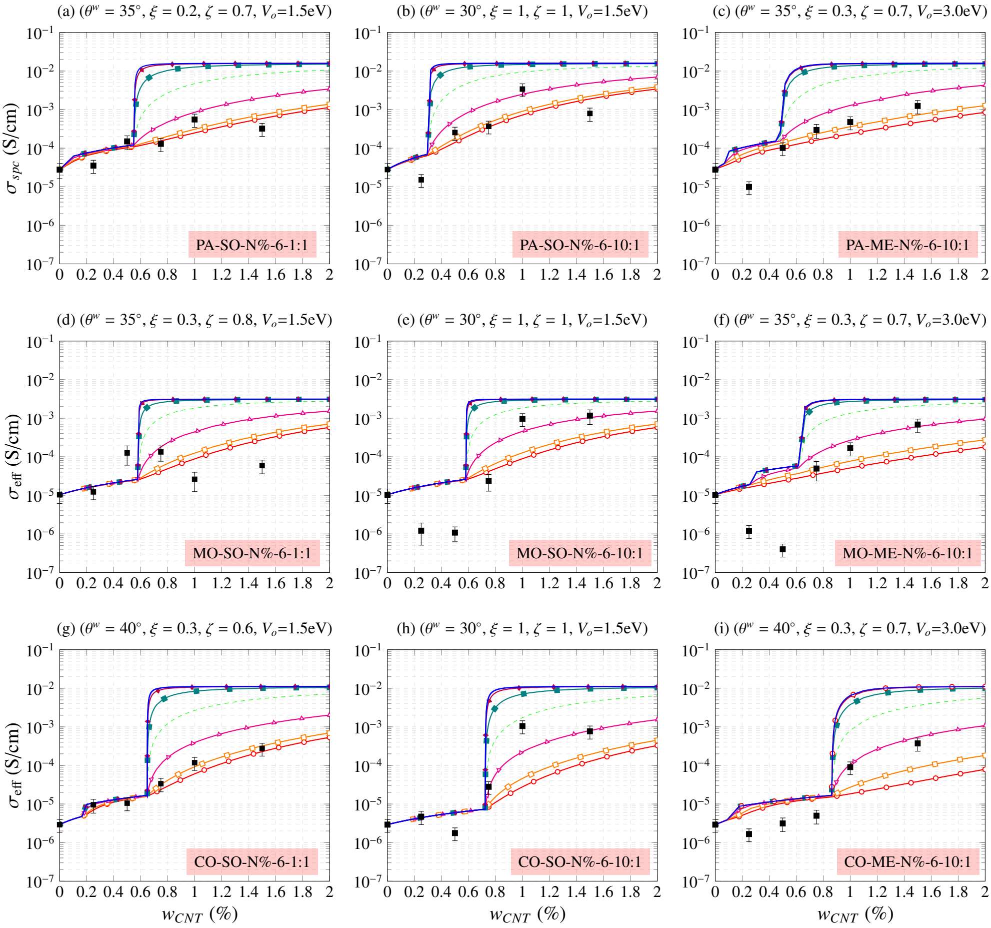

Figure 3.33 Comparison between modeling results and experimental data: composite pastes (a,b,c); composite mortars (d, e, f); composite concretes (g, h, i). (—○— σ_c=1E+0 S/m; —□— σ_c=1E+1 S/m; —△— σ_c=1E+2 S/m; - - - σ_c=1E+3 S/m; —■— σ_c=1E+4 S/m; —◆— σ_c=1E+5 S/m; —— σ_c=1E+6 S/m; ■ experimental data; the error bars denote ± standard deviation intervals, with standard deviations computed by varying the electrodes; L_{CNT} = 1 µm; D_{CNT} = 15 nm).

The experimental results also reveal abrupt decreases in the electrical conductivity with respect to the plain material for specimens with high dispersant concentration and low MWCNTs content (see, e.g., Figs. 3.33 (e) and (f)). This phenomenon may be caused by the formation of a partially isolating coating on the surface of the nanotubes induced by the dispersants. This isolating coating has been also reported in the literature [339] in terms of the formation of surfactant-induced electromechanical double-layers (polarization resistance), what may make the nanotubes behave as non-conductive fibers when their separation distances are large. However, as the content of nanotubes increases, the separation distance decreases and this effect is canceled. In the present work, attempts have been made to simulate this effect by means of reductions of the conductivity of the equivalent solid cylinders at low MWCNT concentrations. Nonetheless, this approach was insufficient to reproduce these falls of the electrical conductivity. Hence, it is hypothesized that the employment of high concentrations of dispersants at low MWCNT concentrations, does not only isolate the nanoinclusions but may also increase the resistivity of the matrix and the contact resistance. Further research is needed on this issue in order to count on more accurate models of MWCNT cement-based materials with high dispersant concentration doped with low MWCNTs contents.

Sensitivity analyses In order to assess the propagation of potential statistical randomness in the overall electrical conductivity of MWCNT cement-based composites, an input sensitivity analysis is presented. In particular, the sensitivity of the effective electrical conductivity of two different MWCNT concentrations has been analyzed, namely w_{CNT}=0.8% and 1.5%, as shown in Figs. 3.34 and 3.35, respectively. The input variables have been categorized into constituents properties $\{L_{CNT}, D_{CNT}, \sigma_m, \sigma_c\}$, waviness $\{\theta^w\}$ and agglomeration $\{\xi, \zeta\}$. Defining an independent input variation of 20% with respect to the initial value, the sensitivity coefficient S_σ with respect to an input variable x can be computed as follows:

$$S_\sigma(\%) = 100 \frac{\Delta\sigma_{eff}}{\Delta x} \frac{x}{\sigma_{eff}} \tag{3.60}$$

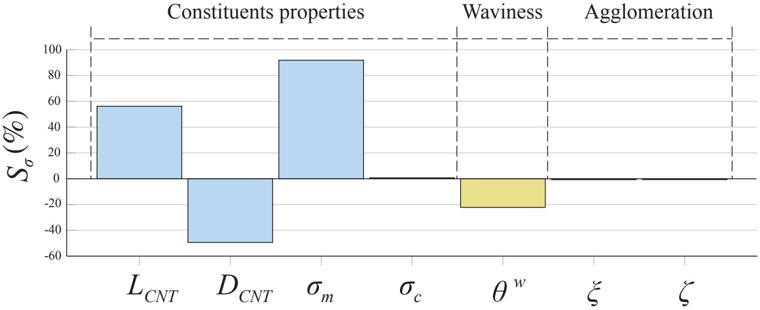

Figure 3.34 Sensitivity analysis of the overall electrical conductivity of MWCNTs cement paste nanocomposites with respect to the variation of the main variables associated with constituents properties, waviness and agglomeration (w_{CNT}=0.8%, σ_c=1E+4 S/m, L_{CNT} = 2 μm, D_{CNT} = 10 nm, V_o=0.36 eV, θ^w = 90°, ξ = 0.4, ζ = 0.4).

The first study (Fig. 3.34) represents the sensitivity analysis of a MWCNT content close to the percolation threshold. In this case, it is observed that the most influential variable is the conductivity of the matrix. A significant effect of the fiber aspect ratio, i.e. length and diameter, is also found as well as a considerable contribution of the helical waviness. It is also noticeable the limited influence of the agglomeration parameters and an almost null sensitivity due to variation of the conductivity of the nanotubes. Likewise, the

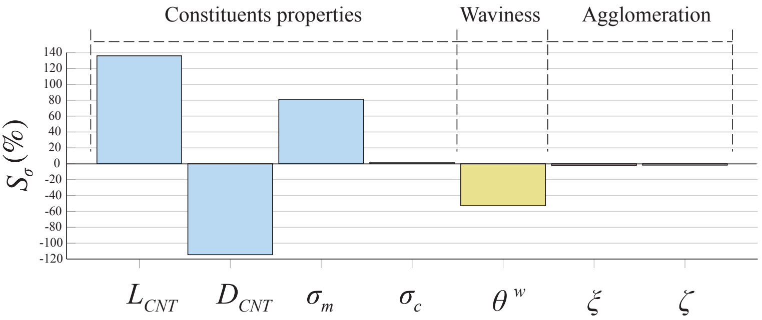

Figure 3.35 Sensitivity analysis of the overall electrical conductivity of MWCNTs cement paste nanocomposites with respect to the variation of the main variables associated with constituents properties, waviness and agglomeration (w_{CNT}=1.5%, σ_c=1E+4 S/m, L_{CNT} = 2 μm, D_{CNT} = 10 nm, V_o=0.36 eV, θ^w = 90°, ξ = 0.4, ζ = 0.4).

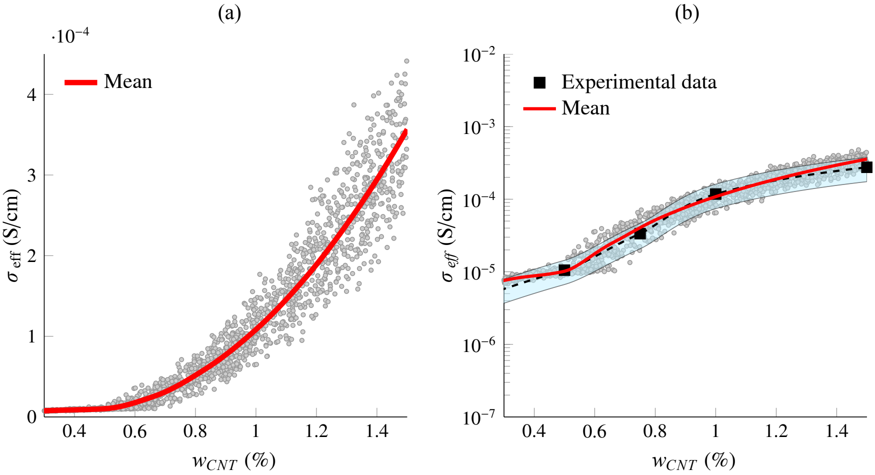

Figure 3.36 Scatter plot of the overall electrical conductivity of MWCNTs cement paste nanocomposites for random simultaneous variation of 5% with respect to the mean value of the parameters $\left\{L, D, \sigma_m, \theta^w\right\}$; (a) analytic overall electrical conductivity in linear scale, (b) Comparison between the analytical results and the max/min experimental band data in logarithmic scale (CO-SO-N%-6-1:1, σ_c=1E+1 S/m, $\overline{L}_{CNT}$ = 1 μm, $\overline{D}_{CNT}$ = 15 nm, V_o=1.5 eV, $\overline{\theta^w}$ = 40°, ξ = 0.14, ζ=0.42).

second case (Fig. 3.35) analyzes the sensitivity of the overall conductivity with a MWCNT content far from the percolation threshold. It is noticed here that the aspect ratio of the MWCNTs becomes predominant. Moreover, once some conductive paths are formed, the conductivity of the matrix loses relevance and, conversely, the waviness gains importance.

In the light of these last results, the comparison between the analytical and experimental data has been updated treating the main variables as random, namely $\{L_{CNT}, D_{CNT}, \sigma_m, \theta^w\}$, and neglecting the variation of the conductivity of the nanotubes σ_c and the agglomeration parameters, ξ and ζ. A random variation of 5% has been considered for all the variables with respect to their mean value. Fig. 3.36 (a) represents a scatter plot of the overall electrical conductivity of concrete with low dispersant concentration with respect to the MWCNT concentration. This result remarks a stronger influence of the variation of the variables on the overall conductivity for filler concentrations above the percolation threshold, where the dispersion of the results is higher. In Fig. 3.36 (b), these results are compared to the experimental data. The max/min band of the experimental data is also represented. It can be noticed that most of the analytical results lie within the experimental band, what demonstrates a further validation of the proposed approach and the feasibility of developing further stochastic analyses in future works.

3.5.2.3 Conclusions

This subsection has presented a micromechanics model to predict the overall conductivity of CNT cement-based nanocomposites with the consideration of waviness and non-uniform spatial distributions of nanoinclusions. The two mechanisms that contribute to the conductivity of CNT composites, namely electron hopping and conductive networks, have been contemplated in the mixed micromechanics framework. The electron hopping mechanism, corresponding to a quantum tunneling phenomenon, has been simulated through a conductive interphase surrounding the nanotubes, whereas the conductive networking mechanism has been modeled by means of changes in the aspect ratios of fibers. Moreover, a helical waviness model and a two-parameter agglomeration approach have been proposed, for the first time, on the basis of SEM inspections.

In order to count on an experimental basis to use as benchmark to validate the analytical model, several nanocomposite cement-based specimens have been manufactured and tested. In particular, specimens of cement pastes, mortars and concretes with different concentrations of MWCNTs have been prepared using three specific preparation techniques. The first one consists of using a high amount of dispersant and mechanical mixing. The two remaining strategies consider similar and lower dispersant concentrations with ultrasonic treatment. The quality of the dispersion has been evaluated using SEM.

Detailed parametric analyses have been carried out in order to illustrate the influence of the constituents properties, waviness and agglomeration. Finally, the accuracy of the proposed approach has been proved by comparison with the experimental data from the tested specimens. In addition, two sensitivity analyses of the effective conductivity of the composites with MWCNT contents close and far from the percolation threshold, respectively, have been presented in order to gain some insight into the structure of the proposed model.

The main contributions of this paper are summarized below.

- The overall electrical conductivity of MWCNT cement-based composites is governed by the simultaneous contribution of the electron hopping and conductive networks mechanisms. The analysis of the effects of the conductivity of the MWCNTs remarks a dominant role of the conductive network mechanism above the percolation process.
- The parametric analyses highlight the importance of the aspect ratio of the nanotubes for the design of MWCNT-based nanocomposites. Increments in the length and

reductions of the diameter, i.e. increments in the CNT aspect ratio, lead to decrements in the percolation threshold and, therefore, higher likelihood of forming conductive paths.

- The analytical predictions show that the dispersion of the nanoinclusions has a strong influence on the overall conductivity of the composite. The results reveal that the higher is the concentration of MWCNTs within the clusters, the lesser is the nanoinclusions uniformity and, thus, the lesser is the overall conductivity of the composite.
- The comparison of the analytical predictions against experimental data demonstrates that the consideration of straight uniformly distributed MWCNTs leads to overestimated conductivity. On the contrary, it is shown that the incorporation of waviness and agglomeration effects, on the basis of SEM inspections, provides closer fits to the experimental data. Hence, it is concluded that the wavy state of the fibers as well as their agglomeration in bundles play a key-role in the conductivity of cement-based nanocomposites.
- The sensitivity analysis shows that, in the case of MWCNT content close to the percolation threshold, the most influential variable in the sensitivity of the overall electrical conductivity of the composite is the conductivity of the matrix. A significant effect of the fiber aspect ratio is also found as well as a considerable contribution of the helical waviness. It is also noticeable the limited influence of the agglomeration parameters and an almost negligible role played by the conductivity of the nanotubes. On the contrary, in the case of MWCNT content above the percolation threshold, the aspect ratio of the MWCNTs becomes predominant. Moreover, once some conductive paths are formed, the conductivity of the matrix loses relevance and, conversely, the waviness gains importance.

3.5.3 Uniaxial piezoresistivity of CNT-reinforced cement-matrix composites

3.5.3.1 Introduction

In this subsection, the developed uniaxial piezoresistivity model is tested against experimental data from MWCNT-reinforced cement-based specimens. Moreover, the influence of the different variables affecting the strain-sensitivity is also examined. The values of the micromechanical variables involved in the calculations are taken from Subsection 3.5.3.

3.5.3.2 Numerical results

In this first set of analyses, detailed parametric studies have been carried out in order to give some insight into the structure of the proposed model, as well as to extract valuable conclusions for the design of self-sensing MWCNT-reinforced cement-based composites.

Effects of constituents properties Fig. 3.37 shows the relative change in resistance $\Delta R/R_o$ of MWCNT-reinforced cement paste (PA) with different filler concentrations f_{CNT}. For illustrative purposes, the variation parameters of the inter-particle properties, C_1 and C_2, have been chosen from reference [290] as 8.9045 and 0.0243, respectively. According to the physical properties of cement paste, the Poisson's ratio has been set to 0.2. The externally applied strain has been imposed in the range $-1\times10^{-4}/+1\times10^{-4}$. Despite only compression tests have been carried out, theoretical results dealing with tensile strains are also shown here for the sake of completeness and potential application of this approach for stretchable materials. It can be seen that the proposed approach reproduces some of the effects evidenced in the experiments. For compressive loadings ($\varepsilon < 0$), the composites exhibit higher values of conductivity, unlike for tensile strains. In both cases, the percolation threshold increases although for the considered ranges of deformation the effect of the volume expansion and variation of the inter-particle properties becomes predominant. This behavior can be also seen in Fig. 3.38, where the overall electric conductivity for different MWCNT concentrations and strain levels is represented. In Fig. 3.37 (a), different MWCNT contents have been selected according to different parts of the percolation curve from Fig. 3.37 (b). It is noticeable that for MWCNT concentrations below and above the percolation threshold, the strain-sensitivity of the composite is considerably low. On the contrary, filler concentrations close to the percolation threshold lead to the highest sensitivity values. This fact justifies the evidence from the experiments about the existence of a critical concentration where the gauge factor reaches a maximum. This maximum is obtained for filler concentrations around the percolation threshold.

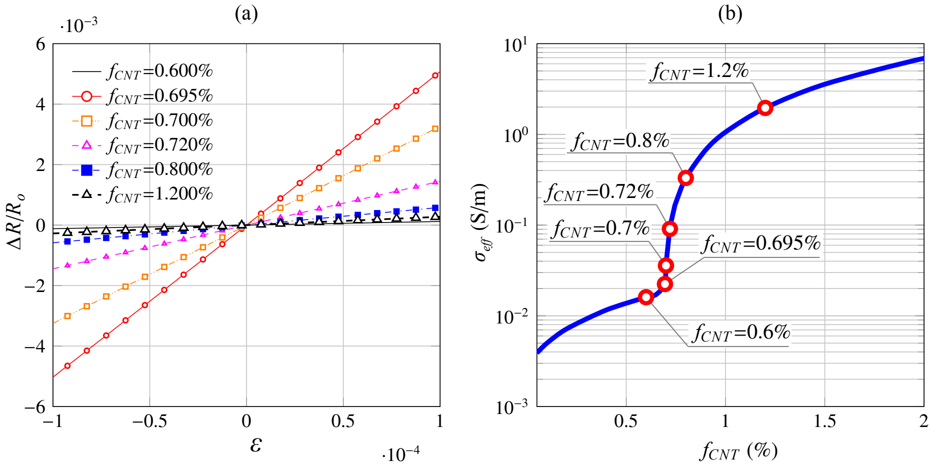

Figure 3.37 Strain-sensing capabilities of MWCNT-reinforced cement paste with different filler concentrations (a) and unloaded overall electrical conductivity of MWCNT-reinforced cement paste (PA, ν=0.2, L_{CNT} = 1 μm, D_{CNT}=10 nm, V_o=0.36 eV, d_c=0.5 nm, σ_c = 10^4 S/m, C_1=8.9045, C_2=0.0243).

In order to gain a better insight into the underlying mechanisms that control the piezoresistivity of the composites, Figs. 3.39 (a) and (b) present the relative resistance change induced by the isolated contribution of the different mechanisms and filler concentrations of 0.965% and 1.2%, respectively. Four different cases S_i have been selected with S_1, S_2, S_3 and S_4 standing for the isolated contribution of the volume expansion, change of the percolation threshold, filler orientation, and tunneling resistance, respectively. It can be seen that for the first concentration, Fig. 3.39 (a), close to the percolation threshold, the

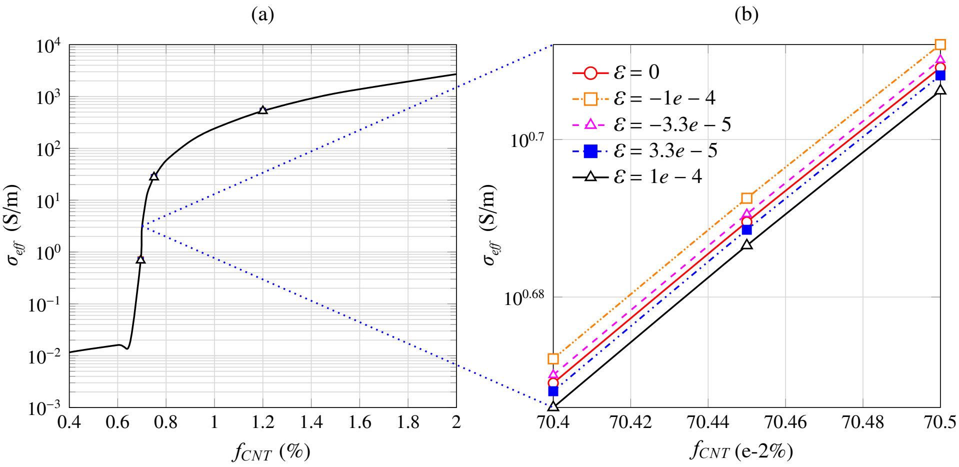

Figure 3.38 Overall electrical conductivity of MWCNT-reinforced cement paste under different strain levels (a), and detail view (b) (PA, ν=0.2, L_{CNT} = 1 µm, D_{CNT}=10 nm, V_o=0.36 eV, d_c=0.5 nm, $\sigma_c = 10^7$ S/m, C_1=8.9045, C_2=0.0243).

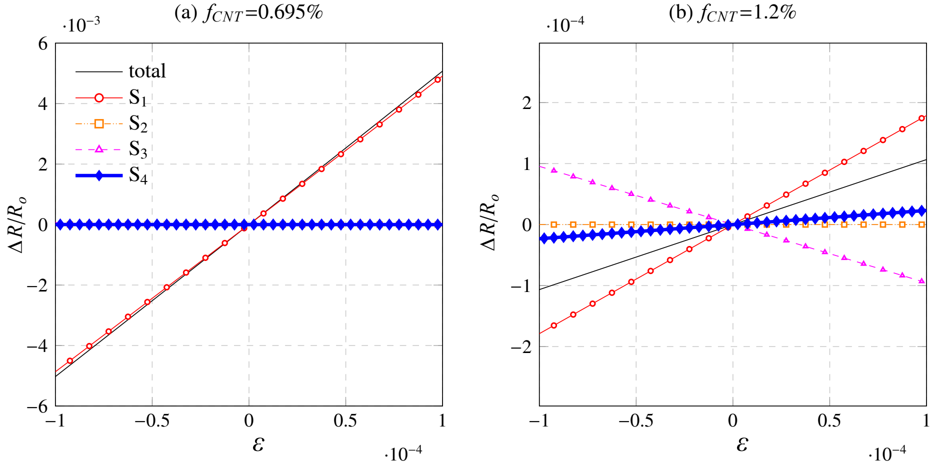

Figure 3.39 Piezoresistive behavior of MWCNT-reinforced cement paste with isolated contributions of the strain-sensing mechanisms (S_1 volume expansion contribution, S_2 contribution of change the in the percolation threshold, S_3 effect of the fiber reorientation and, S_4 change in the tunneling resistance)(PA, ν=0.2, L_{CNT} = 1 µm, D_{CNT}=10 nm, V_o=0.36 eV, d_c=0.5 nm, $\sigma_c = 10^4$ S/m, C_1=8.9045, C_2=0.0243).

strain sensitivity is dominated by the volume expansion (S_1). This fact makes sense since for this concentration only a few conductive paths have been formed. Thus, a change in the effective volume fraction has a deep impact as directly varies the number of formed paths. On the other hand, for filler concentrations far above the percolation threshold,

Fig. 3.39 (b), the number of conductive paths is larger and the strain sensing capability is held by the different mechanisms. In this case, the volume expansion continues being dominant although the reorientation of the fillers has gained importance. The change in the tunneling resistance has limited influence and the change of the percolation threshold has little influence. Fig. 3.40 represents each contribution from Fig. 3.39 (b) separately. From this figure, it is interesting noticing that the change of the percolation threshold increases the resistance for both compressive and tensile strains, in accordance with Fig. 3.12. The strain sensitivity induced by the volume expansion and change in the tunneling resistance reduces the resistance for compressive strains and vice versa. This behavior is also expected as both an increase of the volume fraction and a reduction of the inter-particle distance lead to higher values of conductivity for compressive loadings. The reasoning is the same in the case of tensile strains. Conversely, the contribution of the reorientation of the fillers exhibits an opposite behavior. As we are measuring the resistivity along the direction of the applied strain, for compressive loadings the fillers tend to align in the transverse direction reducing the measured conductivity. In the case of tensile loadings, the fillers tend to align in the direction of the load increasing the measured conductivity.

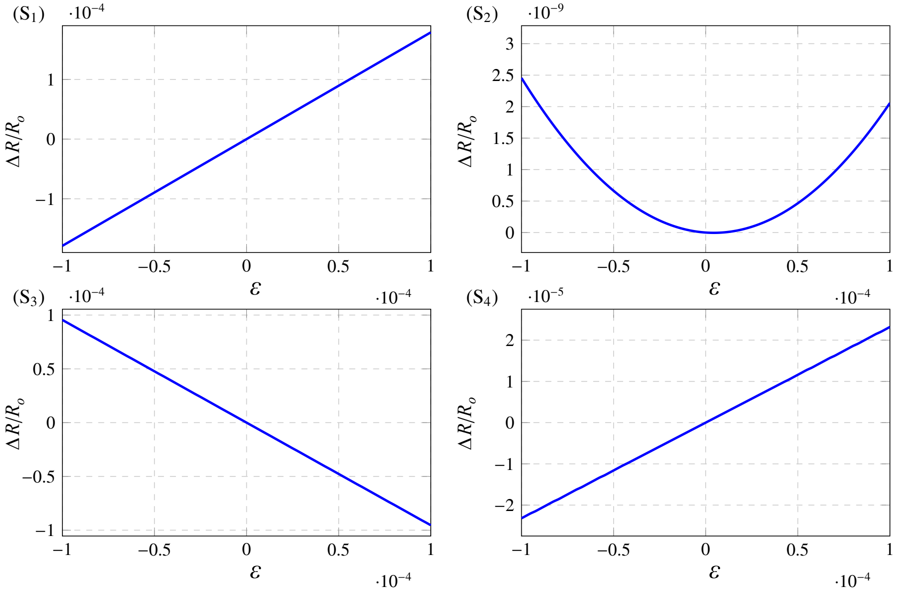

Figure 3.40 Isolated contributions of the strain-sensing mechanisms (S$_1$ volume expansion contribution, S$_2$ contribution of change the in the percolation threshold, S$_3$ effect of the fiber reorientation and, S$_4$ change in the tunneling resistance)(PA, ν=0.2, L_{CNT} = 1 µm, D_{CNT}=10 nm, V_o=0.36 eV, d_c=0.5 nm, $\sigma_c = 10^4$ S/m, C_1=8.9045, C_2=0.0243).

Literature studies have reported about the dominant role of the tunneling-type contact resistance in the strain-sensing capabilities of CNT-reinforced composites [290]. In this regard, as it can be seen in Eq. (3.2), the height of the potential barrier V_o and the initial inter-particle distance d_c play a key-role in the electron hopping mechanism. The relative

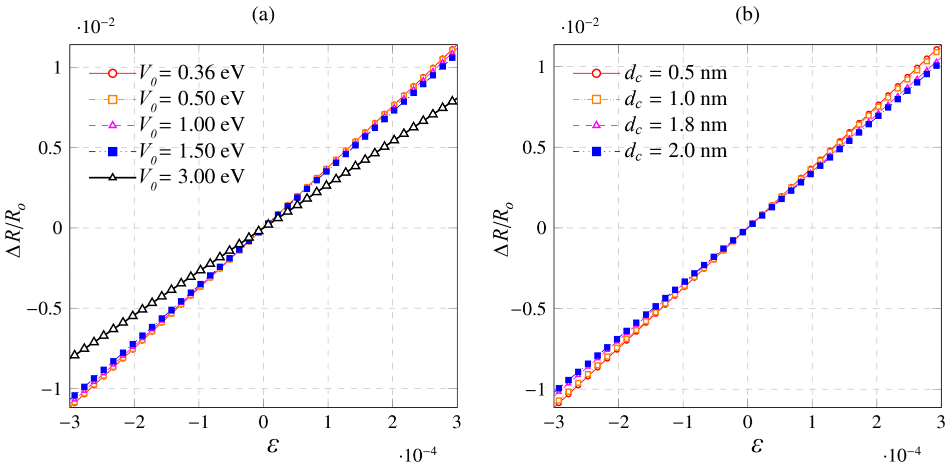

Figure 3.41 Strain-induced relative resistance change $\Delta R/R_o$ of MWCNT-reinforced cement paste for different heights of the potential barrier V_o (a), and different critical separation distances (b) (PA, f_{CNT}=0.695%, ν=0.2, L_{CNT} = 1 µm, D_{CNT}=10 nm, $\sigma_c = 10^4$ S/m, C_1=8.9045, C_2=0.0243).

resistance change for different values of V_o and d_c is presented in Figs. 3.41 (a) and (b), respectively. The MWCNT concentration has been set as f_{CNT}=0.695%, value that is close to the percolation threshold (see Fig. 3.37 (b)). The results presented in these two figures show that the lesser are the values of these two variables, the higher are the strain-induced changes and, thus, the higher is the strain sensitivity of the composite.

Finally, Figs. 3.42 (a) and (b) show the relative resistance change for different values of MWCNT conductivity and two filler concentrations, f_{CNT} = 0.69% and f_{CNT} = 2%, respectively. It can be extracted from these figures that more conductive fillers lead to higher strain sensitivities. Another noticeable aspect is that the nonlinearities, related to the coupled effect of the volume expansion and variation of the percolation threshold, gain importance for concentrations close to the unloaded percolation threshold. On the contrary, the strain-sensing curves exhibit more linear behaviors for concentrations far from this critical concentration. In other words, when the filler concentration is near the percolation threshold, the number of formed conductive paths is still limited so that the breakage or formation of conductive networks has a large impact on the overall conductivity. However, when there exist many conductive paths, the variation of the number of paths does not lead to substantial differences and the composite is thus less piezoresistive. From a mathematical point of view, the strain-induced variations of the effective volume fraction, f^*_{CNT}, and of the percolation threshold, f_c, result in a variation of the fraction of percolated CNTs, $\mathcal{X}$, defined in Eq. (3.16). Hence, the appearance of a nonlinear response for concentrations close to the percolation threshold is justified by the percolation theory. When percolation begins, i.e. for small values of $\mathcal{X}$, the conductivity of CNT-reinforced nanocomposites experiences a sharp increase. Once a sufficient number of conductive paths has been formed, the effective conductivity stabilizes. In this first region is where the strain-induced changes lead to the largest impacts and the most nonlinear effects.

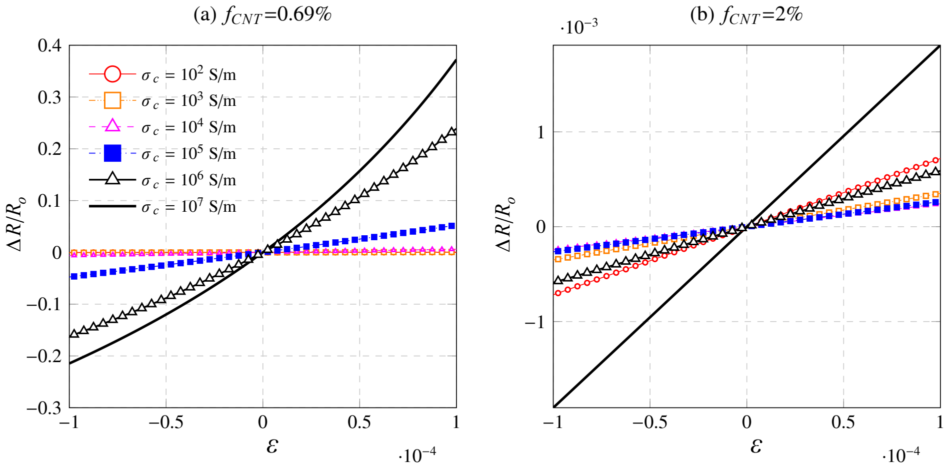

Figure 3.42 Strain-induced relative resistance change $\Delta R/R_o$ of MWCNT-reinforced cement paste for different filler conductivities σ_c and volume fraction $f_{CNT} = 0.69\%$ (a), and $f = 2\%$ (b) (PA, ν=0.2, L_{CNT} = 1 μm, D_{CNT}=10 nm, V_o=0.36 eV, d_c=0.5 nm, C_1=8.9045, C_2=0.0243).

Effects of MWCNT waviness In this section, the effect of MWCNT waviness on the piezoresistive properties of CNT-based composites is investigated. Five wavy geometries, corresponding to helical angles of 90°, 80°, 70°, 60° and 50°, have been considered. Figs. 3.43 (a) and (b) show the relative resistance variation for filler concentrations of 1% and 2%, respectively. The main effect of non-straightness of the fibers is an increase in the percolation threshold as a result of the reduction of the length from the wavy to the equivalent straight fiber. As a result, wavy geometries lead to effective volume fractions closer to the percolation threshold and, therefore, higher values of sensitivity. However, if the geometry is too curved it may result in an effective volume fraction under the percolation threshold and, thus, the strain-sensitivity can get substantially reduced. This is the case of $\theta^w = 50°$ in Fig. 3.43 (a).

Effects of MWCNT agglomeration The effect of MWCNT agglomeration in spherical bundles ($a_1 = a_2 = a_3$) on the conductivity of cement-based composites has been also analyzed. Figs. 3.44 (a) and (b) show the relative resistance change for different agglomeration parameters ξ and filler concentrations of $f_{CNT} = 1\%$ and $f_{CNT} = 2\%$, respectively. In these analyses, the volume fraction of MWCNTs within the bundles is kept constant at 90% ($\zeta = 0.9$), whereas the ratio between the volume of the bundles and the total volume of the RVE, ξ, varies from 0.1 to 0.9. In Fig. 3.44 (a), it is quite clear that the lesser is the value of ξ, i.e. the lesser is the volume of the bundles, the lesser is also the piezoresistivity of the composite. Nevertheless, for volume fractions far away from the percolation threshold, as in Fig. 3.44 (b), this effect is not so clear. Depending on the relative volume fraction of both phases, bundles and surrounding composite, the strain sensitivity may substantially vary.

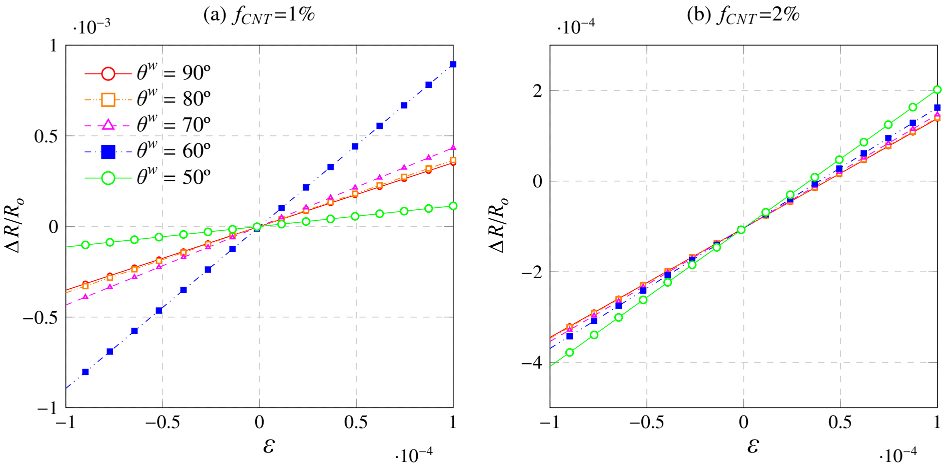

Figure 3.43 Strain-induced relative resistance change $\Delta R/R_o$ of MWCNT-reinforced cement paste for different helical angles θ^w and volume fraction f_{CNT} = 1% (a), and f_{CNT} = 2% (b) (PA, ν=0.2, L_{CNT}^{wavy} = 1 µm, D_{CNT}=10 nm, V_o=0.36 eV, d_c=0.5 nm, $\sigma_c = 10^4$ S/m, C_1=8.9045, C_2=0.0243).

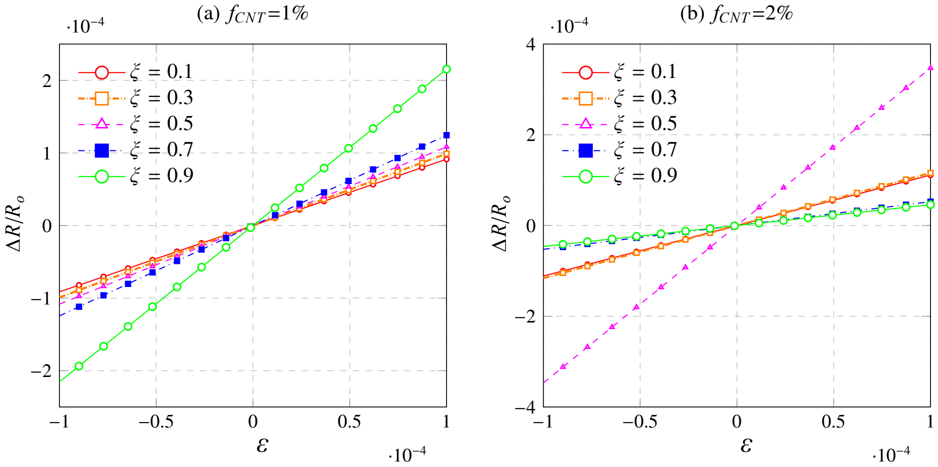

Figure 3.44 Strain-induced relative resistance change $\Delta R/R_o$ of MWCNT-reinforced cement paste for different agglomeration parameters ξ and volume fraction f_{CNT} = 1% (a), and f_{CNT} = 2% (b) (PA, ζ=0.9, ν=0.2, L_{CNT} = 1 µm, D_{CNT}=10 nm, V_o=0.36 eV, d_c=0.5 nm, $\sigma_c = 10^5$ S/m, C_1=8.9045, C_2=0.0243).

Secondly, in Figs. 3.45 (a) and (b) the volume fraction of the bundles ξ is set to 0.4 and the ratio of MWCNT concentration within them, ζ, ranges from 0.4 to 0.9. In Fig. 3.45 (a), it can be seen that the variation from the uniform distribution, $\xi = \zeta$=0.4, to the next degree of agglomeration, ζ=0.6, leads to a higher sensitivity of the composite. However, if this value goes on increasing, such as for ζ=0.8 and ζ=0.9, the effective volume fraction within the bundles moves far away from the percolation threshold and the resulting composite exhibits lesser piezoresistivity. On the contrary, for a global volume fraction far away from the percolation threshold as in Fig. 3.45 (b), the effect of the increment of ζ, i.e. increments of the filler concentration within the bundles, clearly reduces the resulting piezoresistivity.

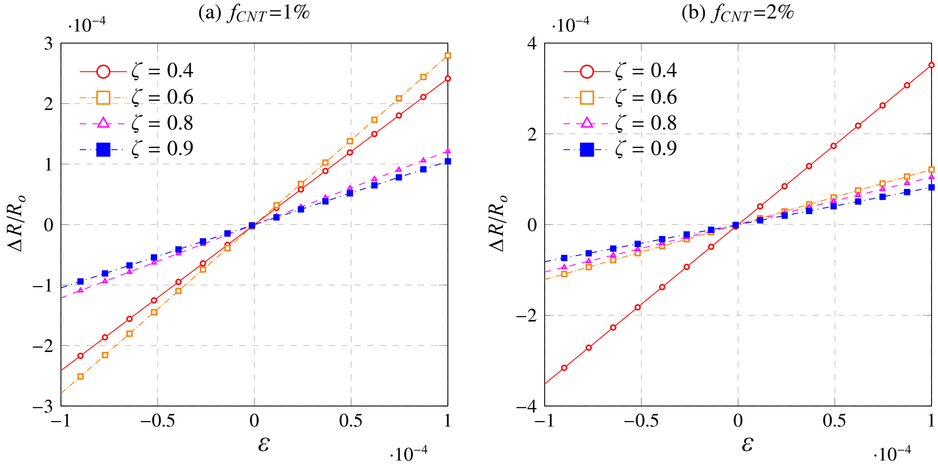

Figure 3.45 Strain-induced relative resistance change $\Delta R/R_o$ of MWCNT-reinforced cement paste for different agglomeration parameters ζ and volume fraction f_{CNT} = 1% (a), and f_{CNT} = 2% (b) (PA, ξ=0.4, ν=0.2, L = 1 µm, D=10 nm, V_o=0.36 eV, d_c=0.5 nm, $\sigma_c = 10^5$ S/m, C_1=8.9045, C_2=0.0243).

Characterization of the gauge factor As mentioned above, the correlation between measured resistance and strain can be modeled, as a first approximation, by means of the same formula used for conventional strain gauges (Eq. 3.58). However, because of the peculiar electromechanical behavior of MWCNT-reinforced composites, the gauge factor λ is rate dependent and also varies with ε, resulting in a nonlinear relationship of strain-to-signal. As it was already shown in Fig. 3.42, as well as it has been evidenced in some other previously published experimental and theoretical works [239], the strain-sensing curves can be approximately modeled with a first linear range followed by a nonlinear one. Although there are a few works dealing with the definition of the nonlinear part, such as the work of Park *et al.* [239] who defined it by an exponential-type function, the linear part is of high interest in the realm of SHM as the accuracy of the measurements is higher within this range. In this work, a linear regression based on a least squares estimator is adjusted in the strain range leading to a coefficient of determination of 0.99, as schematically represented in Fig. 3.46 (a). Hence, two different gauge factors, λ^- and λ^+, can be extracted from the slope of both linear fittings for compressive and tensile strains, respectively, as follows:

$$\frac{\Delta R}{R_o} = \lambda^{-}\varepsilon, \quad \varepsilon < 0 \tag{3.61a}$$

$$\frac{\Delta R}{R_o} = \lambda^{+}\varepsilon, \quad \varepsilon > 0 \tag{3.61b}$$

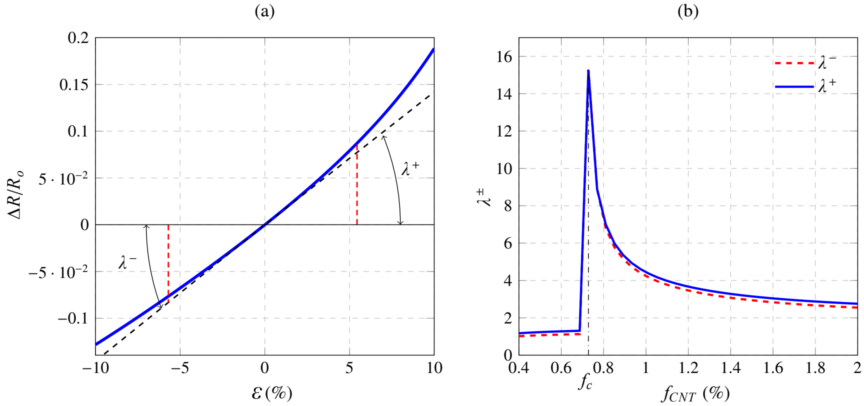

Figure 3.46 Characterization of the gauge factor and the linear strain gauge range (a), and strain gauge of MWCNT-reinforced cement paste versus filler concentration f_{CNT} under compressive λ^{-} and tensile λ^{+} strains (b) (ν=0.2, L_{CNT} = 1 μm, D_{CNT}=10 nm, V_o=0.36 eV, d_c=0.56 nm, $\sigma_c = 10^5$ S/m, C_1=8.9045, C_2=0.0243).

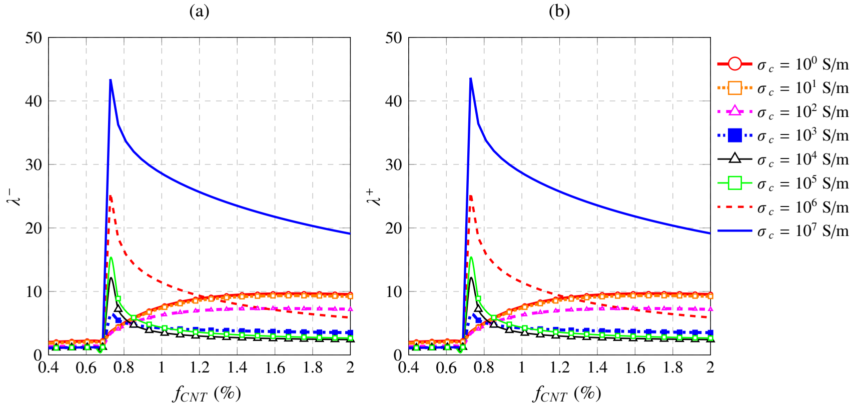

Figure 3.47 Strain gauge of MWCNT-reinforced cement paste versus filler concentration f_{CNT} under compressive λ^{-} (a) and tensile λ^{+} strains (b), for different filler conductivities σ_c (ν=0.2, L_{CNT} = 1 μm, D_{CNT}=10 nm, V_o=0.36 eV, d_c=0.56 nm, $\sigma_c = 10^5$ S/m, C_1=8.9045, C_2=0.0243).

On this basis, the variation of the gauge factor with the filler concentration can be obtained as shown in Fig. 3.46 (b). It should be noted that the gauge factor is slightly higher in the case of tensile stresses. In this case, the percolation threshold increases with increasing inter-particle distance and with volume expansion. However, in the case of compressive strains, the percolation threshold also increases whilst the rest of the parameters decrease (see Fig. 3.40). Moreover, according to results of Fig. 3.37, a maximum value of the gauge factor is observed around the percolation threshold. Figs. 3.47 (a) and (b) depict the gauge factor of MWCNT-reinforced cement paste with different filler concentrations under compressive and tensile strains, respectively. As expected from Fig. 3.42, more conductive fillers lead to higher gauge factor values. It is also noticeable that for higher filler conductivities the peaks are sharper, whilst lower filler conductivities lead to smoother curves.

Experimental validation On the basis of the previous analyses, the proposed micromechanics approach has been compared to the experimental results obtained for different cement-based composites. Fig. 3.48 shows some examples of time histories of applied strain and corresponding electrical resistance obtained in the experiments. In particular, the figures show the response of paste, mortar and concrete specimens containing a filler concentration of 1.5%, 1% and 1% with respect to cement weight, respectively. Hence, according to Eq. (3.58), the values of the gauge factor obtained from the strain sensing tests are compared to the values obtained by the proposed approach in Fig. 3.49. The MWCNT electrical conductivity has been set between 10^1 and 10^4 S/m. The SEM inspections in the analyzed specimens showed good dispersions of the nanoinclusions in the cementitious matrices. This fact has been verified numerically with the use of limited values for the agglomeration parameters with good results for both overall effective conductivity and

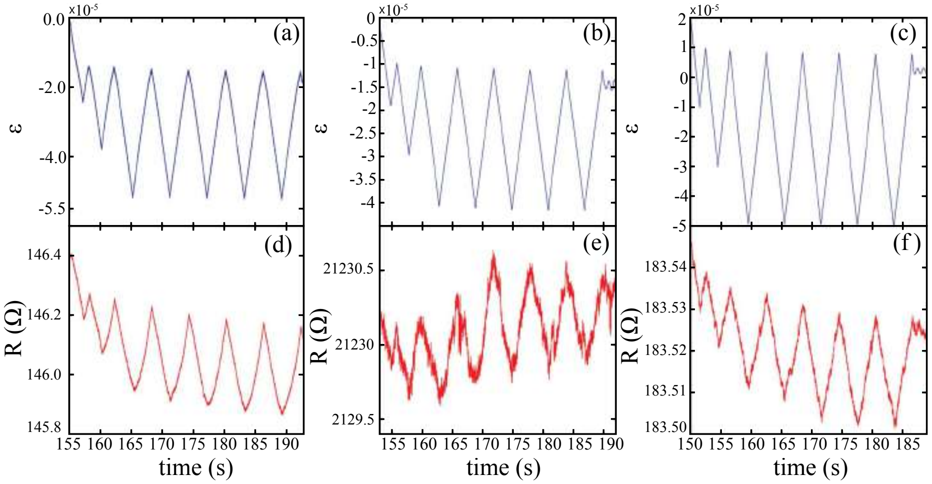

Figure 3.48 Time histories of applied compression strain and corresponding electrical resistance outputted by (a) paste, (b) mortar and (c) cement specimens with filler concentrations of 1.5%, 1% and 1% with respect to cement weight, respectively.

strain-sensing curves. The values of the agglomeration parameters, waviness, geometric properties of the fillers, as well as the variation parameters C_1 and C_2 have been adjusted to fit the experimental data. It is observed that the analytical prediction agrees well with the experimental results and the tendency of the gauge factor λ^- is well captured by the present model. The experimental data also show the existence of an optimal content of nanotubes around 0.75-1% mass content with respect to the mass of cement. This behavior is reproduced by the current approach, as shown above in Fig. 3.37, with the optimal content of nanotubes at the percolation threshold.

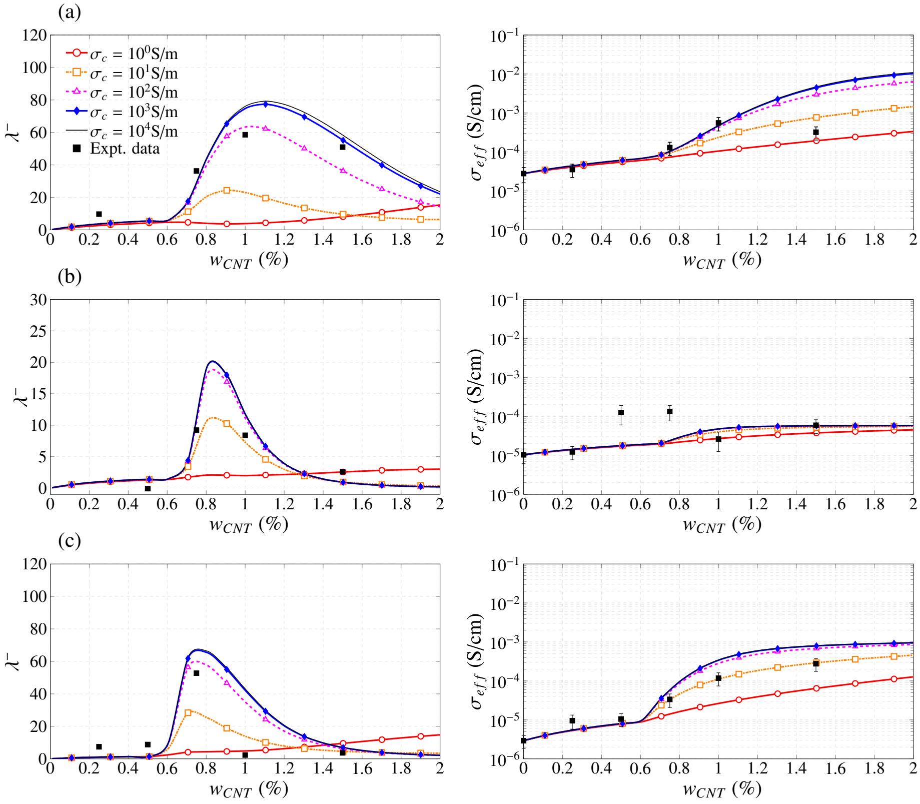

Figure 3.49 Comparison of the theoretical predictions and the experimental electrical compression gauge factors λ^- for cement-based sensors. ((a) PA, L_{CNT} = 0.25 µm, D_{CNT}=10 nm, V_o=0.56 eV, d_c=1.8 nm, ξ=0.90, ζ=0.90, θ^w=35°, C_1=6.8, C_2=1.7; (b) MO, L_{CNT} = 0.25 µm, D_{CNT}=10 nm, V_o=0.56 eV, d_c=1.8 nm, ξ=0.68, ζ=0.90, θ^w=40°, C_1=5.2, C_2=1.5; (c) CO, L_{CNT} = 0.25 µm, D_{CNT}=10 nm, V_o=0.56 eV, d_c=1.8 nm, ξ=0.90, ζ=0.90, θ^w=69°, C_1=5.0, C_2=1.5).

Fig. 3.50 shows the comparison in the $R-\varepsilon$ plane for three samples of cement paste, mortar and concrete with filler concentrations of 1%, 0.75% and 0.75% with respect to the mass of cement, respectively. The material properties have been taken from Fig. 3.49.

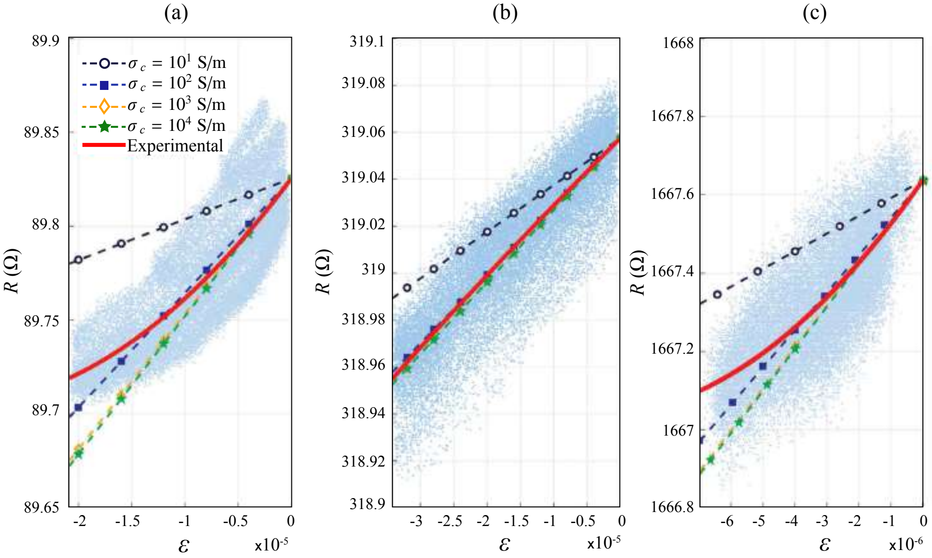

Figure 3.50 Comparison of the theoretical predictions and the experimental electrical resistance versus applied strain for (a) paste, (b) mortar and (c) cement specimens with filler concentrations of 1%, 0.75% and 0.75% with respect to cement weight, respectively.

In order to compare the effective conductivity of the composites from Eq. (3.17) in the direction of application of the external strain, σ_{eff}^{22}, with the electrical resistance, R, measured in the specimens through a high precision LCR meter, the following relation was applied:

$$\sigma_{eff}^{22} = \frac{d}{AR} \tag{3.62}$$

being A the specimen's cross-section and d the electrode's distance with values of 51×51 mm^2 and 10 mm, respectively (see Fig. 3.22). It is noted in this figure that the presented approach can simulate fairly well the linear part of the strain-sensing curves for the three different matrices. According to the results of Fig. 3.49, a filler conductivity around 10^2 S/m leads to very proximate values of the gauge factor. However, for the considered range of small deformations, the appearance of stronger contributions of non-linearities, associated with the variation of the percolation threshold, were not captured by the proposed method. This is the case of cement-paste and concrete specimens, where only the linear behavior was captured by the proposed approach. In the case of mortar specimens, the strain-sensing curve is prominently linear and the theoretical approach provides very proximate values.

3.5.3.3 Conclusions

An extension of the previously proposed micromechanics model has been developed to incorporate the uniaxial piezoresistivity properties of CNT cement-based nanocomposites. The origin of the piezoresistive response of these composites has been attributed to strain-induced changes in the volume fraction, changes in the conductive networks due to the filler reorientation and, therefore, the percolation threshold, and, finally, changes in the tunneling resistance through variation of the inter-particle distance and the height of the potential barrier. The Komoro and Makishima's stochastic method has been implemented in order to evaluate the variation of the percolation threshold following an applied strain through the resulting strain-induced ODF.

Detailed parametric analyses have been carried out in order to illustrate the influence of the properties of the constituents, waviness and agglomeration. In order to highlight the importance of the tunneling effect in the piezoresistivity of MWCNT cement-based composites, the influence of the variation of the height of the tunneling potential barrier and the inter-particle distance have been analyzed. Finally, the accuracy of the proposed approach has been demonstrated by comparison with the experimental data from the tested specimens.

The main contributions of this section are summarized below:

- The strain-sensing capability of MWCNT cement-based composites critically depends on the MWCNT content. Both experiments and theoretical modeling confirm that the largest gauge factors are achieved at the percolation threshold.
- The nonlinear relationship between ohmic resistance and externally applied strains is related to the variation of the percolation threshold. Specimens with filler contents close to the percolation threshold exhibit higher levels of nonlinearity, whilst specimens having concentrations far from this critical value tend to exhibit a more linear behavior.
- More conductive fillers lead to higher gauge factors. In addition, the importance of the non-linear behavior increases with increasing fillers conductivity.
- The comparison of the analytical predictions against experimental data demonstrates that the presented mixed micromechanics model can predict fairly well the gauge factor of MWCNT cement-based composites. Furthermore, the incorporation of waviness and agglomeration enhanced the analytical results.
- The results also showed that the presented approach can model the linear range of piezoresistivity, useful for the development of monitoring applications of CNT cement-based nanocomposites in the realm of SHM. Moreover, the proposed approach also proved capable to model the non-linear response associated with the variation of the percolation threshold, similar to experimental evidence. However, some discrepancies have been found in some specimens with filler contents close to the percolation threshold. These differences are hypothesized to be due to the consideration of uniform average distance among nanotubes and small deformations. However, this approach offers a suitable framework in which incorporate more complex distributions in further research.

3.5.4 3D piezoresistivity of CNT-reinforced cement-matrix composites

In this section, extensive parametric analyses are presented in order to improve understanding of the piezoresistive behavior of CNT-reinforced smart concretes in view of their applications for strain monitoring in Reinforced-Concrete (RC) structural elements.

Further, discussion on the characterization of the piezoresistivity matrix is presented. Afterward, a simulation of a cubic CNT-reinforced mortar sensor is conducted and compared with experimental data. In this way, an easily mathematically tractable model for cubic smart concrete strain sensors is achieved.

3.5.4.1 Parametric analyses

In this first set of analyses, detailed parametric studies have been carried out in order to give some insight into the structure of the proposed model, as well as to extract valuable conclusions for the design of self-sensing CNT-reinforced cement-based composites. For illustrative purposes, cement paste (PA) is chosen as matrix material with electrical conductivity $2.8{\times}10^{-3}$ S/m. The reinforcing phase consists of MWCNTs with electrical conductivities ranging from 10^0 to 10^7 S/m. The rest of the variables have been taken from reference [103] unless otherwise indicated.

Effects of constituents properties on the strain-induced electrical response First, uni-axial laterally constrained dilation (ε_1,0,0) and distortion (ε_{12}) tests are conducted. Fig. 3.51 shows the relative change in resistivity $\Delta\rho/\rho_0$ of MWCNT-reinforced cement paste with different filler concentrations f_{CNT}. For illustrative purposes, the variation parameters of the inter-particle properties under dilation, C_1 and C_2, have been taken from [290] as 8.9045 and 0.0243, respectively. According to the physical properties of cement paste, the Poisson's ratio has been set to 0.2. The externally applied strain has been imposed in the range $(-500, +500)$ $\mu\varepsilon$. In a similar way to previous work by the authors [103], it is noted in Fig. 3.51 (a) that the proposed approach reproduces some of the effects evidenced in the experiments under uni-axial strain. For compressive loadings, $\varepsilon < 0$, the composites exhibit higher values of conductivity, unlike for tensile strains. In both cases, the percolation threshold increases, although, for the considered ranges of deformation, the effect of the volume expansion and variation of the inter-particle properties becomes predominant. Also, it is noticeable that for MWCNT concentrations below and above the percolation threshold, the strain-sensitivity of the composite is considerably low. On the contrary, filler concentrations close to the percolation threshold lead to the highest sensitivity values. This fact justifies the evidence from the experiments about the existence of a maximum strain-sensitivity around the percolation threshold as shown in reference [103] for laterally unconstrained conditions. Solid and dashed lines denote longitudinal ($\Delta\rho_1/\rho_0$) and transverse ($\Delta\rho_2/\rho_0 = \Delta\rho_3/\rho_0$) relative changes in resistivity, respectively. It is observed that transverse relative changes are very similar to the longitudinal ones. This fact indicates that the sensor provides almost the same output (in this case almost proportional to uni-axial strain) regardless of the layout of the electrodes. A closer inspection of the results reveals that the transverse sensitivity is slightly higher than the longitudinal one. This behavior finds an explanation in the re-orientation effect. For instance, in the case of tensile strains, fillers tend to align in the direction of the strain and, thus, the longitudinal resistivity experiences comparatively smaller reductions. This behavior can be also seen in Fig. 3.52, where the overall electric conductivity for different MWCNT concentrations and strain levels is represented. For clarity purposes, higher strain values of ±5% and ±2% are considered. It is important to note that both longitudinal and transverse effective

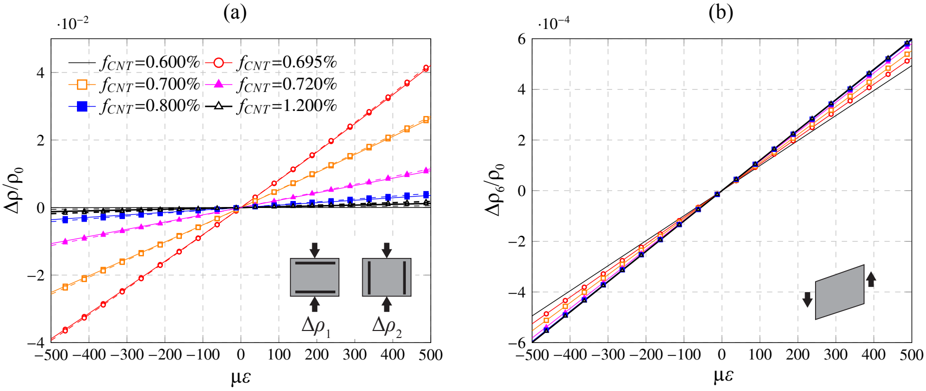

Figure 3.51 Strain-sensing capabilities of MWCNT-reinforced cement paste with different filler concentrations under laterally constrained uni-axial dilation (a) and distortion (b) (ν=0.2, L_{CNT} = 1 μm, D_{CNT}=10 nm, V_o=0.36 eV, d_c=0.5 nm, σ_c = 10^4 S/m, C_1=8.9045, C_2=0.0243). Solid and dashed lines in (a) denote longitudinal, ($\Delta\rho_1/\rho_0$), and transverse, ($\Delta\rho_2/\rho_0 = \Delta\rho_3/\rho_0$), relative changes in resistivity, respectively.

conductivities are close at the percolation threshold and differences raise as the filler concentration increases. This effect remarks the increasing role of filler-reorientation effect at higher filler contents. Fig. 3.51 (b) depicts the relative change in resistivity $\Delta\rho_6/\rho_0$ under shear strain ε_{12}. First, it is important to note that the strain sensitivity is considerably lower than in the dilation case. Moreover, the relative change in resistivity exhibits considerably linear variations with shear strain, desirable feature both for modeling and designing of strain-sensing composites. In this case, the strain sensitivity is higher with increasing filler contents. This fact can be readily ascribed to the isolated contribution of re-orientation effects, since the volume of the composite stays constant.

Fig. 3.53 is aimed at inspecting the differences between previous work by the authors [103] and the present approach, that is the comparison between uni-axial unconstrained ($\overline{\varepsilon}_1 = \overline{\varepsilon}_2 = \overline{\varepsilon}_3^{-\nu}$) and constrained dilations ($\overline{\varepsilon}_1 = \overline{\varepsilon}_2 = 1$). It is first noted that constrained conditions yield considerably higher electrical strain sensitivities. In spite of the fact that filler re-orientation is less influential in the case of constrained conditions as previously shown in Fig. 3.14, volume expansion effect is indeed more predominant as evidenced in Fig. 3.20, what explains the higher sensitivity for laterally constrained conditions. Furthermore, it is also observed here that the transverse sensitivities are slightly higher than the longitudinal ones in both conditions.

Fig. 3.54 shows the relative resistance change for different values of MWCNT conductivity under laterally constrained uni-axial dilation. Two filler concentrations, f_{CNT} = 0.695% and f_{CNT} = 2%, are selected in Figs. 3.54 (a) and (b), respectively, as filler contents proximate and far from the percolation threshold of the unstrained system. It can be extracted from these figures that more conductive fillers lead to higher strain sensitivities. It is important to note that nonlinearities, related to the coupled effect of the volume expansion and variation of the percolation threshold, gain importance for concentrations close to the unloaded percolation threshold. On the contrary, the strain-sensing curves exhibit more

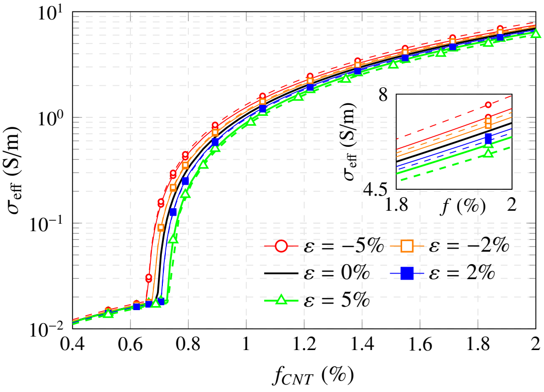

Figure 3.52 Overall electrical conductivity of MWCNT-reinforced cement paste under different laterally constrained uni-axial dilation levels (ν=0.2, L_{CNT} = 1 µm, D_{CNT}=10 nm, V_o=0.36 eV, d_c=0.5 nm, $\sigma_c = 10^7$ S/m, C_1=8.9045, C_2=0.0243). Solid and dashed lines denote in-plane, $\sigma_{eff}(1{,}1)$, and normal, $\sigma_{eff}(1{,}2)$, electrical conductivities, respectively.

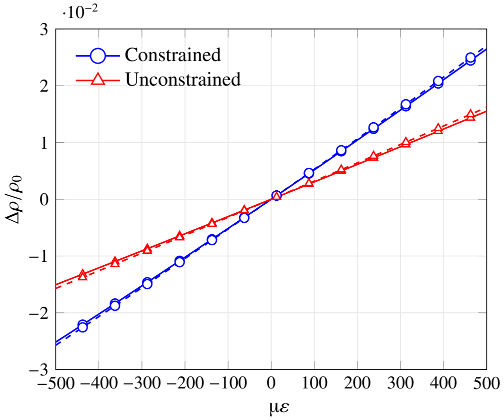

Figure 3.53 Strain-sensing capabilities of MWCNT-reinforced cement paste under uni-axial laterally constrained and unconstrained dilations (ν=0.2, L_{CNT} = 1 µm, D_{CNT}=10 nm, V_o=0.36 eV, f_{CNT} = 0.7%, d_c=0.5 nm, $\sigma_c = 10^4$ S/m, C_1=8.9045, C_2=0.0243). Solid and dashed lines denote longitudinal, ($\Delta\rho_1/\rho_0$), and transverse, ($\Delta\rho_2/\rho_0 = \Delta\rho_3/\rho_0$), relative changes in resistivity, respectively.

linear behaviors for concentrations far from this critical concentration. In other words, when the filler concentration is near the percolation threshold, the number of formed conductive paths is still limited so that the breakage or formation of conductive networks has a strong impact on the overall conductivity. However, when there exist many conductive paths, the variation of the number of paths does not lead to substantial differences and the composite is thus less piezoresistive. From a mathematical point of view, the strain-induced variations of the effective volume fraction and of the percolation threshold result in a variation of the fraction of percolated CNTs, χ. Hence, the appearance of a nonlinear response for concentrations close to the percolation threshold is justified by the percolation theory. When percolation begins, i.e. for small values of χ, the conductivity of CNT-reinforced nanocomposites experiences a sharp increase. In this first region is where the strain-induced changes lead to the largest impacts and the composites exhibit the most nonlinear response. Once a sufficient number of conductive paths has been formed, the overall conductivity stabilizes and the composites respond to strain in a more linear way.

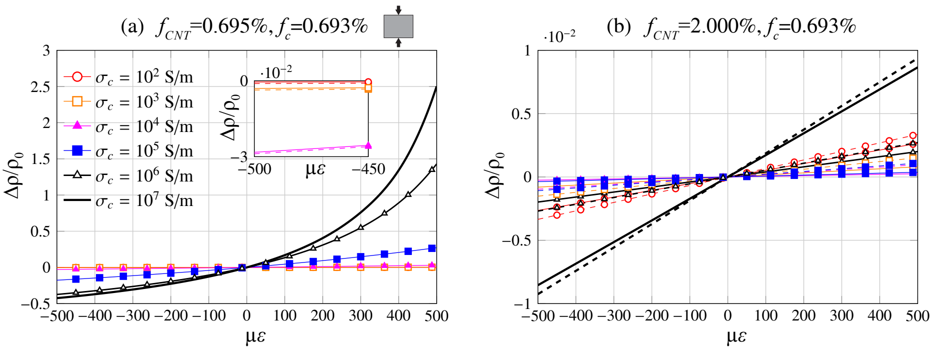

Figure 3.54 Strain-induced relative resistance change $\Delta\rho/\rho_o$ of MWCNT-reinforced cement paste for different filler conductivities σ_c and volume fraction f_{CNT} = 0.695% (a), and f_{CNT} = 2.000% (b) under uniaxial constrained dilation (ν=0.2, L_{CNT} = 1 μm, D_{CNT}=10 nm, V_o=0.36 eV, d_c=0.5 nm, C_1=8.9045, C_2=0.0243). Solid and dashed lines denote longitudinal, ($\Delta\rho_1/\rho_0$), and transverse, ($\Delta\rho_2/\rho_0 = \Delta\rho_3/\rho_0$), relative changes in resistivity, respectively.

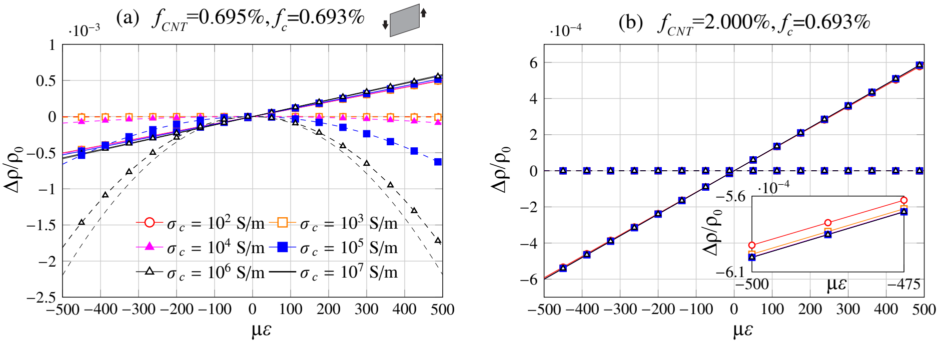

Figure 3.55 Strain-induced relative resistance change $\Delta\rho/\rho_o$ of MWCNT-reinforced cement paste for different filler conductivities σ_c and volume fraction f_{CNT} = 0.695% (a), and f_{CNT} = 2.000% (b) under distortion strain ε_{12} (ν=0.2, L_{CNT} = 1 μm, D_{CNT}=10 nm, V_o=0.36 eV, d_c=0.5 nm, C_1=0, C_2=0). Solid and dashed lines refer to $\Delta\rho_6/\rho_o$ and $\Delta\rho_1/\rho_o$ terms, respectively.

Fig. 3.55 shows the relative resistance change for different values of MWCNT conductivity under shear strain ε_{12}. In order to assess the correctness of the assumption of cubic crystal symmetry of the piezoresistivity matrix in Eq. (3.55), terms $\Delta\rho_6/\rho_o$ and $\Delta\rho_1/\rho_o$ are represented with solid and dashed lines, respectively. Two filler concentrations, f_{CNT} = 0.695% and f_{CNT} = 2%, are again selected here as filler contents. On the basis of the hypothesis of cubic crystal symmetry of the piezoresistivity matrix, when the composite is subjected to a shear strain ε_{12}, only variations in $\Delta\rho_6/\rho_o$ should be observed, whilst the rest of the terms should be constantly zero. However, it can be seen in Fig. 3.55 (a) that the term $\Delta\rho_1/\rho_o$ not only does not disappear but exhibits higher variations than $\Delta\rho_6/\rho_o$. Terms $\Delta\rho_2/\rho_o$ and $\Delta\rho_3/\rho_o$ are not included in this analysis for the sake of clarity as identical conclusions are extracted for them. This effect is ascribed to the re-orientation of the fillers which does not only affect the shear direction but also the rest of orientations. It is also noticeable that the term $\Delta\rho_6/\rho_o$ is highly linear with the shear strain, whilst diagonal terms of the resistivity matrix are highly non-linear. On the other hand, it can be seen in Fig. 3.55 (b) that variations of the diagonal terms of the resistivity matrix are drastically minimized for filler volume fractions above the percolation threshold. The term $\Delta\rho_6/\rho_o$ is clearly shown dominant and linear with the strain. Overall, it can be concluded that the hypothesis of cubic crystal symmetry of the piezoresistivity matrix fails to reproduce the response of CNT-reinforced cement-matrix composites at filler contents very close to the percolation threshold. Nonetheless, the variation of the diagonal terms of the resistivity matrix can be neglected for filler contents slightly higher than the percolation threshold. In these cases, the cubic crystal symmetry condition of the piezoresistivity matrix can be accepted, as well as the linearity of the coefficient λ_{44}. Finally, let us remark that the shear strain sensitivity increases with the filler content.

Characterization of the piezoresistivity matrix In this section, the piezoresistivity coefficients are determined as the ratios between relative variations of electrical resistance and strain according to the virtual experiments in Eqs. (3.56) and (3.57). Fig. 3.56 depicts the piezoresistivity coefficients λ_{11} and λ_{12}, indicated by solid and dashed lines, as a function of the filler concentration. As previously shown, because of the peculiar electromechanical behavior of CNT-reinforced composites subjected to uni-axial dilation, λ_{11} is rate dependent and also varies with ε_1, resulting in a nonlinear relationship of strain-to-signal. According to some other previously published experimental and theoretical works [239], it has been shown in Fig. 3.54 that the strain-sensing curves can be approximately modeled with a first linear range followed by a nonlinear one. In this work, a linear regression based on a least squares estimator is adjusted in the strain range that leads to a coefficient of determination of 0.99. Hence, the piezoresistivity coefficients λ_{11} and λ_{12} are computed as the slope of the regression of their corresponding strain-sensitivity curves. It is important to note that, in accordance with the results in Fig. 3.51, maximum values of piezoresistivity coefficients λ_{11} are found in Fig. 3.56 around the percolation threshold. Also, as expected from Fig. 3.54, more conductive fillers lead to higher sensitivity coefficients. It is also noticeable that the maximum peaks are sharper for higher filler conductivities, whilst less conductive fillers lead to smoother curves. It is observed that λ_{12} exhibits slightly higher values along the whole range of filler concentrations as expected from previous analyses.

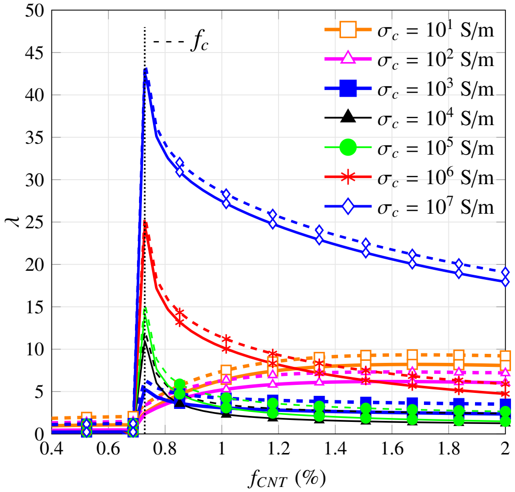

Figure 3.56 Piezoresistivity coefficients of MWCNT-reinforced cement paste versus filler concentration f_{CNT} under uni-axial constrained compression for different filler conductivities σ_c (L_{CNT} = 1 μm, D_{CNT}=10 nm, V_o=0.36 eV, d_c=0.56 nm, C_1=8.9045, C_2=0.0243). Solid and dashed lines stand for longitudinal and transverse strain gauges, λ_{11} and λ_{12}, respectively.

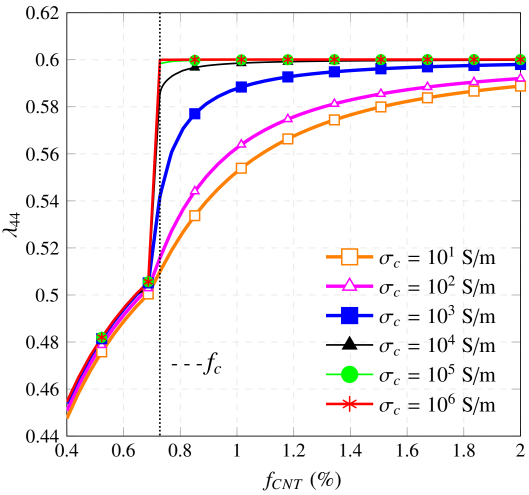

Figure 3.57 Piezoresistivity coefficient λ_{44} of MWCNT-reinforced cement paste versus filler concentration f_{CNT} under uni-axial constrained compression for different filler conductivities σ_c (L_{CNT} = 1 μm, D_{CNT}=10 nm, V_o=0.36 eV, d_c=0.56 nm).

Fig. 3.57 shows the piezoresistivity coefficient λ_{44} for different filler conductivities. In this case, λ_{44} continuously increases with the filler content. A sharp increase in the sensitivity is found at filler contents around the percolation threshold after which slow increasing rates are detected. In a similar way to the previous analysis, more conductive fillers lead to higher sensitivity coefficients. Overall, it can be concluded that the piezoresistivity coefficient under shear strain, λ_{44}, is substantially lower than those associated to dilation. Finally, the piezoresistivity matrix can be computed according to Eq. (3.55). For instance, in the case of MWCNT-reinforced cement paste (PA) with filler volume fraction $f_{CNT} = 1\%$ and filler conductivity $\sigma_c = 10^6$ S/m, the piezoresistivity matrix $\mathbf{\Pi}$ reads:

$$\mathbf{\Pi} = \left[\begin{array}{c:c} \mathbf{\Pi}^{dil} & 0 \\ \hdashline 0 & \mathbf{\Pi}^{dis} \end{array}\right] = \left[\begin{array}{ccc:ccc} 10.04 & 11.19 & 11.19 & 0 & 0 & 0 \\ 11.19 & 10.04 & 11.19 & 0 & 0 & 0 \\ 11.19 & 11.19 & 10.04 & 0 & 0 & 0 \\ \hdashline 0 & 0 & 0 & 0.6 & 0 & 0 \\ 0 & 0 & 0 & 0 & 0.6 & 0 \\ 0 & 0 & 0 & 0 & 0 & 0.6 \end{array}\right] \tag{3.63}$$

In light of the similarity between λ_{11} and λ_{12}, as well as the small values of λ_{44}, it can be concluded that CNT-reinforced smart concretes are essentially sensitive to volumetric strain. It follows that cubes made of such multifunctional materials can be used as volumetric strain sensors to be embedded into concrete elements before casting. In particular, the relative change in electrical resistance outputted by similar sensors, whatever the deployment of electrodes, in a typical 2-probe or 4-probe configuration (see Fig. 3.58), can be approximated by means of a constant piezoresistivity coefficient or gauge factor λ as follows:

$$\frac{\Delta\rho}{\rho_o} = \frac{\Delta R}{R_o} \approx \lambda(\varepsilon_1 + \varepsilon_2 + \varepsilon_3) \tag{3.64}$$

with ΔR the variation of the electrical resistance of the specimen, and R_o the electrical resistance of the unloaded specimen.

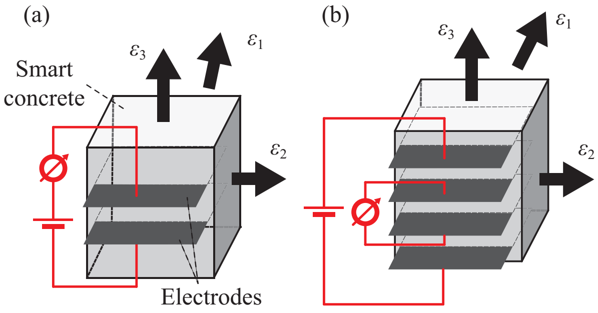

Figure 3.58 Schematic of 2-probe (a) and 4-probe (b) resistivity measurement setups.

3.5.4.2 Case study: embeddable smart blocks

In this section, a three-dimensional case study is presented in order to illustrate the combination of the proposed micromechanics approach with a FEM formulation. More specifically, a smart sensor made of self-sensing MWCNT-reinforced mortar subjected to laterally unconstrained quasi-static compressive loading has been modeled by the present micromechanics approach, introducing its mixed mechanical-electrical constitutive behavior within a FEM analysis, in the present case it is carried out using the commercial software ANSYS v15.0 [299]. This case study was already analyzed in previous work by the authors [103]. On the basis of the experimental results in [61], the variables of the micromechanics model, including filler properties, waviness and agglomeration effects, were fitted by parametric studies with very good agreements. Let us recall that the scope of previous work was restricted to laterally unconstrained uni-axial compression/stretching. In this work, the piezoresistivity coefficients are determined for laterally constrained uni-axial compression and, Afterward, the electrical response is computed by a coupled electro-mechanical calculation in ANSYS. It is also important to note that, as previously demonstrated in [103], the strain sensitivity of CNT-reinforced cement-matrix composites is slightly different under compression and stretching. However, the difference between the piezoresistivity coefficients under compression and traction is small enough that a common strain sensitivity is assumed.

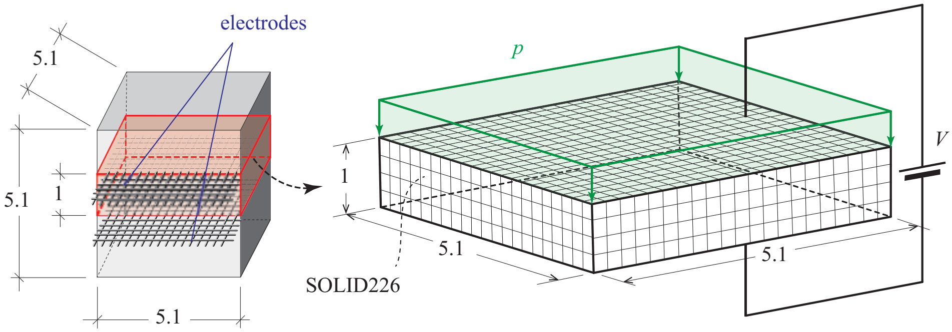

Figure 3.59 Geometry and dimensions of the self-sensing MWCNT-reinforced mortar and of the electrodes (units in cm) (a), and finite element modeling of the active region of the sensor (b).

The sensor is a cube with sides of 5.1 cm instrumented with two stainless steel nets as electrodes, placed at a mutual distance of 1 cm as shown in Fig. 3.59 (a). The electrical conductivity of mortar is chosen as 1.04×10^{-3} S/m and MWCNTs are type Graphistrength C100 with electrical conductivities in the range 10^0 to 10^7 S/m. In particular, a sensor with filler content of 0.75% mass content with respect to mass of cement is selected. The mass content with respect to mass of cement can be related to the filler volume fraction as $wt = f\rho_N/m_{cem}$, with ρ_N and m_{cem} being the mass density of CNTs and the mass of cement in the composite, equal to 50 kg/m^3 and 654 kg/m^3, respectively. Fig. 3.60 shows the electrical resistance as a function of the applied strain obtained in the experiments [61]. Furthermore, the theoretical results computed in previous work [103], denoted by "MA-1D", are plotted for a filler electrical conductivity of 10^4 S/m. In this work, the piezoresistivity coefficients have been computed under virtual experiments of laterally constrained uni-axial dilation and distortion as illustrated above. The rest of the micromechanical parameters of the model, including waviness and agglomeration effects, have been taken from reference [103] (readers are invited to refer to Figs. 26 and 27 in [103]). The active region of the sensor, defined as the material region (5.1×5.1×1 cm^3) between electrodes, has been discretized for computational purposes as shown in Fig. 3.59 (b). Assuming that the electrodes are much more conductive than the composite, it is assumed that the electrodes can be modeled as a coupling condition of constant voltage on the upper and lower faces of the active region. Standard elements SOLID226, defined with twenty nodes and four degrees of freedom per node (three translations and electric potential), have been chosen for the electromechanical numerical modeling. The experimental setup corresponds to a two-probe method, in which the lower electrode is grounded and the upper one is defined with a differential potential of 2.5 V. Finally, the Young's modulus and Poisson ratio of the composite are taken from the experiments as E=18 GPa and ν=0.2. By fitting the experimental results, inter-particle variation constants C_1=8.658, C_2=2.498 are computed and, accordingly, piezoresistivity coefficients λ_{11}=15.7, λ_{12}=16.20, λ_{44}=0.51 are obtained. It is observed in Fig. 3.60 that excellent agreements are found between the present approach and the experimental results, as well as with the previous theoretical model (MA-1D).

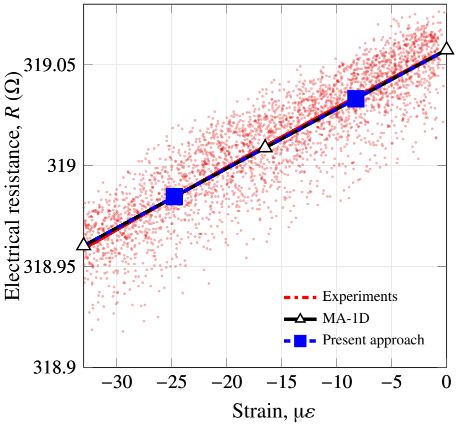

Figure 3.60 Comparison of the theoretical predictions and the experimental electrical resistance versus applied strain for mortar specimens with MWCNT concentration of 0.75% with respect to cement weight (λ_{11}=15.7, λ_{12}=16.20, λ_{44}=0.51, L_{CNT} = 0.25 μm, D_{CNT}=10 nm, V_o=0.56 eV, d_c=1.8 nm, ξ=0.68, ζ=0.90, θ^w=40°, C_1=8.658, C_2=2.498). MA-1D stands for the micromechanics approach of laterally unconstrained compression presented in reference [103], and the experimental data have been taken from reference [61].

Once the consistency of the present micromechanics approach in conjunction with a FEM analysis has been demonstrated, a variety of applications where the strain state is three-dimensional in nature can be now handled. In order to illustrate this, Fig. 3.61 (a) shows a more sophisticated model of the previous sensor. In this case, the electrodes are modeled in detail accounting for their geometry, the penetration depth of the electrodes into the specimen, as well as the influence of the material region surrounding the active region. Fig. 3.61 (b) shows the electric potential field computed by the present mixed micromechanics-FEM approach. This type of results opens a vast range of applications such as the optimization of the electrodes configuration, different sensor geometries, presence of damages, and simulation of sensor's embedding into full-scale RC structural components.

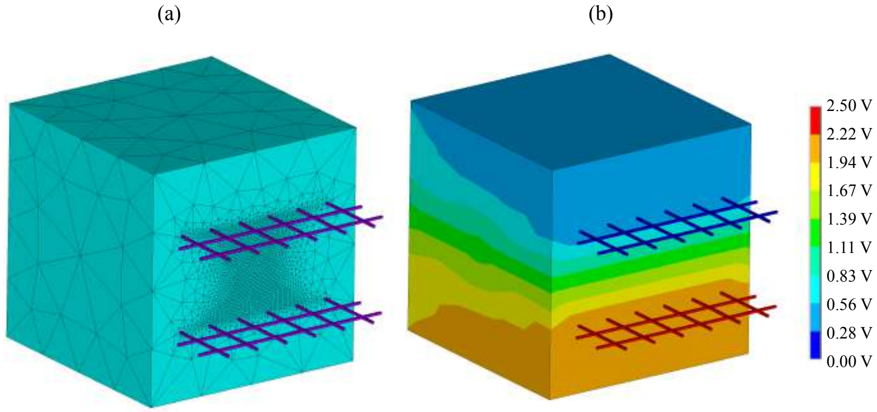

Figure 3.61 Detailed finite element model of MWCNT-reinforced mortar sensor (a), and electric potential field when a differential potential of 2.5 V is applied between the electrodes (b).

3.5.4.3 Conclusions

This subsection has presented a micromechanics approach in combination with a finite element formulation for the analysis of the response of CNT-reinforced smart concrete sensors subjected to arbitrary 3D strain states. The origin of the piezoresistive response of these composites is ascribed to (i) strain-induced changes in the volume fraction, (ii) changes in the conductive networks due to filler reorientation and, finally, (iii) changes in the tunneling resistance through variation of the inter-particle properties. New closed-form expressions of the ODFs of random arrangements of fillers under arbitrary dilation and distortion have been presented. On this basis, the variation of the percolation threshold is directly related to the ODFs by means of the Komori and Makishima model. Also, assuming that CNT-reinforced composites possess a cubic crystal symmetry, only three independent piezoresistivity coefficients are necessary to fully define the piezoresistivity matrix. The proposed approach has been shown capable of determining the piezoresistivity coefficients by two virtual tests, namely laterally constrained dilation and distortion. Afterward, utilizing the computed piezoresistivity matrix within a multiphysics FE formulation, using a commercial computational environment, it has been shown possible to analyze three-dimensional CNT-reinforced structures. Detailed parametric analyses have been carried out in order to illustrate the influence of the different properties of the constituents on the strain-sensing response of CNT-reinforced smart concretes. Finally, the accuracy of the proposed approach has been demonstrated by comparison with published experimental data.

The main contributions of this paper are summarized below:

- It has been shown that the dilation strain sensitivities of CNT-reinforced cement-based composites along the longitudinal (λ_{11}) and transverse (λ_{12}) directions are very similar, with slightly higher sensitivities in the transverse direction.
- The results showed that strains do not only generate variations of the shear components of the resistivity matrix but also of the diagonal terms. It has been shown that the interaction between shear strains and longitudinal/transverse resistivity terms is highly non-linear. However, for filler contents immediately above the percolation threshold, these terms disappear and the assumption of cubic crystal symmetry becomes valid. Overall, it has been shown that CNT-reinforced cement-based composites are also weakly sensitive to shear strains.
- Due to the similarities between the longitudinal and transverse piezoresistivity coefficients, as well as the low sensitivity under distortion, smart concrete strain sensors can be approximately modeled as volumetric strain sensors with one single piezoresistivity coefficient or gauge factor. This simplified model is ready to be applied in practical applications dealing with the use of smart concrete sensors embedded into RC structural components.
- The results of the parametric study have shown that the dilation piezoresistivity coefficients reach their maximum values for filler volume fractions at the percolation threshold. On the other hand, the shear piezoresistivity coefficients continuously increase with the filler content.
- Very close agreements of the present approach with experimental data from previous work have been reported. In addition, a comparison with previous theoretical results considering the ODFs of laterally unconstrained compression demonstrates the consistency of the assumptions imposed on the structure of the piezoresistivity matrix.

3.6 Conclusions

This chapter has presented the main contributions of this thesis in the study of the potential applications of CNTs for the development of smart composites. Firstly, a micromechanics model has been developed to estimate the overall electrical conductivity of CNT cement-based nanocomposites. The proposed approach distinguishes electron hopping and conductive networking as two different mechanisms contributing to the overall conductivity. In addition, waviness and agglomeration effects have been incorporated following similar frameworks to those previously used for the mechanical homogenization. An experimental campaign has been carried out to benchmark the theoretical results. Different cement-based composites, including paste, mortar and concrete, and loaded with different CNT contents have been manufactured. Afterward, the previously developed micromechanics approach has been extended to account for the uniaxial strain-sensing properties. To this aim, strain-induced effects have been considered such as (i) volume expansion and reorientation of CNTs, (ii) changes in the conductive networks, and (iii) changes in the tunneling resistance. A remarkable aspect of this approach refers to the use of ODFs to compute the strain-induced reorientation of the fillers and, consequently, the variation of the percolation threshold. Finally, the latter micromechanics approach has been extended, in combination with a finite element formulation, for the modeling of CNT-reinforced smart concrete sensors under arbitrary 3D strain loadings. By assuming that CNT-reinforced composites possess a cubic crystal symmetry, only three independent coefficients are necessary to fully define the piezoresistivity matrix. Utilizing the computed piezoresistivity matrix within a multiphysics FE formulation, it has been shown possible to analyze three-dimensional CNT-reinforced structures. The comparison of the theoretical results against the experimental data have demonstrated the validity of the proposed approaches.

The main findings of this chapter can be summarized as follows:

- The theoretical simulations confirm that the overall electrical conductivity of CNT-reinforced cement-based materials is governed by electron hopping and conductive networking mechanisms. The good agreements between theoretical and experimental data strengthen the consideration of the electrical response of CNT-reinforced cement-based composites of percolative-type.
- The aspect ratio of the nanofillers determines, along with the filler orientation distribution, the percolation threshold and, thus, is a critical design variable.
- Waviness and agglomeration of CNTs substantially affect the percolation threshold of composites. This fact, together with the previously stated conclusions regarding the mechanical properties, highlights the importance of developing efficient dispersion techniques.
- Both experiments and theoretical results confirm that the largest gauge factors are achieved at the percolation threshold.
- The theoretical simulations exhibit non-linear strain-sensing curves, predominantly for composites loaded with filler contents close to the percolation threshold and high strain levels.
- Overall, it has been shown that CNT-reinforced cement-based composites are weakly sensitive to shear strains.
- It has been shown that the dilation strain sensitivities of CNT-reinforced cement-based composites along the longitudinal and transverse directions are very similar. This fact, along with the low sensitivity under distortion, justifies the use of simplified modelings of CNT-reinforced cement-based sensors as volumetric strain sensors with one single gauge factor.

- Very close agreements of simulations with experimental data have proved the consistency of the cubic crystal symmetry assumption imposed on the structure of the piezoresistivity matrix.

The presented micromechanics models are envisaged to provide a valuable tool for the analysis of three-dimensional CNT-reinforced cement-matrix composites, including simulation of the embedding of smart concrete sensors into full-scale RC components. The proposed theoretical framework is efficient in terms of computational cost and, more importantly, it models the complex coupled electro-mechanical behavior of smart concretes on a well-founded physical basis. Overall, it can be concluded that the second objective of this thesis has been achieved.

4 CNTs for SHM applications in civil engineering

This chapter presents the works conducted for the analysis of the potential applications of CNT-reinforced composites in the realm of SHM. Together with the first experience of the author in the application of OMA techniques, this chapter introduces a novel electromechanical modeling of the dynamic response of CNT cement-based sensors in the time domain. This chapter is a summarized version of papers F and G.

4.1 Introduction

The aim of this chapter focuses on the application of CNT-reinforced Cement composites (CNTCs) as dynamic strain sensors for Structural Health Monitoring (SHM). To this end, the author was first introduced in the field of Operational Modal Analysis (OMA) with traditional off-the-shelf accelerometers. As a result of these first works, the author took part in a refereed journal article (paper G). In that work, the dynamic properties of the Montoro footbridge were identified by means of a multi-scale model updating approach in conjunction with ambient vibration tests. Afterward, and as a result of the research stay at the University of Perugia and the collaboration with professor Filippo Ubertini, the author developed a novel electromechanical modeling of CNT-reinforced cement-based sensors, apt for signal processing applications. On this topic there were some open issues that needed to be addressed. First, the experimental results in reference [205] showed that the electrical response of CNT-reinforced cement-based sensors under the action of sinusoidal loads contains superharmonics. In addition, the experiments also showed that the Frequency Response Function (FRF) of the sensors increases with the frequency of the excitation. The theoretical studies conducted by D'Alessandro *et al*. [63] could explain the superharmonics content in the electrical response by the differential equation governing the equivalent lumped circuit of a piezoresistive strain transducer. However, that sort of equivalent lumped circuit could not explain the increasing FRF, phenomenon that remained an unresolved issue. In order to find an explanation, the author developed a novel equivalent piezoresistive/piezoelectric lumped circuit inspired by a universal equivalent circuit proposed by Wanson *et al.* [339]. This model represents an enhanced version and a generalization of the model previously proposed in reference [63]. The results demonstrate that the proposed model can explain both phenomena affecting CNTCs, namely the superharmonic response under cyclic loading, as well as the amplification of the electrical signals with the frequency of excitation.

This chapter is organized as follows: Subsections 4.1.1 and 4.1.2 review the state of art of modal identification of footbridges and the electromechanical modeling of CNT-reinforced cement-based sensors, respectively. Then, Section 4.2 briefly introduces the ambient-vibration tests conducted in the Montoro footbridge, the numerical modeling, and the model updating process as a case study of OMA. Section 4.3 concisely presents the theoretical framework of the electromechanical modeling of CNT-reinforced composites. Section 4.4 presents a summary of the results achieved with the proposed equivalent electromechanical circuit and comparison with experimental results. Finally, Section 4.5 concludes this chapter.

4.1.1 Novel smart composite materials as a solution to the scalability limitations of traditional monitoring systems

The critical socio-economical and environmental importance of civil infrastructures makes condition-based maintenance of the utmost relevance for structural engineering. The growing concern with the aging and degradation of civil infrastructures (see e.g. [84]), the increasing complexity of new constructions, as well as the possible occurrence of catastrophic natural events have promoted a large number of Structural Health Monitoring (SHM) programs in the last two decades [64, 356, 161, 56, 295, 351, 256, 60, 167, 223, 255]. To monitor the health of a structure, SHM systems collect data from the structure to infer its structural integrity. Measurements are used to evaluate the state of the structure and detect the possible appearance of damage and its location. Hence, SHM is a wide field that encompasses several methodologies aimed to assess the health condition of a structure and reduce its life-cycle cost [35, 31]. In particular, continuous assessment of structural health has become one of the key issues of SHM. This online monitoring is typically conducted through an automated monitoring of the structure and the temporal variations of its properties. Recent field applications of continuous monitoring evidence its potential to enhance structural safety and life expectancy [241, 218, 107]. However, despite these great benefits, the number of continuous SHM applications is still scarce. One factor impeding the extensive applicability of SHM solutions stems from the inherent size of structures to be monitored, that is, their limited scalability. Most existing sensing solutions are hardly scalable without necessitating substantial costs and complex signal processing algorithms, making SHM financially unattractive to infrastructures owners due to their apparent low return on investments.

In the quest for feasible solutions to this scalability issue, Smart Materials/Structures (SMSs) are conceived as especially promising monitoring solutions. The concept of SMS can be understood as the last step in the objects produced by mankind. Originally, the human production started with the use of homogeneous materials directly provided by nature, followed by composite materials in which several constituents are combined so that the resulting properties can be adjusted. A further step is the development of materials with multifunctional properties in such a way that their properties can be adapted to in-service conditions. Overall, three types of SMS can be distinguished: SMS controlling their shape, SMS controlling their vibrations, and SMS controlling their health. Up to date, most

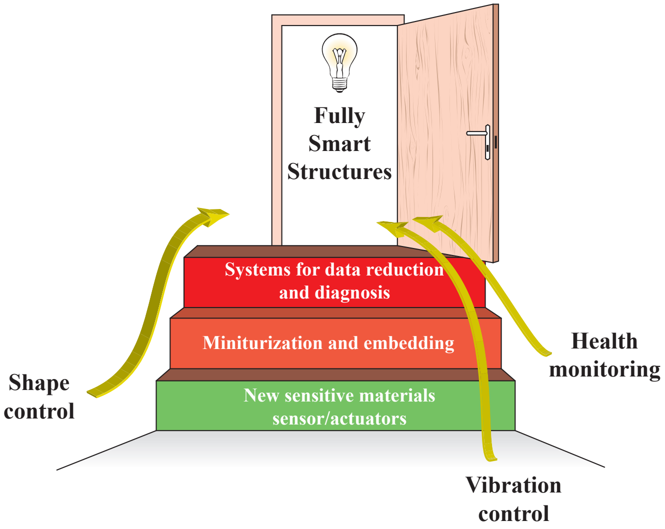

Figure 4.1 Schematic of SHM, shape control and vibration control in the context of Smart Materials/Structures (SMSs).

achievements in this field have only managed to create materials/structures that are self-sensitive by means of embedded sensors. The next step towards smarter structures would be to produce self-healing materials or with damage-mitigation properties. For damage mitigation, embedded actuators made of Shape Memory Alloys (SMAs) [300] have been shown capable of inducing compensating strains in regions of stress concentrations. On the other hand, just very few attempts have been done to manufacture self-healing materials. It is noteworthy the development of self-healing concretes doped with hollow-adhesive brittle fibers. The operating mechanism of these materials consists of releasing the adhesive when the fibers are broken in the region where cracks appear [109]. The development of these types of advanced materials can aid SHM at different levels at shown in Fig. 4.1, including [20]:

- Development of new self-sensing materials to produce sensors and actuators.
- Technologies to miniaturize sensors/actuators and embedding solutions without compromising the durability of the host structure.
- Development of efficient systems for optimization of data management and diagnosis.

In this line, the rapid growth of nanotechnologies represents a pioneering revolution in the development of novel sensors, including multifunctional materials that enable substantial improvements in the cost-effectiveness of SHM solutions for geometrically large systems. The development of new multifunctional and smart materials, and particularly electrically conductive CNT cement-based composites, offers a broad range of possibilities in the realm of SHM [118, 325, 92]. As shown in previous chapters, these composites exhibit strain-sensing capabilities (i.e. composites themselves also behave as sensors) by means of measurable variations of their electrical properties under applied mechanical deformations [99, 171, 324]. This exceptional property, together with the similarity and compatibility between these composites and structural concrete, can be used to develop distributed embedded strain-sensing systems with substantial improvements in the cost-effectiveness in applications to large-scale concrete structures [184, 120, 136, 277, 121, 125, 123]. Currently, the majority of the methods used for the local monitoring of concrete structures (e.g. strain gauges, optic sensors, piezoelectric ceramic, shape memory alloy, etc.) do not offer efficient solutions for embedded monitoring systems capable of getting information about the structural integrity and detecting damage [122].

Some recent results in the literature evidence the potential application of CNT-reinforced cement-based composites as continuous embedded dynamic strain sensors. It is worth noting the work of Materazzi *et al.* [205] who reported on the applicability of carbon nanotube-cement based composites as dynamic strain sensors. The electrical response of prismatic carbon nanotube-cement sensors was studied under harmonic loadings in the typical frequency range of civil structures. Their results demonstrated that a sinusoidal compression as input produces a sinusoidal variation of the electrical resistance plus harmonics as output. The contributions of Ubertini *et al.* [323, 325] furthered the study of the potential application of CNT-reinforced cement-based sensors for output-only modal identification of large concrete structures. In particular, those authors reported on the identification of the resonant frequencies of a large scale steel-reinforced concrete beam under laboratory conditions. Their results showed that CNTCSs can allow for modal identification over a frequency range up to 500 Hz. Another noteworthy contribution was made by Naeem *et al.* [226] who investigated the stress and crack sensing capabilities of MWCNT/cement composites subjected to flexural loadings. Specifically, those authors embedded long prismatic MWCNT/cement sensors at different locations of steel-reinforced mortar beams. Their results showed steep changes in the electrical resistance of the sensors at failure of the mortar, what proves the applicability of MWCNT cement-based nanocomposites as embedded continuous transducers for crack detection applications. Most literature works utilize Direct Current (DC) resistivity measurements. However, it has been reported that DC resistance measurement of CNTCSs exhibit time-based drift in the material's measured electrical output [205, 323, 325]. This phenomenon is often attributed to the material polarization, changes in the material's dielectric constant, piezoelectric effects or the combination of other electrical effects. Electrical polarization of CNTCSs results in signal distortions at low frequencies, what may make it difficult to monitor structures with relatively low resonant frequencies. Conversely, Alternating Current (AC) measurements have been shown to minimize the time-based drift. It is worth noting the work by Downey *et al.* [74] who presented a novel biphasic DC measurement approach for resistance measurements of self-sensing multi-functional materials. Their results demonstrated that the drift is eliminated by applying a periodic square charge/discharge signal. Also, those authors demonstrated the applicability of the proposed approach for damage detection and localization using two CNTCS beams.

4.1.2 Electromechanical behavior of CNT-reinforced cement composites

Although many authors have striven to develop pilot applications of CNT-reinforced cement-based composites, the development of theoretical approaches for the modeling of the dynamic response of these composites is still lacking and, as a consequence, the output of the sensors cannot be properly interpreted. Firstly, it is well known that cementitious materials primarily behave as dielectrics. When subjected to an electric field, the molecular dipoles of dielectric materials tend to get oriented in the direction of the field and, as a consequence, an opposite electric field to the applied one is induced. As a result of this so-termed polarization, the electric current decreases over time under the application of a constant potential difference [346, 40]. Hence, modeling of DC resistivity of CNT-reinforced cement-based composites must include both strain-dependent electrical properties and polarization effects. With this purpose, different equivalent lumped-circuit have been proposed in the literature. It is worth noting the work by Kang *et al*. [154] who performed Electrochemical Impedance Spectroscopy (EIS) testing to characterize the electrical properties of SWNT/PMMA composites. On the basis of impedance analysis, those authors developed a modified Randles circuit to represent the dynamic behavior of the sensors. As in common practice, strain sensing was incorporated by a linear dependence of the relative change of the internal resistance on the applied strain. Another noteworthy contribution was done by Loh *et al*. [195] on SWNT-PSS/PVA thin films. On the basis of frequency-domain EIS, an RC-circuit model was tuned to fit the experimental data. D'Alessandro *et al*. [63] proposed an electromechanical modeling of CNTCSs based on the Randles equivalent circuit. The lumped-circuit consisted of two resistors and a capacitor, accounting for the contact resistance, internal dissipation and electric polarization. A relevant conclusion of that work, in accordance with previously published experimental results [205], was that the dynamic response of CNTCSs contains superharmonics. Unfortunately, the proposed model failed to reproduce the increasing amplitude of the response with increasing frequency. Sanli *et al*. [270] proposed an RC equivalent circuit based on the impedance response of sensitive CNT/epoxy films. A noticeable aspect of that work concerns the consideration of not only strain-dependent internal resistance but also strain-dependent capacitance.

4.2 Ambient-vibration OMA for SHM applications

In this section, the use of OMA for ambient-vibration SHM applications is concisely outlined. In addition, the works developed in the field campaign of the Montoro footbridge in Córdoba (Spain) are presented as an application example.

4.2.1 Introduction

Structural Health Monitoring (SHM) aims at making a diagnosis of the actual state of a structure during its life cycle, that is, the condition of the constituent materials and the different structural members, as well as their full assembly [20]. The state of the structure must remain in the condition specified in the design in such a way that safety and serviceability are preserved. However, structures may be deteriorated by normal aging processes under environmental conditions, as well as by the appearance of damages caused by accidental events. From a structural perspective, damages are related to changes in the material or geometric properties of the system, as well as changes in the boundary conditions or connectivity, which adversely alter the structural performance of the system. The appearance of damage in a structure does not necessarily imply a complete loss of functionality, but rather that it is no longer operating in its optimal manner. Nonetheless, if damage progresses, the performance of the structure may reach a critical point where it ceases being operational, or even collapses. Note that implicit in the term damage there is a comparison with the original unaltered state of the structure. Therefore, damage detection techniques are based upon an assessment of the properties of interest during the life of the structure. The process of implementing a damage identification strategy is referred to as SHM. In virtue of the time-dimension of monitoring, the environmental and in-service conditions can be evaluated and, together with Usage Monitoring, it is also possible to estimate prognosis, including the evolution of certain damages, residual life, etc. Sensing systems on structures can alert the appearance of damages and maintenance operations can be planned accordingly, what is known as condition-based maintenance. Therefore, the life-safety and economic benefits arising from this philosophy depend upon the detection capability of the system so that corrective actions can be implemented before the damage implies a structural failure.

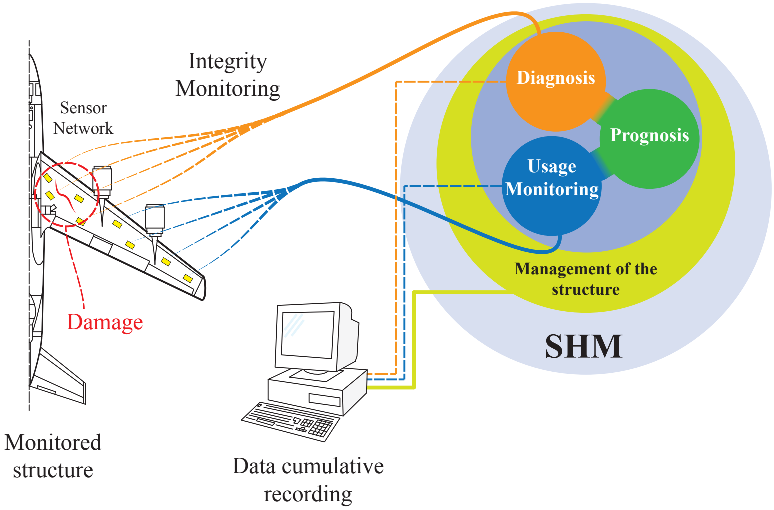

Figure 4.2 Organization of a SHM system.

A SHM system involves the integration of a sensor network, data transmission and processing of the measurements as schematically illustrated in Fig. 4.2. The first part of the system corresponds to the Integrity Monitoring function devoted to monitoring a certain damage. Other sensors on the structure of interest monitor the environmental conditions, which allows for performing the Usage Monitoring function. Through the comparison with the unaltered condition, the signals supplied by the Integrity Monitoring sub-system allow us to make a diagnostic. Combining the information of the Integrity Monitoring and the Usage Monitoring sub-systems, along with the knowledge of the principles of fracture mechanics and constitutive laws, it is also possible to make a prognosis of the damage evolution. Therefore, it is possible to carry out the health management of structures with condition-based repairs and maintenance operations.

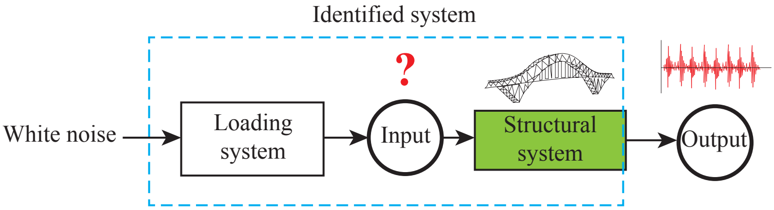

Figure 4.3 System scheme for output-only OMA.

Within this framework, vibration-based monitoring systems play an important role in many industrial and engineering applications such as design optimization, health monitoring, vibration control, and damage detection. This set of techniques is based on linear modal analysis, which assumes that the vibrational properties of a structure are completely defined by its resonant frequencies, corresponding mode shapes and modal damping. One possibility is to test structural systems under the action of controlled inputs, also termed Experimental Modal Analysis (EMA). However, most structures are subjected to in-service conditions and ambient excitations that cannot be controlled. In these cases, the use of output-only monitoring systems is imperative. Operational Modal Analysis (OMA) provides information concerning the dynamic behavior of in-service structures without inducing artificial excitations nor monitoring the loading conditions. Fig. 4.3 illustrates the system scheme for OMA. Given that in-service loads are unknown, they are assumed to be the result of a virtual loading system loaded by zero-mean Gaussian white noise. OMA can assist SHM systems as it identifies the properties of a structure in an operational environment, and damage appearance can be inferred by variations of the modal properties. Numerous OMA/SHM applications in the literature have been successfully applied to large-scale structures such as bridges [241, 356, 295, 223, 201, 167], multi-storey or tall buildings [56], dams [64, 351], historic buildings [256, 255], or offshore structures like wind turbines [80].

4.2.2 Case study: Montoro wooden footbridge[1]

The Montoro footbridge (Fig. 4.4) with a total length of 125.30 m is currently claimed to be the longest wooden footbridge in Spain. It is located in the village of Montoro in

---

[1] An extended version of this subsection is found in paper G.

Córdoba and crosses the Guadalquivir river.

In recent years, structural engineers have focused public attention on the need for improved footbridge monitoring and maintenance [397, 36, 328, 11]. All of these studies analyzed the dynamic response of these civil engineering structures under crowd induced loading. Zivanovic *et al*. [397] reported a detailed review about vibration serviceability of footbridges under human-induced excitation. This literature survey identified humans as the most important source of vibration for footbridges. That work highlighted that, of all vibration properties of the footbridge, damping is the most uncertain but is an extremely important parameter as the resonant behavior tends to govern the vibration serviceability of footbridges. Van Nimmen *et al*. [328] studied the methodology of two current codes of practice, the French SÉTRA guideline and the European guideline HIVOSS, both widely applied in engineering practice. In both evaluation procedures, it is required to estimate the dynamical characteristics of the structure, i.e. the natural frequencies, mode shapes, and damping factors.

The modern trend to construct light and slender footbridges has highlighted the importance of the dynamics of such structures. Moschas and Stiros [222] described the measurement and analysis of the deflections of a short-span pedestrian bridge in Athens, analyzed on the basis of geodetic techniques. A comparison between design and real ('as built') dynamic and static characteristics of the footbridge was presented. Bayraktar *et al*. [22] conducted ambient vibration tests of a 18.40 m span steel footbridge located in Trabzon, Turkey. The modal vibration based assessment of the Podgorica footbridge over the Moraca River in Podgorica, capital of Montenegro, was investigated by Zivanovic *et al*. [398]. That paper describes this lively full-scale footbridge, its numerical modelling and dynamic testing by modal analysis. Afterward, those authors proposed the finite element model updating of the Podgorica footbridge [399]. The ambient vibration-based assessment of the Morca suspension footbridge was studied by Gentile and Gallino [107]. Their experimental investigation was preceded by the development of a 3D FE model, where some uncertain parameters of the model were updated to enhance the agreement between theoretical and experimental natural frequencies. Ivorra *et al*. [145] studied the dynamic behavior of a pedestrian bridge in Alicante, Spain, which presented vertical and horizontal vibration problems. Caetano *et al.* [37, 38] studied the human-induced vibration of the Pedro e Inês footbridge at Coimbra, Portugal. The first article describes the studies undertaken at the design stage and the results of a thorough experimental assessment of the constructed bridge properties. The second article discusses the strategy adopted in the design and assessment of the efficiency of a vibration control system. The effects of the changing ambient temperature of the Dowling Hall footbridge was studied by Moaveni and Behmanesh [218]. Hu *et al.* [142] considered the feasibility of applying a vibration based damage detection approach, based on principal component analysis, to eliminate environmental effects for the Pedro e Inês footbridge, Portugal.

Monitoring of timber bridges, however, has received much less research attention. Stiros and Moschas [298] studied the lateral deflections of a timber pedestrian bridge in Patras, Greece. By using a robotic total station, the authors found a drop of 1.6 Hz in the natural frequencies of the bridge between 2007 and 2008 and then a gradual drop of approximately 8% between 2008 and 2012. The hygro-thermal response of a glulam beam of a pedestrian bridge located in Lisbon, Portugal, was simulated by Fortino *et* *al.* [96]. A 3D multi-Fickian numerical method was proposed to integrate the sensor-based hygro-thermal monitoring of timber bridges. The authors highlighted the need to extend their approach to incorporate the mechanical response of timber elements under the service life of bridges. The monitoring of the moisture content of a block-laminated timber bridge was also investigated by Tannert et al. [307]. Very recently, the monitoring of a long-span cable-stayed timber bridge was also investigated by Saracoglu and Bergstrand [271] with particular attention on the environmental effects.

In spite of the above valuable research works, we must note that studies on the vibration performance of timber bridges are still very limited, particularly when considering the influence of the anisotropic mechanical response of wood and its micromechanics on the structural behavior. We remark here that the anisotropy of microstructural phases may play a crucial role in determining both the effective as well as local response of the material [244].

The main contribution of this work is to produce a high-fidelity numerical simulation platform to acquire reliable information about the actual structural behavior of the Montoro timber footbridge. To achieve this purpose, ambient vibration tests were conducted in situ. An Optimal Sensor Placement (OSP) technique was applied to plan the measurements. This technique requires preliminary information on the modal parameters of the structure. Thus, a preliminary FE model defined by beam elements and isotropic constitutive relationships was implemented. Once the experimental data were collected and post-processed, natural frequencies were obtained and compared with the numerical values predicted by the preliminary model. The disagreement found between the numerical and experimental results revealed the limitations of this type of model. To improve our numerical predictions, a more reliable three-dimensional multi-scale FE model was prepared, taking into account the data collected experimentally and the strong anisotropic effects found in wood. In addition, several microstructural features coming from the ultrastructural scale and the mesoscopic scale were incorporated in the model, along with the macroscopic or structural scale (at the order of meters). A Genetic Algorithm (GA) optimization technique was adopted to update those micromechanical parameters which are either not well-known or subject to considerable variation. Hence, the differences among the experimental and numerical natural frequencies were minimized.

4.2.2.1 Description of the structure

The studied footbridge crosses the Guadalquivir river as it passes through Montoro, Spain (Fig. 4.4 (a)). The whole structure consists of four longitudinal girders stiffened by two lateral trusses linked at both ends. All the primary members are made of glued laminated timber with strength grade GL28h. The cross section presents a mean width of 2 m (Fig. 4.5) and is defined by four longitudinal girders with rectangular cross sections of dimensions 0.48 x 0.22 m and 0.36 x 0.22 m, for the upper and lower girders, respectively. These girders are connected by two lateral warren-type trusses with constant sections of 0.26 x 0.22 m. The joints between the elements are defined by embedded steel plates fixed with bolts that ensures highly stiff connections. The footbridge has a longitudinal length of 125.30 m, divided into five hyperstatic spans of 33.725-10.35-37.15-10.35-33.725 m (Fig. 4.5). The structure is supported at its two ends, in addition to the two intermediate reinforced concrete piles. The deck has a longitudinal slope of 3.5% and consists of a first

(a) Montoro bridge over the Guadalquivir river

(b) Cross section (c) Deck detail

Figure 4.4 General view and details of the bridge structure.

group of small transverse members laying on a second set of beams rotated by 30° with respect to the longitudinal axis of the bridge (Fig. 4.4 (b), (c)). The stiffness contribution of these two groups of beams is considered negligible when compared to the primary structure.

The bridge was constructed in 2010, and partial damage present in the lamination of some members of the footbridge (such as fiber separation) has been confirmed after a visual inspection of the structure. In order to assess the effect of these apparent damages, a rigorous modeling of the structure along with field tests are needed in order to assess the actual state of the structure at present, as well as to develop a basis for future SHM programs.

4.2.2.2 The numerical model

Macroscopic scale: Preliminary FE modeling of the Montoro footbridge. As a first approach, a preliminary 3D model of the footbridge was developed using the commercial finite element software ANSYS 15 [16] (Fig. 4.6). The type of element chosen for this analysis was the linear two-noded BEAM188 with six degrees of freedom per node and based on Timoshenko beam theory. It is important to note that the standard beam element formulation cannot capture the full rank stress-strain state developed in a

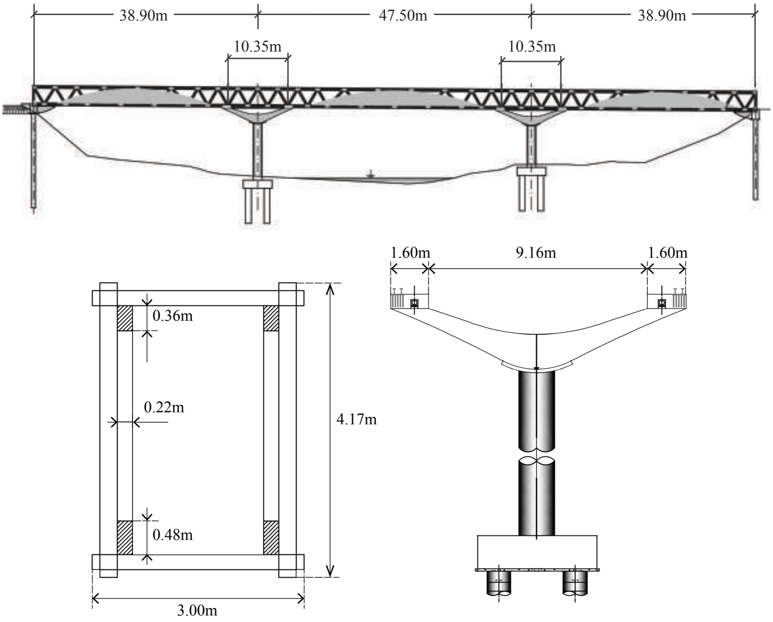

Figure 4.5 Elevation, cross section and pile geometry of the Montoro bridge.

highly anisotropic material such as wood. Nevertheless, the use of this type of element efficient in terms of computational memory requirements and CPU times so it is a good approach to conduct preliminary simulations. At this stage, eccentricities found among the longitudinal axes of adjacent structural members were ignored. All the connections between two or more members were modeled as rigid joints. The deck was not explicitly modeled due to its small contribution to the overall stiffness of the structure but its mass was incorporated to the model by means of lumped mass elements MASS21 at the level of the deck.

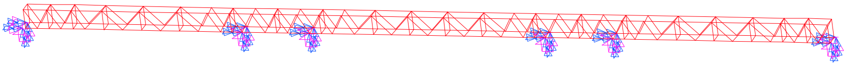

Figure 4.6 Preliminary 3D beam model of the bridge.

The footbridge's structure is made of glued laminated timber whose mechanical properties are extracted from the original structural design project [229]. Here, an isotropic material behavior was assumed, with a Young's modulus of 12.6 GPa, a Poisson's ratio of 0.2, and a density of 500 kg/m^3. Fixed boundary conditions were assumed at one end of the bridge, and rollers at the remaining supports.

The aim of this approach is to build a sufficiently simple model to determine the optimal location of a limited number of sensors on the structure in order to ensure the reliability of the modal data acquired from the vibration-based monitoring testing.

Macroscopic scale: Detailed FE modeling of the Montoro footbridge. In a second stage, a detailed 3D model was created using hexahedral solid finite elements. The type of element chosen in ANSYS was SOLID186, which exhibits quadratic displacement behavior. The element is defined by 20 nodes having three translational degrees of freedom per node. The main justification of adopting this type of element is that 3D solid elements are able to capture the full 3D stress-strain state developed in an orthotropic material. The macroscopic mechanical response of wood is defined by 9 material constants which are calculated by the computational homogenization scheme described below. Attention was paid to the orientation of the material principal axes in order to align the wood fibre direction with the longitudinal axis of each structural member. The finite element mesh consisted of 27920 hexahedral elements and 244538 nodes (Fig. 4.7).

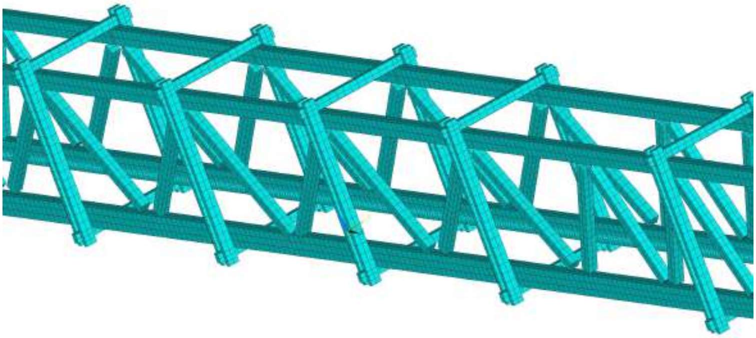

Figure 4.7 Detailed 3D solid FE model of the bridge.

The deck was also modeled by means of MASS21 type elements. Eccentricities between two (or more) member axes at joints were naturally introduced in the model by the use of 3D solid elements. Nevertheless, in some cases it was necessary to define sets of coupling equations among the degrees of freedom of those nodes located at the ends of converging members at some joints (for instance, between adjacent diagonals and main girders). By following this approach, we circumvented the physical modeling of those connections in which several members of different cross-sections converge at a common point. Thus, we avoided a possibly large number of degrees of freedom associated with the modeling of these connections. Finally, the boundary conditions were similar to those described in the preliminary FE model. However, in this new model, the boundary conditions were imposed by restraining the displacements to supporting surfaces, equivalent to the area of the neoprene bearings.

Microscopic scales: Multi-scale material modeling The computational homogenization scheme adopted to compute the anisotropic constitutive response of wood corresponds to the periodic boundary displacement fluctuations model typically associated with the modeling of (heterogeneous) periodic media [263, 264, 94, 45].

In the present multi-scale constitutive theory, it is assumed that the macroscopic or homogenized strain tensor at any arbitrary point of the macroscopic continuum is the volume average of the microscopic strain tensor field over the domain of a Representative Volume Element (RVE) of the material.

The procedure adopted here consists of modeling the mechanical response of timber by means of two fundamental spatial scales. These are the smallest or ultrastructural scale and the mesoscopic or intermediate scale. The homogenization of these two scales provides the material law to be used in all of our 3D solid model of the footbridge at the macroscopic or structural scale.

Ultrastructural scale: The ultrastructural or smallest scale is represented by the wood cell-wall, of the order of a few nanometers. At this level, wood contains three fundamental constituents: cellulose, hemicellulose and lignin. These basic constituents are considered to be universal, with properties inherent to all wood species [135]. The cellulose is a long and stiff polymeric fibre organised into crystalline and amorphous regions which alternate periodically along its length. The length of each crystalline cellulose portion, L_{cc}, varies between 26.5 and 36.4 nm [13]. This periodic arrangement is further covered by an outer surface made up of amorphous cellulose. The crystalline cellulose's width is about 3.2 nm [14], and the total width of the cellulose fibres (including the crystalline core and the outer amorphous sheeting) is 3.6 nm [72]. The degree of cellulose crystallinity, f_{cc}, is defined as the volume fraction of the crystalline portion of cellulose with respect to the total volume of cellulose, and varies between 45 and 60% [14, 42]. The volume fraction of (crystalline and amorphous) cellulose with respect to the total volume of cell-wall, f_c, ranges between 30 and 50% [314, 30]. Hemicellulose is a polymer with little strength built up of sugar units, with mechanical properties highly sensitive to moisture changes. The volume fraction of hemicellulose, f_h, with respect to the total volume of cell-wall, varies between 25 and 29% [289]. Lignin is an amorphous and hydrophobic polymer whose purpose is to cement the individual cells together and to provide shear strength.

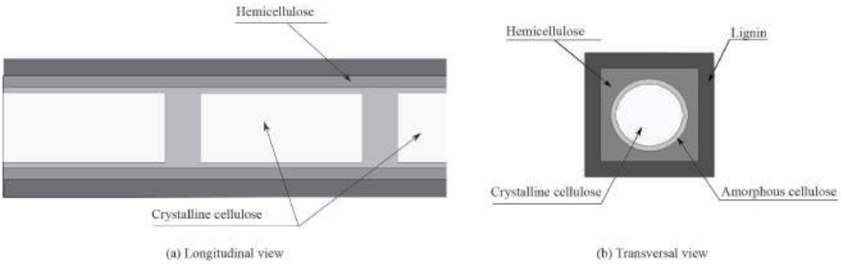

(a) Longitudinal view

(b) Transversal view

Figure 4.8 Schematic representation of a typical microfibril (not to scale). Note that crystalline and amorphous cellulose regions alternate periodically along the length of the microfibril.

These three fundamental constituents form a spatial arrangement called a microfibril which can be represented as a periodic unit building block of rectangular cross-section as shown in Fig. 4.8. A typical FE mesh of the RVE chosen to describe the mechanical response of the microfibril is shown in Fig. 4.9. For the sake of clarity, only one half of the geometry is shown here. The mesh consists of 4495 nodes and 3960 SOLID186 hexahedral elements. The mechanical properties of each of the basic constituents considered in our study are summarized in Table 4.1. This set of data corresponds to an equilibrium moisture content of 12% and are considered to be constants for all our multi-scale FE simulations.

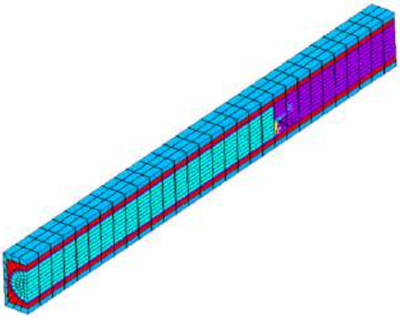

Figure 4.9 Typical finite element mesh of the microfibril RVE at the smallest scale considered in this study. For the sake of clarity, only one half of the mesh is shown here.

Table 4.1 Summary of the elastic mechanical properties of the fundamental constituents of wood adopted in all our multi-scale FE simulations [268, 49].

Constituent and its mechanical properties	**Value**
Crystalline cellulose	
Longitudinal Young's modulus, E_L^{cc} (GPa)	134
Transversal Young's modulus, E_T^{cc} (GPa)	27.2
Shear modulus, G_{LT}^{cc} (GPa)	4.4
Poisson ratio, ν_{LT}^{cc}	0.1
Amorphous cellulose	
Young's modulus, E^{ac} (GPa)	10.42
Poisson ratio, ν^{ac}	0.23
Hemicellulose	
Longitudinal Young's modulus, E_L^h (GPa)	2
Transversal Young's modulus, E_T^h (GPa)	0.8
Shear modulus, G_{LT}^h (GPa)	1
Poisson ratio, ν_{LT}^h	0.2
Lignin	
Longitudinal Young's modulus, E_L^l (GPa)	2
Transversal Young's modulus, E_T^l (GPa)	1
Shear modulus, G_{LT}^l (GPa)	0.6
Poisson ratio, ν_{LT}^l	0.3

Mesoscopic scale: At the mesoscopic or intermediate scale, of the order of tens to hundreds of micrometers, wood is composed mainly of an arrangement of long slender tubular cells, oriented nearly parallel to the axis of the stem and firmly cemented together. The cross-sections of the wood cells are (normally) hexagonal, and can be defined by means of four geometric parameters: T, R, θ and tc, as shown in Fig. 4.10. The parameters T and R correspond to the cell dimensions along the tangential and radial directions (of the fibres in the tree trunk). The length T varies between 23 and 30 µm and the length R between 30 and 40 µm [306]; the value of the angle θ ranges between 10 and 18° [341, 306]; and the

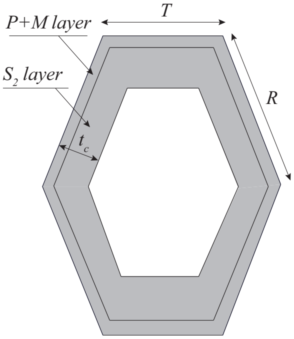

Figure 4.10 Schematic representation of a wood cell with hexagonal cross-section.

cell-wall thickness *tc* between 3 and 8 μm [306, 341]. A growth ring is typically formed by 71% of earlywood and 29% of latewood [269].

Depending on the proportions of the constituents and the specific orientation of the microfibrils with respect to the cell axis, that is, the MicroFibril Angle (*MFA*), the wall of wood cells can be divided into the compound middle lamella (*P*+*M*), which is characterized by a significant abundance of lignin (and therefore of shear strength), and the secondary layer (S), which is formed in turn by the layers S_1, S_2 and S_3. Among all these layers, the S_2 is the thickest and most influential factor in the mechanical behaviour of wood cells. It comprises about 80 – 90% of the total volume of cell-wall [135] and concentrates a high content of cellulose of about 50% in weight [30]. Because of this, we consider the wood cell-wall to be composed of only two layers: the compound middle lamella (*P*+*M*), comprising a relative volume of 20%, and the secondary S_2 layer, with a corresponding relative volume of 80%, both with respect to the total volume of cell-wall. Typically, the *MFA* of the S_2 layer varies between 0 and 22° [327]. Table 4.2 summarizes all these parameters with their corresponding intervals of variation.

Table 4.2 Summary of the micro-mechanical parameters chosen for this study and their corresponding intervals of variation [13, 14, 42, 314, 30, 289, 306, 341, 269, 327].

Micromechanical parameter	Interval of variation
Degree of cellulose crystallinity, f_{cc} (%)	45–60
Volume fraction of cellulose, f_c (%)	30–50
Volume fraction of hemicellulose, f_h (%)	25–29
Length of cellulose crystallites, L_{cc} (nm)	26.5–36.4
Radial dimension of wood cell, R (μm)	30–40
Tangential dimension of wood cell, T (μm)	23–30
Cell-wall thickness, t_c (μm)	3–8
Cell angle, θ (°)	10–18
Microfibril angle, *MFA* (°)	0–22

The *P*+*M* layer is assumed to be isotropic because of the random orientation of the *microfibrils* [251]. Its elastic properties are taken from [340]. These correspond to a Young's modulus of 2 GPa and a Poisson's ratio of 0.3. The (orthotropic) mechanical properties of the S_2 layer are calculated by means of the computational homogenization of the cellulose microfibril RVE of Figure 4.9, taking into account the direction of the cellulose microfibrils according to the *MFA*.

A typical finite element mesh of the RVE chosen to model the wood cell is shown in Fig. 4.11. The mesh consists of 1917 nodes and 1088 SOLID186 hexahedral elements. Finally, the periodic repetition of the wood cell forms the base (orthotropic) material for the macroscopic scale whose 3D solid FE modeling is detailed in Section 4.2.2.2.

Figure 4.11 Typical finite element mesh of the wood cell RVE at the intermediate scale.

4.2.2.3 Results and discussion

Pre-test analysis In order to plan the field testing of the structure, the vibration properties of the preliminary numerical model were calculated by performing modal analysis. The structural dynamic characteristics, including the first five modes of vibration, were obtained; the frequencies are shown in Table 4.3 and the first five mode shapes are illustrated in Fig. 4.12. The complex structural configuration results in very complex mode shapes, usually involving simultaneous lateral and vertical displacements. Furthermore, most of the mode shapes are localized and mainly develop in isolated spans because the short spans at the pile supports define a very stiff section. It is also important to note that the structure has a band of modes with low natural frequencies that are also close in frequency and highly coupled.

Table 4.3 Natural frequencies obtained from the preliminary FE model.

Mode	Frequency (Hz)	Description of mode shape	Nomenclature
1	0.81	First Lateral/bending mode of central span	1LBC
2	0.97	First Lateral/bending mode of end span	1LBE
3	1.97	Second Lateral/bending mode of central span	2LBC
4	2.24	Second Lateral/bending mode of end span	2LBE
5	6.47	First Vertical/bending mode of end span	1VBE

This preliminary model is utilized to define the optimal position of the accelerometers by means of an OSP method. The most often employed technique in practical applications is the Effective Independence (EFI) method introduced by Kammer [151]. The aim of this method is to search for the best set of sensor locations from the set of all candidate locations

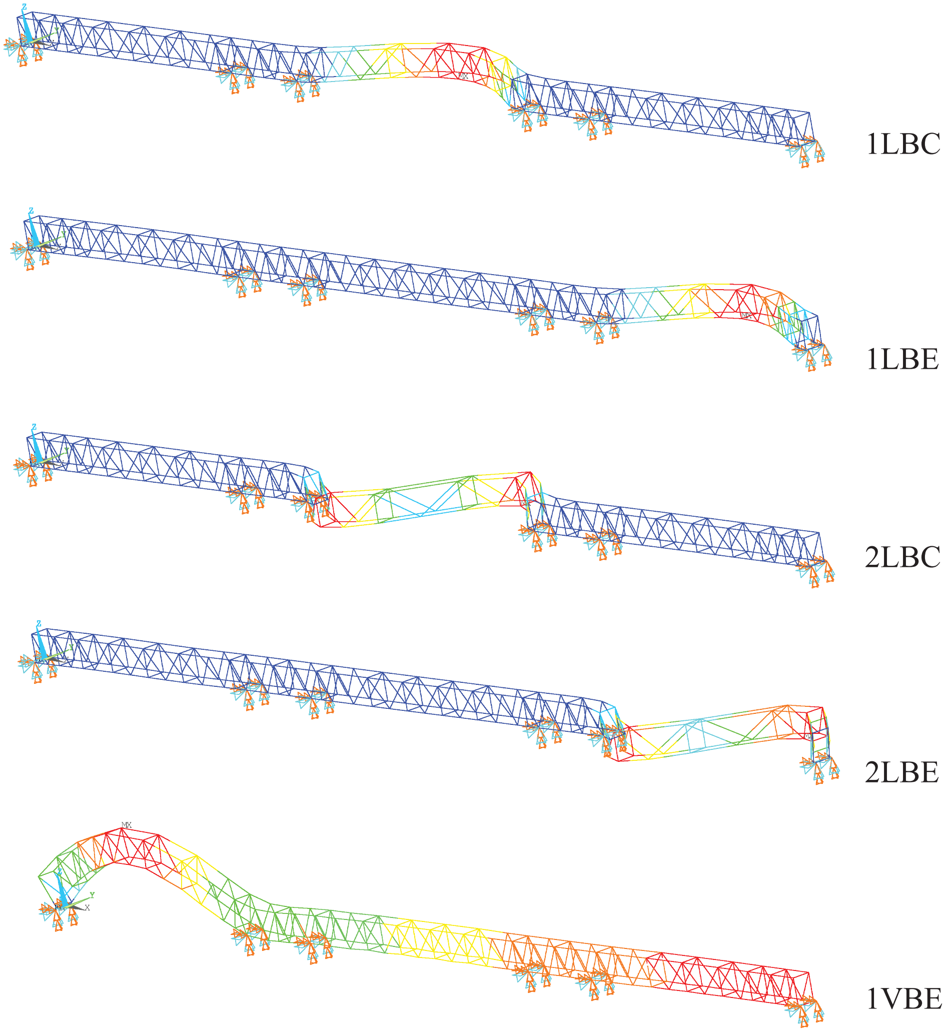

Figure 4.12 Modes of vibration calculated from the preliminary (beam) FE model.

in the structure, such that the linear independence of the mode shapes is maintained. The starting point of this method is the full modal matrix from a finite element model. All of the Degrees Of Freedom (DOFs) used in the FE model cannot be measured in the real structure due to physical limitations. Therefore, the DOFs corresponding to rotations and coordinates that cannot be measured are eliminated from the full modal matrix. Similarly, not all of the mode shapes can be experimentally measured, and hence some target modes are selected to be optimally detected. Hence, the rows corresponding to DOFs that can be measured are kept and the columns corresponding to target modes are retained in the full modal matrix. Hence, the Fisher Information Matrix (**FIM**) is then defined as:

$$\mathbf{FIM} = \boldsymbol{\phi}^T \boldsymbol{\phi} \tag{4.1}$$

where $\boldsymbol{\phi}$ is the mode shape matrix (computed by the preliminary numerical model). The **FIM** matrix has the following properties:

- It is symmetric.
- It is positive semi-definite, that is, its determinant is always positive and all of its the eigenvalues are positive.
- If the column vectors (in this case the mode shapes) are linearly independent, the matrix is full rank, i.e. the rank is equal to the number of the target mode shapes.

If the determinant of the **FIM** is zero, the columns of the modal matrix (i.e. the target modes) are linearly dependent. Therefore, the purpose of the EFI method is to select the best DOFs to place the sensors which maximizes the determinant of the **FIM**. To this aim, it is necessary to define the orthogonal projection matrix **E** as follows:

$$\mathbf{E} = \boldsymbol{\phi}\,\mathbf{FIM}^{-1}\,\boldsymbol{\phi}^T \tag{4.2}$$

Each element of the diagonal of the matrix **E** represents the fractional contribution of the i^{th} DOF to the rank of this matrix and, in particular, to the linear independence of the mode shapes. This is because the matrix **E** is an idempotent matrix whose rank is equal to the sum of the diagonal terms. Hence, the selection process results in an iterative process that can be summarized in the following steps:

1. The DOFs which cannot be measured physically are eliminated. The rows corresponding to DOFs from the modal matrix are deleted.
2. The DOFs which are required a priori for engineering reasons should be retained.
3. Target modes are selected from those of interest. Only the columns from the modal matrix that correspond to those target modes are retained.
4. Matrix **E** is computed. The diagonal of matrix **E** is sorted from the higher elements to the lower ones. The DOF with the lowest value is eliminated from the modal matrix.
5. This process is repeated until the number of DOFs that remain are equal to the desired sensor number of sensors.
6. At every step the FIM determinant determines the evolution of the process.
7. This procedure for the EFI optimal sensor placement method produces a sub-optimal solution in an iterative way.

The research group only could count on ten sensors. Therefore, three different setups were chosen to apply in the experimental measurements and are shown in Fig. 4.13. The first setup, called EFI-Total, was chosen by using the EFI optimal sensor methodology. Two specific setups were also considered to detect the particular behavior of specific spans with a reference sensor that remained fixed during the testing (sensor denoted with R-z).

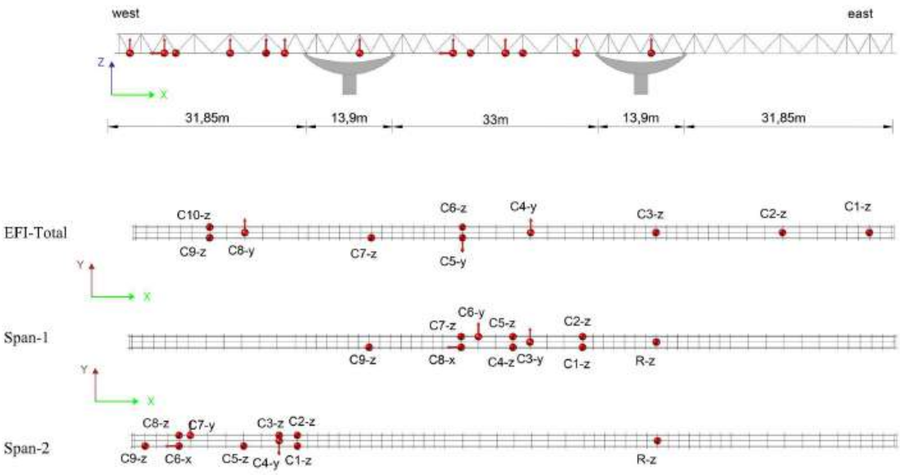

Figure 4.13 Deck measurement points for different setups: EFI-Total, SPAN-1, and SPAN-2.

Field vibration test Ambient vibration tests were conducted determine the vibrational properties of the bridge following the schedule described above. For the ambient vibration tests, a LMS Scadas mobile with 16 channels and 24-bit ADC technology controlled by LMS Test.Lab software was employed. Two types of accelerometers were considered: 8 PCB seismic accelerometers model 393B31 (PCB Piezotronics) with a sensitivity of 10 V/g ±5%, a broadband resolution of 0.000001 g·rms, a measurement range of 0.5 g peak value, and a frequency range of 0.1 - 200 Hz; and 8 Columbia force balance accelerometers model SA-107BHPC with an output voltage of ± 7.5 V, a range of ±0.5 g with a 1 g counterbias, two of them with horizontal sensitivity (shown in Fig. 4.14). The time responses were recorded for 15 minutes, and excitations were provided from natural effects (wind, soil movement, river crossing, etc.).

An example of the time series collected during ambient vibration tests is depicted in Fig. 4.15. It can be observed that the level of excitation in the bridge produced by the ambient excitation is considerably low (of the order of 10^{-3} g). The LMS PolyMAX system identification method [240] was used to identify the first three natural frequencies by using cross power spectra between the recorded measurements (see Fig. 4.16). Table 4.4 shows the natural frequencies experimentally assessed. We can observe that significant differences were found between these experimental measurements and the numerical results obtained by the preliminary FE beam model. The relative errors found between the numerical results coming from this preliminary model and the experimental values are 42%, 48% and 46% for the mode shapes 1LBC, 2LBC and 2LBE, respectively.

Model tuning and numerical results. As we are interested in improving the predictions of our multi-scale model, we set up an updating strategy based on a GA algorithm

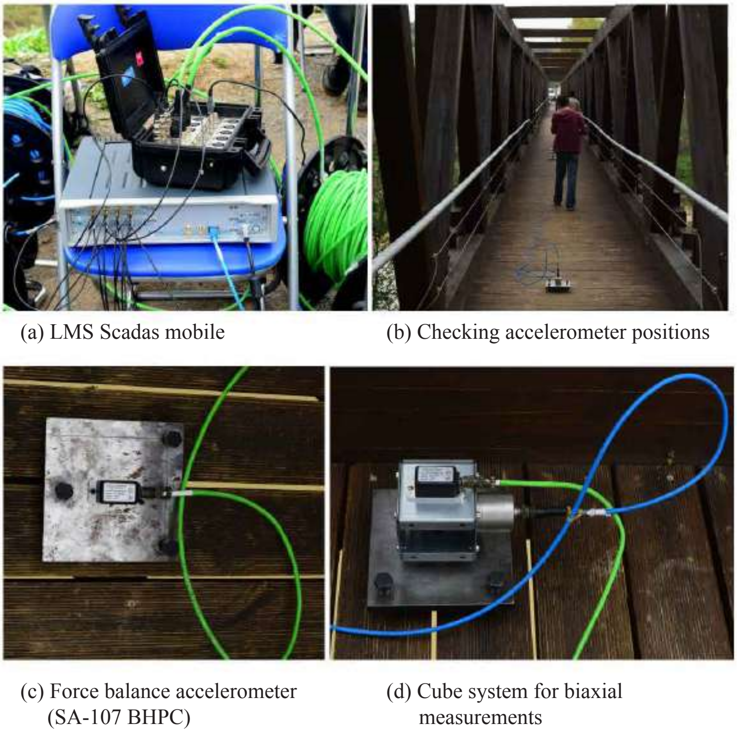
(a) LMS Scadas mobile

(b) Checking accelerometer positions

(c) Force balance accelerometer (SA-107 BHPC)

(d) Cube system for biaxial measurements

Figure 4.14 Ambient vibration testing and details of accelerometer connections.

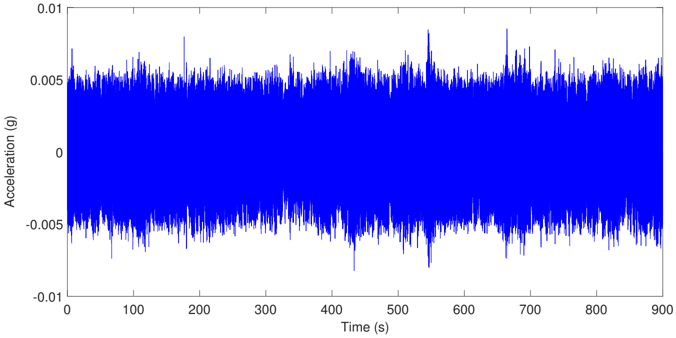

Figure 4.15 Acceleration time series collected during the ambient vibration test at reference C1-z.

[215] to calibrate the micro-mechanical parameters defined in Table 4.2. The optimization process starts with the creation of a trial set of micromechanical parameters for each individual according to the genetic methodology. The performance is estimated by the fitness function which is quantified as the sum of the relative errors between each of the three natural frequencies measured experimentally (shown in Table 4.4) and their numerical

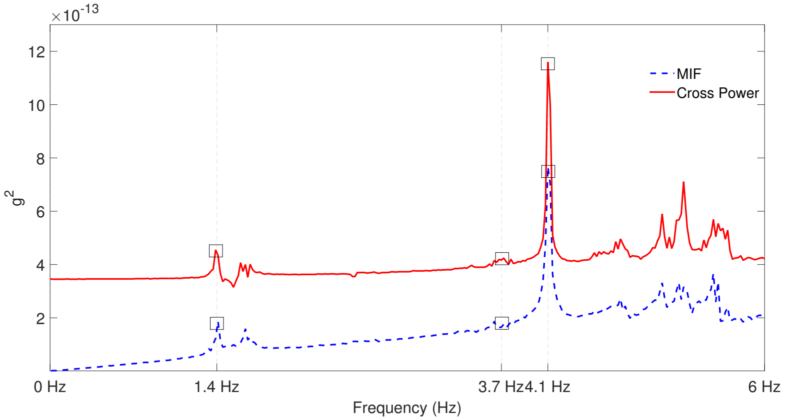

Figure 4.16 Crosspower estimated from auto-correlation functions and the mode indicator function (MIF).

Table 4.4 Modal frequencies and damping ratios from vibration parameter estimation.

Mode	Mode shape	EFI-Total		Span-1		Span-2	
		f (Hz)	ζ (%)	f (Hz)	ζ (%)	f (Hz)	ζ (%)
1	1LBC	1.40	0.64	1.40	0.85	-	-
2	2LBC	3.79	0.76	3.77	1.12	3.79	1.90
3	2LBE	4.18	0.18	4.28	0.26	-	-

counterparts. Each relative error was calculated as the frequency error normalized by its corresponding experimental frequency. Furthermore, no weighing of the different frequencies was considered. After investigating different convergence criterion, the number of individuals per generation was fixed to 20. Using the Parallel Computing Toolbox in Matlab [208], this optimization problem ran on 8 different processors. A cross-over rate of 0.8, which is the default value in Matlab, was adopted.

The GA was applied on our multi-scale model by following a bottom-up approach. That is, at each GA iteration, the algorithm seeks candidate solutions of individuals at the ultrastructural and mesoscopic RVE levels. With a preliminary set of micromechanical parameters at hand, the computational homogenization process is performed at the (bottom) ultrastructural scale, delivering the effective mechanical properties for the next (upper) mesoscopic scale. The homogenization is repeated again at the the mesoscopic RVE level in order to produce the effective material properties for the simulations which involve the macroscopic solid FE model. The fitness value is computed at the end of each iteration of the GA search until convergence is reached. The criterion adopted to stop the optimization process is to set a tolerance of 0.05 to the average change in the value of the fitness function. Once the GA is completed, the chromosomes of the best fit individuals are selected. At this point, the optimization scheme delivers the specific values of the micromechanical parameters so that the differences found between the experimental measurements and our numerical predictions are minimized. Table 4.5 lists the final values of the optimized micromechanical parameters. By adopting the above values in our multi-scale material model we obtain a set of nine (orthotropic) constants which are shown in Table 4.6. Here, the 3-axis represents the longitudinal direction of wood fibres.

Table 4.5 Optimal values of micromechanical parameters optimized by the GA.

Micromechanical parameter	Optimal value
Degree of cellulose crystallinity, f_{cc} (%)	55.59
Volume fraction of cellulose, f_c (%)	48.87
Volume fraction of hemicellulose, f_h (%)	27.65
Length of cellulose crystallites, L_{cc} (nm)	34.98
Radial dimension of wood cell, R (µm)	37.89
Tangential dimension of wood cell, T (µm)	27.09
Cell-wall thickness, t_c (µm)	4.87
Cell angle, θ (°)	10.00
Microfibril angle, MFA (°)	0.22

Table 4.6 Orthotropic macromechanical properties obtained by updating the multi-scale 3D solid FE model.

E_1 (GPa)	0.123	G_{12} (GPa)	0.128	ν_{12}	0.144
E_2 (GPa)	1.018	G_{23} (GPa)	0.484	ν_{23}	0.062
E_3 (GPa)	5.885	G_{13} (GPa)	0.204	ν_{13}	0.007

As one of the purposes of this study is to investigate the actual anisotropic properties of the wood found in the footbridge, we proceed to model a 3D solid beam made of the above material properties and subject to three point bending (simulation not shown here). By analyzing this model, we obtain an updated longitudinal effective Young's modulus of 13.15 GPa. We note that the above Young's modulus is close to the (isotropic) value of 12.6 GPa adopted in the original structural design (which was prepared with glued laminated timber members of strength grade GL28h [111]) and in the preliminary beam FE model. A similar analysis, but with the material principal axes rotated in 90°, allows us to determine a transverse effective Young's modulus of 0.31 GPa, which is near the design value of 0.42 GPa reported for the same structural strength class [111]. The fact that the updated longitudinal and transverse Young's moduli approach the corresponding design values allows us to confirm that the structure is not significantly damaged to compromise the elastic properties of the material. In addition, we studied the sliding and rolling shear modulus (G_o and G_r, respectively) [389] for a timber specimen subjected to shear loads. The modeling (not shown here) consisted of applying a linearly-increasing displacement field in a 4-cm-thick parallelepiped-shaped specimen. For the sliding shear modulus, the displacements were applied in the longitudinal direction of wood fibres, producing angular distortion (uniform shear strain) in the plane formed by the longitudinal axis and the thickness direction. We measured the applied shear strain and the resulting shear stress, and with this information we calculated the sliding shear modulus. The rolling shear modulus was computed similarly, but the displacements were applied in the direction perpendicular to wood fibres, producing shear strains in the plane perpendicular to the longitudinal axis of wood fibres. For these two numerical tests, we obtained a G_o of 315.1 MPa and a G_r of 105.76 MPa. Furthermore, the density updated by means of the present approach is 548.8 kg/m^3, which is almost 10% greater than the density of 500 kg/m^3 adopted in the preliminary beam FE model.

Table 4.7 Numerical frequencies (Hz) obtained by ambient testing (EFI), preliminary FEM and updated solid FEM.

Mode No.	Mode shape	Exp. (EFI)	Preliminary FEM	Updated solid FEM
1	1LBC	1.40	3.04	1.89
2	1LBE	-	3.26	1.99
3	1LBE	-	3.51	2.13
4	2LBE	-	-	3.7
5	2LBC	3.79	5.92	3.79
6	2LBE	4.18	6.03	3.97

Table 4.7 shows the first 6 natural frequencies obtained from the preliminary and the updated solid FE model in comparison with the experimental results obtained by ambient testing. Our first numerical frequency reveals a difference of 35% with respect to the first experimental frequency, corresponding to the mode shape 1LBC. A perfect agreement is found between the fifth numerical frequency and the second experimental frequency, corresponding to the mode shape 2LBC. Our sixth numerical frequency shows a 5% of difference with respect to the third experimental frequency, corresponding to the mode shape 2LBE. The better fitting between the experimental and analytic frequencies for the solid FEM pinpoints the great importance of anisotropy in this type of structures.

4.2.2.4 Conclusions

A multi-scale modeling strategy has been proposed to investigate the modal response of a timber footbridge. The multi-scale framework takes material information coming from sub-micrometer dimensions up to the macroscopic scale. The structural behavior has been monitored experimentally using ambient vibration testing. The modal parameters obtained experimentally have been compared with FE simulations. A first preliminary model has been developed by means of standard beam elements and with an isotropic material. Furthermore, a second model has been elaborated with 3D solid elements. The material properties considered here have been computed numerically by means of the proposed multi-scale modeling approach. A model updating process based on a GA technique has been adopted to improve the predictions of the multi-scale 3D solid FE model. By following this optimization scheme, uncertain micro-mechanical parameters of the material have been calibrated in order to capture the actual behavior of the structure.

The present multi-scale approach has made it possible to capture the strong anisotropy found between the longitudinal and transversal directions of wood lumbers. Great differences have been found between the results produced by an isotropic solid 3D model and the updated (anisotropic) multi-scale model, highlighting the importance of considering the anisotropic effects of wood in the modeling process. The analysis of the numerical results have allowed us to conclude that the structure does not show signs of significant damage. Finally, the overall good agreement found between the results of our updated numerical simulations and the corresponding experimental measurements reveals the potential predictive capabilities of the present GA/multi-scale/experimental approach to capture accurately the actual behavior of complex materials and structures.

4.3 Modeling of CNT-reinforced dynamic transducers[2]

In this section, we present an electromechanical model for CNTCSs inspired by a universal equivalent circuit proposed by Wanson *et al.* [339]. The model represents an enhanced version and a generalization of the model previously proposed by some of the authors in [63].

Prismatic samples of nanocomposite cement paste doped with CNTs are considered in this work and denoted as CNTCS. The samples exhibit a change in their electrical resistivity under applied mechanical deformation, what can be measured by connecting an external data acquisition (DAQ) system to electrodes embedded in the specimens. To elucidate the electrical behavior of CNTCSs under applied mechanical deformations, the samples are connected to a power source providing a stabilized potential difference across their electrodes, V, and to a digital multimeter measuring the time trace of the current passing through the specimen, $I(t)$, as illustrated in Fig. 4.17, where t is the time variable. This configuration is commonly referred to as two-probe configuration. Coaxial cables are used to make connections so as to limit electromagnetic interference and noise.

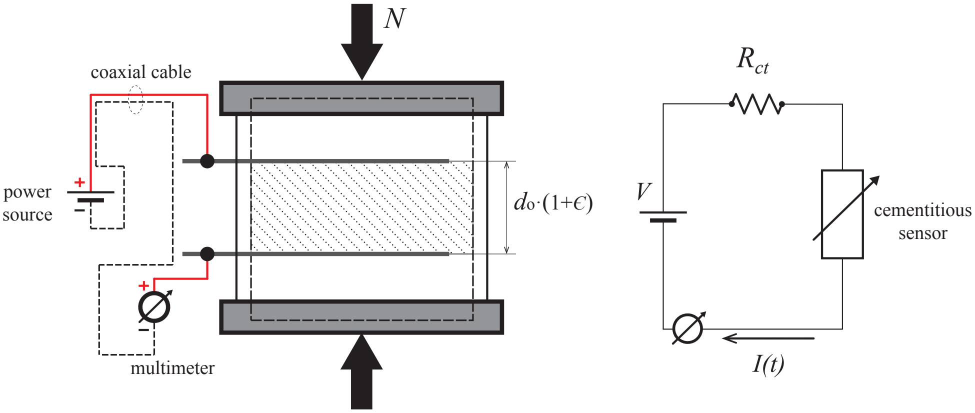

Figure 4.17 Layout of the two-probe method set-up.

As discussed above, many experimental studies have reported on the dynamic response of these smart materials, and they agree on two different phenomena:

- The response in terms of apparent electric resistance of CNTCSs, that is, the ratio between applied voltage and measured current, subjected to a cyclic mechanical loading, N, is defined by an harmonic distortion with respect to the monochromatic input.

---

[2] An extended version of this section is found in paper G.

- The Frequency Response Function (FRF) of the electric resistance of CNTCSs, that is, the amplitude of the response over the amplitude of the mechanical input, increases with the frequency of excitation, i.e., the amplitude of the resistance time series increases with the frequency of excitation.

An adequate electromechanical modeling must simultaneously reproduce both phenomena.

4.3.1 Piezoresistive equivalent circuit

All the studies conducted so far have ascribed the strain-sensitivity of CNT reinforced nanocomposites to a piezoresistive behavior. The change in the electrical resistivity under applied mechanical strain is attributed to three main mechanisms: (i) strain-induced changes in the volume fraction, (ii) filler reorientation and, (iii) changes in the tunneling resistance [103]. All the previously proposed lumped-circuit models for the electromechanical characterization of CNTCSs are based on this principle and, thus, the strain-sensing capability is assumed to be only caused by changes in the internal resistance or capacitance [154, 195, 126, 63]. Although some variants can be found in the literature, the main sensing cell is the one represented in Fig. 4.18 (a). From this modeling approach, the active volume of the specimen, defined as the portion d_o of the sensor in between the selected pair of electrodes, is modeled as a capacitor and a resistor in parallel. R_{ip} and C_{ip} denote internal resistance and capacitance, respectively, while R_{ct} comprises contact resistances for cables, electrodes, and the specimens. In the case of the DC two-probe measurement method, represented in Fig. 4.17, the time evolution of the current through the sample is governed by the following differential equation [63]:

$$\frac{\mathrm{d}I(t)}{\mathrm{d}t} + \frac{I(t)}{\tau} = \frac{V}{\tau \overline{R}} \tag{4.3}$$

where $\overline{R} = R_{ct} + R_{ip}$, and

$$\tau = \frac{C_{ip} R_{ct} R_{ip}}{\overline{R}} \tag{4.4}$$

is the characteristic time of the circuit.

When a mechanical strain ϵ (negative in compression) is applied to the sensor, the distance between the selected electrodes varies from d_o to $d_o(1+\epsilon)$ and, consequently, R_{ip} and C_{ip} vary, while R_{ct} remains approximately constant. In this first stage, we hypothesize that only the internal resistance is influenced by the mechanical deformation, so that the resistance changes as $R_{ip} = R_{ip}^o + \Delta R_{ip}$, where ΔR_{ip} represents the incremental change. In addition, the relationship between the relative change in the internal electrical resistance, $\Delta R_{ip}/R_{ip}^o$, and the axial strain, $\epsilon(t)$, is assumed to be linear:

$$\frac{\Delta R_{ip}}{R_{ip}^o} = \lambda \epsilon(t) \tag{4.5}$$

where λ denotes the gauge factor of the sensor.

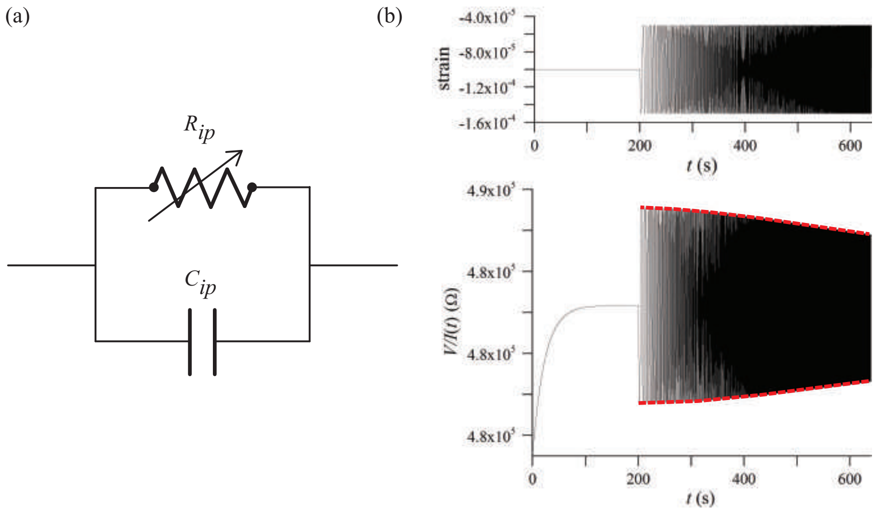

Figure 4.18 Sketch of the sensing unit commonly used in the literature for electromechanical piezoresistive modeling of CNTCSs (a), and numerical test showing apparent electrical resistance with forward sweep of the frequency from 0.1 to 3.0 Hz (b).

As illustrated in Fig. 4.17, the current passing through the sensor, $I(t)$, under a stabilized voltage, V, and axial strain, $\epsilon(t)$, is measured using a multimeter. From this model, the ordinary differential equation defining the time evolution of the current $I(t)$ is obtained by substituting Eq. (4.5) into Eq. (4.4), and after some rearranging of Eq. (4.3) one finds:

$$\frac{\mathrm{d}I(t)}{\mathrm{d}t} + \frac{1}{\tau\overline{R}}\left(R^o_{ip} + \frac{R_{ct}}{1+\lambda\epsilon(t)}\right)I(t) = \frac{1}{1+\lambda\epsilon(t)}\frac{V}{\tau\overline{R}} \tag{4.6}$$

Hence, the response of the sensor subjected to a harmonic axial deformation, $\epsilon(t) = -E\sin(wt)$, of amplitude E and circular frequency w, is governed by the following linear differential equation with time-varying coefficients:

$$\frac{\mathrm{d}I(t)}{\mathrm{d}t} + \frac{1}{\tau\overline{R}}\left(R^o_{ip} + \frac{R_{ct}}{1-\lambda E\sin(wt)}\right)I(t) = \frac{1}{1-\lambda E\sin(wt)}\frac{V}{\tau\overline{R}} \tag{4.7}$$

The solution of this differential equation, in terms of apparent electrical resistance, $R_a(t)$, defined as the ratio between the imposed voltage and the measured current, can be approximated as [329]:

$$R_a(t) = \frac{V}{I(t)} \approx R^o_a(t) + R^t_a(t) \tag{4.8}$$

where $R^o_a(t)$ is a slowly varying component related to charge build-up in the capacitor, and $R^t_a(t)$ is a fast component associated with strain sensing. This latter quantity is generally written as:

$$R_a^o(t) = R_{ip}^o \lambda E \sum_{n=1}^{\infty} a_n \sin(nwt + \phi_n) \tag{4.9}$$

This equation describes an harmonic distortion with respect to the monochromatic input, thus suggesting that the response of the sensor is characterized by superharmonic components of coefficients a_n and phase lags ϕ_n. The presence of superharmonics is not related to nonlinearities, but only to the time-varying nature of the governing linear differential equation. This behavior complies with the first requirement expected for the modeling and, therefore, it is possible to fit the response of a CNTCS subjected to a cyclic loading as shown in references [154, 63]. However, if Eq. (4.6) is solved for the case of an axial loading under a frequency sweep, the second requirement is not met. As can be seen in Fig. 4.18 (b), the amplitude of the electrical resistance series decreases with increasing frequency of excitation and, consequently, the FRF is a decreasing function which is in disagreement with the experimental results presented in the literature.

4.3.2 Piezoelectric equivalent circuit

The reason for the amplification of the electrical signal with increasing frequency of excitation may be attributed to the formation of certain energy source. A similar behavior can be found with traditional piezoelectric materials, such as certain crystals and ceramics, in which an electric charge is accumulated in response to applied mechanical stress. To the best knowledge of the authors, all the published works to date have only associated the self-sensing capabilities of CNTCSs to a piezoresistive behavior. However, since this behavior apparently does not explain the frequency response and the amplification of the electric signal under sweep frequency tests, the authors conducted experimental tests to determine whether some kind of piezoelectric effect can alter the dynamic response of the nanocomposites. Fig. 4.19 shows an example of the results obtained for this aim. In this case, a S1 type MWCNT/cement-paste sensor (later defined in Subsection 4.4.1) was subjected to external strains without power supply (V=0 V) using an universal testing machine. The voltage drop across the specimen was measured through a PXIe-4302 24-bit analog input module mounted on a PXIe-1071 chassis. Data from a load cell monitoring the compression force applied to the sensor were obtained using a 24-bit bridge input module (PXIe-4330). A correlation between the voltage and the applied loading can be observed. This confirms the coupling between the electric and the mechanical fields.

In order to verify whether this piezoelectric behavior in combination with the previous model can explain the increasing frequency response function, a new sensing cell, as represented in Fig. 4.20 (a), is analyzed. Assuming an ideal piezoelectric behavior, the charge generated by strain, q, can be related to the current introduced into the system I_p, as:

$$I_p(t) = \frac{\mathrm{d}q(t)}{\mathrm{d}t} = S_q \frac{\mathrm{d}\epsilon(t)}{\mathrm{d}t} \tag{4.10}$$

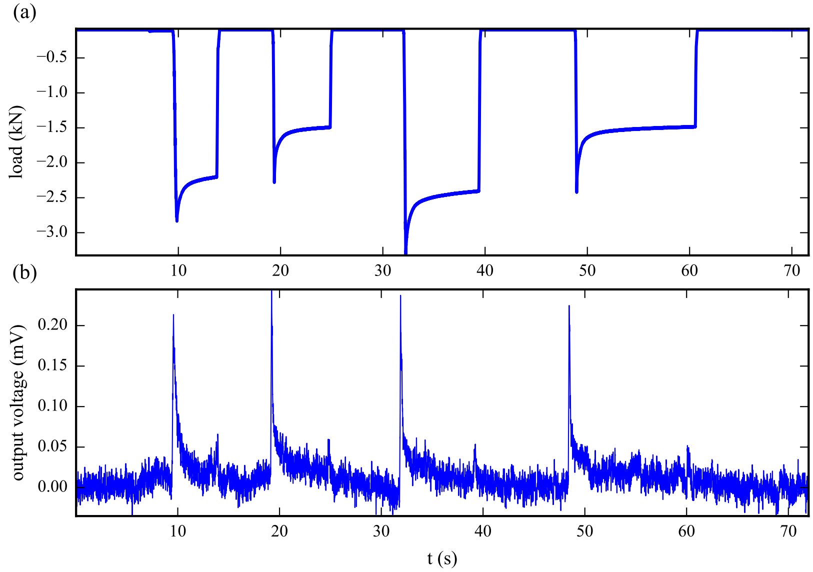

Figure 4.19 Time series of uni-axial compressive load acting on CNTCS without power supply (a), and output voltage (b) (V=0 V, specimen S1).

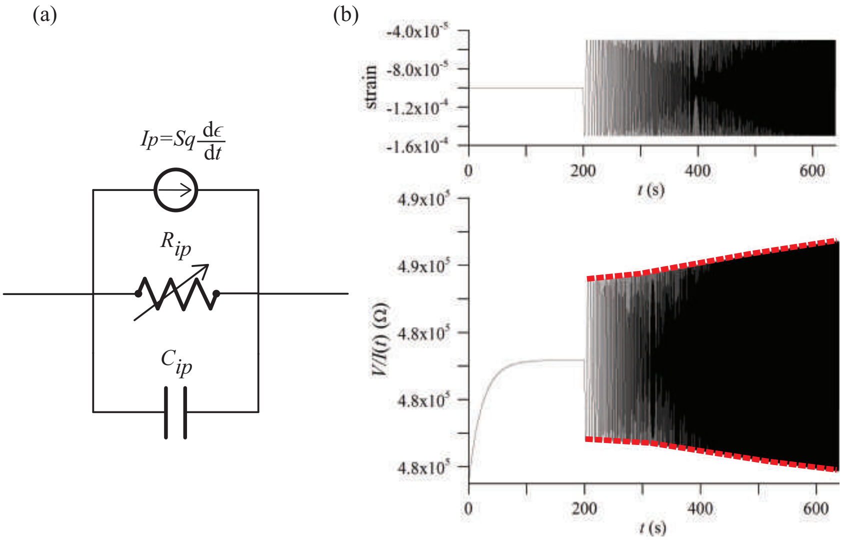

Figure 4.20 Sketch of the new sensing unit proposed for electromechanical piezoresistive modeling of CNTCSs (a) and numerical test showing apparent electrical resistance with forward sweep of the frequency from 0.1 to 3.0 Hz (b).

with S_q being a piezoelectric parameter. Hence, Eq. (4.6) can be rewritten by simply applying Kirchoff's circuit laws as:

$$\frac{\mathrm{d}I(t)}{\mathrm{d}t}+\frac{1}{\tau\overline{R}}\left(R_{ip}^{o}+\frac{R_{ct}}{1+\lambda\epsilon(t)}\right)I(t)=\frac{1}{1+\lambda\epsilon(t)}\frac{V}{\tau\overline{R}}+\frac{S_q}{C_{ip}R_{ct}}\frac{\mathrm{d}\epsilon(t)}{\mathrm{d}t} \tag{4.11}$$

The resulting differential equation with time-varying coefficients preserves a similar structure to Eq. (4.6), and the response under cyclic loadings also contains superharmonic components. However, in this case, the response under sweep frequency exhibits an amplification of the electrical signal with increasing frequency, as can be seen in Fig. 4.20 (b).

4.3.3 Novel piezoresistive/piezoelectric equivalent circuit

In the light of the experimental evidence of the piezoelectric response of CNTCSs, a new lumped-circuit model is proposed to characterize its dynamic electromechanical behavior. The universal equivalent circuit model by Wansom *et al.* [339] is modified so as to include the piezoresistive effect associated with changes in the interparticle resistance following an applied mechanical strain, as well as the new piezoelectric effect. Regarding the piezoresistive effect, as adopted in the first model, many authors consider that only the internal resistance is influenced by the mechanical deformation. The origin of this assumption comes from the experimental results published by Han *et al.* [126]. However, there are also some other works defending the influence of the external strain on the internal capacitance, such as the work of Sanli *et al.* [270]. In that work, experimental results on MWCNT/epoxy composites showed that, for small strains, there exists a linear relationship between the external strain and the internal capacitance. An explanation for this relationship is illustrated in Fig. 4.21. Each nanotube (or nanotube agglomerates) has a resistance R_{CNT}, and due to the inevitable coating of matrix material around the MWCNTs, there exists a dielectric gap which can be modeled as R_c and C_{gap} corresponding to the contact resistance and capacitance, respectively. Under the action of an external strain, the distance between CNTs is on average reduced, which will result in a decrease of R_c and an increase in the C_{gap} value. Hence, for completeness, the strain-induced internal changes are assumed to be caused by variation of not only the internal resistance but also the internal capacitance. Therefore, a second gauge factor based on the relative capacitance change, λ_C, is defined as [270]:

$$\lambda_C=-\frac{\Delta C/C_o}{\epsilon(t)} \tag{4.12}$$

where C_o is the unstrained capacitance and ΔC is the change in capacitance.

The proposed equivalent circuit is illustrated in Fig. 4.22 (a). The sensing cell consists of two resistor-capacitor combinations (in parallel). The first branch is defined by R_{ip} and C_{ip} denoting the internal resistance and capacitance, respectively. It is followed by a second set of resistor-capacitor element defined by R_{pm} and C_{pm}. Regarding the universal equivalent circuit proposed by Wansom *et al.* [339], the first resistor-capacitor set stands for the inter-particle matrix path, in which the origin of piezoresistivity/piezoelectricity is hypothesized to take place, and the second one represents the interface response. For simplicity, the branches that represent the unreinforced matrix and the percolation path

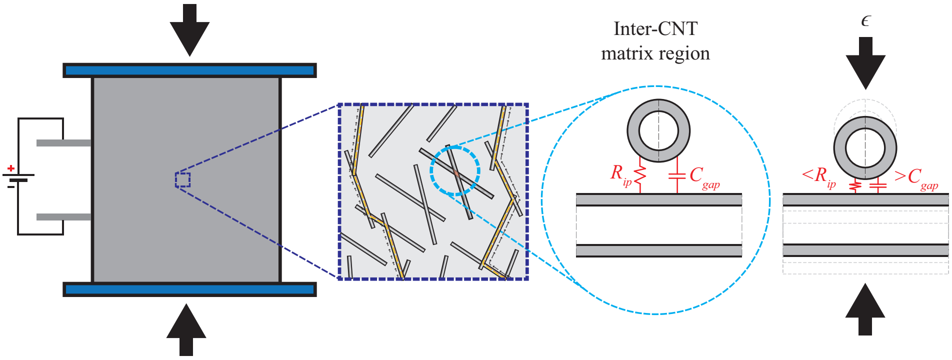

Figure 4.21 Schematic illustration at the micromechanical level of the equivalent RC model of the MWCNTs reinforced cement-based nanocomposite.

have been neglected as they presumably do not significantly contribute to the overall piezoresistivity of the CNTCSs. Moreover, the resistor R_{ct} encapsulates the contact resistances for cables, electrodes, and the specimens. In total, eight unique variables are required to characterize the behavior of the CNTCSs according to this model. In this thesis, the proposed equivalent circuit was modeled using Simulink in MATLAB®. The equivalent complex impedance ($Z_{eq}(w)$) can be calculated as:

$$Z_{eq}(\omega) = R_{ct} + \frac{1}{R_{ip}^{-1} + i\omega C_{ip}} + \frac{1}{R_{pm}^{-1} + i\omega C_{pm}} \tag{4.13}$$

Fig. 4.22 (b) shows a schematic of how the compression strain-induced changes lead to changes in CNTCS Nyquist impedance plot. The proposed model has an impedance response similar to previously published results (e.g. see [339]).

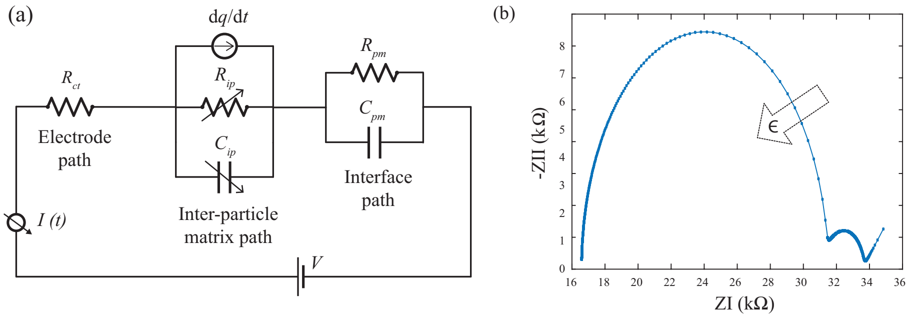

Figure 4.22 Equivalent electrical model (a) and simulated Nyquist diagram of CNTCS (b).

4.4 Results and discussion

The numerical tests presented in this section have been organized into three sections: step response under unloaded condition, harmonic excitation and frequency sweep analysis. At first, the analyses are used to verify the accuracy of the proposed equivalent circuit with comparison against experimental data. Furthermore, the tests are intended to demonstrate the capability of this approach to reproduce the two main features expected in the dynamic response of CNTCSs:

- The electric response of CNTCSs under harmonic excitations contains superharmonics.
- The frequency response function (FRF) of the sensor increases with the frequency of excitation.

4.4.1 Experimental methodology

With the objective of validating the proposed model for CNTCSs, the model is used to reproduce the response of different CNTCS samples previously fabricated by the authors for material characterization and model validation. In particular, experimental data presented in references [205] and [63] are here considered and a comparison with the previous model is conducted. The samples were made of cement paste doped with 2wt.% of MWCNTs type Arkema Graphistrenth C100, with respect to the weight of cement. Cement-paste matrix was utilized because it provides more homogeneous materials in comparison with mortar or concrete. The nanofillers were dispersed in the cement matrix by 15 minutes of mechanical mixing and 15 minutes of sonication with a power of 225 W. Two different types of prismatic specimens were used as shown in Fig. 4.23. The first type, (S1), has a cross-section of 40 x 50 mm^2, and height of 50 mm. The embedded electrodes are stainless steel nets. Specifically, the two inner electrodes are placed at a distance of 2 cm, the external electrodes have a relative distance of 4 cm, and the distance between an internal and an external electrode is 1 cm. The second sample, (S2), has a square cross-section of 40 x 40 mm^2, and height of 160 mm. In this case, the electrodes are copper wires with a diameter of 1 mm, embedded in the middle of the sample. To avoid significant amplification phenomena within the working frequency range, the sensors were designed to have a natural vibration frequency similar to that of the acceleration transducers commonly used in civil engineering applications. The natural frequency of the sensors, f_o, was estimated using a well-known formula for the axial vibration of continuous rods:

$$f_o = \frac{1}{2L}\sqrt{\frac{E}{\rho}} \tag{4.14}$$

where L is the length of the sensor, E is its Young's modulus and ρ is the mass density. Eq. (4.14) is valid assuming a linearly elastic material, fixed axial displacements at both ends of the specimen and modeling the sensor as a monodimensional element. This assumption is a rough approximation of the natural frequency of the sensors which is useful for estimating at least its order of magnitude. In particular, assuming a tangent Young modulus equal to 7000 MPa, and using the measured value for ρ, equal to 1680 kg/m^3, Eq. (4.14) yields f_o=6.4 kHz in the case of S1 specimens.

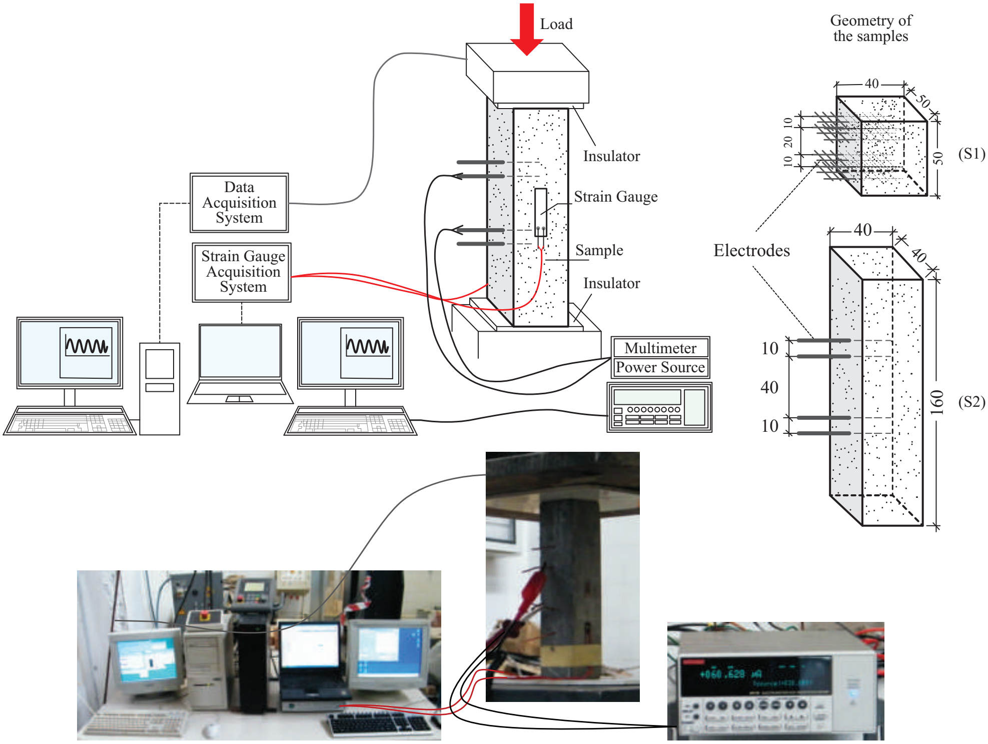

Figure 4.23 Setup of harmonic sinusoidal tests and geometry of the samples.

Fig. 4.23 shows the configuration of the dynamic tests. Two teflon sheets provided insulation between the sample and the testing machine. The samples were instrumented with two strain gauges placed at mid-height on opposite lateral sides. The axial loads were applied with a hydraulic press, type MTS Model 243.40T. The tests were conducted applying sinusoidal compressive loads with both constant and sweep variation of frequencies. The electromechanical tests were carried out after a polarization of 1000 s. The acquisition system of the load consisted of an MTS Force Transducer Model 661.23F-01. The measurements were sampled with a Spider8 device at a sampling frequency of 25 Hz. During the tests, a stabilized voltage of 30 V was applied with an electrometer type Keithley, model 6517B, with resistivity test fixture, model 8009. The electrical current was acquired and then sampled at 13.5 Hz.

Four electrodes were embedded in the samples with the purpose of allowing measurements in different configurations, namely two-probe and four-probe methods. In the case of four-probe measurements, a stabilized current source is applied to the outer electrodes, while inner electrodes are only used for measuring [121]. However, the scope of this work is limited to the two-probe method and therefore only the internal electrodes were used as schemed in Fig. 4.17. The reason for this choice is that the two-probe method permits the use of higher voltages what results in a more accurate measurement and a higher evidence of electrical variations. In addition, the particular position of the internal electrodes, at the same height of the strain gauges, allowed us to correlate the strain condition with the electrical response of the CNTCSs. Nevertheless, future developments of this work shall explore the applicability of the proposed lumped circuit to different test configurations, such as the four-probe method.

4.4.2 Step response in the absence of loads

The objective of this first series of tests is to verify the validity of the proposed lumped electrical circuit model in the absence of mechanical deformations. The apparent electrical resistance is derived from the measured time history of the electrical current, $I(t)$, in response to a constant voltage difference, $V = 1.5$ V, and taking $R(t) = V/I(t)$. The numerical solution is obtained by the Runge-Kutta method and a model-updating algorithm is implemented in order to fit the model parameters $\left\{R_{ct}, R_{ip}, R_{pm}, C_{ip}, C_{pm}, \lambda, \lambda_C, S_q\right\}$. The objective function seeks to minimize the least-squares difference between the numerical and the experimental results. In particular, R_{ct} is directly obtained from the initial value of measured current intensity. The resulting parameters are presented in Table 4.8. In this case, the sensing capability is not activated, so there are not significant differences compared to previous piezoresistive modeling approaches. The accuracy of the model is verified by the quality of the fitting in Fig. 4.24.

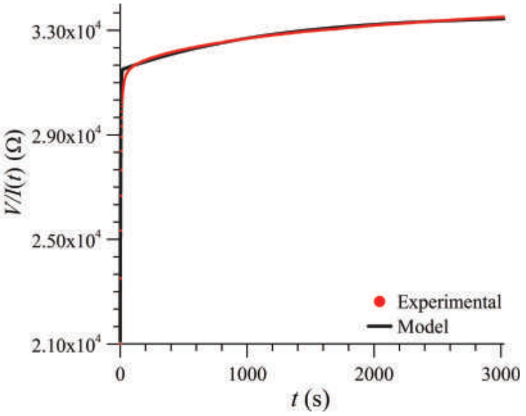

Figure 4.24 Comparison between experimental results and analytical predictions for the step response of CNTCS (V=1.5 V, specimen S1).

4.4.3 Response under cyclic loading

The objective of the second set of tests is to assess the possibility of characterizing the strain sensitivity under harmonic excitations using the proposed circuit model. The experiments

Table 4.8 Fitted model parameters for the electrical step response of CNTCS (V=1.5 V, specimen S1).

R_{ct} (kΩ)	21.12	C_{ip} (μF)	385.70	λ	-
R_{ip} (kΩ)	10.36	C_{pm} (μF)	5.59E+5	λ_C	-
R_{pm} (kΩ)	2.12			S_q (A)	-

were conducted with the specimen S2 on different dates, and different room conditions. Therefore, the model parameters have been fitted to every test. In this particular case, two different frequencies of excitation, 0.1 Hz and 0.2 Hz, have been selected. Figs. 4.25 (a) and (b) show the full-length time histories of measured strain for the frequencies of 0.1 Hz and 0.2 Hz, respectively. The tests were conducted after the application of a constant potential difference of 30 V. A constant compression load of 2 kN was applied for a duration of 240 s followed by sinusoidal loads with intensity varying from 2 kN to 4 kN. The values of the applied stresses were chosen to investigate the electrical response of the sensors in the elastic uncracked state. The total duration of the tests was 360 s. In this case, the updating algorithm has been defined as a multi-objective optimization problem to simultaneously fit both experiments. In addition, in order to highlight the improvements of the present circuit with respect to previously proposed approaches, the piezoresistive modeling shown in Section 4.3.1 and documented in reference [63] is also analyzed. The fitted parameters for the newly proposed piezoresistive/piezoelectric model, A, and the previous piezoresistive model, B, are presented in Table 4.9. It is noted that in this test, as well as in all of the analyzed cases, the gauge factor based on the relative capacitance change, λ_C, has not shown a substantial effect on the response. A similar conclusion was reached by Han *et al.* [126] who experimentally showed that the compressive loading only causes a little insensitive and irregular change in capacitance of MWCNT/cement composites. The time traces of the electrical resistance measured in the experiments, as well as the ones predicted by models A and B, are shown in Fig. 4.26. It can be seen that the proposed equivalent circuit, model A, leads to accurate results for both frequencies of excitation. Conversely, model B which only considers the piezoresistive behavior is shown unable to reproduce the frequency-dependent amplitude of the electrical resistance.

Table 4.9 Fitted model parameters for cyclic loadings of 0.1 Hz and 0.2 Hz (V=30 V, specimen S2). Models A and B correspond to the newly proposed piezoresistive/piezoelectric and previously published piezoresistive modeling, respectively.

Model A (piezoresistive/piezoelectric)						**Model B** (piezoresistive)					
R_{ct} (kΩ)	200.00	C_{ip} (μF)	300.00	λ	300.00	R_{ct} (kΩ)	404.01	C_{ip} (μF)	19.98	λ	802.55
R_{ip} (kΩ)	289.50	C_{pm} (μF)	2.00E+04	λ_C	2.21E-09	R_{ip} (kΩ)	46.41	C_{pm} (μF)	745.78	λ_C	3.08E-14
R_{pm} (kΩ)	50.00			S_q (A)	-0.40	R_{pm} (kΩ)	54.84			S_q (A)	-

In order to gain a better insight into the potential of the studied equivalent circuit, the electrical response in the frequency domain is analyzed. In this case, similarly to the latter tests, a frequency of excitation of 2 Hz is selected. The fitted parameters for models A and B are presented in Table 4.10. It is worth noting that parameters of model A are similar

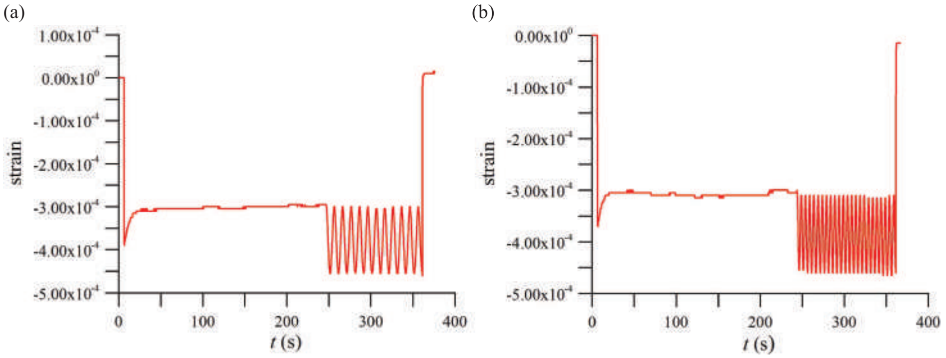

Figure 4.25 Strain series for cyclic loadings of 0.1 Hz (a) and 0.2 Hz (b) (V=30 V, specimen S2).

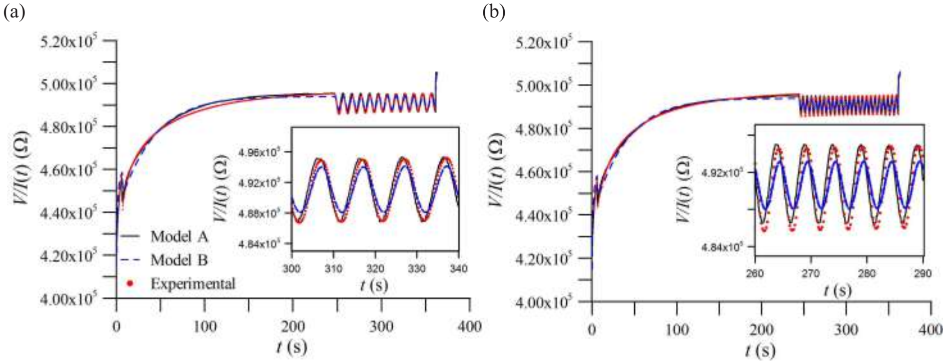

Figure 4.26 Comparison between experimental results and analytical predictions of the response of CNTCS for cyclic loadings of 0.1 Hz (a) and 0.2 Hz (b) (V=30 V, specimen S2). Models A and B correspond to the newly proposed piezoresistive/piezoelectric and previously published piezoresistive modeling, respectively.

in Tables 4.9 and 4.10, even though some differences are evidenced, that are conceivably determined by different testing conditions. On the contrary, parameters of model B as identified in Tables 4.9 and 4.10 show large differences, what most likely indicates that modeling errors are more significant in this case. Figs. 4.27 (a), (b) and (c) show the time history of the apparent electrical resistance obtained in the experiment, by model A, and model B, respectively. The slowly varying component, $R_a^o(t)$, associated with the polarization of cement-based materials, has been eliminated with a high-pass filter with a cutoff frequency of 0.2 Hz. Fig. 4.27 (d) shows the power spectral density (PSD) of these three signals. In agreement with Eq. (4.9), the results reported therein demonstrate that the dynamic response of the sensor is not monochromatic, but rather contains superharmonics at 4 Hz, 6 Hz, and other multiples of 2 Hz. Both methodologies can reproduce the superharmonic content of the electrical signals with fairly good agreements with the experimental data. This explains why previous piezoresistive modelings have been shown able to reproduce the response of CNTCSs under the action of one single value of harmonic loading.

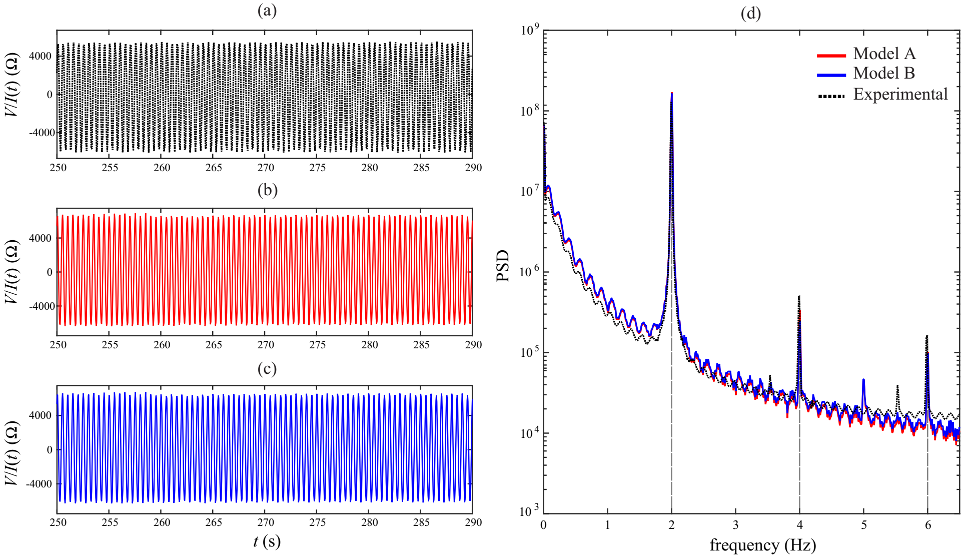

Figure 4.27 Variation of the apparent resistance obtained in experiments (a), model A (b) and model B (c) and their PSDs (d) under 5 Hz sinusoidal axial loading (V=30 V, specimen S2). Models A and B correspond to the newly proposed piezoresistive/piezoelectric and previously published piezoresistive modeling, respectively.

Table 4.10 Fitted model parameters for cyclic loading of 2 Hz (V=30 V, specimen S2). Models A and B correspond to the newly proposed piezoresistive/piezoelectric and previously published piezoresistive modeling, respectively.

Model A (piezoresistive/piezoelectric)						**Model B** (piezoresistive)					
R_{ct} (kΩ)	129.74	C_{ip} (μF)	285.00	λ	300.00	R_{ct} (kΩ)	13.20	C_{ip} (μF)	0.00	λ	196.00
R_{ip} (kΩ)	313.53	C_{pm} (μF)	2.13E+04	λ_C	0.00	R_{ip} (kΩ)	320.30	C_{pm} (μF)	1.49E+05	λ_C	0.00
R_{pm} (kΩ)	49.74			S_q (A)	-0.50	R_{pm} (kΩ)	12913.00			S_q (A)	-

4.4.4 Frequency sweep analysis

Having shown the capability of the proposed equivalent circuit in reproducing the superharmonics in the dynamic response of CNTCSs under cyclic loadings, a sweep test has been conducted to investigate the response under varying frequency of excitation. The tests consisted of the initial application of a constant compression load of 2 kN for 70 s followed by concatenated sinusoidal compression loads with different frequencies and amplitudes varying from 2 kN to 4 kN. In total, 10 load cycles were applied at 13 different load frequency values: from 0.1 to 0.5 Hz with step increments of 0.1 Hz, 0.75 Hz, and from 1.0 to 3.5 Hz with step increments of 0.5 Hz. The total duration of the test was approximately 340 s. The fitted parameters for models A and B are shown in Table 4.11. Note the fitted parameters for the newly proposed model A, unlike model B, are still consistent with the previous results in Tables 4.9 and 4.10. Fig. 4.28 (a) shows the time series of measured strain. Fig. 4.28 (b) shows the comparison of the experimental results and the fitted numerical results obtained by models A and B. As mentioned above, the amplitude of the relative electrical resistance is frequency-dependent. In particular, the amplitude has been shown to be increasing with the frequency. Model B, which only considers piezoresistive effects, exhibits the opposite behavior. On the contrary, the proposed approach, model A, does reproduce a direct frequency-dependent amplitude of the electrical resistance leading to a very good agreement with the experimental data. The proposed approach for a forward and backward frequency sweep analysis is shown in Fig. 4.29. The slowly varying component has been removed by a high-pass filter and the mean value has been extracted. The envelope of the signal was extracted with the amplitude of the analytical signal obtained by a Hilbert transform. Hence, it can be seen that this model provides electrical resistance amplitude increasing with the frequency of excitation for both forward and backward frequency sweep analyses.

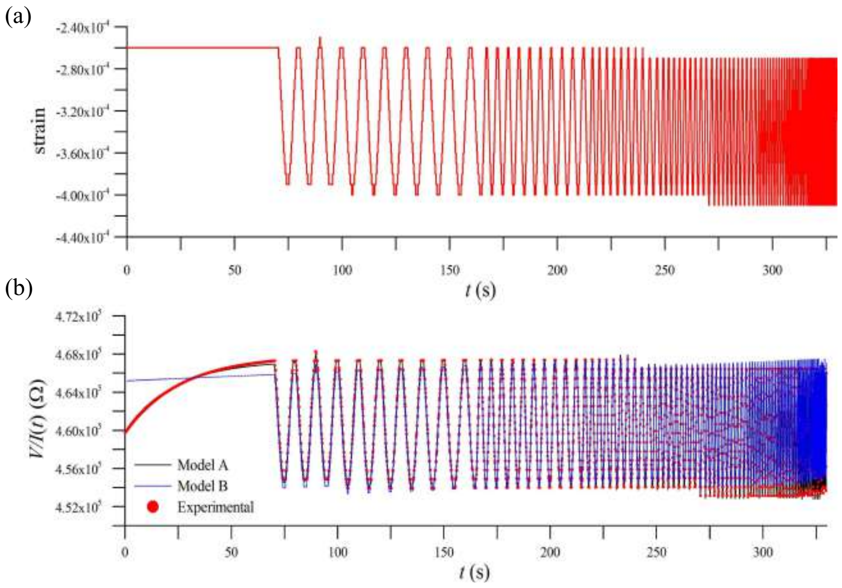

Figure 4.28 Strain series (a) and comparison between experimental results and analytical predictions of the response of CNTCS for forward sweep test from 0.1 to 3.5 Hz (b) (V=30 V, specimen S2). Models A and B correspond to the newly proposed piezoresistive/piezoelectric and previously published piezoresistive modeling, respectively.

The response of a dynamic transducer governed by a linear input-output differential equation is fully described by its frequency response function. The frequency response function is a transfer function that describes the system response to an external excitation force as a function of frequency as:

$$\mathrm{FRF}(f) = \frac{Y(f)}{X(f)} \tag{4.15}$$

Table 4.11 Fitted model parameters for sweep test from 0.1 to 3.5 Hz (V=30 V, specimen S2). Models A and B correspond to the newly proposed piezoresistive/piezoelectric and previously published piezoresistive modeling, respectively.

Model A (piezoresistive/piezoelectric)						**Model B** (piezoresistive)					
R_{ct} (kΩ)	129.85	C_{ip} (μF)	284.75	λ	300.00	R_{ct} (kΩ)	13.31	C_{ip} (μF)	0.00	λ	195.20
R_{ip} (kΩ)	313.42	C_{pm} (μF)	2.13E+04	λ_C	0.00	R_{ip} (kΩ)	320.16	C_{pm} (μF)	1.49E+05	λ_C	0.00
R_{pm} (kΩ)	49.74			S_q (A)	-0.50	R_{pm} (kΩ)	12913.00			S_q (A)	-

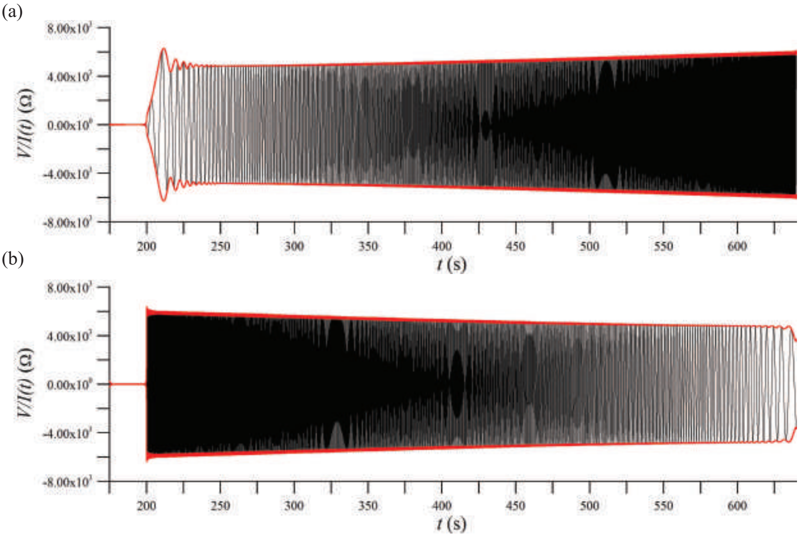

Figure 4.29 Analytical predictions of the response of CNTCS for forward (a) and backward (b) sweep test from 0.1 to 3.5 Hz obtained by the newly proposed piezoresistive/piezoelectric modeling (V=30 V, specimen S2).

where $Y(f)$ is the Fourier transform of the output response $y(t)$, $X(f)$ is the Fourier transform of the input $x(t)$, and f denotes frequency. The dynamic response of transducers commonly used for measuring vibrations is generally described by a second order differential input-output equation. The FRF of this type of systems only depends on the resonant frequency of the sensor and its damping. When the excitation frequency remains far below the resonant frequency of the sensor, f_o, as it is the case, the FRF can be approximated with a constant function with zero phase. This approach corresponds to the response of an ideal linear input-output transducer without delay. In this situation, the level of approximation of a constant FRF is essentially independent of the damping.

The results of the sweep tests have been used to characterize the amplitude of the FRF. To this end, the oscillating components have been first obtained by removing the best-fitting linear trend from the full-length records after the initial 70 s. Next, time windows with 10 cycles at constant frequencies have been extracted, and the average peak-to-peak amplitude of both electrical resistance and the applied load has been evaluated. Finally, the FRF has been obtained using Eq. (4.15), and the resulting curve has been normalized by its value corresponding to the lowest frequency (0.1 Hz). The results, obtained for both the forward and backward frequency sweep tests, are shown in Fig. 4.30 (a). Only the interval 0.1-3.5 Hz is shown because sampling errors became unacceptable for higher frequencies. For comparative purposes, Fig. 4.30 (a) also shows the mechanical FRF that would result from the ideal behavior of the sensors modeled as second-order systems with natural frequency equal to f_o. A critical damping ratio of 0.01 has been considered as representative of the internal damping of hardened cement paste in uncracked state [301]. The experimental results in Fig. 4.30 (a) confirm the prediction of a slight amplitude increase of the response with the frequency. It must be noted that the comparison between the FRFs extracted from forward and backward frequency sweep responses shows a close match what indicates that the errors associated with the elimination of the trend from the time histories and to the sampling were limited in this range.

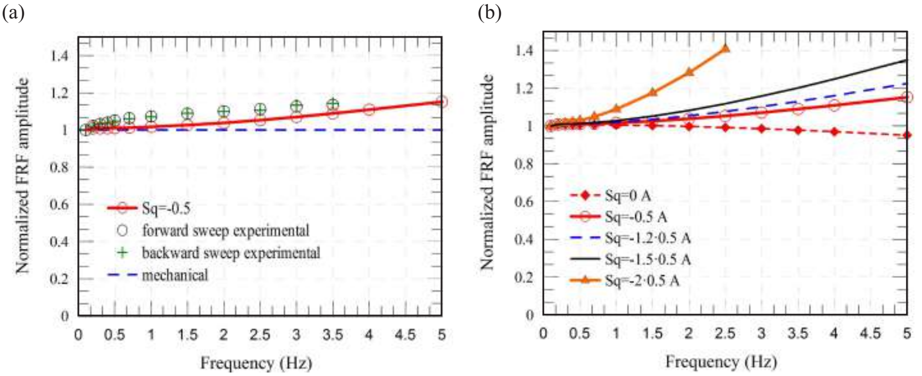

Figure 4.30 Comparison of the experimental and numerical frequency response functions (FRFs) of CNTCSs (a), and sensitivity analysis of the piezoelectric parameter S_q (V=30 V, specimen S2).

The FRF has been similarly obtained with the newly proposed equivalent circuit and represented in Fig. 4.30 (a). The model parameters have been taken from the frequency sweep analysis in Table 4.11. It can be seen that the solution with the fitted piezoelectric parameter in the frequency sweep analysis, S_q =-0.50 A, provides a reasonably good agreement with the experimental data. The FRF has been also obtained with the proposed equivalent circuit for different values of piezoelectric parameter, S_q, as shown in Fig. 4.30 (b). It is noted that the amplification of the electric resistance with frequency can be modulated with different piezoelectric parameters, that is, higher values of S_q lead to higher increasing FRFs. The case of $S_q = 0$, corresponding to the case of only piezoresistive model and equivalent to model B, provides decreasing FRFs with excitation frequency. These results demonstrate that the proposed equivalent circuit is superior in comparison to the previous one in reproducing the dynamic response of the sensors. Moreover, this modeling confirms that the weakly non-linear FRF is not due to mechanical reasons but rather to the peculiar eletrodynamic behavior of the cement paste prepared with carbon nanotubes in this study.

4.4.5 Conclusions

In this section, we have presented an electromechanical model for CNTCSs based on an equivalent lumped circuit. The model consists of a resistor in series with two RC elements, standing for the contact resistance, inter-particle matrix path, and the interface response, respectively. On the basis of experimental evidence, this paper has proposed a novel piezoelectric/piezoresistive approach for the dynamic modeling of CNTCSs. The piezoresistive effect is simulated by a linear variation of the bulk resistance with strain, and the piezoelectric effect is modeled as an additional current source originated by external loadings. Experimental tests of step response of unloaded specimens, harmonic excitations and frequency sweep tests have been performed as a benchmark for validation. The parameters have been fitted by least-square differences optimization and excellent agreements have been found with experimental data. The results have demonstrated that the proposed model can reproduce the superharmonic response of CNTCSs under cyclic loadings, as well as the amplification of the electric resistance with the frequency of excitation.

The main contributions of this research work are summarized below:

- Experimental results evidenced that mechanical deformations in the absence of externally applied power source generate voltage impulses between the electrodes of the specimen. This fact demonstrates the existence of certain level of piezoelectricity in cement-based materials doped with CNTs.
- The proposed model can accurately reproduce the step response of CNTCSs under unloaded conditions.
- The electrical response of CNTCSs in terms of electrical resistance under cyclic loadings contains superharmonics. Both piezoresistive and piezoelectric/piezoresistive modelings can reproduce this behavior.
- The variation of the internal capacitance with external strain has been shown to be negligible.
- The amplitude of the electric resistance is increasing with the frequency of excitation. Approaches that only take into account the piezoresistive effect have shown an opposite behavior, leading to decreasing amplitudes with increasing frequencies of excitation. On the contrary, the proposed piezoresistive/piezoelectric modeling has shown able to reproduce this effect and accurate fittings have been obtained for sweep analyses.
- The fitted parameters have been shown consistent under different experimental conditions and, therefore, the proposed model has proved capable of reproducing the internal behavior of CNTCSs.
- The amplification of the electrical resistance can be modulated with the piezoelectric parameter.

4.5 Conclusions

This chapter has presented the main contributions of this thesis in the study of the potential applications of CNT-reinforced composites in the realm of SHM. Firstly, research studies have been conducted in the field of ambient-vibration SHM. Specifically, an OMA campaign has been conducted with conventional accelerometers in the Montoro footbridge in Córdoba, Spain. Afterward, a theoretical modeling has been developed to study the dynamic response of CNTCSs in the time domain. In particular, the proposed electromechanical model is based on an piezoelectric/piezoresistive equivalent lumped circuit. A series of experiments have been conducted to verify the proposed modeling. To investigate the electrical behavior under applied mechanical deformations, the samples were connected to a power source providing a stabilized potential difference across their electrodes, and to a digital multimeter measuring the time history of the current passing through the specimen. Dynamic characterization has been conducted using a servo-controlled pneumatic universal testing machine equipped with an environmental constant temperature chamber. The applied axial deformation has been measured through two off-the-shelf resistive strain gauges attached to the opposite lateral faces of the specimen. Three different sets of tests have been performed, including step response under unloaded conditions, harmonic excitations and sweep analyses.

The overall findings of this chapter can be summarized as follows:

- Both experiments and theoretical simulations demonstrate that there exists not only a piezoresistive principle, but also a piezoelectric effect governing the response of CNTCSs.
- Piezoresistive/piezoelectric equivalent circuits can reproduce the main features of the response of CNTCSs: (i) the apparent resistance under cyclic excitations contains superharmonics, and (ii) the frequency response function of CNTCs is increasing with the frequency of excitation.
- CNTCs have been shown apt for ambient-vibration testing. In addition, the similarity of CNTCs with conventional structural concrete has been shown key to develop continuous embedded monitoring applications.

The present equivalent circuit is envisioned to provide a useful tool for signal processing applications of CNTCs in the realm of SHM. It is important to note that, despite the developed numerical tool is readily applicable to field experiments, there are still some open issues that have to be addressed in future research. In particular, although the capacitive contribution of the sensors can be eliminated by high-pass filtering, the loss of information at low frequencies limits their application to full-scale civil infrastructures. In this regard, several attempts have been done during this thesis to characterize the resonant frequencies of flexible in-service bridges. However, the experience evidences that the filtering of the signals to eliminate the polarization limits the information to frequency ranges above around 10-15 Hz, far beyond the typical first resonant frequencies of bridges (see e.g. Table 4.7). As will be later indicated as future developments, one possible solution may be the development of experimental setups with Alternating Current (AC) resistivity measurements.

Overall, it can be concluded that the third objective of this thesis has been also fulfilled.

5 Conclusions and future development

5.1 Conclusions

The primary aim of this thesis is twofold: the study of the potential applications of carbon nanotubes as mechanical reinforcements and electrically conductive fillers for the development of multifunctional composites. In this context, the theoretical framework in which most of the work has been formulated corresponds to the mean field homogenization theory. This framework is well suited to scale up the diverse material properties of the different constituent phases of composites into the macroscopic scale. Furthermore, this type of approaches offers a tractable theoretical formulation that enables the consideration of the physically meaningful mechanisms that govern the overall response of the composites (e.g. quantum tunneling effects, conductive networking, waviness, …etc.) without too high computational demands, unlike other widely used methodologies such as molecular dynamics or multi-scale FE modeling.

With regard to the analysis of CNTs as mechanical nanoreinforcements, numerical simulations have been presented to investigate the effect of micromechanical features such as filler content, aspect ratio, orientation distribution, waviness, and agglomeration. The numerical results have pinpointed the outstanding mechanical enhancements of composites doped with reduced CNT contents. Moreover, the design optimization possibilities of functionally graded CNT distributions have been assessed by analyzing the macroscopic response of several full-scale structural elements, including flat shells, skew shells, and curved panels. The results have showed that it is possible to tune the stiffness of CNT-reinforced composites by tailoring design parameters such as filler orientation, volume fraction, dispersion, and functionally graded doping across the thickness of the specimens. Finally, two surrogate models, namely the Kriging and RS-HDMR metamodels, have been implemented to evaluate the uncertainty propagation of the main micromechanical variables in the macroscopic response of FG-CNTRCs. Overall, the presented results support the benefits of CNTs as mechanical reinforcements for the development of high-strength and light-weight composites.

Micromechanics models have been also developed to predict the electrical conductivity of CNT-reinforced cement-based composites. In particular, the contribution of the electron hopping and conductive networking mechanisms have been incorporated in a mixed micromechanics formulation. The relative contribution of these two transport mechanisms have been formulated within a percolative-type behavior. Afterward, the previous approach has been extended to account for uni-axial and three-dimensional strain-sensing properties. To this end, the effect of quasi-static strain loadings has been modeled by strain-induced alterations of the electron hopping and conductive networking mechanisms. The studies included (i) composite volume expansion, (ii) reorientation of fillers and (iii) changes in the percolation threshold. Finally, experimental testing of CNT-reinforced sensors has been conducted under unloaded and quasi-static conditions in order to serve as a validation basis. The comparison against theoretical predictions has demonstrated close agreements, and the developed approach showed capable of estimating the unloaded electrical conductivity and the piezoresistivity matrix (gauge factors), essential for the characterization of CNT-reinforced composites as static strain transducers.

Finally, the last part of this thesis has focused on the study of the potential application of CNT-reinforced composites as smart sensors for SHM. The interest has been especially centered on vibration-based SHM and, therefore, the focus has shifted into the time-domain. With this purpose, an equivalent piezoresistive/piezoelectric lumped circuit has been proposed and experimentally validated. Specifically, DC resistivity measurements have been conducted to characterize the dynamic response of CNT-reinforced cement-based sensors under unloaded conditions, cyclic sinusoidal loadings, and sweep frequency tests. The results have demonstrated that the proposed approach can reproduce the main features that define the dynamic response of the sensors, namely (i) the apparent electrical resistance contains superharmonics when subjected to cyclic excitations, and (ii) the amplitude of the apparent resistance increases with the frequency of the excitation.

Overall, the main contributions of this thesis include:

- A micromechanics approach has been fully developed for the mechanical homogenization of CNT-reinforced composites. Micromechanical features such as complex filler orientation distributions, waviness and agglomeration have been included. Two different waviness models have been studied, namely planar sinusoidal and helical geometries. With regard to the filler agglomeration effects, both fully aligned and randomly oriented filler arrangements have been studied.
- Several CNT-reinforced shell structures (skew, rectangular and cylindrical shells) have been studied. The shell theory has been formulated in the realm of functionally graded materials. In this way, the filler dosage is defined as a continuous function across the thickness. In addition, two different surrogate models, including the Kriging and RS-HDMR metamodels, have been implemented for the analysis of the uncertainty propagation in the structural response.
- A mixed micromechanics approach of the electrical conductivity of CNT-reinforced composites has been developed. The theoretical framework distinguishes the different transport mechanisms underlying the overall electrical conductivity, namely

electron hopping and conductive networking. On the basis of SEM inspections, agglomeration and waviness effects have been also incorporated.

- A micromechanics approach has been presented for the modeling of the piezoresistivity properties of CNT-reinforced composites under uniaxial and three-dimensional strain loadings. Strain-induced effects comprise (i) composite volume expansion, (ii) filler reorientation, and (iii) variation of the percolation threshold. A remarkable feature of the proposed approach lays on the definition of the percolation threshold as a function of the filler ODF. In this manner, the strain-induced reorientation effect reduces the randomness of the fillers and, consequently, it also alters the unstrained percolation threshold. Furthermore, agglomeration and waviness effects have been also taken into account.
- An equivalent piezoresistive/piezoelectric lumped circuit has been proposed for the electromechanical modeling of CNT-reinforced composites. The proposed approach has been shown capable of reproducing the main features present in the dynamic response of these composites, namely (i) the apparent electrical resistance contains superharmonics when subjected to cyclic excitations, and (ii) the amplitude of the apparent resistance increases with the frequency of the excitation.

On the basis of the research results reached in this thesis, the following conclusions can be remarked:

- Limited filler contents lead to elevated increases in the stiffness of CNT-reinforced composites. In addition, functionally graded distributions of fillers can optimize the macroscopic response of composite structures under certain loading conditions. It has been shown that fillers located at the bottom and top layers of CNT-reinforced composite shells yield the highest stiffness values.
- The Mori-Tanaka model provides consistent estimates for composites doped with fully aligned CNT arrangements. Nonetheless, the estimates may be inconsistent for general distributions of fillers. In particular, it has been shown that the predictions for randomly oriented fillers at high volume fractions violate the Hashin-Shtrikman-Walpole bounds. Also, the computed stiffness tensors are diagonally asymmetric for general filler orientation distributions and wavy CNTs. In these cases, alternative approaches such as those proposed by Dunn and co-authors or Schjødt-Thomsen and Pyrz can be used.
- Heterogeneous dispersions with agglomeration of CNTs have detrimental effects on the macroscopic properties of CNT-reinforced composites and, therefore, can be understood as defects in the microstructure.
- Filler waviness has been shown to yield critical reductions in the macroscopic longitudinal Young's modulus and slight increases in the transverse moduli. Also, the numerical results demonstrate that the coupled weakening effect of waviness and agglomeration can only be estimated by considering ad hoc Eshelby's tensors of particular wavy geometries, along with the two-parameter agglomeration model.
- The electrical conductivity of CNT-reinforced composites is governed by the simultaneous contribution of the electron hopping and conductive networking mechanisms.

The relative contribution of both transport mechanisms is defined by the percolation threshold, which is highly dependent upon the filler aspect ratio.

- Both experiments and theoretical results prove that the largest gauge factors of CNTCs are achieved for filler contents close to the percolation threshold. Moreover, the strain sensitivity curves exhibit a non-linear behavior, predominantly for composites loaded with filler contents close to the percolation threshold and high strain levels.
- Overall, it has been shown that CNTCs are weakly sensitive to shear strains. In addition, the results have shown that the dilation strain sensitivities along the longitudinal and transverse directions are very similar. Hence, a simplified modeling of CNTCs as volumetric strain sensors can be defined with one single gauge factor.
- Very close agreements of simulations with experimental data have proved the consistency of the cubic crystal symmetry assumption imposed on the structure of the piezoresistivity matrix of CNTCs.
- Experimental results have evidenced that mechanical deformations in the absence of any externally applied power source generate voltage impulses between the electrodes of CNTCs. This fact has evidenced the existence of certain level of piezoelectricity in cement-based materials doped with CNTs.
- Equivalent piezoelectric/piezoresistive lumped circuits have been shown capable of reproducing the main features underlying the dynamic behavior of CNTCs: the apparent electrical resistance contains superharmonics when subjected to cyclic excitations, and (ii) the amplitude of the apparent resistance increases with the frequency of the excitation.

On the whole, it can be concluded that the proposed objectives at the beginning of this thesis, as previously indicated in Section 1.3, have been successfully accomplished.

5.2 Recommendations for future development

In the light of the experience built-up over the development of this thesis, the following future developments are proposed regarding the mechanical homogenization of CNT-reinforced composites:

- Use of SEM/TEM micrographs and image processing algorithms to characterize the filler orientation distribution functions. In this manner, the experimentally identified ODFs could assist the micromechanics approaches and provide more accurate predictions.
- Mean-field homogenization of elasto-plastic composites based on the linearization of the return-mapping algorithm, and analysis of particle debonding effects.
- Further the definition of heterogeneous dispersions of CNTs. A statistical description of the agglomeration effects, presumably governed by the filler aspect ratio and the use of chemical dispersants, is still lacking in the literature. In this way, the optimum CNT contents could be more precisely determined.

- Statistical description of the CNT waviness effect on the basis of micrograph inspections. In addition, although some efforts have been made to characterize the interaction between curved CNTs and the surrounding matrix, advanced MD or FE multi-scale analyses are yet to be conducted in order to fully explain this interaction.
- Development of atomistic-based FE multi-scale approaches for the accurate modeling of the load transfer mechanisms at the matrix/CNT interfaces. On this basis, it would be possible to determine a library of equivalent continuous micro-fibers to be used in micromechanics approaches. It would be particularly interesting to characterize the efficiency parameters of the EROM as continuous functions of the filler volume fraction, a definition that is still missing in the literature.

Secondly, there are still some open issues that must be addressed with regard to the piezoresistive modeling of CNT-reinforced composites:

- Statistical definition of the average distance among nanotubes in order to estimate more accurately the formation of electrical conductive networks, as well as the thickness of the conductive interphases.
- Further research must be pursued on the determination of the initial inter-particle distance and the height of the potential barrier, along with more sophisticated definitions of the corresponding strain-induced variation parameters, namely C_1 and C_2.
- Extension of the developed micromechanics modeling for large deformation regimes. This topic is of high interest for the design of high-performance stretchable electronics.
- Study of practical applications of CNT-reinforced composite sensors such as: smart coatings for buckling failure detection, electrical resistivity tomography applications of CNT-reinforced patches for crack detection, thermo-piezoresistive sensors, embedded strain sensors, …etc.

Finally, the use of CNT-reinforced composites for SHM is certainly the most challenging application. Along these lines, there are still many open issues that need to be addressed such as:

- Analysis of equivalent lumped circuits for AC resistivity measurements. The optimization of the frequency of the power source may be a key-point to devise efficient monitoring systems with a trade-off between time-based drifts derived from polarization effects and electrical noise.
- Application of the developed equivalent circuit for load identification systems such as traffic loads, high-speed trains loadings, vehicle counting, …etc.
- Use of the developed equivalent circuit for signal processing applications of structures with embedded sensors under seismic loadings.
- Experimental characterization of the piezoelectric coefficients of CNT-reinforced sensors.

- Operational modal analysis identification of large-scale civil infrastructures with CNT-reinforced composite sensors. In this context, the low frequency components introduced by polarization effects may pose an important obstacle to the identification of resonant frequencies below 10-15 Hz with DC resistivity measurements. Hence, the development of AC resistivity measurements with adequate signal-to-noise ratios, and capable of eliminating the capacitive transient components may be a feasible solution.

6 Appendices

A Finite element formulation of FG skew plates

Parametrization of the geometry

Consider a CNTRC skew plate of length a, width b, thickness t and skew angle α as shown in Fig. 2.25 in Section 2.5.2. The midsurface of the shell is given in terms of skew coordinates (θ^1, θ^2), hence the change of coordinates is given by:

$$\begin{aligned} x &= \theta^1 + \theta^2 \cos\alpha \\ y &= \theta^2 \sin\alpha \\ z &= \theta^3 \end{aligned} \tag{6.1}$$

This parametrization leads a covariant basis $\mathbf{a_r}$ defined by:

$$\vec{a}_1 = \begin{Bmatrix} 1 \\ 0 \\ 0 \end{Bmatrix}, \ \vec{a}_2 = \begin{Bmatrix} \cos\alpha \\ \sin\alpha \\ 0 \end{Bmatrix} \ \text{and} \ \vec{a}_3 = \begin{Bmatrix} 0 \\ 0 \\ 1 \end{Bmatrix} \tag{6.2}$$

The covariant metric tensor is noted by a has a value of $\sin^2\alpha$ and leads a contravariant basis $\mathbf{a^r}$ defined as:

$$\vec{a}^1 = \begin{Bmatrix} 1 \\ -\tan^{-1}\alpha \\ 0 \end{Bmatrix}, \ \vec{a}^2 = \begin{Bmatrix} 0 \\ \csc\alpha \\ 0 \end{Bmatrix} \ \text{and} \ \vec{a}^3 = \vec{a}_3 \tag{6.3}$$

Variational formulation, displacement field, stresses and strains of CNTRC skew plates

The theoretical formulation is derived by a variational formulation. Denoting by $\mathcal{U}(\gamma)$ the strain energy and by γ and σ the vectors containing the strain and stress components, respectively, a modified potential of Hu-Washizu assumes the form [343]:

$$\Pi_{HW}[\mathbf{v},\gamma,\sigma] = \int_V [\mathcal{U}(\gamma) - \sigma^T(\gamma - \mathbf{D}\,\mathbf{v}) - \Pi_b]\,\mathrm{d}V - \int_{S_{\hat{v}}} (\mathbf{v} - \hat{\mathbf{v}})\sigma\,\mathbf{n}\,\mathrm{d}S - \int_{S_t} \Pi_t\,\mathrm{d}S \tag{6.4}$$

In Eq. (6.4), $\mathbf{v}$ and the index b represent the displacement vector and the body forces, respectively, whereas $\hat{\mathbf{v}}$ are prescribed displacements on the part of the boundary in which displacements are prescribed $(S_{\hat{v}})$. If the body forces in volume (V) and surface tractions on the bounding surface where tractions are prescribed (S_t) are conservative, then Π_b and Π_t denote the corresponding body forces and surface tractions potentials. The reliability of the foregoing approach stems from the fact that the functional of Hu-Washizu is a modification of the potential. If the approximations of strains (and stresses) are compatible with displacements, then that functional is equal to the potential of the elastic body.

The displacement field is constructed by first-order shear deformation. Hence the in-plane deformation $\gamma_{\alpha\beta}$ is expressed in terms of the extensional $({}_0\gamma_{\alpha\beta})$ and flexural $({}_1\gamma_{\alpha\beta})$ components of the Cauchy-Green strain tensor as:

$$\gamma_{\alpha\beta} = {}_0\gamma_{\alpha\beta} + \theta^3 \, {}_1\gamma_{\alpha\beta}. \tag{6.5}$$

Denoting by V_α and V_3 the tangential displacements of the midsurface in the θ^α and θ^3 directions, and by ϕ_α the rotations about the θ^α lines, the strains in terms of the aforementioned displacements and rotations have the form:

$$\text{Extensional strains} : {}_0\gamma_{\alpha\beta} = \frac{1}{2}\left(V_{\alpha\|\beta} + V_{\beta\|\alpha}\right), \tag{6.6a}$$

$$\text{Flexural strains} : {}_1\gamma_{\alpha\beta} = \frac{1}{2}\left(\sqrt{a}\, e_{\alpha\mu}\phi^{\mu}_{\|\beta} + \sqrt{a}\, e_{\beta\mu}\phi^{\mu}_{\|\alpha}\right), \tag{6.6b}$$

$$\text{Shear strains} : 2\gamma_{\alpha 3} = V_{3,\alpha} + \sqrt{a}\, e_{\alpha\mu}\phi^{\mu} \tag{6.6c}$$

In Eqs. (6.6) $e_{\alpha\beta}$ denote the permutation tensor associated with the undeformed surface and a double bar $(.)_{\|}$ signifies covariant differentiation with respect to the undeformed surface. In vectorial form:

$$ {}_0\gamma = \left\{ \begin{array}{c} {}_0\gamma_{11} \\ {}_0\gamma_{22} \\ 2\,{}_0\gamma_{12} \end{array} \right\}, \quad {}_1\gamma = \left\{ \begin{array}{c} {}_1\gamma_{11} \\ {}_1\gamma_{22} \\ 2\,{}_1\gamma_{12} \end{array} \right\} \quad \text{and} \quad \gamma_S = \left\{ \begin{array}{c} \gamma_{13} \\ \gamma_{23} \end{array} \right\} \tag{6.7}$$

The thin body assumption is considered in the z-direction, and thus it is often possible to neglect the transverse normal stress s^{33}. The stress-strain relationships are defined by:

$$\begin{aligned} s^{\alpha\beta} &= \frac{\partial\Phi}{\partial\gamma_{\alpha\beta}} = C^{\alpha\beta\gamma\delta}\gamma_{\gamma\delta} \\ s^{\alpha 3} &= 2E^{\alpha 3\beta 3}\gamma_{\beta 3} \\ s^{33} &= 0 \end{aligned} \tag{6.8}$$

And the free-energy density takes the form:

$$\Phi = \frac{1}{2} C^{\alpha\beta\gamma\delta}\gamma_{\alpha\beta}\gamma_{\gamma\delta} + 2\,E^{\alpha 3\beta 3}\gamma_{\alpha 3}\gamma_{\beta 3} \tag{6.9}$$

Linearly elastic transversely isotropic constitutive matrix in non-orthogonal coordinates

The definition of non-orthogonal coordinates requires a coherent definition of the stress-strain relationships. On the basis of the representation theorems of transversely isotropic tensors developed by Spencer [296], Lumbarda and Chen [199] obtained the constitutive tensor of linear elastic transversely isotropic materials in a general coordinates system as:

$$C_{ijkl} = \sum_{r=1}^{6} c_r I^r_{ijkl} \tag{6.10}$$

The I^r are a set of linearly independent fourth-order tensors that form a basis of an algebra of order 6 and the c_r are six elastic parameters. In component form, the fourth-order tensors I_r are defined by:

$$I^1_{ijkl} = \frac{1}{2}(a^{ik}a^{jl} + a^{il}a^{jk}) \tag{6.11a}$$

$$I^2_{ijkl} = a^{ij}a^{kl} \tag{6.11b}$$

$$I^3_{ijkl} = n_i n_j a^{kl} \tag{6.11c}$$

$$I^4_{ijkl} = a^{ij}n_k n_l \tag{6.11d}$$

$$I^5_{ijkl} = \frac{1}{2}(a^{ik}n_j n_l + a^{il}n_j n_k + a^{jk}n_i n_l + a^{jl}n_i n_k) \tag{6.11e}$$

$$I^6_{ijkl} = n_i n_j n_k n_l \tag{6.11f}$$

where n_i are the rectangular components of an unit vector parallel to the axis of the transverse isotropy, defined in the mid-plane of the skew plate as $\vec{n} = (\cos\varphi, \sin\varphi, 0)$ (see Fig. 2.25), and a^{ij} are the components of the contravariant basis $\mathbf{a^r}$ defined in Eq. (6.3). The material parameters, c_r, are defined as:

$$\begin{aligned} c_1 &= 2\mu, & c_2 &= \lambda, \quad c_3 = c_4 = \alpha, \\ c_5 &= 2(\mu_o - \mu), & c_6 &= \beta \end{aligned} \tag{6.12}$$

The material parameters c_r depend on five elastic constants: μ and λ, shear modulus within the plane of isotropy and the Lamé constant, the out-of-plane elastic shear modulus μ_0, α and β. In matrix notation the fourth-order elasticity tensor of transversely isotropic material for a preferred x direction in a Cartesian coordinate system gives:

$$C = \begin{bmatrix} 2\alpha+\beta+\lambda-2\mu+4\mu_0 & \alpha+\lambda & \alpha+\lambda & 0 & 0 & 0 \\ \alpha+\lambda & \lambda+2\mu & \lambda & 0 & 0 & 0 \\ \alpha+\lambda & \lambda & \lambda+2\mu & 0 & 0 & 0 \\ 0 & 0 & 0 & \mu & 0 & 0 \\ 0 & 0 & 0 & 0 & \mu_0 & 0 \\ 0 & 0 & 0 & 0 & 0 & \mu_0 \end{bmatrix} \tag{6.13}$$

The relation between elastic invariant constants and the engineering constants can be found by comparing Eq. (6.13) with the classical transversely isotropic stiffness tensor. This comparison leads to:

$$\alpha = \frac{E_{11}(E_{11}-E_{22})E_{22}\nu_{12}}{(E_{11}+E_{22}\nu_{12})(E_{11}-E_{22}\nu_{12}(1+2\nu_{12}))} \tag{6.14a}$$

$$\lambda = \frac{E_{11}E_{22}^2\nu_{12}(1+\nu_{12})}{(E_{11}+E_{22}\nu_{12})(E_{11}-E_{22}\nu_{12}(1+2\nu_{12}))} \tag{6.14b}$$

$$\mu = \frac{E_{11}E_{22}}{2E_{11}+2E_{22}\nu_{12}} \tag{6.14c}$$

$$\mu_o = G_{12} \tag{6.14d}$$

$$\beta = \frac{1}{2}\left(-8G_{12}+\frac{E_{11}E_{22}}{E_{11}+E_{22}\nu_{12}}+\frac{E_{11}(2E_{11}+E_{22}-6E_{22}\nu_{12})}{E_{11}-E_{22}\nu_{12}(1+2\nu_{12})}\right) \tag{6.14e}$$

Once the constitutive tensor is obtained, the plane stress stiffness matrix can be obtained numerically by deleting the rows and columns associated with the z-direction in the compliance matrix. By inverting the resulting compliance matrix, the constitutive equations are written in Voigt's notation in the form:

$$\begin{bmatrix} s_{11} \\ s_{22} \\ s_{12} \\ s_{23} \\ s_{13} \end{bmatrix} = \begin{bmatrix} Q_{11}(z) & Q_{12}(z) & 0 & 0 & 0 \\ Q_{12}(z) & Q_{22}(z) & 0 & 0 & 0 \\ 0 & 0 & Q_{66}(z) & 0 & 0 \\ 0 & 0 & 0 & Q_{44}(z) & 0 \\ 0 & 0 & 0 & 0 & Q_{55}(z) \end{bmatrix} \cdot \begin{bmatrix} \gamma_{11} \\ \gamma_{22} \\ \gamma_{12} \\ \gamma_{23} \\ \gamma_{13} \end{bmatrix} \tag{6.15}$$

$$\begin{aligned} &(C_E^{ij},C_C^{ij},C_B^{ij}) = \textstyle\int_{-h/2}^{h/2} Q_{ij}(z)\cdot(1,z,z^2)\mathrm{d}z \quad (i,j=1,2,6), \\ &C_S^{ij} = \tfrac{1}{ks}\textstyle\int_{-h/2}^{h/2} Q_{ij}\mathrm{d}z \quad (i,j=4,5) \end{aligned} \tag{6.16}$$

Note that Q_{ij} varies with z according to the grading profile of the CNTRC along the thickness. ks denotes the transverse shear correction factor for FGM, given by [79]:

$$ks = \frac{6-(\nu_i V_i+\nu_m V_m)}{5} \tag{6.17}$$

Stiffness matrix of skew plate element

The strain-energy density per unit of area at the reference surface can be defined by:

$$U = \int_{-h/2}^{h/2} \Phi\,\mathrm{d}z \tag{6.18}$$

From Eq. (6.5) and Eq. (6.9), the strain-energy density can be expressed as:

$$U = \textstyle\int_{-h/2}^{h/2} \left[\tfrac{1}{2}C^{\alpha\beta\gamma\delta}\left({}_0\gamma_{\alpha\beta}+\theta^3\;{}_1\gamma_{\alpha\beta}\right)\left({}_0\gamma_{\gamma\delta}+\theta^3\;{}_1\gamma_{\gamma\delta}\right)+2\,E^{\alpha3\beta3}\gamma_{\alpha3}\gamma_{\beta3}\right]\mathrm{d}z \tag{6.19}$$

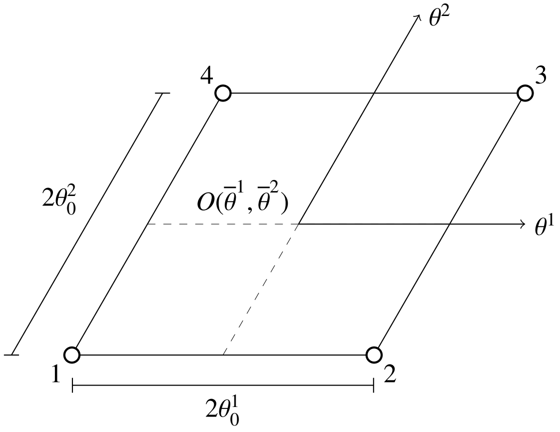

Figure 6.1 Four node skew quadrilateral shell finite element.

Expression (6.19) for the strain energy can be represented as the sum of the extensional (U_E), bending (U_B), coupling (U_C) and transverse shear (U_S) strain energy as:

$$\begin{aligned} &U_{Total} = U_E + U_B + U_C + U_S = \\ &= \tfrac{1}{2}\left({}_0\gamma^T\, \mathbf{C_E}\, {}_0\gamma + {}_1\gamma^T\, \mathbf{C_B}\, {}_1\gamma + {}_0\gamma^T\, \mathbf{C_C}\, {}_1\gamma + {}_1\gamma^T\, \mathbf{C_C}\, {}_0\gamma + \gamma_\mathbf{S}^\mathbf{T}\, \mathbf{C_S}\, \gamma_\mathbf{S}\right) \end{aligned} \tag{6.20}$$

Discretization The shell element derived in the present study is a four-noded skewed isoparametric finite element (see Fig. 6.1) with five degrees of freedom at each node: three physical components of the displacements u_1, u_2, u_3 and two components of the rotations φ_1,φ_2 Eq. (6.21). Bilinear shape functions N_k are chosen for the physical components of the displacements and rotations in the following way:

$$u_i = \sum_{k=1}^{4} u_i^k N_k \quad \text{and} \quad \varphi_\alpha = \sum_{k=1}^{4} \varphi_\alpha^k N_k \;; \tag{6.21}$$

$$N_k = \frac{1}{4}(1+\xi_k\xi)(1+\eta_k\eta)\,, \quad i = 1,2,3 \;\text{ and }\; \alpha = 1,2\,. \tag{6.22}$$

As mentioned before, the use of the Hu-Washizu principle and the independent approximation of strain and stress yields a series of desirable features important for the reliability, convergence behavior, and efficiency of the elemental formulation such as the avoidance of superfluous energy and zero energy modes. Furthermore, the discrete approximation is drawn in a consistent manner from the general theory of the continuum and the mechanical behavior of the finite element, without resorting to special manipulations or computational procedures. In addition, it has been shown [343, 304, 344, 321] that essential prerequisites for the achievement of these goals are: the identification of constant and higher-order deformational modes which are contained in the displacement/rotation assumptions, the realization that the constant terms are necessary for convergence, and that higher-order

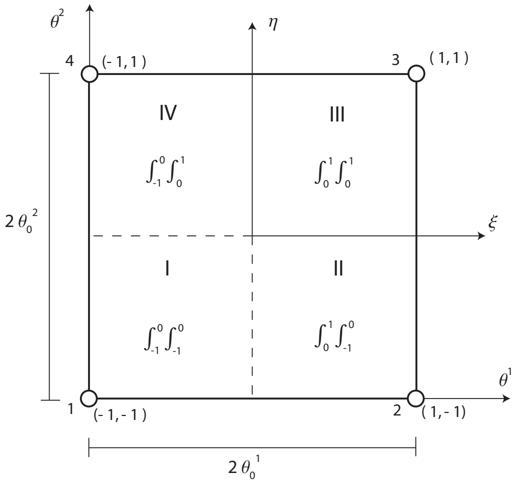

Figure 6.2 Subdomain areas throughout the finite element.

terms reappear in different strain components. Therefore, our approximation does not need to retain the higher-order terms in two different strain components (they are needed only to inhibit a mode).

For instance, the following assumptions for the extensional strains have been shown to serve the aforementioned goals:

$$
\begin{aligned}
\gamma_{11} &= \bar{\gamma}_{11} + \bar{\bar{\gamma}}_{11}\,\eta\,, \\
\gamma_{22} &= \bar{\gamma}_{22} + \bar{\bar{\gamma}}_{22}\,\xi \\
\gamma_{12} &= \bar{\gamma}_{12} + \underline{\hat{\bar{\gamma}}_{11}\,\xi} + \underline{\hat{\bar{\gamma}}_{22}\,\eta}\,.
\end{aligned}
\tag{6.23}
$$

Note that, according to the above ideas, the underlined terms in Eqs. (6.23) are not considered. The elimination of such terms allows the reduction of excessive internal energy and to improve convergence. Furthermore, the replacement of the linear variation of the strains and stresses by piecewise constant approximations leads to computational advantages that are most important in repetitive computations. The piecewise constant approximations can be improved by introducing four subdomains over the finite element (see Fig. 6.2). For example, Fig. 6.3 illustrates the piecewise approximation of γ_{11} and γ_{22} over two subdomains. The membrane shear strain γ_{12} is approximated by a constant.

Considering the piecewise approximations through the four subdomains and expressing strains in physical components (ε, κ, γ), the extensional, bending and shear strain over every subdomain are defined as:

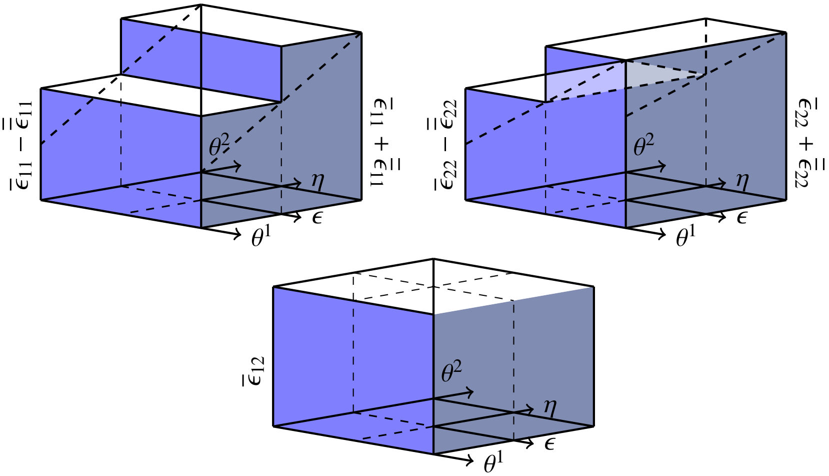

Figure 6.3 Schematic representation of the piecewise constant extensional strain approximation.

Extensional strains $(\varepsilon_{11}, \varepsilon_{22}, \varepsilon_{12})$

$$\varepsilon_{11} = \begin{cases} \varepsilon_{11}^{A} & \text{in} \quad A_I + A_{II} \\ \varepsilon_{11}^{B} & \text{in} \quad A_{III} + A_{IV} \end{cases}, \quad \varepsilon_{22} = \begin{cases} \varepsilon_{22}^{C} & \text{in} \quad A_I + A_{IV} \\ \varepsilon_{22}^{D} & \text{in} \quad A_{II} + A_{III} \end{cases} \quad \text{and} \quad \varepsilon_{12} = \bar{\varepsilon}_{12} \quad \text{in} \quad A \tag{6.24}$$

Bending strains $(\kappa_{11}, \kappa_{22}, \kappa_{12})$

$$\kappa_{11} = \begin{cases} \kappa_{11}^{A} & \text{in} \quad A_I + A_{II} \\ \kappa_{11}^{B} & \text{in} \quad A_{III} + A_{IV} \end{cases}, \quad \kappa_{22} = \begin{cases} \kappa_{22}^{C} & \text{in} \quad A_I + A_{IV} \\ \kappa_{22}^{D} & \text{in} \quad A_{II} + A_{III} \end{cases} \quad \text{and} \quad \kappa_{12} = \bar{\kappa}_{12} \quad \text{in} \quad A \tag{6.25}$$

Shear strains $(\gamma_{13}, \gamma_{23})$

$$\gamma_1 = \begin{cases} \gamma_1^{A} & \text{in} \quad A_I + A_{II} \\ \gamma_1^{B} & \text{in} \quad A_{III} + A_{IV} \end{cases} \quad \text{and} \quad \gamma_2 = \begin{cases} \gamma_2^{C} & \text{in} \quad A_I + A_{IV} \\ \gamma_2^{D} & \text{in} \quad A_{II} + A_{III} \end{cases} \tag{6.26}$$

As a consequence of this approximation, the strain energy term in the Hu-Washizu variational principle takes the form of:

$$\begin{aligned} \int_A U \, \mathrm{d}A &= \int_{A_I} U_I \, \mathrm{d}A + \ldots + \int_{A_{IV}} U_{IV} \, \mathrm{d}A = \sum_{i=I}^{IV} \int_{A_i} U_i \, \mathrm{d}A = \\ &= \tfrac{1}{2} \bar{\varepsilon}^T \, \bar{\mathbf{D}}_{\mathbf{E}} \, \bar{\varepsilon} + \tfrac{1}{2} \bar{\kappa}^T \, \bar{\mathbf{D}}_{\mathbf{B}} \, \bar{\kappa} + \tfrac{1}{2} \bar{\varepsilon}^T \, \bar{\mathbf{D}}_{\mathbf{C}} \, \bar{\kappa} + \tfrac{1}{2} \bar{\kappa}^T \, \bar{\mathbf{D}}_{\mathbf{C}} \, \bar{\varepsilon} + \tfrac{1}{2} \bar{\gamma}^T \, \bar{\mathbf{D}}_{\mathbf{S}} \, \bar{\gamma} \end{aligned} \tag{6.27}$$

where the vectors $\bar{\varepsilon}$, $\bar{\kappa}$ and $\bar{\gamma}$ are defined by:

$$\bar{\varepsilon} = \left\{ \begin{array}{c} \varepsilon_{11}^{A} \\ \varepsilon_{11}^{B} \\ \varepsilon_{22}^{C} \\ \varepsilon_{22}^{D} \\ 2\varepsilon_{12} \end{array} \right\}, \ \bar{\kappa} = \left\{ \begin{array}{c} \kappa_{11}^{A} \\ \kappa_{11}^{B} \\ \kappa_{22}^{C} \\ \kappa_{22}^{D} \\ 2\kappa_{12} \end{array} \right\}, \ \bar{\gamma} = \left\{ \begin{array}{c} \gamma_{1}^{A} \\ \gamma_{1}^{B} \\ \gamma_{2}^{C} \\ \gamma_{2}^{D} \end{array} \right\} \tag{6.28}$$

The matrices $\bar{\mathbf{D}}_{\mathbf{E}}$, $\bar{\mathbf{D}}_{\mathbf{B}}$, $\bar{\mathbf{D}}_{\mathbf{C}}$ and $\bar{\mathbf{D}}_{\mathbf{S}}$ are the discretized elasticity matrices that depend on the geometry of the surface —i.e., on the contravariant ($a^{\alpha\beta}$) and covariant ($a_{\alpha\beta}$) components of the metric tensors— and can be represented as follows:

$$\bar{\mathbf{D}}_{\mathbf{E}} = \begin{bmatrix} \int_{A_1+A_2} D_E(1,1)\,\mathrm{d}A & 0 & \int_{A_1} D_E(1,2)\,\mathrm{d}A & \int_{A_2} D_E(1,2)\,\mathrm{d}A & \int_{A_1+A_2} D_E(1,3)\,\mathrm{d}A \\ & \int_{A_3+A_4} D_E(1,1)\,\mathrm{d}A & \int_{A_4} D_E(1,2)\,\mathrm{d}A & \int_{A_3} D_E(1,2)\,\mathrm{d}A & \int_{A_3+A_4} D_E(1,3)\,\mathrm{d}A \\ & & \int_{A_1+A_4} D_E(2,2)\,\mathrm{d}A & 0 & \int_{A_1+A_4} D_E(2,3)\,\mathrm{d}A \\ & & & \int_{A_2+A_3} D_E(2,2)\,\mathrm{d}A & \int_{A_2+A_3} D_E(2,3)\,\mathrm{d}A \\ sym & & & & \int_{A} D_E(3,3)\,\mathrm{d}A \end{bmatrix}, \tag{6.29}$$

$$\bar{\mathbf{D}}_{\mathbf{S}} = \begin{bmatrix} \int_{A_1+A_2} D_S(1,1)\,\mathrm{d}A & 0 & \int_{A_1} D_S(1,2)\,\mathrm{d}A & \int_{A_2} D_S(1,2)\,\mathrm{d}A \\ & \int_{A_3+A_4} D_S(1,1)\,\mathrm{d}A & \int_{A_4} D_S(1,2)\,\mathrm{d}A & \int_{A_3} D_S(1,2)\,\mathrm{d}A \\ & & \int_{A_1+A_4} D_S(2,2)\,\mathrm{d}A & 0 \\ sym & & & \int_{A_2+A_3} D_S(2,2)\,\mathrm{d}A \end{bmatrix} \tag{6.30}$$

Furthermore, the parameters for the stress resultants are expressed by the following vector forms:

$$\begin{aligned} \mathbf{N}^{T} &= \left[\begin{array}{ccccc} N_{11}^{A} & N_{11}^{B} & N_{22}^{C} & N_{22}^{D} & N_{12} \end{array} \right], \\ \mathbf{M}^{T} &= \left[\begin{array}{ccccc} M_{11}^{A} & M_{11}^{B} & M_{22}^{C} & M_{22}^{D} & M_{12} \end{array} \right] \text{ and} \\ \mathbf{Q}^{T} &= \left[\begin{array}{ccccc} Q_{11}^{A} & Q_{11}^{B} & Q_{22}^{C} & Q_{22}^{D} & Q_{12} \end{array} \right]. \end{aligned} \tag{6.31}$$

In addition, by introducing the matrices:

$$\mathbf{A_N} = \mathbf{A_M} = \begin{bmatrix} A_I + A_{II} & 0 & 0 & 0 & 0 \\ 0 & A_{III} + A_{IV} & 0 & 0 & 0 \\ 0 & 0 & A_I + A_{IV} & 0 & 0 \\ 0 & 0 & 0 & A_{II} + A_{III} & 0 \\ 0 & 0 & 0 & 0 & A \end{bmatrix} \text{ and} \tag{6.32a}$$

$$\mathbf{A_Q} = \begin{bmatrix} A_I + A_{II} & 0 & 0 & 0 \\ 0 & A_{III} + A_{IV} & 0 & 0 \\ 0 & 0 & A_I + A_{IV} & 0 \\ 0 & 0 & 0 & A_{II} + A_{III} \end{bmatrix} \tag{6.32b}$$

along with the discretized strain-displacement relationships, the bilinear approximations for the displacements and rotations, and also the discrete parameters for the strains and stresses, the discrete form of the generalized variational principle of Hu-Washizu is given by:

$$
\begin{aligned}
\Pi_{HW} = {} & \frac{1}{2}\bar{\varepsilon}^T \bar{\mathbf{D}}_{\mathbf{E}}\,\bar{\varepsilon} + \frac{1}{2}\bar{\kappa}^T \bar{\mathbf{D}}_{\mathbf{B}}\,\bar{\kappa} + \frac{1}{2}\bar{\varepsilon}^T \bar{\mathbf{D}}_{\mathbf{C}}\,\bar{\kappa} + \frac{1}{2}\bar{\kappa}^T \bar{\mathbf{D}}_{\mathbf{C}}\,\bar{\varepsilon} + \frac{1}{2}\bar{\gamma}^T \bar{\mathbf{D}}_{\mathbf{S}}\,\bar{\gamma} \\
& - \frac{1}{2}\left(\mathbf{N}^T \mathbf{A}_{\mathbf{N}}\,\bar{\varepsilon} + \bar{\varepsilon}^T \mathbf{A}_{\mathbf{N}}\,\mathbf{N}\right) - \frac{1}{2}\left(\mathbf{M}^T \mathbf{A}_{\mathbf{M}}\,\bar{\kappa} + \bar{\kappa}^T \mathbf{A}_{\mathbf{M}}\,\mathbf{M}\right) - \frac{1}{2}\left(\mathbf{Q}^T \mathbf{A}_{\mathbf{Q}}\,\bar{\gamma} + \bar{\gamma}^T \mathbf{A}_{\mathbf{Q}}\,\mathbf{Q}\right) \\
& + \frac{1}{2}\left(\mathbf{N}^T \mathbf{E}\boldsymbol{\Delta} + \boldsymbol{\Delta}^T \mathbf{E}\,\mathbf{N}\right) + \frac{1}{2}\left(\mathbf{M}^T \mathbf{B}\boldsymbol{\Delta} + \boldsymbol{\Delta}^T \mathbf{B}\,\mathbf{M}\right) + \frac{1}{2}\left(\mathbf{Q}^T \mathbf{G}\boldsymbol{\Delta} + \boldsymbol{\Delta}^T \mathbf{G}\,\mathbf{Q}\right)
\end{aligned}
\tag{6.33}
$$

The Hu-Washizu variational principle establishes that if the variation is taken with respect to nodal displacements and rotations ($\boldsymbol{\Delta}$), strains, and stresses, then all field equations of elasticity and all boundary conditions appear as Euler-Lagrange equations. In particular, the stationary condition for the functional, $\delta\Pi_{HW} = 0$, enforces the following governing discretized field equation:

$$
\begin{aligned}
& \delta\mathbf{N}^T\,(\mathbf{E}\boldsymbol{\Delta} - \mathbf{A}_{\mathbf{N}}\,\bar{\varepsilon}) + \delta\mathbf{M}^T\,(\mathbf{B}\boldsymbol{\Delta} - \mathbf{A}_{\mathbf{M}}\,\bar{\kappa}) + \delta\mathbf{Q}^T\,(\mathbf{G}\boldsymbol{\Delta} - \mathbf{A}_{\mathbf{Q}}\,\bar{\gamma}) \\
& + \delta\bar{\varepsilon}^T\,(\bar{\mathbf{D}}_{\mathbf{E}}\,\bar{\varepsilon} + \bar{\mathbf{D}}_{\mathbf{C}}\,\bar{\kappa} - \mathbf{A}_{\mathbf{N}}\,\mathbf{N}) + \delta\bar{\kappa}^T\,(\bar{\mathbf{D}}_{\mathbf{F}}\,\bar{\kappa} + \bar{\mathbf{D}}_{\mathbf{C}}\,\bar{\varepsilon} - \mathbf{A}_{\mathbf{M}}\,\mathbf{M}) + \delta\bar{\gamma}^T\,(\bar{\mathbf{D}}_{\mathbf{S}}\,\bar{\gamma} - \mathbf{A}_{\mathbf{Q}}\,\mathbf{Q}) \\
& + \delta\boldsymbol{\Delta}^T\,(\mathbf{E}^T\,\mathbf{N} + \mathbf{B}^T\,\mathbf{M} + \mathbf{G}^T\,\mathbf{Q}) - \delta\boldsymbol{\Delta}^T\,\mathbf{p} = 0\,.
\end{aligned}
\tag{6.34}
$$

1. Variation of the stress resultants leads to the discrete strain-displacement relationships:

$$
\begin{aligned}
\mathbf{E}\boldsymbol{\Delta} - \mathbf{A}_{\mathbf{N}}\,\bar{\varepsilon} = 0 \quad & \Longrightarrow \quad \bar{\varepsilon} = \mathbf{A}_N^{-1}\,\mathbf{E}\boldsymbol{\Delta}\,, \\
\mathbf{B}\boldsymbol{\Delta} - \mathbf{A}_{\mathbf{M}}\,\bar{\kappa} = 0 \quad & \Longrightarrow \quad \bar{\kappa} = \mathbf{A}_M^{-1}\,\mathbf{B}\boldsymbol{\Delta} \quad \text{and} \\
\mathbf{G}\boldsymbol{\Delta} - \mathbf{A}_{\mathbf{Q}}\,\bar{\gamma} = 0 \quad & \Longrightarrow \quad \bar{\gamma} = \mathbf{A}_Q^{-1}\,\mathbf{G}\boldsymbol{\Delta}\,.
\end{aligned}
\tag{6.35}
$$

2. Variation of the strain parameters yields the discrete constitutive equations:

$$
\begin{aligned}
\bar{\mathbf{D}}_{\mathbf{E}}\,\bar{\varepsilon} + \bar{\mathbf{D}}_{\mathbf{C}}\,\bar{\kappa} - \mathbf{A}_{\mathbf{N}}\,\mathbf{N} = 0 \quad & \Longrightarrow \quad \mathbf{N} = \mathbf{A}_N^{-1}\,\bar{\mathbf{D}}_{\mathbf{E}}\,\bar{\varepsilon} + \mathbf{A}_N^{-1}\,\bar{\mathbf{D}}_{\mathbf{C}}\,\bar{\kappa} \\
\bar{\mathbf{D}}_{\mathbf{F}}\,\bar{\kappa} + \bar{\mathbf{D}}_{\mathbf{C}}\,\bar{\varepsilon} - \mathbf{A}_{\mathbf{M}}\,\mathbf{M} = 0 \quad & \Longrightarrow \quad \mathbf{M} = \mathbf{A}_M^{-1}\,\bar{\mathbf{D}}_{\mathbf{F}}\,\bar{\kappa} + \mathbf{A}_M^{-1}\,\bar{\mathbf{D}}_{\mathbf{C}}\,\bar{\varepsilon} \\
\bar{\mathbf{D}}_{\mathbf{S}}\,\bar{\gamma} - \mathbf{A}_{\mathbf{Q}}\,\mathbf{Q} = 0 \quad & \Longrightarrow \quad \mathbf{Q} = \mathbf{A}_Q^{-1}\,\bar{\mathbf{D}}_{\mathbf{S}}\,\bar{\gamma}
\end{aligned}
\tag{6.36}
$$

3. Variation of the nodal displacements/rotations leads to the discrete form of the equilibrium equations:

$$\mathbf{E}^T\,\mathbf{N}+\mathbf{B}^T\,\mathbf{M}+\mathbf{G}^T\,\mathbf{Q}-\mathbf{p}=0\,. \tag{6.37}$$

By introducing Eqs. (6.35) in Eqs. (6.36), the parameters for the stress resultants can be expressed in terms of nodal displacements as:

$$\begin{aligned}
\mathbf{N} = &\quad \mathbf{A}_N^{-1}\,\bar{\mathbf{D}}_{\mathbf{E}}\,\mathbf{A}_N^{-1}\,\mathbf{E}\boldsymbol{\Delta}+\mathbf{A}_N^{-1}\,\bar{\mathbf{D}}_{\mathbf{C}}\,\mathbf{A}_M^{-1}\,\mathbf{B}\boldsymbol{\Delta}\,,\\
\mathbf{M} = &\quad \mathbf{A}_M^{-1}\,\bar{\mathbf{D}}_{\mathbf{F}}\,\mathbf{A}_M^{-1}\,\mathbf{B}\boldsymbol{\Delta}+\mathbf{A}_M^{-1}\,\bar{\mathbf{D}}_{\mathbf{C}}\,\mathbf{A}_N^{-1}\,\mathbf{E}\boldsymbol{\Delta}\\
\mathbf{Q} = &\quad \mathbf{A}_Q^{-1}\,\bar{\mathbf{D}}_{\mathbf{S}}\,\mathbf{A}_Q^{-1}\,\mathbf{G}\boldsymbol{\Delta}\,.
\end{aligned} \tag{6.38}$$

In a compact way, the introduction of expressions (6.38) into Eq. (6.37) yields the discrete equilibrium expressed in terms of nodal displacements and rotations as:

$$\left[\mathbf{K}_{Extension}+\mathbf{K}_{Bending}+\mathbf{K}_{Coupling}+\mathbf{K}_{Shear}\right]\boldsymbol{\Delta}=\mathbf{p} \tag{6.39}$$

Therefore, the stiffness matrix, $\mathbf{K}_{20\times20}$, is defined by the sum of the following four terms:

$$\mathbf{K}_{Extension}=\mathbf{A}_N^{-1}\,\bar{\mathbf{D}}_{\mathbf{E}}\,\mathbf{A}_N^{-1}\,\mathbf{E}\,, \tag{6.40}$$

$$\mathbf{K}_{Bending}=\mathbf{B}^T\,\mathbf{A}_M^{-1}\,\bar{\mathbf{D}}_{\mathbf{F}}\,\mathbf{A}_M^{-1}\,\mathbf{B}\,, \tag{6.41}$$

$$\mathbf{K}_{Coupling}=\mathbf{B}^T\,\mathbf{A}_M^{-1}\,\bar{\mathbf{D}}_{\mathbf{C}}\,\mathbf{A}_N^{-1}\,\mathbf{E}+\mathbf{E}^T\,\mathbf{A}_N^{-1}\,\bar{\mathbf{D}}_{\mathbf{C}}\,\mathbf{A}_M^{-1}\,\mathbf{B}\,, \tag{6.42}$$

$$\mathbf{K}_{Shear}=\mathbf{G}^T\,\mathbf{A}_Q^{-1}\,\bar{\mathbf{D}}_{\mathbf{S}}\,\mathbf{A}_Q^{-1}\,\mathbf{G}\,. \tag{6.43}$$

The governing eigenvalue equation

The eigenvalue problem for the undamped free vibration problem takes the well-known form:

$$\mathbf{K}\,\mathbf{u}=\omega^2\,\mathbf{M}\,\mathbf{u}\,, \tag{6.44}$$

where $\mathbf{K}$ is the stiffness matrix of the system, $\mathbf{u}$ represents the eigenvectors, ω is the natural frequency in rad/s and $\mathbf{M}$ is the mass matrix of the structure. The consistent element mass matrix is derived by discretizing the kinetic energy:

$$\delta\mathcal{U}_K=\frac{1}{2}\int_V \rho\,2\,\mathbf{v}\,\delta\ddot{\mathbf{v}}\mathrm{d}V\,, \tag{6.45}$$

and by employing the displacement field defined by first-order shear deformation, the integral (6.45) assumes the form:

$$\delta\mathcal{U}_K = \int_A \rho \begin{bmatrix} \delta\ddot{u}_1 & \delta\ddot{u}_2 & \delta\ddot{u}_3 & \delta\ddot{\varphi}_1 & \delta\ddot{\varphi}_2 \end{bmatrix} \begin{bmatrix} I_1 & I_1\mathcal{A} & 0 & I_2 & I_2\mathcal{A} \\ I_1\mathcal{A} & I_1 & 0 & I_2\mathcal{A} & I_2 \\ 0 & 0 & I_1 & 0 & 0 \\ I_2 & I_2\mathcal{A} & 0 & I_3 & I_3\mathcal{A} \\ I_2\mathcal{A} & I_2 & 0 & I_3\mathcal{A} & I_3 \end{bmatrix} \begin{bmatrix} u_1 \\ u_2 \\ u_3 \\ \varphi_1 \\ \varphi_2 \end{bmatrix} \mathrm{d}A\,, \tag{6.46}$$

where the terms I_1, I_2, I_3 and $\mathcal{A}$ (the contravariant components relationship) are defined by:

$$I_1 = \int_{-h/2}^{h/2} \rho(z)\mathrm{d}z, \quad I_2 = \int_{-h/2}^{h/2} \rho(z)z\mathrm{d}z, \quad I_3 = \int_{-h/2}^{h/2} \rho(z)z^2\mathrm{d}z \tag{6.47}$$

$$\mathcal{A} = \frac{a^{12}}{\sqrt{a^{11}\cdot a^{22}}} = -\cos(\alpha) \tag{6.48}$$

In addition, by the definition of the displacements and rotations through the shape functions, nodal displacements and nodal rotations in Eq. (6.21), the consistent mass matrix can be represented by:

$$\mathbf{M} = \begin{bmatrix} \mathbf{M}_{11} & \mathbf{M}_{12} & \mathbf{M}_{13} & \mathbf{M}_{14} \\ & \mathbf{M}_{22} & \mathbf{M}_{23} & \mathbf{M}_{24} \\ & & \mathbf{M}_{33} & \mathbf{M}_{34} \\ sym & & & \mathbf{M}_{44} \end{bmatrix}_{20\times 20} \tag{6.49}$$

Every $\mathbf{M}_{ij}$ term of the mass matrix, where i and j represent the row and the column respectively, assumes the following form:

$$\mathbf{M}_{ij} = \begin{bmatrix} \int_A I_1 N_i N_j dA & \int_A \mathcal{A} I_1 N_i N_j dA & 0 & \int_A I_2 N_i N_j dA & \int_A \mathcal{A} I_2 N_i N_j dA \\ & \int_A I_1 N_i N_j dA & 0 & \int_A \mathcal{A} I_2 N_i N_j dA & \int_A I_2 N_i N_j dA \\ & & \int_A I_1 N_i N_j dA & 0 & 0 \\ & & & \int_A I_3 N_i N_j dA & \int_A \mathcal{A} I_3 N_i N_j dA \\ sym & & & & \int_A I_3 N_i N_j dA \end{bmatrix}_{5\times 5} \tag{6.50}$$

Finally, we remark that all the aspects of numerical implementation associated with the above expressions are carried out by means of the commercial software package MATHEMATICA [354], which is particularly useful for the treatment of symbolic and algebraic computations.

B Transformation matrices for fourth-rank tensors.

The coordinate transformation in Eq. (2.11) can be conveniently conducted in Voigt matrix notation as $\mathbf{P}'' = \mathbf{W}\mathbf{P}\mathbf{W}^T$ with matrix $\mathbf{W}$ given by:

$$\mathbf{W} = \begin{bmatrix} g_1g_1 & g_2g_2 & g_3g_3 & 2g_2g_3 & 2g_1g_3 & 2g_1g_2 \\ g_4g_4 & g_5g_5 & g_6g_6 & 2g_5g_6 & 2g_4g_6 & 2g_4g_5 \\ g_7g_7 & g_8g_8 & g_9g_9 & 2g_8g_9 & 2g_7g_9 & 2g_7g_8 \\ g_4g_7 & g_5g_8 & g_6g_9 & g_5g_9+g_6g_8 & g_4g_9+g_6g_7 & g_7g_5+g_4g_8 \\ g_1g_7 & g_2g_8 & g_3g_9 & g_2g_9+g_3g_8 & g_1g_9+g_3g_7 & g_2g_7+g_1g_8 \\ g_1g_4 & g_2g_5 & g_3g_6 & g_3g_5+g_2g_6 & g_1g_6+g_3g_4 & g_1g_5+g_2g_4 \end{bmatrix} \tag{6.51}$$

with $\mathbf{g}$ being the rotation matrix written as:

$$\mathbf{g} = \begin{bmatrix} g_1 & g_2 & g_3 \\ g_4 & g_5 & g_6 \\ g_7 & g_8 & g_9 \end{bmatrix} \tag{6.52}$$

C Eshelby's tensor for ellipsoidal inclusions in an isotropic matrix

The Eshelby's tensor for ellipsoidal inclusions in an isotropic matrix was studied by Eshelby [82] and is well-documented in Mura [225]. Being the inclusion defined in the domain:

$$\frac{x_1^2}{a_1^2} + \frac{x_2^2}{a_2^2} + \frac{x_3^2}{a_3^2} \leq 1 \tag{6.53}$$

with a_1, a_2, and a_3 the semi-axes of the inclusion in the x_1, x_2 and x_3 axes, the Eshelby's tensor is defined as:

$$S_{ijkl} = S_{jikl} = S_{ijlk}, \tag{6.54a}$$

$$S_{1111} = \frac{3}{8\pi(1-\nu)} a_1^2 I_{11} + \frac{1-2\nu}{8\pi(1-\nu)} I_1, \tag{6.54b}$$

$$S_{1122} = \frac{1}{8\pi(1-\nu)} a_2^2 I_{12} - \frac{1-2\nu}{8\pi(1-\nu)} I_1, \tag{6.54c}$$

$$S_{1133} = \frac{1}{8\pi(1-\nu)} a_3^2 I_{13} - \frac{1-2\nu}{8\pi(1-\nu)} I_1, \tag{6.54d}$$

$$S_{1212} = \frac{a_1^2 + a_2^2}{16\pi(1-\nu)} I_{12} + \frac{1-2\nu}{16\pi(1-\nu)} I_1, \tag{6.54e}$$

$$\Delta(s) = \sqrt{(a_1^2+s)(a_2^2+s)(a_3^2+s)} \tag{6.55a}$$

$$I_1 = 2\pi a_1 a_2 a_3 \int_0^\infty \frac{\mathrm{d}s}{(a_1^2+s)\Delta(s)} \tag{6.55b}$$

$$I_{11} = 2\pi a_1 a_2 a_3 \int_0^\infty \frac{\mathrm{d}s}{(a_1^2+s)^2\Delta(s)} \tag{6.55c}$$

$$I_{12} = 2\pi a_1 a_2 a_3 \int_0^\infty \frac{\mathrm{d}s}{(a_1^2+s)(a_2^2+s)\Delta(s)} \tag{6.55d}$$

The remaining coefficients are found by simultaneous cyclic permutation of (1,2,3) and (a_1,a_2,a_3). Finally, the definition of the Eshelby's tensor in Voigt matrix notation writes:

$$S_{pq} = \begin{cases} S_{ijkl} & \text{if} \quad p = 1,2,3 \\ 2S_{ijkl} & \text{if} \quad p = 4,5,6 \end{cases} \tag{6.56}$$

D Eshelby's tensor for spheroid inclusions in a transversely isotropic matrix

Lin and Mura [193] gave expressions for the elastic fields of oblate spheroid inclusions in a transversely isotropic matrix with symmetry plane $x_2 - x_3$. The coordinates are assumed to be coincident with the principal directions of the spheroid inclusion. The aspect ratio a_1/a_3 is denoted by $\rho \geq 1$. For a transversely isotropic matrix, the elastic moduli are denoted by:

$$\begin{aligned} &d = C_{11}^m, \quad e = \frac{1}{2}(C_{11}^m - C_{12}^m), \quad f = C_{44}^m, \\ &g = C_{13}^m + C_{44}^m, \quad h = C_{33}^m \end{aligned} \tag{6.57}$$

where C_{ij}^m are the components in Voigt notation of the matrix constitutive tensor. The Eshelby's tensor **S** is calculated as [225]:

$$S_{ijmn} = \frac{1}{8\pi} C_{pqmn}^m \left(\overline{G}_{ipjq} + \overline{G}_{jpiq}\right) \tag{6.58}$$

The non-zero components of $\overline{G}_{ijkl}$ are given by:

$$\begin{aligned}\overline{G}_{1111} =\overline{G}_{2222} = \frac{1}{2}\text{ß}\int_0^1 &\Delta(1-x^2)\Big\{\Big[f(1-x^2)+h\rho^2x^2\Big]\\ &\Big[(3e+d)(1-x^2)+4f\rho^2x^2\Big]-g^2\rho^2x^2(1-x^2)\Big\}\,\mathrm{d}x,\end{aligned} \tag{6.59a}$$

$$\overline{G}_{3333} =4\pi\int_0^1 \Delta\rho^2x^2\Big[d(1-x^2)+f\rho^2x^2\Big]\Big[e(1-x^2)+f\rho^2x^2\Big]\mathrm{d}x, \tag{6.59b}$$

$$\begin{aligned}\overline{G}_{1122} =\overline{G}_{2211} = \frac{1}{2}\pi\int_0^1 &\Delta(1-x^2)\Big\{\Big[f(1-x^2)+h\rho^2x^2\Big]\\ &\Big[(e+3d)(1-x^2)+4f\rho^2x^2\Big]-3g^2\rho^2x^2(1-x^2)\Big\}\,\mathrm{d}x,\end{aligned} \tag{6.59c}$$

$$\begin{aligned}\overline{G}_{1133} =\overline{G}_{2233} = 2\pi\int_0^1 &\Delta\rho^2x^2\Big\{\Big[(d+e)(1-x^2)+2f\rho^2x^2\Big]\\ &\Big[f(1-x^2)+h\rho^2x^2\Big]-g^2\rho^2x^2(1-x^2)\Big\}\,\mathrm{d}x,\end{aligned} \tag{6.59d}$$

$$\begin{aligned}\overline{G}_{3311} =\overline{G}_{3322} = 2\pi\int_0^1 &\Delta(1-x^2)\Big\{\Big[d(1-x^2)+f\rho^2x^2\Big]\\ &\Big[e(1-x^2)+h\rho^2x^2\Big]+f\rho^2x^2\Big\}\,\mathrm{d}x,\end{aligned} \tag{6.59e}$$

$$\begin{aligned}\overline{G}_{1212} =\frac{1}{2}\pi\int_0^1 &\Delta(1-x^2)\Big\{g^2\rho^2x^2-(d-e)\Big[f(1-x^2)\\ &h\rho^2x^2\Big]\Big\}\,\mathrm{d}x,\end{aligned} \tag{6.59f}$$

$$\begin{aligned}&\overline{G}_{1313} =\overline{G}_{2323} =\\ &\quad -(2\pi)\int_0^1 \Delta g\rho^2x^2(1-x^2)\Big[e(1-x^2)+f\rho^2x^2\Big]\mathrm{d}x\end{aligned} \tag{6.59g}$$

where:

$$\begin{aligned}\Delta^{-1} =\Big[e(1-x^2)+f\rho^2x^2\Big]&\Big\{\Big[d(1-x^2)+f\rho^2x^2\Big]\\ &\Big[f(1-x^2)+h\rho^2x^2\Big]-g^2\rho^2x^2(1-x^2)\Big\}\end{aligned} \tag{6.60}$$

E Elastic moduli of composites doped with random fillers agglomerated in spherical bundles

The agglomeration scheme of an isotropic matrix doped with randomly oriented CNTs with agglomeration in spherical bundles was studied by Shi *et al*. [282]. In that work, closed-form solutions of the effective isotropic elastic properties were presented. Thence, the effective bulk moduli K_{in} and K_{out} and the effective shear moduli G_{in} and G_{out} of the bundles and the matrix, as well as the Poisson's ratio of the surrounding composite, ν_{out}, are first computed by:

$$K_{in} = K_m + f_r \frac{(\delta_r - 3K_m\alpha_r)\zeta}{3(\xi - f_r\zeta + f_r\zeta\alpha_r)} \tag{6.61a}$$

$$K_{out} = K_m + f_r \frac{(\delta_r - 3K_m\alpha_r)(1-\zeta)}{3\left[1-\xi-f_r(1-\zeta)+f_r(1-\zeta)\alpha_r\right]} \tag{6.61b}$$

$$G_{in} = G_m + f_r \frac{(\eta_r - 2G_m\beta_r)\zeta}{3(\xi - f_r\zeta + f_r\zeta\beta_r)} \tag{6.61c}$$

$$G_{out} = G_m + f_r \frac{(\eta_r - 2G_m\beta_r)(1-\zeta)}{2\left[1-\xi-f_r(1-\zeta)+f_r(1-\zeta)\beta_r\right]} \tag{6.61d}$$

$$\nu_{out} = (3K_{out} - 2G_{out})/2(3K_{out} + G_{out}) \tag{6.61e}$$

with

$$\alpha_r = \frac{3(K_m + G_m) + k_r - l_r}{3(G_m + k_r)} \tag{6.62a}$$

$$\begin{aligned}\beta_r = \frac{1}{5}\Bigg\{ & \frac{4G_m + 2k_r + l_r}{3(G_m + k_r)} + \frac{4G_m}{G_m + p_r} + \\ & + \frac{2\left[G_m(3K_m + G_m) + G_m(3K_m + 7G_m)\right]}{G_m(3K_m + G_m) + m_r(3K_m + 7G_m)}\Bigg\}\end{aligned} \tag{6.62b}$$

$$\delta_r = \frac{1}{3}\left[n_r + 2l_r + \frac{(2k_r + l_r)(3K_m + 2G_m - l_r)}{G_m + k_r}\right] \tag{6.62c}$$

$$\begin{aligned}\eta_r = \frac{1}{5}\Bigg[& \frac{2}{3}(n_r - l_r) + \frac{8m_rG_m(3K_m + 4G_m)}{3K_m(m_r + G_m) + G_m(7m_r + G_m)} + \\ & + \frac{8G_mp_r}{G_m + p_r} + \frac{2(k_r - l_r)(2G_m + l_r)}{3(G_m + k_r)}\Bigg]\end{aligned} \tag{6.62d}$$

where K_m and G_m are the bulk and shear moduli of the matrix, respectively, and k_r, l_r, m_r, n_r and p_r are fiber Hill's elastic moduli [134]. Finally, considering bundles defined as spherical inclusions, the effective bulk modulus K and the effective shear modulus G of the composite read:

$$K = K_{out}\left[1 + \frac{\zeta\left(\frac{K_{in}}{K_{out}} - 1\right)}{1 + \alpha(1-\xi)\left(\frac{K_{in}}{K_{out}} - 1\right)}\right] \tag{6.63a}$$

$$G = G_{out}\left[1 + \frac{\zeta\left(\frac{G_{in}}{G_{out}} - 1\right)}{1 + \beta(1-\xi)\left(\frac{G_{in}}{G_{out}} - 1\right)}\right] \tag{6.63b}$$

with $\alpha = (1 + \nu_{out})/3(1 - \nu_{out})$ and $\beta = 2(4 - 5\nu_{out})/15(1 - \nu_{out})$.

F Hashin-Shtrikman-Walpole bounds for randomly oriented ellipsoids

In the case of randomly oriented transversely isotropic inclusions embedded in an isotropic matrix, explicit formula for the Hashin-Shtrikman-Walpole (HSW) bounds were derived by Walpole [335]. The elastic moduli of the inclusions and the matrix can be expressed as $L_r = (2k_r, l_r, n_r, 2p_r)$ and $L_o = (3K_o, 2G_o)$, respectively. On this basis, the HSW bounds of a resulting macroscopically isotropic composite write:

$$\overline{K} = \left(\frac{f_r}{K\ast + K_1 - a_1^2/(G^* + G_1)} + \frac{f_m}{K^* + K_o} \right)^{-1} - K^*, \tag{6.64a}$$

$$\begin{aligned} \overline{G} = \Bigg[\frac{1}{5} f_r \bigg(& \frac{1}{G^* + G_1 - a_1^2/(G^* + G_1)} + \frac{2}{G^* + m_r} + \\ & + \frac{2}{G^* + p_r} \bigg) + \frac{f_m}{G^* + G_o} \Bigg]^{-1} - G^* \end{aligned} \tag{6.64b}$$

where:

$$\begin{aligned} K_1 &= \frac{1}{9}(4k_r + 4l_r + n_r), \quad G_1 = \frac{1}{3}(k_r - 2l_r + n_r), \\ K^* &= \frac{4}{3} G^a, \quad G^* = \frac{3}{2} \left[\frac{1}{G^a} + \frac{10}{9K^a + 8G^a} \right]^{-1}, \\ a_1^2 &= \frac{(n_r + l_r - 2k_r)^2}{27} \end{aligned} \tag{6.65}$$

Parameters K^a and G^a in Eq. (6.64) are selected in order to provide the tightest restrictive bounds. A general procedure to determine K^a and G^a was proposed by Walpole [335]. In particular, Eq. (6.64) provides upper bounds for bulk and shear moduli if K^a and G^a are taken as:

$$\begin{aligned} K^a &= K_g + g_1, \quad & G^a &= G_g + g_2, \\ K_g &= \max\{K_1, K_o\}, \quad & G_g &= \max\{G_1, m_r, p_r, G_o\} \end{aligned} \tag{6.66}$$

On the contrary, the lower bounds for bulk and shear moduli are obtained from Eq. (6.64) if K^a and G^a are selected as:

$$\begin{aligned} K^a &= K_l - l_1, \quad & G^a &= G_l + l_2, \\ K_l &= \min\{K_1, K_o\}, \quad & G_l &= \min\{G_1, m_r, p_r, G_o\} \end{aligned} \tag{6.67}$$

Hence, positive parameters g_1, g_2, l_1 and l_2 should be taken as small as possible without violating the following inequalities:

$$\begin{aligned}\left(K_g - K_1 + g_1\right)\left(K_g - K_1 + g_1\right) &\geq a_1^2 \\ (K_1 - K_l + l_1)(G_1 - G_l + l_1) &\geq a_1^2\end{aligned} \tag{6.68}$$

If $K_g > K_l, G_g > G_1$, then $g_1 = g_2 = 0$ and, if $K_1 > K_l, G_1 > G_l$, then $l_1 = l_2 = 0$. Otherwise , g_1 and/or g_2 (l_1 and/or l_2) must be strictly positive and inequalities (6.68) should be changed to equalities. In this case the proper choice for parameters g_1, g_2, l_1, and l_2 is $g_1 = g_2 = l_1 = l_2 = |a_1|$.

G Closed-form expression of orientational average of transversely isotropic tensor with a random distribution

A closed-form solution of the orientational average of a transversely isotropic fourth-rank tensor **L** with symmetry plane $x_2 - x_3$, and weighted by an uniform orientation distribution function can be found in Zheng *et al.* [387]. Writing the tensor **L** as:

$$L = (2K_T, l, l, n, 2G_T, 2G_L) = (c, g, h, d, e, f) \tag{6.69}$$

where

$$\begin{aligned} G_L &= L_{66}, \\ G_T &= \frac{L_{22} - L_{23}}{2}, \\ K_T &= \frac{L_{22} + L_{23}}{2}, \\ l &= L_{12}, \\ n &= L_{11} \end{aligned} \tag{6.70}$$

with L_{ij} being the tensor components in Voigt notation. Then, the orientational average of $\langle L \rangle$ weighted by a random orientation distribution reads:

$$\begin{aligned} \langle L \rangle_{ijkl} = &\left(b_5 + \frac{1}{15} b_1 + \frac{1}{3}(b_3 + b_4)\right)\delta_{ij}\delta_{kl} + \\ &+ \left(b_6 + \frac{1}{15} b_1 + \frac{2}{3} b_2\right)\left(\delta_{ik}\delta_{jl} + \delta_{il}\delta_{jk}\right) \end{aligned} \tag{6.71}$$

where b_i are defined as:

$$\begin{aligned}
b_1 &= d + \frac{c+e}{2} - g - h - 2f, \\
b_2 &= \frac{f-e}{2}, \\
b_3 &= h - \frac{c-e}{2}, \\
b_4 &= g - \frac{c-e}{2}, \\
b_5 &= \frac{c-e}{2}, \\
b_6 &= \frac{e}{2}
\end{aligned} \tag{6.72}$$

List of Figures

List of Tables

Bibliography

[1] Rashid K Abu Al-Rub, Ahmad I. Ashour, and Bryan M. Tyson, *On the aspect ratio effect of multi-walled carbon nanotube reinforcements on the mechanical properties of cementitious nanocomposites*, Construction and Building Materials **35** (2012), 647–655.

[2] Pierre-Claude Aïtcin, *Cements of yesterday and today: concrete of tomorrow*, Cement and Concrete research **30** (2000), no. 9, 1349–1359.

[3] P. M. Ajayan, O. Stephan, C. Colliex, and D. Trauth, *Aligned carbon nanotube arrays formed by cutting a polymer resin–nanotube composite*, Science **265** (1994), no. 5176, 1212–1214.

[4] M. S. Al-Haik, H. Garmestani, D. S. Li, M. Y. Hussaini, S. S. Sablin, R. Tannenbaum, and K. Dahmen, *Mechanical properties of magnetically oriented epoxy*, Journal of Polymer Science Part B: Polymer Physics **42** (2004), no. 9, 1586–1600.

[5] Liu Y. Alamusi and Ning Hu, *Numerical simulations on piezoresistivity of CNT/polymer based nanocomposites*, Computers Materials & Continua **20** (2010), 101–117.

[6] A. R. Alian, S. El-Borgi, and S. A. Meguid, *Multiscale modeling of the effect of waviness and agglomeration of CNTs on the elastic properties of nanocomposites*, Computational Materials Science **117** (2016), 195–204.

[7] A. Alibeigloo and K. M. Liew, *Thermoelastic analysis of functionally graded carbon nanotube-reinforced composite plate using theory of elasticity*, Composite Structures **106** (2013), 873–881.

[8] Akbar Alibeigloo and Ali Emtehani, *Static and free vibration analyses of carbon nanotube-reinforced composite plate using differential quadrature method*, Meccanica **50** (2015), no. 1, 61–76.

[9] Aïssa Allaoui, Shuo Bai, H. M. Cheng, and J. B. Bai, *Mechanical and electrical properties of a MWNT/epoxy composite*, Composites Science and Technology **62** (2002), no. 15, 1993–1998.

[10] Aıssa Allaoui, Suong V. Hoa, and Martin D. Pugh, *The electronic transport properties and microstructure of carbon nanofiber/epoxy composites*, Composites Science and Technology **68** (2008), no. 2, 410–416.

[11] Javier Fernando Jiménez Alonso, *Proposal and calibration of a biodynamic model of human-structure interaction by the resolution of the inverse dynamic problem: application to pedestrian bridges*, Ph.D. thesis, Universidad de Sevilla, 2015.

[12] A Ameli, P. U. Jung, and C. B. Park, *Electrical properties and electromagnetic interference shielding effectiveness of polypropylene/carbon fiber composite foams*, Carbon **60** (2013), 379–391.

[13] S. Andersson, *A study of the nanostructure of the cell wall of the tracheids of conifer xylem by x-ray scattering*, Ph.D. thesis, University of Helsinki, Finland, 2006.

[14] S. Andersson, H. Wikberg, E. Pesonen, S. L. Maunu, and R. Serimaa, *Studies of crystallinity of scots pine and norway spruce cellulose*, Trees - Structure and Function **18** (2004), no. 3, 346–353.

[15] R. Andrews, D. Jacques, A. M. Rao, T. Rantell, F. Derbyshire, Y. Chen, J. Chen, and R. C. Haddon, *Nanotube composite carbon fibers*, Applied Physics Letters **75** (1999), no. 9, 1329–1331.

[16] ANSYS, *Parametric design language guide. release 15.0*, ANSYS, Inc., 2013.

[17] B. S. Aragh, E. B. Farahani, and A. N. Barati, *Natural frequency analysis of continuously graded carbon nanotube-reinforced cylindrical shells based on third-order shear deformation theory*, Mathematics and Mechanics of Solids **18** (2012), no. 3, 264–284.

[18] B. Sobhani Aragh, A. H. Nasrollah Barati, and H. Hedayati, *Eshelby-Mori-Tanaka approach for vibrational behavior of continuously graded carbon nanotube-reinforced cylindrical panels*, Composites Part B: Engineering **43** (2012), no. 4, 1943–1954.

[19] A. Ghorbanpour Arani, S. Maghamikia, M. Mohammadimehr, and A. Arefmanesh, *Buckling analysis of laminated composite rectangular plates reinforced by SWCNTs using analytical and finite element methods*, Journal of Mechanical Science and Technology **25** (2011), no. 3, 809–820.

[20] Daniel Balageas, Claus-Peter Fritzen, and Alfredo Güemes, *Structural health monitoring*, vol. 90, John Wiley & Sons, 2010.

[21] W. S. Bao, S. A. Meguid, Z. H. Zhu, Y. Pan, and G. J. Weng, *Effect of carbon nanotube geometry upon tunneling assisted electrical network in nanocomposites*, Journal of Applied Physics **113** (2013), no. 23, 234313.

[22] A. Bayraktar, A. Altunisik, B. Sevim, and T. Türker, *Ambient vibration tests of a steel footbridge*, Journal of Nondestructive Evaluation **29** (2010), 14–24.

[23] Y. Benveniste, *A new approach to the application of Mori-Tanaka's theory in composite materials*, Mechanics of materials **6** (1987), no. 2, 147–157.

[24] Y. Benveniste, G. J. Dvorak, and T. Chen, *On diagonal and elastic symmetry of the approximate effective stiffness tensor of heterogeneous media*, Journal of the Mechanics and Physics of Solids **39** (1991), no. 7, 927–946.

[25] Claire Berger, Philippe Poncharal, Yan Yi, and Walt de Heer, *Ballistic conduction in multiwalled carbon nanotubes*, Journal of Nanoscience and Nanotechnology **3** (2003), no. 1, 171–177.

[26] L. Berhan and A. M. Sastry, *Modeling percolation in high-aspect-ratio fiber systems. II. the effect of waviness on the percolation onset*, Physical Review E **75** (2007), no. 4, 041121.

[27] D. S. Bethune, C. H. Klang, M. S. de Vries, G. Gorman, R. Savoy, J. Vazquez, and R. Beyers, *Cobalt-catalysed growth of carbon nanotubes with single-atomic-layer walls*, Nature **363** (1993), no. 6430, 605–607.

[28] M. J. Biercuk, M. C. Llaguno, M. Radosavljevic, J. K. Hyun, A. T. Johnson, and J. E. Fischer, *Carbon nanotube composites for thermal management*, Applied Physics Letters **80** (2002), no. 15, 2767–2769.

[29] O. L. Blakslee, D. G. Proctor, E. J. Seldin, G. B. Spence, and T. Weng, *Elastic constants of compression-annealed pyrolytic graphite*, Journal of Applied Physics **41** (1970), no. 8, 3373–3382.

[30] J. Bodig and B. Jayne, *Mechanics of wood and wood composites*, Von Nostrand Reinhold, New York, 1982.

[31] Christian Boller, Fu-Kuo Chang, and Yozo Fujino, *Encyclopedia of structural health monitoring*, Wiley, 2009.

[32] Vladimir V. Bolotin, *Delaminations in composite structures: its origin, buckling, growth and stability*, Composites Part B: Engineering **27** (1996), no. 2, 129–145.

[33] C. Bower, R. Rosen, L. Jin, J. Han, and O. Zhou, *Deformation of carbon nanotubes in nanotube–polymer composites*, Applied Physics Letters **74** (1999), no. 22, 3317–3319.

[34] R. D. Bradshaw, F. T. Fisher, and L. C. Brinson, *Fiber waviness in nanotube-reinforced polymer composites–II: modeling via numerical approximation of the dilute strain concentration tensor*, Composites Science and Technology **63** (2003), no. 11, 1705–1722.

[35] James M. W. Brownjohn, *Structural health monitoring of civil infrastructure*, Philosophical Transactions of the Royal Society of London A: Mathematical, Physical and Engineering Sciences **365** (2007), no. 1851, 589–622.

[36] J. Bujnak, R. Hlinka, J. Odrobinak, and J. Vican, *Diagnosis and evaluation of footbridges*, Procedia Engineering **40** (2012), 56–61.

[37] E. Caetano, A. Cunha, F. Magalhaes, and C. Moutinho, *Studies for controlling human-induced vibration of the Pedro e Inês footbridge, Portugal. Part 1: Assessment of dynamic behavior*, Engineering Structures **32** (2010), 1069–1081.

[38] E. Caetano, A. Cunha, C. Moutinho, and F. Magalhaes, *Studies for controlling human-induced vibration of the Pedro e Inês footbridge, Portugal. Part 2: Implementation of tuned mass dampers*, Engineering Structures **32** (2010), 1082–1091.

[39] Erin Camponeschi, Richard Vance, Marwan Al-Haik, Hamid Garmestani, and Rina Tannenbaum, *Properties of carbon nanotube–polymer composites aligned in a magnetic field*, Carbon **45** (2007), no. 10, 2037–2046.

[40] Jingyao Cao and D. D. L. Chung, *Electric polarization and depolarization in cement-based materials, studied by apparent electrical resistance measurement*, Cement and Concrete Research **34** (2004), no. 3, 481–485.

[41] P Castañeda, *The effect of spatial distribution on the effective behavior of composite materials and cracked media*, Journal of the Mechanics and Physics of Solids **43** (1995), no. 12, 1919–1951.

[42] R. Castro-Triguero, E. I. Saavedra Flores, F. A. DiazDelaO, M. I. Friswell, and R. Gallego, *Optimal sensor placement in timber structures by means of a multiscale approach with material uncertainty*, Structural Control and Health Monitoring **21** (2014), no. 12, 1437–1452.

[43] A. Celzard, E. McRae, C. Deleuze, M. Dufort, G. Furdin, and J. F. Marêché, *Critical concentration in percolating systems containing a high-aspect-ratio filler*, Physical Review B **53** (1996), no. 10, 6209.

[44] Arnon Chaipanich, Thanongsak Nochaiya, Watcharapong Wongkeo, and Pincha Torkittikul, *Compressive strength and microstructure of carbon nanotubes–fly ash cement composites*, Materials Science and Engineering: A **527** (2010), no. 4, 1063–1067.

[45] Y. Chandra, F. Scarpa, R. Chowdhury, S. Adhikari, and J. Sienz, *Multiscale hybrid atomistic-FE approach for the nonlinear tensile behaviour of graphene nanocomposites*, Composites Part A: Applied Science and Manufacturing **46** (2013), 147 – 153.

[46] Li Chang, Klaus Friedrich, Lin Ye, and Patricio Toro, *Evaluation and visualization of the percolating networks in multi-wall carbon nanotube/epoxy composites*, Journal of materials science **44** (2009), no. 15, 4003–4012.

[47] Bing Chen, Keru Wu, and Wu Yao, *Conductivity of carbon fiber reinforced cement-based composites*, Cement and Concrete Composites **26** (2004), no. 4, 291–297.

[48] Li Chen, Xiu-Jiang Pang, and Zuo-Long Yu, *Study on polycarbonate/multi-walled carbon nanotubes composite produced by melt processing*, Materials Science and Engineering: A **457** (2007), no. 1-2, 287–291.

[49] W. Chen, G. C. Lickfield, and C. Q. Yang, *Molecular modeling of cellulose in amorphous state. part I: model building and plastic deformation study*, Polymer **45** (2004), no. 3, 1063–1071.

[50] Yan Chen, Liping Guo, S. Patel, and D. T. Shaw, *Aligned conical carbon nanotubes*, Journal of Materials Science **35** (2000), no. 21, 5517–5521.

[51] Qunfeng Cheng, Jianwen Bao, J. G. Park, Zhiyong Liang, Chuck Zhang, and Ben Wang, *High mechanical performance composite conductor: multi-walled carbon nanotube sheet/bismaleimide nanocomposites*, Advanced Functional Materials **19** (2009), no. 20, 3219.

[52] Manuela Chiarello and Raffaele Zinno, *Electrical conductivity of self-monitoring CFRC*, Cement and Concrete Composites **27** (2005), no. 4, 463–469.

[53] J. Cho, J. J. Luo, and I. M. Daniel, *Mechanical characterization of graphite/epoxy nanocomposites by multi-scale analysis*, Composites science and technology **67** (2007), no. 11, 2399–2407.

[54] T. W. Chou, Seiichi Nomura, and Minoru Taya, *A self-consistent approach to the elastic stiffness of short-fiber composites*, Journal of Composite Materials **14** (1980), no. 3, 178–188.

[55] Rajib Chowdhury and B. N. Rao, *Assessment of high dimensional model representation techniques for reliability analysis*, Probabilistic Engineering Mechanics **24** (2009), no. 1, 100–115.

[56] John F. Clinton, S. Case Bradford, Thomas H. Heaton, and Javier Favela, *The observed wander of the natural frequencies in a structure*, Bulletin of the Seismological Society of America **96** (2006), no. 1, 237–257.

[57] Jonathan N. Coleman, Umar Khan, Werner J. Blau, and Yurii K. Gun'ko, *Small but strong: a review of the mechanical properties of carbon nanotube–polymer composites*, Carbon **44** (2006), no. 9, 1624–1652.

[58] Carole A. Cooper, Diana Ravich, David Lips, Joerg Mayer, and H. Daniel Wagner, *Distribution and alignment of carbon nanotubes and nanofibrils in a polymer matrix*, Composites Science and Technology **62** (2002), no. 7-8, 1105–1112.

[59] H. Corte and O. J. Kallmes, *Statistical geometry of a fibrous network*, The Formation and Structure of Paper, 1962, pp. 13–46.

[60] A. Cunha, E. Caetano, F. Magalhães, and C. Moutinho, *Recent perspectives in dynamic testing and monitoring of bridges*, Structural Control and Health Monitoring **20** (2013), no. 6, 853–877.

[61] Antonella D'Alessandro, Marco Rallini, Filippo Ubertini, Annibale Luigi Materazzi, and Josè Maria Kenny, *Investigations on scalable fabrication procedures for self-sensing carbon nanotube cement-matrix composites for SHM applications*, Cement and Concrete Composites **65** (2016), 200–213.

[62] Antonella D'Alessandro, Filippo Ubertini, Simon Laflamme, Marco Rallini, Annibale L Materazzi, and Josè M Kenny, *Strain sensitivity of carbon nanotube cement-based composites for structural health monitoring*, SPIE Smart Structures and Materials+ Nondestructive Evaluation and Health Monitoring, vol. 9803, 2016, pp. 980319–980319–8.

[63] Antonella D'Alessandro, Filippo Ubertini, Annibale Luigi Materazzi, Simon Laflamme, and Maurizio Porfiri, *Electromechanical modelling of a new class of nanocomposite cement-based sensors for structural health monitoring*, Structural Health Monitoring (2014), 1475921714560071.

[64] Georges R. Darbre and Jean Proulx, *Continuous ambient-vibration monitoring of the arch dam of mauvoisin*, Earthquake engineering & structural dynamics **31** (2002), no. 2, 475–480.

[65] B. G. Demczyk, Y. M. Wang, J. Cumings, M. Hetman, W. Han, A. Zettl, and R. O. Ritchie, *Direct mechanical measurement of the tensile strength and elastic modulus of multiwalled carbon nanotubes*, Materials Science and Engineering: A **334** (2002), no. 1, 173–178.

[66] Fei Deng and Quan-Shui Zheng, *An analytical model of effective electrical conductivity of carbon nanotube composites*, Applied Physics Letters **92** (2008), no. 7, 071902.

[67] S. Dey, T. Mukhopadhyay, S. K. Sahu, G. Li, H. Rabitz, and S. Adhikari, *Thermal uncertainty quantification in frequency responses of laminated composite plates*, Composites Part B: Engineering **80** (2015), 186–197.

[68] S. Dey, T. Mukhopadhyay, A. Spickenheuer, S. Adhikari, and G. Heinrich, *Bottom up surrogate based approach for stochastic frequency response analysis of laminated composite plates*, Composite Structures **140** (2016), 712–727.

[69] Sudip Dey, Tanmoy Mukhopadhyay, and Sondipon Adhikari, *Stochastic free vibration analyses of composite doubly curved shells - a Kriging model approach*, Composites Part B: Engineering **70** (2015), 99–112.

[70] Sudip Dey, Tanmoy Mukhopadhyay, and Sondipon Adhikari, *Stochastic free vibration analysis of angle-ply composite plates - A RS-HDMR approach*, Composite Structures **122** (2015), 526–536.

[71] Jaehyeok Doh and Jongsoo Lee, *Prediction of the mechanical behavior of double walled-CNTs using a molecular mechanics-based finite element method: Effects of chirality*, Computers & Structures **169** (2016), 91–100.

[72] L. A. Donaldson and A. P. Singh, *Bridge-like structures cellulose microfibrils*, Holzforschung **52** (1998), no. 5, 449–454.

[73] Shuhong Dong, Jianqiu Zhou, Hongxi Liu, and Dexing Qi, *Computational prediction of waviness and orientation effects in carbon nanotube reinforced metal matrix composites*, Computational Materials Science **101** (2015), 8–15.

[74] Austin Downey, Enrique Garcia-Macias, Antonella D'Alessandro, Simon Laflamme, Rafael Castro-Triguero, and Filippo Ubertini, *Continuous and embedded solutions for SHM of concrete structures using changing electrical potential in self-sensing cement-based composites*, Nondestructive Characterization and Monitoring of Advanced Materials, Aerospace, and Civil Infrastructure 2017 (H. Felix Wu, Andrew L. Gyekenyesi, Peter J. Shull, and Tzu-Yang Yu, eds.), SPIE, apr 2017.

[75] Yael Dror, Wael Salalha, Rafail L. Khalfin, Yachin Cohen, Alexander L. Yarin, and Eyal Zussman, *Carbon nanotubes embedded in oriented polymer nanofibers by electrospinning*, Langmuir **19** (2003), no. 17, 7012–7020.

[76] Martin L. Dunn, Hassel Ledbetter, Paul R. Heyliger, and Chang Sun Choi, *Elastic constants of textured short-fiber composites*, Journal of the Mechanics and Physics of Solids **44** (1996), no. 9, 1509–1541.

[77] G. J. Dvorak and A. Bahei-El-Din, *Inelastic composite materials: Transformation analysis and experiments*, Continuum Micromechanics, Springer Nature, 1997, pp. 1–59.

[78] T. W. Ebbesen, H. J. Lezec, H. Hiura, J. W. Bennett, H. F. Ghaemi, and T. Thio, *Electrical conductivity of individual carbon nanotubes*, Nature **382** (1996), 54–56.

[79] E. Efraim and M. Eisenberger, *Exact vibration analysis of variable thickness thick annular isotropic and FGM plates*, Journal of Sound and Vibration **299** (2007), no. 4, 720–738.

[80] Lene Eliassen, Eivind Sæta, and Jørgen Krokstad, *Measurement campaign of a large rotor wind turbine*, Energy Procedia **80** (2015), 159–167.

[81] Merit Enckell, Branko Glisic, Frank Myrvoll, and Benny Bergstrand, *Evaluation of a large-scale bridge strain, temperature and crack monitoring with distributed fibre optic sensors*, Journal of Civil Structural Health Monitoring **1** (2011), no. 1-2, 37–46.

[82] J. D. Eshelby, *The determination of the elastic field of an ellipsoidal inclusion, and related problems*, Proceedings of the Royal Society of London. Series A. Mathematical and Physical Sciences **241** (1957), no. 1226, 376–396.

[83] J. D. Eshelby, *The elastic field outside an ellipsoidal inclusion*, Proceedings of the Royal Society of London. Series A, Mathematical and Physical Sciences (1959), 561–569.

[84] Federal Highway Administration, *Status of the nation's highways, bridges, and transit: Conditions and performance*, US Department of Transportation (2006).

[85] C. Feng and L. Y. Jiang, *Investigation of uniaxial stretching effects on the electrical conductivity of CNT-polymer nanocomposites*, Journal of Physics D: Applied Physics **47** (2014), no. 40, 405103.

[86] Chuang Feng, *Micromechanics modeling of the electrical conductivity of carbon nanotude (cnt)-polymer nanocomposites*, Ph.D. thesis, University of Western Ontario, 2014.

[87] Chuang Feng and Liying Jiang, *Micromechanics modeling of the electrical conductivity of carbon nanotube (CNT)–polymer nanocomposites*, Composites Part A: Applied Science and Manufacturing **47** (2013), 143–149.

[88] Chuang Feng and Liying Jiang, *Micromechanics modeling of bi-axial stretching effects on the electrical conductivity of CNT-polymer composites*, International Journal of Applied Mechanics **7** (2015), no. 01, 1550005.

[89] Mauro Ferrari, *Asymmetry and the high concentration limit of the Mori-Tanaka effective medium theory*, Mechanics of Materials **11** (1991), no. 3, 251–256.

[90] Mauro Ferrari, *Composite homogenization via the equivalent poly-inclusion approach*, Composites Engineering **4** (1994), no. 1, 37–45.

[91] Mauro Ferrari and George C. Johnson, *Effective elasticities of short-fiber composites with arbitrary orientation distribution*, Mechanics of Materials **8** (1989), no. 1, 67–73.

[92] André Duarte B. L. Ferreira, Paulo R. O. Nóvoa, and António Torres Marques, *Multifunctional material systems: A state-of-the-art review*, Composite Structures **151** (2016), 3–35.

[93] F. T. Fisher, R. D. Bradshaw, and L. C. Brinson, *Fiber waviness in nanotube-reinforced polymer composites–I: Modulus predictions using effective nanotube properties*, Composites Science and Technology **63** (2003), no. 11, 1689–1703.

[94] E. I. Saavedra Flores, F. A. DiazDelaO, R. M. Ajaj, M. I. Friswell, and G. F. Fernando, *Mathematical modelling of the stochastic mechanical properties of wood and its extensibility at small scales*, Applied Mathematical Modelling **38** (2014), no. 15–16, 3958–3967.

[95] Giovanni Formica, Walter Lacarbonara, and Roberto Alessi, *Vibrations of carbon nanotube-reinforced composites*, Journal of Sound and Vibration **329** (2010), no. 10, 1875–1889.

[96] S. Fortino, A. Genoese, A. Genoese, L. Nunes, and P. Palma, *Numerical modelling of the hygro-thermal response of timber bridge during their service life: A monitoring case-study*, Construction and Building Materials **47** (2013), 1225–1234.

[97] S. Frank, *Carbon nanotube quantum resistors*, Science **280** (1998), no. 5370, 1744–1746.

[98] Mitsutaka Fujita, Riichiro Saito, G. Dresselhaus, and M. S. Dresselhaus, *Formation of general fullerenes by their projection on a honeycomb lattice*, Physical Review B **45** (1992), no. 23, 13834–13836.

[99] O. Galao, F. J. Baeza, E. Zornoza, and P. Garcés, *Strain and damage sensing properties on multifunctional cement composites with CNF admixture*, Cement and concrete composites **46** (2014), 90–98.

[100] Lei Gao and Zhenya Li, *Effective medium approximation for two-component nonlinear composites with shape distribution*, Journal of physics: Condensed matter **15** (2003), no. 25, 4397.

[101] Enrique García-Macías, Rafael Castro-Triguero, Erick I Saavedra Flores, Michael I Friswell, and Rafael Gallego, *Static and free vibration analysis of functionally graded carbon nanotube reinforced skew plates*, Composite Structures **140** (2016), 473–490.

[102] Enrique García-Macías, Antonella D'Alessandro, Rafael Castro-Triguero, Domingo Pérez-Mira, and Filippo Ubertini, *Micromechanics modeling of the electrical conductivity of carbon nanotube cement-matrix composites*, Composites Part B: Engineering **108** (2017), 451–469.

[103] Enrique García-Macías, Antonella D'Alessandro, Rafael Castro-Triguero, Domingo Pérez-Mira, and Filippo Ubertini, *Micromechanics modeling of the uniaxial strain-sensing property of carbon nanotube cement-matrix composites for SHM applications*, Composite Structures **163** (2017), 195–215.

[104] Enrique García-Macías, Luis Rodríguez-Tembleque, Rafael Castro-Triguero, and Andrés Sáez, *Buckling analysis of functionally graded carbon nanotube-reinforced curved panels under axial compression and shear*, Composites Part B: Engineering **108** (2017), 243–256.

[105] Amar C. Garg, *Delamination – a damage mode in composite structures*, Engineering Fracture Mechanics **29** (1988), no. 5, 557–584.

[106] H. Garmestani, M. S. Al-Haik, K. Dahmen, R. Tannenbaum, D. Li, S. S. Sablin, and M. Y. Hussaini, *Polymer-mediated alignment of carbon nanotubes under high magnetic fields*, Advanced Materials **15** (2003), no. 22, 1918–1921.

[107] C. Gentile and N. Gallino, *Ambient vibration testing and structural evaluation of an historic suspension footbridge*, Advances in Engineering Software **39** (2008), 356–366.

[108] Hamid Ghasemi, Roham Rafiee, Xiaoying Zhuang, Jacob Muthu, and Timon Rabczuk, *Uncertainties propagation in metamodel-based probabilistic optimization of CNT/polymer composite structure using stochastic multi-scale modeling*, Computational Materials Science **85** (2014), 295–305.

[109] Swapan Kumar Ghosh, *Self-healing materials: fundamentals, design strategies, and applications*, John Wiley & Sons, 2009.

[110] Branko Glisic and Daniele Inaudi, *Distributed fiber-optic sensing and integrity monitoring*, Transportation Research Record: Journal of the Transportation Research Board **2150** (2010), no. 1, 96–102.

[111] GLULAM, *Structural glued laminated timber – Design essentials*, Glued Laminated Timber Association (2010).

[112] B. Gommers, I. Verpoest, and P. Van Houtte, *The Mori-Tanaka method applied to textile composite materials*, Acta Materialia **46** (1998), no. 6, 2223–2235.

[113] Shen Gong and Zheng H. Zhu, *On the mechanism of piezoresistivity of carbon nanotube polymer composites*, Polymer **55** (2014), no. 16, 4136–4149.

[114] Michael Griebel and Jan Hamaekers, *Molecular dynamics simulations of the elastic moduli of polymer–carbon nanotube composites*, Computer Methods in Applied Mechanics and Engineering **193** (2004), no. 17, 1773–1788.

[115] Fabienne Grillard, Christèle Jaillet, Cécile Zakri, Pierre Miaudet, Alain Derré, Alexander Korzhenko, Patrice Gaillard, and Philippe Poulin, *Conductivity and percolation of nanotube based polymer composites in extensional deformations*, Polymer **53** (2012), no. 1, 183–187.

[116] G Grimmett, *Percolation Springer-Verlag*, vol. 321, Grundlehren der mathematischen Wissenschaften, 1999.

[117] Noriaki Hamada, Shin ichi Sawada, and Atsushi Oshiyama, *New one-dimensional conductors: Graphitic microtubules*, Physical Review Letters **68** (1992), no. 10, 1579–1581.

[118] B. G. Han, B. Z. Han, and J. P. Ou, *Experimental study on use of nickel powder-filled Portland cement-based composite for fabrication of piezoresistive sensors with high sensitivity*, Sensors and Actuators A: Physical **149** (2009), no. 1, 51–55.

[119] B. G. Han, B. Z. Han, and X. Yu, *Experimental study on the contribution of the quantum tunneling effect to the improvement of the conductivity and piezoresistivity of a nickel powder-filled cement-based composite*, Smart Materials and Structures **18** (2009), no. 6, 065007.

[120] Baoguo Han, Siqi Ding, and Xun Yu, *Intrinsic self-sensing concrete and structures: A review*, Measurement **59** (2015), 110–128.

[121] Baoguo Han, Xinchun Guan, and Jinping Ou, *Electrode design, measuring method and data acquisition system of carbon fiber cement paste piezoresistive sensors*, Sensors and Actuators A: Physical **135** (2007), no. 2, 360–369.

[122] Baoguo Han and Jinping Ou, *Embedded piezoresistive cement-based stress/strain sensor*, Sensors and Actuators A: Physical **138** (2007), no. 2, 294–298.

[123] Baoguo Han, Yunyang Wang, Sufen Dong, Liqing Zhang, Siqi Ding, Xun Yu, and Jinping Ou, *Smart concretes and structures: A review*, Journal of intelligent material systems and structures **26** (2015), no. 11, 1303–1345.

[124] Baoguo Han, Xun Yu, and Eil Kwon, *A self-sensing carbon nanotube/cement composite for traffic monitoring*, Nanotechnology **20** (2009), no. 44, 445501.

[125] Baoguo Han, Xun Yu, and Jinping Ou, *Multifunctional and smart carbon nanotube reinforced cement-based materials*, Nanotechnology in civil infrastructure, Springer, 2011, pp. 1–47.

[126] Baoguo Han, Kun Zhang, Xun Yu, Eil Kwon, and Jinping Ou, *Electrical characteristics and pressure-sensitive response measurements of carboxyl mwnt/cement composites*, Cement and Concrete Composites **34** (2012), no. 6, 794–800.

[127] Yue Han and James Elliott, *Molecular dynamics simulations of the elastic properties of polymer/carbon nanotube composites*, Computational Materials Science **39** (2007), no. 2, 315–323.

[128] Peter John Frederich Harris, *Carbon nanotube science: synthesis, properties and applications*, Cambridge University Press, 2009.

[129] Z. Hashin and S. Shtrikman, *On some variational principles in anisotropic and nonhomogeneous elasticity*, Journal of the Mechanics and Physics of Solids **10** (1962), no. 4, 335–342.

[130] Z. Hashin and S. Shtrikman, *A variational approach to the theory of the elastic behaviour of multiphase materials*, Journal of the Mechanics and Physics of Solids **11** (1963), no. 2, 127–140.

[131] Hiroshi Hatta and Minoru Taya, *Effective thermal conductivity of a misoriented short fiber composite*, Journal of Applied Physics **58** (1985), no. 7, 2478–2486.

[132] Wasim M. K. Helal and Dongyan Shi, *Optimum material gradient for functionally graded rectangular plate with the finite element method*, Indian Journal of Materials Science **2014** (2014).

[133] M. Heshmati and M. H. Yas, *Vibrations of non-uniform functionally graded MWCNTs-polystyrene nanocomposite beams under action of moving load*, Materials & Design **46** (2013), 206–218.

[134] R. Hill, *A self-consistent mechanics of composite materials*, Journal of the Mechanics and Physics of Solids **13** (1965), no. 4, 213–222.

[135] K. Hofstetter, C. Hellmich, and J. Eberhardsteiner, *Development and experimental validation of a continuum micromechanics model for the elasticity of wood*, European Journal of Mechanics A/Solids **24** (2005), no. 6, 1030–1053.

[136] T. C. Hou and J. P. Lynch, *Conductivity-based strain monitoring and damage characterization of fiber reinforced cementitious structural components*, Proc. SPIE, vol. 5765, 2005, pp. 419–429.

[137] R. N. Howser, H. B. Dhonde, and Y. L. Mo, *Self-sensing of carbon nanofiber concrete columns subjected to reversed cyclic loading*, Smart materials and structures **20** (2011), no. 8, 8.

[138] H. M. Hsiao and I. M. Daniel, *Elastic properties of composites with fiber waviness*, Composites Part A: Applied Science and Manufacturing **27** (1996), no. 10, 931–941.

[139] Ning Hu, Hisao Fukunaga, Satoshi Atobe, Yaolu Liu, and Jinhua Li, *Piezoresistive strain sensors made from carbon nanotubes based polymer nanocomposites*, Sensors **11** (2011), no. 11, 10691–10723.

[140] Ning Hu, Yoshifumi Karube, Masahiro Arai, Tomonori Watanabe, Cheng Yan, Yuan Li, Yaolu Liu, and Hisao Fukunaga, *Investigation on sensitivity of a polymer/carbon nanotube composite strain sensor*, Carbon **48** (2010), no. 3, 680–687.

[141] Ning Hu, Yoshifumi Karube, Cheng Yan, Zen Masuda, and Hisao Fukunaga, *Tunneling effect in a polymer/carbon nanotube nanocomposite strain sensor*, Acta Materialia **56** (2008), no. 13, 2929–2936.

[142] W. H. Hu, C. Moutinho, E. Caetano, F. Magalhaes, and A. Cunha, *Continuous dynamic monitoring of a lively footbridge for serviceability assessment and damage detection*, Mechanical Systems and Signal Processing **33** (2012), 38–55.

[143] S. Iijima, *Helical microtubules of graphitic carbon*, Nature (London, United Kingdom) **354** (1991), no. 6348, 56–58.

[144] Sumio Iijima, Charles Brabec, Amitesh Maiti, and Jerzy Bernholc, *Structural flexibility of carbon nanotubes*, The Journal of Chemical Physics **104** (1996), no. 5, 2089–2092.

[145] S. Ivorra, D. Foti, D. Bru, and F. J. Baeza, *Dynamic behavior of a pedestrian bridge in alicante, spain*, Journal of Performance of Constructed Facilities **29** (2014), no. 5, 04014132.

[146] T. Iwakuma and S. Nemat-Nasser, *Finite elastic-plastic deformation of polycrystalline metals*, Proceedings of the Royal Society A: Mathematical, Physical and Engineering Sciences **394** (1984), no. 1806, 87–119.

[147] Sung-Hwan Jang, Shiho Kawashima, and Huiming Yin, *Influence of carbon nanotube clustering on mechanical and electrical properties of cement pastes*, Materials **9** (2016), no. 4, 220.

[148] X. Y. Ji, Y. P. Cao, and X. Q. Feng, *Micromechanics prediction of the effective elastic moduli of graphene sheet-reinforced polymer nanocomposites*, Modelling and Simulation in Materials Science and Engineering **18** (2010), no. 4, 045005.

[149] Gary K. Johns, *Modeling piezoresistivity in silicon and polysilicon*, Journal of Applied Engineering Mathematics April **2** (2006), 1–5.

[150] Saeed Kamarian, Mostafa Salim, Rossana Dimitri, and Francesco Tornabene, *Free vibration analysis of conical shells reinforced with agglomerated carbon nanotubes*, International Journal of Mechanical Sciences **108** (2016), 157–165.

[151] D. C. Kammer, *Sensor placement for on-orbit modal identification and correlation of large space structures*, Journal of Guidance, Control and Dynamics **14** (1991), 251–259.

[152] D. C. Kammer and L. Yao, *Enhancement of on-orbit modal identification of large space structures through sensor placement*, Journal of Sound and Vibration **171** (1994), no. 1, 119–139.

[153] Inpil Kang, Yun Yeo Heung, Jay H. Kim, Jong Won Lee, Ramanand Gollapudi, Srinivas Subramaniam, Suhasini Narasimhadevara, Douglas Hurd, Goutham R Kirikera, Vesselin Shanov, et al., *Introduction to carbon nanotube and nanofiber smart materials*, Composites Part B: Engineering **37** (2006), no. 6, 382–394.

[154] Inpil Kang, Mark J. Schulz, Jay H. Kim, Vesselin Shanov, and Donglu Shi, *A carbon nanotube strain sensor for structural health monitoring*, Smart materials and structures **15** (2006), no. 3, 737–748.

[155] Liao-Liang Ke, Jie Yang, and Sritawat Kitipornchai, *Nonlinear free vibration of functionally graded carbon nanotube-reinforced composite beams*, Composite Structures **92** (2010), no. 3, 676–683.

[156] N. Kharghani and C. Guedes Soares, *Behavior of composite laminates with embedded delaminations*, Composite Structures **150** (2016), 226–239.

[157] Y. Kiani, *Thermal post-buckling of FG-CNT reinforced composite plates*, Composite Structures **159** (2017), 299–306.

[158] T. Kimura, H. Ago, M. Tobita, S. Ohshima, M. Kyotani, and M. Yumura, *Polymer composites of carbon nanotubes aligned by a magnetic field*, Advanced Materials **14** (2002), no. 19, 1380–1383.

[159] Scott Kirkpatrick, *Percolation and conduction*, Reviews of modern physics **45** (1973), no. 4, 574.

[160] F. Ko, Y. Gogotsi, A. Ali, N. Naguib, H. Ye, G. L. Yang, C. Li, and P. Willis, *Electrospinning of continuous carbon nanotube-filled nanofiber yarns*, Advanced Materials **15** (2003), no. 14, 1161–1165.

[161] J. M. Ko and Y. Q. Ni, *Technology developments in structural health monitoring of large-scale bridges*, Engineering structures **27** (2005), no. 12, 1715–1725.

[162] J. R. Koehler and A. B. Owen, *9 Computer experiments*, Handbook of statistics **13** (1996), 261–308.

[163] Takashi Komori and Kunio Makishima, *Numbers of fiber-to-fiber contacts in general fiber assemblies*, Textile Research Journal **47** (1977), no. 1, 13–17.

[164] Maria S. Konsta-Gdoutos and Chrysoula A. Aza, *Self sensing carbon nanotube (CNT) and nanofiber (CNF) cementitious composites for real time damage assessment in smart structures*, Cement and Concrete Composites **53** (2014), 162–169.

[165] Maria S. Konsta-Gdoutos, Zoi S. Metaxa, and Surendra P. Shah, *Highly dispersed carbon nanotube reinforced cement based materials*, Cement and Concrete Research **40** (2010), no. 7, 1052–1059.

[166] Maria S. Konsta-Gdoutos, Zoi S. Metaxa, and Surendra P. Shah, *Multi-scale mechanical and fracture characteristics and early-age strain capacity of high performance carbon nanotube/cement nanocomposites*, Cement and Concrete Composites **32** (2010), no. 2, 110–115.

[167] Ki-Young Koo, J. M. W. Brownjohn, DI List, and R. Cole, *Structural health monitoring of the Tamar suspension bridge*, Structural Control and Health Monitoring **20** (2013), no. 4, 609–625.

[168] Th. V. Kosmidou, A. S. Vatalis, C. G. Delides, E. Logakis, P. Pissis, and G. C. Papanicolaou, *Structural, mechanical and electrical characterization of epoxy-amine/carbon black nanonocomposites*, Express Polymer Letters **2** (2008), no. 5, 364–372.

[169] Vijay Kumar and Amit Rawal, *Tuning the electrical percolation threshold of polymer nanocomposites with rod-like nanofillers*, Polymer **97** (2016), 295–299.

[170] Yu Kuronuma, Tomo Takeda, Yasuhide Shindo, Fumio Narita, and Zhijuan Wei, *Electrical resistance-based strain sensing in carbon nanotube/polymer composites under tension: analytical modeling and experiments*, Composites Science and Technology **72** (2012), no. 14, 1678–1682.

[171] Simon Laflamme, Filippo Ubertini, Hussam Saleem, Antonella D'Alessandro, Austin Downey, Halil Ceylan, and Annibale Luigi Materazzi, *Dynamic characterization of a soft elastomeric capacitor for structural health monitoring*, Journal of Structural Engineering **141** (2014), no. 8, 04014186.

[172] Changgu Lee, Xiaoding Wei, Jeffrey W. Kysar, and James Hone, *Measurement of the elastic properties and intrinsic strength of monolayer graphene*, science **321** (2008), no. 5887, 385–388.

[173] Z. X. Lei, L. W. Zhang, and K. M. Liew, *Vibration analysis of CNT-reinforced functionally graded rotating cylindrical panels using the element-free kp-Ritz method*, Composites Part B: Engineering **77** (2015), 291–303.

[174] Z. X. Lei, L. W. Zhang, and K. M. Liew, *Parametric analysis of frequency of rotating laminated CNT reinforced functionally graded cylindrical panels*, Composites Part B: Engineering **90** (2016), 251–266.

[175] Z. X. Lei, L. W. Zhang, KM Liew, and J. L. Yu, *Dynamic stability analysis of carbon nanotube-reinforced functionally graded cylindrical panels using the element-free kp-Ritz method*, Composite Structures **113** (2014), 328–338.

[176] Chunyu Li, Erik T. Thostenson, and Tsu-Wei Chou, *Dominant role of tunneling resistance in the electrical conductivity of carbon nanotube–based composites*, Applied Physics Letters **91** (2007), no. 22, 223114.

[177] Chunyu Li, Erik T. Thostenson, and Tsu-Wei Chou, *Effect of nanotube waviness on the electrical conductivity of carbon nanotube-based composites*, Composites Science and Technology **68** (2008), no. 6, 1445–1452.

[178] F. Li, H. M. Cheng, S. Bai, G. Su, and M. S. Dresselhaus, *Tensile strength of single-walled carbon nanotubes directly measured from their macroscopic ropes*, Applied physics letters **77** (2000), no. 20, 3161–3163.

[179] Geng Ying Li, Pei Ming Wang, and Xiaohua Zhao, *Pressure-sensitive properties and microstructure of carbon nanotube reinforced cement composites*, Cement and Concrete Composites **29** (2007), no. 5, 377–382.

[180] Genyuan Li and Herschel Rabitz, *Ratio control variate method for efficiently determining high-dimensional model representations*, Journal of computational chemistry **27** (2006), no. 10, 1112–1118.

[181] Genyuan Li, Herschel Rabitz, Sheng-Wei Wang, and Panos G. Georgopoulos, *Correlation method for variance reduction of Monte Carlo integration in RS-HDMR*, Journal of Computational Chemistry **24** (2003), no. 3, 277–283.

[182] Genyuan Li, Sheng-Wei Wang, and Herschel Rabitz, *Practical approaches to construct RS-HDMR component functions*, The Journal of Physical Chemistry A **106** (2002), no. 37, 8721–8733.

[183] Genyuan Li, Sheng-Wei Wang, Herschel Rabitz, Sookyun Wang, and Peter Jaffé, *Global uncertainty assessments by high dimensional model representations (hdmr)*, Chemical Engineering Science **57** (2002), no. 21, 4445–4460.

[184] Hui Li, H. G. Xiao, and J. P. Ou, *A study on mechanical and pressure-sensitive properties of cement mortar with nanophase materials*, Cement and Concrete research **34** (2004), no. 3, 435–438.

[185] Hui Li, H. G. Xiao, and J. P. Ou, *Effect of compressive strain on electrical resistivity of carbon black-filled cement-based composites*, Cement and Concrete Composites **28** (2006), no. 9, 824–828.

[186] Hui Li, H. G. Xiao, Jie Yuan, and Jinping Ou, *Microstructure of cement mortar with nano-particles*, Composites Part B: Engineering **35** (2004), no. 2, 185–189.

[187] Jiang Yu Li, *On micromechanics approximation for the effective thermoelastic moduli of multi-phase composite materials*, Mechanics of Materials **31** (1999), no. 2, 149–159.

[188] Zheling Li, Robert J. Young, Neil R. Wilson, Ian A. Kinloch, Cristina Vallés, and Zheng Li, *Effect of the orientation of graphene-based nanoplatelets upon the Young's modulus of nanocomposites*, Composites Science and Technology **123** (2016), 125–133.

[189] Yishun Liao and Xiaosheng Wei, *Penetration resistance and electrical resistivity of cement paste with superplasticizer*, Materials and structures **47** (2014), no. 4, 563–570.

[190] Charles M. Lieber, Teri Wang Odom, Jin-Lin Huang, and Philip Kim, *Atomic structure and electronic properties of single-walled carbon nanotubes*, Nature **391** (1998), no. 6662, 62–64.

[191] K. M. Liew, Z. X. Lei, and L. W. Zhang, *Mechanical analysis of functionally graded carbon nanotube reinforced composites: a review*, Composite Structures **120** (2015), 90–97.

[192] Chuan Lin, Hongtao Wang, and Wei Yang, *Variable percolation threshold of composites with fiber fillers under compression*, Journal of Applied Physics **108** (2010), no. 1, 013509.

[193] S. C. Lin and T. Mura, *Elastic fields of inclusions in anisotropic media (II)*, Physica Status Solidi (a) **15** (1973), no. 1, 281–285.

[194] K. J. Loh, T. C. Hou, J. P. Lynch, and N. A. Kotov, *Nanotube-based sensing skins for crack detection and impact monitoring of structures*, Proceedings of the 6th International Workshop on Structural Health Monitoring, Stanford, CA, USA, 2007.

[195] Kenneth J. Loh, Jerome P. Lynch, B. S. Shim, and N. A. Kotov, *Tailoring piezoresistive sensitivity of multilayer carbon nanotube composite strain sensors*, Journal of Intelligent Material Systems and Structures **19** (2008), no. 7, 747–764.

[196] Søren Nymand Lophaven, Hans Bruun Nielsen, and Jacob Søndergaard, *DACE-A MATLAB Kriging toolbox, version 2.0*, Tech. report, 2002.

[197] Jian Ping Lu and Jie Han, *Carbon nanotubes and nanotube-based nano devices*, International Journal of High Speed Electronics and Systems **9** (1998), no. 01, 101–123.

[198] Weibang Lu, Tsu-Wei Chou, and Erik T. Thostenson, *A three-dimensional model of electrical percolation thresholds in carbon nanotube-based composites*, Applied Physics Letters **96** (2010), no. 22, 223106.

[199] Vlado Lubarda and Michelle Chen, *On the elastic moduli and compliances of transversely isotropic and orthotropic materials*, Journal of Mechanics of Materials and Structures **3** (2008), no. 1, 153–171.

[200] H. M. Ma and X. L. Gao, *A three-dimensional monte carlo model for electrically conductive polymer matrix composites filled with curved fibers*, Polymer **49** (2008), no. 19, 4230–4238.

[201] F. Magalhães, A. Cunha, and E. Caetano, *Vibration based structural health monitoring of an arch bridge: From automated OMA to damage detection*, Mechanical Systems and Signal Processing **28** (2012), 212–228.

[202] P. Malekzadeh and A. R. Zarei, *Free vibration of quadrilateral laminated plates with carbon nanotube reinforced composite layers*, Thin-Walled Structures **82** (2014), 221–232.

[203] Mario Martin-Gallego, M. M. Bernal, M. Hernandez, Raquel Verdejo, and Miguel A. Lopez-Manchado, *Comparison of filler percolation and mechanical properties in graphene and carbon nanotubes filled epoxy nanocomposites*, European Polymer Journal **49** (2013), no. 6, 1347–1353.

[204] Nicola Marzari and Mauro Ferrari, *Textural and micromorphological effects on the overall elastic response of macroscopically anisotropic composites*, Journal of Applied Mechanics **59** (1992), no. 2, 269.

[205] Annibale Luigi Materazzi, Filippo Ubertini, and Antonella D'Alessandro, *Carbon nanotube cement-based transducers for dynamic sensing of strain*, Cement and Concrete Composites **37** (2013), 2–11.

[206] Bryant Mather, *Concrete durability*, Cement and Concrete Composites **26** (2004), no. 1, 3–4.

[207] Georges Matheron, *Principles of geostatistics*, Economic geology **58** (1963), no. 8, 1246–1266.

[208] MathWorks, *Parallel computing toolbox: For use with MATLAB. User's guide*, 2012.

[209] Anna Y. Matveeva, Sergey V. Pyrlin, Marta M. D. Ramos, Helmut J. Böhm, and Ferrie W. J. van Hattum, *Influence of waviness and curliness of fibres on mechanical properties of composites*, Computational Materials Science **87** (2014), 1–11.

[210] T. Page McAndrew, Pierre Laurent, Mickael Havel, and Chris Roger, *Arkema graphistrength® multi-walled carbon nanotubes*, Technical Proceedings of the 2008 NSTI Nanotechnology Conference and Trade Show, NSTI-Nanotech, Nanotechnology 2008 **1** (2008), 47–50.

[211] Meyya Meyyappan, *Carbon nanotubes: science and applications*, CRC press, 2004.

[212] Yu Miao, Li Chen, Yingzi Lin, R. Sammynaiken, and W. J. Zhang, *On finding of high piezoresistive response of carbon nanotube films without surfactants for in-plane strain detection*, Journal of Intelligent Material Systems and Structures **22** (2011), no. 18, 2155–2159.

[213] J. W. Mintmire, B. I. Dunlap, and C. T. White, *Are fullerene tubules metallic?*, Physical Review Letters **68** (1992), no. 5, 631–634.

[214] Cynthia A. Mitchell, Jeffrey L. Bahr, Sivaram Arepalli, James M. Tour, and Ramanan Krishnamoorti, *Dispersion of functionalized carbon nanotubes in polystyrene*, Macromolecules **35** (2002), no. 23, 8825–8830.

[215] M. Mitchell, *An introduction to genetic algorithms*, MIT Press, 1998.

[216] Toby J. Mitchell and Max D. Morris, *Bayesian design and analysis of computer experiments: two examples*, Statistica Sinica **2** (1992), no. 2, 359–379.

[217] Garima Mittal, Vivek Dhand, Kyong Yop Rhee, Soo-Jin Park, and Wi Ro Lee, *A review on carbon nanotubes and graphene as fillers in reinforced polymer nanocomposites*, Journal of Industrial and Engineering Chemistry **21** (2015), 11–25.

[218] B. Moaveni and I. Behmanesh, *Effects of changing ambient temperature on finite element model updating of the dowling hall footbridge*, Engineering Structures **43** (2012), 56–68.

[219] A. Molinari and M. El Mouden, *The problem of elastic inclusions at finite concentration*, International Journal of Solids and Structures **33** (1996), no. 20-22, 3131–3150.

[220] T. Mori and K. Tanaka, *Average stress in matrix and average elastic energy of materials with misfitting inclusions*, Acta metallurgica **21** (1973), no. 5, 571–574.

[221] M. S. Morsy, S. H. Alsayed, and M. Aqel, *Hybrid effect of carbon nanotube and nano-clay on physico-mechanical properties of cement mortar*, Construction and Building Materials **25** (2011), no. 1, 145–149.

[222] F. Moschas and S. C. Stiros, *Three-dimensional dynamic deflections and natural frequencies of a stiff footbridge based on measurements of collocated sensors*, Structural Control and Health Monitoring **21** (2014), 23–42.

[223] Peter Moser and Babak Moaveni, *Design and deployment of a continuous monitoring system for the dowling hall footbridge*, Experimental Techniques **37** (2013), no. 1, 15–26.

[224] D. Mukherjee, B. N. Rao, and A. Meher Prasad, *Global sensitivity analysis of unreinforced masonry structure using high dimensional model representation*, Engineering Structures **33** (2011), no. 4, 1316–1325.

[225] Toshio Mura, *Micromechanics of defects in solids*, vol. 3, Springer Science & Business Media, 1987.

[226] Faizan Naeem, H. K. Lee, H. K. Kim, and I. W. Nam, *Flexural stress and crack sensing capabilities of MWNT/cement composites*, Composite Structures **175** (2017), 86–100.

[227] S. Nemat-Nasser and M. Obata, *Rate-dependent, finite elasto-plastic deformation of polycrystals*, Proceedings of the Royal Society A: Mathematical, Physical and Engineering Sciences **407** (1986), no. 1833, 343–375.

[228] Sia Nemat-Nasser and Muneo Hori, *Micromechanics: overall properties of heterogeneous materials*, vol. 37, Elsevier, 2013.

[229] M. Nevado, *Pasarela peatonal Montoro – documento final de verificación normativa*, Z047, 2011.

[230] Adam M. Neville, *Properties of concrete*, 4th ed., 1995.

[231] Mark E. J. Newman and Robert M. Ziff, *Fast Monte Carlo algorithm for site or bond percolation*, Physical Review E **64** (2001), no. 1, 016706.

[232] A. N. Norris, *An examination of the Mori-Tanaka effective medium approximation for multiphase composites*, Journal of Applied Mechanics **56** (1989), no. 1, 83.

[233] Kostya S. Novoselov, Andre K. Geim, Sergei V. Morozov, D. Jiang, Y. Zhang, Sergey V. Dubonos, Irina V. Grigorieva, and Alexandr A. Firsov, *Electric field effect in atomically thin carbon films*, science **306** (2004), no. 5696, 666–669.

[234] A. Oberlin, M. Endo, and T. Koyama, *Filamentous growth of carbon through benzene decomposition*, Journal of Crystal Growth **32** (1976), no. 3, 335–349.

[235] Michael J. O'connell, *Carbon nanotubes: properties and applications*, CRC press, 2006.

[236] G. M. Odegard, T. S. Gates, K. E. Wise, C. Park, and E. J. Siochi, *Constitutive modeling of nanotube–reinforced polymer composites*, Composites science and technology **63** (2003), no. 11, 1671–1687.

[237] Gregory M. Odegard and Thomas S. Gates, *Constitutive modeling of nanotube/polymer composites with various nanotube orientations*, Proceedings Annual Conference on Experimental and Applied Mechanical, 2002.

[238] Ning Pan, *A modified analysis of the microstructural characteristics of general fiber assemblies*, Textile Research Journal **63** (1993), no. 6, 336–345.

[239] Myounggu Park, Hyonny Kim, and Jeffrey P. Youngblood, *Strain-dependent electrical resistance of multi-walled carbon nanotube/polymer composite films*, Nanotechnology **19** (2008), no. 5, 055705.

[240] B. Peeters, H. Van der Auweraer, F. Vanhollebeke, and P. Guillaume, *Operational modal analysis for estimating the dynamic properties of a stadium structure during a football game*, Shock and Vibration **14** (2007), no. 4, 283–303.

[241] Bart Peeters and Guido De Roeck, *One-year monitoring of the z 24-bridge: environmental effects versus damage events*, Earthquake engineering & structural dynamics **30** (2001), no. 2, 149–171.

[242] Sven Pegel, Petra Pötschke, Gudrun Petzold, Ingo Alig, Sergej M. Dudkin, and Dirk Lellinger, *Dispersion, agglomeration, and network formation of multiwalled carbon nanotubes in polycarbonate melts*, Polymer **49** (2008), no. 4, 974–984.

[243] Giang T. Pham, Y. B. Park, Zhiyong Liang, Chuck Zhang, and Ben Wang, *Processing and modeling of conductive thermoplastic/carbon nanotube films for strain sensing*, Composites Part B: Engineering **39** (2008), no. 1, 209–216.

[244] J. C. Pina, V. G. Kouznetsova, and M. G. D. Geers, *Thermo-mechanical analyses of heterogeneous materials with a strongly anisotropic phase: the case of cast iron*, International Journal of Solids and Structures **63** (2015), 153–166.

[245] R. Byron Pipes, Roy L. McCullough, and David G. Taggart, *Behavior of discontinuous fiber composites: Fiber orientation*, Polymer Composites **3** (1982), no. 1, 34–39.

[246] René H. Poelma, Xuejun Fan, Z. Y. Hu, Gustaaf Van Tendeloo, Henk W van Zeijl, and Guo Qi Zhang, *Effects of nanostructure and coating on the mechanics of carbon nanotube arrays*, Advanced Functional Materials **26** (2016), no. 8, 1233–1242.

[247] P. Poncharal, *Electrostatic deflections and electromechanical resonances of carbon nanotubes*, Science **283** (1999), no. 5407, 1513–1516.

[248] Philippe Poncharal, Claire Berger, Yan Yi, Z. L. Wang, and Walt A. de Heer, *Room temperature ballistic conduction in carbon nanotubes*, The Journal of Physical Chemistry B **106** (2002), no. 47, 12104–12118.

[249] V. N. Popov, V. E. Van Doren, and M. Balkanski, *Elastic properties of crystals of single-walled carbon nanotubes*, Solid State Communications **114** (2000), no. 7, 395–399.

[250] D. Qian, E. Co Dickey, R. Andrews, and T. Rantell, *Load transfer and deformation mechanisms in carbon nanotube-polystyrene composites*, Applied Physics Letters **76** (2000), no. 20, 2868–2870.

[251] H. Qing and L. Mishnaevsky Jr., *Moisture-related mechanical properties of softwood: 3D micromechanical modeling*, Computational Materials Science **46** (2009), no. 2, 310–320.

[252] Y. P. Qiu and G. J. Weng, *On the application of Mori-Tanaka's theory involving transversely isotropic spheroidal inclusions*, International Journal of Engineering Science **28** (1990), no. 11, 1121–1137.

[253] Herschel Rabitz and Ömer F. Aliş, *General foundations of high-dimensional model representations*, Journal of Mathematical Chemistry **25** (1999), no. 2-3, 197–233.

[254] Mohammad A. Rafiee, Javad Rafiee, Zhou Wang, Huaihe Song, Z. Z. Yu, and Nikhil Koratkar, *Enhanced mechanical properties of nanocomposites at low graphene content*, ACS nano **3** (2009), no. 12, 3884–3890.

[255] Luís F. Ramos, Rafael Aguilar, Paulo B. Lourenço, and Susana Moreira, *Dynamic structural health monitoring of Saint Torcato church*, Mechanical Systems and Signal Processing **35** (2013), no. 1, 1–15.

[256] Luis F. Ramos, Leandro Marques, Paulo B. Lourenço, Guido De Roeck, A. Campos-Costa, and J. Roque, *Monitoring historical masonry structures with operational modal analysis: two case studies*, Mechanical Systems and Signal Processing **24** (2010), no. 5, 1291–1305.

[257] C. D. Reddy, S. Rajendran, and K. M. Liew, *Equilibrium configuration and continuum elastic properties of finite sized graphene*, Nanotechnology **17** (2006), no. 3, 864.

[258] A. Reuss, *Calculation of the flow limits of mixed crystals on the basis of the plasticity of monocrystals*, Z. Angew. Math. Mech **9** (1929), 49–58.

[259] Richard W. Robinett and R. D. Murphy, *Quantum mechanics: classical results, modern systems and visualized examples*, American Journal of Physics **65** (1997), no. 12, 1218–1218.

[260] Hossein Rokni, Abbas S. Milani, and Rudolf J. Seethaler, *2D optimum distribution of carbon nanotubes to maximize fundamental natural frequency of polymer composite micro-beams*, Composites Part B: Engineering **43** (2012), no. 2, 779–785.

[261] M. Rouhi and M. Rais-Rohani, *Modeling and probabilistic design optimization of a nanofiber-enhanced composite cylinder for buckling*, Composite Structures **95** (2013), 346–353.

[262] Mohamed Saafi, *Wireless and embedded carbon nanotube networks for damage detection in concrete structures*, Nanotechnolog (2009).

[263] E. I. Saavedra Flores and E. A. de Souza Neto, *Remarks on symmetry conditions in computational homogenisation problems*, Engineering Computations **27** (2010), no. 4, 551–575.

[264] E. I. Saavedra Flores, F. A. DiazDelaO, M. I. Friswell, and R. M. Ajaj, *Investigation on the extensibility of the wood cell-wall composite by an approach based on homogenisation and uncertainty analysis*, Composite Structures **108** (2014), 212–222.

[265] Jerome Sacks, Susannah B. Schiller, and William J. Welch, *Designs for computer experiments*, Technometrics **31** (1989), no. 1, 41–47.

[266] Jerome Sacks, William J. Welch, Toby J. Mitchell, and Henry P. Wynn, *Design and analysis of computer experiments*, Statistical Science (1989), 409–423.

[267] Wael Salalha, Yael Dror, Rafail L. Khalfin, Yachin Cohen, Alexander L. Yarin, and Eyal Zussman, *Single-walled carbon nanotubes embedded in oriented polymeric nanofibers by electrospinning*, Langmuir **20** (2004), no. 22, 9852–9855.

[268] L. Salmén, *Micromechanical understanding of cell-wall structure*, Comptes Rendus Biologies **327** (2004), no. 9-10, 873–880.

[269] L. Salvo, R. Ananías, and A. Cloutier, *Influencia de la estructura anatómica en la permeabilidad específica transversal al gas del pino radiata*, Maderas. Ciencia y Tecnología **6** (2004), no. 1, 33–44.

[270] Abdulkadir Sanli, Christian Müller, Olfa Kanoun, Cagatay Elibol, and Martin F-X Wagner, *Piezoresistive characterization of multi-walled carbon nanotube-epoxy based flexible strain sensitive films by impedance spectroscopy*, Composites Science and Technology **122** (2016), 18–26.

[271] E. Saracoglu and S. Bergstrand, *Continuous monitoring of a long-span cable-stayed timber bridge*, Journal of Civil Structural Health Monitoring **5** (2015), no. 2, 183–194.

[272] Colin M. Sayers, *Elastic anisotropy of short-fibre reinforced composites*, International Journal of Solids and Structures **29** (1992), no. 23, 2933–2944.

[273] J. Schjødt-Thomsen and R. Pyrz, *Overall creep modelling of short fibre reinforced composites with weakened interfaces and complex fibre orientation distributions*, Mechanics of Materials **32** (2000), no. 6, 349–359.

[274] J. Schjødt-Thomsen and R. Pyrz, *The Mori-Tanaka stiffness tensor: diagonal symmetry, complex fibre orientations and non-dilute volume fractions*, Mechanics of Materials **33** (2001), no. 10, 531–544.

[275] Gary D. Seidel and Dimitris C. Lagoudas, *A micromechanics model for the electrical conductivity of nanotube-polymer nanocomposites*, Journal of Composite Materials **43** (2009), no. 9, 917–941.

[276] Milo S. P. Shaffer and Alan H. Windle, *Fabrication and characterization of carbon nanotube/poly(vinyl alcohol) composites*, Advanced Materials **11** (1999), no. 11, 937–941.

[277] Surendra P. Shah, M. S. Konsta-Gdoutos, Z. S. Metaxa, and P. Mondal, *Nanoscale modification of cementitious materials*, Nanotechnology in Construction 3, Springer, 2009, pp. 125–130.

[278] E. Abdollahzadeh Shahrbabaki and A. Alibeigloo, *Three-dimensional free vibration of carbon nanotube-reinforced composite plates with various boundary conditions using ritz method*, Composite Structures **111** (2014), 362–370.

[279] H. S. Shen, *Nonlinear bending of functionally graded carbon nanotube-reinforced composite plates in thermal environments*, Composite Structures **91** (2009), no. 1, 9–19.

[280] H. S. Shen and C. L. Zhang, *Thermal buckling and postbuckling behavior of functionally graded carbon nanotube-reinforced composite plates*, Materials & Design **31** (2010), no. 7, 3403–3411.

[281] Lianxi Shen and Jackie Li, *Transversely isotropic elastic properties of single-walled carbon nanotubes*, Physical Review B **69** (2004), no. 4, 045414.

[282] D. L. Shi, X. Q. Feng, Yonggang Y. Huang, K. C. Hwang, and Huajian Gao, *The effect of nanotube waviness and agglomeration on the elastic property of carbon nanotube-reinforced composites*, Journal of Engineering Materials and Technology **126** (2004), no. 3, 250–257.

[283] Wonbo Shim, Youbin Kwon, S. Y. Jeon, and W. R. Yu, *Optimally conductive networks in randomly dispersed CNT: graphene hybrids*, Scientific reports **5** (2015).

[284] Masashi Shiraishi and Masafumi Ata, *Work function of carbon nanotubes*, Carbon **39** (2001), no. 12, 1913–1917.

[285] Mahmood M. Shokrieh and Roham Rafiee, *Prediction of mechanical properties of an embedded carbon nanotube in polymer matrix based on developing an equivalent long fiber*, Mechanics Research Communications **37** (2010), no. 2, 235–240.

[286] Rafat Siddique and Ankur Mehta, *Effect of carbon nanotubes on properties of cement mortars*, Construction and Building Materials **50** (2014), 116–129.

[287] John G. Simmons, *Electric tunnel effect between dissimilar electrodes separated by a thin insulating film*, Journal of applied physics **34** (1963), no. 9, 2581–2590.

[288] John G. Simmons, *Generalized formula for the electric tunnel effect between similar electrodes separated by a thin insulating film*, Journal of Applied Physics **34** (1963), no. 6, 1793–1803.

[289] Herbert Sixta, *Handbook of pulp*, vol. 1, Wiley Online Library, 2006.

[290] A. P. Sobha and Sunil K. Narayanankutty, *Improved strain sensing property of functionalised multiwalled carbon nanotube/polyaniline composites in TPU matrix*, Sensors and Actuators A: Physical **233** (2015), 98–107.

[291] Ilya M Sobol, *On the distribution of points in a cube and the approximate evaluation of integrals*, USSR Computational mathematics and mathematical physics (1967), no. 7, 86–112.

[292] Ilya M. Sobol, *Global sensitivity indices for nonlinear mathematical models and their Monte Carlo estimates*, Mathematics and Computers in Simulation **55** (2001), no. 1, 271–280.

[293] Il'ya Meerovich Sobol, *On sensitivity estimation for nonlinear mathematical models*, Matematicheskoe Modelirovanie **2** (1990), no. 1, 112–118.

[294] Anastasia Sobolkina, Viktor Mechtcherine, Vyacheslav Khavrus, Diana Maier, Mandy Mende, Manfred Ritschel, and Albrecht Leonhardt, *Dispersion of carbon nanotubes and its influence on the mechanical properties of the cement matrix*, Cement and Concrete Composites **34** (2012), no. 10, 1104–1113.

[295] Serdar Soyoz and Maria Q. Feng, *Long-term monitoring and identification of bridge structural parameters*, Computer-Aided Civil and Infrastructure Engineering **24** (2009), no. 2, 82–92.

[296] A. J. M. Spencer, *The formulation of constitutive equation for anisotropic solids*, Mechanical Behavior of Anisotropic Solids/Comportment Méchanique des Solides Anisotropes, Springer, 1982, pp. 3–26.

[297] Zdenko Spitalsky, Dimitrios Tasis, Konstantinos Papagelis, and Costas Galiotis, *Carbon nanotube–polymer composites: Chemistry, processing, mechanical and electrical properties*, Progress in Polymer Science **35** (2010), no. 3, 357–401.

[298] S. Stiros and F. Moschas, *Rapid decay of a timber footbridge and changes in its modal frequencies derived from multiannual lateral deflection measurements*, Journal of Bridge Engineering **19** (2014), no. 12, 05014005.

[299] Structural analysis guide, Release 15.0, *ANSYS Inc*, Cannonsburg, PA (2014).

[300] Li Sun, Wei Min Huang, Zhi Ding, Y. Zhao, Chang Chun Wang, Hendra Purnawali, and Cheng Tang, *Stimulus-responsive shape memory materials: a review*, Materials & Design **33** (2012), 577–640.

[301] N. Swamy and G. Rigby, *Dynamic properties of hardened paste, mortar and concrete*, Matériaux et Construction **4** (1971), no. 1, 13–40.

[302] Y. Takao, T. W. Chou, and M. Taya, *Effective longitudinal Young's modulus of misoriented short fiber composites*, Journal of Applied Mechanics **49** (1982), no. 3, 536.

[303] Tomo Takeda, Yasuhide Shindo, Yu Kuronuma, and Fumio Narita, *Modeling and characterization of the electrical conductivity of carbon nanotube-based polymer composites*, Polymer **52** (2011), no. 17, 3852–3856.

[304] D. Talaslidis and G. A. Wempner, *The linear isoparametric triangular element: theory and application*, Computer Methods in Applied Mechanics and Engineering **103** (1993), 375–397.

[305] T. Tallman and K. W. Wang, *An arbitrary strains carbon nanotube composite piezoresistivity model for finite element integration*, Applied Physics Letters **102** (2013), no. 1, 011909.

[306] S. Tang, *Modeling the mechanical properties of Pinus Radiata*, Master's thesis, University of Canterbury, New Zealand, 1998.

[307] T. Tannert, A. Muller, and M. Vogel, *Structural health monitoring of timber bridges*, Proceedings of the International Conference Timber Bridges ICB2010 (Lillehammer, Norway) (K. A. Malo, O. Kleppe, and T. Dyken, eds.), 2010.

[308] Sander J. Tans, Michel H. Devoret, Hongjie Dai, Andreas Thess, Richard E. Smalley, L. J. Geerligs, and Cees Dekker, *Individual single-wall carbon nanotubes as quantum wires*, Nature **386** (1997), no. 6624, 474–477.

[309] M. Taya, W. J. Kim, and K. Ono, *Piezoresistivity of a short fiber/elastomer matrix composite*, Mechanics of materials **28** (1998), no. 1, 53–59.

[310] Minoru Taya, *Electronic composites: modeling, characterization, processing, and MEMS applications*, Cambridge University Press, 2005.

[311] T. C. Theodosiou and D. A. Saravanos, *Numerical investigation of mechanisms affecting the piezoresistive properties of CNT-doped polymers using multi-scale models*, Composites Science and Technology **70** (2010), no. 9, 1312–1320.

[312] Erik T. Thostenson and T. W. Chou, *On the elastic properties of carbon nanotube-based composites: modelling and characterization*, Journal of Physics D: Applied Physics **36** (2003), no. 5, 573.

[313] Erik T. Thostenson, Zhifeng Ren, and Tsu-Wei Chou, *Advances in the science and technology of carbon nanotubes and their composites: a review*, Composites science and technology **61** (2001), no. 13, 1899–1912.

[314] T. E. Timell, *Recent progress in the chemistry and topochemistry of compression wood*, Wood Science and Technology **16** (1982), no. 2, 83–122.

[315] Staffan Toll, *Packing mechanics of fiber reinforcements*, Polymer Engineering & Science **38** (1998), no. 8, 1337–1350.

[316] Francesco Tornabene, Nicholas Fantuzzi, and Michele Bacciocchi, *Linear static response of nanocomposite plates and shells reinforced by agglomerated carbon nanotubes*, Composites Part B: Engineering **115** (2017), 449–476.

[317] Francesco Tornabene, Nicholas Fantuzzi, Michele Bacciocchi, and Erasmo Viola, *Effect of agglomeration on the natural frequencies of functionally graded carbon nanotube-reinforced laminated composite doubly-curved shells*, Composites Part B: Engineering **89** (2016), 187–218.

[318] S. Torquato, *Effective stiffness tensor of composite media : I. Exact series expansions*, Journal of the Mechanics and Physics of Solids **45** (1997), no. 9, 1421–1448.

[319] S. Torquato, *Effective stiffness tensor of composite media : II. Applications to isotropic dispersions*, Journal of the Mechanics and Physics of Solids **46** (1998), no. 8, 1411–1440.

[320] S. Torquato, *Morphology and effective properties of disordered heterogeneous media*, International Journal of Solids and Structures **35** (1998), no. 19, 2385–2406.

[321] Rafael Castro Triguero, *Vibraciones de estructuras laminares con forma de paraboloide hiperbólico de planta rectangular*, Ph.D. thesis, Universidad de Sevilla, 2008.

[322] Chao Tsai, Chuck Zhang, David A. Jack, Richard Liang, and Ben Wang, *The effect of inclusion waviness and waviness distribution on elastic properties of fiber-reinforced composites*, Composites Part B: Engineering **42** (2011), no. 1, 62–70.

[323] Filippo Ubertini, Simon Laflamme, Halil Ceylan, Annibale Luigi Materazzi, Gianluca Cerni, Hussam Saleem, Antonella D'Alessandro, and Alessandro Corradini, *Novel nanocomposite technologies for dynamic monitoring of structures: a comparison between cement-based embeddable and soft elastomeric surface sensors*, Smart Materials and Structures **23** (2014), no. 4, 045023.

[324] Filippo Ubertini, Simon Laflamme, and Antonella D'Alessandro, *Smart cement paste with carbon nanotubes*, Innovative Developments of Advanced Multifunctional Nanocomposites in Civil and Structural Engineering (2016), 97–120.

[325] Filippo Ubertini, Annibale Luigi Materazzi, Antonella D'Alessandro, and Simon Laflamme, *Natural frequencies identification of a reinforced concrete beam using carbon nanotube cement-based sensors*, Engineering Structures **60** (2014), 265–275.

[326] Gururaja Udupa, S. Shrikantha Rao, and K. V. Gangadharan, *Functionally graded composite materials: An overview*, Procedia Materials Science **5** (2014), 1291–1299.

[327] J. Valenzuela, I. Ulloa, and M. Rallo, *Estudio del ángulo fibrilar y su relación con la edad cambial en Pinus Radiata D. Don, proveniente de la Séptima Región, Chile*, Maderas, Ciencia y Tecnología **5** (2003), no. 2, 117–124.

[328] K. Van Nimmen, G. Lombaert, G. De Roeck, and P. Van den Broeck, *Vibration serviceability of footbridges: Evaluation of the current codes of practice*, Engineering Structures **59** (2014), 448–461.

[329] Ferdinand Verhulst, *Nonlinear differential equations and dynamical systems*, Springer Science & Business Media, 2006.

[330] B. Vigolo, *Macroscopic fibers and ribbons of oriented carbon nanotubes*, Science **290** (2000), no. 5495, 1331–1334.

[331] T. Vodenitcharova and L. C. Zhang, *Bending and local buckling of a nanocomposite beam reinforced by a single-walled carbon nanotube*, International Journal of Solids and Structures **43** (2006), no. 10, 3006–3024.

[332] W. Voigt, *Ueber die beziehung zwischen den beiden elasticitätsconstanten isotroper körper*, Annalen der Physik **274** (1889), no. 12, 573–587.

[333] L. J. Walpole, *On bounds for the overall elastic moduli of inhomogeneous systems—I*, Journal of the Mechanics and Physics of Solids **14** (1966), no. 3, 151–162.

[334] L. J. Walpole, *On bounds for the overall elastic moduli of inhomogeneous systems—II*, Journal of the Mechanics and Physics of Solids **14** (1966), no. 5, 289–301.

[335] L. J. Walpole, *On the overall elastic moduli of composite materials*, Journal of the Mechanics and Physics of Solids **17** (1969), no. 4, 235–251.

[336] Junpu Wang, Wenzhi Wang, Chao Zhang, and Wenshan Yu, *The electro-mechanical behavior of conductive filler reinforced polymer composite undergone large deformation: A combined numerical-analytical study*, Composites Part B: Engineering **133** (2018), 185–192.

[337] Long Wang and Kenneth J. Loh, *Wearable carbon nanotube-based fabric sensors for monitoring human physiological performance*, Smart Materials and Structures **26** (2017), no. 5, 055018.

[338] Xin Wang, Philip D. Bradford, Wei Liu, Haibo Zhao, Yoku Inoue, Jon-Paul Maria, Qingwen Li, Fuh-Gwo Yuan, and Yuntian Zhu, *Mechanical and electrical property improvement in CNT/nylon composites through drawing and stretching*, Composites Science and Technology **71** (2011), no. 14, 1677–1683.

[339] S Wansom, N. J. Kidner, L. Y. Woo, and T. O. Mason, *AC-impedance response of multi-walled carbon nanotube/cement composites*, Cement and Concrete Composites **28** (2006), no. 6, 509–519.

[340] U. Watanabe and M. Norimoto, *Three dimensional analysis of elastic constants of the wood cell wall*, Wood Research **87** (2000), 1–7.

[341] U. Watanabe, M. Norimoto, and T. Morooka, *Cell wall thickness and tangential young's modulus in coniferous early wood*, Journal of Wood Science **46** (2000), 109–114.

[342] B. Q. Wei, R. Vajtai, and P. M. Ajayan, *Reliability and current carrying capacity of carbon nanotubes*, Applied Physics Letters **79** (2001), no. 8, 1172–1174.

[343] G. Wempner and D. Talaslidis, *Mechanics of solids and shells*, CRC Press, 2003.

[344] G. A. Wempner, A. R. D. Talaslidis, and C. M. Hwang, *A simple and efficient approximation of shells via quadrilateral elements*, Journal of Applied Mechanics **49** (1982), 115–120.

[345] Sihai Wen and D. D. L. Chung, *Carbon fiber-reinforced cement as a thermistor*, Cement and Concrete Research **29** (1999), no. 6, 961–965.

[346] Sihai Wen and D. D. L. Chung, *Damage monitoring of cement paste by electrical resistance measurement*, Cement and Concrete Research **30** (2000), no. 12, 1979–1982.

[347] Sihai Wen and D. D. L. Chung, *Effect of carbon fiber grade on the electrical behavior of carbon fiber reinforced cement*, Carbon **39** (2001), no. 3, 369–373.

[348] Sihai Wen and D. D. L. Chung, *Double percolation in the electrical conduction in carbon fiber reinforced cement-based materials*, Carbon **45** (2007), no. 2, 263–267.

[349] G. J. Weng, *The theoretical connection between Mori-Tanaka's theory and the Hashin-Shtrikman-Walpole bounds*, International Journal of Engineering Science **28** (1990), no. 11, 1111–1120.

[350] George J Weng, *A dynamical theory for the Mori–Tanaka and Ponte Castañeda–Willis estimates*, Mechanics of Materials **42** (2010), no. 9, 886–893.

[351] Jian Huang Weng and Chin Hsiung Loh, *Structural health monitoring of arch dam from dynamic measurements*, 2010, pp. 2518–2534.

[352] Jacob M. Wernik and Shaker A. Meguid, *Recent developments in multifunctional nanocomposites using carbon nanotubes*, Applied Mechanics Reviews **63** (2010), no. 5, 050801.

[353] Roland Wiesendanger, *Scanning probe microscopy and spectroscopy: methods and applications*, Cambridge University Press, 1994.

[354] S. Wolfram, *Mathematica, 4th edition*, Cambridge University Press, 1999.

[355] E. W. Wong, *Nanobeam mechanics: Elasticity, strength, and toughness of nanorods and nanotubes*, Science **277** (1997), no. 5334, 1971–1975.

[356] Kai-Yuen Wong, *Instrumentation and health monitoring of cable-supported bridges*, Structural control and health monitoring **11** (2004), no. 2, 91–124.

[357] Chih-Ping Wu and Hao-Yuan Li, *Three-dimensional free vibration analysis of functionally graded carbon nanotube-reinforced composite plates with various boundary conditions*, Journal of Vibration and Control (2014), 362–370.

[358] J Wuite and S Adali, *Deflection and stress behaviour of nanocomposite reinforced beams using a multiscale analysis*, Composite structures **71** (2005), no. 3, 388–396.

[359] Sishen Xie, Wenzhi Li, Zhengwei Pan, Baohe Chang, and Lianfeng Sun, *Mechanical and physical properties on carbon nanotube*, Journal of Physics and Chemistry of Solids **61** (2000), no. 7, 1153–1158.

[360] Jing Xu, Wenhui Zhong, and Wu Yao, *Modeling of conductivity in carbon fiber-reinforced cement-based composite*, Journal of materials science **45** (2010), no. 13, 3538–3546.

[361] Boris I. Yakobson and Phaedon Avouris, *Mechanical properties of carbon nanotubes*, Carbon nanotubes, Springer, 2001, pp. 287–327.

[362] Kunitoshi Yamamoto and Yoshikazu Nakayama, *Orientation of carbon nanotubes using electrophoresis*, Japanese Journal of Applied Physics **35** (1996), no. Part 2, No. 7B, L917–L918.

[363] K. Y. Yan, Q. Z. Xue, Q. B. Zheng, and L. Z. Hao, *The interface effect of the effective electrical conductivity of carbon nanotube composites*, Nanotechnology **18** (2007), no. 25, 255705.

[364] K. Yanase, S. Moriyama, and J. W. Ju, *Effects of CNT waviness on the effective elastic responses of CNT–reinforced polymer composites*, Acta Mechanica **224** (2013), no. 7, 1351–1364.

[365] B. J. Yang, K. J. Cho, G. M. Kim, and H. K. Lee, *Effect of CNT agglomeration on the electrical conductivity and percolation threshold of nanocomposites: A micromechanics-based approach*, CMES: Computer Modeling in Engineering & Sciences **103** (2014), no. 5, 343–365.

[366] S. Y. Yang, W. N. Lin, Y. L. Huang, H. W. Tien, J. Y. Wang, C. C. M. Ma, S. M. Li, and Y. S. Wang, *Synergetic effects of graphene platelets and carbon nanotubes on the mechanical and thermal properties of epoxy composites*, Carbon **49** (2011), no. 3, 793–803.

[367] M. H. Yas and M. Heshmati, *Dynamic analysis of functionally graded nanocomposite beams reinforced by randomly oriented carbon nanotube under the action of moving load*, Applied Mathematical Modelling **36** (2012), no. 4, 1371–1394.

[368] Tetsuo Yasuoka, Yoshinobu Shimamura, and Akira Todoroki, *Electrical resistance change under strain of CNF/flexible-epoxy composite*, Advanced Composite Materials **19** (2010), no. 2, 123–138.

[369] K. Yazdchi and M. Salehi, *The effects of CNT waviness on interfacial stress transfer characteristics of CNT/polymer composites*, Composites Part A: Applied Science and Manufacturing **42** (2011), no. 10, 1301–1309.

[370] Y. B. Yi, L. Berhan, and A. M. Sastry, *Statistical geometry of random fibrous networks, revisited: waviness, dimensionality, and percolation*, Journal of applied physics **96** (2004), no. 3, 1318–1327.

[371] Min-Feng Yu, Oleg Lourie, Mark J. Dyer, Katerina Moloni, Thomas F. Kelly, and Rodney S. Ruoff, *Strength and breaking mechanism of multiwalled carbon nanotubes under tensile load*, Science **287** (2000), no. 5453, 637–640.

[372] Izzuddin Zaman, H. C. Kuan, Jingfei Dai, Nobuyuki Kawashima, Andrew Michelmore, Alex Sovi, Songyi Dong, Lee Luong, and Jun Ma, *From carbon nanotubes and silicate layers to graphene platelets for polymer nanocomposites*, Nanoscale **4** (2012), no. 15, 4578–4586.

[373] Xiaomei Zeng, Xiaofeng Xu, Prathamesh M Shenai, Eugene Kovalev, Charles Baudot, Nripan Mathews, and Yang Zhao, *Characteristics of the electrical percolation in carbon nanotubes/polymer nanocomposites*, The Journal of Physical Chemistry C **115** (2011), no. 44, 21685–21690.

[374] Benniu Zhang, Zhixiang Zhou, Kaihong Zhang, Guo Yan, and Zhouzhou Xu, *Sensitive skin and the relative sensing system for real-time surface monitoring of crack in civil infrastructure*, Journal of intelligent material systems and structures **17** (2006), no. 10, 907–917.

[375] L. W. Zhang, Z. X. Lei, and K. M. Liew, *Buckling analysis of FG-CNT reinforced composite thick skew plates using an element-free approach*, Composites Part B: Engineering **75** (2015), 36–46.

[376] L. W. Zhang, Z. X. Lei, and K. M. Liew, *Computation of vibration solution for functionally graded carbon nanotube-reinforced composite thick plates resting on elastic foundations using the element-free IMLS-Ritz method*, Applied Mathematics and Computation **256** (2015), 488–504.

[377] L. W. Zhang, Z. X. Lei, and K. M. Liew, *An element-free IMLS-Ritz framework for buckling analysis of FG-CNT reinforced composite thick plates resting on winkler foundations*, Engineering Analysis with Boundary Elements **58** (2015), 7–17.

[378] L. W. Zhang, Z. X. Lei, and K. M. Liew, *Free vibration analysis of functionally graded carbon nanotube-reinforced composite triangular plates using the FSDT and element-free IMLS-Ritz method*, Composite Structures **120** (2015), 189–199.

[379] L. W. Zhang, Z. X. Lei, K. M. Liew, and J. L. Yu, *Static and dynamic of carbon nanotube reinforced functionally graded cylindrical panels*, Composite Structures **111** (2014), 205–212.

[380] L. W. Zhang and K. M. Liew, *Large deflection analysis of FG-CNT reinforced composite skew plates resting on Pasternak foundations using an element-free approach*, Composite Structures **132** (2015), 974–983.

[381] L. W. Zhang and K. M. Liew, *Postbuckling analysis of axially compressed CNT reinforced functionally graded composite plates resting on Pasternak foundations using an element-free approach*, Composite Structures **138** (2016), 40–51.

[382] L. W. Zhang, Z. G. Song, and K. M. Liew, *Nonlinear bending analysis of FG-CNT reinforced composite thick plates resting on Pasternak foundations using the element-free IMLS-Ritz method*, Composite Structures **128** (2015), 165–175.

[383] L. W. Zhang, Z. G. Song, and K. M. Liew, *State-space levy method for vibration analysis of FG-CNT composite plates subjected to in-plane loads based on higher-order shear deformation theory*, Composite Structures **134** (2015), 989–1003.

[384] T. Zhang and Y. B. Yi, *Monte carlo simulations of effective electrical conductivity in short-fiber composites*, Journal of applied physics **103** (2008), no. 1, 014910.

[385] Y. Zhang and F. L. Matthews, *Postbuckling behaviour of curved panels of generally layered composite materials*, Composite Structures **1** (1983), no. 2, 115–135.

[386] Y. Zhang and F. L. Matthews, *Large deflection behavior of simply supported laminated panels under in-plane loading*, Journal of Applied Mechanics **52** (1985), no. 3, 553.

[387] Xiaoyu Zheng, M. Gregory Forest, Robert Lipton, and Ruhai Zhou, *Nematic polymer mechanics: flow-induced anisotropy*, Continuum Mechanics and Thermodynamics **18** (2006), no. 7-8, 377–394.

[388] Xiaoyu Zheng, M Gregory Forest, Richard Vaia, Michael Arlen, and Ruhai Zhou, *A strategy for dimensional percolation in sheared nanorod dispersions*, Advanced Materials **19** (2007), no. 22, 4038–4043.

[389] Qinyi Zhou, Meng Gong, Ying Hei Chui, and Mohammad Mohammad, *Measurement of rolling shear modulus and strength of cross laminated timber fabricated with black spruce*, Construction and Building Materials **64** (2014), 379–386.

[390] Ping Zhu, Z. X. Lei, and K. M. Liew, *Static and free vibration analyses of carbon nanotube-reinforced composite plates using finite element method with first order shear deformation plate theory*, Composite Structures **94** (2012), no. 4, 1450–1460.

[391] Ping Zhu, L. W. Zhang, and K. M. Liew, *Geometrically nonlinear thermomechanical analysis of moderately thick functionally graded plates using a local Petrov–Galerkin approach with moving Kriging interpolation*, Composite Structures **107** (2014), 298–314.

[392] R. Zhu, E. Pan, and A. K. Roy, *Molecular dynamics study of the stress–strain behavior of carbon-nanotube reinforced Epon 862 composites*, Materials Science and Engineering: A **447** (2007), no. 1-2, 51–57.

[393] Olesya I. Zhupanska, *The effect of orientational distribution of nanotubes on buckypaper nanocomposite mechanical properties*, Mechanics of Advanced Materials and Structures **20** (2013), no. 1, 1–10.

[394] T. Ziehn and A. S. Tomlin, *Global sensitivity analysis of a 3D street canyon model-part I: The development of high dimensional model representations*, Atmospheric Environment **42** (2008), no. 8, 1857–1873.

[395] T. Ziehn and A. S. Tomlin, *GUI-HDMR - a software tool for global sensitivity analysis of complex models*, Environmental Modelling & Software **24** (2009), no. 7, 775–785.

[396] Tilo Ziehn and Alison S. Tomlin, *A global sensitivity study of sulfur chemistry in a premixed methane flame model using HDMR*, International Journal of Chemical Kinetics **40** (2008), no. 11, 742–753.

[397] S. Zivanovic, A. Pavic, and P. Reynolds, *Vibration serviceability of footbridges under human-induced excitation: a literature review*, Journal of Sound and Vibration **279** (2005), 1–74.

[398] S. Zivanovic, A. Pavic, and P. Reynolds, *Modal testing and fe model tuning of a lively footbridge structure*, Engineering Structures **28** (2006), 857–868.

[399] S. Zivanovic, A. Pavic, and P. Reynolds, *Finite element modelling and updating of a lively footbridge: The complete process*, Journal of Sound and Vibration **301** (2007), 126–145.

Curriculum Vitae

Curriculum Vitae – Enrique García-Macías

Personal Information

Enrique García Macías
ID: 76440074B
Researcher ID: L-2005-2015
ORCID: 0000-0001-5557-144X
Date of birth: 15/08/1989
Nationality: Spain
C/Río Duero 94, 18110 Granada, Spain
tel: +34 958584398
egarcia28@us.es
Research Gate profile: www.researchgate.net/profile/Enrique_Garcia_Macias

Enrique G. M. graduated with a Bachelor of Civil Engineering with First Class Honours in 2011 at the University of Granada and is undertaking a Ph.D. at the University of Seville

Education

	Post-secondary Education and Degrees:
2007-2011	Escuela Técnica Superior de Ingeniería de Caminos, Canales y Puertos University of Granada Bachelor's degree (8.56/10)
2012-2013	Escuela Técnica Superior de Ingeniería de Caminos, Canales y Puertos University of Granada Master of Structures (9.55/10)
	Doctorate:

2014-2018	School of Engineering Department of Continuum Mechanics and Structural Analysis Ph.D. Mechanical Engineering and Industrial Organization University of Seville Advisors: Prof. Dr. Andrés Sáez Pérez and Dr. Rafael Castro-Triguero
	Honors and Awards:
2011	Extraordinary Degree Award

Language skills

- Cambridge First Certificate of English

Language	Listening skills	Reading skills	Speaking skills	Writing skills
English	B2	B2	B2	B2

Studies Grants

- University Teaching Staff Training (FPU) Grant for Thesis, from the Ministry of Science and Innovation of Spain (2014-2018).

Research Stays

- Ph.D. student visitor at the College of Engineering, Swansea University, United Kingdom (November 2015–March 2016).
- Ph.D. student visitor in the Dipartimento Di Ingegneria Civile ed Ambientale at the University of Perugia, Italy (June 2016–October 2016).

R&D projects funded through competitive calls of public or private entities

PROYECT TITLE:	Monitorización predictiva de estructuras civiles mediante elementos reforzados con nanotubos de carbono.
FUNDING ENTITY:	Ministerio de Economía y Competitividad (Convocatorias 2014 Proyectos de I+D EXCELENCIA y Proyectos de I+D+I RETOS INVESTIGACIÓN).
DURATION:	2015-2018.
PI:	Felipe García Sánchez.
NUMBER OF RESERACHERS:	8.

PROYECT TITLE:	Análisis y Monitorización Estructural de Silo Asentado CEFUSA 27.5/22.
FUNDING ENTITY:	Silos Córdoba.
DURATION:	2013-2014.
PI:	Rafael Castro Triguero.
NUMBER OF RESERACHERS:	2.

Scientific production

Works submitted to national or international conferences

- 9th International Conference on Structural Dynamics, EURODYN 2014: *Two techniques for fast evaluation of design envelopes in high-speed train railway bridges: Train speed sensitivity and the Hilbert Transform.* 30/06/14-02/07/14; Porto, Portugal. Martínez-Castro, Alejandro and **García-Macías, Enrique**.
- IMAC-XXIII: *Ambient Vibration Testing of Historic Steel-Composite Bridge, the E. Torroja Bridge, for Structural Identification and Finite Element Model Updating.* 02/02/15-02/02/15; Orlando, Florida, USA. **García-Macías, Enrique**, Castro-Triguero, Rafael, Gallego, Rafael and Carretero, Justo.
- IOMAC.6th International Operational Modal Analysis Conference: *Operational Modal Analysis and Detection of Non-linear structural behavior of bowstring Arch bridge.* 10/05/15-14/05/15; Gijón, Spain. **García-Macías, Enrique**, Castro-Triguero, Rafael, Gallego, Rafael, Carretero, Justo and Gómez-Casero, Miguel A.

- IMAC-XXXIV: *Uncertainty Analysis of Mechanical Behavior of Functionally Graded Carbon Nanotube Composite Materials*. 25/01/2016-28/01/2016; Orlando, Florida, USA. **García-Macías, Enrique**, Castro-Triguero, Rafael, Friswell, Michael I., Sáez-Pérez, Andrés y Gallego, Rafael.
- 2nd Mechanics of Composites: *Two metamodeling techniques for optimization of carbon nanotube reinforced composite shells*. 11/07/2016-14/07/2016; Faculdade de Engenharia da Universidade do Porto, Oporto, Portugal. **García-Macías, Enrique**, Castro-Triguero, Rafael, Friswell, Michael I., Adhikari, Sondipon and Sáez, Andrés.
- Congreso Universitario de Innovación Educativa en las Enseñanzas TÃľcnicas XXIV CUIEET: *Desarrollo de software para la enseñanza del cálculo y diseño de silos cilíndricos para el almacenamiento de materiales granulares*. Universidad de Cádiz, Spain. 21/09/2016-23/09/2016. **García-Macías, Enrique**, Gómez-Casero, Miguel A. and Castro-Triguero, Rafael.
- Congreso Universitario de Innovación Educativa en las Enseñanzas TÃľcnicas XXIV CUIEET: *La interdisciplinariedad entre la ingeniería y la biomedicina, aplicada en el análisis del comportamiento humano*. Universidad de Cádiz, Spain. 21/09/2016-23/09/2016. Gómez-Casero, Miguel A., García-Macías, Enrique and Castro Triguero, Rafael.
- SPIE-The International Society for Optical Engineering: *Continuous and embedded solutions for SHM of concrete structures using changing electrical potential in self-sensing cement-based composites*. 26/03/2017-29/03/2017; Portland, USA. Downey, Austin, **E. García-Macías**, D'Alessandro, Antonella, Laflamme, Simmon, Castro-Triguero, Rafael, Ubertini, Filippo.
- 6th International Conference on Experimental Vibration Analysis for Civil Engineering Structures, EVACES 2015: *Structural health monitoring of grandstands: A review*. 19/10/2015-21/10/2015. Dubendorf, Zurich; Switzerland. Gómez-Casero, Miguel A., Castro-Triguero, Rafael, **E. García-Macías**, Gallego Sevilla, Rafael, and Cabrera, José.

Publications:

- **García-Macías, Enrique**, Castro-Triguero, Rafael, Flores, Erick I Saavedra, Friswell, Michael I and Gallego, Rafael. Static and free vibration analysis of functionally graded carbon nanotube reinforced skew plates. Composite Structures (2016) 140 473-490
- **García-Macías, Enrique**, Castro-Triguero, Rafael, Friswell, Michael I, Adhikari, Sondipon and Sáez, Andrés. Metamodel-based approach for stochastic free vibration analysis of functionally graded carbon nanotube reinforced plates. Composite Structures (2016) 152 183-198.
- **García-Macías, Enrique**, Rodríguez-Tembleque, Luis, Castro-Triguero, Rafael and Sáez, Andrés. Buckling analysis of functionally graded carbon nanotube-reinforced

curved panels under axial compression and shear. Composites Part B: Engineering (2017) 108 243-256.

- **García-Macías, Enrique**, D'Alessandro, Antonella, Castro-Triguero, Rafael, Pérez-Mira, Domingo and Ubertini, Filippo. Micromechanics modeling of the electrical conductivity of carbon nanotube cement-matrix composites. Composites Part B: Engineering (2017) 108 451-469.
- **García-Macías, Enrique**, D'Alessandro, Antonella, Castro-Triguero, Rafael, Pérez-Mira, Domingo and Ubertini, Filippo. Micromechanics modeling of the uniaxial strain-sensing property of carbon nanotube cement-matrix composites for SHM applications. Composite Structures (2017) 163 195-215.
- **García-Macías, Enrique**, Downey, Austin, D'Alessandro, Antonella, Castro-Triguero, Rafael, Laflamme, Simon and Ubertini, Filippo. Enhanced lumped circuit model for smart nanocomposite cement-based sensors under dynamic compressive loading conditions. Sensors and Actuators A: Physical (2017) 260 45-57.
- Castro-Triguero, Rafael, **García-Macías, Enrique**, Saavedra Flores, Erick, Friswell, M and Gallego, Rafael. Multi-scale model updating of a timber footbridge using experimental vibration data. Engineering Computations (2017) 34(3) 754-780.
- **García-Macías, Enrique**, Rodríguez-Tembleque, Luis, Castro-Triguero, Rafael and Sáez, Andrés. Eshelby-Mori-Tanaka approach for post-buckling analysis of axially compressed functionally graded CNT/polymer composite cylindrical panels. (2017) 128 208-224.
- Downey, Austin, D'Alessandro, Antonella, Baquera, Micah, Rolfes, Daniel, Ubertini, Filippo, **García-Macías, Enrique**, Laflamme, Simmon and Castro-Triguero, Rafael. Damage detection, localization and quantification in conductive smart concrete structures using a resistor mesh model. Engineering Structures (2017) 148 924-935.
- D'Alessandro, Antonella, Ubertini, Filippo, **García-Macías, Enrique**, Castro-Triguero, Rafael, Downey, Austin, Laflamme, Simmon, Meoni, Andrea and Materazzi, Annibale L. Static and Dynamic Strain Monitoring of Reinforced Concrete Components through Embedded Carbon Nanotube Cement-Based Sensors. Shock and Vibration (2017) 2017,3648403.
- **García-Macías, Enrique**, Rodríguez-Tembleque, Luis, Sáez, A. Bending and free vibration analysis of functionally graded graphene vs. carbon nanotube reinforced composite plates. Composite Structures (2018) 86 123-138.